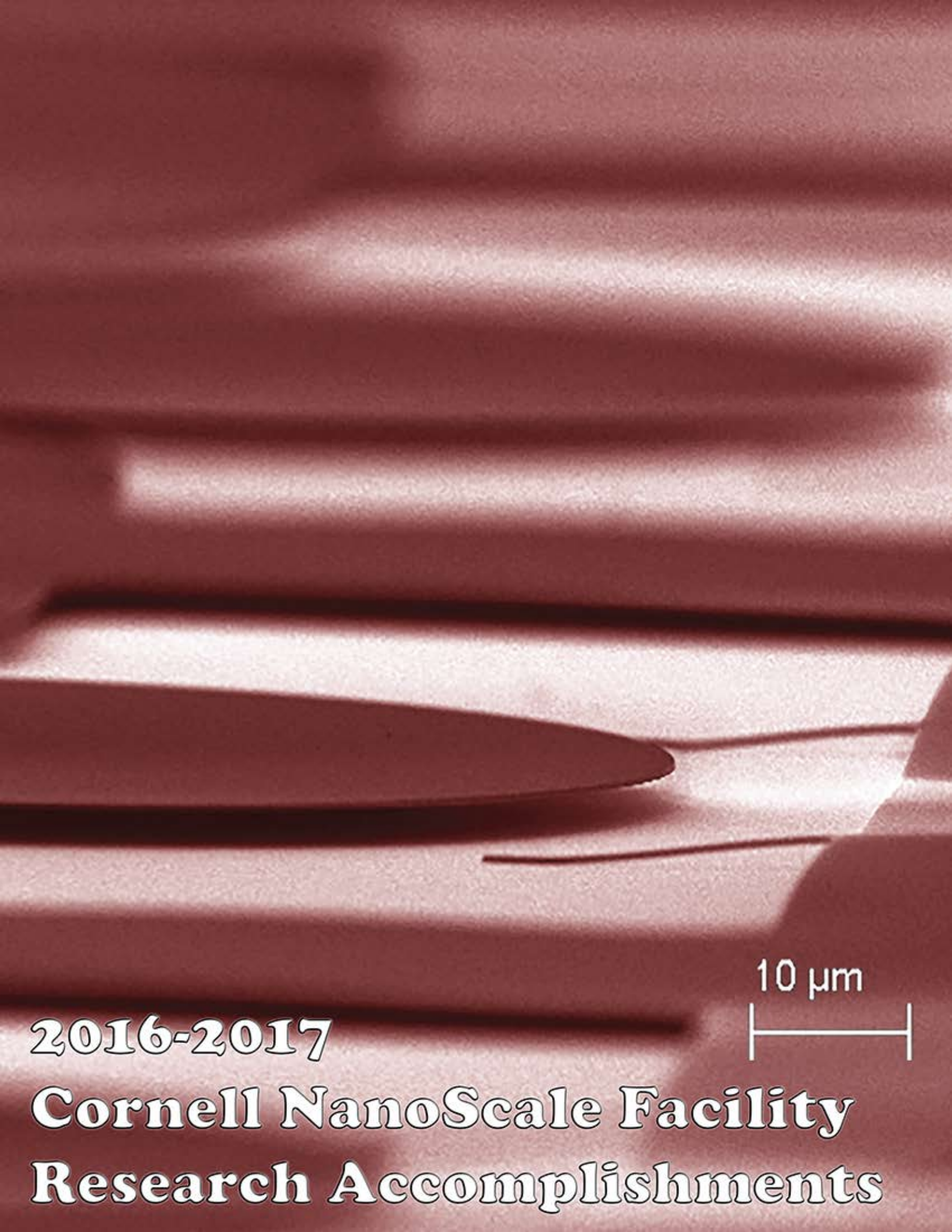

2016-2017
Cornell NanoScale Facility
Research Accomplishments

250 Duffield Hall
343 Campus Road
Ithaca NY 14853-2700

Phone: 607.255.2329 • Fax: 607.255.8601
Email: information@cnf.cornell.edu • Web Site: www.cnf.cornell.edu

CNF Lester B. Knight Director: Christopher Ober

Director of Operations: Donald Tennant

CNF is a member of the National Nanotechnology Coordinated Infrastructure

(www.nnci.net)

and is supported by:
The National Science Foundation,
the New York State Office of Science, Technology and Academic Research,
Cornell University, Industry, and our Users.

The 2016-2017 CNF Research Accomplishments
are also available on the web as secure PDF documents:
http://www.cnf.cornell.edu/cnf_2017cnfra.html

Cornell NanoScale Science & Technology Facility (CNF)

2016–2017 Research Accomplishments

Table of Contents

Technical Reports by Section . . . . . II-IV

Photography Credits IV

Directors' Introduction . . . . . V-VI

A Selection of 2016 Patents, Presentations & Publications . . . . . VII-XXIII

Abbreviations & Their Meanings . . . . . XXIV-XXXI

Technical reports 2-239

Indexes 240-244

Biological Applications, 2-69

Bacterial Mechanics on a Chip 2

Nanostamp Optimization for Single-Molecule DNA/ Protein Array Studies 4

Multi-Organ Microphysiological Systems for Drug Screening 6

Improved Single Cell Whole Genome via Microfluidic Platform 8

Graphene Transistors for Biological Sensing 10

A MEMS Microtensiometer for Sensing Water Potential in Plants and Soils 12

Silicon Nitride Cantilevers for Muscle Myofibril Force Measurements 14

Biomimetic Models of the Tumor Microenvironment and Angiogenesis 16

Stamping and Twisting: Using Bio-Nanotechnology to Enhance Single Molecule Experiments 18

Biocompatible and High Stiffness Tunable Nanophotonic Array Traps with Enhanced Force and Stability . . 20

Generalized Microfluidic Immunosensor for Antibody Detection 22

A Portable, Quantitative Nucleic Acid Amplification System for Disease Diagnostics in Limited Resource Settings 24

Fabrication of Elastomeric Microposts with Step-Changes in Rigidity 26

Development of a Salivary Microfluidic Diagnostic Device using Hot Embossing 28

Increasing Endothelial Retention on Mechanical Heart Valves via Surface Micropatterning 30

Microconcentrator for Biological Small Angle X-Ray Scattering 32

Microfluidic Mixer for Biological Small Angle X-Ray Scattering 34

Design and Application of Microfluidic Devices to Study Cell Migration in Confined Environments . . 36

Microfluidics for Modeling Biological Flows in Breast Tumor Cell Invasion 38

Zero-Mode Waveguides on Thin Silicon Nitride Membranes for Efficient Single-Molecule Sequencing 40

Microfabricated Devices for Cell Organization 42

Electrochemical Detection Array Combining Amperometry and Total Internal Reflection Fluorescence 44

Microfluidics for Automated Long-Term High-Resolution Imaging of *C. Elegans* Larval Development 46

Evaluating and Improving a Novel Bioreactor for Mammalian Cell Culture 48

Synthetic Small Intestines 50

Separation of Submicron Particles in a Surface Acoustic Wave Acoustofluidic Resonator 52

High Confinement and Low Loss Si3N4 Waveguides for Miniaturizing Optical Coherence Tomography 54

Handheld Chem/Biosensor Combining Metasurfaces and Engineered Sensor Proteins to Enhance Surface Plasmon Resonance (SPR) 56

Scalable Sensor Array Platform for Analysis of Quantal Transmitter Release Events 58

Droplet- Microfluidic Device for Stem Cell Culture 60

Graphene Film Protein Crystal Mount 62

Metamaterials for Biosensing 64

Retinal Implant Project 66

Biosensor Wafer-Level Device Fabrication 68

Chemistry, 70-81

Attonewton Sensitivity Cantilevers for Single-Electron Spin Detection 70

Design and Characterization of a Microreactor for Thin Film Deposition and *in situ* Surface Analysis 72

Chemical Bonding Across the Periodic Table at High and Ambient Pressures 74

Substrate Preparation for Ultrafast Vibrational Spectroscopy Experiments 76

Biomechanics of Bacteria 78

Micrometer-Scale Coplanar Waveguides for Nanoscale Magnetic Resonance Imaging 80

Electronics, 82-109

Piezoelectric RF SAW-Based Energy Detectors 82

Individually Detachable Polymer-Silicon Micro-Parts for Vaporizable Electronics 84

High-Capacitance Gating of Nanocrystal Superlattices 86

Design and Realization of GaN Trench Junction-Barrier-Schottky-Diodes 88

Investigation of GaN p-Channel Transistors 90

Two-Dimensional Heterojunction Interlayer Tunneling Field Effect Transistor (Thin-TFET) . .. 92

Self-Assembled Silica Nano-Spheres for Dual Metal Junction-Barrier-Schottky Diodes 94

Material Processing and Device Characterization of β-Ga_2O_3 96

Single Crystal Boron Nitride Devices 98

Calibrated MEMS Switches for Near-ZERO Power RF Detector and Sensors Network 100

Multiple Resonant Features in GaN/AlN Resonant Tunneling Diodes 102

High Temperature Epitaxial Growth of AlN/GaN/AlN Quantum Well HEMTs on SiC 104

Molybdenum Diselenide MOSFET and CMOS Integration 106

Description of the Exploratory Etching and Electrodeposition Project 108

Materials, 110-135

Multi-Functional Platform for Characterization of Nanostructured Polymer Brushes 110

Texturing and Electrical Performance of CAAC IGZO Thin Film Transistors 112

Oxide Nanoparticle EUV (One) Photoresist Studies .. 114

Approaching the Ultimate Size-Limit of Organometallic Silver-Thiolate AgSCn 2D Lamellae: Synthesis and Characterization 116

Transferable Gyroidal Mesoporous Resin/Carbon Thin Films as Potential 3D Templates 118

Nanostructured Polymer Brushes 120

Patterning of Liquid Crystal Elastomers 122

Nanotwins in Copper Thin Films 124

MBE Selective Area Growth of N-polar GaN Nanowires 126

Nanotube Transistor Arrays on a TEM Substrate 128

Transient Fiber Mats of Electrospun Poly(Propylene Carbonate) Composites with Remarkable Mechanical Strength 130

Surface Morphology of Heavily Doped GaN-Based p-n Diodes 132

CVD Graphene Growth on Copper and Refractory Metal Substrates 134

Mechanical Devices, 136-149

Zero-Power Sensors with Near-Zero-Power Wakeup Switches for Reliable Sensor Platforms 136

The Nanoaquarium - A Device for *in situ* Electron Microscopy of Processes in Liquids 138

Hydrophobic/Hyrophilic Nanoscale Patterns for Enhanced Pool Boiling 140

Pool Boiling Critical Heat Flux Enhancement by Early Evaporation of Microlayer 142

Making a Microfluidic Device to Mimic Flow Through Porous Medium 144

Graphene-Based Bimorphs for the Fabrication of µm-Sized, Autonomous Origami Machines 146

Silicon-Based Variable Capacitors for Sound Energy Harvesting 148

Optics & Opto-Electronics, 150-179

Investigation of Atomic Layer Deposition for Distributed Bragg Reflectors 150

Process Optimization for Silicon Photonic Device Fabrication 152

Quaternary Semiconductors for Integrated Nonlinear Optics 154

Visible 3D Metallic Photonic Crystal 156

Lithium Niobate Micro-Structures 158

Optics, continued....

Fabrication of Silicon Single-Photon Avalanche Diodes (SPADs) .. 160
Silicon-Based PN Junction Linear Modulator .. 162
Pixelated Polarizer for IR Focal Plane Array .. 164
Wide Bandgap Semiconductor Deep UV Devices .. 166
Xenon Difluoride Release of MEMS Three-Dimensional Micro-Mirror .. 168
Development of Single and Double Layer Anti-Reflective Coatings for Astronomical Instruments .. 170
Large Area Electrically Tunable Metasurface Lens .. 172
Tunable Semiconductor Metasurfaces for Mid-Infrared Photonics .. 174
III-Nitride and Light-Emitting Diodes .. 176
L-Couplers for Efficient Fiber-Chip Coupling .. 178

Physics & Nanostructure Physics, 180-221

Efficient Switching of Three-Terminal Magnetic Tunnel Junction Devices Powered by the Giant Spin Hall Effect of PtHf Alloys .. 180
Tuning Write Current in Tungsten Based Magnetic Tunnel Junctions with an Ultrathin Hf Insertion Layer .. 182
Reduction of the Spin Hall Angle in Oxygen-Doped Beta Tungsten .. 184
Anomalous Hall Generation of Spin Currents with Controllable Spin Polarization .. 186
Creating Skyrmions Using Spin Transfer Torque .. 188
Platforms for Probing the Electronic Properties of Covalent Organic Frameworks .. 190
Spin Hall Effect in $YbAl_3$ .. 192
Magnetic Actuation of Graphene Microstructures .. 194
Vortex Dynamics in Nanofabricated Superconducting Devices .. 196
Fabrication of Nanofluidic Cavities for Superfluid ^{3}He Studies .. 198
Fabrication of Nanoscale Josephson Junctions for Quantum Coherent Superconducting Circuits .. 200
Development of Superconductor Circuits for Readout of Quantum Nanomechanical Resonators .. 202
Fabrication of Superconducting Devices for Quantum Information Science .. 204
Imaging Magnetization Structure and Dynamics in Ultrathin YIG/Pt Bilayers with High Sensitivity Using the Time-Resolved Longitudinal Spin Seebeck Effect .. 206
Imaging of Topological Spin Textures by Time-Resolved Anomalous Nernst Effect in FeGe .. 208
Properties of Isolated Defects in Hexagonal Boron Nitride .. 210
Fabrication of Aligned Substrates and Suspended Membranes .. 212
Development of Scanning Graphene Hall Probes for Magnetic Microscopy .. 214
Tailoring the Spin-Orbit Torques in PtPd/FeCoB Bilayers by Composition .. 216
Heusler *B*2-Co2MnSi-Based Magnetic Tunneling Junctions on Silicon .. 218
Two-Dimensional Devices to Probe Emergent Properties of Ionic Liquid Interfaces .. 220

Process & Characterization, 222-239

Improving Dopant Activation in III-V Materials using LSA .. 222
Vector Electric field Measurements Using Position-Modulated Kelvin Probe Force Microscopy .. 224
Fabrication of Semiconductor Nanostructured Thin Film Using Inkjet Printing .. 226
Microfabricated Germanium X-Ray Optics for the Cornell High Energy Synchrotron Source (CHESS) .. 228
Nanocale Periodic Features with DUV Stepper Backside Alignment .. 230
Efficient Template-Based Nano Manufacturing of Carbon Nanotube Arrays .. 232
1.1kV GaN Vertical Power P-N Diodes on Ammonothermal GaN Substrates; Process Development and Device Characteristics .. 234
Deep-Tissue Photonic Needles .. 236
Quest for X-Ray Transparent Multilayer Graphene .. 238

Index by Project Number .. 240

Index of Users & Prinicpal Investigators ..241-244

COVER IMAGE CREDIT

The 2016-2017 cover image is an SEM of "Lithium Niobate Micro-Structures" created by Rui Luo, Hanxiao Liang, Yang He, and Qiang Lin, from the Department of Electrical and Computer Engineering, University of Rochester. Find the full report for CNF Project Number 1997-11 on pages 158-159.

CORNELL NANOSCALE SCIENCE & TECHNOLOGY FACILITY (CNF)
2016-2017 RESEARCH ACCOMPLISHMENTS

DIRECTORS' INTRODUCTION, 2017

This year (2017) the Cornell NanoScale Facility (CNF) is having its 40th anniversary.

Since the beginning, CNF has focused on making the smallest of structures of both scientific and technological interest. Serving both the academic and industrial communities as a national facility, it provides the tools and methods of nanoscience. But more importantly as it has done from its foundation, CNF provides knowledgeable outstanding staff, there to ensure the best results possible.

It is important to recognize the contributions many groups have made to the success of CNF including the equipment vendors who have often enabled CNF to get better equipment than it might otherwise possess. I (cko) would like to single out the Knight family for their generous donation for the facility in which CNF is housed. From the old sub-micron facility (sub-μ as it was on the roof) to today's much larger user facility, we have benefited from generous support from alumni and other donors who have enabled Cornell to stay at the technology forefront. We are counting on Cornell alumni support going forward as we work to continue our excellence in subsequent years.

It has been a year since I became CNF director and it has been exciting as we are putting in place plans for the future of CNF. I have particularly enjoyed working with the staff and the leadership at CNF.

Cornell is a founding member of the National Nanotechnology Coordinated Infrastructure (NNCI), a network focused on nanoscience and nanotechnology. NNCI has developed into a strong national partnership between 16 centers located around the country.

I remain very upbeat about the future of nanoscience and as you will see in this book, we describes much exciting research. One of CNF's goals is to serve the needs of researchers in the fields of nanoscale science, engineering and technology. Along with academics, we work closely with startup companies on topics ranging from improved DNA sequencing to better metrology for the semiconductor industry. We also support the activities of larger companies by providing tools and capabilities they cannot easily find in house or by providing experience that will enable process or technique selection for their future activities.

In recognition of our 40th anniversary, we are holding a special meeting on September 14, 2017, with a group of invited speakers who will share with us new directions and new concepts in nanoscience and technology. Presentations will describe recent developments in the internet of things (IoT), nanophotonics, 2D materials and nanobiotechnology. A planning workshop has been organized for the following day to help CNF as it contemplates the tools and skills needs for the next decade of research. This thinking is also influenced by the merger of a portion of the Nanobiotechnology Center (NBTC) into CNF. A pioneer in the combination of biology with nanotechnology, the NBTC will provide us with new capabilities and directions.

News; New Equipment and Capabilities

The CNF continues to upgrade its capabilities. New processes have been developed by CNF staff over the past year to meet the user demands for new materials or improved process control.

Our plasma etch engineers have developed new processes for: etching Diamond-Like-Carbon and nanocrystalline diamond; HBr etch of silicon and SOI with reduced lag; high and low rate GaAs etching; deep germanium etching; and several modified metal etches (Al, Cr, Ti).

We introduced a block copolymer process into the lab to allow users to access quasi-periodic nanostructures without the need for lithography. And new materials and processes have been introduced using nanoimprint lithography that improve the pattern transfer in etch and liftoff in conjunction with our Nanonex imprint tool.

The merger with NBTC has built on our expertise in synthesis and ALD coating of nanoparticles by adding two instruments, the Malvern Zetasizer and Nanosight, adding nanoparticle characterization to our portfolio.

Through a cooperative effort of the research division and the ECE department at Cornell, we are pleased to announce that we have ordered a new scandium doped-AlN piezoelectric material deposition system. We expect to receive this instrument in early 2018! This will allow us to be a leading lab in research related to rf filters and piezo-MEMS.

Educational Outreach

The CNF participates in numerous educational outreach activities, operating both a national and an international version of the NSF Research Experience for Undergraduates (REU) Program. This program takes undergraduate students from across the United States and exposes them to CNF's state of the art facility and our world class staff. In addition to our five REU students, we adopted seven other interns from other programs at Cornell during the 10 week summer REU program, and funded a second group of six (iREU) students, who spent the summer in Japan.

We are grateful to the National Science Foundation for its continued funding for our REU activities, but we also seek corporate funds to augment this program. Please contact Dr. Lynn Rathbun, our REU Programs Manager, to discuss corporate sponsorship (rathbun@cnf.comell.edu).

CNF continues to host many educational tours, workshops and special events at Cornell. These include our short course, "Technology & Characterization at the Nanoscale" (CNF TCN), open to participants from academia, industry, and government. It includes lectures and demonstrations, and also hands-on lab activities in the cleanroom. The next short course will be offered in January 2018.

Over the past year, CNF has hosted visits and tours and staffed events for over 3500 participants; from prospective graduate students and new faculty members, to visiting dignitaries and corporate executives, public events, and visiting groups. These included over 118 distinct visits and events. We again hosted signature outreach events that included the 4H Career Explorations and the Jr FIRST LEGO League. We also enjoy meeting and working with middle and high school students-introducing them to the nano-world we live in. Contact Melanie-Claire Mallison with your visit request (mallison@cnf.cornell.edu).

Let us close by saying that as always we enjoyed having an excellent group of REU students this last summer. Outreach, that is, sharing our excitement about nanoscience is something we really enjoy doing with the broader community. This group of REU students engaged in projects involving use of CNF's advanced tools working on activities that pushed back the frontiers of nanoscience. The summer ended with a convocation in Atlanta, Georgia, the home of the NNCI coordinating site. We have also put out a new edition of Nanooze, our educational publication aimed at K-12 students and we are updating the Nanooze display located at Disney's EPCOT center. All in all it has been an interesting year. We welcome inquiries from all researchers about CNF's capabilities and the NNCI network, especially those with no previous experience in nanofabrication, since the outstanding staff members of the CNF are highly skilled at teaching new users.

As always, we welcome your comments about CNF and its operations, as well as suggestions for improvement.

Chris Ober
Lester B. Knight Director,
Cornell NanoScale Facility (CNF)
director@cnf.cornell.edu

Donald Tennant
Director of Operations, CNF
tennant@cnf.cornell.edu

A Selection of CNF-Research-Related 2016 Patents, Presentations & Publications

"α-Actinin links extracellular matrix rigidity-sensing contractile units with periodic cell-edge retractions"; Meacci G, Wolfenson H, Liu S, Stachowiak MR, Iskratsch T, Mathur A, Ghassemi S, Gauthier N, Tabdanov E, Lohner J, Gondarenko A, Chander AC, Roca-Cusachs P,8, O'Shaughnessy B, Hone J, Sheetz MP; Molecular biology of the cell, Vol. 27, Issue 22, pgs. 3471-3479; Columbia University, 2016.

"0.89 mW on-chip jitter-measurement circuit for high speed clock with sub-picosecond resolution"; Gantsog, E.; Liu, D.; Apsel, A.B.; European Solid-State Circuits Conference, ESSCIRC Conference 2016: 42nd, pgs 457-460; Cornell University, 2016.

"1.7-kV and 0.55-m Omega . cm(2) GaN p-n Diodes on Bulk GaN Substrates With Avalanche Capability"; Nomoto, K.; Song, B.; Hu, Z.; Zhu, M.; Qi, M.; Kaneda, N.; Mishima, T.; Nakamura, T.; Jena, D.; Xing, H.G.; IEEE Electron Device Letters, Vol. 37, Issue 2, pgs 161-164; Cornell University, 2016.

"250 nm Deep UV LED Using GaN/AlN Heterostructures On Bulk AlN Substrates"; Islam, S M; Protasenko, V.; Xing, H.; Jena, D.; 2016 CLEO; Cornell University, 2016.

"4H-SiC n-channel insulated gate bipolar transistors on (0001) and (000-1) oriented free-standing n- substrates"; Chowdhury, Sauvik; Hitchcock, Collin; Stum, Zachary; Dahal, Rajendra; Bhat, Ishwara B; Chow, T Paul; IEEE Electron Device Letters, Vol. 3, pg. 37; Rensselaer Polytechnic Institute, 2016.

"A 72\times60 Angle-Sensitive SPAD Imaging Array for Lens-less FLIM"; Lee, C.; Johnson, B.; Jung, T.; Molnar, A.; Sensors, Vol. 16, Issue 9, pgs 1422; Cornell University, 2016.

"A Biocompatible and High Stiffness Nanophotonic Trap Array for Precise and Versatile Manipulation"; Wang, Michelle; Patent Docket # 7482, Filed - by Cornell, 7/4/16, Invention; Cornell University, 2016.

"A Biocompatible and High Stiffness Nanophotonic Trap for Precise and Versatile Particle Manipulation"; Badman, Ryan, James Inman, Michelle Wang, Fan Ye; Patent Docket # 7482-01-US, United States, PRO - Provisional, Filed, 7/5/16, 62/358,467; Cornell University, 2016.

"A chemo-mechanical model for nuclear morphology and stresses during cell transendothelial migration"; Cao X, Moeendarbary E, Isermann P, Davidson PD, Wang W, Chen M, Burkart A, Lammerding J, Kamm RD, Shenoy V; Biophysical Journal 111(7):1541-1552; Cornell University, 2016.

"A Comparative Study of Flow Boiling in a Microchannel With Piranha Pin Fins"; Yu, X, C Woodcock, Y Wang, J Plawsky, and Y Peles; Journal of Heat Transfer 138, no. 11 (2016): 111502; Rensselaer Polytechnic Institute, 2016.

"A fully integrated software-defined FDD transceiver tunable from 0.3-to-1.6 GHz"; Yang, Dong; Yüksel, Hazal; Newman, Christopher; Lee, Changhyuk; Boynton, Zachariah; Paya, Noman; Pedrone, Miles; Apsel, Alyssa; Molnar, Alyosha; Radio Frequency Integrated Circuits Symposium (RFIC), 2016 IEEE, pgs 334-337; Cornell University, 2016.

"A high-frequency regenerative optomechanical oscillator on lithium-niobate-on-insulator platform"; Jiang, W C, and Q Lin; CLEO/QELS Proceedings, Conf. Laser and Electro-Optics/ Quantum Electronis and Laser Science (CLEO/QELS), STu4E.6 (2016); University of Rochester, 2016.

"A MEMS Microphone Using Repulsive Force Sensors"; Ozdogan, Mehmet, and Shahrzad Towfighian; ASME 2016 International Design Engineering Technical Conferences and Computers and Information in Engineering Conference, pp. V004T08A017-V004T08A017. American Society of Mechanical Engineers, 2016; Binghamton University, 2016.

"A photonic microscope for observing real-time vibrations of carbon nanotubes"; Barnard, Arthur W, Mian Zhang, Gustavo Wiederhecker, Michal Lipson, and Paul L McEuen; APS Meeting Abstracts. 2016; Cornell University, 2016.

"A Polar Symmetric CMOS Image Sensor for Rotation Invariant Measurement"; Sivaramakrishnan, Sriram; Lee, Changhyuk; Johnson, Ben; Molnar, Alyosha; IEEE Sensors Journal, Vol. 16, Issue 5, pgs 1190-1199; Cornell University, 2016.

"A recellularized human colon model identifies cancer driver genes"; Chen, HJ, Z Wei, J Sun, A Bhattacharya, DJ Savage, R Serda, Y Mackeyer, SA Curley, P Bu, L Wang, S Chen, L Cohen-Gould, E Huang, X Shen, SM Lipkin, NG Copeland NA Jenkins and ML Shuler; Nature Biotechnology 34:845-851. (doi:10.1038/ nbt.3586). 2016; Cornell University, 2016.

"A silicon/plastic hybrid tissue multimodal assay tweezer with integrated polysilicon strain gauge displacement sensor"; Chen, Po-Cheng; Lal, Amit; Micro Electro Mechanical Systems (MEMS), 2016 IEEE 29th International Conference on, pgs. 333-336; Cornell University, 2016.

"A Stretchable Multicolor Display and Touch Interface Using Photopatterning and Transfer Printing"; Li, Shuo; Peele, Bryan N; Larson, Chris M; Zhao, Huichan; Shepherd, Robert F; Advanced Materials, Vol. 28, Issue 44, pgs. 9770-9775; Cornell University, 2016.

"A Telecom-Band Cavity-Enhanced Single-Photon Source with High Klyshko Efficiencies"; Lu, X, S Rogers, T Gerrits, W C Jiang, S W Nam, and Q Lin; CLEO/QELS Proceedings, Conf. Laser and Electro-Optics/Quantum Electronis and Laser Science (CLEO/ QELS), FTh1C.1 (2016); University of Rochester, 2016.

"A wireless FSCV monitoring IC with analog background subtraction and UWB telemetry"; Dorta-Quiñones, Carlos I.; Wang, Xiao Y.; Dokania, Rajeev K.; Gailey, Alycia; Lindau, Manfred; Apsel, Alyssa B.; IEEE transactions on biomedical circuits and systems, Vol. 10, Issue 2, pgs 289-299; Cornell University, 2016.

"Achieving an accurate surface profile of a photonic crystal for near-unity solar absorption in a super thin-film architecture"; Kuang, Ping; Eyderman, Sergey; Hsieh, Mei-Li; Post, Anthony; John, Sajeev; Lin, Shawn-Yu; ACS Nano, Vol. 10, Issue 6, pgs. 6116-6124; Rensselaer Polytechnic Institute, 2016.

"Acoustic Localization Phenomena in Ferroelectric Nanophononic Devices"; Bruchhausen, A; Lanzillotti-Kimura, N D; Jusserand, B; Soukiassian, A; Schlom, D G; Dekorsy, T; Fainstein, A; arXiv preprint arXiv:1605.00147; Cornell University, 2016.

"Active control of flow boiling oscillation amplitude and frequency using a transverse jet in crossflow"; Vutha, A.K.; Rao, S. R.; Houshmand, F.; Peles, Y.; Applied Physics Letters, Vol. 108, Issue 13, pgs. 134104; University of Central Florida, 2016.

"Adipose-derived stem cells increase angiogenesis through matrix metalloproteinase-dependent collagen remodeling"; Song, Young Hye; Shon, Seung Hee; Shan, Mengrou; Stroock, Abraham D; Fischbach, Claudia; Integrative Biology, Vol. 8, Issue 2, pgs. 205-215; Cornell University, 2016.

"Aligned Bacterial Cellulose Arrays as Green Nanofibers for Composite Materials"; Rahman, M.M.; Netravali, A.N.; ACS Macro Letters, Vol. 5, Issue 9, pgs. 1070-1074; Cornell University, 2016.

"All the Ways to have a Bond"; Hoffmann, R; Pennsylvania State University, Nov. 30, 2016; Cornell University, 2016.

"All-optical vector measurement of spin-orbit-induced torques using both polar and quadratic magneto-optic Kerr effects"; Fan, X.; Mellnik, A.R.; Wang, W.; Reynolds, N.; Wang, T.; Celik, H.; Lorenz, V.O.; Ralph, D.C.; Xiao, J.Q.; Applied Physics Letters, Vol. 109, Issue 12, pgs. 122406; Cornell University, 2016.

"Ambiguous anti-fouling surfaces: Facile synthesis by light-mediated radical polymerization"; Pester, Christian W; Poelma, Justin E; Narupai, Benjaporn; Patel, Shrayesh N; Su, Gregory M; Mates, Thomas E; Luo, Yingdong; Ober, Christopher K; Hawker, Craig J; Kramer, Edward J; Journal of Polymer Science, Part A: Polymer Chemistry (2016), 54(2), 253-262; Cornell University, 2016.

"An Angstrom-sensitive, differential MEMS capacitor for monitoring the milliliter dynamics of fluids"; Apigo, David J; Bartholomew, Philip L; Russell, Thomas; Kanwal, Alokik; Farrow, Reginald C; Thomas, Gordon A; Sensors and Actuators A: Physical, Vol. 251, pgs. 234-240; New Jersey Institute of Technology, 2016.

"Analysis of a time dependent injection strategy to accelerate the residual trapping of sequestered CO2 in the geologic subsurface"; Huber, EJ; Stroock, AD; Koch, DL; International J. of Greenhouse Gas Control, Vol. 44, pgs. 185-198; Cornell University, 2016.

"Analysis of Individual Signaling Complexes by mMAPS, a Flow-Proteometric System"; Chou, Chao-Kai; Tsou, Pei-Hsiang; Hsu, Jennifer L; Lee, Heng-Huan; Wang, Ying-Nai; Kameoka, Jun; Hung, Mien-Chie; Current Protocols in Molecular Biology, pgs. 20-11; University of Texas MD Anderson Cancer Center, 2016.

"Angle Sensitive Pixel (ASP) - Based Image Processing System, Method, and Applications"; Gill, P., A. Molnar, A. Wang; Patent Docket # 4893-05-CN, China, Issued, 4/3/13, 201180048089.3, 3/30/16, ZL201180048089.3; Cornell University, 2016.

"Antifouling urinary catheters with shape-memory topographic patterns"; Ren, Dacheng; Gu, Huan; https://www.google.com/patents/US20170056618; Syracuse University, 2016.

"Apodized Grating for Silicon Tunable Delay Lines"; Jiang, Lingjun, Stephen Anderson, Young H Kim, Weimin Zhou, and Zhaoran R Huang; Frontiers in Optics, pp. FTu1D-5. Optical Society of America, 2016; Rensselaer Polytechnic Institute, 2016.

"Apparatus and Method for Point-of-Care Diagnostics and Antibiotic Resistance Identification, and Applications Therof"; Erickson, David, Seoho Lee, Saurabh Mehta; Patent Docket # 7108-02-PC, Not Applicable (PCT App), PCT - Patent Cooperation Treaty, Filed, 7/20/16, PCT/US2016/043102; Cornell University, 2016.

"Applications of high-Q microresonators in cavity optomechanics and nonlinear photonics"; Jiang, Wei C; https://urresearch.rochester.edu/fileDownloadForInstitutionalItem.action?itemId=31829&itemFileId=175320; University of Rochester, 2016.

"ASP vision: Optically computing the first layer of convolutional neural networks using angle sensitive pixels"; Chen, Huaijin G.; Jayasuriya, Suren; Yang, Jiyue; Stephen, Judy; Sivaramakrishnan, Sriram; Veeraraghavan, Ashok; Molnar, Alyosha; IEEE Conference on Computer Vision and Pattern Recognition, Proceedings of the, pgs 903-912; Cornell University, 2016.

"Assessment of trace element impacts on agricultural use of water from the Dan River following the Eden coal ash release"; Hesterberg, D; Polizzotto, ML; Crozier, C; Austin, RE; Integrated Environmental Assessment and Management, Vol. 12, Issue 2, pgs. 353-363; Princeton University, 2016.

"Atomic Layer Deposition of Al2O3 on WSe2 Functionalized by Titanyl Phthalocyanine"; Park, JH; Fathipour, S; Kwak, I; Sardashti, K; Ahles, CF; Wolf, SF; Edmonds, M; Vishwanath, S; Xing, HG; Fullerton-Shirey, SK; Seabaugh, A; Kummel, AC; ACS Nano, Vol. 10, Issue 7, pgs 6888-6896; Cornell University, 2016.

"Atomically engineered ferroic layers yield a room-temperature magnetoelectric multiferroic"; Mundy, Julia A; Brooks, Charles M; Holtz, Megan E; Moyer, Jarrett A; Das, Hena; Rébola, Alejandro F; Heron, John T; Clarkson, James D; Disseler, Steven M; Liu, Zhiqi; Kourkoutis, Lena; others; Nature, Vol. 537, Issue 7621, pgs. 523-527; Cornell University, 2016.

"Atomically Thin Graphene Windows That Enable High Contrast Electron Microscopy without a Specimen Vacuum Chamber"; Han, Y., K.X. Nguyen, Y. Ogawa, J. Park, and D.A. Muller; Nano Letters 16, no. 12 (2016): 7427-7432; Cornell University, 2016.

"Atomically Thin Ohmic Edge Contacts Between Two-Dimensional Materials"; Guimarães, Marcos HD; Gao, Hui; Han, Yimo; Kang, Kibum; Xie, Saien; Kim, Cheol-Joo; Muller, David A; Ralph, Daniel C; Park, Jiwoong; ACS Nano, Vol. 10, Issue 6, pgs. 6392-6399; Cornell University, 2016.

"Atomically Thin Ohmic Edge Contacts Between Two-Dimensional Materials"; Guimarães, Marcos HD, Hui Gao, Yimo Han, Kibum Kang, Saien Xie, Cheol-Joo Kim, David A Muller, Daniel C Ralph, and Jiwoong Park; arXiv preprint arXiv:1606.05393 (2016); Cornell University, 2016.

"Atomically Thin Ohmic Edge Contracts Between Two-Dimensional Materials"; Gao, Hui, Marcos Guimaraes, Kibum Kang, Jiwoong Park, Daniel Ralph, Saien Xie; Patent Docket # 7404-01-US, United States, EPR - Enhanced Provisional, Filed, 6/12/16, 62/349,193; Cornell University, 2016.

"AuO: Evolving from Dis-to Comproportionation and Back Again"; Hermann, Andreas; Derzsi, Mariana; Grochala, Wojciech; Hoffmann, Roald; Inorganic chemistry, Vol. 55, Issue 3, pgs. 1278-1286; Cornell University, 2016.

"Automated Analysis of Cancer Cell Migration and Nuclear Envelope Rupture in Confined Environments"; Elacqua J, McGregor AL, Lammerding J; Platform presentation selected from submitted abstract; Biomedical Engineering Society (BMES) Annual Mtg. Minneapolis, MN (October 8, 2016); Cornell University, 2016.

"Automated Analysis of Evolving Interfaces during In Situ Electron Microscopy"; Schneider, Nicholas M; Jeung Hun Park; Michael M Norton; Frances M Ross; Haim H Bau; Advanced Structural and Chemical Imaging 2:2. DOI: 10.1186/s40679-016-0016-z. 26 February 2016; University of Pennsylvania, 2016.

"Automated electrorotation shows electrokinetic separation of pancreatic cancer cells is robust to acquired chemotherapy resistance, serum starvation, and EMT"; Lannin, Timothy; Su, Wey-Wey; Gruber, Conor; Cardle, Ian; Huang, Chao; Thege, Fredrik; Kirby, Brian; Biomicrofluidics, Vol. 10, Issue 6, pgs. 64109; Cornell University, 2016.

"Automated Leukocyte Processing by Microfluidic Deterministic Lateral Displacement"; Civin, CI; Ward, T; Skelley, AM; Gandhi, K; Lee, ZP; Dosier, CR; D'Silva, JL; Chen, Y; Kim, M; Moynihan, J; Chen, X; Aurich, L; Gulnik, S; Brittain, GC; Recktenwald, DJ; Austin, RH; Sturm, JC; Cytometry Part A, Vol. 89A, Issue 12, pgs. 1073-1083; Princeton University, 2016.

"Betavoltaic Apparatus and Method"; Lal, Amit, Steven Tin; Patent Docket # 4941-04-CN, China, Issued, 7/18/12, CN201080061778.3, 1/6/16, ZL201080061778.3; Cornell University, 2016.

"Biocompatible and High Stiffness Nanophotonic Trap Array for Precise and Versatile Manipulation"; Ye, F, RP Badman, JT Inman, M Soltani, JL Killian, MD Wang; Nano Letters, Vol. 16, Issue 10, pgs. 6661-6667; Cornell University, 2016.

"Biocompatible and High-Stiffness Nanophotonic Trap for Precise and Versatile Particle Manipulation"; Wang, Michelle D, Fan Ye, Ryan Badman, James Inman; U.S. Patent Application No. 62/358,467; Cornell University, 2016.

"Biphoton statistics of quantum light generated on a silicon chip"; Lu, Xiyuan; Jiang, Wei C; Zhang, Jidong; Lin, Qiang; ACS Photonics, Vol. 3, Issue 9, pgs. 1626-1636; University of Rochester, 2016.

"Body-on-a Chip; improving drug development"; Shuler, ML (Keynote Speaker); 8th International Conference on Microtechnologies in Medicine and Biology. Seoul, Korea. April 20-22. 2016; Cornell University, 2016.

"Body-on-a-Chip; a self-contained microphysiological system"; Shuler, ML (Keynote Address); Biofabrication. Winston-Salem, NC. Oct. 29-31, 2016; Cornell University, 2016.

"Body-on-a-Chip; systems for animal-free toxicity testing"; Mahler, GJ, MB Esch, T Stokol, JJ Hickman and ML Shuler; ATLA 44: 469-478. 2016; Cornell University, 2016.

"Breaking the Loss Limitation of On-chip High-confinement Resonators"; Ji, Xingchen, Felippe AS Barbosa, Samantha P Roberts, Avik Dutt, Jaime Cardenas, Yoshitomo Okawachi, Alex Bryant, Alexander L Gaeta, and Michal Lipson; arXiv:1609.08699 (2016). Publisher's Version Abstract; Columbia University, 2016.

"Broadband Swept-Source Laser in 1.1 to 1.3 μm with InAs Quantum Dot Gain Chip Devices"; Yao, R., N. Weir, C.-S. Lee, Z. Wang, S.F. Preble, and W. Guo; Frontiers in Optics, pp. FW5C-4. Optical Society of America; Rochester Institute of Technology, 2016.

"Broadly tunable frequency division duplex transceiver: Theory and operation"; Yuksel, H.; Yang, D.; Boynton, Z.; Enroth, E.; Tapen, T.; Molnar, A.; Apsel, A.; ICECS, 2016 IEEE International Conference on, pgs 688-691; Cornell University, 2016.

"Building a "Body-on-a-Chip" to improve drug development"; Shuler, ML Plenary Speaker; Korean Society for Biotechnology and Bioengineering Spring Meeting and International Symposium. Gyeong ju, Korea. April 21-22,2016; Cornell University, 2016.

"Building in vitro models of human barrier tissues"; Shuler, ML; AICHE Meeting. San Francisco, CA. Nov. 13-18, 2016; Cornell University, 2016.

"Capillarity-driven flows at the continuum limit"; Vincent, Olivier; Szenicer, Alexandre; Stroock, Abraham D; Soft Matter, Vol. 12, Issue 31, pgs. 6656-6661; Cornell University, 2016.

"Challenges and approaches to software defined duplexing radio"; Apsel, Alyssa; Molnar, Alyosha; Yang, Dong; Yuksel, Hazal; Tappen, Thomas; Enroth, Emory; Mohiuddin, Mashrur; Boynton, Zachariah; Circuits and Systems (ISCAS), 2016 IEEE International Symposium on, pgs 2779-2782; Cornell University, 2016.

"Characterizations of InAs quantum dot lasers butt-joint coupled with silicon photonics waveguides"; Wang, Zihao, Ruizhe Yao, Stefan Preble, Chi-Sen Lee, and Wei Guo; SPIE OPTO, pp. 975316-975316. International Society for Optics and Photonics, 2016; Rochester Institute of Technology, 2016.

"Chip-scale cavity optomechanics in lithium niobate"; Jiang, WC; Lin, Q; Scientific Reports, Vol. 6; University of Rochester, 2016.

"Chiral atomically thin films"; Kim, C.-J.; Sánchez-Castillo, A.; Ziegler, Z.; Ogawa, Y.; Noguez, C.; Park, J.; Nature Nanotechnology, Vol. 11, Issue 6, pgs. 520-524; Cornell University, 2016.

"Chiral atomically thin films"; Park, Jiwoong; Energy (eV), Vol. 2, Issue 3, pgs. 4; Cornell University, 2016.

"Chiral magnetic excitations in FeGe films"; Turgut, Emrah, Albert Park, Austin Moehle, and Gregory D Fuchs; 61st Annual Conference on Magnetism and Magnetic Materials, New Orleans, LA 2016; Cornell University, 2016.

"Chiral magnetic excitations in FeGe films"; Turgut, E.; Park, A.; Nguyen, K.; Moehle, A.; Muller, D.A.; Fuchs, G.D.; arXiv preprint arXiv:1608.03582; Cornell University, 2016.

"Circuits and Devices Based on Spin Hall Effect to Apply a Spin Transfer Torque with a Component Perpendicular to the Plane of Magnetic Layers"; Buhrman, Robert, Daniel Ralph; Patent Docket # 6495-03-US, United States, US from PCT, Prosecution, 4/18/16, 15/030,291; Cornell University, 2016.

"Coherent control of superconducting transmon qubits with an on-chip single flux quantum driver (poster)"; Leonard Jr, Edward, Ted Thorbeck, Shaojiang Zhu, Caleb Howington, Matthew D Hutchings, JJ Nelson, Britton Plourde, Robert McDermott, Matthew Beck; Applied Superconductivity Conference, 2016, Denver, CO; Syracuse University, 2016.

"Coherent mid-infrared frequency combs in silicon-microresonators in the presence of Raman effects"; Griffith, Austin G; Yu, Mengjie; Okawachi, Yoshitomo; Cardenas, Jaime; Mohanty, Aseema; Gaeta, Alexander L; Lipson, Michal; Optics Express, Vol. 24, Issue 12, pgs. 13044-13050; Columbia University, 2016.

"Combining dynamic nuclear polarization and mechanically detected magnetic resonance to achieve nanoscale magnetic resonance imaging of individual biomolecules and assemblies"; Marohn, JA, CE Isaac, HL Nguyen, PT Nasr, EA Curley, and MC Boucher; Breckenridge, Colorado; July 17-21; Cornell University, 2016.

"Comparing Buffer Leakage in PolarMOSH on SiC and Free-Standing GaN Substrates"; Zhu, Mingda; Song, Bo; Hu, Zongyang; Nomoto, Kazuki; Pan, Ming; Gao, Xiang; Jena, Debdeep; Xing, Huili Grace; 25th Biennial Lester Eastman Conference on High Performance Devices (lec), Proceedings of the, pgs 27-30; Cornell University, 2016.

"Competitive Lateral Flow Assay"; Erickson, David, Seoho Lee, Saurabh Mehta, Sasank Vemulapati; Patent Docket # 7259-02-PC, Not Applicable (PCT App), PCT - Patent Cooperation Treaty, Filed, 11/18/16, PCT/US16/62828; Cornell University, 2016.

"Constructing "Body-on-a-Chip" devices for drug development"; Shuler, ML; Microfluidics Congress: USA. Philadelphia, PA. July 11-12, 2016; Cornell University, 2016.

"Continuous dynamical decoupling of a single diamond nitrogen-vacancy center spin with a mechanical resonator"; MacQuarrie, E R, T A Gosavi, S Bhave, and G D Fuchs; March Meeting of the American Physical Society Bulletin, 2016, Baltimore, MD; Cornell University, 2016.

"Control of cancer cell invasion by A- and B-type lamin-regulated nuclear deformability"; Krause M, te Riet J, te Boekhorst V, Marke R, Perera Rm, te Lindert M, Alexander S, Zwerger M, Cenais C, Friedl P, Lammerding J, Wolf K Platform presentation selected from submitted abstract; Mechanobiology Conference. Amsterdam, The Netherlands (March 22, 2016); Cornell University, 2016.

"Control of spin-orbit torques through crystal symmetry in WTe2/ ferromagnet bilayers"; MacNeill, D, G M Stiehl, M H D Guimaraes, R A Buhrman, J Park, and D C Ralph; Nature Physics (2016); Cornell University, 2016.

"Controllable growth of layered selenide and telluride heterostructures and superlattices using molecular beam epitaxy"; Vishwanath, S; Liu, X; Rouvimov, S; Basile, L; Lu, N; Azcatl, A; Magno, K; Wallace, R; Kim, M; Idrobo, J; Furdyna, J Jena, De; Xing, H; Journal of Materials Research, Vol. 31, Issue 7, pgs 900-910; Cornell University, 2016.

"Coupling a Transmon Qubit to a Superconducting Metamaterial Resonator (poster)"; Wang, Haozhi, Matthew D Hutchings, Francisco Rouxinol, Britton Plourde, Bruno Taketani, Frank K Wilhelm, Sagar Indrajeet, Matthew LaHaye; Applied Superconductivity Conference, 2016, Denver, CO; Syracuse University, 2016.

"Coupling a Transmon Qubit to a Superconducting Metamaterial Resonator"; Wang, H, M Hutchings, S ndrajeet, F Rouxinol, M LaHaye, BLT Plourde, BG Taketani, FK Wilhelm; March Meeting of the American Physical Society Bulletin, 2016, Baltimore, MD; Syracuse University, 2016.

"Covalent bonding modulated graphene-metal interfacial thermal transport"; Jiang, Tao; Zhang, Xueqiang; Vishwanath, Suresh; Mu, Xin; Kanzyuba, Vasily; Sokolov, Denis A; Ptasinska, Sylwia; Go, David B; Xing, Huili Grace; Luo, Tengfei; Nanoscale, Vol. 8, Issue 21, pgs 10993-11001; Cornell University, 2016.

"Current control of magnetic anisotropy via stress in a ferromagnetic metal waveguide"; An, Kyongmo, Xin Ma, Chi-Feng Pai, Jusang Yang, Kevin S Olsson, James L Erskine, Daniel C Ralph, Robert A Buhrman, and Xiaoqin Li; Physical Review B 93, no. 14 (2016): 140404; Cornell University, 2016.

"Deconstructing the Heterogeneity of Surface-Bound Catalysts: Rutile Surface Structure Affects Molecular Properties"; Bell ES, Shah P, Davidson PM, McGregor AL, Fedorchak GR, Isermann P, Lammerding J; Platform presentation selected from submitted abstract; American Society for Cell Biology (ASCB) Annual Meeting. San Francisco, CA (December 7, 2016); Cornell University, 2016.

"Deconstructing the Heterogeneity of Surface-Bound Catalysts: Rutile Surface Structure Affects Molecular Properties"; Calabrese, Carmella; Vanselous, Heather; Petersen, Poul B; Journal of Physical Chemistry C, Vol. 120, Issue 3, pgs. 1515-1522; Cornell University, 2016.

"Deep Reactive Ion Etched Anti-Reflection Coatings for Sub-millimeter Silicon Optics"; Gallardo, P; Koopman, B; Cothard, N; Bruno, S; Cortes-Medellin, G; Marchetti, G; Miller, K; Mockler, B; Niemack, M; Stacey, G; others; arXiv preprint arXiv:1610.07655; Cornell University, 2016.

"Demonstration of GaN HyperFETs with ALD VO 2"; Verma, Amit, Bo Song, David Meyer, Brian Downey, Virginia Wheeler, Huili Grace Xing, and Debdeep Jena; Device Research Conference (DRC), 2016 74th Annual, pp. 1-2. IEEE, 2016; Cornell University, 2016.

"Dephasing of superconducting asymmetric transmon qubits"; Hutchings, M, Matthew Ware, Yebin Liu, Jared B Hertzberg, Jerry M Chow, BLT Plourde; March Meeting of the American Physical Society Bulletin, 2016, Baltimore, MD; Syracuse University, 2016.

"Depth Field Imaging Apparatus, Methods, and Applications"; Jayasuriya, Suren, Alyosha Molnar, Sriram Sivaramakrishnan; Patent Docket # 6955-02-PC, Not Applicable (PCT App), PCT - Patent Cooperation Treaty, Filed, 3/17/16, PCT/US16/22741; Cornell University, 2016.

"Design and characterization of enhanced angle sensitive pixels"; Sivaramakrishnan, Sriram; Wang, Albert; Gill, Patrick; Molnar, Alyosha; IEEE Transactions on Electron Devices, Vol. 63, Issue 1, pgs. 113-119; Cornell University, 2016.

"Design and demonstration of a pumpless 14 compartment microphysiological system"; Miller, PG, and ML Shuler; Biotechnol Bioeng 13: 2213-2227. doi: 10.1002/bit.25989. 2016; Cornell University, 2016.

"Development of Integrated Single Flux Quantum - Superconducting Qubit Circuits"; Leonard Jr, Edward, Ted Thorbeck, Shaojiang Zhu, Caleb Howington, Matthew Hutchings, JJ Nelson, Britton Plourde, Robert McDermotts; March Meeting of the American Physical Society Bulletin, 2016, Baltimore, MD; Syracuse University, 2016.

"Device and Methods for Epigenetic Analysis"; Cipriany, Benjamin, Harold Craighead, Stephen Levy, Paul Soloway; Patent Docket # 4823-05-EP, Europe, Issued, 2/6/12, 10807270.3, 10/5/16, 2462245; Cornell University, 2016.

"Device and Methods for Epigenetic Analysis"; Cipriany, Benjamin, Harold Craighead, Stephen Levy, Paul Soloway; Patent Docket # 4823-06-CN, China, Issued, 3/5/12, 201080039585.8, 8/3/16, ZL2010800395858; Cornell University, 2016.

"Device and Methods for Epigenetic Analysis"; Cipriany, Benjamin, Harold Craighead, Stephen Levy, Paul Soloway; Patent Docket # 4823-07-US, United States, Issued, 4/23/14, 14/260,082, 9/20/16, 9,447,451; Cornell University, 2016.

"Device and Methods for Epigenetic Analysis"; Cipriany, Benjamin, Harold Craighead, Stephen Levy, Paul Soloway; Patent Docket # 4823-08-DE, Germany, Issued, 2/6/12, 10807270.3, 10/5/16, EP2462245; Cornell University, 2016.

"Device and Methods for Epigenetic Analysis"; Cipriany, Benjamin, Harold Craighead, Stephen Levy, Paul Soloway; Patent Docket # 4823-09-GB, United Kingdom, Issued, 2/6/12, 10807270.3, 10/5/16, EP2462245; Cornell University, 2016.

"Device and Methods for Epigenetic Analysis"; Cipriany, Benjamin, Harold Craighead, Stephen Levy, Paul Soloway; Patent Docket # 4823-11-US, United States, CON - Continuation, Filed, 8/26/16, 15/249,275; Cornell University, 2016.

"Device and methods for epigenetic analysis"; Craighead, H; U.S. Patent #9,477,451 issued 9/20/16; Cornell University, 2016.

"Device and Methods for Molecular Analysis"; Cipriany, Benjamin, Harold Craighead, Stephen Levy, Paul Soloway; Patent Docket # 4837-06-CN, China, Issued, 2/27/12, 201080038285.8, 5/4/16, ZL2010800382858; Cornell University, 2016.

"Devices and methods for pharmacokinetics based cell culture systems"; Shuler, M, GT Baxter, A Sin, RA Harrison, and S Meyers; Assigned to Cornell University. US Patent 9,273,276 B2, March 1, 2016; Cornell University, 2016.

"Diffraction Based Transit-receive Delay Element with Zero Temperature Coefficient"; Abdelmejeed, Mamdouh, Justin Kuo, Amit Lal; Patent Docket # 7369-01-US, United States, MPR - Manuscript Provisional, Converted, 3/17/16, 62/309,611; Cornell University, 2016.

"Diffraction Based Transit-receive Delay Element with Zero Temperature Coefficient"; Lal, Amit; Patent Docket # 7369, Filed - by Cornell, 2/26/16, Invention; Cornell University, 2016.

"Direct Observation of Electrostatically Driven Band Gap Renormalization in a Degenerate Perovskite Transparent Conducting Oxide"; Lebens-Higgins, Z; Scanlon, D O; Paik, H; Sallis, S; Nie, Y; Uchida, M; Quackenbush, N F; Wahila, M J; Sterbinsky, G E; Arena, Dario A; Woicik, J C; Schlom, D G; Piper, L F J; Physical Review Letters, Vol. 116, Issue 2, pgs. 27602; Cornell University, 2016.

"Distinguishing Direct and Indirect Photoelectrocatalytic Oxidation Mechanisms Using Quantitative Single-Molecule Reaction Imaging and Photocurrent Measurements"; Sambur, Justin B; Chen, Peng; Journal of Physical Chemistry C, Vol. 120, Issue 37, pgs. 20668-20676; Cornell University, 2016.

"DNA Microgels as a Platform for Cell-Free Protein Expression and Display"; Kahn, Jason S; Ruiz, Roanna CH; Sureka, Swati; Peng, Songming; Derrien, Thomas L; An, Duo; Luo, Dan; Biomacromolecules, Vol. 17, Issue 6, pgs. 2019-2026; Cornell University, 2016.

"Drug-Eluting Conformal Coatings on Individual Cells"; Zhang, Yu; An, Duo; Song, Wei; Pardo, Yehudah; Ma, Minglin; Cellular and Molecular Bioengineering, Vol. 9, Issue 3, pgs. 382-397; Cornell University, 2016.

"Dual-Calibration Technique for Improving Static Linearity of Thermometer DACs for I/O"; Mukhopadhyay, Ishita; Mukadam, Mustansir Y.; Narayanan, Rajendran; O'Mahony, Frank; Apsel, Alyssa B.; IEEE Transactions on Very Large Scale Integration (VLSI) Systems, Vol. 24, Issue 3, pgs 1050-1058; Cornell University, 2016.

"Dual-pumped degenerate optical parametric oscillator in a silicon nitride microresonator"; Okawachi, Yoshitomo, et al; CLEO: Science and Innovations. Optical Society of America, 2016; Columbia University, 2016.

"Dynamic nuclear polarization in a magnetic resonance force microscope experiment"; Issac, Corinne E; Gleave, Christine M; Nasr, Paméla T; Nguyen, Hoang L; Curley, Elizabeth A; Yoder, Jonilyn L; Moore, Eric W; Chen, Lei; Marohn, John A; Physical Chemistry Chemical Physics, Vol. 18, Issue 13, pgs. 8806-8819; Cornell University, 2016.

"Dynamic self-organization of microwell-aggregated cellular mixtures"; Song, Wei; Tung, Chih-Kuan; Lu, Yen-Chun; Pardo, Yehudah; Wu, Mingming; Das, Moumita; Kao, Der-I; Chen, Shuibing; Ma, Minglin; Soft Matter, Vol. 12, Issue 26, pgs. 5739-5746; Cornell University, 2016.

"Dynamics of mode-coupling-assisted microresonator frequency combs"; Jang, Jae K, et al; CLEO: QELS_Fundamental Science. Optical Society of America, 2016; Columbia University, 2016.

"Dynamics of mode-coupling-induced microresonator frequency combs in normal dispersion"; Jang, Jae K, Yoshitomo Okawachi, Mengjie Yu, Kevin Luke, Xingchen Ji, Michal Lipson, and Alexander L Gaeta; Optics Express 24, no. 25 (2016): 28794 - 28803; Columbia University, 2016.

"Early Evaporation of Microlayer for Boiling Heat Transfer Enhancement"; Zou, A, DP Singh, and SC Maroo; Langmuir 32, no. 42 (2016): 10808-10814; Syracuse University, 2016.

"Effect of substrate composition on atomic layer deposition using self-assembled monolayers as blocking layers"; Zhang, Wenyu; Engstrom, James R; Journal of Vacuum Science & Technology A: Vacuum, Surfaces, and Films, Vol. 34, Issue 1, pgs. 01A107; Cornell University, 2016.

"Effects of RF Sputtering Parameters on C-axis Aligned Crystalline (CAAC) InGaZnO4 Films Using Design of Experiment (DOE) Approach"; Zhu, Bin; Roach, Kate E; Lynch, David M; Chung, Chen-yang; Ast, Dieter G; Greene, Raymond G; Thompson, Michael O; ECS Journal of Solid State Science and Technology, Vol. 5, Issue 6, pgs. P368-P375; Cornell University, 2016.

"Efficiently heralded silicon ring resonator photon-pair source"; Steidle, Jeffrey A, Michael L Fanto, Christopher C Tison, Zihao Wang, Paul M Alsing, and Stefan F Preble; SPIE Commercial+ Scientific Sensing and Imaging, pp. 987304-987304. International Society for Optics and Photonics, 2016; Rochester Institute of Technology, 2016.

"Electrically Gated Three-Terminal Circuits and Devices Based on Spin Hall Torque Effects in Magnetic Nanostructures"; Buhrman, Robert, Luqiao Liu, Chi-Feng Pai, Daniel Ralph; Patent Docket # 6029-03-US, United States, Issued, 2/6/15, 14/420,335, 1/5/16, 9,230,626; Cornell University, 2016.

"Electrically Gated Three-Terminal Circuits and Devices Based on Spin Hall Torque Effects in Magnetic Nanostructures"; Buhrman, Robert, Luqiao Liu, Chi-Feng Pai, Daniel Ralph; Patent Docket # 6029-04-KR, South Korea, Issued, 3/6/15, 10-2015-7006023, 8/16/16, 10-1649978; Cornell University, 2016.

"Electrically Gated Three-Terminal Circuits and Devices Based on Spin Hall Torque Effects in Magnetic Nanostructures Apparatus, Methods and Applications"; Buhrman, Robert, Luqiao Liu, Chi-Feng Pai, Daniel Ralph; Patent Docket # 6029-06-US, United States, Issued, 12/31/15, 14/986,331, 11/22/16, 9,502,087; Cornell University, 2016.

"Electrically Gated Three-Terminal Circuits and Devices Based on Spin Hall Torque Effects in Magnetic Nanostructures Apparatus, Methods and Applications"; Buhrman, Robert, Luqiao Liu, Chi-Feng Pai, Daniel Ralph; Patent Docket # 6029-07-US, United States, CON - Continuation, Filed, 11/21/16, 15/357,391; Cornell University, 2016.

"Electrically gated three-terminal circuits and devices based on spin hall torque effects in magnetic nanostructures apparatus, methods and applications"; Buhrman, Robert A, Daniel C Ralph, Chi-Feng Pai, and Luqiao Liu; U.S. Patent 9,230,626, issued January 5, 2016; Cornell University, 2016.

"Electrically gated three-terminal circuits and devices based on spin hall torque effects in magnetic nanostructures apparatus, methods and applications"; Buhrman, Robert A, Daniel C Ralph, Chi-Feng Pai, and Luqiao Liu; U.S. Patent 9,502,087, issued November 22, 2016; Cornell University, 2016.

"Electrically gated three-terminal circuits and devices based on spin hall torque effects in magnetic nanostructures apparatus, methods and applications"; Buhrman, Robert A, Daniel C Ralph, Chi-Feng Pai, and Luqiao Liu; U.S. Patent Application 15/357,391, filed November 21, 2016; Cornell University, 2016.

"Electro-Ultrasonic Devices for Nerve Stimulation and Treatment"; Lal, Amit; Patent Docket # 7004-02-US, United States, US from PCT, Filed, 3/16/16, 15/072,232; Cornell University, 2016.

"Emergent Network Topology within the Respiratory Rhythm-Generating Kernel Evolved In Silico"; Lal, Amit; Oku, Yoshitaka; Someya, Hiroshi; Miwakeichi, Fumikazu; Tamura, Yoshiyasu; PloS One, Vol. 11, Issue 5, pgs. e0154049; Cornell University, 2016.

"Encapsulation and transport properties of quantum dot thin-film transistors using scanning Kelvin probe force microscopy"; Tirmzi, S A M, R P Dwyer, T Hanrath, and J A Marohn; Materials Research Society Fall Meeting; Boston, Massachusetts; November 27 - December 2, 2016; Cornell University, 2016.

"Enhanced spin Hall ratios by Al and Hf impurities in Pt thin films"; Nguyen, Minh-Hai, Mengnan Zhao, Daniel C Ralph, and Robert A Buhrman; APS Meeting Abstracts. 2016; Cornell University, 2016.

"Enhanced spin Hall torque efficiency in Pt100-xAlx and Pt100-xHfx alloys arising from the intrinsic spin Hall effect"; Nguyen, MH, MN Zhao, DC Ralph, and RA Buhrman; Applied Physics Letters 108, 242407, (2016), 10.1063/1.4953768; Cornell University, 2016.

"ESCRT-III proteins CHMP7 and CHMP4B mediate nuclear membrane repair during interphase"; Isermann P, Denais CM, Gilbert RM, Lammerding J Poster presentation selected from submitted abstract; American Society for Cell Biology (ASCB) Annual Meeting. San Francisco, CA (December 4, 2016); Cornell University, 2016.

"Ethics Information Seeking and Sharing Among Scientists: The Case of Nanotechnology"; Kahlor, Lee Ann; Dudo, Anthony; Liang, Ming-Ching; Lazard, Allison J; AbiGhannam, Niveen; Science Communication, Vol. 38, Issue 1, pgs. 74-98; The University of Texas at Austin, 2016.

"EUV metal oxide photoresists: finding common features between systems"; Ober, Christopher K, invited talk; Lithography Workshop, Kona, HI, Nov. 6-10, 2016; Cornell University, 2016.

"Exceptional Terahertz Wave Modulation in Graphene Enhanced by Frequency Selective Surfaces"; Yan, Rusen; Arezoomandan, Sara; Sensale-Rodriguez, Berardi; Xing, Huili Grace; ACS Photonics, Vol 3, Issue 3, pgs 315-323; Cornell University, 2016.

"Experimental Demonstration of a Resonator-Induced Phase Gate in a Multiqubit Circuit-QED System"; Paik, H, A Mezzacapo, M Sandberg, DT McClure, B Abdo, AD Córcoles, O Dial, DF Bogorin, BLT Plourde, M Steffen, AW Cross, JM Gambetta, JM Chow; Phy Review Letters 117, 250502 (2016); Syracuse Univ, 2016.

"Experimental determination of the rate of water filling of large diameter carbon nanotubes"; Pilgrim, Gregory A; Nano/Micro Engineered and Molecular Systems (NEMS), 2016 IEEE 11th Annual International Conference on, pgs. 540-544; University of Rochester, 2016.

"Experimental Study of Electronic Quantum Interference, Photonic Crystal Cavity, Photonic Band Edge Effects for Optical Amplification"; Lin, Shawn-Yu; No. AFRL-RV-PS-TR-2016-0003. Rensselaer Polytechnic Institute Troy United States, 2016; Rensselaer Polytechnic Institute, 2016.

"Explorations and discoveries in Slonczewski torque"; Buhrman, R A, Invited Lecture; IBM 20th Anniversary Spin-Torque MRAM Symposium, IBM T.J. Watson Research Center, Yorktown Heights, NY November 7, 2016; Cornell University, 2016.

"Extending the Capabilities of Heterodyne-Detected Sum-Frequency Generation Spectroscopy: Probing Any Interface in Any Polarization Combination"; Vanselous, Heather; Petersen, Poul B; Journal of Physical Chemistry C, Vol. 120, Issue 15, pgs. 8175-8184; Cornell University, 2016.

"Fabrication of a Vascular System Using Sacrificial Structures"; Bellan, Leon, Harold Craighead, Jason Spector; Patent Docket # 4343-03-US, United States, Issued, 4/15/11, 13/054,450, 1/26/16, 9,242,027; Cornell University, 2016.

"Fabrication of a vascular system using sacrificial structures"; Craighead, H; U.S. Patent #9,242,027 issued January 26, 2016; Cornell University, 2016.

"Fermi Level Tunability of A Novel 2D Crystal: Tin Diselenide (SnSe2)"; Lit, Mingda; Xiao, Shudong; Yan, Rusen; Vishwanathl, Suresh; Fullerton-Shirey, Susan; Jena, Debdeep; Xing, Huili Grace; 2016 74th Annual Device Research Conference (drc); Cornell University, 2016.

"Ferromagnetic resonance phase imaging in spin Hall multilayers"; Guo, Feng; Bartell, Jason M; Fuchs, Gregory D; Physical Review B, Vol. 14, pg. 93, 144415 (2016); Cornell University, 2016.

"Few-nanosecond pulse switching with low write error for in-plane nanomagnets using the spin-Hall effect"; Aradhya, Sriharsha, Graham Rowlands, Shengjie Shi, Junseok Oh, D C Ralph, and Robert Buhrman; APS Meeting Abstracts. 2016; Cornell University, 2016.

"Fiber-based platforms for bioanalytics"; Marcus, R Kenneth; Baeumner, Antje J; Analytical and Bioanalytical Chemistry, Vol. 408, Issue 5, pgs. 1281-1283; Cornell University, 2016.

"Fibrous nonlinear elasticity enables positive mechanical feedback between cells and ECMs"; Hall, Matthew S, Farid Alisafaei, Ehsan Ban, Xinzeng Feng, Chung-Yuen Hui, Vivek B Shenoy, and Mingming Wu; PNAS doi:10.1073/pnas.1613058113 (2016); Cornell University, 2016.

"Fifty Years of Moore's Law: Towards fabrication at molecular dimensions"; Ober, Christopher K, invited talk; 2016 Rauscher Memorial Lecture in Chemistry, Rensselaer Polytechnic Institute, Rensselaer, NY, Oct. 25, 2016; Cornell University, 2016.

"Fifty Years of Moore's Law: Towards fabrication at molecular dimensions"; Ober, Christopher K, invited talk; Department of Chemistry Seminar, UNC Charlotte, Charlotte, NC, Jan. 14, 2016; Cornell University, 2016.

"Fifty Years of Moore's Law: Towards fabrication at molecular dimensions"; Ober, Christopher K, invited talk; Joint School of Nanoengineering and Nanoscience (JSNN) Seminar, UNC Greensboro, Greensboro, NC, Jan. 15, 2016; Cornell, 2016.

"Fifty Years of Moore's Law: Towards fabrication at molecular dimensions"; Ober, Christopher K, invited talk; LBL Seminar, Berkeley, CA, May 17, 2016; Cornell University, 2016.

"Fifty Years of Moore's Law: Towards fabrication at molecular dimensions"; Ober, Christopher K, invited talk; Tufts University CBE Dept Seminar, Boston, MA, May 2, 2016; Cornell, 2016.

"Fifty Years of Moore's Law: What is next in nanoscale fabrication?"; Ober, Christopher K, invited talk; Clemson Materials Science and Engineering Colloquium, Clemson University, Clemson, SC, Oct. 21, 2016; Cornell University, 2016.

"First Demonstration of Strained AlN/GaN/AlN Quantum Well FETs on SiC"; Islam, S M; Qi, Meng; Song, Bo; Nomoto, Kazuki; Protasenko, Vladimir; Wang, Jingshan; Rouvimov, Sergei; Faye, Patrick; Xing, Huili; Jena, Debdeep; 2016 74th Annual Device Research Conference (drc); Cornell University, 2016.

"First demonstration of strained AlN/GaN/AlN quantum well FETs on SiC"; Islam, S M, Meng Qi, Bo Song, Kazuki Nomoto, Vladimir Protasenko, Jingshan Wang, Sergei Rouvimov, Patrick Fay, Huili Grace Xing, and Debdeep Jena; Device Research Conference (DRC), 2016 74th Annual, pp. 1-2. IEEE, 2016; Cornell, 2016.

"First Person: Michael Spencer"; Spencer, Michael; American Scientist, Vol. 104, Issue 4, pgs. 201-202; Cornell University, 2016.

"Flash Track Practices Distilled via Structured Interviews from EPC Projects"; Pishdad-Bozorgi, Pardis; Austin, Robert; De La Garza, Jesus M; Construction Research Congress 2016: Old and New Construction Technologies Converge in Historic San Juan, pgs. 168-178; Princeton University, 2016.

"Flow boiling heat transfer of HFE-7000 in nanowire-coated microchannels"; Yang, Fanghao; Li, Wenming; Dai, Xianming; Li, Chen; Applied Thermal Engineering, Vol. 93, pgs. 260-268; University of South Carolina, 2016.

"Fluidic Actuators for Sensorimotor Feedback in Brain-Driven Scenarios with Magnetoencephalogaphy Recordings"; Heinze, Nicolai, Tim Pfeiffer, Robert Shepherd, Huichan Zhao; Patent Docket # 7495-01-US, United States, EPR - Enhanced Provisional, Filed, 10/28/16, 62/414,439; Cornell University, 2016.

"Fluidic Actuators for Sensorimotor Feedback in Brain-Driven Scenarios with Magnetoencephalogaphy Recordings"; Shepherd, Robert; Patent Docket # 7495, Filed - by Cornell, 7/14/16, Invention; Cornell University, 2016.

"Folded graphene nanochannels via pulsed patterning of graphene"; Lacerda, Rodrigo G, Ive Silvestre, Arthur W Barnard, Samantha P Roberts, and Paul McEuen; APS Meeting Abstracts. 2016; Cornell University, 2016.

"Force analysis and bubble dynamics during flow boiling in silicon nanowire microchannels"; Alam, Tamanna; Li, Wenming; Yang, Fanghao; Chang, Wei; Li, Jing; Wang, Zuankai; Khan, Jamil; Li, Chen; International Journal of Heat and Mass Transfer, Vol. 101, pgs. 915-926; University of South Carolina, 2016.

"Functionalized electrospun poly (vinyl alcohol) nanofibers for on-chip concentration of E. coli cells"; Matlock-Colangelo, Lauren; Coon, Barbara; Pitner, Christine L; Frey, Margaret W; Baeumner, Antje J; Analytical and bioanalytical chemistry, Vol. 408, Issue 5, pgs. 1327-1334; Cornell University, 2016.

"GaN tunnel switch diodes"; Chaney, Alexander, Meng Qi, S M Islam, Huili Grace Xing, and Debdeep Jena; Device Research Conference (DRC), 2016 74th Annual, pp. 1-2. IEEE, 2016; Cornell, 2016.

"GaN Tunnel Switch Diodes"; Chaney, Alexander; Qi, Meng; Islam, S M; Xing, Huili; Jena, Debdeep; 2016 74th Annual Device Research Conference (drc); Cornell University, 2016.

"Gated III-V Semiconductor Structure and Method"; Brown, Richard, James Shealy; Patent Docket # 5018-03-US, United States, Issued, 3/8/13, 13/389,127, 3/29/16, 9,299,821; Cornell University, 2016.

"Gated III-V Semiconductor Structure and Method"; Brown, Richard, James Shealy; Patent Docket # 5018-04-CN, China, Issued, 3/28/12, CN201180004026.8, 1/27/16, ZL201180004026.8; Cornell University, 2016.

"Generation of dual frequency combs using cascaded microring resonators"; Dutt, Avik, et al; CLEO: Science and Innovations. Optical Society of America, 2016; Columbia University, 2016.

"Giant Resistive Switching via Control of Ferroelectric Charged Domain Walls"; Li, Linze; Britson, Jason; Jokisaari, Jacob R; Zhang, Yi; Adamo, Carolina; Melville, Alexander; Schlom, Darrell G; Chen, Long-Qing; Pan, Xiaoqing; Advanced Materials, Vol. 28, Issue 31, pgs. 6574-6580; Cornell University, 2016.

"GPU-accelerated micromagnetic simulations using cloud computing"; Jermain, C L; Rowlands, G E; Buhrman, R A; Ralph, D C; Journal of Magnetism and Magnetic Materials, Vol. 401, pgs. 320-322; Cornell University, 2016.

"Graphene Resonator Based Mixer-First Receiver on CMOS for Digitally Controlled and Widely Tunable RF Interface"; Hone, James, Sunwoo Lee, Changhyuk Lee, Alyosha Molnar; Patent Docket # 6724-02-US, United States, Issued, 11/24/14, 14/552,449, 5/17/16, 9,344,127; Cornell University, 2016.

"Graphene-enhanced plasmonic nanohole arrays for environmental sensing in aqueous samples"; Genslein, Christa; Hausler, Peter; Kirchner, Eva-Maria; Bierl, Rudolf; Baeumner, Antje J; Hirsch, Thomas; Beilstein Journal of Nanotechnology, Vol. 7, pgs. 1564-1573; Cornell University, 2016.

"Group members presented contributed talks"; Buhrman Group; 2016 Magnetism and Magnetic Materials Conference in New Orleans, November 1-4 2016; Cornell University, 2016.

"Group members presented contributed talks"; Buhrman Group; 2016 March Meeting of the American Physical Society, March 14-18, 2016. Baltimore, MD; Cornell University, 2016.

"Gyroscope Based on Optomechanical Sensing"; Bhave, S., R. Wang; Patent Docket # 5520-03-US, United States, Issued, 5/28/14, 14/232,880, 12/27/16, 9,528,829; Cornell University, 2016.

"Handheld chem/biosensor using extreme conformational changes in designed binding proteins to enhance surface plasmon resonance (SPR)"; Lepak, Lori A; Schnatz, Peter; Bendoym, Igor; Kosciolek, Derek; Koder, Ronald; Crouse, David T; SPIE 9862 Proc., Advanced Environmental, Chemical, and Biological Sensing Technologies XIII, 9862-7 (17 April 2016); doi:10.1117/12.2222305; City College of New York, 2016.

"Handheld chem/biosensor using extreme conformational changes in designed binding proteins to enhance surface plasmon resonance (SPR)"; Lepak, Lori A; Schnatz, Peter; Bendoym, Igor; Kosciolek, Derek; Koder, Ronald; Crouse, David T; SPIE Commercial+ Scientific Sensing and Imaging, pgs. 986208-986208; City College of New York, 2016.

"Handheld Chem/biosensor Using Supercharged Binding Proteins to Enhance Surface Plasmon Resonance (SPR)"; Lepak, L, Schnatz, P, Bendoym, I, Kosciolek, D, Koder, R, and Crouse, DT; SPIE Commercial + Scientific Sensing and Imaging, Conference #9862, Advanced Environmental, Chemical, and Biological Sensing Technologies XIII,, Baltimore, MD, 17 April 2016; City College of New York, 2016.

"Hard and Soft Physics with 2D Materials"; McEuen, Paul; APS Meeting Abstracts. 2016; Cornell University, 2016.

"Heralding single photons from a high-Q silicon microdisk"; Lu, X, S Rogers, T Gerrits, W C Jiang, S W Nam, and Q Lin; Optica 3, 1331 (2016); University of Rochester, 2016.

"High Dynamic Range Pixel Array Detector for Scanning Transmission Electron Microscopy"; Tate, M W, P Purohit, D Chamberlain, K X Nguyen, R M Hovden, C S Chang, P Deb, E Turgut, J T Heron, D G Schlom, D C Ralph, G D Fuchs, K S Shanks, H T Philipp, D A Muller, and S M Gruner; Microscopy and Microanalysis, Vol. 22, Issue 1, pgs. 237-249; Cornell, 2016.

"High Mobility Of Sputtered In2Ga2Zno7 (Igzo) Thin Film Transistors (Tfts)"; Chung, Chen-Yang; https://ecommons.cornell.edu/handle/1813/44274; Cornell University, 2016.

"High Performance Electrodes"; Fei, Ling, Seon Gong, Yong Joo, Sunchan Park; Patent Docket # 7167-02-US, United States, MPR - Manuscript Provisional, Converted, 3/24/16, 62/312,871; Cornell University, 2016.

"High Performance Electrodes"; Fei, Ling, Seon Gong, Yong Joo, Sunchan Park; Patent Docket # 7167-03-PC, Not Applicable (PCT App), PCT - Patent Cooperation Treaty, Filed, 11/10/16, PCT/US16/61404; Cornell University, 2016.

"High Performance Electrodes"; Fei, Ling, Seon Gong, Yong Joo, Sunchan Park; Patent Docket # 7167-04-KR, South Korea, FOR - Foreign, Filed, 12/30/16, 10-2016-7037051; Cornell, 2016.

"High Performance Wick"; Stroock, Abraham; Tobias Wheeler; Patent Docket # 4197-04-EP, Europe, Issued, 12/3/10, 9743458.3, 2/10/16, 2288430; Cornell University, 2016.

"High Performance Wick"; Stroock, Abraham; Tobias Wheeler; Patent Docket # 4197-06-ES, Spain, Issued, 12/3/10, ES 2570980 T3, 2/10/16, 2288430; Cornell University, 2016.

"High Performance Wick"; Stroock, Abraham; Tobias Wheeler; Patent Docket # 4197-07-NL, Netherlands, Issued, 12/3/10, EP09743458.3, 2/10/16, 2288430; Cornell University, 2016.

"High Performance Wick"; Stroock, Abraham; Tobias Wheeler; Patent Docket # 4197-08-DE, Germany, Issued, 12/3/10, EP09743458.3, 2/10/16, 2288430; Cornell University, 2016.

"High Performance Wick"; Stroock, Abraham; Tobias Wheeler; Patent Docket # 4197-09-FR, France, Issued, 12/3/10, EP09743458.3, 2/10/16, 2288430; Cornell University, 2016.

"High quality factor Si3N4 ring resonators achieved by surface roughness reduction"; Ji, X, Barbosa, F A, Bryant, A, Cardenas, J, Roberts, S P, and Lipson, M; Lasers and Electro-Optics (CLEO), 2016 Conference on (pp. 1-2). IEEE. (2016, June); Columbia University, 2016.

"High visibility time-energy entangled photons from a silicon nanophotonic chip"; Rogers, Steven; Mulkey, Daniel; Lu, Xiyuan; Jiang, Wei C; Lin, Qiang; ACS Photonics, Vol. 3, Issue 10, pgs. 1754-1761; University of Rochester, 2016.

"High visibility time-energy entangled photons from a silicon nanophotonic chip"; Rogers, Steven; Mulkey, Daniel; Lu, Xiyuan; Jiang, Wei C; Lin, Qiang; CLEO/QELS Proceedings, Conf. Laser and Electro-Optics/Quantum Electronis and Laser Science, FM2N.3 (2016); University of Rochester, 2016.

"High voltage 4H-SiC Bi-directional IGBTs"; Chowdhury, S; Hitchcock, C; Dahal, R; Bhat, I B; Chow, T P; 2016 28th International Symposium on Power Semiconductor Devices and ICs (ISPSD); Rensselaer Polytechnic Institute, 2016.

"High Voltage 4H-SiC Bi-Directional IGBTs"; Chowdhury, S; Hitchcock, C; Dahal, R; Bhat, I B; Chow, T P; 2016 28th International Symposium on Power Semiconductor Devices and Ics (ispsd), pgs. 463-466; Rensselaer Polytechnic Institute, 2016.

"High-bandwidth link with single laser input using silicon modulators and mode multiplexing"; Stern, Brian, and Michal Lipson; Lasers and Electro-Optics (CLEO), 2016 Conference on. IEEE, 2016; Columbia University, 2016.

"High-quality InN films on GaN using graded InGaN buffers by MBE"; Islam, S M; Protasenko, Vladimir; Rouvimov, Sergei; Xing, Huili; Jena, Debdeep; Japanese Journal of Applied Physics, Vol. 55, Issue 5, pgs 05FD12; Cornell University, 2016.

"High-speed optical sampling by temporal stretching using four-wave mixing"; Lipson, Michal, et al; U.S. Patent No. 9,291,509. 22 Mar. 2016; Columbia University, 2016.

"High-Throughput Detection of Thiamine Using Periplasmic Binding Protein-Based Biorecognition"; Edwards, Katie A; Seog, Woo Jin; Han, Lu; Feder, Seth; Kraft, Clifford E; Baeumner, Antje J; Analytical Chemistry, Vol. 88, Issue 16, pgs. 8248-8256; Cornell University, 2016.

"Highly multiplexed RNA aptamer selection using a microplate-based microcolumn device"; Reinholt, Sarah J; Ozer, Abdullah; Lis, John T; Craighead, Harold G; Scientific Reports, Vol. 6; Cornell University, 2016.

"HORSE-SHOE: High Operational Rate and Shock Enabled SAW H-filed Optical EIT Inertial Sensors"; Lal, Amit; Patent Docket # 7370, Filed - by Cornell, 3/2/16, Invention; Cornell, 2016.

"How Escherichia coli lands and forms cell clusters on a surface: a new role of surface topography"; Gu, Huan; Chen, Aaron; Song, Xinran; Brasch, Megan E; Henderson, James H; Ren, Dacheng; Scientific Reports, Vol. 6; Syracuse University, 2016.

"How to connect time-lapse recorded trajectories of motile microorganisms with dynamical models in continuous time"; Pedersen, Jonas N; Li, Liang; Gradinaru, Cristian; Austin, Robert H; Cox, Edward C; Flyvbjerg, Henrik; Physical Review E, Vol. 94, Issue 6, pgs. 62401; Princeton University, 2016.

"Human "Body-on-a-Chip" devices as a tool to improve drug development"; Shuler, ML (Keynote Address); Select Bio, Lab-on-a-Chip, Microfluidics and Microarrays World Congress. San Diego, CA. Sept 26-28, 2016; Cornell University, 2016.

"Hydroxyl Radical Generation and DNA Nuclease Activity: A Mechanistic Study Based on a Surface-Immobilized Copper Thioether Clip-Phen Derivative"; Romo, A; Abreu, D; Paulo, T; Carepo, M Sousa, E; Lemus, L; Aliaga, C; Batista, A; Nascimento, O; Abruna, H; Diogenes, I; Chemistry-a European Journal, Vol. 22, Issue 29, pgs. 10081-10089; Cornell University, 2016.

"Identifying and Prioritizing Best Practices to Achieve Flash Track Projects"; Austin, Robert B; Pishdad-Bozorgi, Pardis; de la Garza, Jesus M; Journal of Construction Engineering and Management, Vol. 142, Issue 2, pgs. 4015077; Princeton University, 2016.

"III-V Semiconductor Structures Including Aluminum-Silicon Nitride Passivation"; Brown, Richard, James Shealy; Patent Docket # 5017-02-US, United States, Issued, 3/2/12, 13/380,104, 4/5/16, 9,306,050; Cornell University, 2016.

"Image restoration and analysis of influenza virions binding to membrane receptors reveal adhesion-strengthening kinetics"; Lee, DW; Hsu, H-L; Bacon, KB; Daniel, S; PloS One, Vol. 11, Issue 10, pgs. e0163437; Cornell University, 2016.

"Imaging Magnetization Structure and Dynamics in Ultrathin YIG/Pt Bilayers with High Sensitivity Using the Time-Resolved Longitudinal Spin Seebeck Effect"; Bartell, JM; Jermain, CL; Aradhya, SV; Brangham, JT; Yang, F; Ralph, DC; Fuchs, GD; arXiv preprint arXiv:1612.07610; Cornell University, 2016.

"Imaging precessional phase variations in spin Hall devices using picosecond heat pulses"; Guo, Feng, J M Bartell, G D Fuchs; March Meeting of the American Physical Society Bulletin, 2016, Baltimore, MD; Cornell University, 2016.

"Imbibition triggered by capillary condensation in nanopores"; Vincent, Olivier; Marguet, Bastien; Stroock, Abraham; arXiv preprint arXiv:1612.06684; Cornell University, 2016.

"Implantable Therapeutic Delivery System and Methods Thereof"; An, Duo, James Flanders, Minglin Ma; Patent Docket # 6480-03-US, United States, US from PCT, Filed, 12/9/16, 15/317,657; Cornell University, 2016.

"In situ electrochemical characterization of poly-3,4-ethylenedioxythiophene/tetraalkylphenylene diamine films and their potential use in electrochemical energy storage devices"; Rodriguez-Calero, Gabriel G; Conte, Sean; Lowe, Michael A; Burkhardt, Stephen E; Gao, Jie; John, Jimmy; Hernandez-Burgos, Kenneth; Abruna, Hector D; Journal of Electroanalytical Chemistry, Vol. 765, pgs. 65-72; Cornell University, 2016.

"In Situ Measurements of Graphene Mechanics During Annealing"; Hui, A, R De Alba, A Sebastian, J Parpia; March Meeting 2016 Abstract ID: BAPS.2016.MAR.A17.9; Cornell University, 2016.

"In-Run Scale factor and Drift Calibration of MEMS Gyroscopes with Rejection of Acceleration Sensitivities"; Nadig, Sachin; Pinrod, Visarute; Ardanuc, Serhan; Lal, Amit; 2016 3rd IEEE International Symposium on Inertial Sensors and Systems, pgs. 144-145; Cornell University, 2016.

"Inertial Measurement Unit Calibration Stage, Method and Applications"; Lal, Amit; Patent Docket # 7250-02-PC, Not Applicable (PCT App), PCT - Patent Cooperation Treaty, Filed, 10/31/16, PCT/US2016/059679; Cornell University, 2016.

"Innovations in Knowledge Management The Impact of Social Media, Semantic Web and Cloud Computing Foreword"; Austin, Robert D; Innovations in Knowledge Management: The Impact of Social Media, Semantic Web and Cloud Computing, Vol. 95, pgs. V-VII; Princeton University, 2016.

"Inorganic Bulk Multijunction Materials and Processing for Preparing Same"; Engstrom, James, Tobias Hanrath; Patent Docket # 4308-03-CN, China, Issued, 8/10/09, 200980137196.6, 10/26/16, ZL200980137196.6; Cornell University, 2016.

"Integrated Circuits Based Biosensors"; Gund, Ved, Amit Lal; Patent Docket # 6595-03-US, United States, US from PCT, Allowed, 7/27/16, 15/114,814; Cornell University, 2016.

"Integrated Circuits Based Biosensors"; Gund, Ved, Amit Lal; Patent Docket # 6595-04-EP, Europe, EPC - European Patent Convention, Filed, 8/29/16, 15739947.8; Cornell University, 2016.

"Integrated polarized light emitting diode with a built-in rotator"; Lin, Shawn-Yu, Yong Sung Kim, and Mei-Li Hsieh; U.S. Patent 9,362,460, issued 6/7/16; Rensselaer Polytechnic Institute, 2016.

"Integrated thermal tuning of suspended micro-resonators"; Lee, B S, Zhang, M, Barbosa, F A, Miller, S, Mohanty, A, and Lipson, M; CLEO: Science and Innovations (pp. SF2P-2). Optical Society of America. (2016, June); Columbia University, 2016.

"Integration of InAs QD comb lasers with silicon photonics ring resonators"; Yao, Ruizhe, Zihao Wang, Stefan Preble, Chi-Sen Lee, and Wei Guo; Progress in Electromagnetic Research Symposium (PIERS), pp. 3163-3163. IEEE, 2016; Rochester Institute of Technology, 2016.

"Intra-molecular triplet energy transfer is a general approach to improve organic fluorophore photostability"; Zheng, Qinsi; Jockusch, Steffen; Rodriguez-Calero, Gabriel G; Zhou, Zhou; Zhao, Hong; Altman, Roger B; Abruna, Hector D; Blanchard, Scott C; Photochemical & Photobiological Sciences, Vol. 15, Issue 2, pgs. 196-203; Cornell University, 2016.

"Intrinsic electron mobility limits in beta-Ga2O3"; Ma, Nan; Tanen, Nicholas; Verma, Amit; Guo, Zhi; Luo, Tengfei; Xing, Huili Grace; Jena, Debdeep; Applied Physics Letters, Vol. 109, Issue 21, pgs 212101; Cornell University, 2016.

"Investigation of Forward Transient Characteristics of Vertical GaN-on-GaN p-n Diodes"; Miao, Meng; Liou, Juin J; Song, Bo; Nomoto, Kazuki; Xing, Huili Grace; Salcedo, Javier A; Hajjar, Jean-Jacques; Nanoelectronics Conference (INEC), 2016 IEEE International, pp. 1-2. IEEE, 2016; Cornell University, 2016.

"Investigations of a transmon-coupled nanoresonator in a CPW cavity"; Hao, Yu; American Physical Society March Meeting - Baltimore, MD, 17 March 2016; Syracuse University, 2016.

"Is nanotech failing casual learners?"; Maynard, Andrew D; http://www.nature.com/nnano/journal/v11/n9/full/nnano.2016.167.html; Arizona State University, 2016.

"Kinetics of Block Copolymer Phase Segregation during Sub-millisecond Transient Thermal Annealing"; Jacobs, Alan G; Liedel, Clemens; Peng, Hui; Wang, Linxi; Smilgies, Detlef-M; Ober, Christopher K; Thompson, Michael O; Macromolecules, Vol. 49, Issue 17, pgs. 6462-6470; Cornell University, 2016.

"Kirigami graphene transistors for biological sensing"; Reynolds, Michael, Morgan Brown, Kathryn McGill, Patricia Davidson, Jan Lammerding, Ethan Minot, Jesse Goldberg, and Paul McEuen; APS Meeting Abstracts. 2016; Cornell University, 2016.

"KS-Detect-validation of solar thermal PCR for the diagnosis of Kaposi's sarcoma using pseudo-biopsy samples"; Snodgrass, Ryan; Gardner, Andrea; Jiang, Li; Fu, Cheng; Cesarman, Ethel; Erickson, David; PloS One, Vol. 11, Issue 1, pgs. e0147636; Cornell University, 2016.

"Lamins modulate nuclear mechanics, migration efficiency, and nuclear envelope integrity during cancer cell migration in confined 3-D environments"; Lammerding J Platform presentation selected from submitted abstract; American Society for Cell Biology (ASCB) Annual Meeting. San Francisco, CA (December 4, 2016); Cornell University, 2016.

"Large-scale arrays of single- and few-layer MoS2 nanomechanical resonators"; Jia, Hao; Yang, Rui; Nguyen, Ariana E; Alvillar, Sahar Naghibi; Empante, Thomas; Bartelsb, Ludwig; Feng, Philip X-L; Nanoscale, Vol. 8, Issue 20, pgs. 10677-10685; Case Western Reserve University, 2016.

"Lateral Temperature-Gradient Method for High-Throughput Characterization of Material Processing by Millisecond Laser Annealing"; Bell, Robert T; Jacobs, Alan G; Sorg, Victoria C; Jung, Byungki; Hill, Megan O; Treml, Benjamin E; Thompson, Michael O; ACS Combinatorial Science, Vol. 18, Issue 9, pgs. 548-558; Cornell University, 2016.

"Layered transition metal dichalcogenides: promising near-lattice-matched substrates for GaN growth"; Gupta, P; Rahman, A; Subramanian, S Gupta, S; Thamizhavel, A; Orlova, T; Rouvimov, S; Vishwanath, S; Protasenko, V; Laskar, M; Xing, H; Jena, D; Bhattacharya, A; Scientific Reports, Vol. 6, pgs 23708; Cornell University, 2016.

"Leading in the Age of Super-Transparency"; Austin, Robert D; Upton, David M; Mit Sloan Management Review, Vol. 57, Issue 2, pgs. 25-+; Princeton University, 2016.

"LF-powered, piezo-surface acoustic wave apparatus and method"; Lal, Amit, Steven Tin; Patent Docket # 4603-06-KR, South Korea, FOR - Foreign DIV, Allowed, 7/22/16, 10-2016-7020153; Cornell University, 2016.

"Light Field Image Sensor, Method and Applications"; Molnar, Alyosha, Albert Wang; Patent Docket # 4337-05-KR, South Korea, Issued, 2/23/11, 10-2011-7004231, 6/2/16, 10-1629044; Cornell University, 2016.

"LINC Complex Disruption Enhances Nuclear Deformability And Cell Transit Through Narrow Constrictions"; Fedorchak G, Patel J, Davidson P, Lammerding J Platform presentation selected from submitted abstract; Biomedical Engineering Society (BMES) Annual Meeting. Minneapolis, MN (October 6, 2016); Cornell University, 2016.

"Linear graphene on silicon nitride electroabsorption modulators for RF-over-fiber links"; Phare, C T, Cardenas, J, Lee, Y H D, and Lipson, M; CLEO: Science and Innovations (pp. SF2G-2). Optical Society of America. (2016, June); Columbia University, 2016.

"Lone-pair stabilization in transparent amorphous tin oxides: a potential route to p-type conduction pathways"; Wahila, M; Butler, K; Lebens-Higgins, Z; Hendon, C; Nandur, A; Treharne, R; Quackenbush, N; Sallis, S; Mason, K; Paik, H; others; Chemistry of Materials, Vol. 28, Issue 13, pgs. 4706-4713; Cornell, 2016.

"Long wavelength optical response of graphene-MoS2 heterojunction"; Kwak, Joon Young; Hwang, Jeonghyun; Calderon, Brian; Alsalman, Hussain; Spencer, Michael G; Applied Physics Letters, Vol. 108, Issue 9, pgs. 91108; Cornell University, 2016.

"Long-Term High-Resolution Imaging of Developing C. elegans Larvae with Microfluidics"; Keil, Wolfgang; Kutscher, Lena M; Shaham, Shai; Siggia, Eric D; Dev Cell. 2017 Jan 23;40(2):202-214. doi: 10.1016/j.devcel.2016.11.022. Epub 2016 Dec 29; Cornell University, 2016.

"Looking for evidence of photo-induced Marcus electron transfer in organic semiconductor films using scanned-probe photocapacitance measurements pushed to nanosecond time resolution"; Marohn, J A, S R Nathan, and R P Dwyer; Materials Research Society Fall Meeting; Boston, Massachusetts; November 27 - December 2, 2016; Cornell University, 2016.

"Low-cost fabrication of high efficiency solid-state neutron detectors"; Wu, Jia-Woei; Huang, Kuan-Chih; Weltz, Adam; English, Erik; Hella, Mona M; Dahal, Rajendra; Lu, James J-Q; Danon, Yaron; Bhat, Ishwara B; SPIE Defense+ Security, International Society for Optics and Photonics; Rensselaer Polytechnic Institute, 2016.

"Low-damping sub-10-nm thin films of lutetium iron garnet grown by molecular-beam epitaxy"; Jermain, C L, H Paik, S V Aradhya, R A Buhrman, D G Schlom, and D C Ralph; Applied Physics Letters 109, 192408, (2016), 10.1063/1.4967695; Cornell, 2016.

"Low-energy Consumption Quaternary Magnetoelectric Spin Hall Effect Based Logic and Memory Device"; Schlom, Darrell; Patent Docket # 7453, Filed - by Cornell, 6/1/16, Invention; Cornell University, 2016.

"Low-loss air-clad suspended silicon platform for mid-infrared photonics"; Miller, Steven, et al; CLEO: Science and Innovations. Optical Society of America, 2016; Columbia University, 2016.

"Low-power photothermal self-oscillation of bimetallic nanowires"; De Alba, Roberto, TS Abhilash, Richard Rand, Harold G Craighead and Jeevak M Parpia; Nano Letters (Under Consideration), November 2016 https://arxiv.org/abs/1610.07591; Cornell University, 2016.

"Low-resistance Ohmic Edge Contacts between Two-dimensional Materials for Large-scale Atomically-thin Circuitry"; Park, Jiwoong, Daniel Ralph; Patent Docket # 7404, Filed - by Cornell, 4/11/16, Invention; Cornell University, 2016.

"Manipulating Magnetic Devices with Spin-Orbit Torques"; Ralph, Daniel C; 2016 74th Annual Device Research Conference (drc); Cornell University, 2016.

"MBE Deep-UV LEDs on Bulk AlN Substrates"; Islam, Sm Moudud; Protasenko, Vladimir; Xing, Huili; Jena, Debdeep; 2016 Compound Semiconductor Week; Cornell University, 2016.

"Measurement of current-generated torques in transition metal dichalcogenide/ferromagnet bilayers"; Stiehl, Gregory M, David MacNeill, Marcos HD Guimarães, Hui Gao, Jiwoong Park, and Daniel C Ralph; APS Meeting Abstracts. 2016; Cornell, 2016.

"Measurement of DNA Translocation Dynamics in a Solid-State Nanopore at 100 ns Temporal Resolution"; Shekar, Siddharth, David J Niedzwiecki, Chen-Chi Chien, Peijie Ong, Daniel A Fleischer, Jianxun Lin, Jacob K Rosenstein, Marija Drndi, Kenneth L Shepard; Nano Letters, 2016, 16 (7), pp 4483-4489; Syracuse University, 2016.

"Measurement of Spin Torques in WTe2/Ferromagnet Bilayers"; MacNeill, D, GM Stiehl, MHD Guimarães, J Park, and DC Ralph; APS Meeting Abstracts. 2016; Cornell University, 2016.

"Measurement, Enhancement and Utilization of Spin Orbit Torques"; Buhrman, R A, Invited Lecture; Marie Curie School on Domain Wall Motion and Spintronics, Spetses, Greece, September 12-16, 2016; Cornell University, 2016.

"Measurements of nanoresonator-qubit interactions in a hybrid quantum electromechanical system"; Rouxinol, F; Hao, Y; Brito, F; Caldeira, A O; Irish, E K; LaHaye, M D; Nanotechnology, Vol. 27, Issue 36, pgs. 364003; Syracuse University, 2016.

"Measurements of Qubit-Nanoresonator Interactions in a Hybrid Quantum Electromechanical System"; Rouxinol, F, Hao, Y, Brito, F, Caldeira, AO, Irish, EK, & LaHaye, MD; Nanotechnology, Focus Session: Quantum Information 27, 36 (2016); Syracuse University, 2016.

"Measuring photo-capacitance transients in organic semiconductor films using a scanned probe microscopy cantilever as a mechanical integrator"; Dwyer, R P, S R Nathan, and J A Marohn; 58th Electronic Materials Conference; Newark, Delaware; June 22 - 24, 2016; Cornell University, 2016.

"Measuring photo-capacitance transients in organic semiconductor films with sub-cycle time resolution"; Dwyer, R P, S R Nathan, and J A Marohn; Materials Research Society Fall Meeting; Boston, Massachusetts; November 27 - December 2, 2016; Cornell University, 2016.

"Megatelescope releases its first image"; Austin, Robert; Physics Today, Vol. 69, Issue 12, pgs. 42-45; Princeton University, 2016.

"Method for Reducing Flow Resistance in Suspension Processing"; Cohen, Itai; Patent Docket # 7480, Filed - by Cornell, 6/29/16, Invention; Cornell University, 2016.

"Method for Reducing Sequence Bias in DNA Amplification"; Craighead, Harold, Harvey Tian; Patent Docket # 7443-01-US, United States, EPR - Enhanced Provisional, Converted, 5/22/16, 62/339,945; Cornell University, 2016.

"Methods and apparatus for event detection, propagation and localization using UWB impulse radios"; Dokania, Rajeev K.; Wang, Xiao Y.; Dorta-Quinones, Carlos I.; Godycki, Waclaw; Apsel, Alyssa B.; Patent Number: US 9468038 B2, PCT/US2011/034765, 11. Okt. 2016; Cornell University, 2016.

"Methods and Apparatus for high-throughput formation of nano-scale arrays"; Craighead, H; Patent Application Number 13/389/113 filed; Cornell University, 2016.

"Methods and Apparatus for High-Throughput Formation of Nano-scale Arrays"; Craighead, Harold, David Lin, Christine Tan; Patent Docket # 4869-04-US, United States, Issued, 4/5/12, 13/389,113, 11/15/16, 9,493,022; Cornell University, 2016.

"Methods and apparatus for high-throughput formation of nano-scale arrays"; Craighead, H; U.S. Patent #9,493,022 issued November 15, 2016; Cornell University, 2016.

"Methods for Reducing Sequence Bias in DNA amplification"; Craighead, H; Provisional patent application CU ID 7443 5/22/2016; Cornell University, 2016.

"Methods of Making Patterned Structures of Materials, Patterned Structures of Materials, and Methods of Using Same"; Chan, Wei, Jin-Kyun Lee, Christopher Ober, Evan Schwartz, Sandip Tiwari; Patent Docket # 5266-03-US, United States, Issued, 4/2/14, 14/005,964, 7/12/16, 9,389,511; Cornell University, 2016.

"Microcontact-printed hydrogel microwell arrays for clonal muscle stem cell cultures"; Aguilar VM, Cosgrove BD; Methods in Molecular Biology: Skeletal Muscle Development, ed: Ryall J. Springer Science + Business Media. (in press); Cornell University, 2016.

"Microenvironment-on-chip: Development of a microfluidics-based tumor ecosystem"; Torga, G; Lin, K-C; Austin, RH; Pienta, KJ; Cancer Research, Vol. 76; Princeton University, 2016.

"Microfluidic Chip Having On-chip Electrically Tunable High-Throughput Nanophotonic Trap"; Lin, Jun, Michal Lipson, Summer Saraf, Mohammad Soltani, Michelle Wang; Patent Docket # 6163-03-US, United States, Issued, 6/22/15, 14/654,839, 9/6/16, 9,433,941; Cornell University, 2016.

"Microfluidic Device for Aptamer-based Cancer Cell Capture and Gene Mutation Detection"; Craighead, Harold, Sarah Reinholt; Patent Docket # 7428-01-US, United States, EPR - Enhanced Provisional, Converted, 5/22/16, 62/339.924; Cornell University, 2016.

"Microfluidic Device for Aptamer-based Cancer Cell Capture and Gene Mutation Detection"; Craighead, Harold; Patent Docket # 7428, Filed - by Cornell, 5/9/16, Invention; Cornell, 2016.

"Microfluidic Device for Aptamer-based Cancer Cell Capture and Gene Mutation Detection"; Craighead, H; Provisional patent application CU ID 7428 5/22/2016; Cornell University, 2016.

"Microfluidic Device for Aptamer-based Cancer Cell Capture and Gene Mutation Detection"; Reinholt, SJ, HG Craighead; TechConnect World Innovation Conference, Washington, DC, May 22-2,5 2016; Cornell University, 2016.

"Miniature Ion Accelerator"; Lal, Amit; Patent Docket # 7390, Filed - by Cornell, 3/23/16, Invention; Cornell University, 2016.

"Misfit P-Type Transparent Conductive Oxide (TCO) Films, Methods and Applications"; Aksit, Mahmut, Richard Robinson; Patent Docket # 6669-03-US, United States, US from PCT, Filed, 10/6/16, 15/302,319; Cornell University, 2016.

"Mode-locked mid-infrared frequency combs in a silicon microresonator"; Yu, Mengjie, Yoshitomo Okawachi, Austin G Griffith, Michal Lipson, and Alexander L Gaeta; Optica 3, no. 8 (2016): 854 - 860; Columbia University, 2016.

"Modeling barrier tissues in vitro: methods, achievements, and challenges"; Sakolish, CM, MB Esch, JJ Hickman, ML Shuler, and GJ Mahler; E Bio Medicine. http://www.ncbi.nlm.nih.gov/pmc/articles/PMC4816829/ 2016; Cornell University, 2016.

"Modeling Life"; Shuler, ML SNU-Dongjin Distinguished Lectureship of 2016; Seoul National University. SNU-Dongjin Distinguished Lectureship of 2016; Cornell University, 2016.

"Modular, pumpless body-on-a-chip platform for the co-culture of GI tract epithelium and primary liver tissue"; Esch, MB, H Ueno, DR Applegate, and ML Shuler; Lab on a Chip, 16: 2719 - 2729. (doi: 10.1a39/c6lc00461i).. 2016; Cornell University, 2016.

"Monolayer Films of Semiconducting Metal Dichalcogenides, Methods of Making Same, and Uses of Same"; Kang, K, J Park, S Xie; Patent Docket # 6967-02-US, United States, US from PRV, Filed, 4/15/16, 15/130,407; Cornell University, 2016.

"Monolayer Films of Semiconducting Metal Dichalcogenides, Methods of Making Same, and Uses of Same"; Kang, Kibum, Jiwoong Park, Saien Xie; Patent Docket # 6967-03-EP, Europe, EPC - European Patent Convention, Prosecution, 4/15/16, 16165628.5; Cornell University, 2016.

"Monolayer Films of Semiconducting Metal Dichalcogenides, Methods of Making Same, and Uses of Same"; Kang, Kibum, Jiwoong Park, Saien Xie; Patent Docket # 6967-04-CN, China, FOR - Foreign, Prosecution, 4/18/16, 2.0161E+11; Cornell University, 2016.

"Monolayer Films of Semiconducting Metal Dichalcogenides, Methods of Making Same, and Uses of Same"; Kang, K, J Park, S Xie; Patent Docket # 6967-05-KR, South Korea, FOR - Foreign, Filed, 4/15/16, 10-2016-0046063; Cornell University, 2016.

"Multi-frequency LiNbo3 Lamb wave resonators with< 3$Ømega$ impedance"; Wang, Renyuan; Bhave, Sunil A; Zhgoon, Sergei; Bhattacharjee, Kushal; Micro Electro Mechanical Systems (MEMS), 2016 IEEE 29th International Conference on, pgs. 679-682; Cornell University, 2016.

"Multi-Organ toxicity demonstration in a functional human in vitro system composed of four organs"; Oleaga, C, Bernabini, Smith, Srinivasan, Jackson, McLamb, Platt, Bridges, Cai, Santhanam, Berry, Najjar, Akanda, Guo, Martin, Eckman, Esch, Langer, Ouedraogo, Cotovio, Breton, Shuler and Hickman; Scientific Reports, Vol. 6, Article 20030 (2016); Cornell University, 2016.

"Multi-qubit measurements with a Josephson Photomultiplier"; Howington, Caleb, M Hutchings, Guilhem Ribeill, Ivan Pechenezhskiy, Maxim G Vavilov, Frank K Wilhelm, R McDermott, BLT Plourde; March Meeting of the American Physical Society Bulletin, 2016, Baltimore, MD; Syracuse University, 2016.

"Multiplexed electrospray deposition apparatus"; Craighead, H; U.S. Patent #9,289,786 issued March 22, 2016; Cornell, 2016.

"Nano-MRI: Achieving nanoscale magnetic resonance imaging of individual biological molecules and assemblies using mechanical detection and dynamic nuclear polarization"; Marohn, J A, C E Isaac, H L Nguyen, P T Nasr, E A Curley, and M C Boucher; 252nd American Chemical Society National Meeting; Philadelphia, Pennsylvania; August 21 - 25, 2016; Cornell University, 2016.

"Nano-scale technologies: Impact on biology and medicine"; Craighead, H G, Keynote Presentation; Bionano Technology Workshop, IBM Research Center, Yorktown Heights, NY, October 19, 2016; Cornell University, 2016.

"Nanobiotechnology and DNA Analysis"; Craighead, H; Cornell School of Integrated Plant Sciences and Plant Pathology, Seminar talk, September 19, 2016; Cornell University, 2016.

"Nanofabrication and Biosystems"; Craighead, H G, Keynote Address; Grand Opening of U. Delaware Nanofabrication Facility, March 8, 2016; Cornell University, 2016.

"Nanofluidic structures for the study of mesoscopic topological superfluidity"; Rojas, Xavier, Andrew Casey, Petri J Heikkinen, Lev V Levitin, TS Abhilash, Nikolay Zhelev, Jeevak Parpia, John Saunders; QFS 2016 Prague (Poster P1.27); Cornell, 2016.

"Nanomaterial datasets to advance tomography in scanning transmission electron microscopy"; Levin, B; Padgett, E; Chen, C; Scott, M; Xu, R; Theis, W; Jiang, Y; Yang, Y; Ophus, C; Zhang, H; Ha,

D; Wang, D; Yu, Y; Abruna, H Robinson, R; Ercius, P; Kourkoutis, L; Miao, J; Muller, D; Hovden, R; Scientific Data, Vol. 3, pgs. UNSP 160041; Cornell University, 2016.

"Nanomaterials as versatile tools for signal amplification in (bio) analytical applications"; Fenzl, Christoph; Hirsch, Thomas; Baeumner, Antje J; Trac-Trends in Analytical Chemistry, Vol. 79, pgs. 306-316; Cornell University, 2016.

"Nanopatterning of Stable Radical Containing Block Copolymers for Highly Ordered Functional Nanomeshes"; Liedel, Clemens; Ober, Christopher K; Macromolecules, Vol. 49, Issue 16, pgs. 5884-5892; Cornell University, 2016.

"Nanopores in zero mode waveguides"; Wanunu, Meni, Jonas Korlach, Mathieu Foquet, and Stephen Turner; U.S. Patent 9,267,917, issued February 23, 2016; Pacific Biosciences of California, Inc., 2016.

"Nanoscale functional imaging of organic materials"; Marohn J A; ExxonMobil Research and Engineering Co., Annandale, New Jersey; June 3, 2016; Cornell University, 2016.

"Nanoscale functional imaging of organic materials"; Marohn J A; National Institute of Standards and Technology, Gaithersburg, Maryland; October 28, 2016; Cornell University, 2016.

"Nanoscale lateral displacement arrays for the separation of exosomes and colloids down to 20 nm"; Wunsch, BH; Smith, JT; Gifford, SM; Wang, C; Brink, M; Bruce, RL; Austin, RH; Stolovitzky, Gustavo; Astier, Yann; Nature Nanotechnology, Vol. 11, Issue 11, pgs. 936-940; Princeton University, 2016.

"Nanoscale Optofluidic Devices for Molecular Detection"; Erickson, David, Sudeep Mandal; Patent Docket # 4186-03-US, United States, Issued, 9/14/10, 12/675,370, 8/9/16, 9,410,892; Cornell University, 2016.

"Nanosecond- Timescale Low- Error Switching of 3-Terminal Magnetic Tunnel Junction Circuits through Dynamic Oersted-Field Assisted Spin-Hall Effect"; Aradhya, Sriharsha, Robert Buhrman, Daniel Ralph, Graham Rowlands; Patent Docket # 7376-01-US, United States, MPR - Manuscript Provisional, Converted, 3/17/16, 62/309,875; Cornell University, 2016.

"Nanosecond-Timescale Low Energy Switching of In-Plane Magnetic Tunnel Junctions through Dynamic Oersted-Field-Assisted Spin Hall Effect"; Aradhya, Sriharsha V; Rowlands, Graham E; Oh, Junseok; Ralph, Daniel C; Buhrman, Robert A; Nano Letters 16, 5987 (2016), 10.1021/acs.nanolett.6b01443; Cornell, 2016.

"Nanosecond-timescale low error switching of in-plane magnetic tunnel junctions through dynamic Oersted-field assisted spin-Hall effect"; Aradhya, Sriharsha V, Graham E Rowlands, Junseok Oh, Daniel C Ralph, and Robert A Buhrman; arXiv preprint arXiv:1605.02104 (2016); Cornell University, 2016.

"Nanosecond-timescale Low Write Error Switching of Magnetic Tunnel Junctions through the Spin-Hall Effect"; Buhrman, Robert, Daniel Ralph; Patent Docket # 7376, Filed - by Cornell, 3/8/16, Invention; Cornell University, 2016.

"Nanosecond-Timescale Low-Error Switching of 3-Terminal Magnetic Tunnel Junction Circuits through Dynamic Oersted-Field Assisted Spin-Hall Effect"; Buhrman, R A, Aradhya S; Rowlands G; Ralph D C; U.S. Serial No. 62/309,875 filed on March 17, 2016; Cornell University, 2016.

"Nanowire Arrays Structures for Sensing, Solar Cell and Other Applications"; Lal, Amit, Yuerui Lu; Patent Docket # 4926-03-US, United States, Issued, 4/16/12, 13/448,384, 2/16/16, 9,263,519; Cornell University, 2016.

"Near-field Enhancement and Optimal Performance in Metamaterial Terahertz Modulators Based on 2D-materials"; Arezoomandan, Sara, Rusen Yan, Prashanth Gopalan, Kun Tian, Ashish Chanana, Ashutosh Tiwari, Huili Grace Xing, Ajay Nahata, and Berardi Sensale-Rodriguez; Latin America Optics and Photonics Conference, pp. LW2B-4. Optical Society of America, 2016; Cornell University, 2016.

"Near-field radiative heat transfer between parallel structures in the deep subwavelength regime"; St-Gelais, Raphael; Zhu, Linxiao; Fan, Shanhui; Lipson, Michal; Nature Nanotechnology 11 (2016): 515; Columbia University, 2016.

"Neuromorphic event-driven neural computing architecture in a scalable neural network"; Akopyan, Filipp; Arthur, John V.; Manohar, Rajit; Merolla, Paul A.; Modha, Dharmendra S.; Molnar, Alyosha; Risk III, William P.; U.S. Patent 8909576 B2, US20160224886, US 20160224886 A1, 4. Aug. 2016; Cornell University, 2016.

"Next generation lithography: addressing the challenge of sub-20 nm patterning"; Ober, Christopher K, invited talk; International SanDisk Technology Conference (ISTC 2016), Milpitas, California, March 7-9, 2016,; Cornell University, 2016.

"Nonaffine deformation under compression and decompression of a flow-stabilized solid"; Ortiz, CP; Riehn, R; Daniels, KE; Journal of Statistical Mechanics: Theory and Experiment, Vol. 2016, Issue 8, pgs. 84003; North Carolina State University, 2016.

"Novel materials for next generation photonic devices"; Lipson, Michal; Device Research Conference (DRC), 2016 74th Annual. IEEE, 2016; Columbia University, 2016.

"Nuclear envelope rupture and repair during cancer cell migration"; Denais CM, Gilbert RM, Isermann P, McGregor AL, te Lindert M, Weigelin B, Davidson PM, Friedl P, Wolf K, Lammerding J; Science. 2016. 352(6283): 353-8; Cornell University, 2016.

"Nuclear mechanics during migration in 3-D environments"; Lammerding J Invited presentation; "Mechanical forces in physiology and disease" conference at the Centro Nacional de Investigaciones Cardiovasculares (CNIC). Madrid, Spain (November 4, 2016); Cornell University, 2016.

"Nuclear Rupture and Mechanics during Cancer Cell Migration in Confined Environments"; Lammerding J Invited platform presentation; Biomedical Engineering Society (BMES) Annual Meeting. Minneapolis, MN (October 7, 2016); Cornell, 2016.

"Observation of semilocalized dispersive states in the strongly correlated electron-doped ferromagnet Eu 1- x Gd x O"; Shai, Daniel E; Fischer, Mark H; Melville, Alex J; Monkman, Eric J; Harter, John W; Shen, D W; Schlom, Darrell G; Lawler, Michael J; Kim, E-A; Shen, Kyle M; Physical Review B, Vol. 94, Issue 19, pgs. 195102; Cornell University, 2016.

"Observation of the Polar Phase of 3He in a Nematic Aerogel"; Zhelev, N, M Reichl, TS Abhilash, E N Smith, KX Nguyen, EJ Mueller, and J M Parpia; Nature Communications, {\bf 7} 12975 (2016). doi:10.1038/ncomms12975}; Cornell University, 2016.

"On the Benefits of a Symmetric Redox Flow Battery"; Potash, Rebecca A; McKone, James R; Conte, Sean; Abruna, Hector D; Journal of the Electrochemical Society, Vol. 163, Issue 3, pgs. A338-A344; Cornell University, 2016.

"On-chip dual comb source for spectroscopy"; Dutt, Avik; Joshi, Chaitanya; Ji, Xingchen; Cardenas, Jaime; Okawachi, Yoshitomo; Luke, Kevin; Gaeta, Alexander L; Lipson, Michal; arXiv preprint arXiv:1611.07673; Columbia University, 2016.

"On-demand removal of bacterial biofilms via shape memory activation"; Gu, Huan; Lee, Sang Won; Buffington, Shelby Lois; Henderson, James H; Ren, Dacheng; ACS Applied Materials & Interfaces, Vol. 8, Issue 33, pgs. 21140-21144; Syracuse University, 2016.

"Optical and electronic properties of single defects in ZnO and h-BN"; Fuchs, G D Invited Talk; Gordon Research Conference on Semiconductor Defects, New London, NH 2016; Cornell University, 2016.

"Optical Fibers for Embedded Curvature Sensors in Soft Actuators"; Huang, Rukang, Robert Shepherd, Huichan Zhao; Patent Docket # 7179-01-US, United States, EPR - Enhanced Provisional, Converted, 2/25/16, 62/299,582; Cornell University, 2016.

"Optical Force Based Biomolecular Analysis in Slot Waveguides"; Erickson, D, M Lipson, S Moore, B Schmidt, A Yang; Patent Docket # 4438-03-US, United States, Issued, 10/28/11, 13/062,867, 4/26/16, 9,322,995; Cornell University, 2016.

"Optoelectronically innervated soft prosthetic hand via stretchable optical waveguides"; Zhao, Huichan; O'Brien, Kevin; Li, Shuo; Shepherd, Robert F; Science Robotics, Vol. 1, Issue 1, pgs. 7529; Cornell University, 2016.

"Optofluidic Photobioreactor Apparatus, Method, and Applications"; Erickson, David, David Sinton; Patent Docket # 5200-03-US, United States, Issued, 7/30/13, 13/885,478, 12/13/16, 9,518,248; Cornell University, 2016.

"Optofluidic Photobioreactor Apparatus, Method, and Applications"; Erickson, David, Perry Schein; Patent Docket # 5200-06-US, United States, CIP - Continuation in Part, Filed, 11/15/16, 15/351,715; Cornell University, 2016.

"Optomechanical disk vibratory gyroscope"; Lee, J, O Painter, and Q Lin; U.S. Patent #: 9,389,079; University of Rochester, 2016.

"Optomechanical non-reciprocal device"; Manipatruni, Sasikanth, Michal Lipson, and Jacob T Robinson; U.S. Patent No. 9,423,605. 23 Aug. 2016; Columbia University, 2016.

"Optomechanical Oscillator Network, Control and Synchronization Methods, and Applications"; Barnard, A, M Lipson, S Manipatruni, P McEuen, G Wiederhecker, M Zhang; Patent Docket # 5050-03-US, United States, Issued, 7/11/14, 14/130,967, 7/12/16, 9,389,413; Cornell University, 2016.

"Organic electronics for high-resolution electrocorticography of the human brain"; Khodagholy, Dion; Gelinas, Jennifer N; Zhao, Zifang; Yeh, Malcolm; Long, Michael; Greenlee, Jeremy D; Doyle, Werner; Devinsky, Orrin; Buzsaki, Gyorgy; Science Advances, Vol. 2, Issue 11, pgs. e1601027; New York University, 2016.

"Oriented collagen fibers direct tumor cell intravasation"; Han, Weijing; Chen, Shaohua; Yuan, Wei; Fan, Qihui; Tian, Jianxiang; Wang, Xiaochen; Chen, Longqing; Zhang, Xixiang; Wei, Weili; Liu, Ruchuan; Qu, Junle; Jiao, Yang; Austin, Robert H; Liu, Liyu; National Academy of Sciences of the United States of America, Proceedings of the, Vol. 113, Issue 40, pgs. 11208-11213; Princeton University, 2016.

"Origin of field-like spin-orbit torques in heavy metal/ferromagnet/oxide thin film heterostructures"; Ou, Y X, C F Pai, S J Shi, D C Ralph, and R A Buhrman; Physical Review B 94, 140414, (2016), 10.1103/Physrevb.94.140414; Cornell University, 2016.

"Orthogonal Processing of Organic Materials Used in Electronic and Electrical Devices"; Chatzichristidi, M, P Dodson (f/k/a Taylor), J-K Lee, G Malliaras, C Ober, A Zakhidov; Patent Docket # 4385-09-US, United States, Issued, 12/11/15, 14/966,570, 11/22/16, 9,500,952; Cornell University, 2016.

"Oxide Driven Strength Degradation of (1 1 1) Silicon Surfaces"; Grutzik, Scott J; Zehnder, Alan T; MEMS and Nanotechnology, Volume 5, pgs. 1-7; Cornell University, 2016.

"Oxygen evolution reaction electrocatalysis on SrIrO3 grown using molecular beam epitaxy"; Tang, Runbang; Nie, Yuefeng; Kawasaki, Jason K; Kuo, Ding-Yuan; Petretto, Guido; Hautier, Geoffroy; Rignanese, Gian-Marco; Shen, Kyle M; Schlom, Darrell G; Suntivich, Jin; Journal of Materials Chemistry A, Vol. 4, Issue 18, pgs. 6831-6836; Cornell University, 2016.

"Oxygen tension and riboflavin gradients cooperatively regulate the migration of Shewanella oneidensis MR-1 revealed by a hydrogel-based microfluidic device"; Kim, BJ, Chu, I, Jusuf, S, Kuo, T, Teravest, M, Angenent, L, and Wu, M; Frontiers in Microbiology 7 (2016); Cornell University, 2016.

"Parametric Comb Generation via Nonlinear Wave Mixing in High-Q Optical Resonator Coupled to Built-In Laser Resonator"; Gaeta, Alexander, Adrea Johnson, Michal Lipson, Yoshitomo Okawachi; Patent Docket # 6264-03-US, United States, Issued, 10/22/15, 14/786,319, 11/8/16, 9,490,605; Columbia University, 2016.

"Particle Accelerator Apparatus, Methods, and Applications"; Ardanuc, Serhan, Qing Ji, Amit Lal, Arun Persaud, Thomas Schenkel, Peter Seidl, Will Waldron; Patent Docket # 7390-01-US, United States, MPP - Manuscript Plus Provisional, Filed, 5/4/16, 62/331,614; Cornell University, 2016.

"Passive Mixing Capabilities of Micro- and Nanofibres When Used in Microfluidic Systems"; Matlock-Colangelo, Lauren; Colangelo, Nicholas W; Fenzl, Christoph; Frey, Margaret W; Baeumner, Antje J; Sensors, Vol. 16, Issue 8, pgs. 1238; Cornell University, 2016.

"Patterning methods for flexible electronics: a start-up company in a start-up industry"; Ober, Christopher K, invited talk; 251st ACS National Meeting, San Diego, CA, March 13-17, 2016; Cornell University, 2016.

"Patterning of Biomaterials Using Fluorinated Materials and Fluorinated Solvents"; Dodson (f/k/a Taylor), Priscilla, Jin-Kyun Lee, Christopher Ober; Patent Docket # 4959-03-US, United States, Issued, 1/14/13, 13/582,082, 2/16/16, 9,259,759; Cornell University, 2016.

"Phase diagram of a thin film of 3He confined within a 1.08 μm deep cavity"; Zhelev, Nikolay, Abhilash Sebastian, Eric Smith, Jeevak Parpia; March Meeting 2016 Abstract ID: BAPS.2016.MAR.R24.5; Cornell University, 2016.

"Phase-sensitive imaging of ferromagnetic resonance and current using heat and light"; Guo, Feng, Jason M Bartell, Darryl H Ngai, Minh-Hai Nguyen, Robert A Buhrman, and Gregory Fuchs; Joint Intermag and 60th Annual Conference of Magnetism and Magnetic Materials, San Diego, CA, 2016; Cornell University, 2016.

"Phonon-Mediated Quasiparticle Poisoning of Superconducting Microwave Resonators"; Patel, U, Ivan V Pechenezhskiy, B L T Plourde, M G Vavilov, R McDermott; arXiv:1610.09351 (2016); Syracuse University, 2016.

"Photobioreactor Apparatus, Method and Application"; Angenent, Largus, Devin Doud, David Erickson, Eunjung (Erica) Jung, Michael Kalontarov; Patent Docket # 6147-03-US, United States, Issued, 8/25/15, 14/770,246, 12/20/16, 9,523,070; Cornell University, 2016.

"Photonic chips based on multimode fiber-to-waveguide coupling"; Stern, Brian, Michal Lipson, Aseema Mohanty, Felippe Barbosa, and Jaime Cardenas; U.S. Patent Application 15/150,350, filed May 9, 2016; Columbia University, 2016.

"Photosensitive Materials: New Materials Solving Old Problems"; Ober, Christopher K, invited talk; 17th Symposium on Polymer for Microelectronics, Winterthur, DE Apr 25-27; Cornell, 2016.

"Piezoelecrtically Powered Sensor RFID"; Lal, Amit; Patent Docket # 7431, Filed - by Cornell, 5/9/16, Invention; Cornell, 2016.

"Piezoelectric and Logic Integrated Delay Line Memory"; Kuo, Justin, Amit Lal; Patent Docket # 6542-03-US, United States, US from PCT, Filed, 8/3/16, 15/116,441; Cornell University, 2016.

"Piezoelectric Inertial Sensors with 3DOF Sense Mass Actuation and Transduction"; Lal, Amit, Sachin Nadig, Visarute Pinrod; Patent Docket # 7520-01-US, United States, MPR - Manuscript Provisional, Filed, 9/9/16, 62/385,322; Cornell University, 2016.

"Piezoelectric Inertial Sensors with 3DOF Sense Mass Actuation and Transduction"; Lal, Amit; Patent Docket # 7520, Filed - by Cornell, 8/17/16, Invention; Cornell University, 2016.

"Piezoelectric micro dither stage calibration of 6-axis IMU"; Pinrod, Visarute; Nadig, Sachin; Ardanuç, Serhan; Lal, Amit; Micro Electro Mechanical Systems (MEMS), 2016 IEEE 29th International Conference on, pgs. 990-993; Cornell University, 2016.

"Piezoelectric Micromachined Ultrasonic Transducers in Consumer Electronics: The Next Little Thing?"; Pinrod, Visarute; Nadig, Sachin; Ardamuc, Serhan; Lal, Amit; 2016 IEEE 29th International Conference on Micro Electro Mechanical Systems (mems), pgs. 990-993; Cornell University, 2016.

"Polarization spectroscopy of defect-based single photon sources in ZnO"; Jungwirth, N R, H -S Chang, M Jiang, and G D Fuchs; March Meeting of the American Physical Society Bulletin, 2016, Baltimore, MD; Cornell University, 2016.

"Polarization spectroscopy of defect-based single photon sources in ZnO"; Jungwirth, N R, H-S Chang, M Jiang, and G D Fuchs; ACS Nano 10, 1210 (2016); Cornell University, 2016.

"Positive Tone Nanoparticle Photoresists: New Insight on the Patterning Mechanism"; Ober, Christopher K, invited talk; International Conference on Photopolymer Science and Technology, Chiba, Japan, June 22 - 24, 2016; Cornell, 2016.

"Positive Tone Nanoparticle Photoresists: New Insight on the Patterning Mechanism"; Yu, Mufei; Xu, Hong; Kosma, Vasiliki; et al; Journal of Photopolymer Science And Technology 2016, 29(3) 509-512; Cornell University, 2016.

"Positive tone oxide nanoparticle EUV (ONE) photoresists; Recent progress in nanoparticle photoresists development for EUV lithography"; Kasahara, K (Ober); SPIE Advanced Lithography, San Jose, CA, Feb. 21-25, 2016; Cornell University, 2016.

"Positive Tone Oxide Nanoparticle EUV (ONE) Photoresists"; Yu, Mufei; Giannelis, Emmanuel P; Ober, Christopher K; SPIE Advances In Patterning Materials and Processes XXXIII, Proceedings of SPIE 2016, 9779, 977905, Hohle, CK; Younkin, TR; eds; Cornell University, 2016.

"Preparation of Micronutrients Fortified Spirulina Supplemented Rice-Soy Crisps Processed through Novel Supercritical Fluid Extrusion"; Bashir, Shahid; Sharif, Mian Kamran; Butt, Masood Sadiq; Rizvi, Syed SH; Paraman, Ilankovan; Ejaz, Rebia; Journal of Food Processing and Preservation; Cornell University, 2016.

"Probing spin-dynamic lattice strain interactions within the ground and excited-states of nitrogen-vacancy centers in diamond"; Fuchs, G D Invited Talk; SPINOS VI, International Meeting on Spins in Organic Semiconductors, Chicago IL, 2016; Cornell University, 2016.

"Probing the intrinsic optical Bloch-mode emission from a 3D photonic crystal"; Hsieh, Mei-Li, James A Bur, Qingguo Du, Sajeev John, and Shawn-Yu Lin; Nanotechnology 27, no. 41 (2016): 415204; Rensselaer Polytechnic Institute, 2016.

"Processing of Block Copolymers for Long Range Order using Solvent Vapour and Laser Spike Annealing"; Ober, Christopher K, invited talk; EUPOC Conference on Block Copolymers for Nanotechnology Applications, Gargnano, Italy, 22-26 May, 2016; Cornell, 2016.

"Protective Layers for Metal Electrodes Batteries"; Archer, Lynden, Snehashis Choudhury, Zhengyuan Tu, Shuya Wei; Patent Docket # 7607-01-US, United States, EPR - Enhanced Provisional, Filed, 12/19/16, 62/436,248; Cornell University, 2016.

"Q: How many folded angels can we fit on the head of pin? A: 22+/- 5"; Cohen, Itai, Tom Hull, Robert Lang, Christian Santangelo, Marc Miskin, Kyle Dorsey, and Paul McEuen; APS Meeting Abstracts. 2016; Cornell University, 2016.

"Quantitative dissection of heterogeneous muscle stem cell dysfunction in aging"; Cosgrove BD; Northeast Bioengineering Conference, Invited Talk. 04/06/16; Cornell University, 2016.

"Quantitative real-time detection of carcinoembryonic antigen (CEA) from pancreatic cyst fluid using 3-D surface molecular imprinting"; Yu, Yingjie; Zhang, Qi; Buscaglia, Jonathan; Chang, Chung-Chueh; Liu, Ying; Yang, Zhenhua; Guo, Yichen; Wang, Yantian; Levon, Kalle; Rafailovich, Miriam; Analyst, Vol. 141, Issue 14, pgs. 4424-4431; Stony Brook University, 2016.

"Quantum Electromechanical System"; LaHaye, MD; Quantum Science Symposium. 01 Nov. 2016; Syracuse University, 2016.

"Quantum random number generator using a microresonator-based Kerr oscillator"; Jang, Jae K, Yoshitomo, Okawachi, Mengjie Yu, Kevin Luke, Daniel O Carvalho, Michal Lipson, and Alexander L Gaeta; Optics Letters, 41 (2016): 4194-4197; Columbia University, 2016.

"Quantum simulation of the Anderson Hamiltonian with an array of coupled nanoresonators: delocalization and thermalization effects"; Lozada-Vera, J Carrillo, A de Sá Neto, OP, Moqadam, JK, LaHaye, MD, and de Oliveira, MC; Europhysics Journal Quantum Technology 3:9 (2016); Syracuse University, 2016.

"Qubit parity measurements with a Josephson Photomultiplier"; Howington, Caleb, Matthew D Hutchings, Guilhem Ribeill, Ivan Pechenezhskiy, Maxim G Vavilov, Robert McDermott, Britton Plourde; Applied Superconductivity Conference, 2016, Denver, CO; Syracuse University, 2016.

"Qubit Readout with the Josephson Photomultiplier"; Pechenezhskiy, Ivan, Guilhem Ribeill, M Hutchings, Caleb Howington, Maxim G Vavilov, Frank K Wilhelm, BLT Plourde, Robert McDermott; March Meeting of the American Physical Society Bulletin, 2016, Baltimore, MD; Syracuse University, 2016.

"Quest for Ultra Strong Multilayer Graphene as X-ray Transparent SAXS/WAXS Vacuum Window"; Illava, Gabrielle (Richard Gillilan, Sol Gruner); 2016 CNF annual user mtg; Cornell University, 2016.

"Radiation-Sensitive Composition and Pattern-Forming Method"; Giannelis, Emmanuel, Kazuki Kasahara, Vasiliki Kosma, Christopher Ober, Jeremy Odent, Hong Xu, Mufei Yu; Patent Docket # 7359-01-US, United States, PRO - Provisional, Converted, 2/19/16, 62/297,430; Cornell University, 2016.

"Radiation-sensitive Composition and Pattern-forming Method"; Giannelis, Emmanuel, Christopher Ober; Patent Docket # 7359, Filed - by Joint Owner, 2/19/16, Invention; Cornell, 2016.

"Radiation-Sensitive Composition, and Pattern-Forming Method"; Giannelis, Emmanuel, Kazuki Kasahara, Christopher Ober, Hong Xu; Patent Docket # 7491-01-US, United States, PRO - Provisional, Not Converted, 3/28/16, 62/314,035; Cornell University, 2016.

"Radiation-Sensitive Composition, and Pattern-Forming Method"; Giannelis, E, K Kasahara, V Kosma, C Ober, M Yu; Patent Docket # 7492-01-US, United States, PRO - Provisional, Converted, 3/28/16, 62/314,019; Cornell University, 2016.

"Radiation-Sensitive Composition, and Pattern-Forming Method"; Giannelis, Emmanuel, Christopher Ober; Patent Docket # 7491, Filed - by Joint Owner, 7/12/16, Invention; Cornell, 2016.

"Radiation-Sensitive Composition, and Pattern-Forming Method"; Giannelis, Emmanuel, Christopher Ober; Patent Docket # 7492, Filed - by Joint Owner, 7/12/16, Invention; Cornell, 2016.

"Raman-assisted coherent, mid-infrared frequency combs in silicon microresonators"; Griffith, A G, Yu, M, Okawachi, Y, Cardenas, J, Mohanty, A, Gaeta, A L, and Lipson, M; arXiv preprint arXiv:1604.06436 (2016); Columbia University, 2016.

"Rapid emergence and mechanisms of resistance by U87 glioblastoma cells to doxorubicin in an in vitro tumor microfluidic ecology"; Han, Jeonghun; Jun, Yukyung; Kim, So Hyun; Hoang, Hong-Hoa; Jung, Yeonjoo; Kim, Suyeon; Kim, Jaesang; Austin, Robert H; Lee, Sanghyuk; Park, Sungsu; National Academy of Sciences of the United States of America, Proceedings of the, Vol. 113, Issue 50, pgs. 14283-14288; Princeton University, 2016.

"Rapid synthesis of Li4Ti5O12/grapheme composite with superior rate capability by a microwave-assisted hydrothermal method (vol 8, pg 297, 2014)"; Shia, Yi; Gao, Jie; Abruna, Hector D; Liu, Huakun; Li, Huijun; Wang, Jiazhao; Wu, Yuping; Nano Energy, Vol. 30, pgs. 910-910; Cornell University, 2016.

"Reactions of Atomic Carbon with Butene Isomers: Implications for Molecular Growth in Carbon-Rich Environments"; Bourgalais, J; Spencer, Michael; Osborn, David L; Goulay, F; Le Picard, S D; Journal of Physical Chemistry A, Vol. 120, Issue 46, pgs. 9138-9150; Cornell University, 2016.

"Readiness Assessment for Flash Tracking"; Pishdad-Bozorgi, Pardis; de la Garza, Jesus M; Austin, Robert B; Journal of Construction Engineering and Management, Vol. 142, Issue 12, pgs. 6016005; Princeton University, 2016.

"Recent Progress in GaN Power Devices with BV> 1200 V"; Xing, Huili Grace, Kazuki Nomoto, Zongyang Hu, Bo Song, Mingda Zhu, and Debdeep Jena (Invited); Electrochemical Society Meeting Abstracts, no. 24, pp. 1223-1223.; Cornell University, 2016.

"Reduced Dephasing in Tunable Superconducting Transmon Qubits"; Hutchings, Matthew D, Matthew Ware, Yebin Liu, Jared Hertzberg, Jerry M Chow, Britton Plourde; Applied Superconductivity Conference, 2016, Denver, CO; Syracuse University, 2016.

"Repeatable Room Temperature Negative Differential Conductance in GaN/AlN Resonant Tunneling Diodes"; Encomendero, Jimy, Faiza Afroz Faria, S M Islam, Vladimir Protasenko, Sergei Rouvimov, Patrick Fay, Debdeep Jena, and Huili Grace Xing; arXiv preprint arXiv:1606.08100(2016); Cornell University, 2016.

"Resolving and Tuning Mechanical Anisotropy in Black Phosphorus via Nanomechanical Multimode Resonance Spectromicroscopy"; Wang, Zenghui; Jia, Hao; Zheng, Xu-Qian; Yang, Rui; Ye, G J; Chen, X H; Feng, Philip X-L; Nano Letters, Vol. 16, Issue 9, pgs. 5394-5400; Case Western Reserve University, 2016.

"Resonant tunneling assisted propagation and amplification of plasmons in high electron mobility transistors"; Bhardwaj, Shubhendu; Sensale-Rodriguez, Berardi; Xing, Huili Grace; Rajan, Siddharth; Volakis, John L; Journal of Applied Physics, Vol. 119, Issue 1, pgs 13102; Cornell University, 2016.

"Room temperature weak ferromagnetism in Sn1-xMnxSe2 2D films grown by molecular beam epitaxy"; Dong, Sining; Liu, Xinyu; Li, Xiang; Kanzyuba, Vasily; Yoo, Taehee; Rouvimov, Sergei; Vishwanath, Suresh; Xing, Huili G; Jena, Debdeep; Dobrowolska, Margaret; Furdyna, Jacek K; Applied Materials, Vol. 4, Issue 3, pgs 32601; Cornell University, 2016.

"Scanning SQUID susceptometers with sub-micron spatial resolution"; Kirtley, John R; Paulius, Lisa; Rosenberg, Aaron J; Palmstrom, Johanna C; Holland, Connor M; Spanton, Eric M; Schiessl, Daniel; Jermain, Colin L; Gibbons, Jonathan; Fung, Y-K-K; others; Review of Scientific Instruments, Vol. 87, Issue 9, pgs. 93702; Cornell University, 2016.

"Scanning Tunneling Microscopy and Spectroscopy of Air Exposure Effects on Molecular Beam Epitaxy Grown WSe2 Monolayers and Bilayers"; Park, J; Vishwanath, S; Liu, X; Zhou, H; Eichfeld, S; Fullerton-Shirey, S; Robinson, J; Feenstra, R; Furdyna, J; Jena, D; Xing, H; Kummel, A; ACS Nano, Vol 1; Cornell University, 2016.

"Search for new Superfluid States in 3He"; Parpia, Jeevak [Invited Talk]; Condensed Matter Seminar, Michigan State Sept 2016; Cornell University, 2016.

"Search for spatially-modulated phases in confined superfluid 3He"; Levitin, Lev V, Nikolay Zhelev, Robert G Bennett, Jeevak M Parpia, Andrew J Casey, John Saunders; QFS 2016 Prague (Poster P3.26); Cornell University, 2016.

"Self-Folding With Graphene Bimorphs"; Miskin, Marc, Kyle Dorsey, Peter Rose, Itai Cohen, and Paul McEuen; APS Meeting Abstracts. 2016; Cornell University, 2016.

"Semiconductor Circuits and Devices Based on Low Energy Consumption Semi Conductor Structures Exhibiting Multi-Valued Magnetoelectric Spin Hall Effect"; Heron, John, Kelin Kuhn, Mostafizur Rahman, Darrell Schlom; Patent Docket # 7453-01-US, United States, MPR - Manuscript Provisional, Filed, 6/10/16, 62/348,803; Cornell University, 2016.

"Semiconductor Tweezers and Instrumentation for Tissue Detection and Characterization"; Chen, Po-Cheng, Amit Lal, Fabrizio Michelassi, Connie Wu; Patent Docket # 6424-03-US, United States, US from PCT, Filed, 2/5/16, 14/910,660; Cornell University, 2016.

"Sensor Apparatus, Methods and Applications"; Ardanuc, Serhan, Amit Lal; Patent Docket # 7370-01-US, United States, MPR - Manuscript Provisional, Converted, 3/2/16, 62/302,422; Cornell University, 2016.

"Sensor Apparatus, Methods and Applications"; Davaji, Benyamin, Sahil Gupta, Amit Lal, Sachin Nadig; Patent Docket # 7431-01-US, United States, PRO - Provisional, Filed, 5/10/16, 62/334,114; Cornell University, 2016.

"Silicon technologies for arrays of Single Photon Avalanche Diodes"; Gulinatti, A, F Ceccarelli, I Rech, and M Ghioni [Invited]; DCS 2016: SPIE Defense + Commercial Sensing 2016 - Advanced Photon Counting Techniques X, Baltimore (Maryland - USA), April 17-21, 2016; Politecnico di Milano, Italy, 2016.

"Silicon technologies for arrays of Single Photon Avalanche Diodes"; Gulinatti A, F Ceccarelli, I Rech, and M Ghioni [Best Paper Award]; SPIE Commercial + Scientific Sensing and Imaging - Advanced Photon Counting Techniques X, 2016, vol. 9858, 98580A, pp. 1-13, (2016), http://dx.doi.org/10.1117/12.2223884; Politecnico di Milano, Italy, 2016.

"Silicon-Based Dual-Pumped Degenerate Kerr Oscillator"; Okawachi, Yoshitomo, et al; Nonlinear Photonics. Optical Society of America, 2016; Columbia University, 2016.

"Silicon-chip-based mid-infrared dual-comb spectroscopy"; Yu, Mengjie, Yoshitomo Okawachi, Austin G Griffith, Nathalie Picqué, Michal Lipson, and Alexander L Gaeta; arXiv:1610.01121 (2016); Columbia University, 2016.

"Simultaneous optical and electrical in vivo analysis of the enteric nervous system"; Rakhilin, N; Barth, B; Choi, J; Muñoz, NL; Kulkarni, S; Jones, JS; Small, DM; Cheng, Y-T; Cao, Y; LaVinka, C; others; Nature Communications, Vol. 7, pgs. 11800; Binghamton University, 2016.

"Single Cell DNA Methylation Analysis via On-Chip Whole Genome Amplification and Bisulfite Treatment"; Tian, HC, JJ Benitez, HG Craighead; TechConnect World Innovation Conference, Washington, DC, May 22-25, 2016; Cornell University, 2016.

"Single- and few-layer WTe2 and their suspended nanostructures: Raman signatures and nanomechanical resonances"; Lee, Jaesung; Ye, Fan; Wang, Zenghui; Yang, Rui; Hu, Jin; Mao, Zhiqiang; Wei, Jiang; Feng, Philip X-L; Nanoscale, Vol. 8, Issue 15, pgs. 7854-7860; Cornell University, 2016.

"Single-Cell Dissection of Muscle Stem Cell Functional Heterogeneity"; Cosgrove BD; AICHE/SBE International Conference on Stem Cell Engineering, Invited Talk. 10/24/16; Cornell University, 2016.

"Single-particle tracking shows that a point mutation in the carnivore parvovirus capsid switches binding between host-specific transferrin receptors"; Lee, Donald W; Allison, Andrew B; Bacon, Kaitlyn B; Parrish, Colin R; Daniel, Susan; Journal of Virology, Vol. 90, Issue 9, pgs. 4849-4853; Cornell, 2016.

"Size modulated transition in the fluid-structure interaction losses in nano mechanical beam resonators"; Vishwakarma, S, A Pandey, J Parpia, S Verbridge, H G Craighead, R Pratap; Journal of Applied Physics, 119, 1174-4501, DOI: 10.1063/1.4950758 (2016); Cornell University, 2016.

"Soft Robot Device and Related Fabrication Methods"; Elsamadisi, Ahmed, Robert Shepherd, Huichan Zhao; Patent Docket # 6501-04-US, United States, US from PCT, Filed, 4/19/16, 15/030,501; Cornell University, 2016.

"Soil Weathering as an Engine for Manganese Contamination of Well Water"; Gillispie, Elizabeth C; Austin, Robert E; Rivera, Nelson A; Bolich, Rick; Duckworth, Owen W; Bradley, Phil; Amoozegar, Aziz; Hesterberg, Dean; Polizzotto, Matthew L; Environmental Science & Technology, Vol. 50, Issue 18, pgs. 9963-9971; Princeton University, 2016.

"Solar-thermal complex sample processing for nucleic acid based diagnostics in limited resource settings"; Gumus, Abdurrahman; Ahsan, Syed; Dogan, Belgin; Jiang, Li; Snodgrass, Ryan; Gardner, Andrea; Lu, Zhengda; Simpson, Kenneth; Erickson, David; Biomedical optics express, Vol. 7, Issue 5, pgs. 1974-1984; Cornell University, 2016.

"Solubility studies of inorganic-organic hybrid nanoparticle photoresists with different surface functional groups"; Li, Li; Chakrabarty, Souvik; Jiang, Jing; Zhang, Ben; Ober, Christopher; Giannelis, Emmanuel P; Nanoscale (2016), 8(3), 1338-1343; Cornell University, 2016.

"Spatially-annealed nanoparticle films and methods of making and using same"; Hanrath, Tobias; Treml, Ben E; https://www.google.com/patents/US20170040488; Cornell University, 2016.

"Special Issue: Complementarity Problems and Applications Preface"; Facchinei, Francisco; Ferris, Michael C; Luo, Zhi-Quan; Ralph, Daniel; Mathematical Programming, Vol. 157, Issue 2, pgs. 343-347; Cornell University, 2016.

"Spin Hall effect (SHE) and spin transfer torque (STT) effect based device has metal insertion layer which is in contact with and located between, ferromagnetic layer and SHE layer"; Buhrman, R A, Nguyen M; Pai C; Ralph D C; Patent Number: WO2016011435A1; Cornell University, 2016.

"Spin Hall Effect Magnetic Apparatus, Method, and Applications"; Buhrman, Robert, Luqiao Liu, Chi-Feng Pai, Daniel Ralph; Patent Docket # 5587-07-CN, China, Issued, 4/15/14, 201280050731.6, 9/21/16, ZL201280050731.6; Cornell University, 2016.

"Spin Seebeck measurements of current-induced switching in YIG"; Bartell, J M, C Jermain, H Wang, R A Buhrman, F Yang, D C Ralph, and G D Fuchs; March Meeting of the American Physical Society Bulletin, 2016, Baltimore, MD; Cornell University, 2016.

"Spin Torque Study of the Spin Hall Conductivity and Spin Diffusion Length in Platinum Thin Films with Varying Resistivity"; Nguyen, M H, D C Ralph, and R A Buhrman (Web of Science denoted "highly cited paper"); Physical Review Letters 116, 126601, (2016), 10.1103/Physrevlett.116.126601; Cornell, 2016.

"Spin-Hall Torques Generated by Rare-Earth (Lanthanide) Thin Films"; Reynolds, Neal; Jadaun, Priyamvada; Heron, John T; Jermain, Colin L; Gibbons, Jonathan; Collette, Robyn; Buhrman, R A; Schlom, D G; Ralph, D C; arXiv preprint arXiv:1612.01927; Cornell University, 2016.

"Squish and Squeeze - Nuclear Mechanics in 3D Cell Migration"; Lammerding J Invited seminar as Distinguished Lecturer in the Cell Biology Seminar Series, selected by the students and postdoctoral fellows; National Institutes of Health (NIH). Bethesda, MD (March 3, 2016); Cornell University, 2016.

"Squish and Squeeze - Nuclear Mechanics in 3D Cell Migration"; Lammerding J Invited presentation; Research Tumour Biology Workshop on Cancer Cell Migration in Space and Time. Lisbon, Portugal (October 17, 2016); Cornell University, 2016.

"Stability Limit of Water by Metastable Vapor-Liquid Equilibrium with Nanoporous Silicon Membranes"; Chen, I-Tzu; Sessoms, David A; Sherman, Zachary; Choi, Eugene; Vincent, Olivier; Stroock, Abraham D; Journal of Physical Chemistry B, Vol. 120, Issue 23, pgs. 5209-5222; Cornell University, 2016.

"Stability of modelocked microresonator frequency combs"; Klenner, Alexander, Chaitanya S Joshi, Jae K Jang, Kevin Luke, Xingchen Ji, Yoshitomo Okawachi, Michal Lipson, and Alexander L Gaeta; CLEO: Science and Innovations, pp. STu1H-5. Optical Society of America, 2016; Columbia University, 2016.

"Steady state vapor bubble in pool boiling"; Zou, An, Ashish Chanana, Amit Agrawal, Peter C Wayner Jr, and Shalabh C Maroo; Scientific Reports, Vol. 6 (2016); Syracuse University, 2016.

"Still and rotating myosin clusters determine cytokinetic ring constriction"; Wollrab, Viktoria; Thiagarajan, Raghavan; Wald, Anne; Kruse, Karsten; Riveline, Daniel; Nature Communications 7, Article number: 11860 (2016) doi:10.1038/ncomms11860; Université de Strasbourg & CNRS, 2016.

"Strain control of Fermiology and many-body interactions in two-dimensional ruthenates"; Burganov, B, C Adamo, A Mulder, M Uchida, P D C King, J W Harter, D E Shai, A S Gibbs, A P Mackenzie, R Uecker, M Bruetzam, M R Beasley, C J Fennie, D G Schlom, K M Shen; Physical Review Letters, Vol. 116, Issue 19, pgs. 197003; Cornell University, 2016.

"Stress-Based Sensor, Method and Applications"; Bellan, Leon, Harold Craighead, Jeevak Parpia, Darren Southworth; Patent Docket # 5066-04-CN, China, Issued, 11/30/12, 201180027080.4, 6/1/16, ZL201180027080.4; Cornell University, 2016.

"Stressed out Cells - Getting to the Nucleus of It"; Lammerding J Invited speaker; 2016 Gordon Research Conference on Musculoskeletal Biology and Bioengineering. Andover, NH (August 10, 2016); Cornell University, 2016.

"Stressed out Cells - Getting to the Nucleus of It"; Lammerding J Keynote speaker; 2016 University of California Santa Cruz (UCSC) Program in Biomedical Science and Engineering Annual Research Conference. Santa Cruz, CA (Sept. 14, 2016); Cornell, 2016.

"Stressed out Cells - Getting to the Nucleus of It"; Lammerding J Invited speaker; British Society for Matrix Biology (BSMB) Annual Conference. Cardiff, UK (September 5, 2016); Cornell, 2016.

"Stretchable Electroluminescent Devices and Methods of Making and Using Same"; Larson, Chris, Shuo Li, Bryan Peele, Sanlin Robinson, Robert Shepherd; Patent Docket # 6857-02-US, United States, EPR - Enhanced Provisional, Converted, 4/4/16, 62/317,834; Cornell University, 2016.

"Stretchable Electroluminescent Devices and Methods of Making and Using Same"; Larson, Chris, Shuo Li, Bryan Peele, Sanlin Robinson, Robert Shepherd; Patent Docket # 6857-03-PC, Not Applicable (PCT App), PCT - Patent Cooperation Treaty, Filed, 11/3/16, PCT/US16/60346; Cornell University, 2016.

"Stretchable Waveguide Fabrication"; Shepherd, Robert, Huichan Zhao; Patent Docket # 7503-01-US, United States, EPR - Enhanced Provisional, Converted, 9/1/16, 62/382,484; Cornell, 2016.

"Stretching of Tethered DNA in Nanoslits"; Yeh, Jia-Wei; Szeto, Kylan; ACS Macro Letters, Vol. 5, Issue 10, pgs. 1114-1118; Cornell University, 2016.

"Strong spin Hall effect in the antiferromagnet PtMn"; Ou, Y X, S J Shi, D C Ralph, and R A Buhrman; Physical Review B 93, 220405 (2016), 10.1103/Physrevb.93.220405; Cornell University, 2016.

"Structural Diversity and Electron Confinement in Li4N: Potential for 0-D, 2-D, and 3-D Electrides"; Tsuji, Y, P L V K Dasari,, S F Elatresh, R Hoffmann, N W Ashcroft; Journal of the American Chemical Society, 2016, 138, 14108-14120; Cornell University, 2016.

"Structure of the Photo-catalytically Active Surface of SrTiO3"; Plaza, M; Huang, X; Ko, J; Shen, M; Simpson, B Rodriguez-Lopez, J; Ritzert, N Letchworth-Weaver, K; Gunceler, D; Schlom, D; Arias, T; Brock, J; Abruna, H; Journal of the American Chemical Society, Vol. 138, Issue 25, pgs. 7816-7819; Cornell University, 2016.

"Structured Illumination Microscopy Image Reconstruction Algorithm"; Lal, Amit; Shan, Chunyan; Xi, Peng; IEEE Journal of Selected Topics in Quantum Electronics, Vol. 22, Issue 4, pgs. 6803414; Cornell University, 2016.

"Study of topological spin texture in B20 crystalline FeGe films"; Turgut, Emrah, Albert Park, Kayla Nguyen, Robert Hovden, Lena Kourkoutis, David Muller, and Gregory Fuchs; Joint Intermag and 60th Annual Conference of Magnetism and Magnetic Materials, San Diego, CA, 2016; Cornell University, 2016.

"Study of topological spin texture in B20 crystalline FeGe films"; Turgut, Emrah, Albert Park, Kayla Nguyen, Robert Hovden, Lena Kourkoutis, David Muller, and G D Fuchs; March Meeting of the American Physical Society Bulletin, 2016, Baltimore, MD; Cornell University, 2016.

"SU-8 clamped CVD graphene drum resonators"; Lee, Sunwoo, Changyao Chen, Vikram V Deshpande, Gwan-Hyoung Lee, Ilkyu Lee, Michael Lekas, Alexander Gondarenko et al; arXiv preprint arXiv:1612.04279 (2016); Columbia University, 2016.

"Sub-230nm deep-UV emission from GaN quantum disks in AlN grown by a modified Stranski-Krastanov mode"; Islam, S M; Protasenko, Vladimir; Rouvimov, Sergei; Xing, Huili; Jena, Debdeep; Japanese Journal of Applied Physics, Vol. 55, Issue 5, pgs 05FF06; Cornell University, 2016.

"Sub-particle reaction and photocurrent mapping to optimize catalyst-modified photoanodes"; Sambur, Justin B; Chen, Tai-Yen; Choudhary, Eric; Chen, Guanqun; Nissen, Erin J; Thomas, Elayne M; Zou, Ningmu; Chen, Peng; Nature, Vol. 530, Issue 7588, pgs. 77-80; Cornell University, 2016.

"Sub-superfluid 3-He coherence length cross-section SiNN (Silicon Nitride - Niobium) wires"; De Alba, R, Abhilash TS, Rand R and Parpia, JM; QFS 2016 Prague (Poster P4.12); Cornell, 2016.

"Superconducting resonators with trapped vortices under direct injection of quasiparticles"; Nsanzineza, I, Umesh Patel, KR Dodge, RF McDermott, BLT Plourde; March Meeting of the American Physical Society Bulletin, 2016, Baltimore, MD; Syracuse University, 2016.

"Superior Charge Storage and Power Density of a Conducting Polymer-Modified Covalent Organic Framework"; Mulzer, Catherine R; Shen, Luxi; Bisbey, Ryan P; McKone, James R; Zhang, Na; Abruna, Hector D; Dichtel, William R; ACS Central Science, Vol. 2, Issue 9, pgs. 667-673; Cornell University, 2016.

"Suppressing the Fundamental Thermo-Optic Noises of A High-Q Microresonator"; Sun, X B, H Liang, R Luo, X -C Zhang, and Q Lin; CLEO/QELS Proceedings, Conf. Laser and Electro-Optics/ Quantum Electronis and Laser Science (CLEO/QELS), STu1E.2 (2016); University of Rochester, 2016.

"Surface Functionalized Graphene Biosensor on Sapphire for Cancer Cell Detection"; Joe, Daniel J; Hwang, Jeonghyun; Johnson, Christelle; Cha, Ho-Young; Lee, Jo-Won; Shen, Xiling; Spencer, Michael G; Tiwari, Sandip; Kim, Moonkyung; Journal of Nanoscience and Nanotechnology, Vol. 16, Issue 1, pgs. 144-151; Cornell University, 2016.

"Surface Protected Active Metal Electrodes for Rechargeable Batteries"; Archer, Lynden; Patent Docket # 7607, Filed - by Cornell, 11/10/16, Invention; Cornell University, 2016.

"Systems and methods for assembling two-dimensional materials"; Shepard, Kenneth L, Inanc Meric, Cory R Dean, Lei Wang, and James Hone; U.S. Patent Application 15/016,933, filed February 5, 2016; Cornell University, 2016.

"Technologies for Next Generation Silicon Photonics"; Lipson, Michal; Frontiers in Optics. Optical Society of America, 2016; Columbia University, 2016.

"Temperature Dependence of Wavelength Selectable Zero-Phonon Emission from Single Defects in Hexagonal Boron Nitride"; Jungwirth, N R, B Calderon, Y Ji, M G Spencer, M E Flatté, and G D Fuchs; Gordon Research Conference on Semiconductor Defects, New London, NH 2016; Cornell University, 2016.

"Temperature Dependence of Wavelength Selectable Zero-Phonon Emission from Single Defects in Hexagonal Boron Nitride"; Jungwirth, Nicholas R; Calderon, Brian; Ji, Yanxin; Spencer, Michael G; Flatte, Michael E; Fuchs, Gregory D; Nano Letters, Vol. 16, Issue 10, pgs. 6052-6057; Cornell University, 2016.

"Terahertz amplification in RTD-gated HEMTs with a grating-gate wave coupling topology"; Quispe, Hugo O Condori; Encomendero-Risco, Jimy J; Xing, Huili Grace; Sensale-Rodriguez, Berardi; Applied Physics Letters, Vol. 109, Issue 6, pgs 63111; Cornell University, 2016.

"Terahertz Plasmon Amplification in RTD-gated HEMTs with a Grating-gate"; Quispe, Hugo O Condori; Encomendero, Jimy; Xing, Huili Grace; Rodriguez, Berardi Sensale; Active Photonic Materials Viii, Vol. 9920, pgs UNSP 992027; Cornell University, 2016.

"Terahertz plasmon amplification in RTD-gated HEMTs with a grating-gate"; Quispe, Hugo O Condori, Jimy Encomendero, Huili Grace Xing, and Berardi Sensale Rodriguez; SPIE Nanoscience+ Engineering, pp. 992027-992027. International Society for Optics and Photonics, 2016; Cornell University, 2016.

"The A-B transition for superfluid 3He confined to a 1.08 micrometer tall geometry"; Parpia, Jeevak [Invited Talk]; QFS 2016 Prague; Cornell University, 2016.

"The A-B transition in superfluid 3He under confinement in a thin slab geometry"; Zhelev, N, TS Abhilash, EN Smith, RG Bennett, X Rojas, L Levitin, J Saunders, and JM Parpia; Nature Communications (under consideration at) 2016. https://arxiv.org/abs/1610.07186; Cornell University, 2016.

"The Next Generation of Nanophotonic Standing-Wave Array Traps for Precision Manipulation"; Lin, Jun, Fan Ye, Ryan Badman, James Inman, Michelle Wang; Biophysical Journal 110, 633a (2016); Cornell University, 2016.

"The response of small SQUID pickup loops to magnetic fields"; Kirtley, John R; Paulius, Lisa; Rosenberg, Aaron J; Palmstrom, Johanna C; Schiessl, Daniel; Jermain, Colin L; Gibbons, Jonathan; Holland, Connor M; Fung, Y K K; Huber, Martin E; others; Superconductor Science and Technology, Vol. 29, Issue 12, pgs. 124001; Cornell University, 2016.

"The Sodium-Oxygen/Carbon Dioxide Electrochemical Cell"; Xu, Shaomao; Wei, Shuya; Wang, Hongsen; Abruna, Hector D; Archer, Lynden A; Chemsuschem, Vol. 9, Issue 13, pgs. 1600-1606; Cornell University, 2016.

"Themo-Optic Oscillation Dynamics in A High-Q Lithium Niobate Microresonator"; Liang, H, W C Jiang, X B Sun, X -C Zhang, and Q Lin; CLEO/QELS Proceedings, Conf. Laser and Electro-Optics/ Quantum Electronis and Laser Science (CLEO/QELS), STu1E.4 (2016); University of Rochester, 2016.

"Thermal reorganization of alkyl-substituted thienothiophene semiconductors"; Pozdin, Vladimir A; Smilgies, Detlef-M; Fong, Hon Hang; Sorensen, Michael; He, Mingqian; Journal of Materials Chemistry C, Vol. 4, Issue 23, pgs. 5255-5262; Cornell, 2016.

"Thermally controlled comb generation and soliton modelocking in microresonators"; Joshi, Chaitanya, Jae K Jang, Kevin Luke, Xingchen Ji, Steven A Miller, Alexander Klenner, Yoshitomo Okawachi, Michal Lipson, and Alexander L Gaeta; Optics Letters, 41 (2016): 2565-2568; Columbia University, 2016.

"Thermally-controlled single-soliton modelocking in silicon nitride microresonators"; Joshi, C S, Jang, J K, Luke, K, Ji, X, Klenner, A, Okawachi, Y,and Gaeta, A L; CLEO: Science and Innovations (pp. STu4Q-3). Optical Society of America. (2016, June); Columbia University, 2016.

"Thickness-dependent magnetoelasticity and its effects on perpendicular magnetic anisotropy in Ta/CoFeB/MgO thin films"; Gowtham, P G, G M Stiehl, D C Ralph, and R A Buhrman; Physical Review B 93, 024404 (2016), 10.1103/Physrevb.93.024404; Cornell University, 2016.

"Thin Film Plasmonic Optical Modulator"; Rana, Farhan, Michael Spencer; Patent Docket # 7432, Filed - by Joint Owner, 5/10/16, Invention; Cornell University, 2016.

"Thin Film Plasmonic Optical Modulator"; Rana, Farhan, Thomas Sommer, Michael Spencer, Jared Strait; Patent Docket # 7432-01-US, United States, PRO - Provisional, Filed, 6/30/16, 62/356,837; Cornell University, 2016.

"TiO2 nanophotonic sensors for efficient integrated evanescent-Raman spectroscopy"; Evans, C C, C Liu, and J Suntivich; ACS Photonics, Vol. 3, Issue 9, pgs; Cornell University, 2016.

"Tissue Scaffold Materials for Tissue Regeneration and Methods of Making"; Morgan, John, Jason Spector, Abraham Stroock; Patent Docket # 6458-03-US, United States, US from PCT, Filed, 5/18/16, 15/037,417; Cornell University, 2016.

"Titanium dioxide enables visible integrated-evanescent Raman sensors"; Evans, C C, C Liu, and J Suntivich; CLEO: 2016, OSA Technical Digest, paper SM1E.1; Cornell University, 2016.

"Toward Nanoscale Magnetic Imaging of Local Magnetization Dynamics Using Picosecond Thermal Gradients"; Bartell, Jason M, Darryl H Ngai, Feng Guo, Jonathan C Karsch, Gregory Fuchs; Joint Intermag and 60th Annual Conference of Magnetism and Magnetic Materials, San Diego, CA, 2016; Cornell University, 2016.

"Transfer-free Batch Fabrication of Single Layer Graphene Devices"; Brown, Lola, Mark Levendorf, Jiwoong Park, Carlos Ruiz-Vargas; Patent Docket # 4854-03-US, United States, Issued, 3/26/12, 13/384,663, 6/7/16, 9,362,364; Cornell University, 2016.

"Transient dynamics of a superconducting nonlinear oscillator"; Bhupathi, P, Peter Groszkowski, M P DeFeo, Matthew Ware, Frank K Wilhelm, and B L T Plourde; Physical Review Applied, Vol. 5, Issue 2, pgs. 24002; Syracuse Univ, 2016.

"Transient force analysis and bubble dynamics during flow boiling in silicon nanowire microchannels"; Alam, Tamanna; Khan, Ahmed Shehab; Li, Wenming; Yang, Fanghao; Tong, Yan; Khan, Jamil; Li, Chen; International Journal of Heat and Mass Transfer, Vol. 101, pgs. 937-947; University of South Carolina, 2016.

"Transient materials from thermally-sensitive polycarbonates and polycarbonate nanocomposites"; Camera, Katherine L; Wenning, Brandon; Lal, Amit; Ober, Christopher K; Polymer, Vol. 101, pgs. 59-66; Cornell University, 2016.

"Transient micropackets for silicon dioxide and polymer-based vaporizable electronics"; Gund, V; Ruyack, A; Camera, K; Ardanuc, S; Ober, C; Lal, A; Micro Electro Mechanical Systems (MEMS), 2016 IEEE 29th International Conference on, pgs. 1153-1156; Cornell University, 2016.

"Trap-clearing spectroscopy in perylene diimide derivatives"; Smieska, L M, Z Li, D Ley, A B Braunschweig, and J A Marohn; Chemistry of Materials, 2016, 28, 813 - 820. doi = 10.1021/acs.chemmater.5b04025; Cornell University, 2016.

"Tunable phonon cavity coupling in graphene membranes"; De Alba, Roberto, Isaac Storch, Thanniyil Sebastian Abhilash, Francesco Massel, Paul L McEuen, Harold G Craighead, Jeevak M Parpia; Nature Nanotechnology, Vol. 11, Issue 9, pgs. 741-746 {\bf11} 741-746 (2016) doi:10.1038/nnano.2016.86; Cornell University, 2016.

"Tunable squeezing using coupled ring resonators on a silicon nitride chip"; Dutt, A; Miller, S; Luke, K; Cardenas, J; Gaeta, AL; Nussenzveig, P; Lipson, Ml; Optics Letters, Vol. 41, Issue 2, pgs. 223-226; Columbia University, 2016.

"Tunable, full-color nanowire light emitting diode arrays monolithically integrated on Si and sapphire"; Wang, Renjie, Yong-Ho Ra, Yuanpeng Wu, Songrui Zhao, Hieu PT Nguyen, Ishiang Shih, and Zetian Mi; SPIE OPTO, pp. 97481S-97481S. International Society for Optics and Photonics, 2016; McGill University, 2016.

"Two New Games for Carbon"; Hoffmann, R; Braunschweig University of Technology, Germany, Jan. 29, 2016; Cornell University, 2016.

"Two-dimensional heterojunction interlayer tunnel FET (Thin-TFET): From theory to applications"; Li, Mingda Oscar, Rusen Yan, Debdeep Jena, and Huili Grace Xing; Electron Devices Meeting (IEDM), 2016 IEEE International, pp. 19-2. IEEE, 2016; Cornell University, 2016.

"Ultra small cross-section photonic probes for deep tissue non-invasive light delivery"; Fain, R, Wang, T, Wang, M, Charan, K, Barbosa, F A, Cardenas, J, and Lipson, M; CLEO: Science and Innovations (pp. JW2A-141). Optical Society of America. (2016, June); Columbia University, 2016.

"Ultra-broadband Dispersion Engineering of Nanophotonic Devices with Five Zero-Dispersion Wavelengths"; Liang, H, Y He, R Luo, and Q Lin; CLEO/QELS Proceedings, Conf. Laser and Electro-optics/Quantum Electronis and Laser Science (CLEO/QELS), JTh2A.114 (2016); University of Rochester, 2016.

"Ultra-thin superconducting film coated silicon nitride nanowire resonators for low-temperature applications"; Sebastian, Abhilash, Nikolay Zhelev, Roberto De Alba, Jeevak Parpia; March Meeting 2016 Abstract ID: BAPS.2016.MAR.B52.3; Cornell University, 2016.

"Ultralow-Leakage AlGaN/GaN High Electron Mobility Transistors on Si With Non-Alloyed Regrown Ohmic Contacts"; Song, Bo; Zhu, Mingda; Hu, Zongyang; Qi, Meng; Nomoto, Kazuki; Yan, Xiaodong; Cao, Yu; Jena, Debdeep; Xing, Huili Grace; IEEE Electron Device Letters, Vol. 37, Issue 1, pgs 16-19; Cornell University, 2016.

"Unleashing Creativity With Digital Technology"; Austin, Robert D; Mit Sloan Management Review, Vol. 58, Issue 1, pgs. 22-23; Princeton University, 2016.

"Using human "Body-on-a-Chip" devices to aid drug development"; Shuler, ML; Select Bio Organ-on-a-Chip World Congress. Boston, MA. July 7-8, 2016; Cornell University, 2016.

"Vertical Ga2O3 Schottky barrier diodes on single-crystal β-Ga2O3 (- 201) substrates"; Song, Bo; Verma, Amit Kumar; Nomoto, Kazuki; Zhu, Mingda; Jena, Debdeep; Xing, Huili Grace; Device Research Conference (DRC), 2016 74th Annual, pp. 1-2. IEEE, 2016; Cornell University, 2016.

"Vibration Powered RF-Transponder for Sensing Low Frequency Motion Events"; Gupta, S K; Pinrod, V; Nadig, S; Davaji, B; Lal, A; Journal of Physics: Conference Series, Vol. 773, pgs. 12034; Cornell University, 2016.

"Vortices and Quasiparticles in Superconducting Microwave Resonators"; Nsanzineza, Ibrahim; http://surface.syr.edu/etd/446/; Syracuse University, 2016.

"Weakly-tunable transmon qubits in a multi-qubit architecture"; Hertzberg, Jared, Nicholas Bronn, Antonio Corcoles, Markus Brink, George Keefe, Maika Takita, M Hutchings, BLT Plourde, Jay Gambetta, Jerry Chow; March Meeting of the American Physical Society Bulletin, 2016, Baltimore, MD; Syracuse University, 2016.

"Zero-Power Sensor Apparatus, Method and Applications"; Lal, Amit, Alyosha Molnar; Patent Docket # 7221-02-PC, Not Applicable (PCT App), PCT - Patent Cooperation Treaty, Filed, 10/13/16, PCT/US16/56826; Cornell University, 2016.

ABBREVIATIONS & THEIR MEANINGS

µl ... microliter
µm ... micron, micrometer
µN ... micro-Newtons
µs ... microsecond
Ω ... Ohm
< ... is less than
> ... is greater than
~ ... approximately
1D ... one-dimensional
2D ... two-dimensional
2DEG ... two-dimensional electron gas
3D ... three-dimensional
3DOM carbon ... three-dimensionally ordered macroporous carbon
^{3}He ... helium-3
^{4}He ... helium-4
α-Al_2O_3 ... sapphire
α-Si ... amorphous silicon
A&M ... Agricultural & Mechanical
AC ... alternating current
AFM ... atomic force microscopy/microscope
AFOSR ... Air Force Office of Scientific Research
Ag ... silver
agLDL ... aggregated low-density lipoproteins
$AgNO_3$ ... silver nitrate
AgSR ... silver-alkanethiolate
AIC ... aluminum-induced crystallization
Al ... aluminum
Al_2O_3 ... aluminum oxide
ALD ... atomic layer deposition
AlGaN ... aluminum gallium nitride
AM ... amplitude modulation
APD ... avalanche photodiode
APS ... advanced photon source
Ar ... argon
ARC ... anti-reflective coating
ArF ... argon fluoride
As ... arsenic
AST ... aspartate transaminase
atm ... standard atmosphere (as a unit of pressure)
ATRP ... atom transfer radical polymerization
Au ... gold
AuNPs ... gold nanoparticles
B ... boron
B_4C ... boron carbide
B. subtilis ... *Bacillus subtilis*
BAM ... bisphenol aminomethyl
BCL_3 ... boron trichloride
BDM ... 2,3-butanedione monoxime
BES ... bioelectrochemical system
BHJ ... bulk heterojunction
Bi ... bismuth
BiOCl ... bismuth oxychloride
BioSAXS ... biological small angle x-ray scattering
BN ... boron nitride
BOE ... buffered oxide etch
BOX ... buried oxide layer
BPB ... bisphenol base
BPF ... bisphenol F
Br ... bromine
BRDF ... bidirectional reflectance distribution function
BSA ... bovine serum albumin
BST ... barium strontium titanate
BTO ... barium titanate
C ... carbon
C ... centigrade
C-V ... capacitance-voltage
C_3N_4 ... carbon nitride
C_4F_8 ... octafluorocyclobutane, or perfluorocyclobutane
CAAC ... c-axis-aligned crystalline
$CaCl_2$ ... calcium chloride
$CaCO_3$ ... calcium carbonate
CAD ... computer-aided design
CaF_2 ... calcium fluoride
CCI ... Centers for Chemical Innovation
CCMR ... Cornell Center for Materials Research

CCS .. .. continuous compositional spreads
Cd ... ... cadmium
CdS .. .. cadmium sulfide
CdSe ... ... cadmium selenide
CDW ... ... charge-density-wave
Ce ... ... cerium
CF_4 ... ... carbon tetrafluoride or tetrafluoromethane
CFD . ... computational fluid dynamics
CFMA . ... carbon-fiber microelectrode amperometry
CH_4 .. .. methane
CHESS ... ... Cornell High Energy Synchrotron Source
CHF_3 ... ... trifluoromethane
CIGS ... ... copper indium gallium diselenide
CION ... ... colloidal iron oxide nanoparticles
Cl . ... chlorine
Cl_2 ... ... chlorine gas
Cl_2/SF_6 ... ... chlorine sulfur hexafluoride
cm ... ... centimeter
CMOS . ... complementary metal oxide semiconductor
CMOSFET . ... complementary metal oxide field effect transistor
CMP ... ... chemical mechanical polishing
CNF . ... Cornell NanoScale Science & Technology Facility
CNL . ... charge neutrality level
CNS . ... Cornell Center for Nanoscale Systems
CNTFET . ... carbon nanotube field-effect transistor
Co ... ... cobalt
CO_2 .. .. carbon dioxide
Co_3O_4 .. .. cobalt oxide
COF . ... covalent organic framework
CoFeAl ... ... cobalt iron aluminum
CoFeB . ... cobalt iron boron
CoP .. .. cobalt porphyrin
CPC . ... colloidal photonic crystal
CPD . ... contact potential difference
CpG . ... cytosine-phosphate-guanine
Cr . ... chromium
CRDS .. .. cavity ring-down spectrometer
cryoSAXS .. .. cryogenic small angle x-ray scattering
CTC . ... circulating tumor cell
CTC . ... composite thermal capacitors
CTE . ... coefficients of thermal expansion
CTL . ... confinement tuning layer
Cu ... ... copper
Cu_2ZnSnS_4 ... . copper zinc tin sulfide
$CuAlO_2$ ... ... copper aluminum oxide
CVD . ... cardiovascular disease
CVD . ... chemical vapor deposition
CW .. .. continuous wave
CXRF ... ... confocal x-ray fluorescence microscopy
DARPA ... ... Defense Advanced Research Projects Agency
DC ... ... direct current
DCB . ... double cantilever beam
DCE 1,2-dichloroethane
DCM ... ... dichloromethane
de novo .. .. Latin expression meaning "from the beginning," "afresh," "anew," "beginning again."
DEP . ... dielectrophoresis
DFT . ... density functional theory
DFT . ... discrete Fourier transform
DH-PSF .. .. double helix point-spread function
DI . ... de-ionized
DIC .. .. differential interference contrast
DMF ... ... dimethyl formamide
DNA ... ... deoxyribonucleic acid
DNP ... ... dynamic nuclear polarization
DODAB .. .. dimethyl dioctadecyl ammonium bromide
DOE ... ... United States Department of Energy
DPPC .. .. 1,2-dipalmatoyl-sn-glycero -3-phosphocholine
DPPG .. .. 1,2-dimyristoyl-sn-glycero-[phospho-rac-(1-glycerol)]
DRAM ... ... dynamic random access memory
DRIE ... ... deep reactive ion etch
DSA . ... directed self assembly
dsDNA ... ... double-stranded DNA
DUV ... ... deep ultraviolet
e-beam .. .. electron beam lithography
E. coli .. .. *Escherichia coli*
EB ... ... exchange bias
EBID ... ... electron beam induced deposition
EBL . ... electron beam lithography
ECD . ... electrochemical detectors
ECM ... ... extracellular matrix
EDS . ... energy dispersive spectroscopy
EDTA .. .. ethylenediaminetetraacetic acid

EELS ... electron energy loss spectroscopy
EG ... ethylene glycol
EIS ... electrochemical impedance spectroscopy
ELISA ... enzyme-linked immunosorbent assays
EMCCD ... electron multiplying charge coupled device
EO ... electro-optic
EOT ... equivalent oxide thickness
EPICs ... electronic photonic integrated circuits
EPR ... enhanced permeability and retention
Er ... erbium
ErAs ... erbium arsenide
ESM ... effective screening medium
EUV ... extreme ultraviolet
ex situ ... Latin phrase which translated literally as 'off-site' — to examine the phenomenon in another setting than where it naturally occurs
ex vivo ... Latin for "out of the living" — that which takes place outside an organism
F ... fluorine
FcCOOH ... ferrocenecarboxylic acid
FDA ... United States Food & Drug Administration
FDMA ... fluorinated perfluorodecyl methacrylate
FDMNES ... finite-difference method approach to predicting spectroscopic transitions
Fe ... iron
Fe_2O_3 ... iron oxide
$FeCl_3$ ... iron(III) chloride, aka ferric chloride
FeDRAM ... ferroelectric dynamic random access memory
FEM ... finite element method
FES ... functional electrical stimulation
FESEM ... field-emission scanning electron microscopy/microscope
FET ... field-effect transistor
FFTs ... fast Fourier transforms
fg ... femto gram
FIB ... focused ion beam
FIR ... far infrared
fJ ... femto Joules
FLT ... field-like torque
FM ... frequency modulation
FMR ... ferromagnetic resonance
FOTS ... fluorosilane, tridecafluoro-1,1,2,2-tetrahydrooctyltrichlorosilane
FRAP ... fluorescence recovery after photobleaching
FRET ... fluorescence resonance energy transfer
FTIR ... Fourier transform infrared spectroscopy
FWM ... four-wave mixing
Ga ... gallium
GaAs ... gallium arsenide
GaAsN ... gallium arsenide nitride
GaInNAs ... gallium indium nitride arsenide
GaN ... gallium nitride
GaP ... gallium phosphide
GaSb ... gallium antimonide
GASP ... growth advantage in stationary phase
GB ... glass bead
GBLMA ... α-gamma butyrolactone methacrylate
GC ... gas chromatograph
GC-C-IRMS ... gas chromatography combustion isotope ratio mass spectrometry
Gd ... gadolinium
Ge ... germanium
GEDI µdevices ... geometrically enhanced differential immunocapture microdevices
GFET ... graphene field effect transistor
GHz ... gigahertz
GI ... gastrointestinal
GMFI ... gross mean fluorescence intensity
GMR ... giant magnetoresistance
GNR ... gold nanorod
GNR ... graphene nanoribbons
GPa ... gigapascal
GPC ... gel permeation chromatography
GPS ... global positioning system
GRIN ... gradient refractive index
GUI ... graphical user interface
GVD ... group-velocity dispersion
h ... hours
H ... hydrogen
H-NMR ... hydrogen-1 nuclear magnetic resonance spectroscopy
H_2O_2 ... hydrogen peroxide
HAMA ... hydroxyl adamantyl methacrylate
$HAuCl_4$ ... chloroauric acid
HBAR ... high-overtone bulk acoustic resonator
hBN ... hexagonal boron nitride

HBr ..... hydrogen bromide
hcp ..... hexagonal close packing
HCP1 ..... Heme Carrier Protein 1
He ..... helium
HEMTs ..... high electron mobility transistors
Hf ..... hafnium
HF ..... hydrofluoric acid
HfB_2 ..... hafnium diboride
HFEs ..... hydrofluoroethers
HfO_2 ..... hafnium dioxide
Hg ..... mercury
high-k ..... high dielectric constant
HMDS ..... hexamethyldisilazane
HMGB ..... high-mobility group box protein
HOMO-LUMO ..... highest occupied molecular orbital & lowest unoccupied molecular orbital
HOPG ..... highly oriented pyrolytic graphite
HRS ..... high resistance state
HRTEM ..... high-resolution transmission electron microscopy
HS-ssDNA ..... thiol terminated single stranded deoxyribonucleic acid
HSQ ..... hydrogen silsesquioxane
HSQ/FOx ..... negative electron beam resist hydrogen silsesquioxane
Hz ..... Hertz
I-V ..... current-voltage
I/O ..... input/output
IARPA ..... Intelligence Advanced Research Projects Activity
IC ..... integrated circuit
ICP ..... inductively coupled plasma
ICP-MS ..... inductively coupled plasma mass spectroscopy
ICP-RIE ..... inductively coupled plasma reactive ion etcher
IFVD ..... impurity free vacancy diffusion
IGERT ..... Integrative Graduate Education and Research Traineeship
IGZO ..... indium gallium zinc oxide
IID ..... impurity induced disordering
IIEI ..... ion implant enhanced interdiffusion
IJCMSSE ..... International Journal of Computational Materials Science & Surface Engineering
In ..... indium
in situ ..... Latin phrase which translated literally as 'in position' — to examine the phenomenon exactly in place where it occurs
in vitro ..... Latin for "within glass" — refers to studies in experimental biology that are conducted using components of an organism that have been isolated from their usual biological context in order to permit a more detailed or more convenient analysis than can be done with whole organisms.
in vivo ..... Latin for "within the living" — experimentation using a whole, living organism
InAlN ..... indium aluminum nitride
InAs ..... indium arsenide
InAs NWs ..... indium arsenide nanowires
INDEX ..... Institute for Nanoelectronics Discovery and Exploration
InGaAsN ..... indium gallium arsenide nitride
$InGaZnO_4$ ..... indium gallium zinc oxide
InP ..... indium phosphide
IPA ..... isopropyl alcohol
IPE ..... Ion & Plasma Equipment, Inc.
IPT ..... in-plane torque
IR ..... infrared
IRMS ..... isotope ratio mass spectrometry
IrO_2 ..... iridium oxide
IrOx ..... iridium oxide
ISFET ..... ion-sensitive field effect transistor
ITO ..... indium tin oxide
J/m ..... Joules/meter
JP-8 ..... Jet Propellant 8
k ..... dielectric constant
K ..... Kelvin (a unit of measurement for temperature)
K ..... potassium
kDa ..... kilodaltons
KFM ..... Kelvin force microscopy
kg ..... kilogram
kHz ..... kilohertz
KOH ..... potassium hydroxide
KPFM ..... Kelvin probe force microscopy
L/D ..... length-to-diameter ratio
La ..... lanthanum
LAO ..... lanthanum aluminum oxide
LASSP ..... Laboratory of Atomic & Solid State Physics

LED . . . . . light-emitting diode
LER . . . . . line edge roughness
Li . . . . . lithium
LO . . . . . local oscillator
low-κ . . . . . low dielectric constant
LPCVD . . . . . low pressure chemical vapor deposition
lpm . . . . . liter per minute
LRS . . . . . low resistance state
LSPR . . . . . localized surface plasmon resonance
LTMD . . . . . layered transition metal dichalcogenide
Lu . . . . . lutetium
LWGs . . . . . liquid-core/liquid-cladding waveguides
LWR . . . . . line width roughness
M-OPTG . . . . . microring-based optical pulse-train generator
MACE . . . . . metal-assisted chemical etching
MAMA . . . . . methyl adamantyl methacrylate
MBE . . . . . molecular beam epitaxy
MCBJ . . . . . mechanically controllable break junction
MD . . . . . molecular dynamics
ME . . . . . magnetoelectric
MEG . . . . . maleimide-ethylene glycol disulfide
MEMs . . . . . microelectromechanical systems
MFC . . . . . microbial fuel
MFMR . . . . . microfabricated micro-reactors
MgO . . . . . magnesium oxide
MGs . . . . . molecular glasses
MHz . . . . . megahertz
micron . . . . . micrometer, aka µm
MIFIS . . . . . metal-insulator-ferroelectric-insulator-semiconductor
min . . . . . minutes
ml . . . . . milliliter
mm . . . . . millimeter
mM . . . . . millimolar
MMA-MAA . . . . . methyl-methacrylate-co-methacrylic acid
mmHg . . . . . millimeters of mercury; unit of pressure measurement
MnO_2 NPs . . . . . manganese oxide nanoparticles
Mo . . . . . molybdenum
MOCVD . . . . . metal oxide chemical vapor deposition
MONOS . . . . . metal/oxide/nitride/oxide/semiconductor
MOS . . . . . metal oxide semiconductor
MoS_2 . . . . . molybdenum disulfide
$MoSe_2$ . . . . . molybdenum diselenide
MOSFET . . . . . metal oxide semiconductor field effect transistor
MOVPE . . . . . metal organic vapor phase epitaxy
MPM . . . . . multiphoton microscopy
MQCA . . . . . magnetic quantum-dot cellular automata
MQW . . . . . multiple quantum well
MRA . . . . . multifunction reconfigurable antenna
MRAM . . . . . magnetic random access memory
MRFM . . . . . magnetic resonance force microscopy
MRI . . . . . magnetic resonance imaging
ms . . . . . millisecond
MSM . . . . . metal-semiconductor-metal
MTJ . . . . . magnetic tunneling junction
mTorr . . . . . millitorr
mV . . . . . millivolt
MVD . . . . . molecular vapor deposition
MWNT . . . . . multiwalled carbon nanotube
MΩ . . . . . megaohms
N . . . . . nitrogen
N_2 . . . . . nitrous oxide
nA . . . . . nanoAmperes
NaCl . . . . . sodium chloride
NASA . . . . . National Aeronautics & Space Administration
Nb . . . . . niobium
Nb_3Sn . . . . . triniobium-tin
NBTC . . . . . Nanobiotechnology Center, Cornell University
NCRR . . . . . National Centers for Research Resources
NCs . . . . . nanocrystals
Nd . . . . . neodymium
NEMs . . . . . nanoelectromechanical systems
NEXAFS . . . . . near edge x-ray absorption fine structure
NH_4F . . . . . ammonium fluoride
Ni . . . . . nickel
NIDCD . . . . . National Institute on Deafness & Other Communication Disorders
NIH . . . . . National Institutes of Health
NIR . . . . . near-infrared
nL . . . . . nanoliter
nm . . . . . nanometer
NMP n-methyl-2-pyrrolidone

NMR ... nuclear magnetic resonance microscopy / spectroscopy

NNCI ... National Nanotechnology Coordinated Infrastructure

NORIS ... nanometrology optical ruler imaging system

NPR ... nonlinear polarization rotation

NPs ... nanoparticles

NPs ... nanopores

ns ... nanosecond

NSF ... National Science Foundation

NSF-SGER ... National Science Foundation Small Grants for Exploratory Research

NSOM ... near-field scanning optical microscopy

NSSP ... nanostructured semipolar

NV ... nitrogen-vacancy

NVM ... non-volatile memory

NW FETs ... nanowire field-effect transistors

NYSTAR ... New York State Office of Science, Technology & Academic Research, Empire State Development's Division of Science, Technology and Innovation

O ... oxygen

OFET ... organic field effect transistor

Oh number ... Ohnesorge number

OLED ... organic light-emitting diode

ONO ... oxide/nitride/oxide

ONR-MURI ... Office of Naval Research Multidisciplinary University Research Initiative

OPS ... optical particle sizer

OPV ... organic photovoltaic cells

OST-MRAM ... orthogonal spin-transfer magnetic random access memory

OTFT ... organic thin-film transistor

P(VDF-TrFE) ... poly[(vinylidenefluoride-co-trifluoroethylene]

P/E ... program/erase

Pa ... Pascals

PAB ... post-apply bake

PaC ... Parylene-C

PAE ... power-added efficiency

PAG ... photoacid generator

PAMAM ... polyamidoamine

PANOMs ... planarized aperatures for near-field optical microscopy

Pb ... lead

PBG ... photonic bandgap

PBPK ... physiologically-based pharmacokinetic

PbS ... lead sulfide

PBS ... phosphate-buffered saline

PbSe ... lead selenide

PC ... persistent current

PC ... photocurrent

PCB ... printed circuit board

PCBM ... [6,6]-phenyl-C61-butyric acid methyl ester; a fullerene derivative

PCM ... phase change material

PCN ... photonic crystal nanocavity

Pd ... palladium

PD ... photodetector

PDMS ... polydimethylsiloxane

PE-GNR ... polyelectrolyte gold nanorod

PEB ... post-exposure bake

PEC ... photoelectrochemical

PECVD ... plasma enhanced chemical vapor deposition

PEDOT:PSS ... poly(3,4-ethylenedioxythiophene): poly(styrenesulfonate)

PEG ... polyethylene glycol

PEI ... polyethyleneimine

PFM ... piezo-response force microscopy

PGMA ... poly(glycidyl methacrylate)

pH ... a measure of the activity of hydrogen ions (H+) in a solution and, therefore, its acidity.

Ph.D. ... doctorate of philosophy

PhC ... photonic crystal

PID ... proportional-integral-derivative

PL ... photoluminescence

pL ... picoliter

PLD ... pulsed laser deposition

PLGA ... poly(lactic-co-glycolic) acid

PMGI ... poly(methyl glutarimide)

PMMA ... poly(methyl methacrylate)

PmPV ... poly(m-phenylenevinylene-co-2,5-dioctoxy-p-phenylenevinylene)

poly-Si ... polycrystalline silicon

POP ... polyolefin plastomer

PPM ... photolithographic phase masks

PS ... polystyrene

PS-*b*-PMMA ... polystyrene-*block*-poly (methyl methacrylate)

PSL ... polysterene latex

PSMO ... praseodymium strontium manganite

PSμM ... phase separation micro-molding
Pt ... platinum
Pt/Ir ... platinum/iridium
PTX ... paclitaxel
PV ... photovoltaic
PVA ... poly-vinyl alcohol
PVC ... polyvinyl chloride
PVD ... physical vapor deposition
PVDF ... polyvinylidene fluoride
PVP ... polyvinylpyrrolidone
Py ... permalloy, $Ni_{81}Fe_{19}$
PZT ... lead zirconate titanate ($PbZr_{0.52}Ti_{0.48}O_3$)
Q ... quality factor
QD ... quantum dots
QW ... quantum well
QWI ... quantum well intermixing
RA ... resistance-area
Re number ... Reynolds number
REU ... Research Experience for Undergraduates Program
RF ... radio frequency
RF MEMS ... radio frequency microelectromechanical systems
RFID ... radio frequency identification
RIE ... reactive ion etch
RMS or rms ... root mean square
RNA ... ribonucleic acid
ROS ... reactive oxygen species
RPEVCD ... remote plasma-enhanced chemical vapor deposition
RRAM ... resistive random access memory
RTA ... rapid thermal anneal
RTD ... resistance temperature device
s ... seconds
S ... sulfur
SA-MOVPE ... selective area metal organic vapor phase epitaxy
SABC ... surface active block copolymers
SAED ... selected area electron diffraction
SAMs ... self-assembled monolayers
SAXS ... small angle x-ray scattering
Sb ... antimony
SBH ... Schottky barrier height
Sc ... scandium
SCAN ... single-chromatin analysis at the nanoscale
sccm ... standard cubic centimeters per minute
$scCO_2$ ... supercritical carbon dioxide
SCOFET ... single crystal organic field effect transistor
SCORE ... SNARE Complex Reporter
SDS ... sodium dodecyl sulfate
Se ... selenium
sec ... seconds
SECM ... scanning electrochemical microscopy
SEM ... scanning electron microscopy/microscope
SERS ... surface enhanced Raman spectroscopy
SF_6 ... sulfur hexafluoride
SFLS ... supercritical fluid-liquid-solid
SH ... second harmonic
Si ... silicon
Si_3N_4 ... silicon nitride
SiAlON ... silicon aluminum oxynitride
SiC ... silicon carbide
SiH_4 ... silane
SiN ... silicon nitride
SiNWs ... silicon nanowires
SiO_2 ... silicon dioxide
SIROF ... sputtered iridium oxide film
SLBs ... supported lipid bilayers
SLG ... single-layer graphene
SLM ... spatial light modulator
SLUG ... superconducting low-inductance undulatory galvanometer
SML ... spin memory loss
SMS ... single molecule spectroscopy
Sn ... tin
SNARE ... soluble n-ethylmaleimide-sensitive factor attachment protein receptor complex
SnO_2 ... tin oxide
SNPs ... silver nanoparticles
SNR ... signal-to-noise ratio
SOFC ... solid oxide fuel cells
SOI ... silicon-on-insulator
SPCM ... scanning photocurrent microscopy
SPD ... switching phase diagram
SPR ... surface plasmon resonance
SQUID ... superconducting quantum interference device
Sr_2RuO_4 ... strontium ruthenate

SRC .. ..Semiconductor Research Corporation
$SrTiO_3$ ... ...strontium titanate
ssDNA ... ...single-stranded deoxyribonucleic acid
ST-FMR .. ..spin torque ferromagnetic resonance
STEM .. ..scanning transmission electron microscopy/microscope
STJ ... ...superconducting tunnel junction
STM ... ...scanning tunneling microscopy/microscope
STO . ...strontium titanate
STT . ...spin-transfer torques
STT-MRAM ... .spin-transfer torque magnetic random access memory
SVA .. ..solvent vapor annealing
t-BOC .. ..tert-butoxycarbonyl
Ta . ...tantalum
Ta_2O_5 .. ..tantalum pentoxide
TaN . ...tantalum nitride
TAOx ... ...tantalum oxide
TCO . ...transparent conducting oxide
Te . ...tellurium
TE ... ...transverse electric
TEC . ...thermionic energy converter
TEER .. ..transepithelial electrical resistance
TEM ... ...transmission electron microscopy/microscope
TER . ...transepithelial resistance
TFET .. ..tunnel field effect transistor
TFM ... ...traction force microscopy
TFT . ...thin-film transistor
Tg . ...glass transition temperature
TH ... ...third harmonic
THz . ...terahertz
Ti . ...titanium
TiN .. ..titanium nitride
TiO_2 . ...titanium dioxide
TIR-FRET .. ..total internal reflection - fluorescence resonance energy transfer
TLM ... ...transfer length measurement
TM ... ...transverse magnetic
TMAH ... ...tetramethylammonium hydroxide
TMOS . ...tetramethylorthosilicate
TMR ... ...tunneling magnetoresistance
TO ... ...thermo-optic
TO ... ...torsional oscillator
TO ... ...transformation optics
TPoS ... ...thin-film piezoelectric-on-substrate
TRT . ...thermal release tape
TSVs ... ...through silicon vias
TTD . ...transverse translational diversity
TTV . ...total thickness variation
TXM ... ...transmission x-ray microscopy
UHV ... ...ultra-high vacuum
USDA .. ..United States Department of Agriculture
UV ... ...ultraviolet
UV-Vis ... ...ultraviolet-visible
V ... ...vanadium
V ... ...voltage
VA-CNT .. ..vertically aligned carbon nanotube
vdW ... ...van der Waals
VLS .. ..vapor-liquid-solid
VRMs .. ..voltage regulator modules
VSM ... ...vibrating sample magnetometry
W . ...tungsten
WDM .. ..wavelength-division multiplexing
We number .. ..Weber number
WGM .. ..whispering gallery mode
WSe_2 ... ...tungsten diselenide
XeF_2 ... ...xenon difluoride
XMCD . ...x-ray magnetic circular dichroism
XPM ... ...cross-phase modulation
XPS .. ..x-ray photoelectron spectroscopy
XRD . ...x-ray diffraction
XRR . ...x-ray reflectivity
YB_{25} . ...yttrium boride
YBCO .. ..yttrium-barium-copper-oxide
YBS . ...y-branch switch
ZMW ... ...zero-mode waveguide
Zn ... ...zinc
$ZnCl_2$ ... ...zinc chloride
ZnO . ...zinc oxide
ZnO:Al ... ...zinc aluminum oxide
ZnS .. ..zinc sulfide or zinc-blende
Zr . ...zirconium
ZrO_2 ... ...zirconium dioxide
ZTO . ...zinc tin oxide

The 2016-2017 CNF Research Accomplishments reports were formatted by Ms. Melanie-Claire Mallison and proof-read by the CNF Staff. We welcome your comments at mallison@cnf.cornell.edu

The reports are also online at http://www.cnf.cornell.edu/cnf_2017ra.html

Cornell NanoScale Science & Technology Facility (CNF)

2016-2017

Research Accomplishments

Bacterial Mechanics on a Chip

2017 CNF REU Intern: Gabriel Guisado

CNF REU Affiliation: Biomedical Engineering, University of Rochester

CNF Project: Cornell NanoScale Science & Technology Facility Research Experience for Undergraduates (CNF REU) Program

CNF REU Principal Investigator: Prof. Christopher Hernandez, Sibley School of MAE, Cornell University

CNF REU Mentor: Melanie Roberts, Meinig School of Biomedical Engineering, Sibley School of Mechanical and Aerospace Engineering (MAE); Cornell University

Primary Source of Research Funding: National Science Foundation via NNCI Grant No. ECCS-1542081

Contact: gguisado@u.rochester.edu, cjh275@cornell.edu, mfr75@cornell.edu

Website: http://www.cnf.cornell.edu/cnf5_reuprogram.html

Primary CNF Tools Used: Heidelberg, Gamma, ASML, Oxford 80s/100, Trion, MOS furnaces, VersaLaser, AJA

Abstract:

The ability of bacteria to squeeze into constrictions a fraction of their size can lead to bacterial infections such as osteomyelitis. In osteomyelitis, bacteria cells squeeze into small channels in the bone where they are protected from immune cells and become much more difficult to treat with antibiotics. To simulate the mechanical loading conditions bacteria experience as they move through sub-micron channels, bacteria are analyzed in similarly sized tapered channels through the fabrication of a microfluidic device. The sub-micron channels were created using Deep UV (DUV) Photolithography in the CNF, and then etched to transfer the design to a fused silica device. The design includes an inlet of approximately 1.2 µm, an outlet of 250 nm, and is 75 µm long. The bacteria trapped in the channels are imaged with both traditional and super-resolution microscopy. The distance travelled is then measured and compared to the pressure drop experienced by the bacteria in the channels. This pressure drop is defined as the difference in pressure across the bacteria trapped in the channel. Data collected this summer revealed that under a high inlet pressure, the bacteria can go into a channel width a fraction of their size. At a low inlet pressure, the bacteria will not squeeze into a constriction less than half their diameter. However, with the introduction of a large pressure drop, the bacteria can squeeze into a constriction up to a quarter of their diameter (Figure 1).

Figure 1: MRSA [yellow and arrows] penetrating bone [gray] to point where immune cells [pink] can't reach the MRSA (Nishitani, et al., 2016).

Summary of Research:

"Extrusion loading" is the loading mechanism the lab refers to as the mechanical stimuli that *E. coli* undergo when in the designed tapered channels. Extrusion loading is unique among methods of mechanically stimulating bacteria in that it achieves a non-uniform stress and strain experienced by the bacteria.

Manufacturing the microfluidic device begins with a CAD design (Figure 2). The channels in the design are tapered, ranging from an inlet width of 1.2 µm and an outlet width of 250 nm. The design is created so there are varying pressure drops across each channel. This varying pressure drop is because of a resistance to fluid flow in the bypass (Figure 3). There is a decline in pressure as the fluid moves through the channels, giving every channel its own distinct upstream pressure.

The device uses 600 different channels so that several different pressure drops can be examined at once. The silica glass device is created with DUV lithography. Fused silica was chosen because it is much stiffer than the bacteria and its transparency allows for microscopy. SEM, AFM, and the Profilometer are used to check for proper taper geometry, outlet width, channel depth and to allow optimization of the process in subsequent application.

After characterization, the device is bonded to a thin (170 nm) silica wafer and ready for experimentation. The device is placed on the microscope stage and bacteria in liquid suspension are flowed into the inlet using a syringe pump with a pressure gage reporting pressure at the inlet. Experiments are performed at

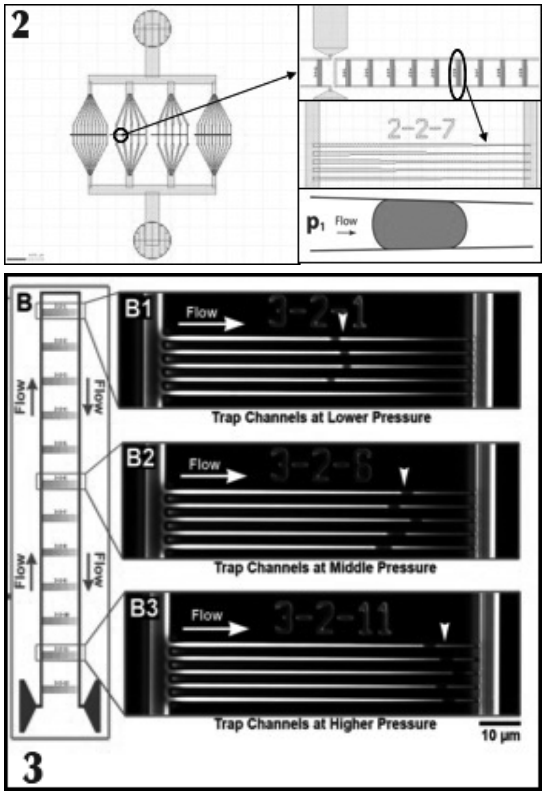

Figure 2, top: The tapered channels used to trap bacteria have a 1.2 µm inlet, a 250 nm outlet, and are 75 µm long. Multiple tapered channels are on each device. Six devices are present on each wafer. Figure 3, bottom: Tapers are placed in sets of five separated by a distance. Each set of tapers experiences a different drop in pressure across its length. This pressure drop is determined by the difference between upstream and downstream pressure (Sun, et al., Lab Chip 2014).

inlet pressures of 25 kPa and 60 kPa. Using a syringe pump that controls flow rate, the bacteria in M9 media are transported into the device. A pressure sensor is connected to the tube and a computer so that the pressure can be monitored and controlled based on the flow rate of the syringe pump. Images of the bacteria in the tapered channels are collected using transmission microscopy and the distance traveled by the bacteria was determined. The pressure drop across each bacterium in a tapered channel is determined using hydraulic circuit calculations. The distance traveled by bacteria is determined using the channel's number labels as a positional marker in the experimental images. The results indicate the relationship between loading conditions and how far the bacteria travel.

Results and Conclusions:

Over 1000 cells from over 20 different experiments were analyzed. Experiments were performed at both 60 kPa and 25 kPa inlet pressure. At a 60 kPa inlet pressure, the regression line shows an intercept of 52 µm traveled (75 µm channel length), and an average width of 500 µm under a 1 kPa pressure drop. R_2 = 0.39. At a 25 kPa inlet pressure, the regression line shows an intercept of an average of 30 µm traveled. R_2 = 0.71. In regards to reaching max constriction (250-300 nm) in the channels, this can be done in the 60 kPa experiments at approximately 6 kPa pressure drop, while it takes at least double that in the 25 kPa conditions. It was previously undetermined whether in the 25 kPa experiments the bacteria would be able to reach the end of the channels where it is under the max constriction. Therefore, these findings present the lab with new information regarding loading conditions that enable bacteria to squeeze deep into these channels (Figure 4).

Future Work:

Future work would be to conduct a similar experiment, but with bacteria known to cause infections, such as *Staphylococcus aureus*. Since this strain of bacteria has a higher safety level than the *E. coli* used, the study would have to be moved to a different lab facility. As more of a long-term goal, we want to find out what component or components of bacteria play the biggest role in how they are able to squeeze into these sub-micron channels. Finding the biological pathways in which bacteria squeeze into these sub-micron channels could eventually lead to better antibiotics for treating bacterial infections.

Acknowledgements:

NSF grant nos. ECCS-1542081 and CMMI-1463084, NNCI, CNF REU Program Coordinators and Staff. Thank you to Professor Christopher Hernandez and Melanie Roberts for affording me this opportunity, and the Peng Cheng Group for collaborating on this study.

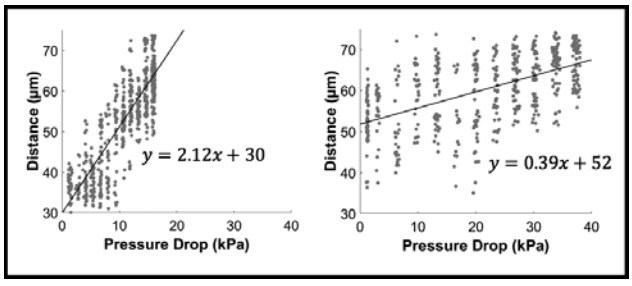

Figure 4: Shown here are over 1000 analyzed cells. The relationship between pressure drop across the channel and penetration of the bacteria differs between an external pressure of 25 kPa (left) and an external pressure of 60 kPa (right).

Nanostamp Optimization for Single-Molecule DNA/Protein Array Studies

2017 CNF REU Intern: Mónica M. López Martínez

CNF REU Affiliation: Chemical Engineering, University of Puerto Rico-Mayaguez Campus

CNF Project: Cornell NanoScale Science & Technology Facility Research Experience for Undergraduates (CNF REU) Program

CNF REU Principal Investigator: Dr. Michelle D. Wang, Laboratory of Atomic and Solid State Physics, Howard Hughes Medical Institute; Cornell University

CNF REU Mentors: Ryan Badman, Dr. James E. Baker; Laboratory of Atomic and Solid State Physics, Cornell University

Primary Source of Research Funding: National Science Foundation via NNCI Grant No. ECCS-1542081

Contact: monica.lopez8@upr.edu, mdw17@cornell.edu, rpb226@cornell.edu, jeb94@cornell.edu

Website: http://www.cnf.cornell.edu/cnf5_reuprogram.html

Primary CNF Tools Used: JEOL JBX-6300FS, Oxford Cobra ICP etcher

Abstract:

Over the past two decades, biophysical single molecule DNA, RNA and motor protein studies have demonstrated the important role that the structural and mechanical properties of single molecules play in gene replication and expression. Specifically, genetic processes can be significantly affected when DNA experiences torque or protein interaction forces, which happens often *in vivo*. Single molecule DNA studies typically "tether" DNA between a protein anchor on a surface, and a microbead in solution, that can be twisted or pulled with optical or magnetic tweezers. Nanostamping of protein spot anchor arrays, compared to blanket coating a substrate with protein for DNA anchoring, aids in single molecule studies by precisely controlling the DNA anchor position. This improves resolution and throughput of the technique. Thus, we are exploring a nanostamping method called the "Ink-Subtract-Print" method by optimizing the dimensions of electron beam-patterned nanostamps that can selectively pattern arrays of 100-300 nm wide circles of protein on a glass surface.

Summary:

Introduction. The deoxyribonucleic acid molecule (DNA) has a double helix structure with unique mechanical properties that subsequently influence the way that other proteins interact with DNA to achieve complex biological functions of transcription and replication.

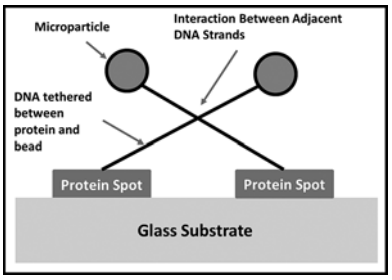

Figure 1: Schematic of protein-DNA-bead tethers.

Our lab is interested in studying the interactions between DNA and motor proteins that are present in DNA processing activities. Although DNA can be macroscopically long, it is only 2 nm wide and cannot be visualized with light microscopy. DNA is therefore tethered between a microsphere handle and microscope slide for observation and manipulation. To obtain organized observations of these microscopic molecules and investigate interactions between a protein and multiple DNA strands, we precisely placed the position of the separate DNA molecules on a glass slide so that the distance between strands was well-defined. Specifically, we patterned a protein surface array using the Ink-Subtract-Print (ISP) nanostamping method [1], so the DNA could be anchored on the surface at one end of the DNA molecule with high spatial precision (Figure 1).

Methods; I. Ink-Subtract-Print Method. This protein patterning procedure consists of inking a PDMS square with protein to cover the whole surface, and then stamping the square on the patterned silicon template to remove the protein everywhere on the PDMS except in the array of small circles [1]. This subtractive step is physically possible because plasma cleaning the silicon template gives hydrophilic properties to the wafer. Since the protein on the PDMS is also hydrophilic, it will be attracted to the top surface of the subtraction template wafer. When the PDMS is pulled away, the protein will be attached to the wafer in the non-patterned areas. In contrast, the PDMS will retain protein where the silicon wafer had holes. The patterned protein spots on the PDMS after subtraction are, then, stamped or "printed" on a plasma-cleaned glass surface which will be the area used to perform the DNA-binding experiments (Figure 2).

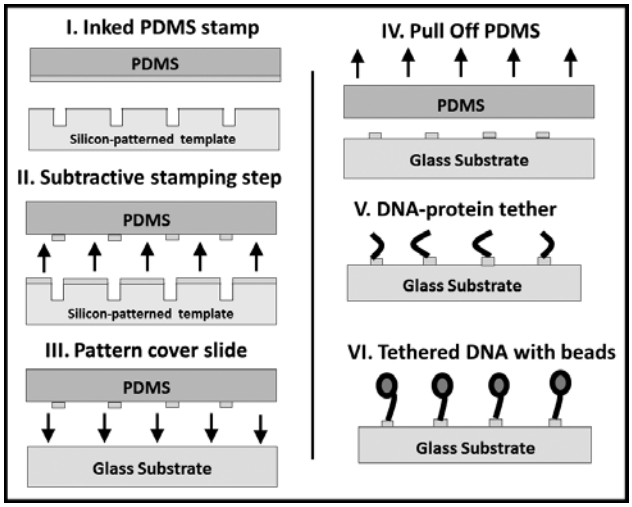

Figure 2. Ink Substract Print stamping method.

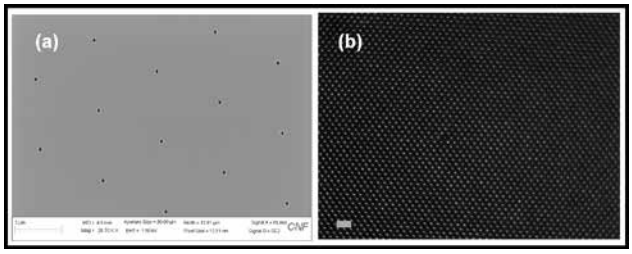

Figure 3: (a) A scanning electron microscope image of the silicon template with a hexagonal array of holes for subtractive stamping, scale bar is 2 µm. (b) A fluorescent microscope image of the final protein array on glass, scale bar is 6 µm.

Methods; II. Nanofabrication of Patterned Silicon Template. Our main goal thus was to create patterned silicon templates containing periodic hexagonal arrays of 100-300 nm circular holes spaced at a 3-µm pitch that could be used as a subtraction template (Figure 3a) to produce patterned protein spots on PDMS (Figure 3b).

To acquire the target pattern needed to perform the Ink-Subtract-Print stamping procedure on our silicon wafer, the first step was to expose a silicon wafer coated with ZEP520A resist using the JEOL JBX-6300FS 100kV electron beam (e-beam) lithography system. Once the wafer was exposed and developed, the Oxford Cobra inductively coupled plasma (ICP) etcher was used to etch the silicon wafer according to the e-beam pattern. To remove the ZEP520A and obtain our final cleaned, patterned nanostamp template, we used a bath of 1165 organic stripper for approximately four hours. Finally, we obtained four 1 cm × 1 cm stamp areas patterned on each wafer.

Results:

After four hours of DNA incubation time (13.7 kbp DNA, 25 pM), we observed an average of 10 tethers in each microscope field of view, which contained ~ 1,500,

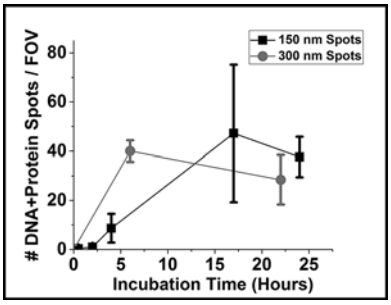

Figure 4: The number of DNA tethers bound to protein anchors per field of view (FOV) under a fluorescent microscope, per hour of incubation, using (1) 150 nm wide protein anchors and (2) 300 nm wide protein anchors.

150 nm wide protein spots. To increase the number of tethers, the incubation time was increased to 17 hours and yielded ~ 50-100 DNA-protein tethers per field of view. By increasing anchor protein spots to 300 nm in diameter, we were able to obtain more tethers in a shorter amount of time compared to 150 nm wide protein spots. An analysis of these results shows that since the area of each protein anchor spot is small compared to anchor spots described in previously published reports [2], it will take more time for the DNA to bind to these small features (Figure 4).

Future Work:

There are several ways to improve the number of DNA tethers in the future work: (1) Increase DNA concentration (2) tether DNA to magnetic beads and place a magnet under the glass so the DNA is more likely to dwell near the cover slide surface and thus more likely to bind to the protein anchor or (3) test larger stamp circles.

Acknowledgements:

NSF and NNCI funding via NSF grant no. ECCS-1542081, Cornell NanoScale Facility, PI Dr. Michelle Wang, Mentors Ryan Badman and Jim Baker, Lab Members Jaeyoon Lee, Guillermo V. Vargas, and Seong Ha Park, CNF REU Program Coordinator Melanie-Claire Mallison, CNF Staff Michael Skvarla, Tom Pennell, Jeremy Clark, and Edward Camacho.

References:

[1] Coyer, Sean R., Andrés J. García, and Emmanuel Delamarche. "Facile Preparation of Complex Protein Architectures with Sub.100.nm Resolution on Surfaces." Angewandte Chemie International Edition 46.36 (2007): 6837-6840.

[2] De Vlaminck, Iwijn, et al. "Highly parallel magnetic tweezers by targeted DNA tethering." Nano letters 11.12 (2011): 5489-5493.

Multi-Organ Microphysiological Systems for Drug Screening

CNF Project Number: 731-98
Principal Investigators: Michael L. Shuler, Harold G. Craighead
Users: Ying Wang, Paula Miller, Chen-yu Chen

Affiliations: Nancy E. and Peter C. Meinig School of Biomedical Engineering, Robert Frederick Smith School of Chemical and Biomolecular Engineering; Cornell University

Primary Sources of Research Funding: National Center for Advancing Translational Sciences, National Science Foundation, National Institutes of Health

Contact: MLS50@cornell.edu, hgc1@cornell.edu, ying.wang@cornell.edu, pgm6@cornell.edu, cc2569@cornell.edu

Website: https://www.bme.cornell.edu/people/profile.cfm?netid=mls50

Primary CNF Tools Used: VersaLaser laser cutter, ObJet30 Pro 3D printer, PDS 2010 Labcoter2parylene coater

Abstract:

Novel preclinical screening models that can better predict clinical outcomes are in urgent need to expedite drug development at sustainable cost. Human cell culture-based, multi-compartmental multi-cellular microphysiological systems (MPS) hold the potential of recreating the dynamic *in vivo* drug process and human cell response *in vitro* and are thus promising to serve as a "human surrogate" for drug screening. These microphysiological systems are featured with microfluidic interconnections among chambers that mimic the blood circulation in the body allowing for organ-organ interactions. We are currently developing several multi-organ MPS, with different emphases on lung drug inhalation, spleen immune responses and central nervous system (CNS) drug uptake.

Summary of Research:

Lung-on-a-Chip Platform for Inhalation Drug Screening and Development. Pulmonary diseases such as asthma and chronic obstructive pulmonary disease (COPD) are the leading causes of respiratory death. Current preclinical drug screening process for inhalation drugs for treatment relies on animal models and is often costly and time consuming. Drug administration through inhalation for long-term sustained release has also gained substantial recognition in recent years. The development of Lung-on-a-Chip models aims to bypass animal models and provide a high adaptive way to fit into the human anatomy. We have developed a pumpless microfluidic inhalation drug screening system that could be used to evaluate drug inhalation, metabolism and toxicity. This microphysiological system includes a "breathing" lung chamber, a liver and a tumor chamber with 3D tissue constructs (Figure 1). The lung chamber was designed to mimic human alveolar-capillary interface and active air flow breath function. The expansion of the lung chamber was driven by vacuum pump via an expandable silicone membrane (Figure 1). The Lung-on-a-Chip platform consists of two poly(methyl methacrylate) (PMMA) layers and two silicone layers, which were patterned using a CO_2 laser cutter VersaLaser at CNF. The microfluidic channels and reservoirs were etched to desired dimensions into the bottom PMMA layer using the CO_2 laser.

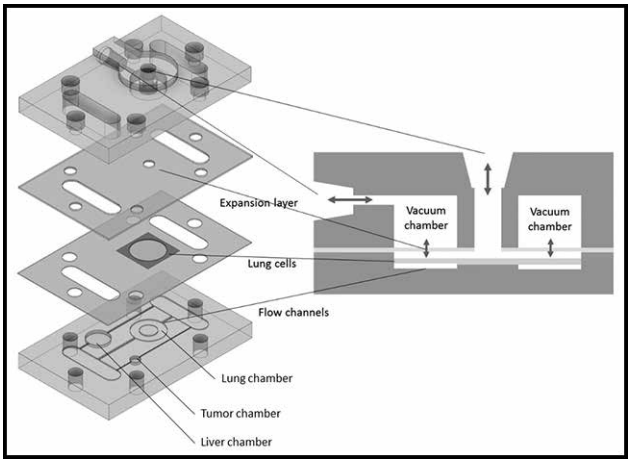

Figure 1: Design of the lung-on-a-chip device.

Liver-BBB-Tumor Chip. We are developing a three-organ human microphysiological system that could be used for central nervous system (CNS) drug screening. The device contains three cell chambers, representing "liver," "blood brain barrier (BBB)," and "tumor," respectively. The organ chambers are interconnected via microfluidic channels and perfused with blood surrogate at physiologically relevant flow rates using a

pumpless microfluidic platform [1,2]. The microfluidic platforms were fabricated using a 3D object printer (Objet 30Pro at CNF) and coated with a conformal layer of parylene-C via a vapor deposition system (PDS-2010 Lab LABCOTER® 2 at CNF) for enhanced chemical resistance and biocompatibility. The BBB constructs were prepared with brain microvascular endothelial cells (BMECs) derived from human induced pluripotent stem cells (hiPSCs) and primary human astrocytes that were co-cultured on the two sides of a porous polycarbonate membrane [3]. Liver 3D cultures were prepared from human primary hepatocytes and non-parenchymal cells (NPCs) encapsulated in hydrogels. The tumor chamber was filled with hydrogel encapsulated MCF-7 cells. Our Liver-BBB-tumor model could be used to evaluate drug metabolism by liver cells, brain uptake of drug and its metabolites across the BBB and the toxicity towards tumor cells. This model will be a valuable tool for screening of brain drug candidates.

Design and Demonstration of a Five-Compartment Microphysiological System. We describe a human "Body-on-a-Chip" device (or microphysiological system) that can be used to emulate the *in vivo* drug process of absorption, distribution, metabolism and toxicity as well as immune responses. The device contains five different chambers representing bone marrow, inflamed spleen, GI tract, liver and fat (Figure 2). The design of the 5-organ MPS is based a physiologically based pharmacokinetic (PBPK) model.

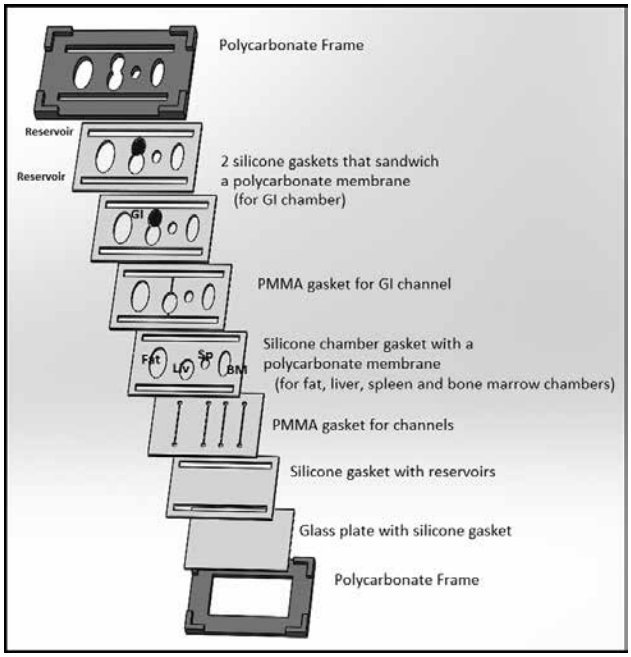

Figure 2: Design of the 5-compartment microphysiological system. Schematic exploded view of the microfluidic platform.

The barrier chamber layer (GI tract) allows direct access for administration of chemical or biological compounds, which must pass through the GI barrier and undergo a first-pass hepatic metabolism before entering the circulation. The non-barrier chambers were created as three-dimensional configurations by encapsulating cells in PGMatrix (Pepgel, Manhattan, KS). The reported average human male organ volumes and organ flow rates [4] were used to estimate the fluid retention times in each organ chamber. A custom programmed rocker platform was used to create circulation using gravity-drive flows. The silicone cell culture chamber layers and plastic channel layers were patterned using the CO_2 laser VersaLaser at CNF. The device is optically transparent and thus allows for daily monitoring. This five-chamber device will be used to study preclinical anti-leishmaniesis drug toxicity and response.

References:

[1] J. H. Sung, C. Kam, M. L. Shuler, Lab Chip 2010, 10, 446.

[2] Y. I. Wang, C. Oleaga, C. J. Long, M. B. Esch, C. W. McAleer, P. G. Miller, J. J. Hickman, M. L. Shuler, Exp. Biol. Med. 2017, 153537021769410.

[3] Y. I. Wang, H. E. Abaci, M. L. Shuler, Biotechnol. Bioeng. 2016, 9999, 1.

[4] R. Keenan, J. Dunn, V. N. Shlyaptsev, R. F. Smith, P. K. Patel, D. F. Price; October 16, 2003, SPIE UCRL-PROC-200323.

Improved Single Cell Whole Genome via Microfluidic Platform

CNF Project Number: 762-99
Principal Investigator: Harold G. Craighead
Users: Harvey C. Tian, Sarah Reinholt

Affiliation: Applied and Engineering Physics, Cornell University, Ithaca
Primary Source of Research Funding: National Cancer Institute
Contact: hgc1@cornell.edu, hct33@cornell.edu, sjr236@cornell.edu
Primary CNF Tools Used: ABM contact aligner, Unaxis deep silicon etcher

Abstract:

We present a valveless microfluidic device for single cell capture and on-chip whole genome amplification of immobilized deoxyribonucleic acid (DNA). This device uses a series of closely spaced micropillars to physically entrap single cells and its genomic DNA (gDNA) upon cell lysis. Our past work has demonstrated high efficiency DNA capture using micropillar arrays from varying cell counts (hundreds) down to a single cell [1]. Here, we demonstrate the ability to perform in-channel chemistries, such as DNA amplification, to the immobilized gDNA in our device by sequentially introducing reagents into our channels. We describe a method for using our device to reduce amplification bias during isothermal whole genome amplification (WGA) of single cells. We report that out of six gene loci sampled, we detect all six loci from the single cell WGA product collected from our device compared to two out of six in control samples. Single cell WGA has long suffered from amplification bias. To this end, several technologies have been developed to improve genome coverage and reduce amplification bias including emulsion based techniques [2], linear amplification [3], and microfabricated devices [4,5]. Our approach fundamentally differs from existing methods as we perform WGA under a constant flow of reagents across extracted gDNA that has been elongated and immobilized within our device.

Summary of Research:

Our device, as shown in Figure 1(A), contains a single input port leading to multiple separate yet identical channels each containing a micropillar array region, Figure 1(B). A suspension of human cervical cancer cells (HeLa cells) are loaded into the input single cells were captured at the apex of the micropillar array as depicted in Figure 1(B) while excess uncaptured cells flow through to the output ports where they were removed. Upon introducing a cell lysis agent into the channel, the gDNA of entrapped cell become physically entangled on the micropillars immediately downstream from the original position of the cell and this gDNA can be labeled and visualized as in Figure 1(C).

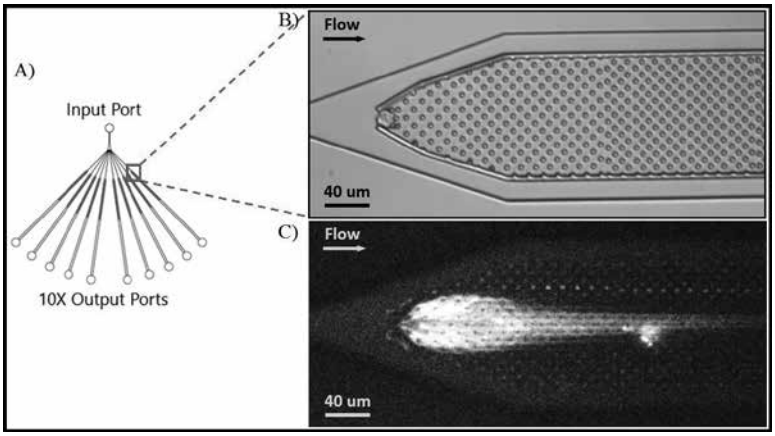

Figure 1: Microfluidic device schematic and micrograph of entrapped single cell and extracted DNA. The fabrication of this device was done using the CNF ABM contact aligner and Unaxis deep silicon etcher.

The extracted gDNA can then be isothermally whole genome amplified on-chip using commercially available multiple displacement amplification (MDA) reagents. Because the amplified DNA fragments are below the size threshold necessary to become entangled upon the 2 μm diameter micropillars, they flow through the pillars and can be collected at the output port at the end of the amplification.

To assess amplification bias, we sampled six cancer gene loci spaced across the human genome. We used PCR and targeted primer pairs to determine the presence or absence of each loci within the WGA product. Positive controls were performed on single cells isolated through fluorescence activated cell sorting (FACS).

Our results indicate that single cell genomes amplified with our device showed 6/6 gene loci detected as compared to 2/6 from samples in which single cells isolated via FACS. We believe the ability to perform amplification and other processes on immobilized but accessible DNA in a flowing system is responsible for the reduced amplification bias and provides a system for other processes on single cell genomes.

References:

[1] "Microfluidic extraction, stretching and analysis of human chromosomal DNA from single cells," J. J. Benitez, J. Topolancik, H. C. Tian, C. B. Wallin, D. R. Latulippe, K. Szeto, P. J. Murphy, B. R. Cipriany, S. L. Levy, P. D. Soloway, H. G. Craighead, Lab Chip, 12, (2012).

[2] "Uniform and accurate single-cell sequencing based on emulsion whole-genome amplification," Y. Fu, C. Li, S. Lu, W. Zhou, F. Tang, X. S. Xie, Y. Huang, PNAS, 112, 38 (2015).

[3] "Genome-Wide Detection of Single-Nucleotide and Copy-Number Variations of a Single Human Cell," C. Zhong, S. Lu, A. R. Chapman, X. S. Xie, Science, 338, (2012).

[4] "Massively parallel polymerase cloning and genome sequencing of single cells using nanoliter microwells," J. Gole, A. Gore, A. Richards, Y. Chiu, H. Fung, D. Bushman H. Chiang, J. Chun, Y. Lo, K. Zhang, Nature Biotech, 31, 12 (2013).

[5] "A Quantitative Comparison of Single-Cell Whole Genome Amplification Methods," C. F. A. deBourcy, I. D. Vlaminck, J. N. Kanbar, J. Wang, C. Gawad, S. R. Quake, PLOS One, 9, 8 (2014).

Graphene Transistors for Biological Sensing

CNF Project Number: 900-00

Principal Investigator: Paul L. McEuen

Users: Michael F. Reynolds, Samantha Norris, Kathryn L. McGill

Affiliations: Laboratory of Atomic and Solid State Physics, Department of Physics, Cornell University; Department of Physics, Oregon State University

Primary Sources of Research Funding: National Science Foundation (DMREF DMR-1435999), Cornell Center for Materials Research (CCMR DMR-1120296), Brain Research through Advancing Innovative Neurotechnologies Initiative through Early Concept Grants for Exploratory Research (NSF DBI-1450967)

Contact: plm23@cornell.edu, mfr74@cornell.edu, sn588@cornell.edu, klm274@cornell.edu

Website: http://www.mceuengroup.lassp.cornell.edu/

Primary CNF Tools Used: Oxford ALD, graphene furnace, Autostep i-line stepper, Oxford 81

Abstract:

Two-dimensional materials provide a platform for biocompatible yet conformal cellular sensing devices. We report a releasable graphene field-effect transistor fabricated using standard photolithography, and we demonstrate the electrical response of these devices to action potentials from cardiomyocytes and mouse neurons *in vitro*.

Summary of Research:

Presently, there are numerous methods for single-cell action potential detection, but all struggle to simultaneously obtain high spatial, temporal, and electrical resolution The use of moveable microscopic graphene field-effect transistors (FETs) has the potential to solve many of these problems.

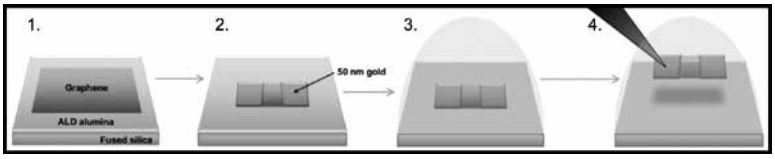

Figure 1: The fabrication process for flexible, releasable graphene FETs.

Since graphene has remarkable voltage sensitivity, the action potential passing through a nearby cell can be easily detected by measuring the current flowing through the device. Moreover, freely-released graphene devices can be manipulated to conform to the cells of interest [1], thereby maximizing the signal recorded in this extracellular measurement. Finally, graphene absorbs only 2% of white light. Its effective transparency allows electrical measurements to be performed simultaneously with numerous imaging techniques, granting high spatial resolution coincident to an electrical measurement of cell action potentials.

We pattern the graphene using standard photo-lithography techniques. This allows us to play with designs to allow for a more conformal placement on the cell without degrading the electrical responsivity of the device [1]. To prepare these samples, we initially cover our substrate with 20 nm of aluminum oxide (alumina) grown via atomic layer deposition (Oxford ALD), as shown in Figure 1.1. This layer of alumina is a sacrificial layer and will be etched away shortly before the experiment (see Figure 1.3). After transferring graphene, grown via chemical vapor deposition, on top of the substrates, we evaporate 50 nm of gold on top of these samples and pattern it using standard photolithographic processes (exposing with the Autostep i-line Stepper). As shown in Figure 1.2, the final photolithography step is to oxygen plasma etch the graphene into the desired shape (Oxford 81).

After etching away the alumina in hydrochloric acid, the devices, now weakly adhered to the substrate, are placed into the same Petri® dish in which the neural or cardiac cells were cultured. In order to manipulate the devices, platinum-iridium probes were attached to micromanipulators; by forcing these probes into the gold pads, sufficient contact is made to pick up the device. To reduce electrical noise but still allow current to flow, the shafts of the probes were insulated except for a small exposed tip. It is important to note that from the time the alumina is etched away, the devices must remain in fluid; otherwise, we are unable to remove them from the surface and freely manipulate them in space. After picking up a device, it is then placed upon a cell. Experiments are performed in standard cell media,

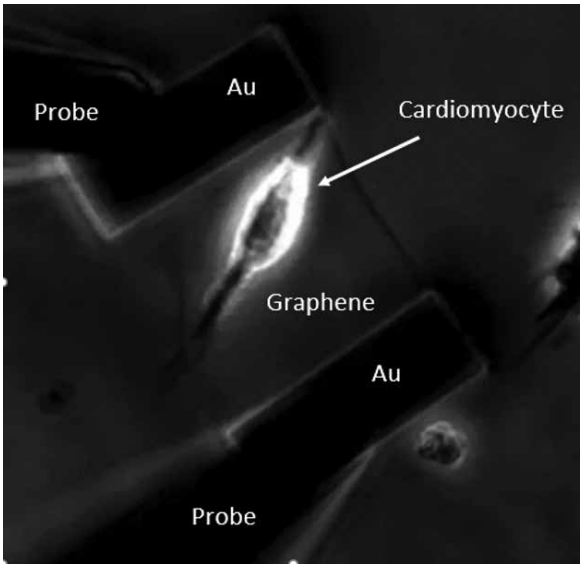

Figure 2: Using probes to manipulate a graphene device on top of a single cardiomyocyte.

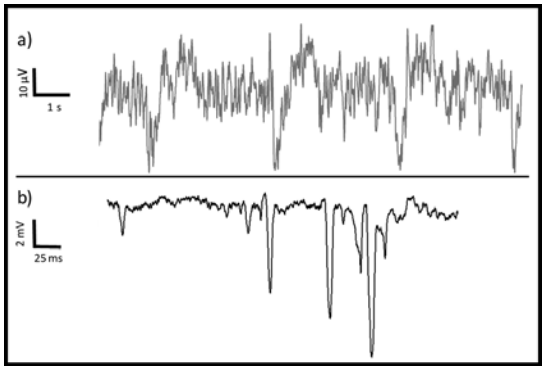

Figure 3: Experimental data obtained from a) cardiomyocytes grown on top of graphene devices at Cornell, and b) graphene devices placed on top of mouse neurons at Oregon State University.

and the electrolyte potential of the media is controlled by a Ag/AgCl reference electrode inserted into the fluid.

An experiment with graphene devices placed on top of cardiomyocytes is shown in Figure 2. As expected, the graphene appears as a mostly transparent sheet stretched between the two gold pads. To monitor the current through the graphene device, a small voltage bias of ~ 100 mV is placed across the device by connecting one of the probes to a battery. We monitor the current flowing through the device using an amplifier connected to either an oscilloscope or data acquisition hardware, depending on our experimental needs.

Successful experiments have been performed with non-released devices (upon which cells are grown) using cardiomyocytes at Cornell and with releasable (free-floating) devices on mouse neurons by collaborators at Oregon State University. The devices used at Cornell were fabricated at CNF, and the cardiomyocytes were cultured by Tyler Kirby, a postdoctoral fellow in the Lammerding lab at Cornell. The resulting data is shown in Figure 3. The neuronal data agrees with the literature [2], yet the cardiomyocyte action potential spike is ~ 100x wider and smaller than anticipated.

Moving forward, we plan to improve our graphene devices to increase the signal-to-noise ratio of our data and improve device-cell contact to capture more of this trans-membrane current. Presently, we are experimenting with device geometries and characterizing a process to put silicon dioxide o-rings between the graphene devices and cells. In doing so, we hope to trap the ions released by the cell during a firing event, thereby increasing the local voltage gating of the graphene. We will also be considering new methods for manipulating our devices with the ultimate goal of performing an electrical measurement *in vivo*.

References:

[1] Blees, M., et al. Graphene kirigami. Nature 524, 204-207 (2015).

[2] Blaschke, B. M., et al. Flexible graphene transistors for recording cell action potentials. 2D Materials 3, (2016).

[3] Hess, L.H., et al. Graphene transistor arrays for recording action potentials from electrogenic cells. Advanced Materials 23, 5045-5049 (2011).

A MEMS Microtensiometer for Sensing Water Potential in Plants and Soils

CNF Project Number: 1119-03

Principal Investigator: Abraham D. Stroock

Users: Michael Santiago-Pinero, Winston L. Black II, Siyu Zhu, Olivier Vincent, Antoine Robin

Affiliation: Department of Chemical and Biomolecular Engineering, Cornell University

Primary Sources of Research Funding: National Science Foundation (CBET-0747993 and CHE-0924463), the Air Force Office of Scientific Research (FA9550-15-1-0052), the National Institute of Food and Agriculture, U.S. Department of Agriculture (under Agreement No. 2010-51181-21599)

Contact: abe.stroock@cornell.edu, ms2343@cornell.edu, wlb62@cornell.edu, sz393@cornell.edu, robin.antoine93@gmail.com

Website: www.stroockgroup.org

Primary CNF Tools Used: Thermal oxide furnace, LPCVD furnace, Oxford 81/82, SÜSS SB8e, Oxford PECVD, DISCO dicing saw

Introduction:

We have been pursuing the application of the second generation micro-tensiometer in environmental and agricultural contexts and for the study of related fundamental phenomena. A micro-tensiometer (μTM) measures the temperature and water potential (equivalent to the chemical potential of water) in its immediate environment for applications in physical chemical research on the properties of liquid water.

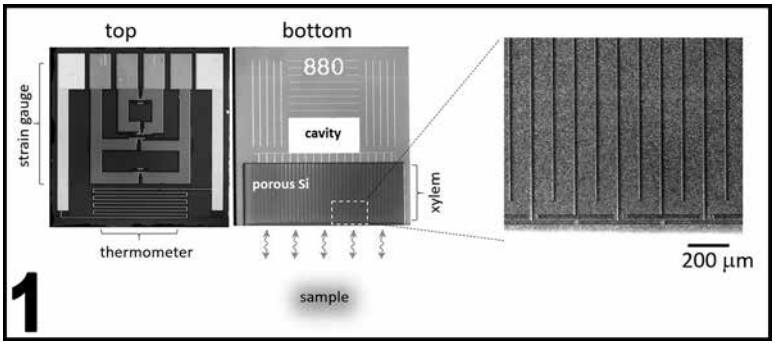

We have reported the design of the second generation μTM, and the preliminary results about the response of embedded sensors in trees last year. This year, we focused on applying the μTM for monitoring the plant water status, and the study of metastable solid-liquid equilibrium of water. We have developed the methodology to install a μTM into the trunk of a tree, and conduct diurnal stem water potential measurements; the observed values agree well with the benchmark, manual technique. We have also managed to provide the first direct measurement of the Gibb-Thomson equilibrium between ice and liquid in the doubly metastable state of tension and supercooling.

Summary of Research:

Motivation. This project seeks to develop a microelectromechanical system (MEMS) tensiometer capable of sensing water potential. Water potential, Ψ (MPa) is a thermodynamic quantity that defines the thermodynamic availability of water for chemical reactions and physical processes such as mass transfer. Of particular interest is the range of Ψ near saturation that occurs in the plants and soil that make up the biosphere. Accurate, *in situ* measurements in this range have not been achievable with current technologies. The ability to perform such measurements has important implication for studying the basic biology of plants, for precision agricultural techniques such as deficit irrigation, and for basic questions about the thermodynamics of water itself.

Design. Figure 1 presents images of our micro-tensiometer. The top view shows the wiring associated with a strain gauge in the form of a Wheatstone bridge of poly(silicon) piezoresistors and a platinum resistance thermometer. The bottom view shows a cavity that we fill with pure liquid water; the layer of silicon above this cavity acts as a diaphragm, the deflection of which is measured by the strain gauge on the top side. This cavity is connected to the bottom edge via channels and a zone of nano-porous silicon that we form as a thin layer on the bottom side of the wafer; the design of this structure was inspired by the structure of xylem, the conductive tissue in plants. The cavity and microchannels are seal by bonding the bottom side of a glass wafer. As water leaves the cavity through the nanoporous membrane, the pressure of the liquid in the cavity drops until it comes to equilibrium with the external phase of water. We measure the difference in pressure between the inside and outside gives us Ψ and is measured with the calibrated strain gauge.

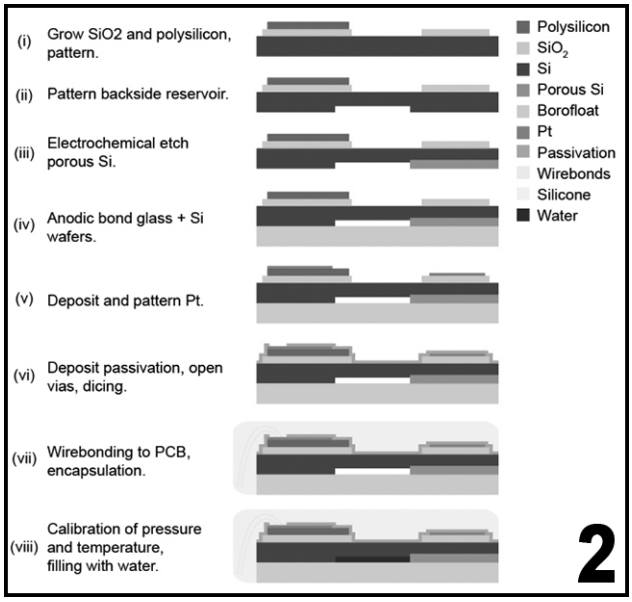

Method. Figure 2 presents an abbreviated representation of our process flow. The important steps in this process are: growth of insulating oxide (B2 thermal oxide furnace), deposition and patterning of poly(silicon) (LPCVD furnace C4), etching of cavity and microchannels (Oxford 81/82), anodic etching of porous silicon membrane, anodic bonding of silicon to glass (SÜSS SB8e), deposition and patterning of platinum with titanium adhesion layer, deposition of passivation layers (Oxford PECVD), and dicing. After dicing, chips were mounted and wire bonded to custom PCBs and selectively encapsulated in various materials to protect electronic elements from water and while allowing for exchange through the membrane.

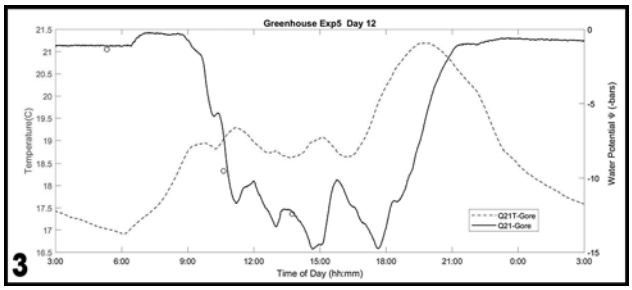

Application in Plants. Figure 3 presents the comparison between the response of a µTM embedded directly within the stem of a potted apple tree (solid curve, right y-axis) and a Scholander pressure chamber (black circles, right y-axis). As expected, temperature

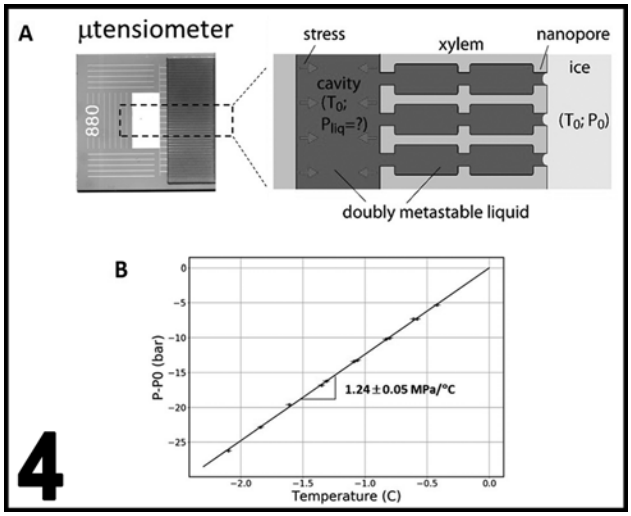

(dashed curve, left y-axis) rises during the day and decreases at night, and the water potential decreases during the day after transpiration starts in response to sunrise, and increases when the transpiration slows down and the stem rehydrates with water feed from the soil. The measured stem water potential was within the range for a well-watered apple tree (> -15 bars), and matched the Scholander pressure chamber, a widely accepted hygrometer that requires point by point manual measurements and high-pressure gas.

Studies on Metastable Solid-Liquid Equilibrium of Water. Figure 4 presents the water potential of ice measured by direct submersion of a µTM inside ice and with cooling of the system down to -2.2°C. Figure 4A presents a schematic diagram of the direct contact between ice and metastable liquid water in the sensor. Figure 4B shows the linear correlation between the system temperature and measured water potential (MPa). The tension increases with the decreasing of temperature at the rate predicted by the Gibbs-Thomson relation (-1.2 MPa/°C).

Current Efforts:

We are building a mathematical model to predict the stem water potential in plants as a function of environmental parameters for comparison with the measurements. We would also like to proceed with the studies on the metastable solid-liquid equilibrium of water by improving the packaging of the sensor and the experiment set-up, or by modifying the design of the current generation of µTM to measure tension under lower temperature (i.e., -10°C or lower).

Silicon Nitride Cantilevers for Muscle Myofibril Force Measurements

CNF Project Number: 1255-04
Principal Investigator: Walter Herzog
Users: Timothy Leonard, Andrew Sawatsky

Affiliation: Faculty of Kinesiology, University of Calgary, Calgary, Canada

Primary Sources of Research Funding: Natural Sciences and Engineering Research Council of Canada, Canadian Institutes of Health Research and the Canada Research Chair for Cellular and Molecular Biomechanics

Contact: wherzog@ucalgary.ca, leonard@ucalgary.ca, ajsawats@ucalgary.ca

Website: www.ucalgary.ca/knes

Primary CNF Tools Used: GCA 5x Stepper, Oxford 81, Si_2N_3 furnace, critical point dryer system

Abstract:

To measure muscle forces in the nano-Newton range, silicon nitride cantilever pairs were manufactured using the GCA 5x-Stepper photolithography system and the Oxford 81 ion etching system at the CNF, and then used in our lab in Canada. We investigated titin mechanical properties using a skeletal muscle myofibril model. Our experiments demonstrate that in myofibrils at long sarcomere length, the free-spring length of titin, which is present in the I-band region of the sarcomere, is an adjustable spring and allows for a tunable length.

Summary of Research:

Titin is a giant molecular spring present within the sarcomere and is responsible for most of the passive force found in muscle. Titin has elements with different stiffness and visco-elastic properties that come into play in an orderly fashion with increasing sarcomere length. In skeletal muscle, the I-band region of titin contains two distinct immunoglobulin (Ig) domains, a small N2A portion, and the PEVK segment [1]. Lengthening a skeletal muscle sarcomere within the physiologically relevant range first causes the Ig domains to straighten out and is then followed by extension of titin's PEVK domain. Both of the Ig regions (proximal and distal) and the PEVK region are thought to be essentially elastic at physiologically relevant sarcomere lengths (SL). However, at SL greater than the physiological range, Ig domains start to unfold during stretch, and this unfolding is thought to be responsible for titin then behaving in a highly visco-elastic manner.

Previous work by our group has shown that elevated passive forces in activated and lengthened muscle at very long SL (when myofilament overlap is lost) are much higher than the purely passive forces at matched SL [2]. A proposed mechanism for this is that the free-spring length of the titin is shortened by titin-actin interactions, thereby effectively producing a shorter and hence stiffer spring. If this is the case, then the question arises, does this interaction occur at one specific location on both filaments (titin and actin)? If so, then the free-spring length of titin has only two configurations; one long with no interactions (as in the passive state), and one shorter, due to interactions (in the active state). A 2-state model would mean that at long SL in active and then lengthened muscle, all forces should be similar since all free-spring lengths are similar.

Myofibrils were harvested from psoas muscle obtained from New Zealand White rabbits and were chemically and mechanically isolated as described in our previous work [3]. Single myofibrils were attached to nanofabricated silicon-nitride cantilevers (stiffness 68pN/nm) [4] for force measurement at one end of the myofibril (resolution < 0.5 nN), and at the other end, a glass pipette needle attached to a piezo-motor for controlling specimen length (Figure 1). Testing was done using an activating solution that contained ATP and free calcium with a pCa of 3.5. Passive data was provided by previous experiments [2]. Submaximal active forces were obtained by adding BDM (2,3-butanedione monoxime) to the activating solution. Myofibrils were either fully activated (n=1) or submaximally activated (n=4), and then stretched from an average sarcomere length of 2.6 μm to a final SL of approximately 5 μm at a speed of 0.1 μm/s/sarcomere. At a long SL, in this case 4.5 μm, stress was measured for all samples so as to provide a matched SL for all tests. Stress was reported by normalizing force with the cross-sectional area of each myofibril.

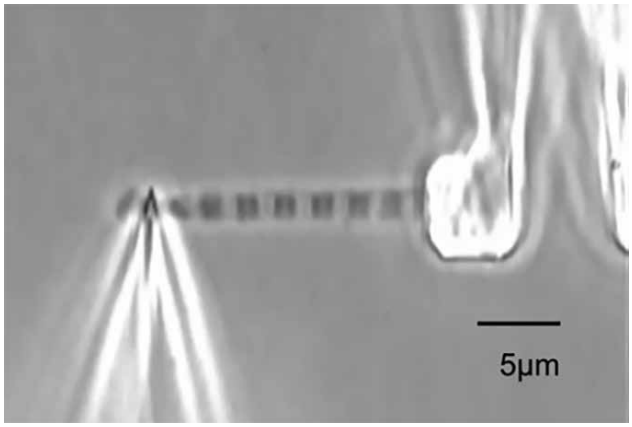

Figure 1: Myofibril attached to a glass needle for stretch-shortening and nano-levers for force measurement. An example of a single myofibril with eight sarcomeres in-series.

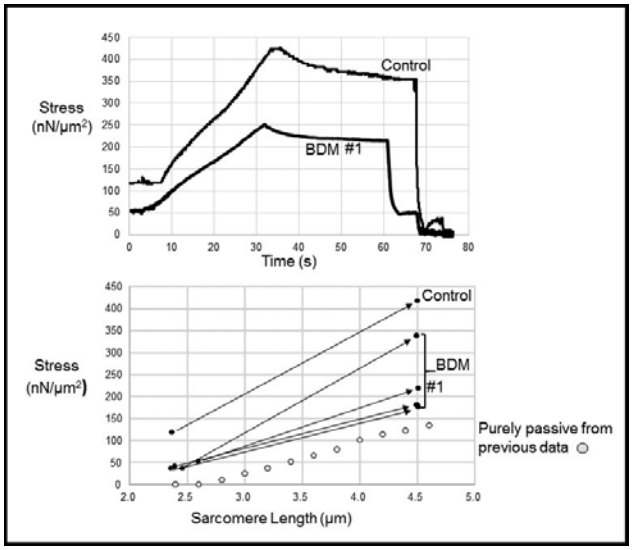

Figure 2: Stress-time data for two of the experiments (upper) and stress-sarcomere length results (lower) taken at SL of 4.5 μm for all tests.

Figure 2 (upper panel) is the stress-time data for two of the tests. Note that in the fully activated (control) test, the stress is substantially higher compared to one of the activated (with BDM) trials. Figure 2 (lower panel) shows all five activated trials and at matched sarcomere lengths, (4.5μm), the stress values range from just above the passive values (approximately 175nN/μm^2) up to fully activated at 425 nN/μm^2. Myofilament overlap in psoas myofibrils is lost at SL beyond 4 μm, and so forces at these long lengths are not the result of cross-bridge cycling, and can only be attributed to titin.

From our results, we conclude that the I-band free-spring length of titin appears to be variable. The variation in stress for specimens at the same length and at very long SL (where active cross-bridge cycling is not possible) can only be explained by a variation in the titin free-spring length. The idea that the titin-actin attachment is a 2-state model only must be incorrect and so the sites for the interaction between these proteins must occur along the length of one or maybe both. If this is so, then the tunability of the free-spring length of titin poses interesting questions for future research.

References:

[1] Granzier and Labeit. Muscle Nerve. 36:740-755, 2007.

[2] Leonard and Herzog AJP-Cell. 299(1):C14-20, 2010.

[3] Joumaa et al. Eur J Physiol. 455:367-371, 2007.

[4] M. E. Fauver, et al. IEEE Trans Biomed Eng 45(7), 891, 1998.

Biomimetic Models of the Tumor Microenvironment and Angiogenesis

CNF Project Number: 1540-07, 1278-04
Principal Investigators: Claudia Fischbach-Teschl, Abraham D. Stroock
Users: Peter DelNero, Lu Ling, John Morgan

Affiliation: Department of Biomedical Engineering, Cornell University
Primary Source of Research Funding: National Institutes of Health (NIH)
Contact: cf99@cornell.edu, abe.stroock@cornell.edu, pfd28@cornell.edu, LL657@cornell.edu, jpm339@cornell.edu
Websites: www.fischbachlab.org, www.stroockgroup.org
Primary CNF Tools Used: SU-8 photolithography; ABM contact aligner, Karl Suss RC-8, SU-8 hotplates

Abstract:

Cancer is a disease of nature and nurture. On the one hand, oncogenic mutations drive the hyperproliferation of malignant cells. On the other hand, tumor growth and metastasis is intimately dependent on the surrounding tissue microenvironment that the cancer cells inhabit. Microvascular perfusion is a critical determinant of this environment. The microcirculatory system mediates the exchange of respiratory gases, metabolites, and drugs. In cancer, abnormal blood flow results in a highly heterogeneous tissue environment, which drives the evolution of increasingly adaptive cancer cell phenotypes. Our project uses tissue engineering and microfluidic approaches to unravel the complex interdependence between cancer cells and the vascular microenvironment, specifically in the context of tissue transport and tumor metabolism.

Summary of Research:

As the primary conduit of oxygen, nutrients, drugs, and other biomolecular signals, the vasculature is a critical determinant of the tumor microenvironment. To explore the interactions between cancer cells and the peripheral blood vessels, we integrated cancer biology and tissue engineering strategies to fabricate artificial tumor mimetics with explicit microvasculature, fully embedded within remodelable hydrogel scaffolds. We are using these *in vitro* models to investigate: 1) the regulation of vascular function and angiogenesis by cancer cells; 2) how microvascular dysfunction disrupts homeostatic tissue perfusion; 3) how populations of tumor cells adapt their metabolic phenotype in response to aberrant transport gradients [1]. By studying tissue-level phenomena, we hope to identity novel insights on disease progression that may inform a more effective use of existing anti-cancer treatments.

To investigate these questions, we use biomaterials-based microfluidic platforms to recapitulate the tumor-vascular microenvironment. In our previous report, we demonstrated the fabrication of endothelialized microvascular structures that displayed membrane barrier function and angiogenic sprouting. This year, we are integrating localized tumor compartments to create a more sophisticated co-culture system. This model allows precise control of microenvironmental

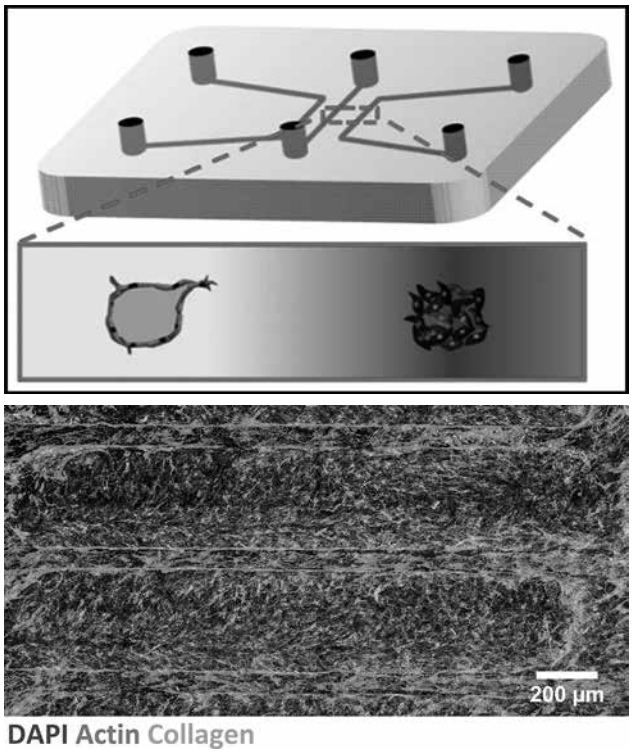

Figures 1-2: Schematic illustration (1) and confocal micrograph (2) of microfluidic biomaterials using lithographically patterned collagen gels.

conditions and *in situ* analysis of cell status. Moving forward, we aim to use the co-culture model to correlate the emergence of heterogeneous phenotypes within the asymmetric microvascular landscape. If successful, this approach will provide a tool to address previously inaccessible questions about tumor adaptation and evolution during disease initiation, progression, treatment, and recurrence.

In addition, we used soft-lithography to generate a collagen-based microwell platform to study the role of extracellular matrix remodeling in tumor angiogenesis [2,3]. Specifically, adipose stromal cells (ASCs), a major stromal component of mammary microenvironment, simultaneously deposit and contract the tumor matrix. In addition, these cells generate potent pro-angiogenic factors that promote blood vessel growth. We have previously shown that in tumor, ASCs become myofibroblastic cells that exhibit increased matrix remodeling and VEGF secretion. To evaluate the relative contributions of matrix structure and soluble factor secretion, we utilized microfabricated biomaterial-based assays to assess 3D endothelial cell sprouting. Our findings indicate that matrix remodeling by ASCs can be as equally, or even more important than, pro-angiogenic factor secretion in facilitating new vessel growth.

References:

[1] P. DelNero, M. Lane, S.S. Verbridge, B. Kwee, P. Rabbany, B. Hempstead, A. Stroock, C. Fischbach, 3D culture broadly regulates tumor cell hypoxia response and angiogenesis via pro-inflammatory pathways, Biomaterials, 2015;55:110-8.

[2] Y.H. Song, S.H. Shon, M. Shan, A. Stroock, C. Fischbach. Adipose-derived Stem Cells Increase Angiogenesis through Matrix Metalloproteinase-dependent Collagen Remodeling, Integrative Biology, 2016;8:205-215.

[3] R. Seo, P. Bhardwaj, S. Choi, J. Gonzalez, R. C. A. Eguiluz, K. Wang, S. Mohanan, P. G. Morris, B. Du, X. K. Zhou, L. T. Vahdat, A. Verma, O. Elemento, C. A. Hudis, R. M. Williams, D. Gourdon, A. J. Dannenberg, C. Fischbach, Obesity-dependent changes in interstitial ECM mechanics promote breast tumorigenesis. Sci. Transl. Med. 7, 301ra130 (2015).

Stamping and Twisting: Using Bio-Nanotechnology to Enhance Single Molecule Experiments

CNF Project Number: 1738-08

Principal Investigator: Michelle D. Wang[1]

Users: Ryan Badman[1], James Baker[1,2], Xiang Gao[1,2]

Affiliations: 1. Department of Physics, Cornell University, Ithaca NY;
2. Howard Hughes Medical Institute, Chevy Chase, Maryland

Primary Source of Research Funding: Howard Hughes Medical Institute

Contact: mdw17@cornell.edu, rpb226@cornell.edu, jeb94@cornell.edu, xg237@cornell.edu

Website: http://wanglab.lassp.cornell.edu/

Primary CNF Tools Used: ASML Deep UV stepper, Oxford 100, PT 72, Trion chrome etcher, MVD 100 molecular vapor deposition, Zeiss Supra SEM

Abstract:

Traditional, single laser optical tweezer deoxyribonucleic acid (DNA) experiments trap, within the focal region of an infrared laser beam, a floating micro- or nanoparticle that is tethered to a glass surface by a single DNA molecule. A DNA tether can be stretched by pulling on the trapped particle, and resulting force-extension spectra can be analyzed to characterize the fundamental properties of bare DNA, or protein-DNA complexes.

The Wang lab is exploring more advanced capabilities beyond the traditional approach discussed above, through two bio-nanotechnology methods: (1) using nanostamps to precisely pattern protein anchor points on a microscope slide for DNA to tether in organized arrays, and (2) using birefringent quartz nanocylinders in angular optical traps to add "twisting" capabilities to optical tweezers that previously could only stretch. The twisting capability of angular optical traps allows measurement of "torque spectra" that provide additional fundamental biophysical information beyond the traditional force-extension spectra generated in DNA stretching.

Summary of Research:

With the goal of pursuing high impact, fundamental biology experiments, the Wang lab has leveraged nanofabrication technologies to augment traditional optical tweezer experiments. We have been pushing beyond the traditional approaches through two nanotechnology methods: (1) using nanostamps [1] to precisely pattern protein anchor points on a glass surface so that DNA molecules are tethered with greater control, and (2) trapping birefringent quartz nanocylinders in angular optical tweezers [2] to add "twisting" capabilities to optical tweezers that previously could only stretch. The twisting functionality allows analysis of "torque spectra" that provide additional fundamental biophysical information beyond the traditional "force-extension spectra" generated in DNA stretching experiments.

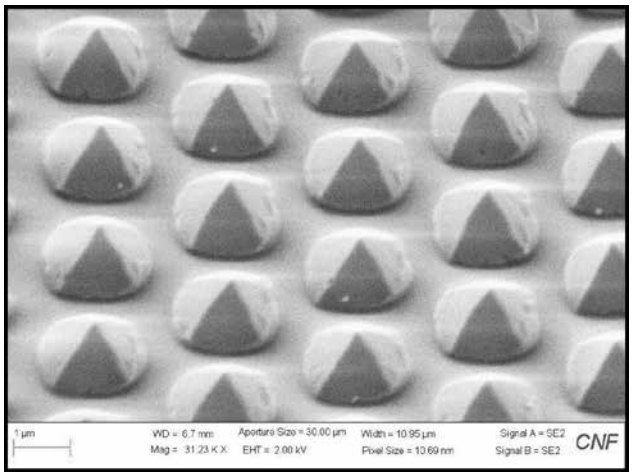

Figure 1: Scanning electron microscope (SEM) image of the stamp surface of a PDMS pyramid array nanostamp. Proteins adsorb on the pyramids, and then transfer to a glass slide during stamping for periodic protein patterning. With these pyramids, protein spots are approximately 500 nm wide, and spaced in an array with 3 µm pitch.

For the nanostamping method, polydimethylsiloxane (PDMS) nanostamps (Figure 1) give the ability to study the interactions between two DNA tethers by precisely controlling the distance between the stamped protein anchor positions. The protein anchors will be spaced

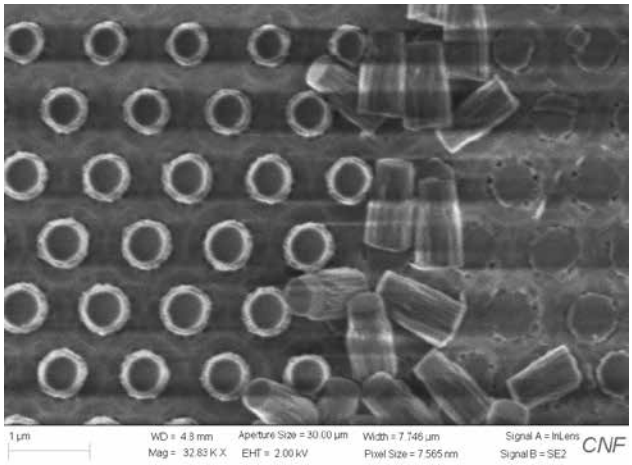

Figure 2: SEM image of quartz cylinders on the quartz wafer. The cylinders on the left side are viewed top down after the cylinders are etched from the quartz wafer. The cylinders on the right side have been knocked over with a razor blade to view the side profile. In an optical trap, these quartz cylinders can be rotated like a light powered motor for applying torque to DNA.

with the same array pitch as the tips of the pyramid on the PDMS stamp. The nanostamps can also increase the local anchor protein density without increasing the overall tether density, which is useful for experiments involving torsionally constrained tethers. The nanostamps can enhance sample preparation outcomes for traditional optical tweezer experiments, angular optical trap studies, and also be used in conjunction with magnetic tweezer setups [3].

For the birefringent trapping targets, while the Wang lab has previously published results using birefringent quartz cylinders [2] for DNA twisting, recently we have been developing newer, faster and highly reproducible protocols using the ASML Deep Ultraviolet (DUV) stepper and the Oxford 100 in CNF to fabricate quartz cylinders with a higher quality than was achieved a decade ago using less advanced nanofabrication tools. Figure 2 shows an example image of recently made quartz cylinders. See Figure 3 for a schematic depicting an example of our experimental setup: a trapped quartz cylinder tethered with DNA to a glass surface.

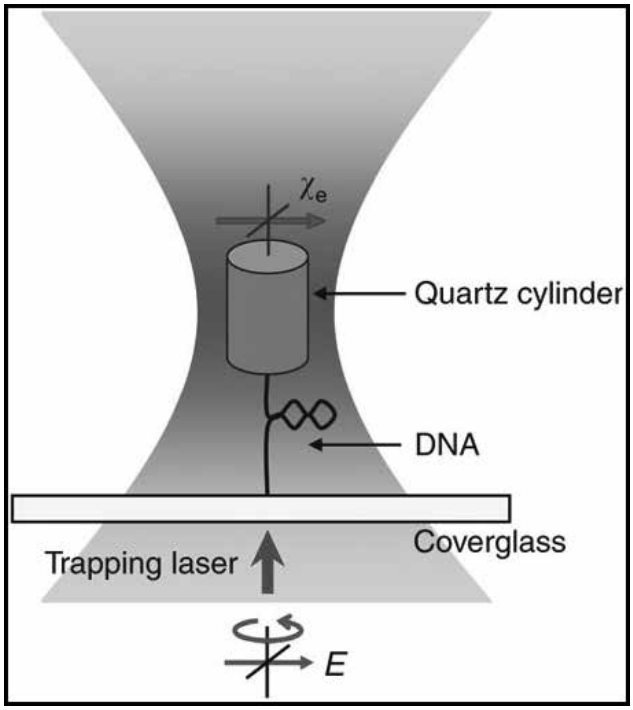

Figure 3: Taken from [2], Figure 3 shows an example of a quartz cylinder attached to a DNA tether that is anchored to protein on a glass coverslip. The quartz cylinder is applying torque to the DNA tether. The protein anchor points on the glass slide can be patterned with nanostamps for more precise and controllable experiments.

References:

[1] Eichelsdoerfer DJ, Liao X, Cabezas MD, Morris W, Radha B, Brown KA, Giam LR, Braunschweig AB, Mirkin CA. Large-area molecular patterning with polymer pen lithography. Nature protocols. 2013 Dec 1;8(12):2548-60.

[2] Deufel C, Forth S, Simmons CR, Dejgosha S, Wang MD. Nanofabricated quartz cylinders for angular trapping: DNA supercoiling torque detection. Nat Methods 2007, 4:223-225.

[3] De Vlaminck, I., and Dekker, C. (2012). Recent advances in magnetic tweezers. Annual review of biophysics, 41, 453-472.

Biocompatible and High Stiffness Tunable Nanophotonic Array Traps with Enhanced Force and Stability

CNF Project Number: 1738-08

Principal Investigator: Michelle D. Wang[1]

Users: Fan Ye[1,2], Ryan Badman[1]

Affiliations: 1. Department of Physics, Cornell University; 2. Howard Hughes Medical Institute, Chevy Chase MD

Primary Source of Research Funding: Howard Hughes Medical Institute

Contact: mdw17@cornell.edu, fy72@cornell.edu, rpb226@cornell.edu

Website: http://wanglab.lassp.cornell.edu/

Primary CNF Tools Used: ASML deep UV stepper, Oxford 100, Unaxis 770, Heidelberg DWL2000, SÜSS MA6-BA6, Gamma automatic coat-develop, LPCVD Nitride - B4, Wet/Dry Oxide - B2, AJA sputter deposition, GSI PECVD, Oxford PECVD, SC4500 odd-hour evaporator, Zeiss Supra SEM, Zeiss Ultra SEM

Abstract:

A nanophotonic trapping platform based on on-chip tunable optical interference allows parallel processing of biomolecules and holds promise to make single molecule manipulation and precision measurements more easily and broadly available. The Wang lab has developed and implemented such an on-chip device based on silicon (Si) or silicon nitride (Si_3N_4) waveguides, coined a nanophotonic standing-wave array trap (nSWAT), that allows for controlled and precise manipulation of trapped nano/micro particle arrays [1,2]. By taking a systematic design approach, we present here a new generation of nSWAT devices with significant enhancement of the optical trapping force, stiffness, and stability, while the quality of the standing wave trap is resistant to fabrication imperfections [3]. The device is implemented on a Si_3N_4 photonic platform and operates at 1064 nm wavelength that permits low optical absorption by the aqueous solution. Such performance improvements open a broader range of applications based on these on-chip optical traps.

Summary of Research:

Optical trapping is a powerful manipulation and measurement technique widely employed in the biological and materials sciences. Miniaturizing bulky and expensive optical trapping instruments onto optofluidic platforms holds promise for high throughput lab-on-chip applications that can be readily integrated with other novel lab-on-chip innovations such as fluorescent detectors or on-chip lasers.

Recently, we have demonstrated a high-throughput, near-field nanophotonic trapping platform that achieved stable trapping with precision controllable repositioning [1-3]. The core concept of the platform is nanophotonic standing-wave interferometry, where laser light travels through a nanophotonic waveguide, is split into two equal intensity laser beams, the two beams are guided by the waveguides and meet each other, which ultimately leads to interference of two counter-propagating laser beams and results in the formation of standing waves. The evanescent field of the antinodes of the standing wave forms an array of stable three-dimensional optical traps. We call this type of trap a nanophotonic standing-wave array trap (nSWAT). By

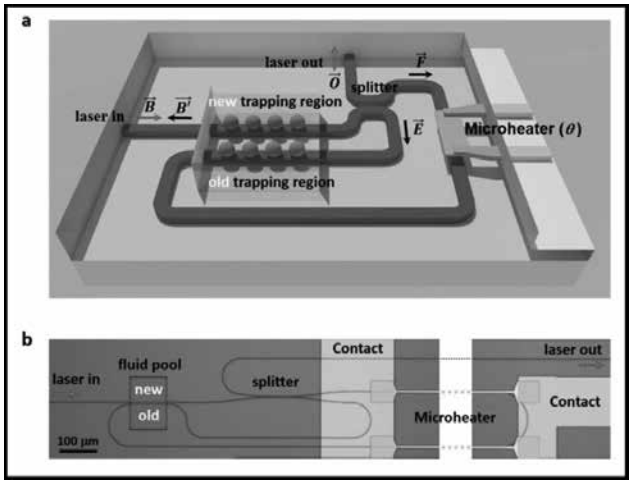

Figure 1: Taken from [3]. nSWAT analysis and fabrication. a) A schematic of the device layout. The electric field vectors at different locations along the waveguide are indicated. b) An optical microscope image of the fabricated device.

tuning the phase difference between the two counter-propagating laser beams, the antinode locations can be precisely repositioned, and consequently, the optical trap positions can be precisely manipulated. The nSWAT device holds the capability for high throughput precision measurements on-chip.

In the past year, we developed a new nSWAT design that significantly improves the stability of the trap and doubles the trapping force and energy for the same input laser power. For a quantitative comparison, we fabricated both the old and the new trap design on the same chip and compared their performance concurrently under the same input laser power. We demonstrated that this new force-doubling design is more resistant to fabrication imperfections than the old design. The CMOS compatible fabrication procedures and numerical simulation details of the nSWAT devices are documented in Refs. [2,3].

Figure 1 (taken from [3]) depicts the structure of the trapping device that contains both the old nSWAT and the new nSWAT design in proximity of each other and operate by the same laser power. Figure 2 (taken from [3]) shows the scattered laser light from the waveguide at both locations to demonstrate the force-doubling nature of the new design. Figure 3 (taken from [2]) shows the stiffness measurement of an array of polystyrene beads trapped on the Si_3N_4 waveguide to demonstrate the built-in capacity for parallelized precision manipulation and measurements of an nSWAT device.

Our development and improvement of the Si_3N_4 waveguide nSWAT platform has led to three publications in the past year, see Refs. [2-4].

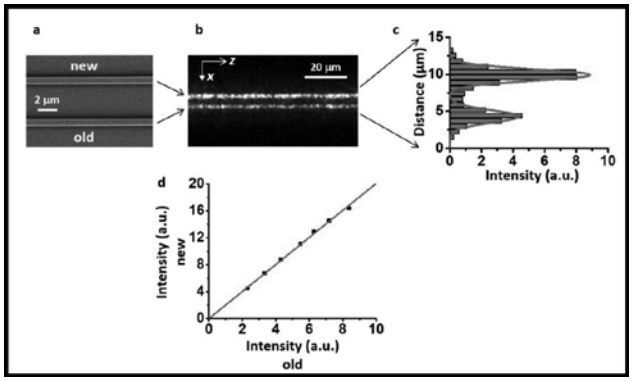

Figure 2: Taken from [3]. Direct comparison of the power in a waveguide in the old and new trapping regions. a) Scanning electron micrograph of the waveguides in the two trapping regions. b) Image of scattered light from the two waveguides. The brightness of the scattered light from each waveguide is proportional to the power transmitted through the waveguide. c) Intensity plot of the waveguides. d) Relation in the cumulative intensities of the scattered light in the waveguides in the new and old trapping regions.

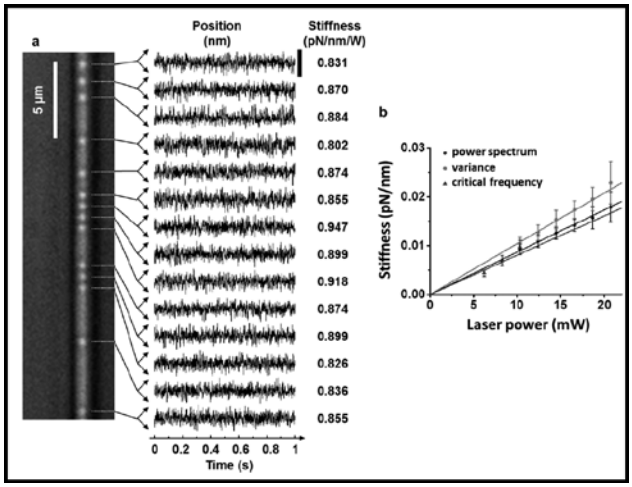

Figure 3: Taken from [2]. Parallel precision measurements. (a) Array of beads trapped on the waveguide. Their positions were monitored over time. The middle panel provides a zoomed in view of the position of each bead versus time, with its stiffness per watt of laser power at the trapping region shown to the right. The black scale bar corresponds to 100 nm. (b) Trap stiffness measurements using three different methods: the power spectrum method, the variance method, and the critical frequency method.

References:

[1] M. Soltani, J. Lin, R. A. Forties, J. T. Inman, S. N. Saraf, R. M. Fulbright, M. Lipson, and M. D. Wang, "Nanophotonic trapping for precise manipulation of biomolecular arrays," Nature Nanotechnology 9(6), 448-452 (2014).

[2] F. Ye, R. P. Badman, J. T. Inman, M. Soltani, J. L. Killian, and M. D. Wang, "Biocompatible and high stiffness nanophotonic trap array for precise and versatile manipulation," Nano Letters 16(10), 6661-6667 (2016).

[3] F. Ye, M. Soltani, J. T. Inman, and M. D. Wang, "Tunable nanophotonic array traps with enhanced force and stability," Optics Express 25 (7) 7907-7918 (2017).

[4] J. E. Baker, R. P. Badman, and M. D. Wang, "Nanophotonic trapping: precise manipulation and measurement of biomolecular arrays," WIREs Nanomed Nanobiotechnol. e1477 (2017).

Generalized Microfluidic Immunosensor for Antibody Detection

CNF Project Number: 1757-09

Principal Investigator: Christopher K. Ober[1]

Users: Aibar Nurmukhanov[1], Roselynn Cordero[2]

Affiliations: 1. Department of Materials Science and Engineering, 2. Department of Chemistry and Chemical Biology; Cornell University

Primary Source of Research Funding: National Science Foundation

Contact: cko3@cornell.edu, an485@cornell.edu, rc634@cornell.edu

Primary CNF Tools Used: ABM contact aligner, Hamatech-Steag Wafer Processor, CVC SC4500, DISCO dicing saw, CorSolutions fluidic probe station

Abstract:

Microfluidics are important devices that control and manipulate fluid flows with volume sizes ranging from microliters to picoliters. These devices received enormous attention in the fields of biology and biotechnology for the recent development of sensing devices that manipulate, analyze, and detect small quantities and operate at smaller volumes. Microfluidics offer numerous advantages such as ability to work with small quantities, potential for cheap and portable immunosensor device fabrication, manipulation of multiple samples at once, and applicability for patient treatments in isolated areas with no laboratory settings, facilities, and well-trained technicians. Microfluidics can also be used as point-of-care systems for diagnostics that provide real clinical value, and help identify and treat serious illnesses such as diabetes or cancer. These lab-on-a-chip (LOC) devices demonstrate reliable diagnostic results and practical application to replace some laboratory tests. This report focuses on the master mold fabrication using different SU-8 permanent epoxy negative photoresist using photolithography and replication of microchannels using polydimethylsiloxane (PDMS) block for LOC applications.

Summary of Research:

A patterned device, consisting of 35 rows of seventeen fused silica squares (300 × 300 μm) surrounded by a patterned gold lines (150 μm wide) was fabricated using lift-off process (Figure 1). A lift-off process includes spin-coating a bilayer of photoresists: lift-off resist LOR 10A (based on polydimethylglutarimide) and positive-tone SPR220-3.0 photoresist (based on cresol novolak resin and diazo photoactive compound) on fused silica substrate followed by baking at 180°C for 3 minutes and 115°C for 1.5 minutes, respectively. An ABM contact aligner with mercury arc lamp (i-line: 365 nm optical source) was used to expose a positive photoresist for 10 seconds followed by post-exposure bake at 115°C for 1.5 minutes. Then, the substrate was developed by Hamatech-Steag Wafer Processor using a double puddle automated process in tetramethylammonium hydroxide (TMAH) solution to obtain an undercut profile for metal deposition. Subsequently, 15 nm of chromium (adhesion layer) and 100 nm of gold layers were deposited on the wafer using a CVC SC4500 electron beam evaporation system.

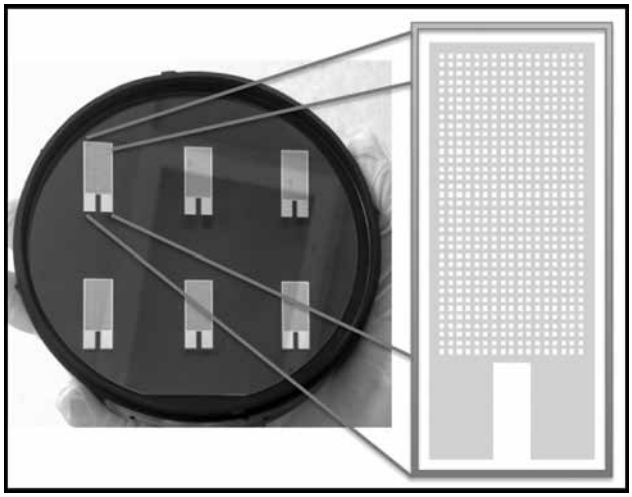

Figure 1: Generalized platform made of fused silica substrate and generated pattern of thin layer of gold lines by lift-off process.

A solution of Remover 1165 was used remove photoresist and obtain isolated patterns of gold lines as shown in Figure 2. The whole wafer was cut into six individual platforms using all-purpose blade on DISCO-dicing saw. The same positive photoresist (SPR220-3.0) was spin-coated on the wafer as a sacrificial layer before dicing.

Microfluidic channels were fabricated using epoxy based SU-8 type negative photoresist by master mold fabrication using photolithography (Figure 2). Preparation of the PDMS and replication of master mold patterns on its surface is done via widely known and relatively simple soft lithography process. PDMS was prepared using polymer base and curing agent, then poured over SU-8 master mold structure and cured in the oven at 60°C for at least two hours. Finally, a PDMS replica with microchannels was peeled away from the substrate to get embossed microstructure.

Polydimethylsiloxane (PDMS) was chosen due to its chemical and physical properties that suit our immunosensor design. PDMS is a non-toxic, cheap and easy-to-mold elastomer making it a strong candidate for integration in portable and inexpensive immunosensor device. Sealing of the PDMS to the surface of the platform was achieved by evaporation of the ethanol between the surfaces of the platform and PDMS replica (Figure 3). This method is non-destructive compared to other conventional methods such as oxygen plasma or corona discharge. Methods that use harsh conditions of oxygen plasma tend to make strong (covalent) bonding between the glass and the PDMS. However, these methods also change and sometimes destroy crucial surface chemistry of the platform, which is needed for successful implementation of the fundamental idea of the antibody catalyzed water oxidation pathway process.

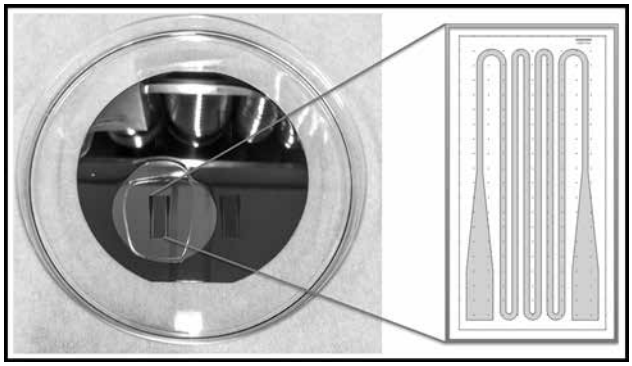

Figure 2: Illustration of one of the master molds using SU-8. Serpentine-like features with polydimethylsiloxane (PDMS) on top.

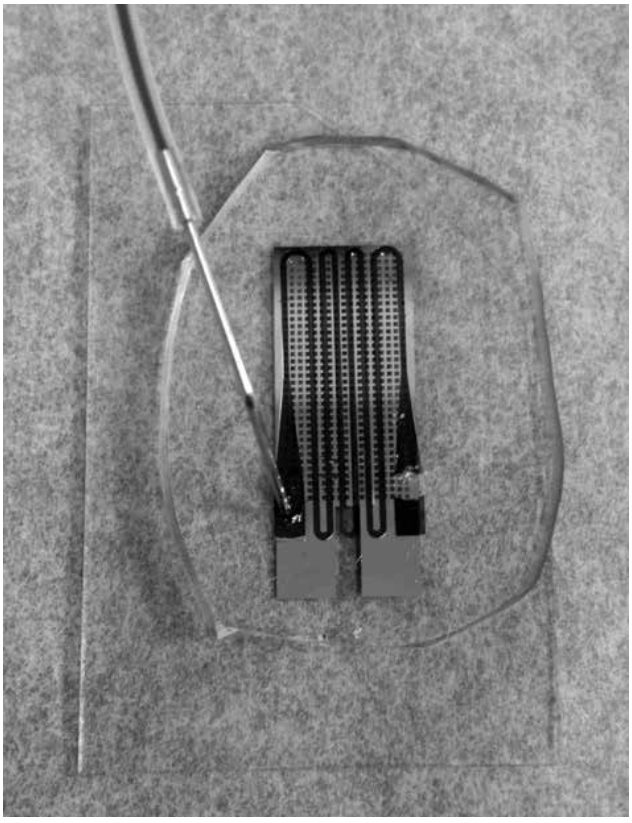

Figure 3: Generation-one microfluidic immunosensor device. Food-dye was used to illustrate continuous flow inside the device.

References:

[1] M. Elizabeth Welch, Nicole L. Ritzert, Hongjun Chen, Norah L. Smith, Michele E. Tague, Youyong Xu, Barbara A. Baird, Héctor D. Abruña, and Christopher K. Ober, Journal of the American Chemical Society, 2014, 136 (5), 1879-1883.

[2] Whitesides, George M. "The origins and the future of microfluidics." Nature442.7101 (2006):368-373.

[3] Xia, Younan, et al. "Replica molding using polymeric materials: A practical step toward nanomanufacturing." Advanced Materials 9.2 (1997): 147-149.

[4] Duffy, David C., et al. "Rapid prototyping of microfluidic systems in poly (dimethylsiloxane)." Analytical chemistry 70.23 (1998): 4974-4984.

[5] Sia, Samuel K., and George M. Whitesides. "Microfluidic devices fabricated in poly (dimethylsiloxane) for biological studies." Electrophoresis 24.21 (2003): 3563-3576.

[6] McDonald, J. Cooper, and George M. Whitesides. "Poly (dimethylsiloxane) as a material for fabricating microfluidic devices." Accounts of chemical research35.7 (2002): 491-499.

A Portable, Quantitative Nucleic Acid Amplification System for Disease Diagnostics in Limited Resource Settings

CNF Project Number: 1858-10
Principal Investigator: David Erickson
User: Ryan Snodgrass

Affiliation: Mechanical Engineering, Cornell University
Primary Source of Research Funding: National Institutes of Health
Contact: de54@cornell.edu, rjs492@cornell.edu
Website: ericksonlab.org
Primary CNF Tools Used: VersaLaser laser cutter

Abstract:

We built a portable diagnostic device for limited resource settings called TINY. TINY performs isothermal nucleic acid amplification with the flexibility of being heated via non-electricity sources if electricity is unavailable (e.g., sunlight or open flame). TINY is also capable of nucleic acid quantification, therefore delivering a technology that is usually contained in a large, immobile laboratory tool to a handheld package weighing just over 1 kg.

Summary of Research:

Nucleic acid tests (NAT) are still largely inaccessible to rural communities in resource limited settings [1]. While PCR (polymerase chain reaction) and qPCR (quantitative PCR) are common diagnostic techniques in expensive laboratory settings, delivering the same diagnostic capability to developing countries calls for unique engineering solutions. Our research during the past year has culminated in the production of TINY, a device for performing NAT in the field using alternative heat sources such as sunlight and open flame. Our lab previously developed a microfluidic chip capable of performing PCR using sunlight, but it was incapable of DNA quantification [2,3]. Other groups have developed portable and quantitative NAT using an isothermal variant of PCR known as LAMP (loop-mediated isothermal amplification) [4], but these devices are designed to be heated via exothermic chemical reaction, and cannot use electricity when available [5].

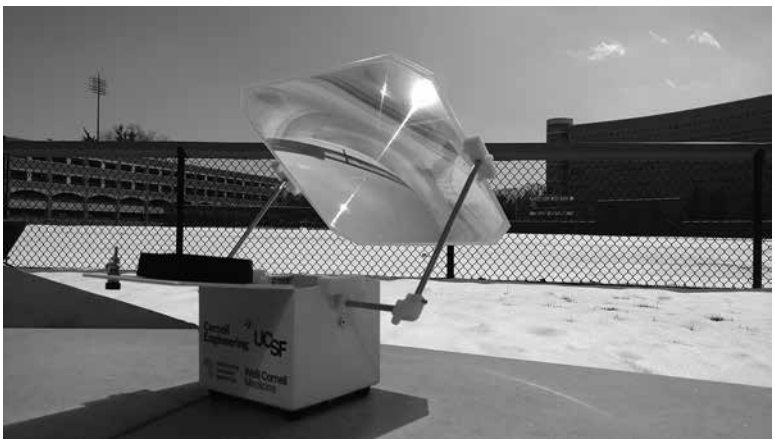

Figure 1: The TINY system while collecting sunlight during a solar heatup experiment: completed on March 21, 2017; ambient temperature was 6°C.

TINY (Tiny Isothermal Nucleic acid amplification sYstem) is a portable tool capable of performing quantitative, isothermal nucleic acid amplification. TINY is unique in that it may be heated via solar energy (Figure 1), flame (from a Bunsen burner), or electricity. This makes it particularly suited for use in locations where electricity is only occasionally accessible or completely inaccessible. TINY tracks fluorescence and absorbance of four samples simultaneously, is designed to be used with standard PCR tubes as sample containers, weighs only 1.1 kg, and occupies just over 2 L of space. It is easily carried in one hand. The optical design in TINY is unique in that only one, stationary excitation source is used and no mechanical actuation is required to track the optical characteristics of the multiple samples simultaneously.

A large concern when using sunlight as a heat source for diagnostic tools is the irregular solar irradiance and its effect on sample temperature. Our previous microfluidic

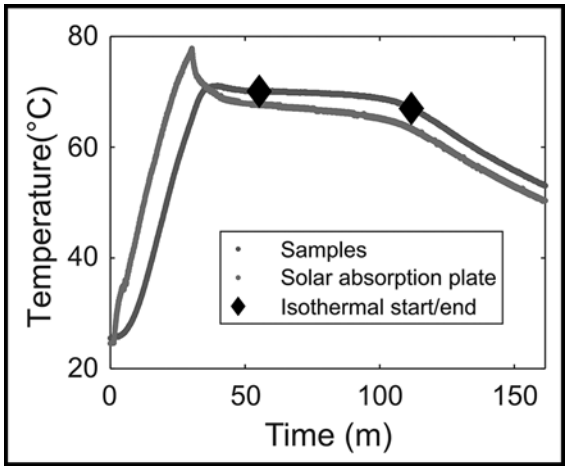

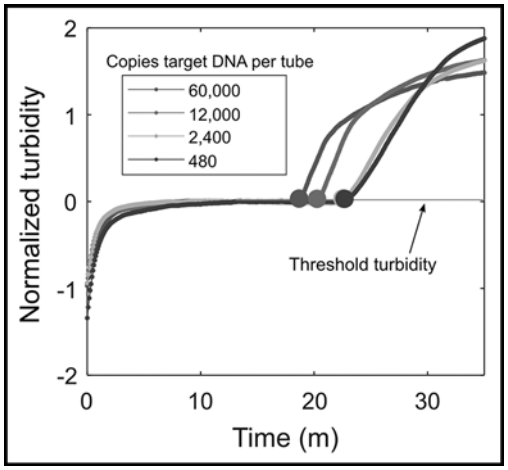

Figure 2, left: Temperature data from the TINY device during a solar heatup experiment. The temperature of the samples stayed isothermal (defined as 67 to 70°C) for 57 min after TINY collected sunlight for 30 min. The peak in the temperature data marks where solar absorption ended and cooling commenced with no further heat collection.

Figure 3, right: Turbidity data for an isothermal amplification experiment. The threshold time is calculated as when the turbidity passes the horizontal threshold line.

device [2,3] showed large temperature fluctuations due to even small changes in weather (e.g., cloud coverage). We therefore designed TINY to store large amounts of heat isothermally in the latent heat of a phase change material. We store approximately 14 kJ of latent heat in 75 mL of a phase change material that melts at 68°C, a temperature optimal for LAMP. If enough heat is stored, the device can maintain isothermal conditions for about an hour even while no longer collecting any heat (Figure 2).

We are currently performing a large trial on more than 40 biopsy samples collected in Kampala, Uganda, from patients suspected of having Kaposi's sarcoma (KS) — a cancer most common in HIV-positive individuals in sub-Saharan Africa. Our results show that TINY can reliably track the fluorescence or absorbance (Figure 3) of multiple samples in real-time allowing for the quantification of target DNA. We have also discovered that TINY has quantitative capability on-par with commercial nucleic acid amplification systems that can perform LAMP, meaning that TINY is capable of performing tests for other nucleic acid targets and that the performance of the diagnostic is limited by the specific assay in use and not the TINY itself.

TINY was designed and built on Cornell's campus. We used the Cornell NanoScale Science and Technology Facility for assistance with fabrication of many of the parts that are used in the construction of TINY. For example, the Versa laser cutter was essential in cutting opaque parts that are necessary for the optical function in the system.

References:

[1] M. Urdea, L. A. Penny, S. S. Olmsted, M. Y. Giovanni, P. Kaspar, A. Shepherd, P. Wilson, C. A. Dahl, S. Buchsbaum, G. Moeller, D. C. Hay Burgess, Requirements for high impact diagnostics in the developing world, Nature 444, 73-79 (2006).

[2] L. Jiang, M. Mancuso, Z. Lu, G. Akar, E. Cesarman, D. Erickson, Solar thermal polymerase chain reaction for smartphone-assisted molecular diagnostics, Sci. Rep. 4 (2014), doi:10.1038/srep04137.

[3] R. Snodgrass, A. Gardner, L. Jiang, C. Fu, E. Cesarman, D. Erickson, KS-Detect – Validation of Solar Thermal PCR for the Diagnosis of Kaposi's Sarcoma Using Pseudo-Biopsy Samples, PLoS ONE 11, e0147636 (2016).

[4] T. Notomi, H. Okayama, H. Masubuchi, T. Yonekawa, K. Watanabe, N. Amino, T. Hase, Loop-mediated isothermal amplification of DNA, Nucl. Acids Res. 28, e63-e63 (2000).

[5] S.-C. Liao, J. Peng, M. G. Mauk, S. Awasthi, J. Song, H. Friedman, H. H. Bau, C. Liu, Smart cup: A minimally-instrumented, smartphone-based point-of-care molecular diagnostic device, Sensors and Actuators B: Chemical 229, 232-238 (2016).

Fabrication of Elastomeric Microposts with Step-Changes in Rigidity

CNF Project Number: 1859-10
Principal Investigator: Cynthia A. Reinhart-King[b]
User name: Jacob VanderBurgh[a,b]

Affiliations: a. Meinig School of Biomedical Engineering, Cornell University, Ithaca, New York, USA; b. Department of Biomedical Engineering, Vanderbilt University, Nashville, Tennessee, USA

Primary Source of Research Funding: National Science Foundation Award 1435755

Contact: cynthia.reinhart-king@vanderbilt.edu, jav244@cornell.edu

Website: http://www.cellmechanics.org/

Primary CNF Tools Used: AutoStep GCA i-line stepper, Unaxis 770 Deep Si etcher, Heidelberg DWL 2000, ABM contact aligner

Abstract:

Arterial stiffening occurs during aging and rigidity sensing of the vascular endothelium plays an important role in atherosclerosis. Recent evidence indicates arterial stiffening is accompanied by greater heterogeneity in stiffness within the intima. To explore the effect of heterogeneity in substrate stiffness upon the endothelium, we fabricated dense arrays of elastomeric micropillars that introduce multiple subcellular step changes in substrate rigidity. Endothelial cell area increased with increasing rigidity, verifying cells respond appropriately to the range of rigidities provided. Future work will focus on further characterizing endothelial barrier integrity in response to spatial changes in rigidity.

Summary:

Cardiovascular diseases are the leading cause of death worldwide and cardiovascular risk can be predicted by vascular stiffness [1,2]. Vascular stiffening occurs with age and is correlated with traditional cardiovascular risk factors such as hypertension [3,4]. Our lab and others have shown that vascular stiffening regulates vascular endothelial permeability permitting cholesterol uptake and leukocyte extravasation into the vessel wall, hallmarks of atherosclerosis [5-7]. Recent evidence indicates that vascular stiffening is accompanied by greater heterogeneity in the rigidity of the intima with areas of high stiffness located directly adjacent to areas of low stiffness [8].

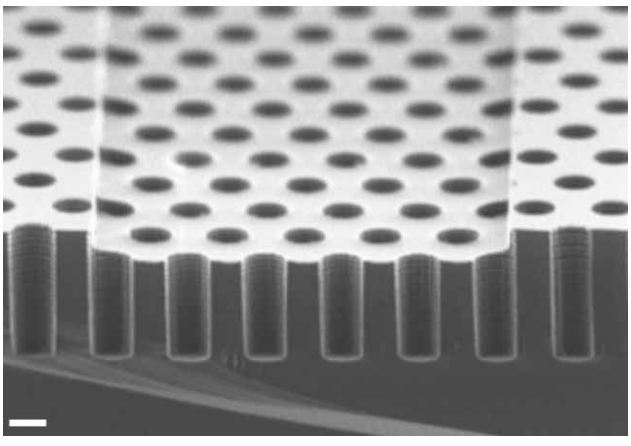

Figure 1: Negative silicon master of micropillars with a step-change in rigidity. Scale bar is 2 µm.

To explore the consequences of heterogeneous intimal stiffening, we have developed a micropillar model to explore the impact of greater complexity in substrate stiffness upon endothelial cell function.

Negative silicon (Si) masters of micropillars with a step-change in rigidity were fabricated with two-stages of deep reactive-ion etching (DRIE) as described previously (Figure 1) [9]. RCA-cleaned Si wafers with a thin layer of photoresist were first patterned with a 5x reduction stepper and a photomask consisting of a hexagonal array of holes. Patterned photoresist was used as a mask for subsequent DRIE on a Unaxis 770 Deep Si Etcher to generate an array of hexagonal holes of uniform depth. Hole depth was controlled by monitoring etch time and utilized to fabricate a library of silicon masters with varying uniform hole depth.

Thick photoresist was subsequently spun onto these arrays to completely fill the cylindrical holes and rectangular strips of photoresist were patterned with an ABM contact aligner. Photoresist was developed such that photoresist dissolved from the surface of the Si wafer, but remained within the cylindrical holes,

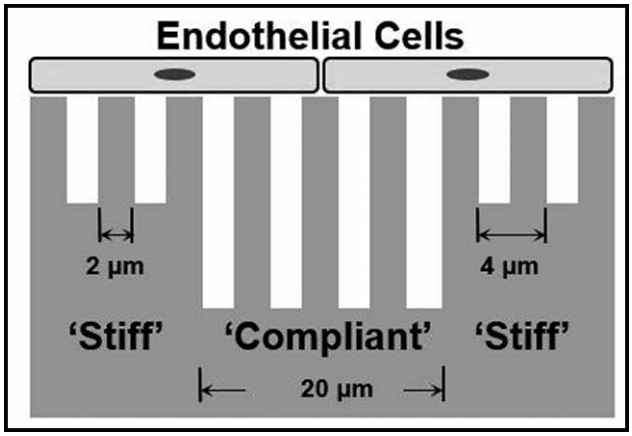

Figure 2: Schematic of micropillars with a step-change in rigidity.

protecting the bottom of the cylindrical holes during the second DRIE step. Replica molding of the Si negative master with silicone elastomer polydimethylsiloxane (PDMS) yields coplanar micropillars with regions of shorter (stiff) and taller (compliant) pillars (Figure 2). Pillar height corresponds to perceived substrate stiffness (E_{eff}) as described in Equation 1 in which E is the bulk PDMS modulus of elasticity, r is the pillar radius, and L is the pillar height [10]. Micropillar substrates were coated with fibronectin and seeded with bovine aortic endothelial cells (BAEC).

$$E_{eff} = \frac{27\,E\,r^3}{16\,L^3}$$

Equation 1

Projected cell area of subconfluent BAECs increased with increasing rigidity, which is consistent with previously reported findings and validates endothelial cells are responding appropriately to the range of micropillar rigidities examined (data not shown) [11]. Future work will characterize endothelial barrier integrity in response to complex cues in substrate rigidity.

References:

[1] Naghavi, M. et al. Global, regional, and national age-sex specific all-cause and cause-specific mortality for 240 causes of death, 1990-2013: A systematic analysis for the Global Burden of Disease Study 2013. Lancet 385, 117-171 (2015).

[2] Mattace-Raso, F. U. S. et al. Arterial stiffness and risk of coronary heart disease and stroke: The Rotterdam Study. Circulation 113, 657-663 (2006).

[3] Benetos, A., Laurent, S., Hoeks, A. P., Boutouyrie, P. H. and Safar, M. E. Arterial alterations with aging and high blood pressure. A noninvasive study of carotid and femoral arteries. Arterioscler. Thromb. Vasc. Biol. 13, 90-97 (1993).

[4] Liu, Z. R., Ting, C. T., Zhu, S. X. and Yin, F. C. Aortic compliance in human hypertension. Hypertension 14, 129-136 (1989).

[5] Huynh, J. et al. Age-Related Intimal Stiffening Enhances Endothelial Permeability and Leukocyte Transmigration. Sci. Transl. Med. 3, 112ra122-112ra122 (2011).

[6] Stroka, K. M. and Aranda-Espinoza, H. Endothelial cell substrate stiffness influences neutrophil transmigration via myosin light chain kinase-dependent cell contraction. Blood 118, 1632-1640 (2011).

[7] Hayenga, H. N. and Aranda-Espinoza, H. Stiffness increases mononuclear cell transendothelial migration. Cell. Mol. Bioeng. 6, 253-265 (2013).

[8] Kohn, J. C. et al. Mechanical heterogeneities in the subendothelial matrix develop with age and decrease with exercise. J. Biomech. 1-7 (2016). doi:10.1016/j.jbiomech.2016.03.016

[9] Breckenridge, M. T., Desai, R. a., Yang, M. T., Fu, J. and Chen, C. S. Substrates with Engineered Step Changes in Rigidity Induce Traction Force Polarity and Durotaxis. Cell. Mol. Bioeng. 7, 26-34 (2013).

[10] Ghibaudo, M. et al. Traction forces and rigidity sensing regulate cell functions. Soft Matter 4, 1836 (2008).

[11] Engler, A. et al. Substrate Compliance versus Ligand Density in Cell on Gel Responses. Biophys. J. 86, 617-628 (2004).

[12] Dejana, E. and Vestweber, D. The role of VE-cadherin in vascular morphogenesis and permeability control. Progress in Molecular Biology and Translational Science 116, (Elsevier Inc., 2013).

Development of a Salivary Microfluidic Diagnostic Device using Hot Embossing

CNF Project Number: 1872-10
Principal Investigator: David Erickson
User: Elizabeth Rey

Affiliation: Sibley School of Mechanical and Aerospace Engineering, Cornell University

Primary Source of Research Funding: National Science Foundation

Contact: de54@cornell.edu, egr42@cornell.edu

Primary CNF Tools Used: Heidelberg DWL2000, YES vapor prime oven, ABM contact aligner, Unaxis 770 Deep Si etcher, P10 profilometer, Zeiss Supra SEM, DISCO dicing saw, hot press, Harrick plasma generator, micro drill

Abstract:

Point of care diagnostic devices allow people to get fast, accurate information about their health and well-being without the need to go to a clinic or hospital. The device that we are designing will determine the concentration of cortisol from a sample of the user's saliva. Cortisol is a steroid hormone associated with stress levels and expressed in human saliva [1,2]. This microfluidic device will contain a microbead-based immunoassay that will determine the cortisol content from a saliva sample. The device is manufactured using a hot embossing process, which uses a silicon master made with traditional lithographic processes. The device will be made from a thermoplastic called Zeonor 1020R, which is a transparent, semi-rigid plastic that can be used in large-scale manufacturing processes such as injection molding and hot embossing. All of the fabrication of the device is being done in the Cornell NanoScale Facility.

Summary of Research:

The microfluidic device is made using a hot embossing process, which involves the high-temperature pressing of a mold into a piece of thermoplastic. The mold used in this process is made of silicon and is fabricated using photolithographic processes. The design for the mold is made using L-Edit and transferred to a photomask using the Heidelberg Mask Writer (DWL2000). This mask is then used to transfer a pattern to a photoresist on a silicon wafer. The photoresist (SPR-220-7.0) is spun onto a bare silicon wafer, which has been previously primed in the YES Vapor Prime Oven, to a thickness of approximately 7 μm. After spinning, the photoresist is soft baked on a 115°C hot plate for 2 minutes and 30 seconds. The wafer is allowed to sit for an hour and then exposed using the mask and the ABM Contact Aligner. The wafer is again allowed to sit for an hour and then is developed using the Hamatech Steag Wafer Processor. The pattern is now developed and can be used to etch the silicon wafer.

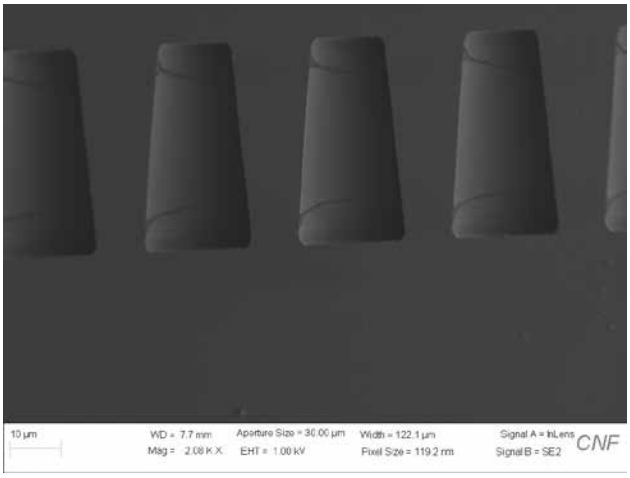

Figure 1: SEM image of small trapezoidal features.

We etched the wafer using the Unaxis 770 Deep Si Etcher to a depth of 100 μm, and monitored the etch depth and etch rate using the P10 Profilometer. Upon reaching the desired depth, we removed the photoresist in the chemical strip bath. In order to ensure that the process was working as desired, we used the scanning electron microscope (SEM) to image the various features of the device. An SEM image of the smallest features, around 20-40 μm in size, can be seen in Figure 1. We then used the Unaxis 770 again to deposit a thin layer of fluoropolymer onto the wafer in order to prevent sticking in the hot emboss process. In order to separate the individual patterns into separate masters, we cut the wafer into pieces using the DISCO Dicing Saw. Masters are then ready to be used in the hot emboss process. Some of these masters can be seen in Figure 2.

Figure 2: Completed masters for hot embossing.

Figure 3: Completed microfluidic chip with blue dye shown for visualization of channels.

The hot emboss process uses the CRC Prepreg Mini Test Press, which applies heat and even pressure. The silicon master is adhered to a glass backing, for strength, and then the plastic piece is placed on top of the master, with another glass backing on top of that. This whole stack is placed in the hot press once the hot press reaches the desired temperature and pressed for several minutes. The setup is allowed to cool below the glass transition temperature of the plastic and then the pressure is released and the plastic is de-embossed. The pattern is transferred from the master to the plastic. We then drill through-holes in a blank piece of plastic using the custom-made micro drill. This blank piece is then bonded to the patterned piece to create the microfluidic device. For the bonding process, we used the Harrick Plasma Generator to activate the surfaces of the plastic pieces and immediately put the pieces together and put them in the hot press again to thermally bond.

The microfluidic device is now complete and ready to be turned into an immunoassay. A completed device with blue dye shown for visualization of the channels can be seen in Figure 3.

References:

[1] Kirschbaum C, Hellhammer DH Salivary cortisol in psychoneuroendocrine research: recent developments and applications.

[2] Umeda T, Hiramatsu R, Iwaoka T, et al (1981) Use of saliva for monitoring unbound free cortisol levels in serum. Clin Chim Acta 110:245–253. doi: 10.1016/0009-8981(81)90353-3.

Increasing Endothelial Retention on Mechanical Heart Valves via Surface Micropatterning

CNF Project Number: 1923-10
Principal Investigator: Dr. Jonathan Butcher
User: Brett Resnick

Affiliation: Biomedical Engineering Department, Cornell University
Primary Source of Research Funding: Cornell University
Contact: JTB47@cornell.edu, BER62@cornell.edu
Primary CNF Tools Used: CVC SC4500, PlasmaTherm deep Si etcher, Zygo optical profilometer, DISCO dicing saw, Heidelberg DWL2000

Abstract:

In treating heart valve disease, physicians try to avoid using mechanical heart valves because of the lifelong anticoagulation therapy they require. Endothelial cells (EC) have antithrombotic properties, which studies suggest can be used to reduce clotting on valve surfaces if they can tolerate severe flow conditions. Success with EC retention was found by creating devices with microtrenches to reduce surface shear. Using the Cornell NanoScale Facility, we aimed to fabricate constructs with microchannels across the surface that would sufficiently reduce EC detachment during flow. After fabrication, endothelial adhesion to these constructs would be tested using shear flow bioreactor experimentation. To create these artificial valves, we patterned resist on a 1 mm thick Si wafer and deposited alumina. The resist was removed such that only an alumina etching mask remained, after which 700 μm trenches were etched into the wafer. Then pyrolytic carbon was deposited and, finally, the trenched wafer was cut into 1 cm^2 square pieces. Resulting images suggest that our micropatterned devices successfully reduce the shear stress experienced by the EC, thus improving their adhesion to the valve surface.

Summary of Research:

The role of heart valves is to ensure the unidirectional flow of blood through the body during circulation [1]. Therefore, any mineralization, degeneration, or damage to heart valves can lead to excessive regurgitation, insufficient circulation, and overall heart failure. Currently, the traditional method of treatment, and last line of defense, for valvular heart disease involves implanting one of two replacement valve types: mechanical or biological [2]. While mechanical heart valves have the superior durability and strength for a longer implantation lifespan, the biomaterials from which they are composed often struggle with hemocompatability [2].

Endothelial cells are known for their ability to counteract this issue with hemocompatability, and can therefore be used as a successful antithrombotic coating on mechanical heart valves. However, endothelial adhesion under cardiovascular flow conditions remains an issue. Frendl, et al., showed how patterning a surface with micro-trenches can reduce the shear effect of fluid flow on endothelial cells, and therefore increase their ability to adhere to the surface [2]. This study aimed to determine a standard fabrication process for these microchanneled constructs. In coordination with the Cornell NanoScale Facility (CNF) and its staff, we micropatterned the surface of a silicon wafer, in order to produce constructs similar to those created by Dr. Mandy Esch in the Frendl study. Unfortunately, due to technological changes and instability of previously made masks, a new fabrication process had to developed.

In attempting to use the older masks, all surface features began to erode once the etching process reached a depth of approximately 450 μm. Additionally, there was great variation in channel depth throughout the wafer, resulting in major dimensional inconsistencies between samples. An alternate attempt at device fabrication involved the wet etching of an alumina mask. However, this process led to significant lateral undercutting of the mask, in addition to deformation of the microchannels, themselves.

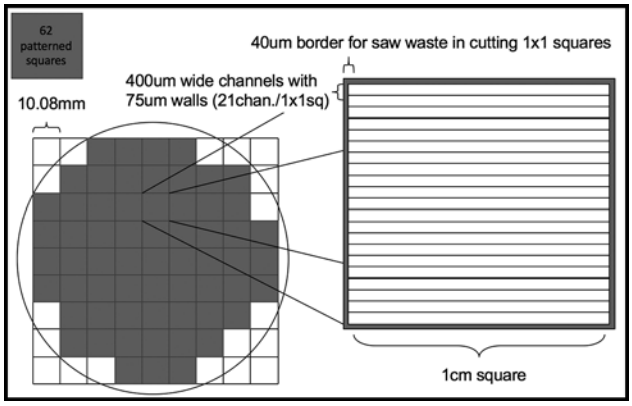

Figure 1: Profile of the alumina etching mask. Produces 62 square constructs, each 1 cm² consisting of 21 trenches. Each trench is approximately 400 µm wide and 700 µm deep.

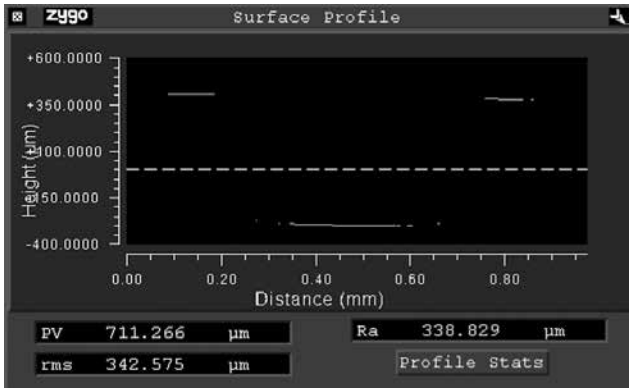

Figure 2: Cross sectional measurements of microchannel depth after etching using the Zygo optical profilometer.

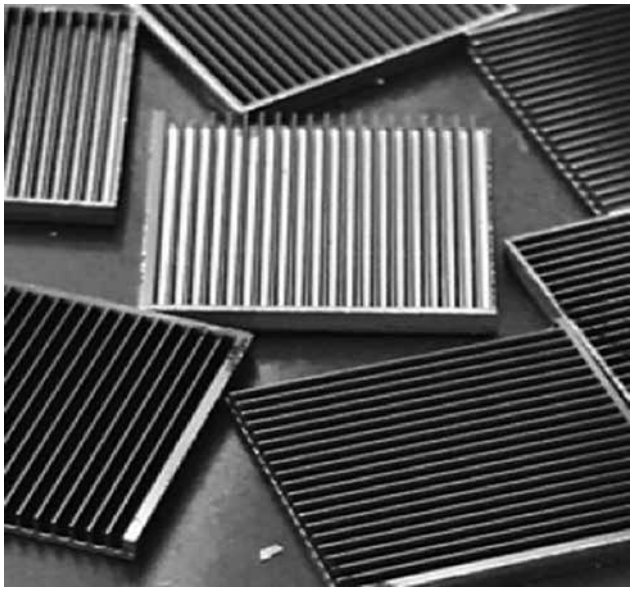

Figure 3: Final product of the microfabrication process.

Eventually, the CNF team was able to agree upon a potential new method. The fabrication procedure would begin with a 1 mm thick SiO_2 wafer, 100 mm in diameter.

First, the oxide was removed from the initial wafer using hydrofluoric acid. Once oxide-free, the wafer was layered with a negative photoresist (nLOF 2020), whose pattern would serve as a guide for alumina deposition in the proceeding step. Once the resist was properly situated, a coating of alumina (aluminum oxide, Al_2O_3) was deposited on the wafer using the CVC SC4500 e-gun evaporation system for thin films. The treated wafer was then soaked for two days in lift-off solution, that would remove the photoresist layer, thus leaving only the desired alumina etching mask behind (Figure 1).

Once lift-off of the negative resist was complete, the wafer was subjected to DRIE silicon etching within the PlasmaTherm Deep Si Etcher. Channel depths were measured after each round of cycling using a Zygo optical profilometer (Figure 2). As the trenches reached a depth of 700 µm, the wafer was once again placed in the CVC SC4500 to deposit a pyrolytic carbon coating of approximately 75 nm. Finally, following the patterning created using the alumina etching mask, the wafer was cut into 1 cm^2 square pieces using a DISCO dicing saw.

This entire process was conducted within the class 1000 particle-controlled environment of the CNF cleanroom. The final product can be seen in Figure 3.

References:

[1] Rajamannan, NM.; Evans, FJ.; Aikawa, E.; et al., Calcific Aortic Valve Disease: Not Simply a Degenerative Process: A Review and Agenda for Research from The National Heart and Lung and Blood Institute Aortic Stenosis Working Group. Circulation. 2011; 124:1783-1791c.

[2] Frendl C.M., Tucker S.M., Esch, M.B., Butcher, J.T. Endothelial retention and phenotype on carbonized cardiovascular implant surfaces. Biomaterials. 2014. 35(27): 7714-23.

Microconcentrator for Biological Small Angle X-Ray Scattering

CNF Project Number: 1940-10
Principal Investigator: Richard E. Gillilan
Users: Manjie Huang, Melanie MacMullan

Affiliations: Macromolecular Diffraction Facility of the Cornell High Energy Synchrotron Source (MacCHESS), Cornell High Energy Synchrotron Source; Cornell University

Primary Source of Research Funding: National Institutes of Health GM-103485

Contact: reg8@cornell.edu, mh2334@cornell.edu, mm2354@cornell.edu

Website: www.macchess.cornell.edu/MacCHESS/bio_saxs.html

Primary CNF Tools Used: VersaLaser laser cutter

Abstract:

Biological small angle x-ray solution scattering (BioSAXS) continues to enjoy widespread popularity as a means of characterizing the structure and behavior of biomolecules in solution. BioSAXS requires not only a minimum concentration to obtain statistically useful scattering signals, but a full range of concentrations to characterize the solution behavior. Many important systems examined by today's researchers are difficult to prepare in quantity and are only marginally soluble. Attempts to concentrate such samples often result in aggregation and subsequent sample loss. *In situ* concentration of samples at the synchrotron beamline allows researchers to explore the full range of concentrations with minimal sample loss. Semipermeable membranes embedded into a modified microfluidic BioSAXS sample cell provide a means of concentrating protein solutions in close proximity to the x-ray beam. Preliminary studies have demonstrated that this concentration process can be achieved on practical time scales at modest pressures without damage to sensitive thin x-ray windows or the formation of leaks.

Summary of Research:

Solubility of complex biological preparations can often be problematic. High concentrations shift equilibrium in favor of the formation of higher oligomers or aggregates. When samples are precious, the point at which sample aggregation occurs is usually not known *a priori*. On the other hand, low concentrations can favor the dissociation of important complexes and contribute to poor x-ray scattering signal. In earlier work [1], we explored concentrating samples at ambient pressure using dialysis. Dialysis and ultrafiltration are closely related techniques. The latter method relies upon pressure to drive separation of biomolecules from solvent rather than diffusion alone. The use of pressure, however, is problematic in x-ray scattering due to the necessity of having very thin x-ray transparent windows. To explore the feasibility of *in situ* ultrafiltration during x-ray solution scattering, students Manjie Huang and Melanie MacMullan adapted our currently-used in-vacuum BioSAXS flow-cell design to incorporate a semipermeable (ultrafiltration) membrane.

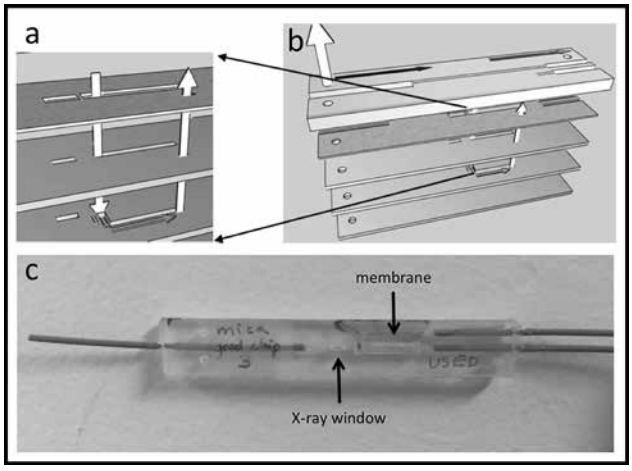

Figure 1: Ultrafiltration chip design and flow scheme. Stack of PMMA sheets allows sample delivery on one side of membrane and filtrate removal on the other (see inset A of B). A third outlet (large white arrow in B, leftmost tube in C) allows concentrated sample to flow past x-ray window.

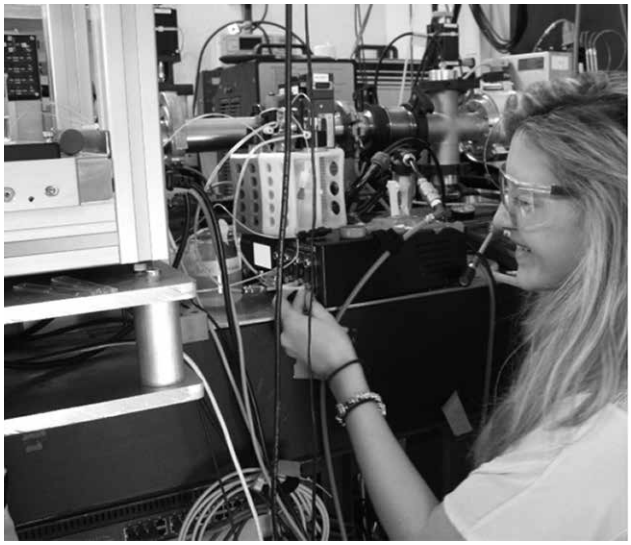

Figure 2: ELVEFLOW™ control system regulates pressure on membrane during concentration phase at synchrotron beamline (Melanie MacMullan shown).

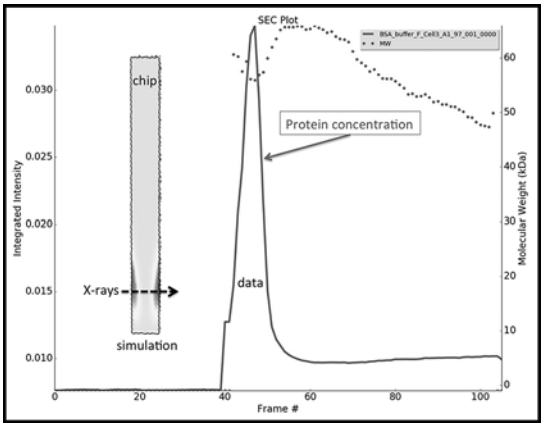

Figure 3: Integrated x-ray scattering intensity of outflow from concentrator chip (grey line). Bovine serum albumin (BSA) peak reaches approximately 20-fold concentration level from input protein, high enough to see interparticle scattering effects in the molecular weight estimate (grey dots). Inset "chip" shows COMSOL simulation of concentration gradients expected near the membrane surface.

Ultrafiltration membranes were sandwiched between multiple layers of PMMA using a design that incorporates standard chromatography (PEEK) tubing for inlets and outlets (Figure 1A-C). PMMA parts were fabricated on the VersaLaser system at CNF. Natural ruby mica (25 μm thick, Attwater, UK) was used for the x-ray windows to reduce distortion due to pressure. Monomeric bovine serum albumin (BSA) (SIGMA Life Science, A1900-500MG, lot 5LBM3178V) was prepared at 0.8 mg/ml for introduction into the chip, with real-time in-chip concentration levels determined by comparison of scattering intensity profiles to solutions of known concentration. Transmembrane pressures of 200-300 mbar produce concentration factors of 10-20 times over the course of less than an hour, a practical timescale similar to chromatography techniques in molecular biology.

After a period of concentration, samples are allowed to exit the membrane region of the chip to flow past the x-ray window. The total integrated x-ray intensity trace as the sample flows past the window is a single peak (Figure 3, grey line). Estimated molecular weight (Figure 3, grey dots) shows a dip at the peak, which is characteristic of high concentrations. COMSOL Multiphysics simulations of the concentration process (inset in Figure 3) show an expected concentration gradient near the x-ray window surface, a phenomenon that limits concentration uniformity in this design. Future designs will explore ways to uniformize concentration and minimize sample volume requirements. A timelapse video of the concentration process can be seen at http://news.chess.cornell.edu/articles/2016/Gillilan161213.html

References:

[1] Skou, M., S. Skou, T. G. Jensen, B. Vestergaard and R. E. Gillilan (2014). "*In situ* microfluidic dialysis for biological small-angle x-ray scattering." Journal of Applied Crystallography 47(4): 1355-1366.

Microfluidic Mixer for Biological Small Angle X-Ray Scattering

CNF Project Number: 1940-10
Principal Investigator: Richard E. Gillilan
User: Jesse Hopkins

Affiliations: Macromolecular Diffraction Facility of the Cornell High Energy Synchrotron Source (MacCHESS), Cornell High Energy Synchrotron Source; Cornell University

Primary Source of Research Funding: National Institutes of Health GM-103485

Contact: reg8@cornell.edu, jbh246@cornell.edu

Website: www.macchess.cornell.edu/MacCHESS/bio_saxs.html

Primary CNF Tools Used: VersaLaser laser cutter, SUEX laminator, ABM contact aligner

Abstract:

Time resolved small angle x-ray solution scattering (TR-SAXS) has provided important new insights in structural biology, but the experiments have remained technically challenging. The so-called continuous-flow mixing strategy is beginning to emerge as the best way to make these types of experiments more practical and accessible to biologists visiting synchrotron beamlines. Based on the concept of chaotic advection mixing [1], using photolithographic methods at CNF, we have fabricated a continuous-flow microfluidic mixing chip that has allowed us to measure benchmark protein unfolding events below the 10 ms timescale.

Summary of Research:

Small-angle x-ray solution scattering (SAXS) is a structural probe for biological macromolecules capable of determining molecular weight, oligomeric state, conformational changes and flexibility under realistic physiological conditions. Time resolved SAXS (TR-SAXS) measures time dependent structural changes of macromolecules in solution and is often used to study conformational changes or unfolding/refolding. The most difficult part of time resolved SAXS is often initiating the reaction in the system. Typically, this is done by fluidic mixing that can change the pH, salt concentration, or other conditions.

Our mixing chip is based on the principle of chaotic advection [1]. As part of our initial design process, we used the COMSOL Multiphysics program to simulate flow and mixing (Figure 1A). We chose a mixer design covering a large range of flow rates (three orders of magnitude), allowing reactions with slower times to be probed with lower sample consumption. Actual fabrication was carried out at the Cornell NanoScale Science and Technology Facility (CNF). X-ray windows and liquid ports were cut in a PDMS backing. Polyimide (7.5 μm thick) was epoxied over the window hole and 500 μm thick SUEX was laminated over the acrylic. Patterning was done using photolithography. ADEX (5 μm) was used as an adhesive layer for a final polyimide layer to seal the mixing channel.

For testing, we measured the well-characterized urea-induced lysozyme refolding reaction [2]. The unfolding was initiated through a tenfold dilution of sample with 8M urea solution. Several time points were measured from 9ms to 1s immediately after mixing. Radius of gyration (R_g) is an easily-extracted parameter from SAXS data that measures the overall size of the protein. Figure 2 shows how our chip produces the characteristic decrease in R_g with time that results from denaturation.

Based on this preliminary test, CNF-fabricated microfluidic mixing chips are expected to provide a basis for our future TR-SAXS user program at CHESS, helping to make time resolved biological scattering experiments practical for novice users with problems on a wide range of timescales.

References:

[1] Kane, et al. Anal. Chem. 2008, 80, 9534-9541.

[2] Segel, et al., J. Mol. Bio. 1999, 288, 489-499.

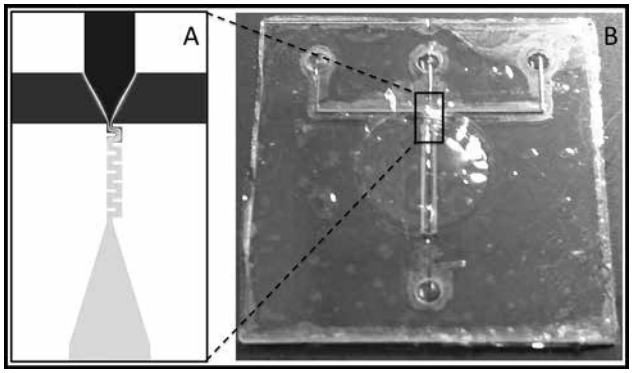

Figure 1: Microfluidic mixer for time-resolved biological small-angle solution scattering. Based on computational fluid dynamics simulations (A) we designed a chip capable of reaching a wide range of timescales relevant to structural biology. A prototype chip was constructed by photolithographic methods at CNF and tested at the G1 beamline of the Cornell High Energy Synchrotron Source (B).

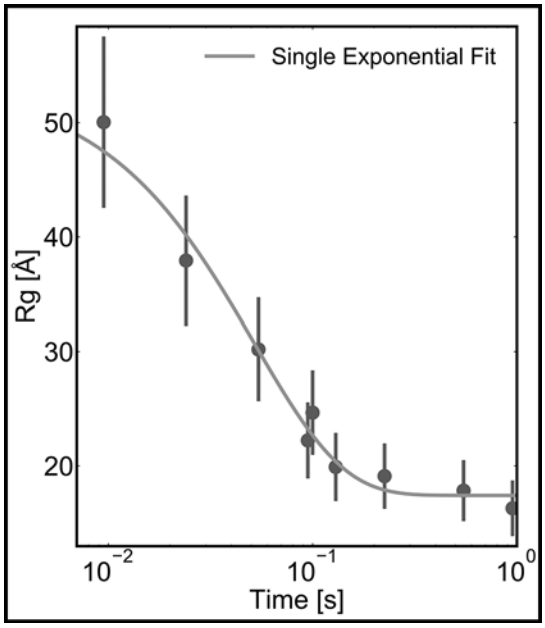

Figure 2: First results from prototype microfluidic mixing chip. The radius of gyration (R_g) of the standard protein lysozyme changes in well-characterized ways when mixed with the denaturant urea. The experiment successfully captured protein unfolding behaviour on a timescale from 1s down to 9ms.

Design and Application of Microfluidic Devices to Study Cell Migration in Confined Environments

CNF Project Number: 2065-11

Principal Investigator: Jan Lammerding[1]

User: Aaron Windsor[2]

Affiliations: 1. Biomedical Engineering Department and Weill Institute, Cornell University; 2. Cornell NanoScale Science & Technology Facility (CNF)

Primary Sources of Research Funding: National Institutes of Health award R01 HL082792; National Institutes of Health award 1U54 CA210184; Department of Defense Breast Cancer Research Program Breakthrough Award BC150580; National Science Foundation CAREER award CBET-1254846

Contact: jan.lammerding@cornell.edu, ajw49@cornell.edu

Website: http://lammerding.wicmb.cornell.edu/

Primary CNF Tools Used: Heidelberg DWL2000, ABM contact aligner, YES polyimide bake oven, MVD100 molecular depositon, SU-8 hotplates

Abstract:

Metastatic spreading of cancer cells is responsible for the vast majority of cancer deaths. To better understand the biophysical processes and molecular consequences involved in cancer cell migration through tight spaces, we designed a novel microfluidic device capable of observing deformation of cells and their nuclei during confined three-dimensional (3-D) migration. Using these devices we observed substantial deformation of the nucleus, including strain on the chromatin, changes in the volume of the nucleus and loss of nuclear envelope integrity, which led to the uncontrolled exchanged of nucleo-cytoplasmic content, herniation of chromatin across the nuclear envelope and DNA damage. Our findings indicate that cell migration incurs substantial physical stress on the nuclear envelope and its content, and requires efficient nuclear envelope and DNA damage repair for cell survival.

Summary of Research:

The ability of cells to migrate through tissues and interstitial spaces is an essential factor during development and tissue homeostasis, immune cell mobility, and in various human diseases. Deformation of the nucleus and its associated lamina during 3-D migration is gathering increasing interest in the context of cancer metastasis, with the underlying hypothesis that a softer nucleus, resulting from reduced levels of lamin A/C, may aid tumour spreading. However, current methods to study the migration of cells in confining 3-D environments are limited by their imprecise control over the confinement, physiological relevance, and/or compatibility with high resolution imaging techniques.

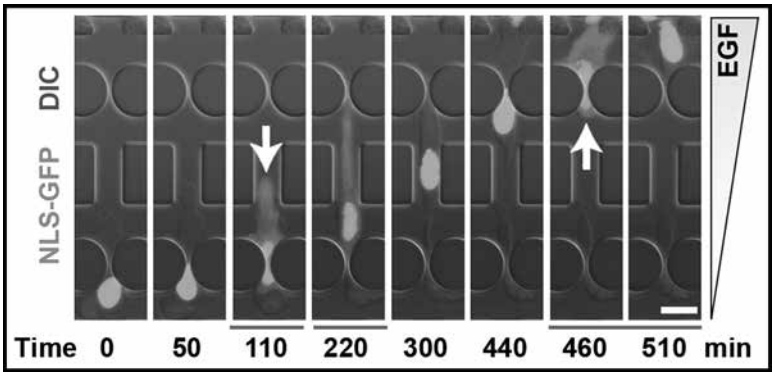

Figure 1: Image sequence of an MDA-MB-231 breast cancer cell that exhibited multiple NE ruptures while moving through 2-5-mm² constrictions. DIC, differential interference contrast; EGF, epidermal growth factor. White arrows and grey lines below frames indicate beginning and duration of NE rupture(s). Scale bar, 20 µm. Figure reproduced from [1].

We designed and built a polydimethylsiloxane (PDMS) microfluidic device composed of channels with precisely-defined constrictions mimicking physiological environments that enable high resolution imaging of live and fixed cells. The device promotes easy cell loading and rapid, yet long-lasting (>24 hours) chemotactic gradient formation without the need for continuous perfusion. Using this device, we obtained detailed, quantitative measurements of dynamic nuclear deformation as cells migrate through tight spaces,

revealing distinct phases of nuclear translocation through the constriction, buckling of the nuclear lamina, and severe intranuclear strain. Furthermore, we found that lamin A/C-deficient cells exhibited increased and more plastic nuclear deformations compared to wild-type cells but only minimal changes in nuclear volume, implying that low lamin A/C levels facilitate migration through constrictions by increasing nuclear deformability rather than compressibility.

We detected nuclear envelope rupture using previously established fluorescent reporters consisting of green or red fluorescent proteins fused to a nuclear localization sequence that rapidly escapes into the cytoplasm when nuclear envelope integrity is lost. Breast cancer, fibrosarcoma, and human skin fibroblast cells displayed transient loss of nuclear envelope integrity, which coincided with the nucleus passing through the constrictions. Nuclear envelope rupture was associated with transient influx of fluorescently labeled cytoplasmic proteins into the nucleus.

Irrespective of the experimental model, the incidence of nuclear envelope rupture increased exponentially with decreasing pore size and reached > 90% when the nuclear height was confined to 3 µm. Nuclear envelope rupture *in vitro* and *in vivo* was often accompanied by protrusion of chromatin through the nuclear lamina. The incidence of such "chromatin herniations" increased significantly with decreasing pore sizes. Furthermore, cells that had passed through microfluidic constrictions had more nuclear fragments positive for g-H2AX, a marker of DNA double-strand breaks than cells that had not yet entered the constrictions. To assess the functional relevance of nuclear envelope repair, we quantified cell viability after rupture. Under normal conditions, the vast majority (>90%) of surviving cells experienced repeated NE rupture. Inhibiting either nuclear envelope repair or DNA damage repair pathways alone did not reduce cell viability, but inhibition of both nuclear envelope and DNA repair substantially increased cell death after NE rupture.

The integration of our migration devices with high resolution time-lapse imaging provides a powerful new approach to study intracellular mechanics and dynamics in a variety of physiologically relevant applications, ranging from cancer cell invasion to immune cell recruitment.

References:

[1] Celine M. Denais, et al., Science, 352, 6283, 353-8 (2016).

[2] Armen Mekhdjian, et al., Mol Biol Cell (2017). doi: 10.1091/mbc.E16-09-0654. [Epub ahead of print].

[3] Philipp Isermann and Jan Lammerding. Nucleus (2017). doi: 10.1080/19491034.2017.1292191. [Epub ahead of print].

Microfluidics for Modeling Biological Flows in Breast Tumor Cell Invasion

CNF Project Number: 2068-11
Principal Investigator: Mingming Wu
User: Yu Ling Huang

Affiliation: Department of Biological and Environmental Engineering, Cornell University
Primary Source of Research Funding: National Cancer Institute
Contact: mw272@cornell.edu, yh486@cornell.edu
Website: http://biofluidics.bee.cornell.edu/
Primary CNF Tools Used: Karl Suss MA/BA 6 aligner, Unaxis 770, Anatech Resist Strip, MVD100, Heidelberg DWL2000

Abstract:

Cancer metastasis is a physical process where tumor cells break away from the primary tumor, invade through the interstitial extracellular matrix, enter and leave the vascular vessels, and establish a secondary tumor at a distant organ. Increasing evidences have demonstrated that the tumor microenvironment critically regulates tumor cell invasion. Microfluidic platforms are a useful tool in modeling the tumor microenvironment because they are compatible with microscopes and allow for dynamical imaging of cell migration. The unique microsized channel features of microfluidics allow us to model biological flows precisely within a tumor microenvironment, including intramural flow through blood vessels and interstitial flow through the interstitial extracellular matrix. We developed and fabricated a microfluidic device that enables us to mimic both intramural flow and interstitial flow for studying their roles on breast tumor cell invasion.

Summary of Research:

The goal of designing the microfluidic device is to simultaneously model intramural flow through engineered vessels and interstitial flow through three-dimensional tumor embedded extracellular matrices. To achieve this goal, we designed a microfluidic device with five parallel cell channels for endothelial tube formation and one horizontal channel for interstitial flow (Figure 1).

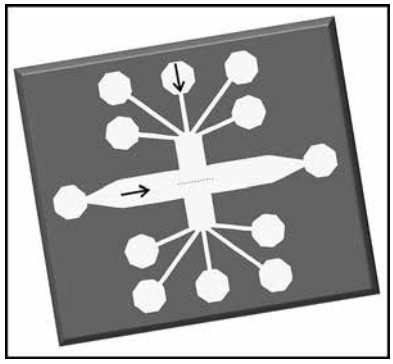

Figure 1: Schematic of the microfluidic device with 5-cell channels (width of 400 μm) and one horizontal channel (width of 2 mm).

A key feature of the device is its use of microsized contact lines placed in between each two neighboring cell channels. The purpose of the contact lines was to confine tumor cells embedded collagen within a desired channel, and endothelial cells (EC) can be seeded and formed a hollow tube surrounding by collagen (Figure 2 as an example). The advantages of the five-channel layout over our previous 3-channel device [1,2] are flexibility to grow one or two endothelial tubes and spatial arrangement of tumor cells and endothelial tubes.

The microfluidic device was fabricated using the standard soft lithography technique. First, the silicon master was fabricated using a two-step etching method, and then the microfluidic device was replicated from the silicon master using PDMS stamping.

To fabricate the negative silicon master, the micro contact lines with dimension of 10 μm in width and 5 μm in depth were first etched, followed by a 200 μm deep etch for the cell and horizontal channels. Photoresist S1813 was first spun on a silicon wafer at 3000 rpm for 45 second, and then baked at 115°C for 60 second before exposed to 128.7 mJ/cm^2 on a contact aligner. After developing the resist with MF-321, the wafer was etched using a Botsch® deep silicon etching method to obtain the 5 μm contact lines.

To make the cell and horizontal channels as a second layer, SPR220-7.0 photoresist was spun on the etched wafer with 2500 rpm for 40 second, and baked at 115°C for 90 second before exposure with dosage of 1.05 J/cm^2, followed by post baked for another 90 second at 115°C. After resist development with AZ 726MIF, the wafer was etched for 200 μm depth. After resist striping with oxygen plasma for one hour, the wafer was silanized with a single layer of (1H,1H,2H,2H-Perfluorooctyl) trichlorosilane (FOTS) using a vapour deposition method. To prepare the microfluidic device, PDMS at 10:1 ratio was then poured onto the silicon master to replicate a positive feature for our experiments.

Figure 3 illustrates our first step to confine collagen at two side cell channels by the contact lines while endothelial cells were introduced into the middle cell channel. Intramural flow was applied through the EC tube to facilitate the formation of an EC tube.

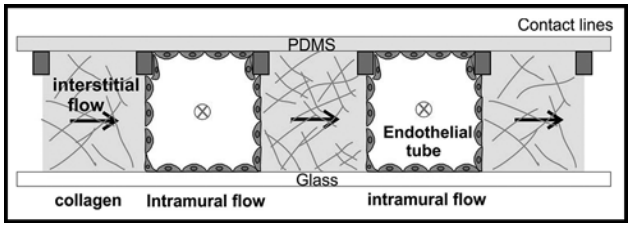

Figure 2: Schematic of cross sectional view of the microfluidic device (zoom in from dash line in Figure 1). Small rectangles in between channels represent the contact lines (10 μm by 5 μm). Collagen gels are confined in individual channels whereas endothelial tubes formed in the empty channel surrounded by collagen. Intramural flow can be applied through the EC tubes and interstitial flow can be applied through the horizontal channel.

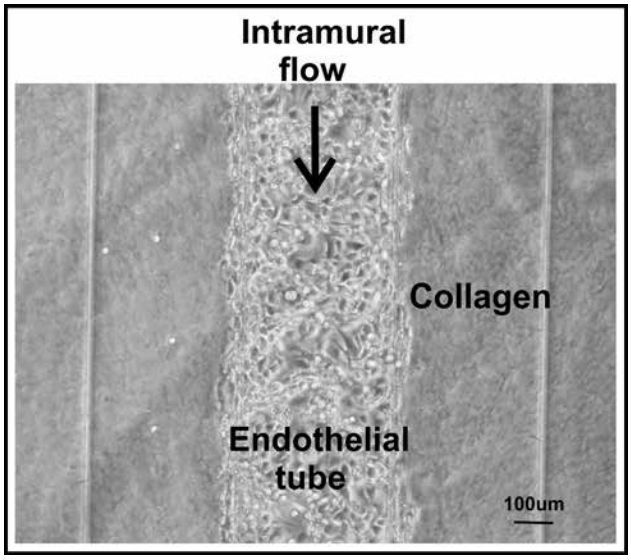

Figure 3: Micrograph of EC tube formation within a channel surrounded by collagen in the two side channels.

References:

[1] Tung, C., Krupa, O., Apyadin, E., Liou, J., Diaz-Santana, A., Kim, B. J., and Wu, M. (2013). A contact line pinning based microfluidic platform for modelling physiological flows. Lab on a Chip, 13(19), 3876-3885. http://doi.org/10.1039/c3lc50489a

[2] Huang, Y. L., Tung, C., Zheng, A., Kim, B. J., and Wu, M. (2015). Interstitial flows promote an amoeboid over mesenchymal motility of breast cancer cells revealed by a three-dimensional microfluidic model. Integrative Biology.: Quantitative Biosciences from Nano to Macro, 7(11), 1402-1411. http://doi.org/10.1039/c5ib00115c

Zero-Mode Waveguides on Thin Silicon Nitride Membranes for Efficient Single-Molecule Sequencing

CNF Project Number: 2214-13
Principal Investigator: Prof. Meni Wanunu
User: Dr. Vivek Jadhav

Affiliation: School of Physics, Northeastern University
Primary Source of Research Funding: NIH award No. 1R01 HG009186
Contact: wanunu@neu.edu, v.jadhav@neu.edu
Website: http://www.northeastern.edu/wanunu/
Primary CNF Tools Used: LPCVD CMOS nitride - E4, JEOL 6300, SC4500 odd-hour evaporator, Zeiss Ultra SEM

Abstract:

Single-molecule, real-time (SMRT) DNA sequencing using zero-mode waveguides (ZMWs) offers long reads by polymerase bound DNA template. We demonstrate low-concentration of DNA capture by constructing ZMW on a 50 nm thick silicon nitride membrane and drilling a nanopore (~3-4nm) at the base of the waveguide using TEM. To protect the aluminum from electrochemical reactions, we coat the ZMWs with a thin layer of silicon dioxide using atomic layer deposition. A polymerase-streptavidin bound DNA template is anchored to the exposed biotin at the bottom of a ZMW by applying a voltage bias. DNA polymerase replicates the sample DNA as it incorporates new fluorescently-labeled phospholinked nucleotides, emitting a burst of light before the phosphate is cleaved off, giving a color sequence that corresponds to the DNA sequence.

Summary of Research:

Single-molecule detection at micromolar concentration is achieved by fabricating zero-mode waveguides (ZMWs) with subwavelength holes in a metal film [1]. An essential component of the single molecule, real-time (SMRT) sequencing is the zero-mode waveguide (ZMW), a cylindrical cavity in which the DNA and DNA polymerase molecules are immobilized [1].

A single molecule of DNA template-bound DNA polymerase is immobilized at the bottom of a ZMW, which has excitation confinement in zeptoliter enables detection of an individual fluorescently-labeled phospholinked nucleotides [2]. The ZMW nanostructure are fabricated on a 50 nm thick silicon nitride (deposited using LPCVD CMOS nitride - E4) membranes using electron-beam lithography (JEOL 6300) at CNF (Figure 1). We showed that making ZMW and drilling a 3.5 nm pore at the bottom of the ZMW, the efficiency of molecular loading into these structures could be enhanced by orders of magnitude [3].

We continue to fabricate these devices for our DNA sequencing experiments. Increasing the size of ZMW (~110nm) we can capture large DNA molecule with ease. To protect the aluminum (deposited using SC4500 odd-hour evaporator) from electrochemistry with chloride buffer, which might occur while apply a voltage bias during an experiment, we passivate the aluminum with ~ 13 nm of silicon oxide using atomic layer deposition technique (done outside CNF, Fig. 2).

These ZMW array chips are used for capturing DNA-polymerase complexes. In Figure 3, we see a sample time trace from our DNA-sequencing experiment. Each fluorescent burst corresponds to individual dATP, dTTP, dGTP, dCTP nucleotide being incorporated into a new DNA strand.

References:

[1] Levene, M.J., et al., Zero-mode waveguides for single-molecule analysis at high concentrations. Science, 2003. 299(5607): p. 682-686.

[2] Eid, J., et al., Real-time DNA sequencing from single polymerase molecules. Science, 2009. 323(5910): p. 133-138.

[3] Larkin, J., et al., Reversible Positioning of Single Molecules inside Zero-Mode Waveguides. Nano Letters, 2014. 14(10): p. 6023-6029.

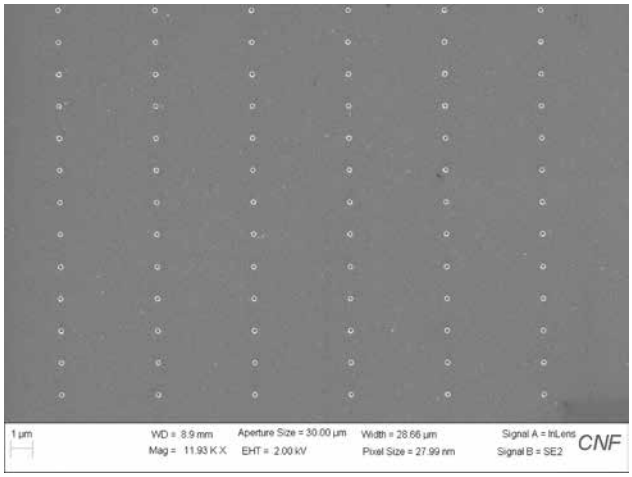

Figure 1: Scanning electron microscopy image of an array of ZMWs on a thin silicon nitride membrane.

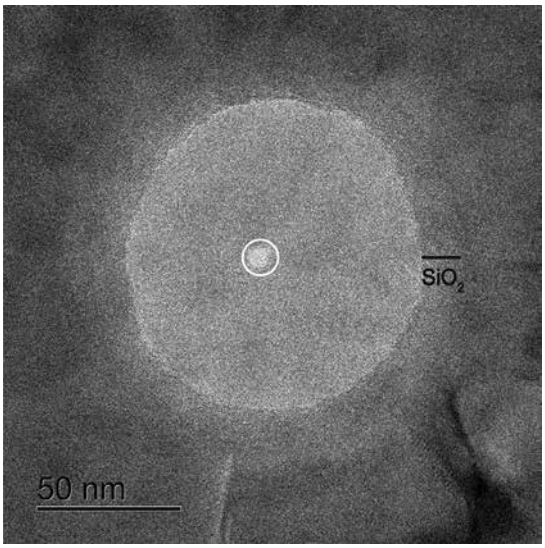

Figure 2: Transmission electron micrograph of a ZMW with a nanopore at its center (white circle). The ~ 13 nm layer of ALD silicon dioxide.

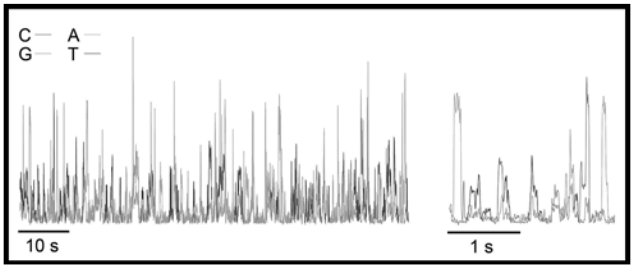

Figure 3: False-color spectrally-resolved fluorescence intensity vs. time data obtained during sequencing experiment. Legend shows the color of each of the dNTPs.

Microfabricated Devices for Cell Organization

CNF Project Number: 2249-13
Principal Investigator: Minglin Ma
User: Wei Song

Affiliation: Department of Biological and Environmental Engineering, Cornell University
Primary Source of Research Funding: American Diabetes Association
Contact: mm826@cornell.edu, ws336@cornell.edu
Website: http://malab.bee.cornell.edu
Primary CNF Tools Used: Heidelberg DWL2000 mask writer, ABM contact aligner, PDMS coating station, SU-8 hotplates

Abstract:

Different types of cells dynamically self-assemble and organize themselves in a spatiotemporal and context-dependent manner [1]. In this study, we report the spatiotemporal dynamics of cell organization of a binary cellular mixture (MDA-MB-231 and MCF10A cells) seeded in microfabricated microwells. The initial seeding ratio of binary cells determined the degree of encapsulation of MCF0A cells by MDA-MB.231 cells. When cells were free to grow, the differential proliferation rate of MDA-MB-231 (low growth rate) and MCF10A cells (high growth rate) resulted in a reversed core (MDA-MB-231)-shell (MCF10A) organization at seeding ratio of 1:1 (MDA-MB-231:MCF10A) and a side-by-side aggregate structure at seeding ratio of 4:1 after long-term culture.

Summary of Research:

Fabrication of Polydimethylsiloxane (PDMS) Microwell. The photomask was prepared using DWL2000 mask writer (Heidelberg Instruments). The silicon wafer was spin-coated with SU-8 2150 photoresist (MicroChem) at 500 rpm for 40 sec and then 2500 rpm for 30 sec. The wafer was covered with the photomask and exposed by a UV photolithography machine (ABM contact aligner) for 32 sec. After being developed and post-baked, the SU-8 master wafer was fabricated. The SU-8 master wafer was then used to create PDMS (Sylgard 184, Dow Corning) mold. A mixture (10:1) of Sylgard 184 silicone elastomer components was casted onto the master wafer and cured at 60°C overnight to prepare a PDMS microwell. Figure 1 is a microscopic image of PDMS microwells.

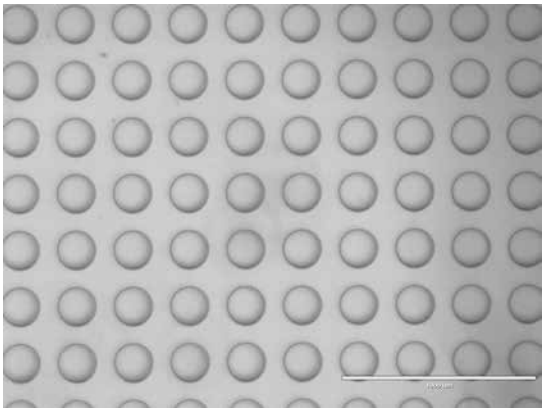

Figure 1: A microscopic image of PDMS microwells. Scale bar: 1000 µm.

Formation of Cell Aggregates in PDMS Microwells. PDMS microwells were autoclaved, placed in a 24-well plate, and coated with 1% (w/v) Pluronic® F127 (Sigma) solution before cell seeding to prevent cell attachment on PDMS surface and facilitate formation of cell aggregates. To form cell aggregates, cell suspensions of MDA-MB-231/MCF10A mixture (MDA.MB-231:MCF10A=1:1 and 4:1, total 1.0×10^6 cells) were added to each well of 24-well plate with PDMS microwells inside. After four hours of static culture, the cells that were adhered to the interspace between microwells were removed by medium change. The cells that fell into the microwells formed cell aggregates after overnight culture. The cell aggregates were cultured in microwells for nine days. The mixed medium (MDA-MB-231 medium:MCF10A medium=1:1 and 4:1) was changed every two days.

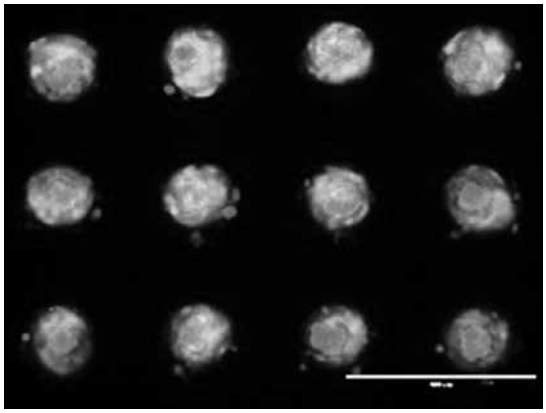

Figure 2: A fluorescent image of cell segregation of MDA-MB-231 [red colour] and MCF10A [green colour] cells at 1:1 cell seeding ratio over nine days of culture. Scale bar: 400 µm.

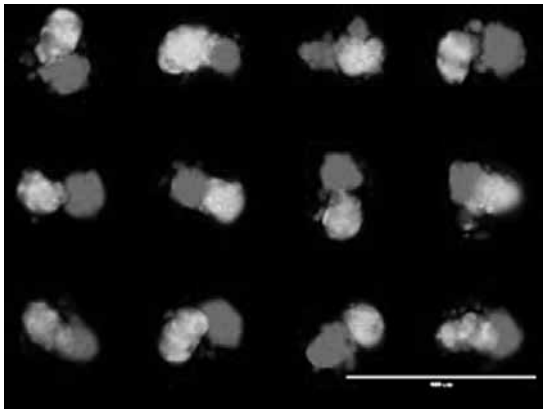

Figure 3: A fluorescent image of cell segregation of MDA-MB-231 [red colour] and MCF10A [green colour] cells at 4:1 cell seeding ratio over nine days of culture. Scale bar: 400 µm.

Figure 2 is a fluorescent image of cell segregation of MDA-MB-231 (red colour / darker grey) and MCF10A (green colour / lighter grey) cells at 1:1 cell seeding ratio over nine days of culture. Figure 3 is a fluorescent image of cell segregation of MDA-MB-231 (red colour / darker grey) and MCF10A (green colour / lighter grey) cells at 4:1 cell seeding ratio over nine days of culture.

In summary, the initial seeding ratio and cell proliferation have significant effects on the evolution of cell organization of binary cellular mixture over long-term culture. Depending on the initial seeding ratios, the cell organization is either a core-shell (1:1) or side-by-side (4:1) aggregate by the differential proliferation rates of MDA-MB-231 and MCF10A cells.

References:

[1] Yoshiki Sasai. Cytosystems dynamics in self-organization of tissue architecture. Nature 2013, 493, 318-326.

Electrochemical Detection Array Combining Amperometry and Total Internal Reflection Fluorescence

CNF Project Number: 2260-13
Principal Investigator: Manfred Lindau
User: Meng Huang

Affiliation: School of Applied and Engineering Physics, Cornell University
Primary Source of Research Funding: National Institutes of Health
Contact: ML95@cornell.edu, mh2236@cornell.edu
Primary CNF Tools Used: ABM contact aligner, CHA Mark 50 evaporator

Abstract:

Neurotransmitters are released in a quantal event by fusion with membranes. The mechanism of this fusion event remains unknown, but is crucial for molecular manipulation and various kinds of disease. We develop and fabricate an electrochemical detection array capable of combining amperometry measurement and total internal reflection fluorescence (TIRF). Amperometry provides the information for the releasing neurotransmitters from vesicles in the cell while TIRF enables direct visualization of vesicles with appropriate fluorescence labels. The combination of the two methods offers a new way for studying the exocytosis process.

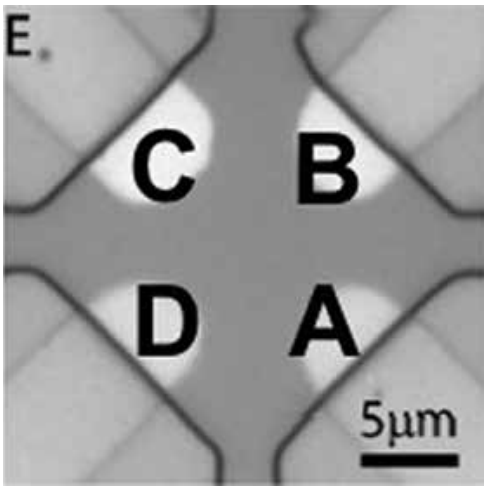

Figure 1: The micrograph showing the geometry of the 4-electrode ECD device.

Summary of Research:

Exocytosis is the process where neurotransmitters are released into the extracellularspace [1]. The amperometry measurement provides precise details about the released transmitters in a single quantal event. While amperometry has the above-mentioned advantages, it measures the releasing contents reaching the electrodes and cannot directly characterize the releasing mechanisms. The total internal reflection fluorescence (TIRF) can detect the fluorescence signals at the substrate surface to visualize the foot print of the cell with its generated evanescence wave. The combination of the two methods offers the availability of monitoring vesicle releasing events and amperometry spikes simultaneously.

To fully utilize the TIRF technology, the specific site of release must be known to locate the fluorescence signal. Therefore, we developed the electrochemical detection (ECD) array with four electrodes between which a cell can be placed, as shown in Figure 1 [1]. Individual fusion events can be detected amperometrically with ~ 200 nm precision, utilizing a map of random walk simulations while the cell surface can be imaged with TIRF microscopy [3].

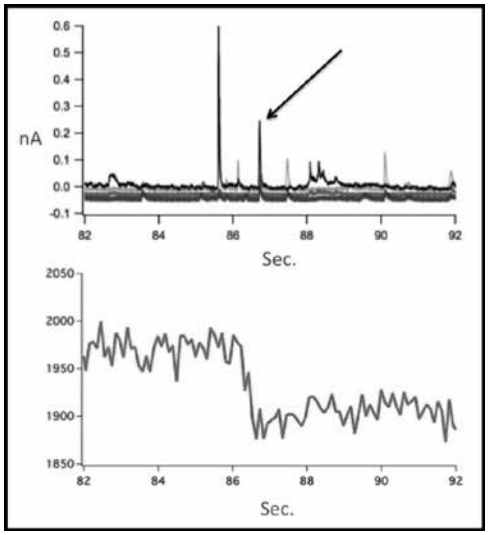

Figure 2: Correlation of amperometry and TIRF imaging for a vesicle release event in chromaffin cells loaded with FFN 511. Top image shows the amperometry recording while the bottom image shows the fluorescence signal from the TIRF microscopy.

A 4-inch, 175 μm thick glass wafer was used for the fabrication of the ECDs. Patterns were transferred onto the wafer through general lithography with NFOL 2020 negative photoresist. The photoresist was spin-coated on the wafer with 3000 rpm for 30s, resulting in a thickness of 2 μm. After the soft bake, alignment and exposure was performed with ABM contact aligner for 7s at 12.14 mJ/s. Following the post exposure bake, the photoresist was developed using 726MIF for 70s. Then 10 nm Ti / 150 nm Pt were deposited on the device using the CHA Mark50 evaporator, followed by a lift off process using 1165. A 2 μm thick SU-8 insulation layer was applied on the ECD using SU-8-2002 and only the tips of the four electrodes were left exposed to the environment.

Fluorescence false neurotransmitter (FFN) 511 was used as the fluorescence marker in the experiment. Bovine chromaffin cells loaded with FFN 511 was plated in the center of the 4-electrode ECD. A fluorescent image of cell pressed on ECD electrode was taken by TIRF microscopy while the release events from vesicles were detected by the electrodes through amperometry. By comparing the random walk simulation and the amperometric spikes of the released neurotransmitters, the precise locations of the specific events could be determined through spatiotemporal correlation. As shown in Figure 2, the TRIF imaging at the specific event location shows a decrease in the intensity, indicating a vesicle loaded with FFN 511 disappearing from the TIRF camera, or releasing its contents to the extracellular space.

References:

[1] Kisler, K., et al., J. Biomater. Nanobiotechnol., 2012. 3(2): p.243-253.

[2] Liu, X., et al. Analytical Chem., 2011, 83: p. 2445-2451.

[3] Zhao, Y., et al., PNAS., 2013. 110(35): p.14249-14254.

Microfluidics for Automated Long-Term High-Resolution Imaging of *C. Elegans* Larval Development

CNF Project Numbers: 2293-14, 2518-17 (REMOTE 155)
Principal Investigators: Eric D. Siggia[1], Shai Shaham[2]
Users: Wolfgang Keil[1,2], Michael Skvarla[3]

Affiliations: 1. Center for Physics and Biology, The Rockefeller University; 2. Laboratory for Developmental Genetics, The Rockefeller University; 3. Cornell NanoScale Science & Technology Facility (CNF)

Primary Source of Research Funding: National Science Foundation

Contact: siggiae@rockefeller.edu, shaham@rockefeller.edu, wkeil@rockefeller.edu

Primary CNF Tools Used: Heidelberg DWL2000, SÜSS MA6-BA6, P10 profilometer, Aura 1000, MVD 100, Unaxis 770

Abstract:

Long-term studies of *Caenorhabditis elegans* (*C. elegans*) larval development traditionally require tedious manual observations because larvae must move to develop, and existing immobilization techniques either perturb development or are unsuited for young larvae. In our project, we developed a simple microfluidic device to image development of *C. elegans* larvae at high spatiotemporal resolution from hatching to adulthood (~3 days). Ten animals, each confined by a circular array of posts, 4.88 µm apart, in a 400 µm diameter chamber, can be periodically immobilized by compression to allow high-quality imaging of even weak fluorescence signals. For the first time, this allows visualization and quantification of developmental processes such as neural arborization, cell divisions, transdifferentiation, and cell death in a feeding, moving, and growing animal. Our technique opens the door to quantitative analysis of time-dependent phenomena governing cellular behavior during *C. elegans* larval development.

Summary of Research:

The nematode *C. elegans* is optically transparent, exhibits an invariant cell lineage, and can be functionally probed using powerful genetic tools, making it a versatile setting for revealing principles of metazoan development. However, long-term high-resolution *in vivo* imaging of *C. elegans* development has been accessible only in embryos, not for developing larvae [1]. The goal of the CNF projects 229314 and 251817/ REMOTE 155 was to close this gap by developing a microfluidics device for fast, reliable, reversible, repeatable, and non-damaging immobilization of *C. elegans* larvae at any given post-embryonic stage.

The main work at the CNF involved developing and optimizing the micro-chamber in which the animals would be kept and imaged throughout their post-embryonic development. We tested dozens of chamber sizes and layout geometries and compared them with respect to ease of animal loading, reliability of animal immobilization, and their ability to confine animals of all larval stages. The latter proved to be most challenging. Very young *C. elegans* larvae are 15 µm wide and 250 µm long, yet proved to be flexible enough to squeeze through 5 µm channels. Late larval stage animals and adults are much larger, typically 30-50 µm wide and 800-1000 µm long. Thus, channels to confine animals had to be smaller than 5 µm while at the same time 20-30 µm high.

Previous *C. elegans* microfluidic devices were fabricated by casting and curing PDMS on molds obtained by photolithography on silicon wafers, mostly using photosensitive epoxy (negative photoresist), e.g. ref. [2]. However, durable features of the required dimensions allowing repeated casts could not be easily accommodated by these techniques. The CNF staff thus suggested deep-reactive ion etching (DRIE) to fabricate the molds. This resulted in precise and durable high-aspect ratio features. The final layout of the two-layer microfluidics device consists of ten 400 µm diameter circular chambers, each formed by an array of posts, 4.88 µm apart (Figure 1, [3]).

Worms are immobilized by a two-step procedure: First, we gradually apply increasing negative pressure to the outlet of the flow layer (Figure 1C, left). This elicits increasing flow toward the outlet, pushing animals to the side of the chamber. At the same time, the negative pressure in the compression layer chamber is gradually released back to ambient pressure. Second, we

gradually increase the pressure applied to the compression layer, deflecting the PDMS membrane toward the flow layer below (Figure 1C, right). The deflected PDMS membrane restricts the animal's movement by pushing it toward the side of the chamber (Figures 1C, right and 1D). Reliable immobilization is achieved within 45-60s. A manuscript describing the technology and several applications has been published in 2017 in Developmental Cell [3].

In collaboration with several labs inside and outside of Rockefeller University, we are currently using our method to study a variety of cellular phenomena, ranging from stochastic cell fate decisions, neurodevelopment to cell death and degradation. We expect the microfluidics setup developed in the course of this CNF project to be highly relevant and extensively applied by a large scientific community and we are in contact with several companies in order to transform our technology into a commercially available platform that could be used by hundreds of *C. elegans* laboratories around the world.

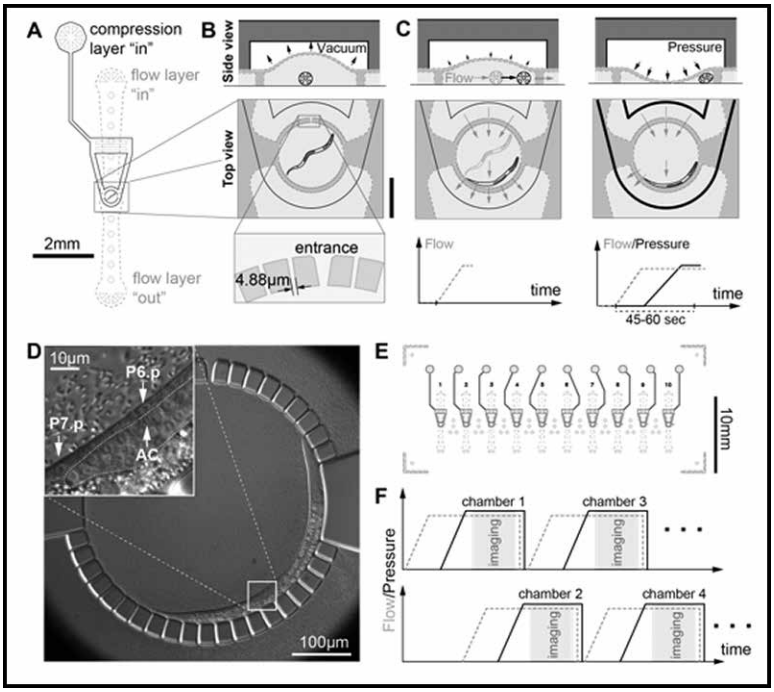

Figure 1: Layout and operating principle of the final device [3].

(A) Worm chamber with inlet and outlet ports for the flow layer (dashed grey) and the inlet port for the pressure layer (solid black).

(B) Side view (top) and top view (bottom) of a worm chamber; Scale bar 250 µm; side view not drawn to scale. Height of flow layer is 20 µm. Height of the pressure layer chamber is 50 µm. Between immobilizations, the pressure layer is kept under vacuum such that the height of the worm chamber is increased.

(C) Illustration of the immobilization procedure. Left: gradually increasing suction at the flow layer outlet (bottom) pushes the animal to the side of the chamber without flushing it through the small channels (top and middle). Right: vacuum in the pressure layer is gradually released and replaced by pressure. This slowly pushes down the membrane between the pressure and flow layers to gently compress and immobilize the worm.

(D) Differential Interference Contrast (DIC) image of an immobilized larva in the chamber. Inset: Magnified view of the mid-body region, showing nuclei of three* C. elegans *cells (P6.p, P7.p and AC). Dashed line indicates gonad outline.

(E) Microfluidic chip with ten identical worm chambers.

(F) To achieve short imaging intervals, immobilization procedures and imaging for chambers 1,3,…9 and 2,4,…10 are staggered using two independent pressure/vacuum pipelines.

References:

[1] Z. Bao, J. I. Murray, T. Boyle, S. L. Ooi, M. J. Sandel, and R. H. Waterston, Proc. Nat'l. Acad. Sci., USA 103, 2707 (2006).

[2] J. Krajniak and H. Lu, Lab Chip 10, 1862 (2010).

[3] W. Keil, L. M. Kutscher, S. Shaham, and E. D. Siggia, Dev Cell 1 (2017).

Evaluating and Improving a Novel Bioreactor for Mammalian Cell Culture

CNF Project Number: 2298-14
Principal Investigators: John C. March, Cait M. Costello
Users: Rohan Acharya, Marek Andrzej Kwasnica

Affiliation: Department of Biological Engineering, Cornell University
Primary Sources of Research Funding: National Institutes for Health, National Science Foundation
Contact: jcm224@cornell.edu, cmc483@cornell.edu, rba49@cornell.edu, mak436@cornell.edu
Primary CNF Tools Used: ObJet30 Pro 3D printer, Labcoter-2 parylene deposition system

Abstract:

To better study complex biological phenomena and interactions of the small intestine, new cell culture systems must be devised that can better mimic the gastrointestinal microenvironment than the standard Petri® dish. To this end, we have evaluated an *in vitro* modeling platform that incorporates a three-dimensional growth scaffold for the cells and fluid flow induced mechanical shear stress that simulate the villi of the intestine and the migratory motor complex respectively. The goal of this project was to evaluate the effect of the periodic fluid shear stress on the proliferation, differentiation, and mucus production of Caco-2 cells grown in the bioreactors compared to standard cell culture dish. Additionally, we made design improvements to simplify the closing mechanism of the bioreactor and reduce the potential for leakage and contamination.

Summary of Research:

The small intestine is a long, tubed-shaped organ that functions in nutrient absorption. In the inmost layer of the mucosa, surrounding the lumen, there is a layer of finger-like projections, called villi, that serve to increase the available surface area for adsorption and create a gradient of shear stresses during passage of food and fluids through the gut. This gradient provides a variety of environments for our cells and bacteria to live and grow, that is called the microbiome. As diagnoses of gastrointestinal and metabolic diseases such as irritable bowel syndrome (IBS) and diabetes are on the rise, there is an increased interest in studying the human microbiome. To better study interactions between bacteria and human cells, a culture platform that supports both cells and simulates the periodic stresses of digestion is needed. Our group sought to evaluate the effects of periodic fluid flow on the differentiation, mucus production, and protein expression of cells lining in the mucosal layer, using Caco-2 cells as a model organism.

Using the ObJet30 Pro 3D printer, and Parylene coater, we created bioreactors that would house a porous polyethylene vinyl acetate scaffold (PEVA) that simulates the mucosal layer. The reactor provides two chambers, separated by the scaffold, to simulate the lumen and the basal layers of the small intestine, seen in Figure 1 and in Figure 2 (a later model of reactor). Fluid was pumped over the cells in the upper chamber in 10 minute intervals, followed by 90 minute periods of no flow, to simulate the median rate of active contractions of the migratory motor complex (rhythms of contractions that move food along the gastrointestinal tract) during rest.

We found that the fluid shear stress gradient, seen in Figure 3, created a differentiation gradient for the Caco-2 cells. Younger proliferating stem cells clustered around the base of the villi in areas of low shear stress, while more mature differentiated cells along the villi in areas of exposed to more shear stress and more nutrients. Near the tips of the villi, the oldest cells would die and be sloughed off. Differentiation was determined by expression of alkaline phosphatase, an enzymatic component of microvilli that seek out nutrients in mature cells, and mucus production, associated with younger cells. We also found a twofold increase in expression of the sugar transport enzymes SGLT-1 and Glut-2, as well as a fourfold increase in glucose transport (Figure 4).

The modified bioreactor, seen in Figure 2, proved to be a worthy step in providing an intestinal model that was a better engineered product. While there was some initial leaking of these, a further experimental modification allowed for a better product. Any leaking

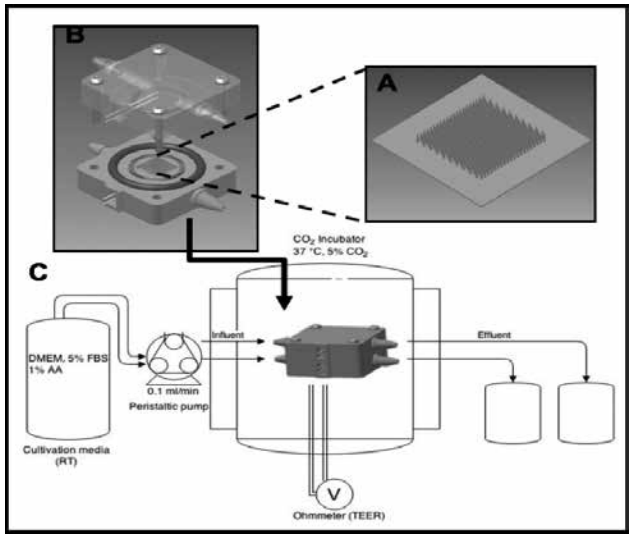

Figure 1: Bioreactor setup. A porous PEVA scaffold (A) was seeded with Caco-2 cells and fitted into the assembled 3D printed bioreactor vessel (B) using the O-rings to seal it in place. After connection to influent and effluent tubing and the peristaltic pump, the device is placed inside the CO_2 incubator for three weeks (C). TEER measurements taken by inserting silver wires connected to chopstick electrodes through the side portal.

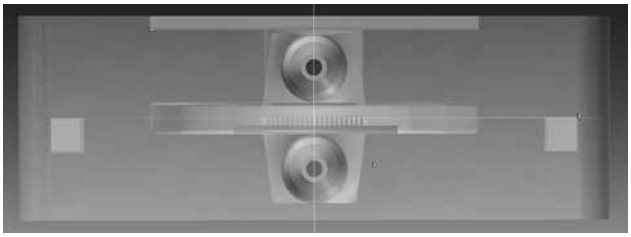

Figure 2: Side view of a reactor that can be placed directly on a microscope. The working distance of the 10x objective lens is 10.6 mm, which is greater than the total depth to the scaffold at 6.25 mm.

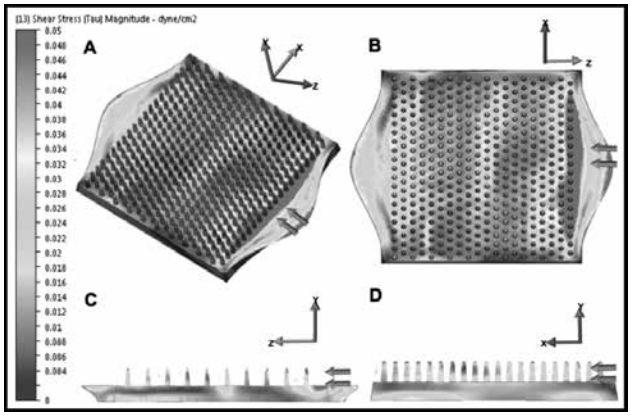

Figure 3: Computational fluid dynamics with intestinally relevant flow rates. (A) shows a 3D profile while (B) shows a top down view. (C) and (D) are planes that were cut through the middle of the scaffold in the z-y and x-y directions respectively. Double arrows represent flow.

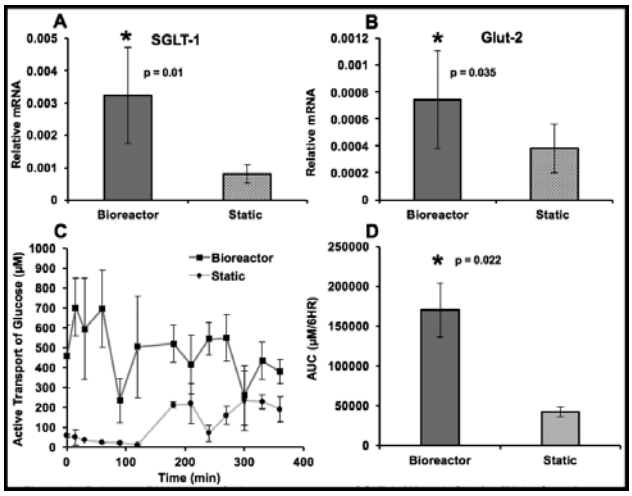

Figure 4: Relative mRNA levels of glucose transporters SGLT-1 (A) and Glut-2 (B) in Caco-2 grown in bioreactors and control scaffolds under static conditions. Significance Student's t-test. N = 6. Active transport of glucose over six hours in the bioreactors and static scaffolds (C). For statistical differences, the area under the curve (AUC) was calculated for each sample and then significance was determined using a Student's t-test (B). N = 3.

in early experiments was shown to result from a lack of vacuum grease or glue and quickly fixed for future experiments.

Further experiments exhibited the accuracy of the resulting culture. Change in mucus production when flow was introduced was drastic and mimicked intestines that did not have inflammation problems. The introduction of a pathogen, PA01, was a good example of changing the microbial environment of the system. The reactor also showed that it could handle multiple bacteria, and accurately display the relationship between them. These experiments provided a good precursor to other possible experiments that could be done with the reactors.

References:

[1] SU-8, C.M., et al. (2016) "Small Intestinal Bioreactors for Studies of Intestinal Absorption." In preparation.

[2] SU-8 C.M., Hongpeng J., Shaffiey S., Yu J., Jain N.K., Hackam D., and March J.C. (2014) "Synthetic small intestinal scaffolds for improved studies of intestinal differentiation." Biotechnology and Bioengineering. doi: 10.1002/bit.25180.

[3] Acharya, R.B. (2017) "Design and Modification of Bioreactors Simulating Intestinal Flow." (Master's Thesis, Cornell Univ.)

Synthetic Small Intestines

CNF Project Number: 2298-14
Principal Investigator: John C. March
User: Cait M. Costello

Affiliation: Department of Biological and Environmental Engineering, Cornell University
Primary Source of Research Funding: NIH
Contact: jcm224@cornell.edu, cmc483@cornell.edu
Primary CNF Tools Used: ObJet30 Pro 3D printer, Labcoter-2 parylene deposition system

Abstract:

The development of artificial small intestines that realistically mimic *in vivo* systems will enable improvement of our understanding of the human gut and its impact on human health. In this work, we demonstrate the importance of gut surface topography and fluid flow dynamics, which are shown to impact epithelial cell growth, proliferation and intestinal cell function. We have constructed a small intestinal bioreactor using three-dimensional (3-D) printing and polymeric scaffolds that mimic the 3-D topography of the intestine and its fluid flow. Our results indicate that transepithelial electrical resistance (TEER) measurements, which are typically high in static 2-D Transwell® apparatuses, is lower in the presence of liquid sheer and 3-D topography compared to a flat scaffold and static conditions. There was also increased cell proliferation and discovered localized regions of elevated apoptosis, specifically at the tips of the villi, where there is highest sheer. Similarly, glucose was actively transported (as opposed to passive) and at higher rates under flow.

Summary of Research:

Transwells have long been used as the standard *in vitro* culture method for studies of intestinal absorption, as they provide both an apical and basolateral spaces to simulate the gut-blood-barrier and enable both active and passive transport of drugs and nutrients. However, intestinal cells seeded onto flat supports exhibit markedly different phenotypes to cells *in vivo* [1], partly due to the poor representation of the 3-D extracellular microenvironments. We have previously shown that recreating the topography of the small intestine with biocompatible collagen or poly-lactic-glycolic acid (PLGA) scaffolds populated with accurately sized villi can lead to improved differentiation and paracellular permeability of Caco-2 monolayers along the villus axis [2]. Cells in a 3-D villus environment experience different nutrient gradients (including oxygen) than cells grown on flat surfaces [3], which can affect their physiology including differentiation. Also, spatial microstructure can influence cell-cell junctions, cell-matrix contacts and molecular communication [4].

In addition to the complex topographical and cellular environment, the human intestine exhibits mechanically active peristaltic motions and fluid flow after ingestion that guide the food bolus down the intestine, facilitating absorption. Specifically, the stomach and small intestine create shear stresses via the hormone-mediated migrating-motor-complex (MMC), an inter-digestive pattern that is dominated by cycles of stasis and short, high-pressure bursts of peristaltic motions, that serve to propel small particles and microorganisms towards the colon [5]. Even during fasting, there is an intermittent flow that exposes the intestinal epithelia to shear stresses. Cyclic strain and shear stress have been shown to modulate signaling pathways in the gut, including those mediated by mechano-sensing β1 and β3 integrins. Importantly, these activate the Rac1 and ERK-signaling pathways (among others) and the downstream wnt/β-catenin pathways which control cellular proliferation and differentiation [6].

What is missing is a device that provides both the accurately-sized villus topography and fluid flow to improve study of intestinal absorption, drug delivery, and intestinal barrier function. Towards this aim, we developed a 3-D printed bioreactor that can both contain villus scaffolds and also create separation of the apical and basolateral spaces in a manner (Figure 1). We cultivated cells in these systems for > 3 weeks, and found site-specific expression profiles of cell differentiation and apoptosis along the crypt-villus axis that are more similar to *in vivo* than Transwell culture or static 3-D

models (Figure 2). In addition, we evaluated intestinal function by measuring the rate of glucose absorption through the epithelial monolayers, finding significantly more uptake than in static systems. Importantly, levels reached are consistent with estimates for physiological conditions.

We anticipate that such small intestinal bioreactors will be useful for future studies of intestinal function, including high throughput drug absorption profiling and studies of bacteria-host interactions.

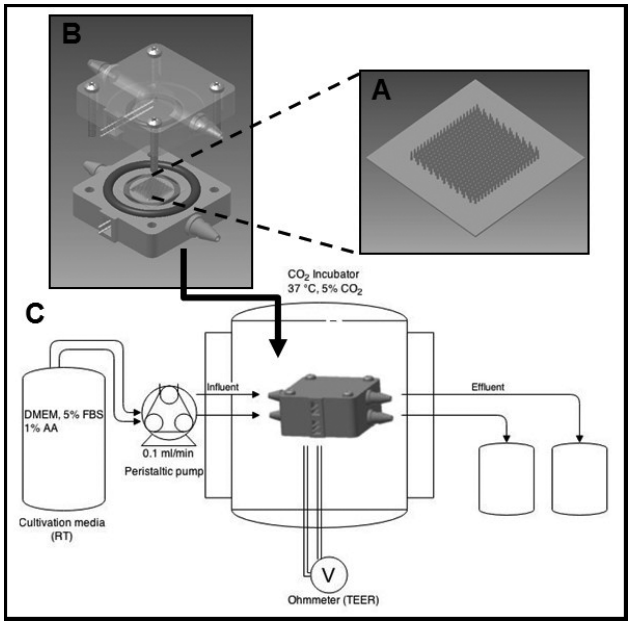

Figure 1: Bioreactor setup. A porous PEVA scaffold (A) was seeded with Caco-2 cells and fitted into the assembled 3-D printed bioreactor vessel (B) using the o-rings to seal it in place. After connection to influent and effluent tubing and the peristaltic pump, the device is placed inside the CO_2 incubator for 3-5 weeks (C). TEER measurements were taken daily by connecting the silver wires to chopstick electrodes and then to a voltohmmeter.

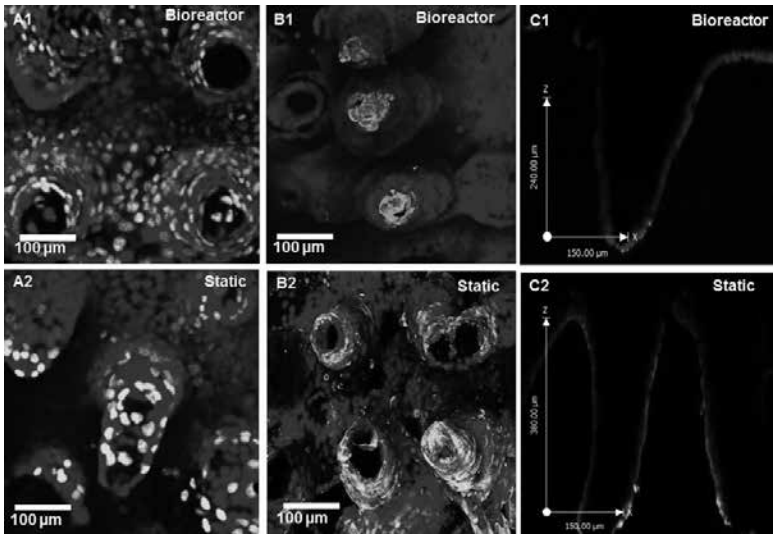

Figure 2: 3-D confocal rendering of PEVA scaffolds after growth of Caco-2 cells in the bioreactors and under static conditions. Images were taken at 20X magnification and stained for proliferation with EdU staining [green] (A1-2) and apoptosis with Tunel Assay [green] (B1-2). Caco-2 monolayers grown in the bioreactors have more proliferating cells and the apoptotic cells are localized to the tips of the villi where the highest shear is. Conversely, the static monolayers have less proliferating cells near the base and a large increase in apoptotic cells.

References:

[1] J. H. Sung, J. Yu, D. Luo, M. L. Shuler and J. C. March, Lab Chip, DOI:10.1039/c0lc00273a.

[2] J. Yu, S. Peng, D. Luo and J. C. March, Biotechnol. Bioeng., DOI:10.1002/bit.24518.

[3] E. Cukierman, R. Pankov, D. R. Stevens and K. M. Yamada, Science, 2001, 294, 1708-1712.

[4] H. Liu and K. Roy, Tissue Eng., 2005, 11, 319-330.

[5] T. Takahashi, J. Neurogastroenterol. Motil., 2012, 18, 246-57.

[6] C. P. Gayer and M. D. Basson, Cell. Signal., DOI:10.1016/j.cellsig.2009.02.011.

Separation of Submicron Particles in a Surface Acoustic Wave Acoustofluidic Resonator

CNF Project Number: 2349-15

Principal Investigator: Brian J. Kirby

User: Prateek Sehgal

Affiliation: Sibley School of Mechanical and Aerospace Engineering, Cornell University

Primary Source of Research Funding: Center on the Physics of Cancer Metabolism (Award number 1U54CA210184-01 from the National Cancer Institute)

Contact: kirby@cornell.edu, ps824@cornell.edu

Website: http://blogs.cornell.edu/kirbyresearch/prateek-sehgal/

Primary CNF Tools Used: SC4500 odd-hour evaporator, ABM contact aligner, Heidelberg DWL2000

Abstract:

Separation of submicron particles, specifically based on their size, has become ubiquitous to numerous biological and chemical studies. One specific example is the need to separate subpopulations of tumor-derived vesicles — microvesicles ranging from 100-1000 nm and exosomes ranging from 30-100 nm [1]. The current approaches, such as ultracentrifugation and ultrafiltration, fail to usefully isolate the subpopulations of tumor-derived vesicles owing to the fragility and small size of these particles. Acoustophoresis has recently emerged as a label-free and gentle technique to separate biological particles based on their physical properties such as size, density, and compressibility. However, separation of submicron particles has been challenging to date because of the weak acoustic radiation force (ARF) on the particles and the domination of secondary effects, such as acoustic streaming, which inhibits the controlled manipulation of the particles. In this work, we have developed a surface acoustic wave (SAW)-based acoustophoretic device that integrates Fabry-Perot acoustic resonators in a novel microfluidic geometry to effectively separate submicron particles. We present numerical simulations of the device that demonstrates the acoustic field generation in a microfluidic channel, which is used for size-based separation of submicron particles. Finally, we experimentally demonstrate the acoustophoretic separation of 500 nm and 100 nm particles in our device at 6.7-fold higher total flow rate and 3-fold lower power density relative to the previous work [2].

Summary of Research:

Theory. Our device is an assembly of Fabry-Perot SAW resonator and the PDMS microfluidic channel that is bonded directly over the resonator. The SAW resonator consists of one interdigitated transducer (IDT) that is bounded by the Bragg reflectors on both sides, creating the Fabry-Perot modality. The PDMS microfluidic channel is aligned at an orientation angle θ_f, as shown in Figures 1 and 2.

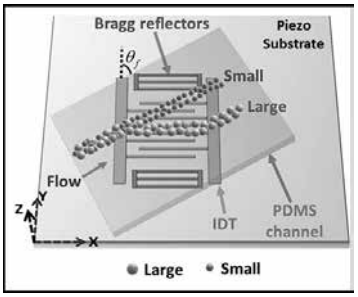

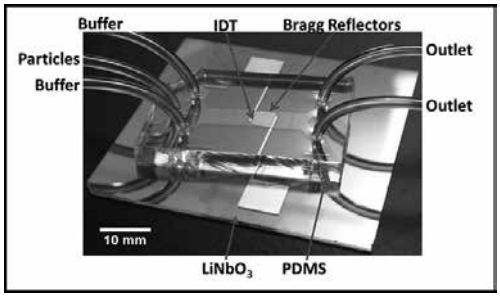

Figure 1, left: The schematic of the Fabry-Perot acoustofluidic device.
Figure 2, right: The fabricated device.

The standing SAW (SSAW) field, which is generated by each finger-pair of the IDT (Figure 3) and strongest at the center of the IDT, is utilized for submicron particle separation. The Bragg reflectors strengthen the SSAW field on the IDT and create a resonant cavity by reflecting the traveling SAW emanated from both sides of the IDT. The SSAW field couples to the fluid and generate standing acoustic field in the channel, as shown in numerical simulations (Figure 3). The particles suspended in the fluid experience size-dependent ARF in this standing

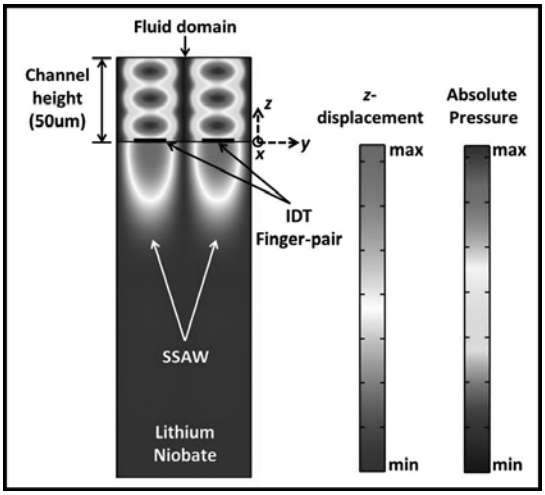

Figure 3: 2D FEM numerical simulations of SSAW displacement field in LiNbO3 and pressure field in fluid for one finger-pair of the IDT with periodic boundary conditions.

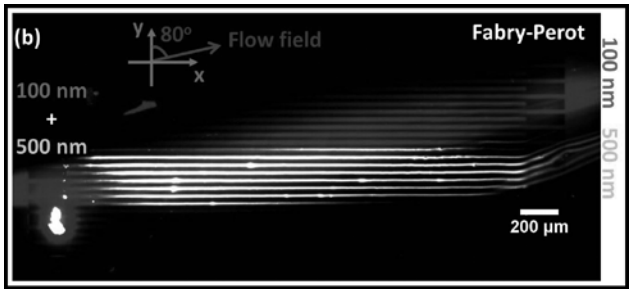

Figure 4: Mean fluorescent composite image of 500 nm (yellow) and 100 nm (blue) particles in the device.

acoustic field. The orientation of the IDT and the flow field results in size-dependent migration trajectories of the particles — the large particles migrate parallel to the IDT and the small particles migrate parallel to the flow field. This differential migration of particles results in the size-based separation of submicron particles in our device. Importantly, the Fabry-Perot modality enhances the overall ARF on the particles and the SAW-based excitation of high frequency waves minimizes the effect of Rayleigh acoustic streaming on the particles. These effects together enable the manipulation of submicron particles in our system.

Methods. The Cr-Au electrodes (10/400 nm, 24 finger-pairs) for a 80 µm SAW wavelength along with 12 reflector strips on each side of the IDT are patterned on 500-µm-thick 128° Y-X cut lithium niobate ($LiNbO_3$) using the standard photolithography and lift-off techniques. Microfluidic channel of height 50 µm are cast in PDMS from SU-8 molds. The PDMS channel and the IDT are bonded at $\theta_f = 80°$ by aligning the alignment marks in each component. The device is characterized with 500 nm fluorescent polystyrene beads injected in the middle channel with DI water as sheath (buffer) fluid. The fluorescent images are acquired using a CCD camera and an upright microscope.

Experiments. Figure 4 shows the migration of 500 nm (yellow) and 100 nm particles (blue) in our device. Both the particles migrate parallel to the flow field, at an angle to the electrodes, before and after the IDT region. The 500 nm particles migrate parallel to the electrodes over the IDT region, whereas the trajectory of the 100 nm particles is still dominated by the flow field over the IDT region. A distinct separation is seen at the exit of the IDT region (right side of the image). The formation of bands by the 500 nm particles is consistent with the acoustic focusing of these particles at the pressure nodes. The separation of two populations is achieved at the power density and the total flow rate of 0.12 W/mm^2 and 12.2 ul/min, respectively. The power density is 3-fold lower and the total flow rate is 6.7-fold-higher than the previously reported parameters for the separation of 500nm/300nm particles [2]. This enhanced acoustic effect in our device is attributed to the Fabry-Perot modality of our system. These results demonstrate the proof of concept of our device to separate submicron biological particles. Because the particles are levitated in the acoustic field over the IDT, we expect that the acoustophoretic separation modality of our device is suitable to separate subpopulations of tumor-derived vesicles without damaging these vesicles.

References:

[1] G. Raposo and W. Stoorvogel, J. Cell Biol., 2013, 200, 373-383.

[2] D. J. Collins, T. Alan and A. Neild, Lab Chip, 2014, 14, 1595-1603.

High Confinement and Low Loss Si_3N_4 Waveguides for Miniaturizing Optical Coherence Tomography

CNF Project Number: 2364-15

Principal Investigator: Michal Lipson[1]

Users: Xingchen Ji[2], Aseema Mohanty[2]

Affiliations: 1. Department of Electrical Engineering, Columbia University, New York, NY 10027; 2. School of Electrical and Computer Engineering, Cornell University, Ithaca, NY 14853

Primary Source of Research Funding: Defense Advanced Research Projects Agency

Contact: ML3745@columbia.edu, xj53@cornell.edu, am2353@cornell.edu

Primary CNF Tools Used: LPCVD, e-beam lithography, Oxford 100 etcher, AJA sputter deposition

Abstract:

We show high confinement thermally tunable, low loss Si_3N_4 waveguides that are 40 cm long. We show that this platform can enable the miniaturization of traditionally bulky active optical coherence tomography (OCT) components.

Summary of Research:

Optical coherence tomography (OCT) has revolutionized fields such as ophthalmology and dermatology with noninvasive real-time micron scale resolution imaging. OCT is an interferometric imaging technique capable of providing high-resolution, cross-sectional and three-dimensional images with micrometer-scale axial resolution at depths above a millimeter [1,2].

The interferometer in commonly used OCT systems is based on fiber or individual free space optical components that limit the stability, cost and size of the systems. Integrated photonics could miniaturize the interferometer by providing a compact, low-loss and tunable optical path. This would not only improve the stability of the interferometric detection but could also significantly reduce the size and cost of the whole system [3]. Recently, interferometers in material platforms such as silicon on insulator, silicon oxynitride and thin silicon nitride (Si_3N_4) have been demonstrated [4-6]. However, all of these studies use an external free-standing reference arm to compensate the optical path length that limits the degree of miniaturization. In order to have a sufficiently long on-chip reference arm, loss becomes a critical issue.

The challenge in integrating the reference arm on-chip, one of the key components needed for miniaturization, is the tradeoff between the need for low loss and for a long tunable arm. While low loss is usually achieved in glass, this platform does not present a tunability mechanism and requires a much larger bending radius. Waveguides consisting of SiO_2 surrounded by a thin layer of Si_3N_4 designed to reduce bending radius have been demonstrated as an on-chip reference arm [7]; however, the minimum bend radius achieved is still a few millimeters and due to the weak light confinement in Si_3N_4, it does not provide enough thermo-optic interaction for tuning.

Here we break the traditional trade-off between loss and tunability using low loss Si_3N_4 waveguide with high confinement for efficient thermo-optic effect. The low loss is achieved by using a new etching process where the polymer residue from the etching process left on the sidewalls is reduced [8]. E-beam lithography is commonly used in photonic device fabrication. For a sufficiently long waveguide, typically multiple e-beam lithography fields have to be crossed. Due to field shifts and stage instability, stitching happens at the field boundary that dramatically increases propagation loss in the waveguide. By adiabatically tapering the size of the waveguide to a wider width at these stitching boundaries, we significantly decrease the propagation loss due to the stitching. The thermo-optic coefficient of Si_3N_4 is about $2.45 \pm 0.09 \times 10^{-5}$ RIU/°C [9], micro-heaters can be integrated with Si_3N_4 structures, which gives us tunability on the centimeter scale.

We fabricate Si_3N_4 waveguides that are tens of centimeters long with losses as low as 0.17 ± 0.01 dB/cm. We compare the 40 cm long waveguide that crosses multiple different e-beam fields with shorter waveguides that have no field crossing. The propagation loss fit is still linear, which shows that

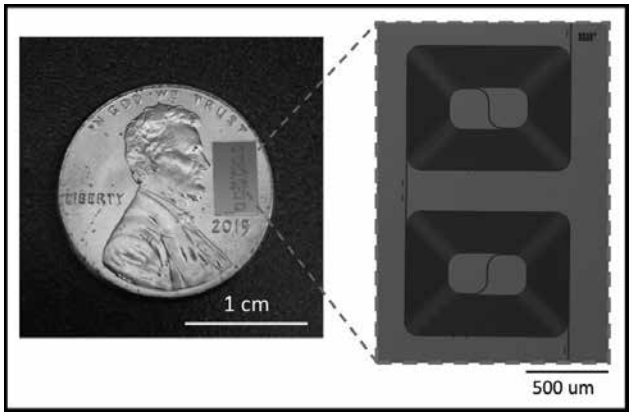

Figure 1: Chip size comparison with a penny and zoomed in microscope image of fabricated devices.

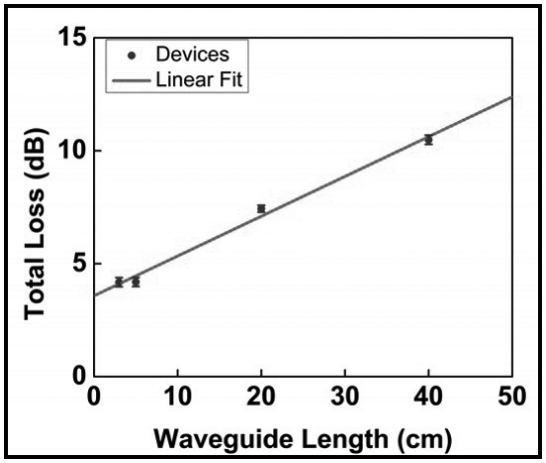

Figure 2: Measured total loss vs different waveguide lengths, from linear fit we extract propagation loss to be 0.17 ± 0.01 dB/cm.

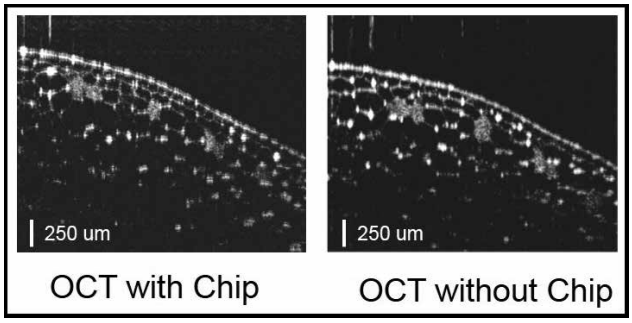

Figure 3: OCT image comparisons of onion slice using Si_3N_4 waveguide and fiber as the reference arm.

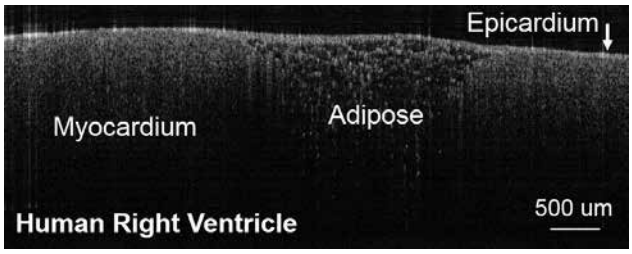

Figure 4: OCT image of human right ventricle sample using Si_3N_4 waveguide as the reference arm.

our novel adiabatic taper design helps to reduce the stitching loss. The propagation loss can be further reduced by applying process described in [8].

We conduct OCT imaging using the thermally tunable Si_3N_4 waveguide as the reference arm of interferometer. A spectral-domain OCT system at 1300 nm was employed to generate the cross-sectional images. As shown in the figure, the quality of the image remains almost the same, which means our on-chip Si_3N_4 waveguide can be used to replace fiber reference arm without sacrificing image quality.

Utilizing low loss high confinement thermally tunable Si_3N_4 waveguide and a novel adiabatic taper design, we are able to fabricate sufficiently long on-chip reference arm for OCT. Integrated photonics has the ability to miniaturize the size and cost of the OCT systems, as well as to increase the stability and provide centimeter scale tunability, which leads to a fully integrated OCT system on chip.

References:

[1] D. Huang, E. A. Swanson, C. P. Lin, J. S. Schuman, W. G. Stinson, W. Chang, M. R. Hee, T. Flotte, K. Gregory, C. A. Puliafito, and J. G. Fujimoto, Science 254 (5035), 1178-1181 (1991).

[2] W. Drexler, M. Liu, A. Kumar, T. Kamali, A. Unterhuber, and R. A. Leitgeb, J. Biomed. Opt. 19, 071412 (2014).

[3] F. Prieto, B. Sepulveda, A. Calle, A. Llobera, C. Domynguez, A. Abad, A. Montoya, and L M Lechuga, Nanotechnology 14, 907 (2003)

[4] G. Yurtsever, K. Komorowska, and R. Baets, Proc. SPIE 8091, 80910 (2011).

[5] V. D. Nguyen, N. Weiss, W. Beeker, M. Hoekman, A. Leinse, R. G. Heideman, T. G. van Leeuwen, and J. Kalkman, Opt. Lett. 37 (23), 4820-4822 (2012).

[6] B. I. Akca, B. Pova.ay, A. Alex, K. Wörhoff, R. M. de Ridder, W. Drexler, and M. Pollnau, Opt. Express 21(14), 16648-16656 (2013).

[7] G. Yurtsever, B. Pova.ay, A. Alex, B. Zabihian, W. Drexler, and R. Baets, Biomedical Opt. Express 5 (4): 1050-1061 (2014).

[8] X. Ji, F. A. Barbosa, S. P. Roberts, A. Dutt, J. Cardenas, Y. Okawachi, A. Bryant, A. L. Gaeta, and M. Lipson, arXiv:1609.08699 (2016).

[9] A. Arbabi and L. L. Goddard, Opt. Lett. 38, 3878-3881 (2013).

Handheld Chem/Biosensor Combining Metasurfaces and Engineered Sensor Proteins to Enhance Surface Plasmon Resonance (SPR)

CNF Project Number: 2430-16

Principal Investigator and User: Lori Lepak

Affiliation: Phoebus Optoelectronics, LLC

Primary Source of Research Funding: Department of Defense

Contact: llepak@phoebusopto.com

Website: www.phoebusopto.com

Primary CNF Tools Used: Heidelberg DWL2000, ASML DUV stepper, SC4500 evaporator, Zeiss SEM

Abstract:

Since 2003, Phoebus Optoelectronics has enabled custom R&D solutions in the fields of Metamaterials, Plasmonics, Antennas, and Sensors. We work closely with our customers throughout device development, from product realization to small volume manufacturing. Our R&D portfolio spans the spectral ranges of visible light, infrared, terahertz, and microwave radiation, for applications in high resolution infrared imaging systems, wavelength and polarization filtering, tunable optical components, beam forming and steering, solar cells and renewable energy devices, and chemical and biological toxin sensors. Our agile team makes extensive use of the resources at the CNF for our nano/micro fabrication and testing, to provide cost efficiency and rapid turnaround.

In the present report, we discuss recent efforts to develop a chem/bio toxin detection system, which provides the state-of-the-art sensitivity of a typical benchtop system with the superior SWaP performance of a handheld system. Our surface plasmon resonance (SPR)-based sensor is expected to be capable of detecting ng/mL concentrations of selected toxins in under five minutes.

Summary of Research:

SPR is a highly sensitive, label-free optical detection technique, whose underlying physics is illustrated in reflection mode in Figure 1. A laser passes through a prism, at an incident angle θ, on a gold film that is in contact with an analyte solution on its opposite side. The illumination produces an evanescent wave (surface plasmon), which significantly reduces the reflectance at a resonant angle. This resonant angle is strongly dependent on the local refractive index, within a few tens of nanometers of the gold surface, and thus is extremely sensitive to enzyme-substrate or antibody-antigen binding events near the surface. The resonance is independent of the geometric configuration of the optical elements (see [8] for mathematical derivation), such that these results also apply to devices that operate in transmission mode.

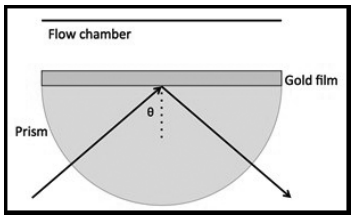

Figure 1: Surface plasmon resonance spectroscopy schematic. Reproduced from reference [8].

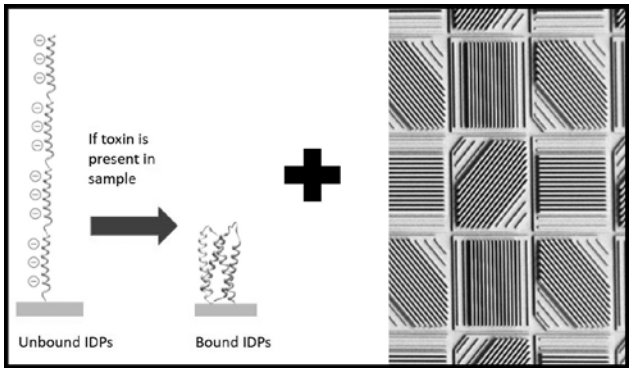

Figure 2: Phoebus-engineered sensor system combines (a) Designed IDPs that undergo extreme conformational changes upon binding target (b) Gold metasurface, patterned to maximize transmission at SPR resonant wavelength. Adapted from ref. [8].

As illustrated in Figure 2, Phoebus has combined two recently developed technologies to enable an SPR sensor system that provides enhanced sensitivity at lower SWaP, relative to technologies currently on the market. First, Phoebus detects toxins using engineered intrinsically disordered proteins (IDP's), designed to

undergo an exceptionally large conformational change upon binding their specific target. This conformation change increases the density of the protein layer, thereby locally increasing the effective refractive index, which in turn enhances the SPR signal by a factor of 100-1000x competing systems.

Second, Phoebus uses the resources of the CNF to fabricate plasmonic chips patterned with a metamaterial surface to enable extraordinary optical transmission (EOT), a phenomenon unique to metastructures in which light is transmitted through apertures much smaller than the incident wavelength, at anomalously large intensities relative to the predictions of conventional aperture theory. EOT was first observed by T.W. Ebbesen in 1998 [1]. Since its founding in 2003, Phoebus has successfully harnessed EOT by incorporating metasurfaces into devices used to perform light filtering [2-3], photon sorting [4-5], polarimetric detection [6], high speed optical detection [7], and most recently, in our SPR plasmonic sensor chips [8].

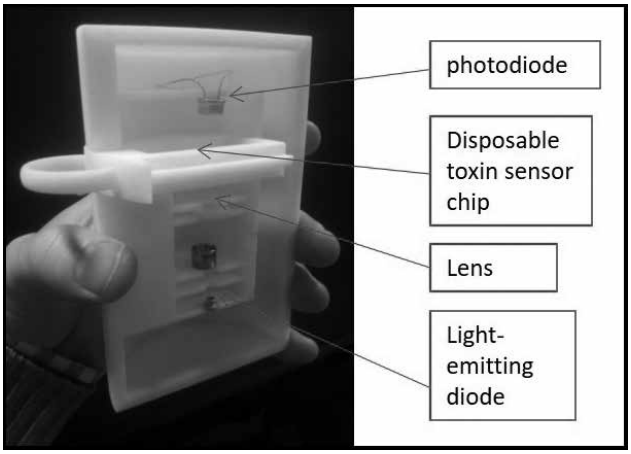

Figure 3: Complete Phoebus handheld biosensor system, Reproduced from reference [8].

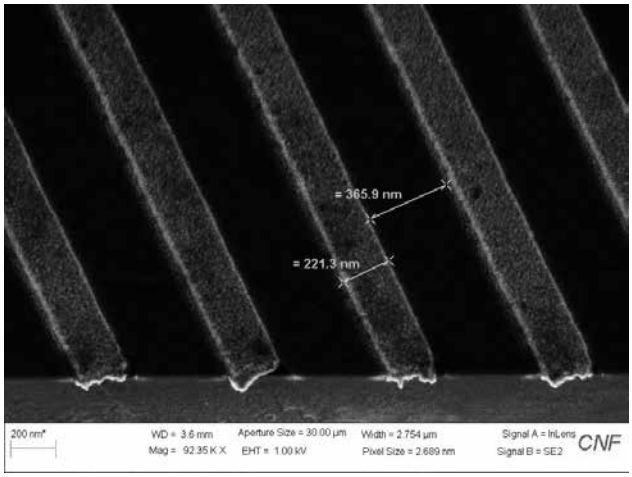

Figure 4: Cross section of a metasurface wire grid used in disposable biosensor chip. Reproduced from reference [8].

These two innovations are combined by attaching the engineered IDP's to the patterned gold metasurface using standard thiol-based attachment chemistry, to make a disposable sensor chip. As shown in Figure 3, this chip is inserted into the complete handheld 3D printed module. All of the optical elements are already assembled in-line as indicated, for a transmission based detection system. Except for Phoebus's disposable sensor chip, all of the optical components are inexpensively commercially available, which helps to make our overall system a highly cost-effective toxin sensing solution.

Our first-generation metasurface chips, imaged in the SEM in cross section in Figure 4, consist of an array of gold wires, which serve both to bind the designed IDPs and to undergo SPR. To make the chip, we patterned the wires using the ASML DUV stepper, evaporated Cr/Au, and performed a liftoff. This process is capable of consistently producing lines down to ~ 200 nm wide, with smooth enough sidewalls for an operable optical device.

References:

[1] Ebbesen, T.W., et al., "Extraordinary optical transmission through sub-wavelength hole arrays." Nature, (1998). 391(6668): p. 667-669.

[2] Crouse, D. "Numerical modeling and electromagnetic resonant modes in complex grating structures and optoelectronic device applications." Electron Devices, IEEE Transactions on 52.11 (2005): 2365-2373.

[3] Crouse, D., and Keshavareddy, P. "Polarization independent enhanced optical transmission in one-dimensional gratings and device applications." Optics Express 15.4 (2007): 1415-1427.

[4] Lansey, E., Crouse, D., et al. "Light localization, photon sorting, and enhanced absorption in subwavelength cavity arrays." Optics Express 20.22 (2012): 24226-24236.

[5] Jung, Y.U; Bendoym, I.; Golovin, A.B.; and Crouse, D.T. "Dual-band photon sorting plasmonic MIM metamaterial sensor." Proc. SPIE 9070, Infrared Technology and Applications XL, 90702X (June 24, 2014); doi:10.1117/12.2050620.

[6] Crouse, D., and Keshavareddy, P. "A method for designing electromagnetic resonance enhanced silicon-on-insulator metal–semiconductor-metal photodetectors." Journal of Optics A: Pure and Applied Optics 8.2 (2006): 175.

[7] Mandel, I.; Gollub, J.; Bendoym, I; Crouse, D. Theory and Design of A Novel Integrated Polarimetric Sensor Utilizing a Light Sorting Metamaterial Grating. Sensors Journal, IEEE, (2012): Vol. PP, 99

[8] Lepak, L., et al. "Handheld chem/biosensor using extreme conformational changes in designed binding proteins to enhance surface plasmon resonance (SPR)" Proc. SPIE 9862, Advanced Environmental, Chemical, and Biological Sensing Technologies XIII, 9862-7 (April 17, 2016); doi:10.1117/12.2222305.

Scalable Sensor Array Platform for Analysis of Quantal Transmitter Release Events

CNF Project Number: 2460-16
Principal Investigator: Manfred Lindau
User: Meng Huang

Affiliation: School of Applied and Engineering Physics, Cornell University
Primary Source of Research Funding: National Institutes of Health
Contact: ML95@cornell.edu, mh2236@cornell.edu
Primary CNF Tools Used: ABM contact aligner, Unaxis 770 Deep Si etcher, AJA sputter depsition system

Abstract:

Neurontransmitters are released in a quantal event by fusion with membranes. We develop and fabricate a CMOS sensor array capable of parallel electrochemical detection of vesicle release events from chromaffin cells. To enable amperometry measurement, polarizable platinum electrodes are deposited on the Al/Cu metal contact on the CMOS chip by sputtering. SU-8 insulation layer is also applied to protect the surface structure of the chip and avoid incomplete coverage of the metal contact by shifting the position of the electrodes as well as form deep wells to trap cells. A silicon wafer with deep etched wells is used as holder for the CMOS chips for better handling and pattern transfer.

Summary of Research:

Neurontransmitters are released into the extracellular space in a process known as exocytosis [1]. The amperometry measurement provides precise details about the released transmitters in a single quantal event. However, amperometric spikes vary from cell to cell even under the same condition [2]. Therefore, a large number of measurements for vesicle release events must be performed to achieve a change in the mean value. Here, we present the CMOS IC sensor array capable of parallel amperometry measurement of vesicle release events and the post-fabrication to enable its functionality.

The CMOS chip has a die dimension of around 3 mm × 4 mm. Therefore, direct spin coating of photoresist on the chip will leave a severe side effect and distort the pattern, especially for the viscous SU-8. Here, we fabricate a silicon wafer holder for the chips for better handling and pattern transfer. First, SPR220-7.0 resist is spin coated on the wafer at 3000 rpm for 30s followed by a 90s soft bake. Then, it is exposed using ABM contact aligner to transfer the pattern (exact dimension of the die but with 50 μm margin) on it as a mask layer for etching. After the post exposure bake and development in 726MIF, the wafer is etched using Unaxis 770 deep silicon etcher to make a 250.m deep well for the chip to fit in.

The CMOS sensor chip is fabricated at MOSIS by On Semiconductor C5F/N. Polarizable electrode materials such as platinum are not offered in this process. Instead, Al/Cu metal contact are deposited to serve as interconnection of the chip. However, amperometry measurement requires polarizable electrodes for low noise current measurement as the oxidation current is usually on the order of pA. Hence, it is necessary to have a post-fabrication process in the CNF clean room to deposit platinum electrodes directly onto the Al/Cu metal contacts for amperometry measurement. AJA sputtering system is used to deposit Ti(60s)/Pt(500s) bilayer with 400w power on the electrode to have a uniform metal film as well as good side wall coverage.

To avoid possible defect such as incomplete coverage of the Pt electrode, a shift electrode strategy is performed to redefine the position and shape of the working electrodes (Figure 1) [4]. The shifted electrodes also enable cell trapping by SU-8 deep wells. The patterned poly(L-lysine) in register with the electrodes will promote cell adhesion, while poly(ethylene glycol) is applied in between wells will resist cell adhesion [5]. Pt electrodes are deposited over the Al/Cu contact, but instead of just covering the contact window, they are extended to cover some part of the overglass. Finally, a 16 μm SU-8 2025 thick layer is fabricated on the surface of the CMOS chip.

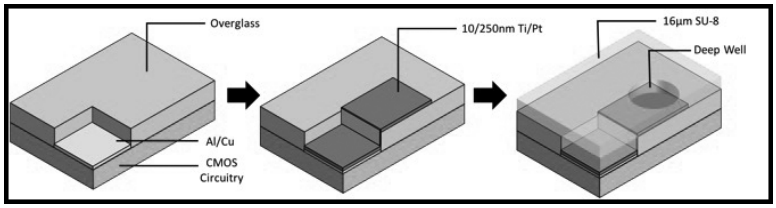

Figure 1: The geometry of shift electrode. The opening of the working area is redefined. In our case, one passivation SU-8 layer is applied with redefined shape (round) of the new opening for better cell trapping.

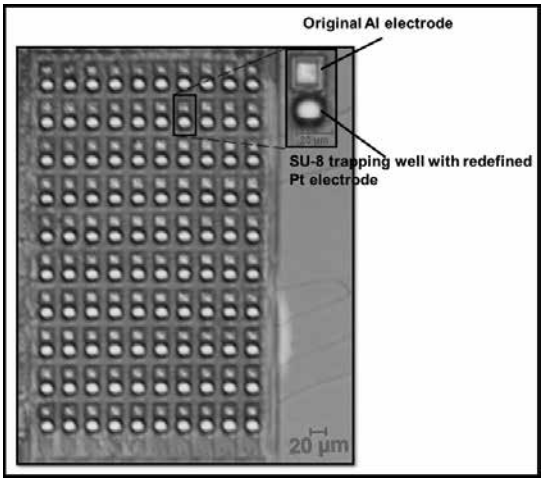

Figure 2: Shift electrode strategy on the CMOS chip. The squares that is out of focus in the image indicate the original electrode while the rounded openings are SU-8 deep wells redefined on the chip.

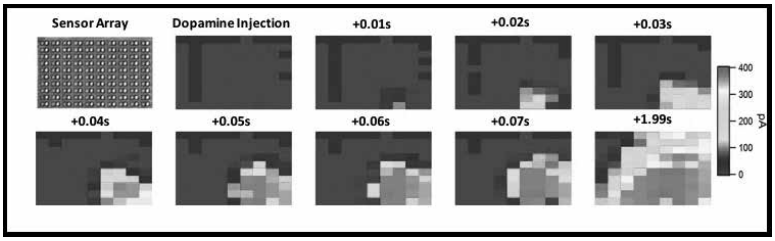

Figure 3: Visualization of dopamine diffusion with 350 μM dopamine solution added on the chip. The color is based on the current level at each individual pixel.

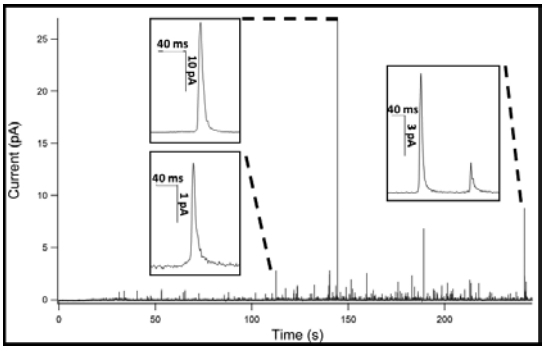

Figure 4: Amperometry recording at one pixel. Many amperometric spikes are observed, validating the function of the device.

Deep wells with 20 μm in diameter are opened by general lithography at the redefined electrode position. The round shape rather than the original square shape of the electrode opening is beneficial for cell trapping (Figure 2). Microcontact printing of poly(L-lysine) and poly(ethylene glycol) will be performed for promotion and resistance of cell adhesion. The product was tested with 350 μM Dopamine solution and the dopamine molecule diffusion can be observed from the current level of each pixel on the chip (Figure 3). Live cell amperometry recordings also show clear and clean amperometric spikes (Figure 4).

The device is able to measure multiple cells in parallel, facilitating the experiment in terms of time and efforts.

References:

[1] Kisler, K., et al., J. Biomater. Nanobiotechnol., 2012. 3(2): p.243-253.

[2] Colliver, TL., et al., J. Neurochem., 2000. 74(3): p. 1086-1097.

[3] Kim, B., et al., Biosens Bioelectron., 2013. 41: p. 736-744.

[4] Heer, F., et al. Biosens Bioelectron., 2004, 20(2): p. 358-366.

[5] Liu, X., et al. Analytical Chem., 2011, 83: p. 2445-2451.

Droplet- Microfluidic Device for Stem Cell Culture

CNF Project Number: 2461-16
Principal Investigator: Benjamin D. Cosgrove
User: Andrea J. De Micheli

Affiliation: Meinig School of Biomedical Engineering, Cornell University
Primary Sources of Research Funding: Cornell start-up funds, NIH Grant # R00AG042491 (Cosgrove)
Contact: bdc68@cornell.edu, ad689@cornell.edu
Website: http://blogs.cornell.edu/cosgrove/
Primary CNF Tools Used: Heidelberg DWL66FS/2000, SÜSS MJB4, SU-8 hotplates

Abstract:

We are working on a droplet-microfluidic device to generated microscopic beads of poly(ethylene glycol), a biomaterial we use to study the interaction between muscle stem cells and their environment. The device is made from PDMS cast on a SU-8 pattered wafer generated by standard SU-8 photolithography techniques at CNF.

Summary of Research:

Microfluidics have enabled a more high-throughput and comprehensive examination of biological systems. In particular, the interaction between stem cells and their local environment (the niche) can be studied using biomaterial constructs that attempt to recreate physical and biological aspects of the niche. We used a droplet-microfluidic device (designed and built at CNF) to generate hundreds of thousands of beads of the biomaterial poly(ethylene glycol) (PEG) with various physical and biochemical properties. We will be using these ~ 100 μm PEG beads as artificial microenvironments to screen for muscle stem-cell-niche interactions that are characteristic of muscle physiology. So far, we were able to create PEG beads with a different level of incorporated Laminin and observe myoblast binding in culture.

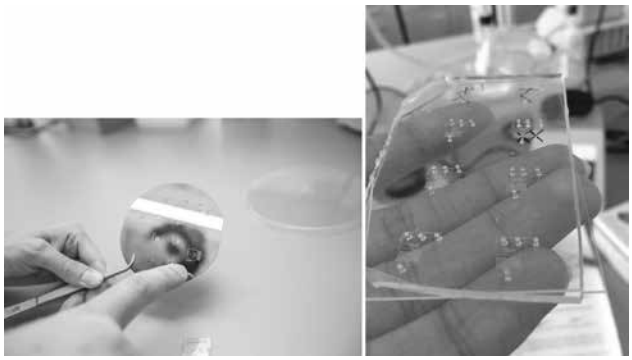

Figure 2: Left: SU-8 wafer with patterned structures. Right: A series of eight PDMS microfluidic devices.

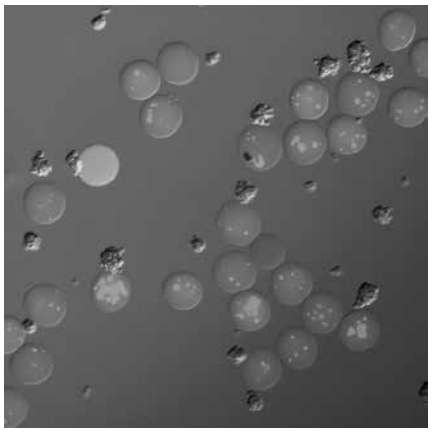

Figure 1: 100-micron PEG beads coated with the fluorescent (Alexa647) protein laminin (red / light grey). Clusters of myoblasts can be seen adhering to the beads.

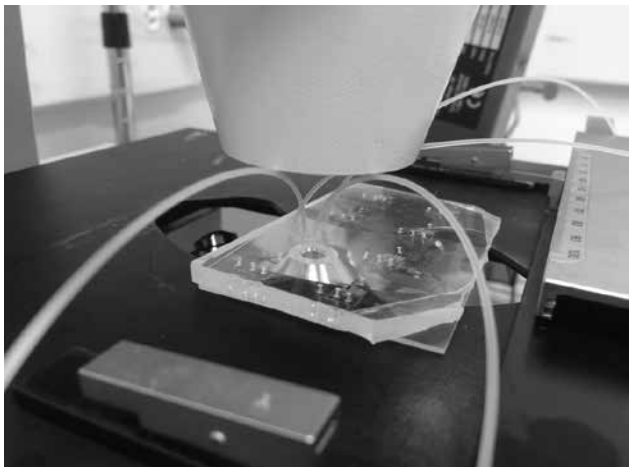

Figure 3: Droplet-microfluidic setup for generating PEG beads. Courtesy De Vlaminck lab.

Graphene Film Protein Crystal Mount

CNF Project Number: 2467-16
Principal Investigator: Marian Szebenyi
User: Irina Kriksunov

Affiliations: CLASSE, MacCHESS; Cornell University
Primary Source of Research Funding: National Institutes of Health
Contact: dms35@cornell.edu, ik29@cornell.edu
Website: www.macchess.cornell.edu
Primary CNF Tools Used: Carbon nanotube/graphene furnace, Zeiss Ultra SEM, VersaLaser engraver/cutter tool

Abstract:

Graphene is a novel material with many distinct properties. Graphene is impermeable to gases and transparent to x-rays. The ability of graphene to reduce the x-ray background and maintain the hydration of protein crystals suggests that graphene could be used as a crystal-mounting platform in protein x-ray crystallography. Multiple layer graphene film is used to construct a protein crystal mount, suitable for x-ray protein crystallography experiment.

Summary of Research:

The graphene-on-copper samples were prepared at the Cornell NanoScale Facility using the carbon nanotube/graphene furnace.

A film consisting of multiple graphene layers was grown on both sides of a thin (100 μm) copper foil. A polymethyl methacrylate (PMMA) coating was applied on top of one side as a support for graphene film. The copper substrate was removed by an etching process using ferric chloride (Transene Company, Inc.). The samples were placed in 100 ml ferric chloride solution in a crystallizing dish for 30 minutes. Once the graphene film with PMMA substrate was free of copper, a series of rinsing procedures were performed using high purity DI water. The graphene film was stored floating on water in the crystallizing dish.

X-ray crystallographic data were collected at Cornell High Energy Synchrotron Source F1 and A1 beamlines using both microbeam set up and 100 μm collimator. Trypsin, ferritin and catalase crystals were mounted on graphene film crystal holders. Two types of crystal mounts were constructed using multiple layer graphene film with 0.5 μm thick PMMA backing layer: graphene wrap mount and graphene window chip.

Graphene Wrap Mount. Graphene wrap mount was constructed using MitegenMesh (MiTeGen, LLC) crystal holder and graphene film with a PMMA layer. Graphene film was wrapped around MitegenMesh mount containing multiple crystals [1]. Data collected at room temperature from Trypsin crystals at 1.35 A (Figure 1).

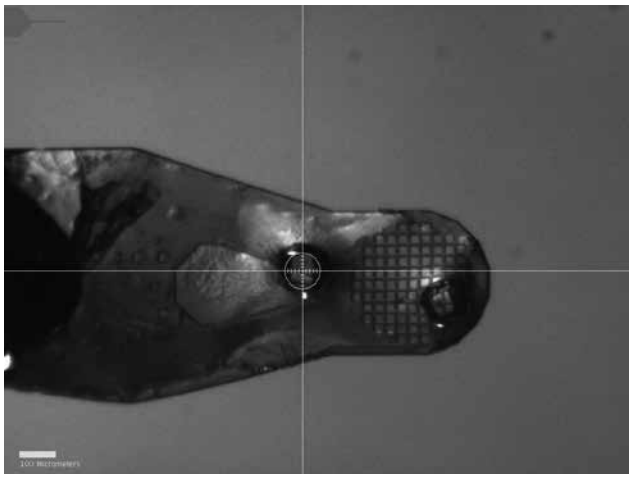

Figure 1: Graphene wrap mount.

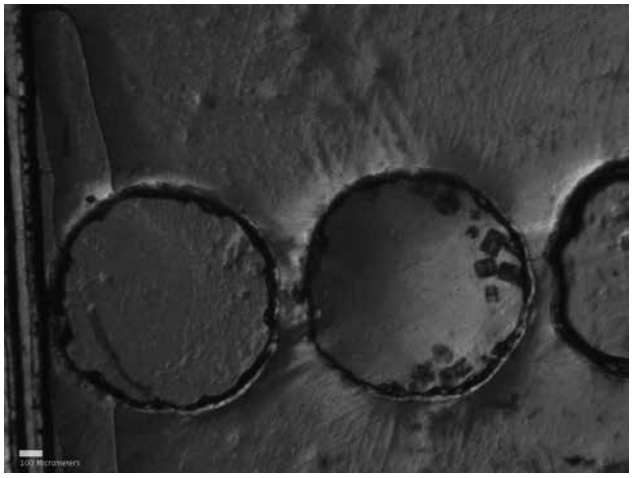

Figure 2: Graphene window chip.

Graphene Window Chip. Nine chips with graphene windows were constructed using samples of multiple layer graphene film with PMMA backing. Various polymer materials were used to make chip insertion and frames [2]. Trypsin crystals were deposited to graphene windows, which were sealed afterward during chip assemble.

Multiple sets of data, consisting of 30 frames and 30 degrees in rotation, were collected from trypsin crystals at room temperature. Trypsin crystals diffracted strongly to 1.35 A at best (Figure 2). Each chip was stored in an individual Petri® dish along with the wet cotton ball to maintain humid environment. In order to assess the diffraction quality of crystals inside the graphene windows, trypsin crystals were exposed to x-rays again in two, five and forty-five days. After being stored for 1.5 month, some of the crystals were still diffracting to about 2A, suggesting the graphene windows were capable of protecting the crystals from drying out.

References:

[1] Wierman J. L., Alden J. S., Kim C. U., McEuen P. L., and Gruner S. M. Graphene as a protein crystal mounting material to reduce background scatter. J. Appl. Cryst. 46(5), doi:10.1107/S002188981301786X, 2013.

[2] Graphene-based microfluidics for serial crystallography. Shuo Sui, Yuxi Wang, Kristopher W. Kolewe, Vukica Srajer, Robert Henning, Jessica D. Schiffman, Christos Dimitrakopoulos and Sarah L. Perry. The Royal Society of Chemistry, 2016.

Metamaterials for Biosensing

CNF Project Number: 2472-16
Principal Investigator: Gennady Shvets
Users: Shourya Dutta Gupta, Glen Kelp

Affiliations: Applied and Engineering Physics, Cornell University; Department of Physics, University of Texas at Austin

Primary Source of Research Funding: Cornell Faculty Development Grant

Contact: gs656@cornell.edu, sd789@cornell.edu, gk389@cornell.edu
Website: http://shvets.aep.cornell.edu

Primary CNF Tools Used: JEOL 9500, CVC SC4500 evaporator, Zeiss Supra SEM, YES asher etcher

Abstract:

Non-invasive and non-destructive identification of different cell types allow for early stage diagnosis and lead to more efficacious potential treatment of various human diseases. For example, early stage cancer detection enables many more treatment options and potential cure as compared to detection in the later stage of cancer. In this respect, circulating tumor cells (CTCs) in the blood stream have been shown to be a strong indicator of early stage of various cancers. However, separation, capturing and identification of CTCs still possess significant challenges with regarding to their extremely low concentration as well as the inability of traditional methods to characterize them accurately. The problem of capturing and identifying CTCs is undertaken using two different approaches in our lab: (a) isolation of CTCs from blood using dielectrophoresis (DEP), and (b) spectroscopic identification of cells using mid-IR plasmon resonant metasurface sensors.

Summary of Research:

Mid-IR spectroscopy is one of the prominent ways of identifying different materials via their fingerprint molecular vibrations. In the past, this has been used for spectroscopically distinguishing cancerous versus non-cancerous tissue.

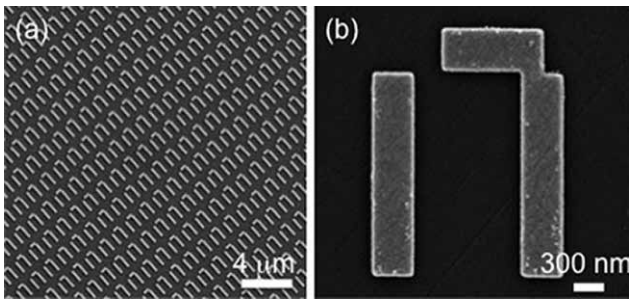

Figure 1: SEM micrographs of the plasmonic metasurface sensor. (a) Low magnification image showing theperiodic arrange of plasmonic microstructures. (b) SEM image of a single unit cell of the metasurface. The metasurface is designed to exhibit very high electric fields in the vicinity of the structure. Depicted unit cells are repeated on the substrate plane to form arrays 100 × 100 (µm)^2 in size. These metasurfaces are made of gold and fabricated on CaF_2 substrates using e-beam lithography.

Typically, at least a complete monolayer of cells is required for performing such a characterization. This limitation on the number of cells creates a large hindrance for adapting this technique for the detection of CTCs, due to their inherently low concentration. It has been previously shown by our group that mid-IR spectroscopy performed using plasmon resonant metasurfaces (Figure 1) allows one to enhance the sensitivity of this technique significantly and we used this approach to accurately characterize a single protein layer [1]. The increase in sensitivity arises from the highly enhanced optical electric fields created near the structures. Furthermore, the metasurface only probes a small region close of the cell membrane due to the rapid decay of the enhanced fields away from the metasurface.

To demonstrate that this technique is viable for cell distinction at a few cell levels, we used these metasurfaces for distinguishing between cancerous (RKO) and non-cancerous (CCD841) colon cells.

A typical image of metasurfaces with cells on them is depicted in Figure 2a, where the darker region indicates the metasurface. Figure 2b shows a set of representative mid-IR spectra from the two different cells that clearly show a large difference. The difference in the spectral features between the two cell types can thus be used for identifying them. Note that the spectra were acquired in the aqueous state, which is generally not the case in most of the studies in literature. Finally, from a device perspective, the whole experiment is performed within a flow chamber enclosing the metasurfaces, which paves the way for automated and rapid identification and characterization of cells. Deposition of cells directly onto the metasurface sensor is improved with the use of dielectrophoresis (DEP).

Since cells act like dielectric particles, a non-uniform AC electric field can be set up around the metasurface using embedded electrodes and a function generator that cause cell movement due to DEP force (proportional to electric field gradient, Figure 3). Attachment of the cells to the sensor surface is further improved by covering the sensor with antibodies. By tuning the electric field frequency, it is also possible to capture specific cells while repelling other kinds of cells in a multi-species cell solution (Figure 3). Separation of different cell types is especially important while working with blood samples that have very low concentration of CTCs. In the case of CTCs, the separation of tumor and blood cells with DEP is very effective, since those cell types have very different dielectric properties and therefore the frequency of the electric field can be chosen such that CTCs move to the sensor while pushing the blood cells away from it.

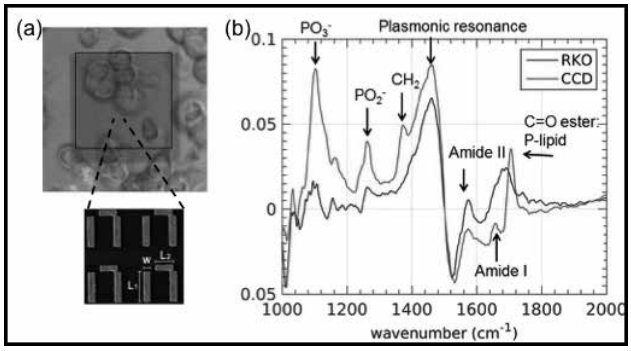

Figure 2: Spectroscopic and non-destructive identification of cancerous cells. (a) Optical image of the metasurface array covered with cells. (b) Absorbance spectra measured from the metasurface samples for colon normal (CCD841) and cancer (RKO) cells.

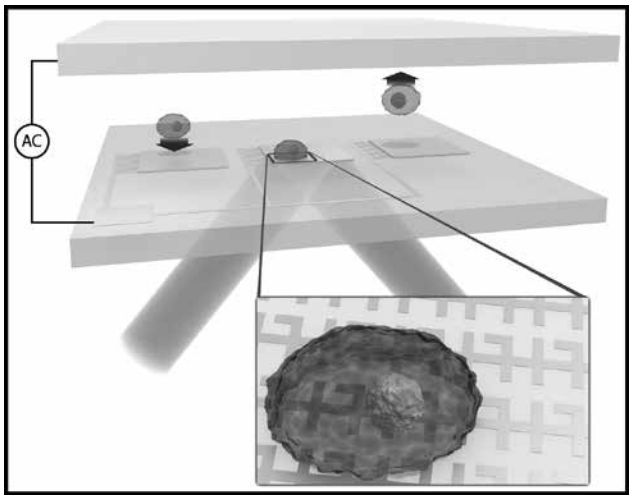

Figure 3: Schematic of the experimental set-up to capture CTCs with DEP. A large ITO plate electrode [green] is placed on one side of a flow channel whereas discrete electrodes run through the metasurface. The electrodes are connected to a function generator to set up non-uniform AC electric field inside the channel. At the correctly chosen frequency CTCs [purple] will move towards the metasurface sensor and get captured while blood cells [blue] will be repelled and flushed away by continuous stream of fluid. IR spectra of the cells can then be collected using an IR microscope.

References:

[1] Fano-resonant asymmetric metamaterials for ultrasensitive spectroscopy and identification of molecular monolayers. Chihhui Wu, Alexander B. Khanikaev, Ronen Adato, Nihal Arju, Ahmet AliYanik, Hatice Altug, Gennady Shvets; Nature Materials 11, 69-75 (2012).

Retinal Implant Project

CNF Project Numbers: 2504-16, 657-97

Principal Investigator: Douglas Shire, PhD

Users: Marcus Gingerich, Ph.D.[1,2,5], Douglas Shire, Ph.D.[1,3,4,5]

Affiliations: 1. Dept. of Electrical Engineering, Cornell University; 2. Dept. of Neuro-Ophthalmology, Massachusetts Eye and Ear Infirmary; 3. Dept. of Electrical Engineering, Massachusetts Institute of Technology; 4. VA Cleveland Healthcare System; 5. Bionic Eye Technologies, Inc.

Primary Sources of Research Funding: Louis Stokes Cleveland VA Medical Center; NIH/NIBIB U01EB018873; NIH/NIBIB R01EB022013, Massachusetts Lions Eye Research Fund

Contact: dbs6@cornell.edu, mdg37@cornell.edu

Website: http://www.bostonretinalimplant.org

Primary CNF Tools Used: Heidelberg DWL2000 mask writer, MA6 contact aligner, polyimide YES curing oven, PT72 RIE, SC4500 evaporator, Gamma Spray Coater, Au electroplating station, K & S Au ball bonder, Zeiss SEM, as well as numerous metrology tools

Abstract:

The purpose of the Retinal Implant Project is to restore useful vision to patients who are blind with degenerative retinal diseases. The primary illnesses we hope to treat are retinitis pigmentosa (a primary cause of inherited blindness) and age-related macular degeneration (the leading cause of blindness in the developed world). Both these diseases cause the eventual destruction of the photoreceptor cells — rods and cones — in the retina, leaving intact the ganglion cells that transmit electrical impulses (and hence visual information) to the brain. The ganglion cells may be stimulated, however, with biphasic current pulses from a microfabricated electrode array. Blind surgical volunteers have consistently described visual percepts that resulted from such stimuli, and this has led our team to develop a wireless, implantable retinal prosthesis.

Summary of Research:

The implanted portion of our device consists of power and data secondary receiving coils, and in a sealed titanium (Ti) can a small number of discrete components, and a custom designed integrated circuit (IC), which consists of circuitry for clock and data recovery, current drivers for electrodes in a stimulating electrode array, and a programmable function generator capable of stimulating with a wide range of pulse widths and amplitudes. The current outputs drive high-charge capacity sputtered iridium oxide film (SIROF) stimulating electrodes, which in turn give rise to the visual percepts mentioned above.

CNF-fabricated components of this system have included various proof-of-concept test structures and tools used in the research effort and an integrated combination flexible circuit and stimulating electrode array. Si wafers serve as carriers for these freestanding films during processing. The electrode leads are fabricated inside of 'sandwiches' of polyimide and amorphous silicon carbide (SiC), while the SIROF electrodes are reactively sputter-deposited.

Assembly of the intraocular components of the prosthesis is accomplished by flip chip stud bumping of the IC and solder attachment of discrete components onto an internal flexible circuit board that is hermetically sealed into an ultraminiature Ti can. The RF coils are soldered and glued to the integrated external flex-array, which is in turn thermosonically bonded to the hermetic feedthrough of the Ti can. Finally, the thermosonic bonds are protected and insulated with an overmold. An external patient interface unit, will consist of a video camera for capturing images, a digital signal processor, and a radio frequency (RF) transmitter and coil to relay power and data to the implanted device.

Scientific challenges still remain in realizing a chronically implantable retinal prosthesis. While our first-generation device was primarily encapsulated in polymers for short term proof-of-concept implant studies, our second generation system focused on a system that would last many years *in vivo*. Our efforts have focused on developing a device with 256+ stimulation channels that is still small enough and of

a configuration to be easily implanted in the ocular orbit and continue to function for many years *in vivo*. Thus, a major effort has been the development of a technological platform to build a robust, hermetically packaged, high-density subretinal visual prosthesis with a lifetime of > 10 years in biological saline that is scalable to hundreds of I/O channels.

Recent efforts in the CNF have been focused on fabricating, testing and redesigning the electrode array (see Figure 1). The project has also been developing and implementing a process to incorporate SU-8-based 3D electrodes (see Figure 2) into a hybrid electrode array to achieve a better interface between the electrode and the target neural cells. Fabrication work at the CNF has included process development required for such high aspect structures including the challenges of lithography with the presence of such extreme topography (see Figure 3). In addition, alternate methods of interconnection have been explored including Au ball stud bumps some examples of which are shown in Figure 4. The latest microfabrication process utilizes numerous CNF tools including the Heidelberg DWL2000 mask writer, MA6 contact aligner, polyimide YES curing oven, PT72 RIE, SC4500 evaporator, Gamma Spray Coater, Au electroplating station, K & S Au ball bonder, Zeiss SEM, as well as numerous metrology tools.

References:

[1] J. F. Rizzo, J. Wyatt, J. Loewenstein, S. Kelly, and D. Shire, "Methods and Perceptual Thresholds for Short-Term Electrical Stimulation of Human Retina with Microelectrode Arrays," Investigative Ophthalmology and Visual Science, vol. 44, no. 12, Dec. 2003, pp. 5355-5361.

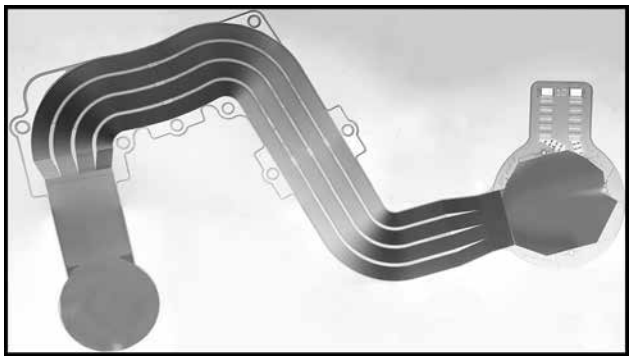

Figure 1: A picture of a single complete electrode array.

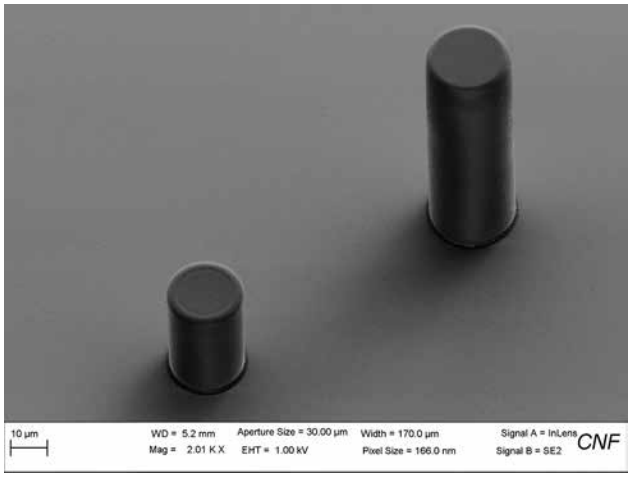

Figure 2: An SEM of two thicknesses of SU-8 structures.

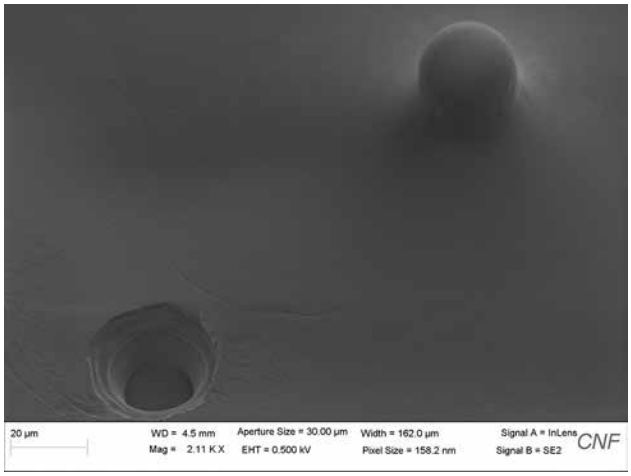

Figure 3: An SEM of an SU-8 structure spray-coated with photoresist to protect during processing and a contact-litho patterned opening to the left.

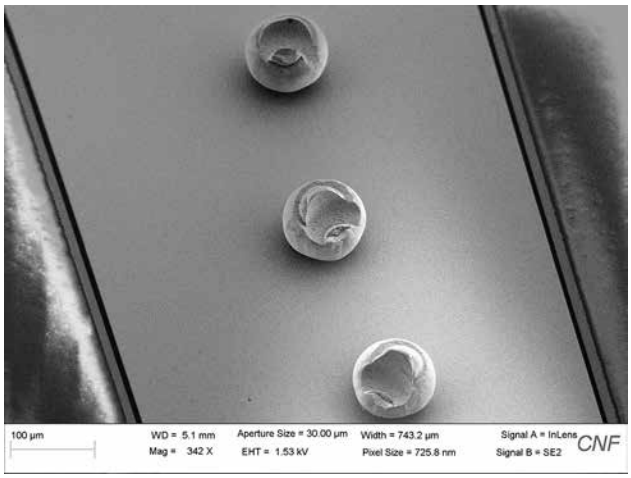

Figure 4: An SEM of Au balls made with the K & S ball bonder to test the feasibility of a stud bump bond interconnection method.

Biosensor Wafer-Level Device Fabrication

CNF Project Number: 2531-17
Principal Investigator: Dr. Carl Boone, Senior Research Scientist[1]
User: Christopher Alpha[2]

Affiliations: 1. FemtoDx, Inc.; 2. Cornell NanoScale Facility
Primary Source of Research Funding: Venture Capital
Contact: carl.boone@femtodx.com, christopher.alpha@gmail.com
Website: www.femtodx.com
Primary CNF Tools Used: AS200 i-line stepper, JEOL 6300, metal evaporator, CVC evaporator, ALD

Abstract:

We are using CNF to make prototype test devices for a point-of-care medical device start-up company. We have just begun work at CNF and have no results at this time.

Summary of Research:

FemtoDx is a biomedical device start-up company developing silicon-based point-of-care diagnostic tools. The technology is based on initial proof-of-concept work done at Boston University using a limited nanofabrication toolset and minimal process, making devices a few at a time. Wafer-scale processing with good cross-wafer uniformity is the goal of the work at the Cornell NanoScale Facility (CNF).

This project at CNF will process 150 mm silicon-on-insulator wafers to create prototype test devices. This will also provide some initial process validation for moving to a foundry. Currently, the project is in the calibration phase, with a full process run expected for late June, 2017. No data or other figures are available at this time.

The patterned Si structure consists of a group of parallel Si nanowires, which will later be chemically modified for molecular detection specificity. Proprietary electrical measurements will be used to measure molecular binding for scientific and diagnostic purposes.

The nanowires are electrically connected through metal electrodes to bonding pads. Building on our prior work, our CNF-produced devices, which will create hundreds of devices with the exact same process flow due to the 6^2 wafer capabilities, will be able to include tests of sensor sensitivity to geometric factors and designs. (Some other facilities we have considered are limited to 4^2 wafers. The SOI wafers we have dedicated for this project only are available in 6^2 and larger.) It will also incorporate new measurement techniques to improve signal to noise ratio. Some devices will have additional microcomponents to perform basic scientific experiments related to the electromechanical response of proteins to electric fields, different environmental temperatures, and the presence of electroosmotic and electrophoretic flow. Such tests are interesting from a purely scientific standpoint, as they can address unanswered questions about protein binding dynamics and electrophoretic processes, plus a technological standpoint, as they give a starting point for further device optimization.

Approximately eight lithography steps (one e-beam, the rest photolithography), plus standard metal and oxide deposition and Si etching, are required for the current process design. We have critical dimensions of 50 nm (for one e-beam step), and 4 μm (for photolithography steps). All steps are standard processing that can be readily converted to CNF's toolset, as has already been verified through communications with Christopher Alpha. We expect to get one to two fully processed wafers, with more wafers consumed in process development, over the course of the next six months.

This project is funded by FemtoDX and will be performed under the supervision of senior research scientist Dr. Carl Boone, with input from device engineer Carsten Madler and CEO Raj Mohanty.

Attonewton Sensitivity Cantilevers for Single-Electron Spin Detection

CNF Project Number: 863-00
Principal Investigator: John A. Marohn
Users: Elizabeth Curley, Michael Boucher, Peter Sun

Affiliation: Department of Chemistry and Chemical Biology, Cornell University
Primary Source of Research Funding: Army Research Office
Contact: jam99@cornell.edu, eac274@cornell.edu, mcb344@cornell.edu, hs859@cornell.edu
Website: marohn.chem.cornell.edu
Primary CNF Tools Used: JEOL 6300, SC4500 evaporator, Oxford 80

Abstract:

Magnetic resonance force microscopy (MRFM) is a scanning-probe technique that overcomes the sensitivity and resolution limitations of conventional magnetic resonance imaging (MRI) by detecting density of magnetic spins as a force or force-gradient on a high-compliance silicon micro-cantilever. One of the primary goals of this research project is to advance MRFM as a tool to image the tertiary structures of individual membrane proteins and biomolecular complexes. This report discusses developments in cantilever fabrication and sample preparation conducted at the Cornell NanoScale Facility (CNF) to enable advancements in nanoscale magnetic resonance imaging through single electron-spin detection of nitroxide spin labels.

Summary of Research:

In 2009, Moore et al. demonstrated a protocol to detect nitroxide electron radical spins, used as a label in electron spin resonance (ESR) studies of biological systems, in an MRFM experiment [1]. In this protocol, the magnetization of electron radicals was modulated, allowing the spin density to be measured as a shift in the resonance frequency of an oscillating magnet-tipped cantilever. This innovation suggests the possibility of attaching spin labels to a protein or complex at known residues, imaging the electrons, and using the locations of the spins to make inferences about the tertiary structure (Figure 1).

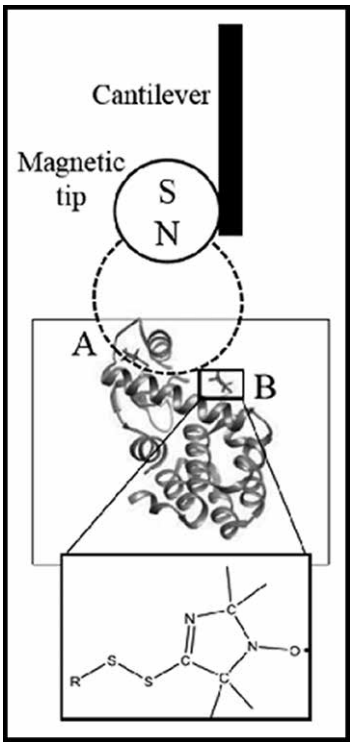

Figure 1: Cartoon of the single electron-spin MRFM experiment showing cantilever, magnet and sample protein. The inset shows the structure of a spin label attached to the protein being studied.

Detecting electron spins, rather than nuclear spins offer a distinct advantage; the large magnetic moment of electrons (660x ^{1}H), offers increased sample polarization, and increased force, i.e. far fewer spins required to measure a signal. Detecting a *single* electron-spin would allow the locations of individual labels on the molecule to be observed.

The magnitude of the MRFM force-gradient signal from an individual spin is proportional to the field-gradient of the cantilever's magnetic tip. Smaller magnets have larger field-gradients, and can detect a smaller number of spins and with better resolution. For this reason, Longenecker et al. developed a batch-and-serial protocol at CNF to prepare cobalt nanomagnets on attonewton-sensitivity microcantilevers [2]. The 200 nm-diameter cobalt nanomagnets were shown to have record field gradients of ~ 5 mT/nm, significantly greater than the micrometer-scale nanomagnets used in previous MRFM ESR experiments. Nuclear magnetic resonance experiments

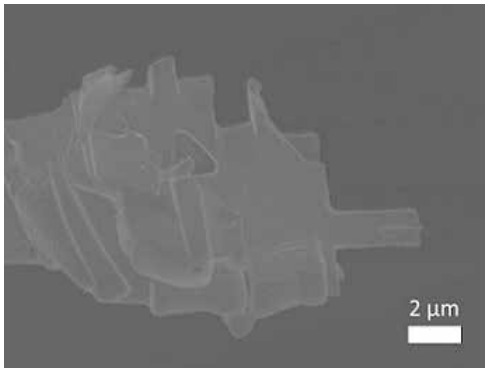

Figure 2: Scanning electron microscopy image of a cantilever tip showing the chip with a 200 nm deposited nanomagnet.

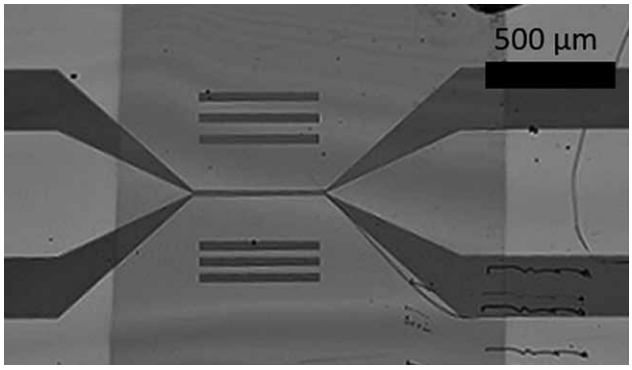

Figure 3: Optical image of a coplanar waveguide with sample and top contact applied. Shaded rectangular region is the gold top contact.

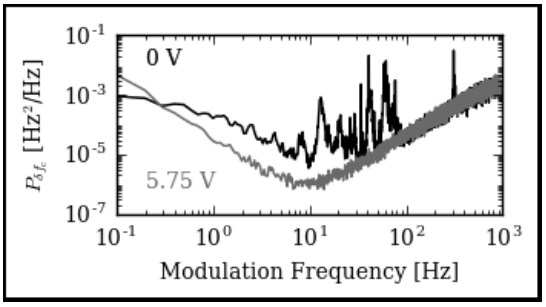

Figure 4: Power spectral density of cantilever frequency fluctuations measured at 4.2 K, 50 nm from the surface of a metal top contact. The frequency fluctuations are significantly reduced when a 5.75 V bias is applied to the cantilever (grey).

were able to detect a signal from just 500 proton magnetic moments, demonstrating the sensitivity required for single electron-spin detection.

Over the past year work has been done at the CNF to fabricate of attonewton-sensitivity magnet-tipped cantilevers, with magnet diameters as small as 100 nm using the Longenecker protocol (Figure 2). In this protocol, cobalt metal was evaporated onto a separate silicon-on-insulator wafer and this chip was later attached to the cantilever body. The wafer was patterned by a JEOL 6300 electron-beam lithography system and the magnetic material was deposited by electron beam evaporation in a SC4500 evaporator. A magnet overhang, ~ 200 nm, was achieved through plasma etching in an Oxford PlasmaLab 80+ RIE System with a sulfur hexafluoride and oxygen recipe. Magnet patterned chips were lifted off via ion beam milling and attached to pre-fabricated silicon cantilevers by platinum deposition using a dual beam FEI Strata 400 STEM FIB system available at the Cornell Center for Materials Research (CCMR).

The main limiting factor in the sensitivity of MRFM experiments to date has been surface noise. Varying electric and magnetic fields in the sample interact with the cantilever tip and are observed as fluctuations in the cantilever resonance frequency. These fluctuations — frequency noise — obscure the signal in force gradient MRFM measurements. Based on the frequency noise observed by Longenecker, et al. [2], we hypothesized that the surface noise was exacerbated by both charges accumulating on the sample surface and eddy currents originating in the metal microwire below the sample. To mitigate this surface frequency noise, we applied a 12 nm gold top contact over the sample using an electron beam evaporator and grounded the gold contact using wire bonds (Figure 3). We then applied a bias to the cantilever tip to minimize contact potential differences between the magnet tip and the metal surface — resulting in significantly reduced frequency noise (Figure 4). We have developed protocols to deposit gold over a narrow region of our sample using a shadow mask or over a larger surface area by taping off the sample surface using Kapton® tape.

With noise mitigation protocols in place, we are currently developing frequency radiation sources to more effectively polarize electron spins and an updated detection protocol for higher resolution electron spin imaging. Efforts are currently underway to prepare samples for a proof-of-concept single-electron spin detection experiment on a biological sample.

References:

[1] Moore, et al. PNAS 2009, 106 (52), 22251-22256.

[2] Longenecker, et al. ACS Nano 2012, 6 (11), 9637-9645.

Design and Characterization of a Microreactor for Thin Film Deposition and *in situ* Surface Analysis

CNF Project Number: 1239-04
Principal Investigator: James R. Engstrom
Users: Taewon Suh, Jiun-Ruey Chen

Affiliation: School of Chemical and Biomolecular Engineering, Cornell University
Primary Source of Research Funding: Semiconductor Research Corporation
Contact: jre7@cornell.edu, ts695@cornell.edu, jc2642@cornell.edu
Website: http://engstromgroup.cbe.cornell.edu
Primary CNF Tools Used: Arradiance ALD Gemstar-6, Oxford ALD FlexAL

Abstract:

Atomic layer deposition (ALD) is a technique capable of precise control of film thickness and conformal film growth due to the self-limiting nature of the precursors involved. The Engstrom research group has built a microreactor that delivers and confines reactants of ALD in a small region for deposition. This microreactor is coupled to an ultra high vacuum (UHV) chamber for surface characterization such that the deposited film is transferred *in vacuo*, without an air break, to the analysis chamber. The most well-studied precursor of in the ALD community, trimethylaluminum (TMA) is used to characterize the microreactor to verify whether it is able to deposit Al_2O_3 film in ALD fashion with water as the co-reactant.

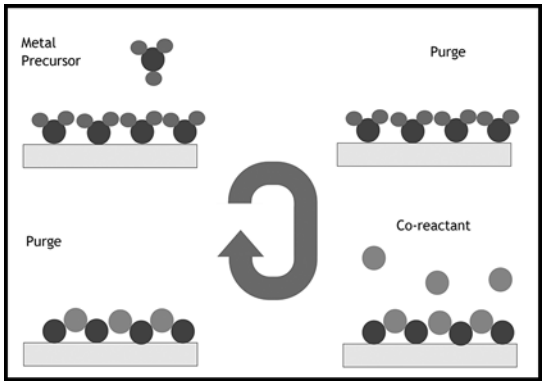

Figure 1: Schematic of an ALD cycle.

Summary of Research:

ALD has emerged as a potential approach capable of matching the rapid rate of downscaling of semiconductor devices. The self-limiting nature of ALD precursors brings about two major advantages unique to the technique: precise control of thickness of deposited film and conformal growth [1]. As described in Figure 1, ALD is sequential binary reaction separated by purge steps to prevent any unwanted parasitic reactions between the precursor and co-reactant in gas phase. TMA, the most-studied precursor in the ALD community, is introduced to a surface in alternating sequence with water as the co-reactant. The deposited alumina film is transferred *in vacuo* to and characterized in a UHV chamber coupled with the microreactor using x-ray photoelectron spectroscopy (XPS).

The thickness of deposited film (~ a few nm) is often in the range that is most effectively probed with surface-sensitive characterization techniques that require UHV, $p < 10^{-9}$ Torr. Conventional ALD is typically conducted at low to medium vacuum conditions ($p \sim 10^{-3}$-10^{2} Torr), thus in most cases UHV based analysis of the deposited thin films occurs in a separate chamber, requiring an air break that may significantly alter the surface composition, oxidation state, structure of the deposited film, and/or underlying substrate. Avoiding this air break is critical for fundamental studies of the growth of ultrathin films, particularly in the early stages. Figure 2 describes how a sample is exposed to precursors at the upper stage and transferred down to the lower stage of the chamber without exposure to air for post-deposition characterization.

In this report, we assess the performance of the microreactor probe with various experiments. In a 10-cycle ALD experiment with $Al(CH_3)_3$ and H_2O,

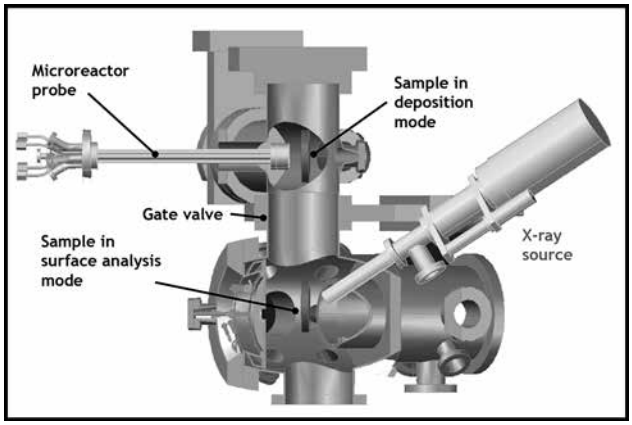

Figure 2: CAD rendering of the microreactor and UHV surface analysis chamber.

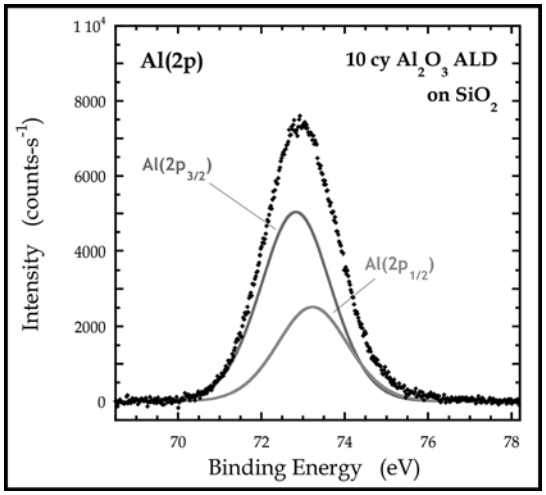

Figure 3: XP spectrum of the Al(2p) feature of 10-cycle Al_2O_3 ALD film deposited on SiO_2 by microreactor probe.

we deposited an ultrathin film of alumina (Al_2O_3) on a hydroxyl-group terminated SiO_2 at substrate temperature of 180°C. From the integrated intensity of a XP spectrum of Al(2p) peak (refer to Figure 3), photoionization cross section, inelastic mean free path, and kinetic energy, thickness of alumina is calculated to be 14.2 Å [2]. Previous studies have reported growth rates ranging from 1.1 to 1.2 Å per cycle, indicating that thickness of the alumina film from ten ALD cycles using the microreactor lies close within the range of reported values [3]. In addition, elemental ratio of oxygen to aluminum is estimated to be 1.52, which corresponds to the stoichiometric ratio of elements in Al_2O_3 film.

A half-cycle ALD experiment is performed with the same precursor, $Al(CH_3)_3$, substrate, and temperature to verify linear correlation between thickness and number of cycles. The thickness of the ultrathin film from this experiment is 1.36 Å, approximately 9.6% of that from the 10-cycle one. This linear relationship between the thickness vs. number of cycles is a unique characteristic of ALD and confirms that the microreactor probe is capable of depositing films via ALD. The absolute atomic density of Al atom is calculated using calibration of semi-infinite Au film and methods described elsewhere [4]. Approximately 1.03×10^{15} Al atoms·cm^{-2} are detected from the half-cycle experiment whereas $\sim 1.02 \times 10^{15}$ Al atoms·cm^{-2} are present in the two top-most layers of α-Al_2O_3 <0001> surface [5].

References:

[1] S. M. George, "Atomic layer deposition: An overview," Chem. Rev., vol. 110, pp. 111-131, 2010.

[2] J. H. Scofield, "Hartree-Slater subshell photoionization cross-sections at 1254 and 1487 eV," J. Electron Spectros. Relat. Phenomena, vol. 8, no. 2, pp. 129-137, 1976.

[3] A. W. Ott, J. W. Klaus, J. M. Johnson, and S. M. George, "Al_3O_3 thin film growth on Si<100> using binary reaction sequence chemistry," Thin Solid Films, vol. 292, no. 1-2, pp. 135-144, 1997.

[4] K. J. Hughes and J. R. Engstrom, "Interfacial organic layers: Tailored surface chemistry for nucleation and growth," J. Vac. Sci. Technol. A Vacuum, Surfaces, Film., vol. 28, no. 5, p. 1033, 2010.

[5] T. Suzuki, S. Hishita, K. Oyoshi, and R. Souda, "Structure of a -Al O (0001) surface and Ti deposited on a -Al O (0001) substrate.; CAICISS and RHEED study," vol. 437, pp. 289-298, 1999.

Chemical Bonding Across the Periodic Table at High and Ambient Pressures

CNF Project Number: 1371-05
Principal Investigator: Roald Hoffmann
User: Martin Rahm

Affiliation: Department of Chemistry and Chemical Biology, Cornell University
Primary Source of Research Funding: National Science Foundation, Grant CHE-1305872
Contact: rh34@cornell.edu, martin.rahm@cornell.edu
Website: http://hoffmann.chem.cornell.edu/roald/
Primary CNF Tools Used: CNF Computer Cluster

Abstract:

We address problems of bonding, structure, and emergent properties such as superconductivity in a wide range of materials – from discrete molecules through polymers to extended solids. The behavior of matter under high pressure is of special interest, as it forms a fruitful collaboration with the group of Neil Ashcroft in Physics. The specific project addressed in 2016-2017 is the design of gold hydrides, as well as ternary gold-hydrogen-alkali metal or earth compounds with potential superconductivity.

Summary of Research:

Gold is one of few elements that does not have a known hydride in the condensed phase, and the making of one presents an extraordinary experimental challenge. A few years ago, we gained some expertise with gold in a study (also done with CNF resources) metastable AuO [1]. In the present work, our structure searches (using CNF computing resources, in last year's report) began by showing that there are no stable binary phases of gold hydride below 300GPa.

More recently, we have concluded a study that comes to a more positive outcome, predicting specific new alkaline/alkali-gold hydride ternaries [2]. One of these, $KAuH_2$, which calculates as thermodynamically favorable with respect to the elements and other decomposition products are shown in Figure 1. We have also used CNF resources to validate our approach by confirming the experimentally known ground states of related A_2PdH_2 (A=alkali metal) ternaries [3].

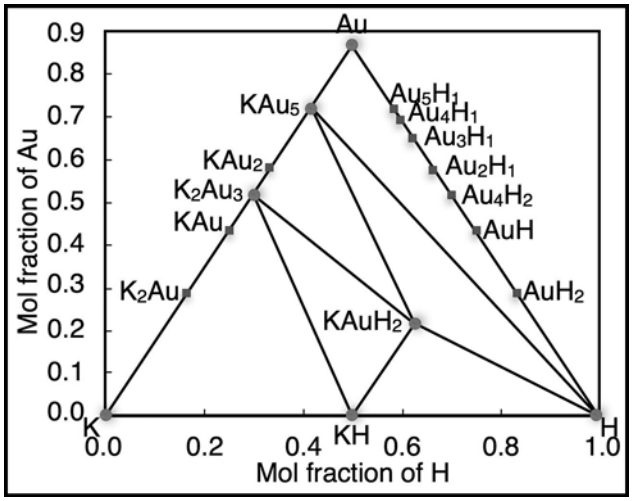

Figure 1: Calculated 3-component phase diagram of K, Au and H as T → 0K. [Red] squares denote unstable compositions (above the convex hull). Black lines between [green] circles connect stable phases. $KAuH_2$ is predicted to be stable with respect to decomposition into all binaries considered here. In addition to running structure prediction calculations, we are also using the CNF cluster to study the behavior of these phases over a range of pressures, to modulate their conductivity, band gap, and relative heat of formation. The mix of light hydrogen and heavier gold gives rise to both high and low frequency phonons in the lattice, which is interesting since electron-phonon coupling is a key ingredient in BCS superconductivity, which we are trying to understand. Three superconducting compounds have thus far been identified following CNF-supported structure searching: $KAuH_2$ (T_c = 0.3K @120GPa), $Ba(AuH_2)_2$ (T_c = 30K @1atm), and $Ba(AuH_2)_2$ (T_c = 10K @1atm) [2]. The predicted structure of one of these, $Ba(AuH_2)_2$, is shown in three views in Figure 2.

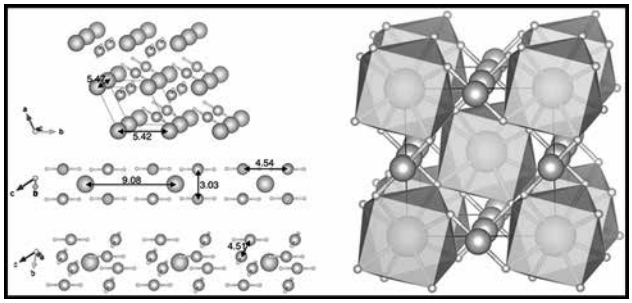

Figure 2: Three views of predicted I4 structure of metastable $Ba(AuH_2)_2$ at 1atm. Large balls are Ba, medium ones Au, smallest ones H. In the view at right, the Ba-H sublattice is highlighted as prisms centered with Ba ions.

References:

[1] AuO: evolving from dis- to comproportionation, and back again, Andreas Hermann, Mariana Derzsi, Wojciech Grochala, and Roald Hoffmann, Inorg Chem, 2016, 55, 1278-1286.

[2] Ternary Gold Hydrides: Designing New, Possibly Superconducting Compounds, Martin Rahm, Roald Hoffmann and Neil Ascroft, J. Am. Chem. Soc, 2017, accepted.

[3] Kadir, K.; Kritikos, M.; Noreus, D.; Andresen, A. F. J. Less-Common Met. 1991, 172-174, 36-41. Bronger, W.; Brassard, L. A. Z. Anorg. Allg. Chem. 1996, 622, 462-464.

Substrate Preparation for Ultrafast Vibrational Spectroscopy Experiments

CNF Project Number: 1936-10
Principal Investigator: Poul B. Petersen
User: Stephanie Sanders

Affiliation: Department of Chemistry and Chemical Biology, Cornell University
Primary Source of Research Funding: National Science Foundation
Contact: pbp33@cornell.edu, ses422@cornell.edu
Website: Petersen.chem.cornell.edu
Primary CNF Tools Used: Oxford ALD FlexAL

Abstract:

Water is ubiquitous and an active component in many natural and technological processes. Vibrational spectroscopy can be used to probe the structure and dynamics of water in a variety of environments. We use sum-frequency generation, a surface specific vibrational spectroscopy, to probe the structure and dynamics of interfacial water at chemically tunable surfaces. Interfaces with tunable surface character are created with self-assembled monolayers. In order to create substrates compatible for both silane self-assembly and sum-frequency generation, infrared and visible transparent CaF_2 windows are coated with SiO_2. Then after surface functionalization with silane monolayers, the water structure and dynamics at the interfaces can be explored with sum-frequency generation.

Summary of Research:

Water is an active component in many natural and technological processes [1]. Interfaces terminates the H-bonded network of water. We aim to study the structure and dynamics of water at self-assembled monolayers (SAMs) with varying surface character using sum-frequency generation (SFG) spectroscopy. In SFG, an infrared photon interacts with a dipole transition of the molecule and a visible photon excites the molecule to a virtual electronic state where it can undergo an anti-Stokes Raman transition resulting in a photon at the sum of the two incident frequencies being emitted [2,3]. In order to collect SFG spectra of solid-aqueous interfaces, we must probe through the window so the infrared photons are not absorbed by water. However, silica, a common SAMs substrate, also absorbs in the infrared.

To create an infrared and visible transparent substrate compatible with SAMs syntheses, we start with a CaF_2 window, which is transparent through the visible and infrared. Then approximately 10 nm of SiO_2 is deposited on the CaF_2 window via atomic layer deposition (ALD) with the Oxford ALD FlexAL. The SiO_2 layer is thin enough to not absorb all the IR photons and prevent SFG spectra of the sample from being collected, but thick enough to form a surface compatible with the self-assembly of silanes.

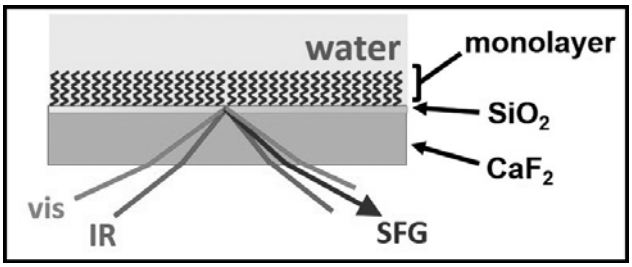

Figure 1: Schematic.

Once the SiO_2 is deposited, hydrophobic, hydrophilic, or mixed monolayer are synthesized with self-assembly of silanes on the surface. Figure 1 shows a schematic of the surface in contact with water. Then, the surfaces and water at the surfaces are analyzed with SFG [2,3].

References:

[1] Ball, P. Life's Matrix: A Biography of Water; University of California Press: Berkeley, 2001.

[2] Barrett, A. R.; Petersen, P. B. Order of Dry and Wet Mixed-Length Self-Assembled Monolayers. J. Phys. Chem. C 2015, 119 (42), 23943-23950.

[3] Vanselous, H.; Petersen, P. B. Extending the Capabilities of Heterodyne-Detected Sum-Frequency Generation Spectroscopy: Probing Any Interface in Any Polarization Combination. J. Phys. Chem. C 2016, 120 (15), 8175-8184.175-8184.

Biomechanics of Bacteria

CNF Project Number: 1970-10
Principal Investigator: Christopher J. Hernandez
Users: Melanie F. Roberts, Lucy Wang

Affiliations: Sibley School of Mechanical and Aerospace Engineering, Meinig School of Biomedical Engineering; Cornell University

Primary Source of Research Funding: National Science Foundation 1463084

Contact: cjh275@cornell.edu, mfr75@cornell.edu
Website: hernandezresearch.com

Primary CNF Tools Used: ASML, Oxford 100, VersaLaser, MOS clean anneal

Abstract:

The mechanical properties of the bacterial cell envelope influence cell growth, cell division and subcellular localization of membrane proteins. Here we demonstrate the ability to apply mechanical loads to live bacteria, the first step toward determination of mechanical properties of bacterial components *in vivo*. Additionally, we show that devices based on the same concept have the ability to separate bacterial species/strains from one another based on the cell mechanical phenotype.

Summary of Research:

In bacteria, the ability to resist mechanical forces is necessary for survival and growth, allowing cells to withstand osmotic pressures while maintaining cell shape, cell growth and division. Hence, the mechanical properties of bacteria and bacterial structural components influence species competition and resistance to toxins and antibiotics.

Our work involves the use of micro/nano fabricated devices as tools for mechanical testing of live bacteria. Within our devices individual bacteria are flowed into tapered channels and trapped at points within the channels based on whole cell stiffness in which less stiff cells are able to travel further in to the channels (Figure 1). Key advantages of this microfluidic platform for profiling the biomechanical properties of bacteria include: minimal sample preparation, no chemical immobilization or labeling, and the ability to analyze hundreds of cells at once.

In our first series of experiments we manufactured devices on silica glass wafers using deep UV photo-

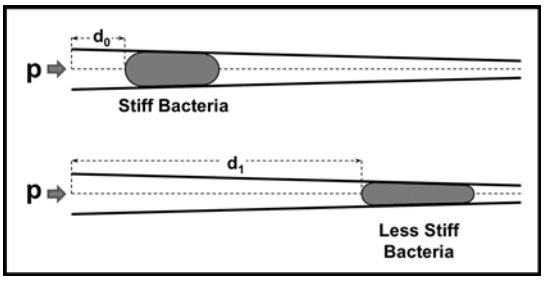

Figure 1: Bacteria under fluid pressure (p) are forced into tapered channels. The distance a cell travels into a tapered channel depends on cell stiffness with more compliant cells traveling further into the channels. The distance traveled by a cell into the tapered channel (d_1) is therefore an indicator of cell stiffness. Viewing the deformation of a cell under two different applied pressures can be used to determine the mechanical properties of the cell envelope.

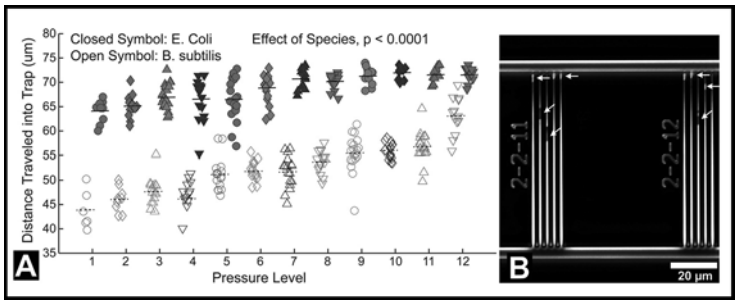

Figure 2: (A) The position of bacteria occupying trap channels at twelve different pressure levels (where level 1 is lowest and level 12 is greatest) in a single experiment are shown. Horizontal lines indicate averages at each pressure level.* E. coli *travel further into the traps than* B. subtilis *overall (p < 0.0001, ANCOVA) as well as at each individual pressure level (p < 0.0001, t tests). (B) Differences in bacteria stiffness between species can be detected in a mixed culture.* E. coli *expressing GFP ([green], indicated by horizontal arrows) traveled further into the trap channels than B. subtilis (indicated by tilted arrows), demonstrating the possibility of separating bacteria based on mechanical phenotype.

lithography to achieve nano-scale features (250 nm smallest dimension). These glass on glass devices were manufactured using the ASML, Oxford 100, VersaLaser and MOS clean anneal tools at the Cornell NanoScale Science & Technology Center.

In the first device design, cells from a population are submitted to up to 12 different applied pressures was used to establish the biomechanical profile of two model organisms, *E. coli* and *B. subtilis*.

Our results demonstrated differences in stiffness between *E. coli* and *B. subtilis* (Figure 2) and suggest that a device with a shorter channel length would allow transport of *E. coli* but not *B. subtilis*, potentially allowing for separation of bacteria based on the biomechanical properties [1]. When combined with theoretical mechanics models, it allows us to determine the stress distribution within individual bacteria and study their response to mechanical stimulation [2]. In our recent work, we have explored the effects of mechanical loads on the assembly/disassembly of multicomponent efflux pumps. Multicomponent efflux pumps are three part channels that cross the inner membrane, periplasm and outer membrane of bacteria and are used to remove toxins (excessive metal ions, antibiotics, etc.) [3].

Our preliminary data suggests that the assembly and function of multicomponent efflux pumps is sensitive to mechanical stress and strain, in particular shear stresses across the cell envelope appear to impair the function of efflux pumps while hydrostatic stresses tend to promote the function of efflux pumps.

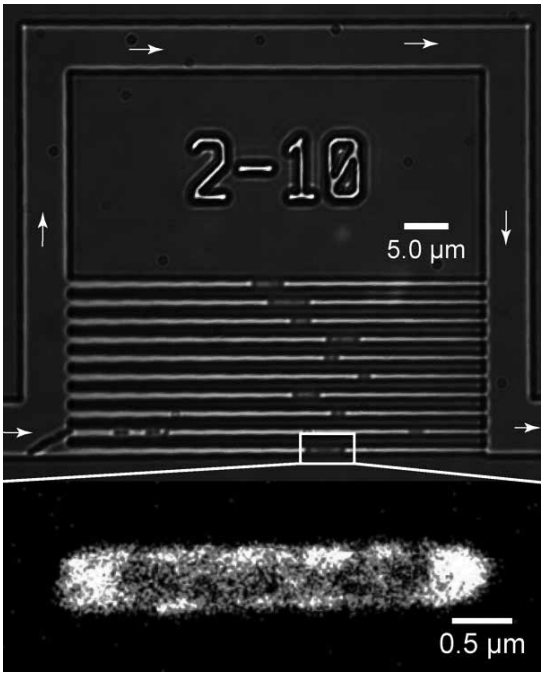

Figure 3: (Top) A single mechanical testing device is shown with arrows indicating direction of flow. Bacteria trapped within the tapered channels are visible in bright field images. PALM microscopy is used to visualize a photo switchable membrane protein, making it possible to view the cell morphology and measure changes in cell shape in response to changes in flow rate/pressure.

References:

[1] Sun, X., Weinlandt, W.H., Patel, H., Wu, M., Hernandez, C.J. (2014) "A Microfluidic Platform for Profiling Biomechanical Properties of Bacteria." Lab Chip. 14 (14), 2491-2498. NIHMS600175.

[2] M. F. Roberts, A. Srivastava, X. Sun, L. Kreminski, L. Ling, L. Wang, P. Chen, C-Y. Hui, C. J. Hernandez. "A Microfluidic Platform for Generating Non-Uniform Mechanical Stress in Cell Envelopes of Live Bacteria" American Society of Microbiology Annual Meeting 2016.

[3] M.F. Roberts, A. Srivastava, L.M. Wang, C-Y Hui, L.A. Genova, P. Chen, C.J. Hernandez "A microfluidic system for mechanical characterization and stimulus of individual bacteria" European Society of Biomechanics 2017.

Micrometer-Scale Coplanar Waveguides for Nanoscale Magnetic Resonance Imaging

CNF Project Numbers: 2125-12, 863-00

Principal Investigator: John A. Marohn

Users: Corinne E. Isaac, Elizabeth Curley, Michael Boucher

Affiliation: Department of Chemistry and Chemical Biology, Cornell University

Primary Source of Research Funding: Army Research Office

Contact: jam99@cornell.edu, cek222@cornell.edu, eac274@cornell.edu, mcb344@cornell.edu

Website: marohn.chem.cornell.edu

Primary CNF Tools Used: Gamma automatic coat-develop, ASML 300C DUV stepper

Abstract:

We report on the design, fabrication, and characterization of broadband micrometer-scale coplanar waveguides capable of delivering millitesla strength magnetic fields on a 200 milliwatt power budget with minimal sample heating. These waveguides, operating from DC up to 40 GHz, have been integrated into a cryogenic scanning probe microscope to enable the detection of electron spin resonance and nuclear magnetic resonance in a single force detected magnetic resonance experiment for the first time. Additionally, the ability to irradiate both nuclear and electron spins with a single device allowed for the first mechanical detection of hyperpolarized proton magnetization achieved via cross-effect dynamic nuclear polarization [1]. These enabling advances are the first steps toward achieving three-dimensional, nano-scale magnetic resonance imaging (nano-MRI) using magnetic resonance force microscopy.

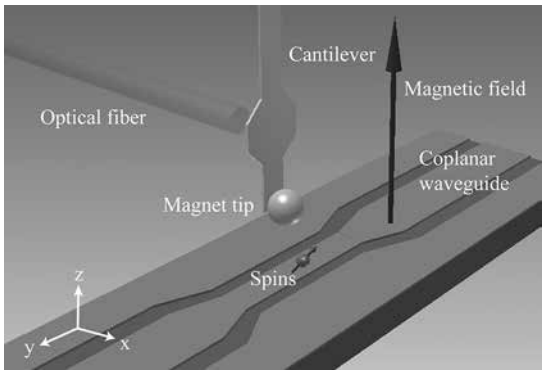

Figure 1: Schematic of a magnetic resonance force microscope experiment showing the magnet-tipped cantilever and coplanar waveguide necessary to modulate sample spins (adapted from Ref. 3).

Summary of Research:

Having a universal platform for imaging individual biomolecules or biomolecular complexes with isotopic specificity and nanometer or sub-nanometer resolution would be an enabling advance for a variety of scientific disciplines. By detecting magnetic resonance as a force on an attonewton-sensitivity microcantilever (Figure 1), magnetic resonance force microscopy (MRFM) offers the sensitivity and depth-of-view required for three-dimensional, nano-MRI. While recent advances in MRFM have demonstrated the ability to perform 3D imaging of a single virus particle with < 10 nanometer resolution [2] and the sensitivity required to detect a few hundred proton magnetic moments with a record-high gradient magnet tipped cantilever [3], these experiments required hours or days of signal averaging as a result of detecting statistical polarization or random spin fluctuations commonly referred to as 'spin-noise'.

To achieve greater imaging resolution, while decreasing signal averaging time, our approach was two-fold: (1) increase nuclear spin polarization to generate a well-defined polarized spin signal and (2) develop a universal sample platform in which biological samples can be deposited for single electron spin imaging. The enabling advance for both experiments was a broadband coplanar waveguide (CPW) to deliver radiofrequency waves for nuclear magnetic resonance (NMR), microwave frequency irradiation for electron spin resonance (ESR) and combining these techniques to transfer polarization from nuclear spins to electron spins via dynamic nuclear polarization (DNP). The challenge in the development of these CPWs was to achieve a high (millitesla) strength oscillating magnetic field, from a few megahertz to tens of gigahertz while operating on the < 200 milliwatt power budget of our microscope to avoid sample heating under operation at 4.2 kelvin. The CPWs were designed and simulated (Sonnet) to have a 50-Ω characteristic impedance

throughout the device. With this design constraint, the waveguides could be coupled via multiple wire bonds to a ceramic coplanar waveguide board equipped with SMA connectors for use with commercial radiofrequency (rf) and microwave (MW) signal generators. To achieve the millitesla rf magnetic fields necessary to invert nuclear spin polarization and microtesla MW magnetic fields required to saturate electron spin resonance, the coplanar waveguides were designed to maintain a 50-Ω impedance while the centerline tapered from a 480 μm wide wire with a 230 μm wide gap to a 5 or 10 μm wide wire with a 3 μm or 6 μm wide gap, respectively. This constriction generated a high current density in the microwire capable of producing magnetic fields up to 5 millitesla for rf waves and a few microtesla for MW frequency irradiation with just 200 mW of input power. Additionally, this coplanar waveguide has demonstrated losses of just a few milliwatt across the device meaning sample, heating at cryogenic temperatures is negligible.

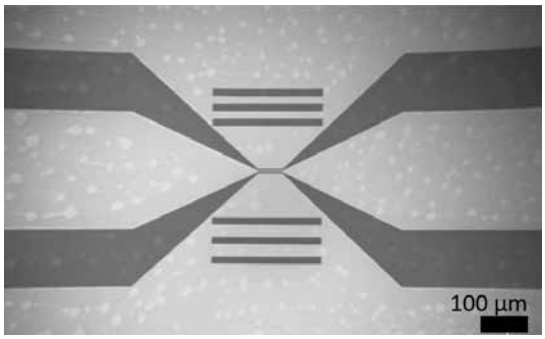

Figure 2: Scanning electron microscopy image of a fabricated coplanar waveguide. The gridlines seen above and below the centerline are used to optically locate the microwire during operation under high vacuum at 4.2 kelvin.

Our coplanar waveguides are fabricated at the Cornell NanoScale Science and Technology Facility. The 2 mm by 10 mm waveguide chips were fabricated on high resistivity silicon wafers patterned with 0.2 μm thick copper. A representative waveguide with a 100 μm long, 5 μm wide microwire can be seen in Figure 2. The tapered design was achieved via a photolithography-based protocol. The Gamma Automatic Coat-Develop tool was used to spin-cast DSK-101-312 and UV-210 resists, which were then exposed using the ASML 300C DUV Stepper. Following developing and descumming, a titanium/copper/gold (5/200/30 nm) film was deposited via electron-beam evaporation.

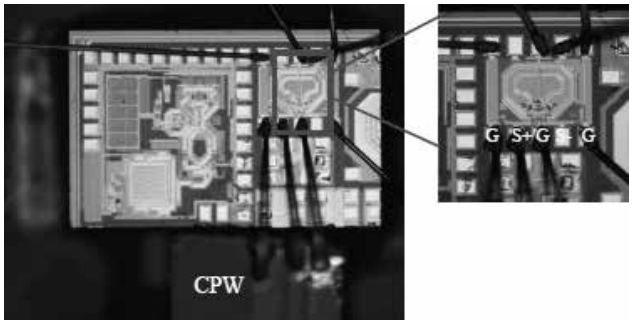

Figure 3: Optical microscope image of 36 GHz CMOS oscillator coupled via aluminum wires bonds to our custom fabricated coplanar waveguide.

Furthermore, patterned silicon gridlines, seen above and below the CPW microwire in Figure 2, have been implemented into the ground plane of the coplanar waveguide to assist in the alignment of the cantilever and microwire under vacuum at temperatures down to 4.2 kelvin. Additional optical features may be added in future biological imaging experiments to rapidly locate specific molecules of interest.

In addition to using CPWs coupled to commercial frequency generators as a universal sample platform, we have further developed coplanar waveguides to be coupled to cryogenic chip scale microwave sources developed by Prof. Ehsan Afshari and coworkers (Figure 3). Coupled to our coplanar waveguides, these 36 GHz CMOS oscillators generate > 300 μW of output power at temperatures down to ~ 12 kelvin. Simulations show that this should be sufficient to saturate electron spin resonance in our magnetic resonance force microscope. This unique combination of CMOS oscillator and coplanar waveguide would be the first of its kind integrated into any cryogenic scanned probe microscope experiment.

References:

[1] Isaac, Marohn, et al. Phys. Chem. Chem. Phys. 2016, 18, 8806.
[2] Degen, Rugar, et al. PNAS, 2009, 106, 1313.
[3] Longenecker, Marohn, et al. ACS Nano, 2012, 6, 9637.

Piezoelectric RF SAW-Based Energy Detectors

2017 CNF REU Intern: Daniel Teal

CNF REU Affiliation: Mechanical Engineering and Mathematics, University of Texas at Austin

CNF Project: Cornell NanoScale Science & Technology Facility Research Experience for Undergraduates (CNF REU) Program

CNF REU Principal Investigator: Dr. Amit Lal, SonicMEMS Lab, Cornell University

CNF REU Mentor: Alex Ruyack, SonicMEMSLab, Cornell University

Primary Source of Research Funding: National Science Foundation via the NNCI Grant No. ECCS-1542081

Contact: dteal@utexas.edu, amit.lal@cornell.edu, arr68@cornell.edu

Website: http://www.cnf.cornell.edu/cnf5_reuprogram.html

Primary CNF Tools Used: Heidelberg 2000, SÜSS MA6, odd-hour evaporator, DISCO dicing saw, ultrasonic wire bonder

Abstract:

Extremely low-power electronic devices promise improvements in remote and distributed sensor networks, among other applications. Thus, we have designed and studied mechanisms based on piezoelectric surface acoustic wave (SAW) and graphene properties that detect and manipulate high frequency (200 MHz) electronic signals characteristic of radio frequency (RF) communications intercepted by such a device in hopes of using these signals as a power source. We demonstrate conversion of RF signals to SAWs on a lithium niobate substrate with standard interdigitated transducers. Electrodes of monolayer graphene placed on top of the substrate intercept the SAWs and convert them back to electric current via the acoustoelectric effect.

Summary of Research:

Our ultimate goal is to create devices that can trigger a nanoelectromechanical (NEMS) switch using a nanowatt radio frequency (RF) signal. To this purpose, here we build mechanisms that have the potential to rectify or otherwise modify such an alternating current (AC) RF signal at the Cornell NanoScale Science and Technology Facility (CNF).

A surface acoustic wave (SAW), a Rayleigh wave, can be excited on a piezoelectric substrate by means of an interdigitated transducer (IDT) — an array of electrodes with alternating electrical bias. Because the substrate is piezoelectric, such a wave carries with it an alternating electric field. Next, monolayer graphene placed on top of the substrate allows electron mobility. Electrons are pushed by the field caused by the SAW, namely, the acoustoelectric effect. This electron current can be captured by electrodes placed across the path of the SAW. The current across these electrodes is proportional to the SAW power density and cross-sectional area of the conductor [1]. We also note a related physical effect: the resistivity of graphene increases whenever the material undergoes strain [2], as when stretched by a passing SAW.

We use 4-inch 128° Y-cut black lithium niobate (LN) wafers as device substrates. SAWs will propagate in the X direction. First, gold electrodes are patterned using a liftoff process — 75 nm of gold are evaporated with a 10 nm Ti adhesion layer on top of a 2.5 µm negative photoresist mask of nLOF 2020. The nLOF is dissolved in 1165 to isolate the electrodes. Gold IDTs use 5 µm electrodes at a 10 µm pitch for a 20 µm wavelength. We designed for 200 MHz signals.

Inspired by Trung, et al. [3], we attempted to use a liftoff process to pattern graphene on top of the gold. An alternative method was to pattern gold with an oxygen plasma RIE etch with a photoresist mask, but the CNF does not allow gold to be used in most RIE tools. We found that graphene transferred via (CITE) on top of our LN wafer with a 2 µm nLOF 2020 mask, baked overnight at 130°C, then placed in 1165 for 30.5 mins in the ultrasonicator produces graphene features reliably. However, graphene resistors with thicknesses less than 100 µm cannot be manufactured reliably. Finally, the chips were diced with the Disco saw and wirebonded to printed circuit boards (PCBs) that connected to external instrumentation.

Among other tests, we placed two IDTs opposing each other with a graphene electrode in the center, as shown in Figure 1. An alternating current fit into either IDT should induce an acoustoelectric current in the graphene, confirming the process functionality. In Figure 2, we plot the current measured across the graphene with a Keithley 2400 when the instrument is set to source zero bias voltage. A 192.733 MHz wave,

its frequency having been chosen as a resonance peak via an earlier frequency sweep on the device, was fed into the left, then right IDT at various powers through a 50-Ω waveform generator. We observed that current was affected linearly with IDT intensity as predicted by Bandhu, et al. [1], and the SAWs sent in opposite directions produced opposite changes, as expected.

We also measured the location intensity of a SAW generated from a curved IDT with a Polytec UHF scanning doppler vibrometer. Focusing the SAW had two benefits: first, it was easier to capture the entirety of the SAW energy with a graphene electrode, and second, the greater strain from the SAW amplitude should increase the graphene resistance, thus increasing the voltage induced across the graphene. The measurement is shown in Figure 3.

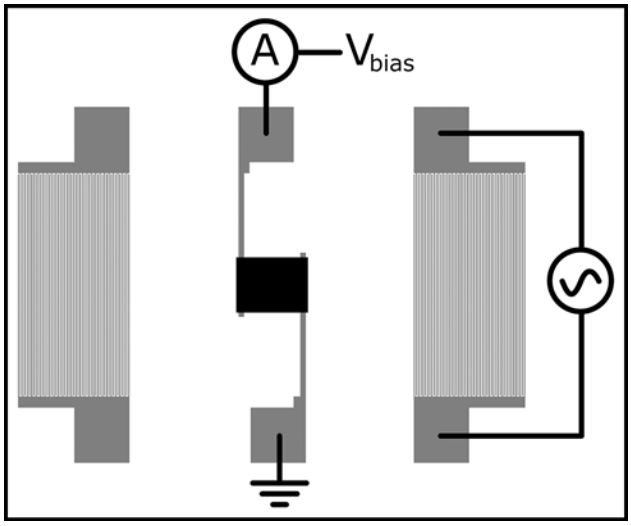

Figure 1: Schematic of tested device. Length of IDT fingers is approximately 1 mm. A rectangle of graphene (black, center) is placed on two electrodes and in between two IDTs.

Results and Conclusions:

We have successfully replicated the acoustoelectric effect using a lithium niobate process in the CNF cleanroom, as well as a focused SAW. We conclude these processes may work for our purposes, namely, triggering a NEMS switch from an extremely low power RF signal.

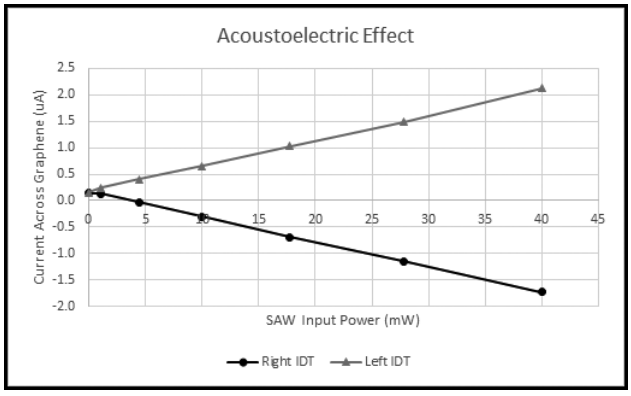

Figure 2: Power input to IDT to create SAW vs. current output from graphene for each IDT.

Future Work:

Now that we can build this system in the CNF, we need to scale it to work with much less power. Once complete, this system can be combined with RF generating sensors and a NEMS switch.

Acknowledgements:

Thanks to my PI, Dr. Amit Lal, my mentor, Alex Ruyack, and acquaintances, Benyamin Davaji and Nabil Shalabi, for technical help, and for the CNF for hosting this. Finally, the National Science Foundation via the National Nanotechnology Coordinated Infrastructure (NNCI) Grant No. ECCS-1542081 provided funding for this Research Experience for Undergraduates Program.

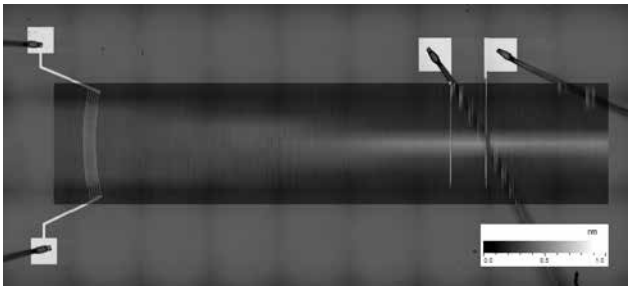

Figure 3: Another device. A curved IDT, left, creates a SAW that propagates right to an invisible piece of graphene placed across two electrodes. The SAW is concentrated at the graphene location.

References:

[1] Bandhu, L., Lawton, L. M., and Nash, G. R. (2013). Macroscopic acoustoelectric charge transport in graphene. Applied Physics Letters, 103 (13), 133101. https://doi.org/10.1063/1.4822121

[2] Fu, X.-W., et al. (2011). Strain dependent resistance in chemical vapor deposition grown graphene. Applied Physics Letters, 99(21), 213107. https://doi.org/10.1063/1.3663969

[3] Trung, T.N., Kim, D.-O., Lee, J.-H., Dao, V.-D., Choi, H.-S., and Kim, E.-T. (2017). Simple and Reliable Lift-Off Patterning Approach for Graphene and Graphene-Ag Nanowire Hybrid Films. ACS Applied Materials and Interfaces, 9(25), 21406-21412. https://doi.org/10.1021/acsami.7b05790

Individually Detachable Polymer-Silicon Micro-Parts for Vaporizable Electronics

CNF Project Number: 1262-04
Principal Investigator: Amit Lal
User: Ved Gund

Affiliation: School of Electrical and Computer Engineering, Cornell University
Primary Source of Research Funding: Defense Advanced Research Projects Agency VAPR
Contact: amit.lal@cornell.edu, vvg3@cornell.edu
Website: http://www.sonicmems.ece.cornell.edu/
Primary CNF Tools Used: GSI PECVD, Unaxis deep Si etcher, SÜSS MA-6 contact aligner, Ziess Ultra SEM

Abstract:

Wireless communications integrated with sensors form the basis of sensor-node networks for data collection and monitoring for defense and environmental applications. The data obtained is often proprietary and needs to be encrypted appropriately. Left unattended, the electronics and data can be acquired by potential adversaries, and can contribute to environmental signatures. Adversaries can use the nodes for technology counterfeiting, and left alone the sensor nodes can have detrimental effects on the environment. Software key encryption provides the first line of security against these adversaries but can be eventually compromised. To address the security and disposal of these devices, we have previously reported on the design, fabrication and testing of MEMS-based triggers for vaporizable electronics [1] and architectures for these systems [2], fabricated at the CNF. However, this approach necessitates the integration of complex chemistries, i.e. hermetically sealed rubidium stored inside polymer chambers, and is also susceptible to long-term device failure due to slow oxidation of the rubidium as a result of oxygen leakage through the polymer-nitride interface. Additionally, the array-based approach achieves a microsystem transience but is not very well controlled due to the volatility of rubidium during oxidation. In this work, we present an approach to transience that does not rely on complex chemistries and one that can produce controlled transience [3].

Summary of Research:

Our device architecture is shown in Figure 1. We post-process silicon substrates with deep reactive ion-etching (DRIE) to etch singulation grooves and transform the contiguous substrate into arrays of silicon pillars. The pillars are held together with the low temperature degradable polypropylene (PPC) handle layer for chip components, and can be patterned with standard photolithography methods. The PPC surrounding each part can be vaporized individually to release pillars using micro-fabricated metal heaters, without affecting other parts of the chip. Electrically controlled release of individual silicon micro-parts to selectively remove components from large die provides a controllable method of transience. Such a device architecture also holds great promise of micro-delivery of payloads from land or airborne robotic platforms.

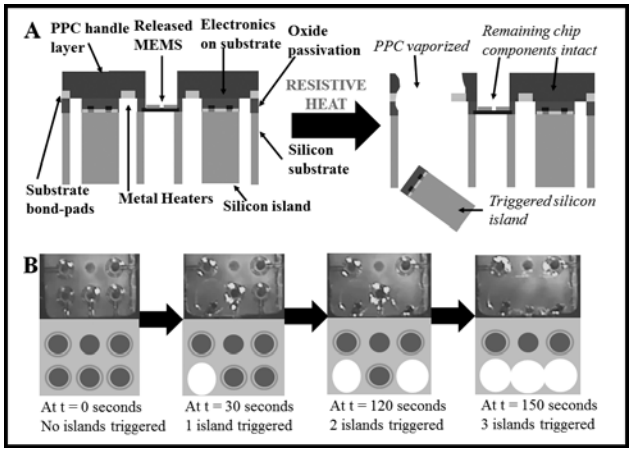

Figure 1: A). Schematic of the proposed transient system with post-processed electronics held together with a PPC handle layer. B). Optical images showing the transition of a substrate with the elimination of three pillars (chip components) in 150 seconds.

Fabrication:

The fabrication process flow is shown in Figure 2. A 0.5 µm-thick silicon dioxide film was deposited on the top side of a 300 µm wafer with the GSI PECVD tool. This oxide film serves as an etch-stop for deep silicon etching, and as a passivation layer for protecting the electronics during the post-processing steps. A 1.5 µm oxide film was deposited on the backside as an etch-mask for DRIE. Titanium/gold (10nm/40nm) heaters were patterned on the top oxide with a lift-off process, using the CVC odd-hour evaporator. Through-wafer trenches were then etched in the substrate with DRIE from the backside, using the Unaxis deep Si etcher. A 3 µm-thick PPC film, loaded with 5 weight % photo-acid generator (PAG), was spun on the top side, followed by a UV exposure dose of 4mJ/cm^2 with the SÜSS MA-6 contact aligner. This UV activation reduces the vaporization temperature of the PPC from 260°C to 170°C.

Following this step, the oxide under the PPC, which is no longer needed to hold the silicon-pillar array together, was etched in 6:1 BOE in the chemical hoods. This step effectively transfers the metal heaters from the oxide to the PPC, leaving it adhered to the polymer. Figure 3 shows an SEM image of the backside of 3 × 3 pillar array taken with the Ziess Ultra SEM in CNF.

The key issues addressed and advances made with this process include: 1) Lithography on large membranes. Our process demonstrates high yield (> 90%) on large area oxide membranes as large as 1.5 mm, with silicon pillars; 2) Choosing and engineering low-stress thin-film: Titanium/gold (Ti/Au) heaters are compatible with etch chemistries of silicon (DRIE) and oxide (HF). Ti is needed for Au adhesion, but can be undercut in the regions exposed for oxide etching, and on the edge of the substrate. However, it is not etched on the substrate; 3) Developing a method to transfer metal from oxide to PPC, without delamination.

Results:

The pillars were tested to determine the power required to vaporize and singulate each silicon micro-part from the substrate by completely vaporizing the polymer surrounding it. Additionally, they were tested to determine the time of triggering required to detach an island from the substrate. Figure 4 shows the setup for testing the time of triggering as well as high speed camera images of the pillar being detached. The entire process occurs over the duration for which the heater conducts current — the pillar is detached over much shorter time scales ~ 100 milliseconds. The power need is 96.7 mW over 5.06 seconds.

References:

[1] V. Gund, et al. "Graphene one-shot micro-valve: Towards Vaporizable Electronics", IEEE MEMS, Estoril, Portugal, 2015.

[2] V. Gund, et al. "Transient Micropackets for Silicon Dioxide and Polymer-based Vaporizable Electronics", IEEE MEMS, Shanghai, China, 2016.

[3] V. Gund, et al. "Individually Detachable Polymer-Silicon Micro-Parts for Vaporizable Electronics", IEEE Transducers, Taiwan, 2017.

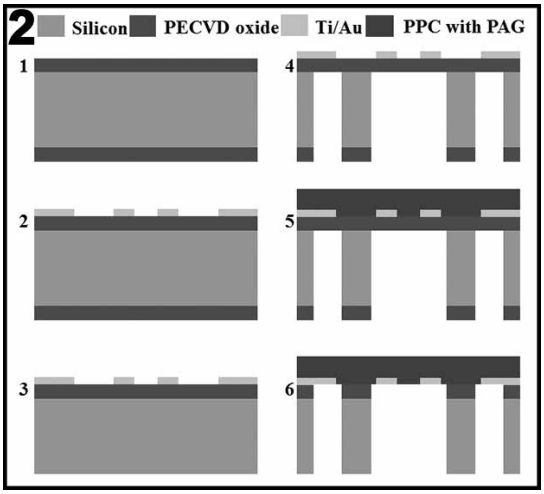

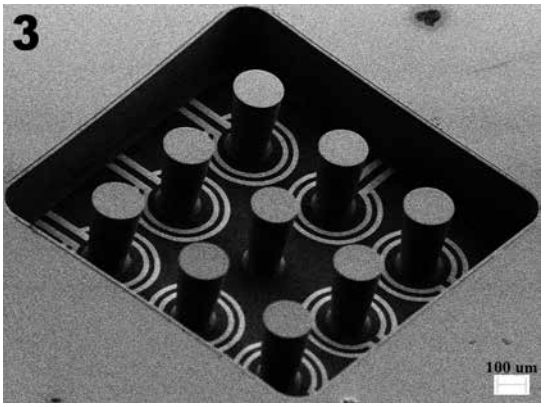

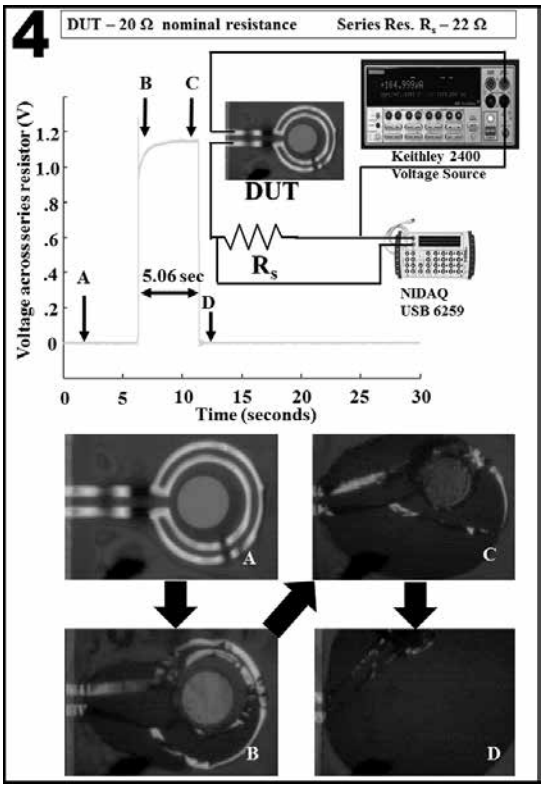

Figure 2, top: Device fabrication process. Figure 3, middle: SEM image of a micro-fabricated device array. Figure 4, bottom: Test setup for determining power of triggering micro-pillars and high-speed camera images of a pillar being detached from the substrate over a five second interval with 96.7 mW power.

High-Capacitance Gating of Nanocrystal Superlattices

CNF Project Number: 1645-08
Principal Investigator: Tobias Hanrath
User: Kevin Whitham

Affiliations: School of Chemical and Biomolecular Engineering, Materials Science and Engineering; Cornell University

Primary Source of Research Funding: Department of Energy through Grant DE-SC0006647 'Charge Transfer Across the Boundary of Photon-Harvesting Nanocrystals'

Contact: th358@cornell.edu, kw242@cornell.edu

Website: hanrath-group.cbe.cornell.edu

Primary CNF Tools Used: GCA Autostep 5x Stepper, Oxford 81, Tthermal evaporator, scanning electron microscopes

Abstract:

Recent discoveries of the formation of epitaxially connected quasi-two-dimensional quantum dot superlattices have opened new horizons to create novel materials with properties by design. Calculations of such 2D quantum dot solids forecast a rich electronic structure with features such as Dirac cones and topological edge states. However, to date, experimental validation of the properties emerging from the delocalization electrons in these systems is still lacking. Here we summarize recent efforts to probe charge transport in field effect transistors with short-channels and ionic gates.

Summary of Research:

The Anderson transition in disordered electronic materials describes the emergence of delocalized electron wavefunctions as the energetic spread of localized states decreases. The boundary between localized and delocalized states in disordered solids is commonly referred to as the mobility edge [1,2]. Despite being an ideal system for studying the Anderson transition, it has not been shown conclusively in nanocrystal (NC) solids. It is suspected that mid-gap defect states pull the Fermi level below the lowest energy quantized states.

A field-effect transistor geometry is usually employed to raise the Fermi level to investigate delocalization. However, the capacitance of an SiO_2-based metal-oxide-semiconductor (MOS) device is limited to $\sim 10^{-8}$ F/cm^2, which translates to about one electron per NC. If each NC has on average one trap state, a conventional MOS transistor will be unable to fill an appreciable number of quantized states without doping.

Unconventional gating strategies can theoretically achieve the carrier densities required to bring the Fermi level deep into the quantized states of a NC solid. Ion gel gating avoids the trade-off between reliability and capacitance, which is the challenge with oxide dielectric layers. Because the electric field is defined by the distance between charge and counter-charge, a thin oxide layer is preferred for high capacitance. With an ion-gel however, the electric field is contained within layers of organic cations and anions at the semiconductor-gel interface. Ion-gels can attain capacitance values of 10^{-5} F/cm^2, sufficient to accumulate several electrons per NC [3]. Combining ion-gel gating with small trap densities could lead to better understanding of the intrinsic transport limitations in NC solids.

Given the four-fold degeneracy of PbSe, a carrier density of four electrons per NC is required to move the Fermi level to the center of the 1Se distribution where states are most delocalized. Schornbaum, et al., showed that an ion-gel consisting of PVDF-HFP polymer with 1-ethyl-3-methylimidazolium tris(pentafluoroethyl) trifluorophosphate (EMIM-FAP) can be used to achieve $\sim 10^{-6}$ F/cm^2 without doping PbSe NCs [4].

In Figure 1, we show that an ion-gel made with 1:4 wt. PVDF-HFP and EMIM-FAP can be used to accumulate the same carrier density at 1 V bias as an MOS transistor with 40 V bias. The preservation of the transport behavior is promising, and the carrier density can be increased with higher ionic liquid loading in the gel. Optimization of the ion-gel gating technique for use with PbSe NC solids may lead to carrier densities as high as four electrons per NC. It remains to be seen if densities of the magnitude (10^{13} cm^{-2}) are possible in NC solids and if electrons at such high energies will exhibit delocalization.

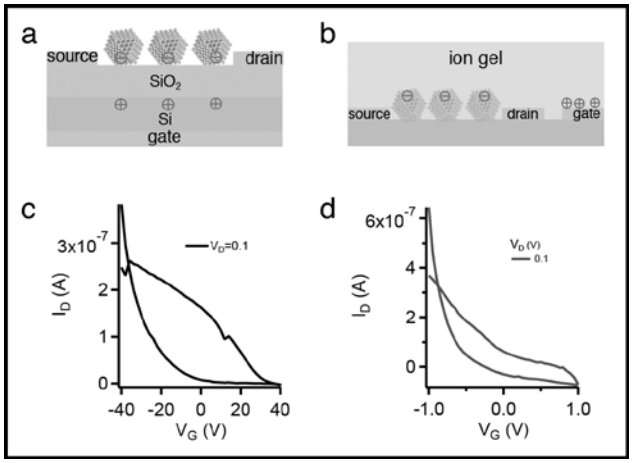

Figure 1: Comparison of conventional MOS gating and ion-gel gating. [a,b] Schematic illustration of device geometries for MOS (a) and ion-gel (b) devices. [c,d] Transfer curves are shown for MOS gating (c) and ion-gel gating (d).

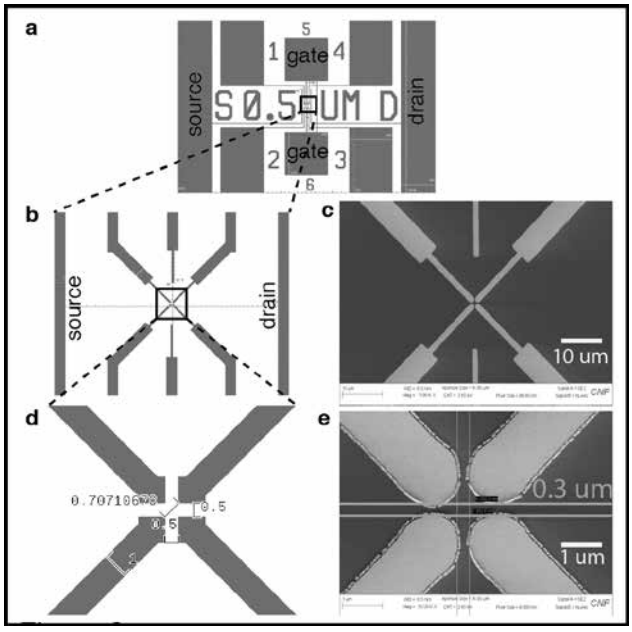

Figure 2: Design and preliminary characterization of short-channel ionic-gate FET device. a, Layout showing source, drain, four voltage probe, and two gate contacts. b, Active area of layout. c, Scanning electron micrograph (SEM) showing four voltage probes and two gate contacts. d, Dimensions of voltage probes in the Van der Pauw geometry. e, SEM of voltage probes showing 0.3 μm dimension.

There are two practical challenges in the fabrication of ion-gel gated transistor devices. Because the ion-gel is deposited on top of the NC layer, the gate electrode must be fabricated on top of the device, rather than the traditional back-gate. Secondly, for accurate measurements of localization length, scattering at grain boundaries must be minimized. This requires fabrication of electrode gaps smaller than the average superlattice grain size, between a few hundred nanometers and a few micrometers. This range of feature sizes is accessible by i-line (365 nm wavelength) photolithography. Additionally, a true measurement of conductance requires four probes to account for contact resistance.

Fabricating sub-micron features by photolithography requires optimization of the lithographic process to achieve the desired critical dimension (CD). The most accurate method for patterning of metal lines is to pattern windows into photoresist through which metal is deposited by evaporation (line of sight). The photoresist mask is then dissolved, lifting-off unwanted metal. Because i-line lithography uses a monochromatic light source, a standing wave interference pattern is created by reflection from the substrate. This pattern is transferred to the resist, thus inhibiting control over CD. Therefore an anti-reflective coating (ARC) is deposited below the photoresist layer. The thickness of the ARC is chosen to minimize the intensity of reflection from the substrate. With this technique, we have fabricated features down to 300 nm, as shown in Figure 2. One optimization step remains in the device fabrication, to remove unwanted metal fringes surrounding the voltage probes, as these could disrupt contact between the quantum dot film and the metal contacts. The fringes could be the result of insufficient plasma etching of the ARC layer, or under-development of the photoresist.

References:

[1] Anderson, P. W. Absence of diffusion in certain random lattices. Physical review 109, 1492 (1958).

[2] Mott, N. The mobility edge since 1967. Journal of Physics C: Solid State Physics 20, 3075 (1987).

[3] Schornbaum, J., et al. Light-emitting quantum dot transistors: emission at high charge carrier densities. Nano letters 15, 1822-1828 (2015).

Design and Realization of GaN Trench Junction-Barrier-Schottky-Diodes

CNF Project Number: 2307-14
Principal Investigator: Huili Grace Xing
User: Wenshen Li

Affiliation: School of Electrical and Computer Engineering, Cornell University
Primary Source of Research Funding: ARPA-E SWITCHES Program
Contact: grace.xing@cornell.edu, WL552@cornell.edu
Primary CNF Tools Used: PT 770, Oxford 81, odd-hour evaporator, AutoStep i-line stepper, Oxford PECVD

Abstract:

We present the design principle and experimental demonstrations of GaN trench junction-barrier-Schottky-diodes (trench JBSDs), where the Schottky contact within the patterned trenches is at the same plane as the adjacent p-n junctions. Assisted by the TCAD simulations, the leakage current reduction mechanism is identified as the reduced surface field (RESURF) effect due to the barrier-height difference between the p-n junction and Schottky junction. Design space for the width of stripe-shaped trenches is found to be < 0.5 μm for a drift layer doping level of 1e15~1e16 cm^{-3}, while for circular trenches the size requirement is relaxed. In the fabricated devices with 1-4 μm diameter circular trenches, approximately a 20X reduction in the reverse leakage is observed with a characteristic shift in the turn-on voltage, which are signatures of the trench JBSD with desired RESURF. The experimental observations are in excellent agreement with the simulation results. This JBSD design shows promising potential in further improving the performance of Schottky-based GaN power devices without the need for ion-implantation or material regrowth.

Summary of Research:

As shown in Figure 1(a), the trench JBSD epi structure is similar to our previous high-BV PNDs grown by metal-organic chemical vapour deposition on freestanding GaN substrates with a threading dislocation density of ~ 2×10^6 cm^{-2} [1]. A net doping concentration of ~ 1×10^{16} cm^{-3} in the drift layer is extracted by the capacitance-voltage (C-V) measurement [Figure 1(b)]. Trench JBSDs are designed to have circular trench patterns with a diameter of 1, 2, 3, and 4 μm.

The trench JBSDs are fabricated by dry-etch first to form trenches and reveal the n-GaN surface, followed by deposition of circular Pd-based anodes. Pd forms an ohmic contact to p-GaN and a Schottky contact to n-GaN in the trench. Figure 1(c) shows the representative transmission line method I-V characteristics of the ohmic contact on p-GaN. An excellent specific contact resistivity of 3.9×10^{-5} Ω·cm^2 is extracted. Conventional SBDs are made on the etched n-GaN surface. No additional field plate (FP) structures are used for edge termination, since the additional leakage often associated with the FP process [2] might mask the trend in the leakage current of trench JBSDs designed with varied trench sizes.

Figure 2 shows the measured I-V characteristics of the fabricated trench JBSDs. An ideal Schottky turn-on behavior is observed for both trench JBSDs and the SBD at ~ 1 V with an ideality factor of ~ 1.00-1.05. A clear shift in the turn-on voltage is observed in the log plot in Figure 2(a) and highlighted in the inset, which agrees well with the simulation results. The linear-scale I-V curves in Figure 2(b) show a two-step turn-on for the trench JBSDs, similar to [3]. The reverse I-V characteristics in Figure 2(c) show a clear reduction of the leakage current density as the trench size decreases from 4 μm to 1 μm. Up to 20 times reduction in leakage current is achieved in the 1 μm trench JBSDs compared with conventional SBDs, reaching the PND leakage level. As the total trench area is designed to have the same total area, the reduction in leakage current is due to the RESURF effect arising from the trench JBSD design.

Finally, the benchmark plot of R_{ON}-BV is shown in Figure 4. The figure-of-merit of the SBD and trench JBSD in this paper is comparable to that of the best SBD reported without field plate.

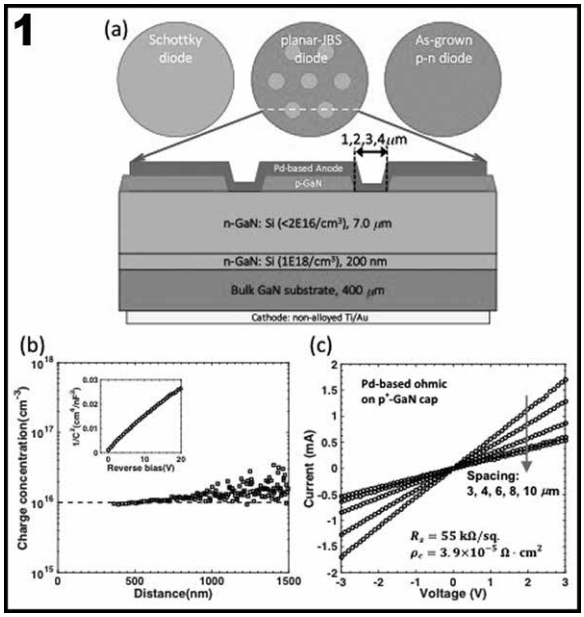

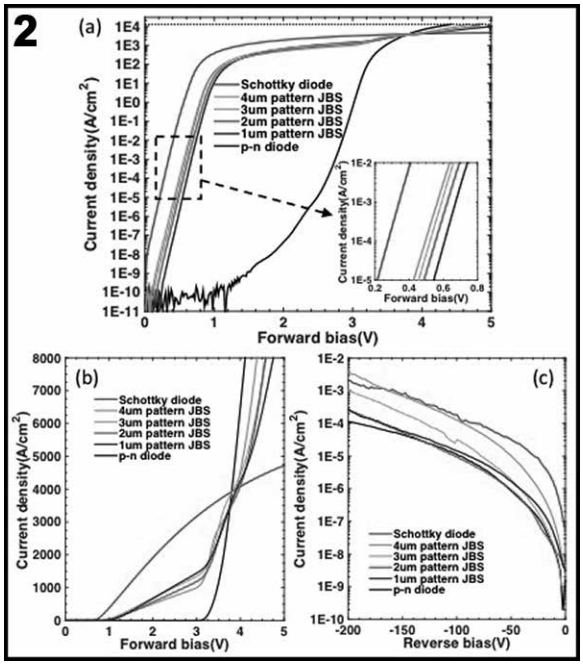

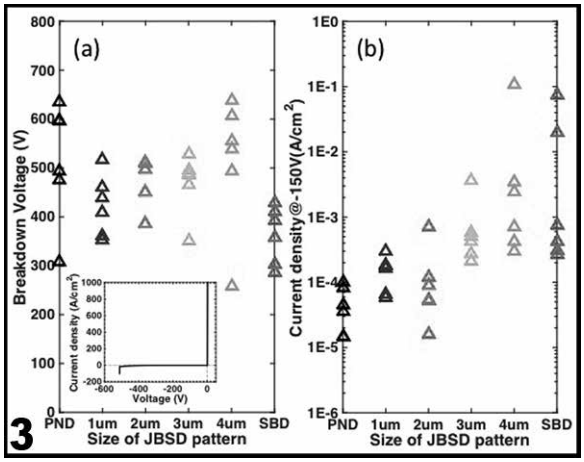

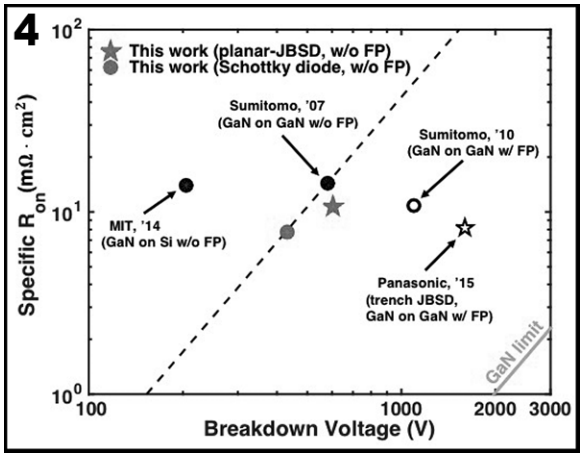

Figure 1: (a) Schematic top view and cross-section of the fabricated trench JBSD. Circular trenches have a diameter of 1, 2, 3, and 4 μm. The total Schottky (trench) area is designed to be the same for each trench diameter. (b) Carrier concentration in the n-GaN drift layer extracted by the C-V measurement at 1 MHz. (c) Representative TLM I-V characteristics of the Pd-based ohmic contact on p-GaN. A low specific contact resistivity of 3.9×10^{-5} Ω·cm² and p-GaN sheet resistance of 55 kW/sq. is extracted.

Figure 2: Measured I-V characteristics of the trench JBSDs. All measured diodes have a diameter of 100 μm. (a) Forward I-V in log scale. (b) Forward I-V in linear scale showing a characteristic two-step turnon. (c) Reverse I-V in log scale. A clear trend of reduction in the reverse leakage is observed for the trench JBSDs over the range of 0 ~ -200 V.

Figure 3: (a) BV distribution and (b) reverse current density at -150 V for each type of measured devices.

Figure 4: Bench mark plot of BV versus specific R_{on}.

References:

[1] Z. Hu, et al., "Near unity ideality factor and Shockley-read-Hall lifetime in GaN-on-GaN pn diodes with avalanche breakdown," Appl. Phys. Lett., vol. 107, no. 24, p. 243501, 2015.

[2] K. Nomoto, et al., "1.7-kV and 0.55-m-cm² GaN p-n diodes on bulk GaN substrates with avalanche capability," IEEE Electron Device Lett., vol. 37, no. 2, pp. 161-164, Feb. 2016.

[3] K. Ryo, et al., "A high current operation in a 1.6 kV GaN-based trench hybrid-junction diode (THD)," IEICE, Japan, Tech. Rep. ED2015-75, vol. 115, no. 329, pp. 39-42, 2015.

Investigation of GaN p-Channel Transistors

CNF Project Number: 2307-14
Principal Investigators: Huili Grace Xing, Debdeep Jena
User: Kazuki Nomoto

Affiliation: Electrical and Computer Engineering, Cornell University

Primary Source of Research Funding: ARPA-E SWITCHES

Contact: grace.xing@cornell.edu, kn383@cornell.edu

Primary CNF Tools Used: Autostep i-line Stepper, JEOL 6300, P7, FilMetrics, AFM Veeco Icon, Zeiss SEM, PT770, Oxford 81, Oxford PECVD, Odd-hour Evaporator, Oxford ALD, RTA AG610

Abstract:

Impurity p-type doping is realized in molecular beam epitaxy (MBE) grown pGaN/un-intentional doped (UID) GaN/semi-insulating (SI) SiC. Depletion-mode p-channel field effect transistors (FETs) are demonstrated. Driven by the high hole density, a 2-μm-long D-mode FET shows improvement of drain current from 1.2 mA/mm (V_{GS} = -2 V, V_{DS} = -10 V) at 27°C to 4.6 mA/mm (V_{GS} = -2 V, V_{DS} = -10 V) at 100°C.

Summary of Research:

Devices were grown by plasma-assisted molecular beam epitaxy in a Veeco GENxplore under metal-rich conditions. The epitaxial structure includes a 100 nm UID buffer, followed by 200 nm of moderately p-doped GaN and 10 nm of heavily p-doped GaN. After device mesa isolation by the PT-770 ICP-RIE system, Pd-based ohmic contacts are deposited at source and drain and used as a mask to ICP etch the p+ GaN and a variable amount of the p GaN. The device is then coated in 10.9 nm of ALD (Oxford ALD FlexAL) aluminum oxide dielectric before a Ti/Au gate is deposited. The resulting structure is shown in Figure 1.

On the processed samples, TLM measurements demonstrated ohmic contacts with R_c = 155 Ω·mm (ρc = 1.5 × 10^{-3} Ω·cm^2), as shown Figure 2. *I-V* and transfer characteristics were measured from 27°C to 100°C (see Figure 3 and 4), notably improving with increasing temperature. Room temperature on-currents on the order of 2 mA/mm are competitive with several of the 2DHG-based candidates [1-5].

References:

[1] Shatalov, IEEE Elec. Dev. Lett. 23:8, 2002.
[2] Li et al IEEE Elec. Dev. Lett. 34:7, 2013.
[3] Reuters et al J. Phys. D: Appl. Phys. 47:175103, 2014.
[4] Herwig Hahn, PhD Thesis, RWTH Aachen University.
[5] Zhang et al, Nature Scientific Reports 6:23683, 2016.

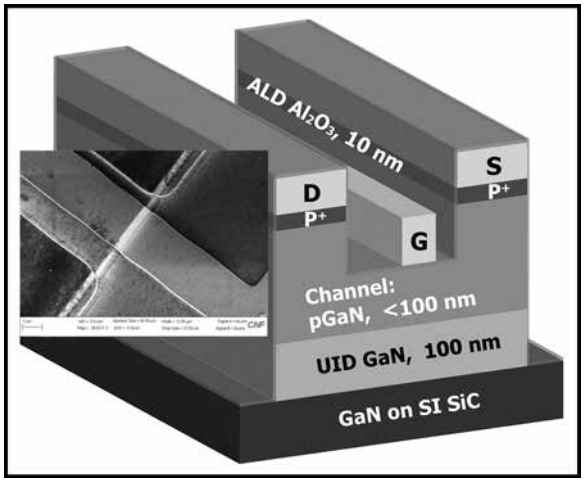

Figure 1: A device cross-section of the fabricated D-mode p-channel FET and an SEM image.

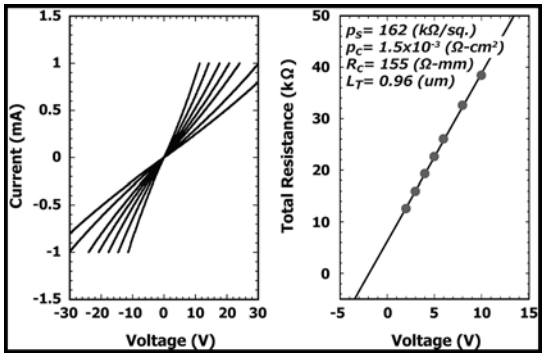

Figure 2: Ohmic characteristics for Pd-based contacts on p⁺GaN.

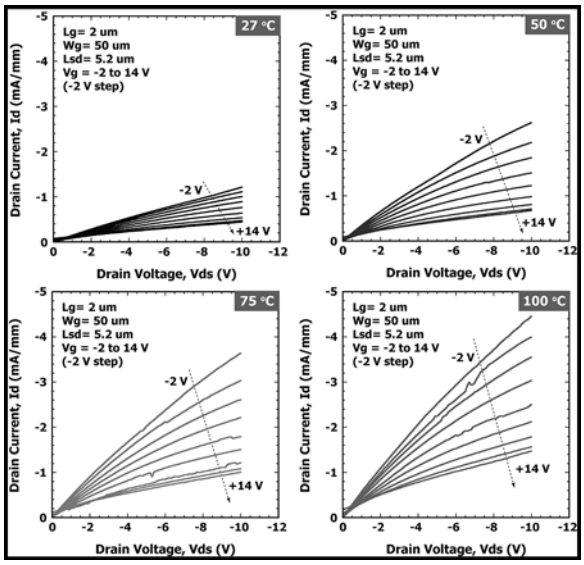

Figure 3: 27/100°C I_d-V_{ds} characteristics for p-channel FETs with Lg = 2 µm.

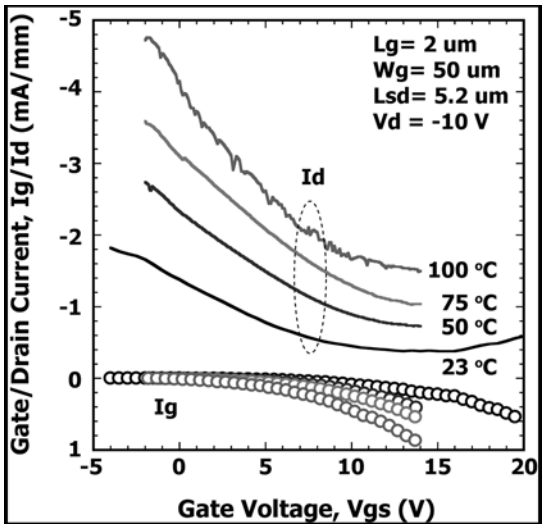

Figure 4: 27/100°C transfer characteristics for p-channel FETs with Lg = 2 µm.

Two-Dimensional Heterojunction Interlayer Tunneling Field Effect Transistor (Thin-TFET)

CNF Project Number: 2324-15

Principal Investigator: Huili Grace Xing

Users: Suresh Vishwanath, Rusen Yan, Mingda Li, Xiang Li, Hyunjea Lee

Affiliation: Electrical and Computer Engineering, Cornell University

Primary Sources of Research Funding: LEAST project (Center for Low Energy Systems Technology), Semiconductor Research Corporation

Contact: grace.xing@cornell.edu, sv372@cornell.edu, ry253@cornell.edu, ML888@cornell.edu, XL633@cornell.edu, HL2255@cornell.edu

Primary CNF Tools Used: Veeco AFM, JEOL 6300, SC4500 evaporator

Abstract:

We propose to investigate the two-dimensional heterojunction interlayer tunneling field effect transistor (Thin-TFET). The objectives of this research are; 1) to understand the vertical tunneling process between two 2-D semiconductor layers, and 2) to demonstrate Thin-TFETs, otherwise stated, vertical 2D crystal TFETs with tunneling aligned with the gate field. Along with common metals (e.g., Au, Ti, Pt) and chemicals found in the cleanroom, we will be using 2D layered materials — Mx2, where M = tungsten (w), tin (Sn), molybdenum (Mo), and x = sulfide (S), selenide (Se), telluride (Te).

Summary of Research:

Tunneling FETS promise sub-60 mV/dec of sub-threshold swing (SS), which cannot be realized in traditional MOSFETs. With this type of device, we can greatly reduce the amount of supply voltage (V_{DD}) that is required to turn on devices, keeping off-state current sufficiently low. To realize TFETs with sub-60 mV/dec of SS, strong gate control should be required to modulate the entire portion of conducting channel. The atomic scale thickness of layered two-dimensional (2D) materials makes it possible to achieve strong gate modulation across the channel, and their surface with no dangling bond provides excellent condition for steep SS [1,2]. Among various layered materials, we focus on WSe_2 and $SnSe_2$ to form nearly broken bandgap alignment, which is a desirable condition for tunneling devices.

$SnSe_2$ was exfoliated from bulk materials using polydimethylsiloxane (PDMS) and examined under microscope to find a flake desirable to be stacked together. Then the target flake was transferred onto SiO_2/Si substrate and the same process was done for WSe_2 flakes to locate it on top of $SnSe_2$ flakes. Veeco atomic force microscope (AFM) was used to characterize the thickness of exfoliated flakes.

Since the band gap of layered materials depends on the number of layers, it is important to know the flake thickness for appropriate band alignment. The typical size of exfoliated flakes is micron-scale, which means the pattern for electrodes cannot be easily formed with traditional photo-lithography facilities. JEOL 6300 electron beam lithography system was used, which allows for the formation of sub-micron size patterns. After the electron beam exposure using resist poly methyl methacrylate (PMMA), followed by development, 5 nm of Cr and 50 nm of Pd were deposited as contact metals using the SC4500 evaporator.

Figure 1 shows the stacked $SnSe_2$ (bottom) and WSe_2 (top) flakes with deposited metal electrodes. Instead of SiO_2 as a back-gate oxide, solid polymer, polyethylene-oxide cesium perchlorate (PEO:$CsClO_4$) was adopted as a top-gate dielectric layer [3]. With high capacitance and no electric conductivity, this polymer is a good candidate for high-efficiency gate dielectrics required for steep SS. The devices were top-gated with side metal pad near the flakes as shown in Figure 1. As it takes time for Cs^+ and ClO_4^- ions to respond to changing gate voltage, 10 seconds of sweep delay was applied per 10-mV-change in gate voltage.

For TFETs operation, the band alignment of two flakes should be modulated to change the size of tunneling window for carriers. When gate voltage is applied, the relative position of Fermi level in band diagram is shifted to the upper or lower side accordingly.

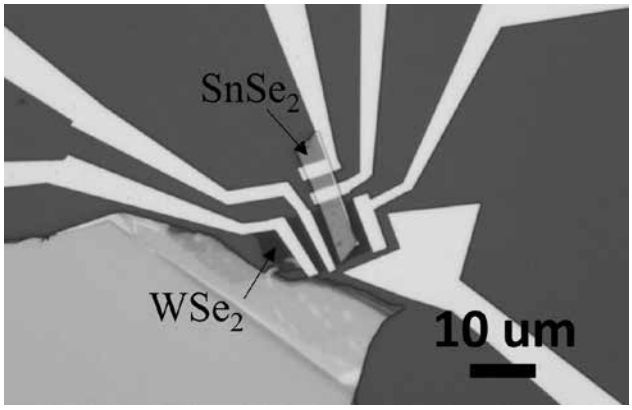

Figure 1: Optical image of the fabricated $WSe_2/SnSe_2$ Thin-TFET.

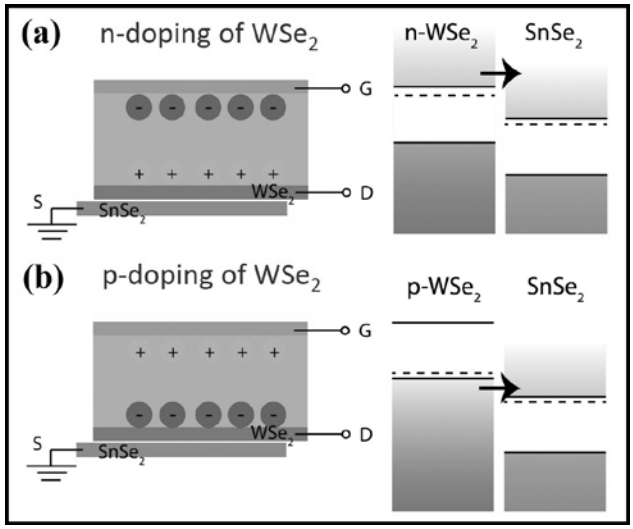

Figure 2: Band alignment of the flakes with respect to gate bias [5].

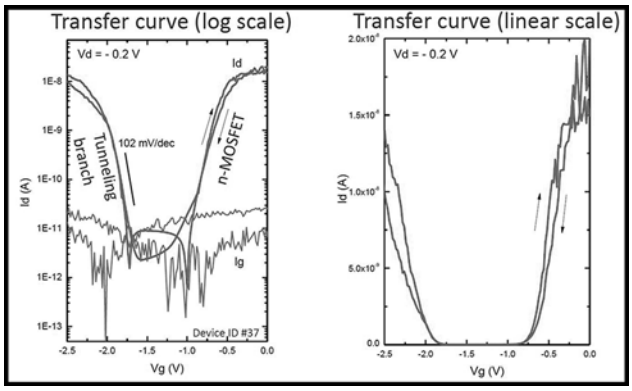

Figure 3: Transfer curves of the $WSe_2/SnSe_2$ Thin-TFET [5].

As for $SnSe_2$ used as a source-side material, it is degenerately n-doped in nature and thus the change in Fermi level of $SnSe_2$ is negligible. In other words, the quantum capacitance of $SnSe_2$ — an important quantity in the design of nanoscale devices — is large enough to make it immune to gating effects [4].

As shown in Figure 2, we can modulate the relative band alignment between $SnSe_2$ and WSe_2 by tuning the band of WSe_2 with gate voltage. When the negative gate voltage is applied (Figure 2a), there is a carrier transport only in between two conduction bands. On the other hand, when the positive voltage is applied (Figure 2b), the tunneling window opens so that electrons can be transported from the valence band of WSe_2 to the conduction band of $SnSe_2$. In this tunneling transport, SS is not restricted by Boltzmann limit (60 mV/dec at room temperature), which makes possible the low power dissipation of TFETs [5].

Figure 3 shows the transfer characteristics of the measured $WSe_2/SnSe_2$ Thin-TFETs. Right hand side n-branch shows the non-tunneling branch in which carriers are transported over the potential barrier through thermionic emission. Left hand side p-branch shows the tunneling branch that has a sharper slope in log scale curves, indicating lower SS. The SS did not reach sub-60 mV/dec in this case; however, we would achieve the goal by reducing contact resistance that restricts ideal performance or choosing a different set of materials with have completely broken band alignment that is the best for tunneling transport.

References:

[1] M. Li, D. Esseni, J. J. Nahas, D. Jena, and H. G. Xing, IEEE Elec. Dev. Soc., 3, 200-207 (2015).

[2] R. Yan, S. Fathipour, Y. Han, B. Song, S. Xiao, M. Li, N. Ma, V. Protasenko, D. A. Muller, D. Jena, and H. G. Xing, Nano Lett., 15, 5791-5798 (2015).

[3] S. Fathipour, P. Pandey, S. Fullerton, and A. Seabaugh, J. Appl. Phys., 120, 234902 (2016).

[4] T. Fang, A. Konar, H. G. Xing, and D. Jena, Appl. Phys. Lett., 91, 092109 (2007).

[5] M. Li, R. Yan, D. Jena, and H. G. Xing, 2016 IEEE International Electron Devices Meeting (IEDM), San Francisco, CA, Dec. 2016.

Self-Assembled Silica Nano-Spheres for Dual Metal Junction-Barrier-Schottky Diodes

CNF Project Number: 2350-15

Principal Investigators: Prof. Debdeep Jena, Prof. Huili Grace Xing

User: Jae Ho Shin

Affiliation: Department of Materials Science and Engineering, Cornell University

Primary Source of Research Funding: Sixpoints

Contact: djena@cornell.edu, grace.xing@cornell.edu, js3366@cornell.edu

Websites: djena.engineering.cornell.edu, grace.engineering.cornell.edu

Primary CNF Tools Used: ABM contact aligner, Zeiss Supra/Ultra SEMs, e-beam evaporator, PT-770 ICP RIE

Abstract:

We report on a time and cost-effective method of selectively depositing thin metal films onto substrates. Silica nanospheres of 50 nm diameter were hexagonally packed using Triton X-100 surfactant on the DI water/air interface, and were transferred onto bulk n type gallium nitride substrates. After inspection using the scanning electron microscope, 20 nm thick metal was deposited on top. After stripping of the silica, a triangular shaped array of metal deposits remained. This technique will enable a quick, simple method of fabricating dual metal junction-barrier-Schottky-diodes, which use the difference in work function of two metals to reduce reverse leakage as in a p-n diode, as well as retain the low turn-on voltage of Schottky barrier diodes.

Summary of Research:

Gallium nitride (GaN), with its superior Baliga's figure-of-merit, is an excellent candidate for high power, high speed devices. GaN Schottky barrier diodes (SBDs) have shown the highest power efficiency in the < 1kV breakdown voltage range [1], but show high reverse leakage current compared to those of p-n diodes, which is detrimental to achieving high breakdown voltage. One method of reducing the reverse leakage current is by fabricating a junction-barrier-Schottky-diode (JBSD) [2]. This structure combines the large breakdown voltage of p-n diodes, and the low turn on voltage of SBDs into one device. Due to the difficulties in ion implantation and regrowth technologies in GaN, designing trench patterns in the p-type GaN and exposing the n-type GaN and making metal contacts on them could circumvent the issue. Results of these trench JBSD devices are further expressed in references [3]. A schematic of the JBSD device is depicted in Fig. 1.

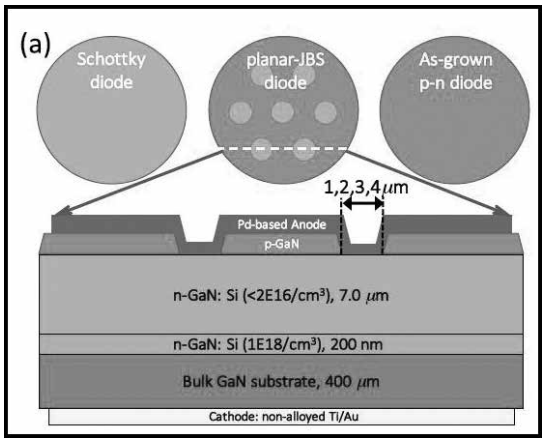

Figure 1: Schematic of trench-JBSD device with p-type GaN and Schottky metal contact on n-GaN [3].

A p-type GaN could be viewed as a Schottky metal contact with a work function of ~ 3eV. Thus, another approach could be taken to replace the p-type GaN with another metal. Due to the difference in work function of the two metals, similar effects as a p-GaN/metal JBSD could be achieved. The goal of this research at CNF was to fabricate a dual metal JBSD. In order to achieve this local metal stack structure, a hard mask consisting of self-assembled monolayer of nano-scale silica spheres was used. The densest packing structure of spheres would be hexagonally close packed structures. However, in that packed structure, there would be an interstitial between every three spheres. Our strategy was to use this interstitial to selectively deposit metal.

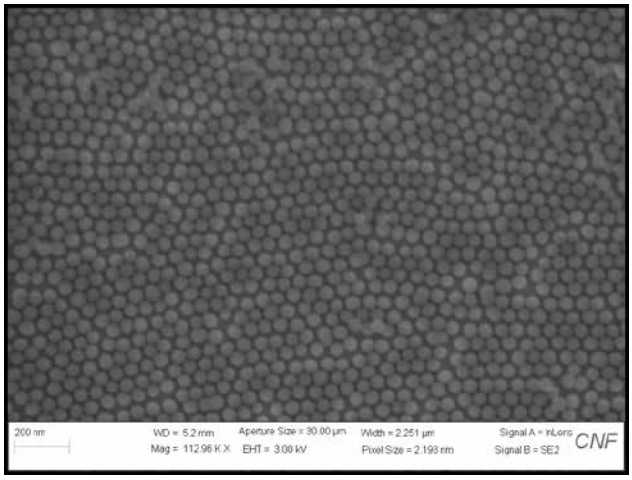

Figure 2: SEM image of HCP monolayer of silica nanospheres with 50 nm diameter.

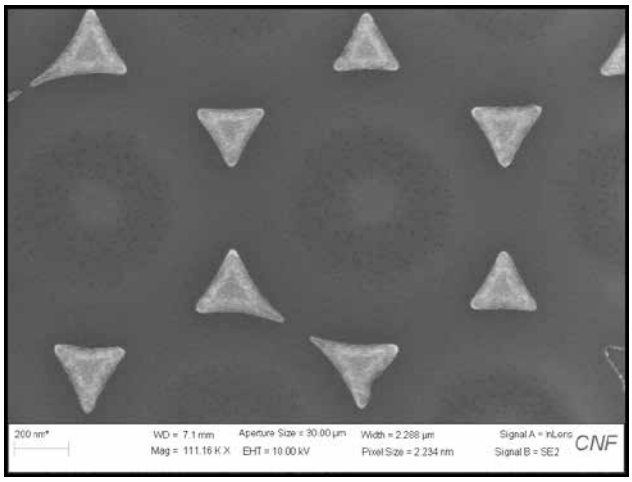

Figure 3: SEM image of 20 nm metal deposition remaining on interstitial area of HCP silica nanosphere monolayer.

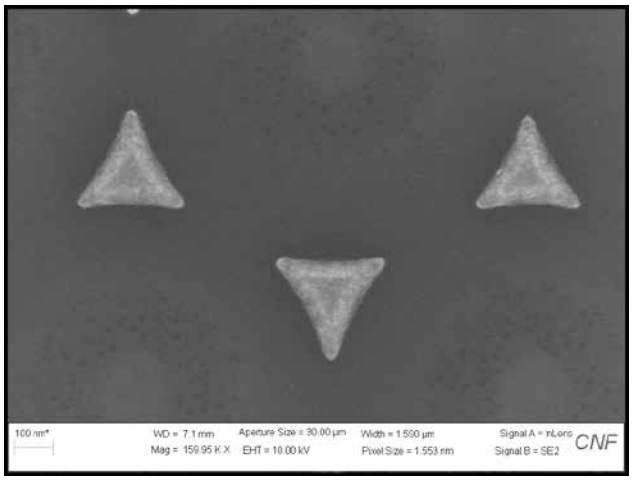

Figure 4: SEM image of 20 nm metal deposition remaining on interstitial area of HCP silica nanosphere monolayer.

Silica nanospheres were self-assembled on the interface between DI water and air using Triton X-100 surfactant, and then were transferred onto an n-GaN substrate and dried. After inspection of the layer with SEM, metal was deposited onto the structure.

Figure 2 is an SEM image of the monolayer assembled onto a bulk GaN substrate. When the silica was stripped off using buffered oxide etch, only the metal that was deposited in the interstitial points remained. Thus, it is able to selectively deposit metal without use of nanoscale patterning such as e-beam lithography. It reduces the process time as well as cost required to pattern nanoscale features.

Figure 3 and Figure 4 are SEM images of the resulting metal depositions on a bulk GaN substrate.

References:

[1] S. Chowdhury and T. P. Chow, "Comparative performance assessment of SiC and GaN power rectifier technologies," Phys. Status-Solidi C, vol. 13, nos. 5-6, pp. 360–364, 2016.

[2] B. J. Baliga, "The pinch rectifier: A low-forward-drop high-speed power diode," IEEE Electron Device Lett., vol. 5, no. 6, pp. 194-196, Jun. 1984.

[3] W. Li, "Design and realization of GaN trench junction-barrier-Schottky-diodes," IEEE Transactions on Electron Devices, vol. 64, no.4, pp.1635-1641.

Material Processing and Device Characterization of β-Ga_2O_3

CNF Project Number: 2428-16

Principal Investigators: Debdeep Jena, Huili Grace Xing

Users: Liheng Zhang, Zongyang Hu, Kazuki Nomoto, Mingda Zhu, Nicholas Tanen

Affiliations: School of Electrical and Computer Engineering, Department of Materials Science and Engineering; Cornell University

Primary Source of Research Funding: NSF DMREF Program (Award Number 1534303)

Contact: djena@cornell.edu, lz388@cornell.edu, zh249@cornell.edu, njt47@cornell.edu, kn383@cornell.edu

Primary CNF Tools Used: JEOL 9300 EBL, Oxford FlexAL ALD, Autostep i-line stepper, AJA sputter system, Oxford PECVD system, Oxford 81, Veeco Icon AFM

Abstract:

β-Ga_2O_3 is a wide-bandgap semiconductor with a bandgap of ~ 4.9 eV, a high breakdown field of ~ 8 MV/cm and an electron mobility of ~ 100 cm^2/V-s [1]. These properties give β-Ga_2O_3 a Baliga's figure-of-merit (BFOM) ~ four times as large as those for GaN and SiC for power efficiency [1]. The availability of large-size high-quality single-crystal wafers grown by low-cost melt-grown methods gives β-Ga_2O_3 an extra advantage for large-scale high-power electronics [1]. In this project, we are developing the material processing technologies as well as fabricating and characterizing switching devices. Our aim is to understand the gap between current device performances and theoretical limits for materials and to shorten this gap by improving processing to realize high-power devices. In 2015~2016, we used CNF to successfully optimize a dry etching process [2], make Schottky barrier diodes (SBDs) [3] and demonstrate the two-dimensional electron gas (2DEG) in the AlN/Ga_2O_3 heterostructure [4]. In the past year (2016~2017), we continued using CNF to optimize ohmic contacts on β-Ga_2O_3, and realized current modulation in field-effect transistors (FETs) such as nanomembrane FETs and lateral MOSFETs. We are currently using the optimized dry etching and ohmic contact processes to develop vertical FETs with high breakdown voltages.

Summary of Research:

Ohmic contacts are critical components of electronic devices to ensure significant current level and reliable device performances. We used Si-ion-implantation for ohmic contacts. Blanket Si-ion-implantation was done on bulk Ga_2O_3 substrates to create an n+Ga_2O_3 layer. The dopants were subsequently activated by annealing at 900~1000°C for 30 minutes in the general annealing furnace. The Ga_2O_3 substrates were patterned using photolithography with the ABM contact aligner. Metals were then deposited using the e-beam evaporation system followed by liftoff. Transmission line measurement (TLM) test structures were thereby fabricated for extracting contact resistance. We obtained < 1 Ω-mm contact resistance and ~ $4*10^{-5}$ Ω-cm^2 specific contact resistivity for both <010> and <-201> face substrates, which were sufficient for demonstrating devices. Figure 1 shows an example of linear I-V characteristics and scaling behavior of the TLM on <-201> face Ga_2O_3.

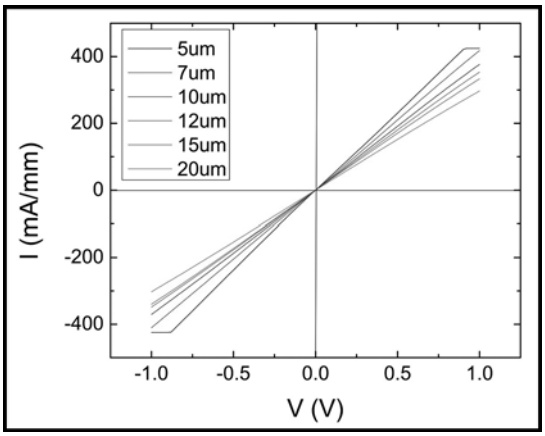

Figure 1: I-V characteristic of TLM test structures on Si-ion-implanted n+Ga_2O_3.

We used optimized processes to fabricate lateral and vertical FETs. Nanomembranes were exfoliated from bulk Ga_2O3 crystal and transferred to SiO_2-on-Si substrates. We then used the JEOL 9300 e-beam lithography (EBL) system to directly write contacts at the source and drain (S/D) followed by similar metal deposition and liftoff processes aforementioned.

Back gate was implemented by blanket depositing metal contact on the back of the substrate. Figure 2 shows the transfer characteristic of the membrane FET in both linear and log scales showing > 100 On/Off, ~ -35V threshold voltage and low drain leakage current at V_{ds} = 1 V. Enhancement-mode MOSFETs were made on Sn-doped Ga_2O_3 epilayers on semi-insulating (SI) substrates. Aforementioned Si-ion-implantation was used for ohmic contacts. The channel became insulating following dopant activation possibly due to Fe-out-diffusion from the SI substrate, but we used a gate overlapping with the S/D to turn the channel back on with positive gate bias. We used the Oxford FlexAL atomic layer deposition (ALD) system to deposit Al_2O_3 gate dielectric and the Autostep i-line stepper to do gate lithography followed by metal deposition and liftoff. Figure 3 shows the output characteristic of the MOSFET. The transfer curve (not shown here) of the MOSFET showed an ~ 10^6 On/off.

We are also fabricating vertical FinFETs with a wrap-around gate. We used the JEOL 6300 EBL to pattern 0.1~0.2 μm lines, which would then be etched into vertical fin-shaped channels using a metal etch mask deposited by e-beam evaporation. MOS gate containing Al_2O_3 gate dielectric deposited by the Oxford FlexAL and Cr gate metal by the AJA sputter system wrapped around the vertical channel to modulate it from the sides. The Oxford PECVD system was used to deposit SiO_2 to isolate source and gate metals and the Oxford 81 etcher to pattern the SiO_2 layers. The Autostep i-line stepper was used to align and pattern the substrates for gate and source metallization, device isolation and contact via openings. Comparison GaN bulk substrates were fabricated along with Ga_2O_3 substrate.

Initial results showed encouraging performances from GaN (Figure 4). We measured > 1000 V reverse breakdown voltages on vertical MOS structures, and > 500 V three-terminal off-state breakdown voltages on vertical power MOSFETs without edge termination. Three-terminal on-state devices showed 0.4 mΩ-cm^2 specific resistance, negligible hysteresis and close-to-enhancement-mode operation.

We are also using CNF to study the fundamental material properties of Ga_2O_3. For example, we use the Veeco Icon AFM to study the surface morphology of MBE grown AlN/GaN films on Ga_2O_3 substrates and used e-beam evaporation to make metal contacts to Ga_2O_3 for transport measurements.

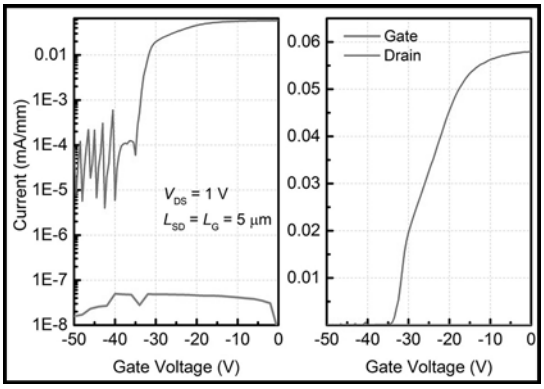

Figure 2: Transfer characteristic of nanomembrane FETs.

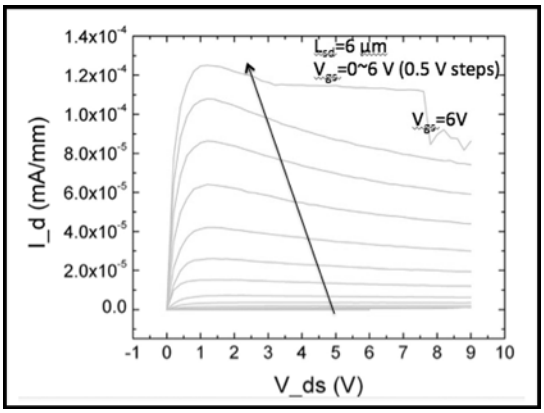

Figure 3: Output characteristic of E-mode MOSFETs.

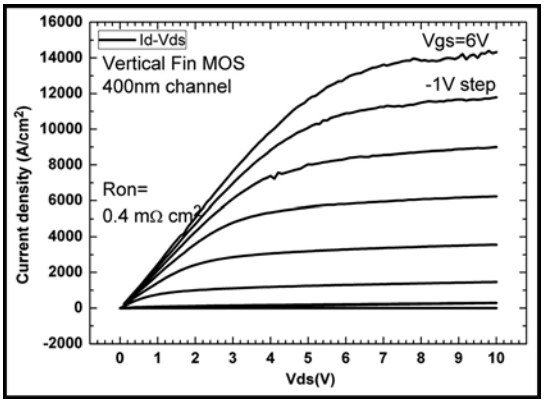

Figure 4: Output characteristic of GaN vertical Fin MOSFET with 400 nm wide channel.

References:

[1] M. Higashiwaki et al., Semicond. Sci. Technol. 31, 034001 (2016).

[2] L. Zhang et al, Japanese J. App. Phy. 56, 030304 (2017).

[3] B. Song et al, Device Research Conference (DRC), 2016.

[4] N. Tanen et al, North American Molecular Beam Epitaxy Conference (NAMBE), 2016.

Single Crystal Boron Nitride Devices

CNF Project Number: 2435-16
Principal Investigator: Dr. Debdeep Jena
User: Brian Calderon

Affiliation: Electrical Engineering, Cornell University
Primary Source of Research Funding: NSF
Contact: djena@cornell.edu, brian.r.calderon@gmail.com, brc65@cornell.edu
Primary CNF Tools Used: ABM contact aligner, CVD, VersaLaser, Zeiss Supra SEM

Abstract:

We demonstrate a novel method to place contacts precisely onto single crystal grown hexagonal boron nitride (hBN) using the ABM contact aligner. This work enables us to study the electronic properties and semiconducting nature of hBN as well as how these properties change with regard to crystal structure.

Summary of Research:

Hexagonal boron nitride (hBN) is a wide bandgap layered 2D crystal consisting of weakly interacting Van der Waals bonds between layers and strongly coupled sp2 hybridized bonds within layers [1]. Due to its atomic flatness and ability to only weakly scatter electrons, as in reference [2], it has primarily been used as a substrate for electronic devices based on other 2D materials, however its own electronic properties have not been well studied [1,3]. Prior work has shown that unwrapping boron nitride nanotubes (BNNT's) into boron nitride nanosheets (BNNS) results in highly conductive layers that can sustain currents on the order of micro-amps [4]. In this work, we study if the same can be accomplished in single crystal monolayers of hBN grown by chemical vapor deposition (CVD).

The hBN was initially grown by CVD on Cu foil and was transferred using a five-step wet transfer approach summarized in Figure 1. We spun polymethylmethacrylate (PMMA) at 3000 rpm for 60s onto the hBN/Cu substrate, the PMMA/hBN/Cu stack was then turned over and O_2 plasma was used to remove hBN on the backside (Step II in Figure 1). The stack was then left to float in Cu etchant CE-100 from Transene for 12hrs (Step III in Figure 1), the floating PMMA/hBN layer was then transferred to DI water and left to float for another 12hrs (Step IV in Figure 1). After this the PMMA/hBN was scooped up in the target substrate and left to dry for 12hrs. Finally, the PMMA/hBN/Substrate was left in a solvent solution (Microposit remover 1165 from Shipley) for 12hrs to remove the PMMA layer (Step V in Figure 1). The target substrate used in this study was a pre-patterned SiO_2 (280nm) on p-type doped Si.

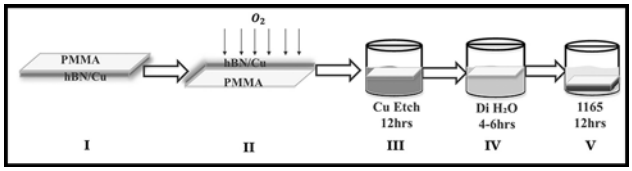

Figure 1: Wet transfer process used to remove the CVD grown hBN from the underlying Cu substrate and transfer it to an arbitrary substrate (SiO_2/Si in this case).

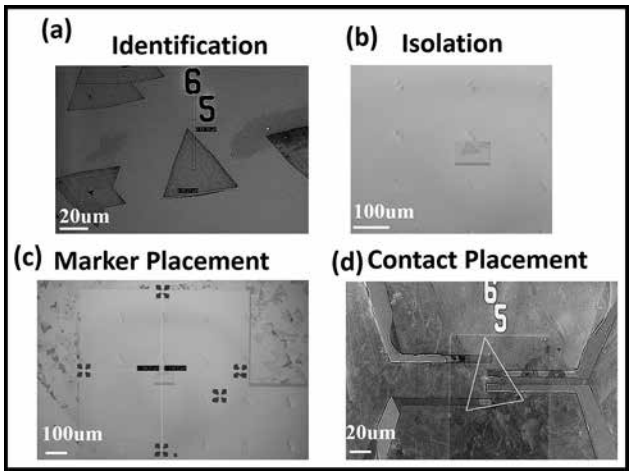

Figure 2: Fabrication procedure used to place contacts onto the single crystal hBN flakes. As can be compared between figures (a) and (d) the contacts were placed precisely within the desired triangular hBN flake.

Our fabrication procedure consisted of finding and measuring the location of a target hBN flake that has been transferred onto our pre-patterned SiO_2/Si substrate, this was done using the scanning electron microscope (SEM) as can be seen in Figure 2a. This step was necessarily done in the SEM due to the complete transparency of hBN under white light, making it impossible to find under microscope. The target flake was then isolated (Figure 2b) and precision alignment marks were placed using a custom-made contact mask (Figure 2c). Finally, the metal contacts were placed to the single crystal flake as shown in Figure 2d. Using this method, we're also able to place contacts across an hBN grain boundary and study its effects on conduction through this monolayer semiconductor.

Results on electrical characterization are still ongoing and will be reported in a future report.

The details of the custom-made mask are presented in Figure 3. A typical chrome mask used for contact alignment was made with alignment markers along the bisectors of a square (Figure 3a). The mask also contained two intersecting chrome rectangles that were used as positioners to measure distance from a given alignment mark on the pre-patterned substrate. A sheet of RubyLith was etched in the VersaLaser tool and four square holes were cut out. These were aligned to the markers in the chrome mask (Figure 3b). The RubyLith and chrome mask result is seen in Figure 3c. RubyLith was used since it's a sheet that is partially transparent in white light but is opaque to i-line and g-line wavelengths, thus it was possible to find the markings in the substrate, measure the desired distance from a given marking and expose only the contact marker regions that were cut into the RubyLith.

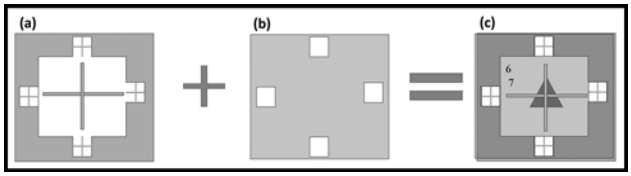

Figure 3: Details of the custom-made mask used to place the alignment markers in the fabrication procedure.

References:

[1] J. Yin, J. Li, Y. Hang, J. Yu, G. Tai, X. Li, Z. Zhang and W. Guo, "Boron Nitride Nanostructures: Fabrication Functionalization and Applications," Small, vol. doi: 10.1002/smll.201600053, pp. 1-27, 2016.

[2] C. R. Dean, A. F. Young, I. Meric, C. Lee, L. Wang, S. Sorgenfrei, K. Watanabe, T. Taniguchi, P. Kim, K. L. Shepard and J. Hone, "Boron Nitride Substrates for high-quality graphene electronics," Nature Communications, vol. 5, pp. 722-726, 2010.

[3] F. Mahvash, E. Paradis, D. Drouin, T. Szkopek and M. Siaj, "Space-Charge Limited Transport in Large-Area Monolayer Hexagonal Boron Nitride," Nano Letters, vol. 15, pp. 2263-2268, 2015.

[4] H. Zeng, C. Zhi, Z. Zhang, X. Wei, W. Guo, Y. Bando and D. Goldberg, ""White Graphenes": Boron Nitride Nanoribbons via Boron Nitride Nanotube Unwrapping," Nano Letters, vol. 10, pp. 5049-5056, 2010.

Calibrated MEMS Switches for Near-ZERO Power RF Detector and Sensors Network

CNF Project Number: 2440-16

Principal Investigator: Alyosha C. Molnar

User: Sunwoo Lee

Affiliation: Electrical and Computer Engineering, Cornell University

Primary Source of Research Funding: Defense Advanced Research Projects Agency

Contact: am699@cornell.edu, SL933@cornell.edu

Website: https://molnargroup.ece.cornell.edu/

Primary CNF Tools Used: Heidelberg DWL2000, SÜSS MA6-BA6, SC4500 odd and even hour evaporator, ASML 300C, Oxford 100, Oxford 81 and 82, AJA ion mill, CVC sputter deposition, PT720-740, Unaxis 770, Oxford Cobra

Abstract:

State-of-the-art military sensors today rely on active electronics to detect vibration, light, sound or other signals, requiring a constant consumption of power, while much of that power and time spent processing what often, unfortunately, turns out to be irrelevant data. N-ZERO program under Defense Advanced Research Projects Agency seeks to overcome such power limitations. Our research group's approach is an implementation of a MEMS switch, calibrated through a low power CMOS controlling circuit such that the MEMS switch is kept just shy of closure, making it extremely sensitive to the incoming RF signal or sensors output, limited only by the Brownian noise. In order to demonstrate a MEMS switch that can be well calibrated digitally, we have fabricated a MEMS switch with around ten biasing electrodes of varying dimensions. We have also designed the spring constant and contact gap in accordance with operating voltage range of the CMOS control circuit. In developing so, CNF has provided crucial supports in fabricating high facility, state-of-the-art low-power Si switches.

Summary of Research:

We start our fabrication using commercial 4-inch silicon-on-insulator (SOI) substrates. The substrates are first coated with titanium (Ti, as an adhesion layer) and chrome of 3 nm and 70 nm respectively to later form a hard mask. The MEMS switch patterns are made using a Heidelberg mask writer DWL2000, while the resist coating and exposure are done through the Gamma automatic coat-develop tool. While the chrome film is highly reflective, AR60 anti-reflection coating available in the Gamma automatic coat-develop tool makes the subsequent exposure in ASML 300C DUV Stepper possible. UVN resist, a negative type, is coated on top of the AR60 film, and is post-exposure baked and developed in the Gamma system. Following the development, the CNF Oxford 82 etcher is used to remove the arc film that is not developable, before the PT720/740 RIE is used to selectively remove the titanium-chrome film. Following the chrome etch, the residual photoresist is stripped in 1165 bath, followed by a deionized water rinse and nitrogen dry.

With the sturdy chrome mask, the device layer of the SOI substrate is etched away using either the Unaxis 770 deep Si etcher or the Oxford 100 ICP. Upon confirming that the etch has gone through the entire device layer using the P-7 profilometer, the residual chrome is etched away in a chrome etchant by soaking for an hour. The patterned SOI substrate is coated with a protective photoresist for dicing (SPR220.2 is used), and is diced using the DISCO dicing saw. Each diced die is then sonicated through acetone and isopropanol, 10 minutes each, before nitrogen drying.

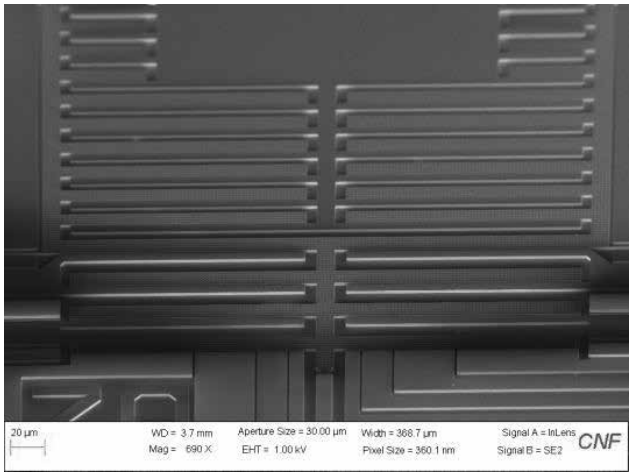

Figure 1: A SEM image of the fabricated a NZERO MEMS switch.

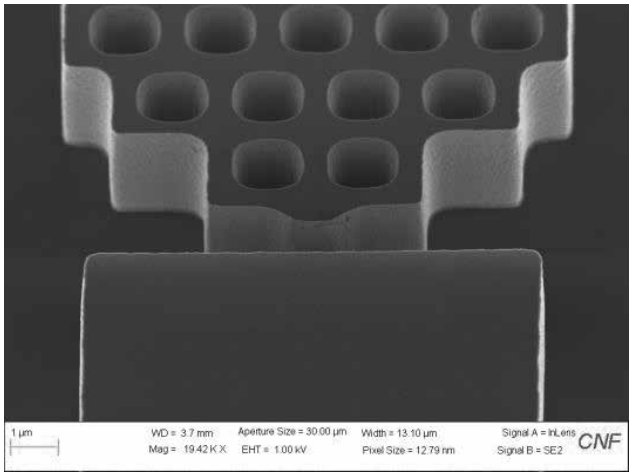

Figure 2: A zoomed-in SEM image of the fabricated a NZERO MEMS switch.

Finally, each die is released by etching away the box oxide using Primaxx Vapor HF system. In addition, to improve the contact resilience as well as resistance, platinum (50 nm) is coated at an angle using an SC4500 Odd hour e-beam evaporator (3 nm titanium is again used as an adhesion layer) for a sidewall coating as the MEMS switch is a lateral-motion one. Finally, ZEISS Ultra and Supra scanning electron microscopes (SEMs) are used to inspect the fabricated switches. Images can be seen in the Figures 1 and 2. For certain switches, in order to alleviate the problems posed by the high stress nature of the platinum, an AJA Ion Mill is used to remove the top platinum, while largely preserving the platinum on the side.

References:

[1] http://www.darpa.mil/program/near-zero-rf-and-sensor-operations

Multiple Resonant Features in GaN/AlN Resonant Tunneling Diodes

CNF Project Number: 2443-16
Principal Investigator: Huili Grace Xing
User: Jimy Encomendero

Affiliation: Electrical and Computer Engineering, Cornell University
Primary Source of Research Funding: Office of Naval Research under the DATE MURI Program
Contact: grace.xing@cornell.edu, jje64@cornell.edu
Primary CNF Tools Used: Veeco AFM, ABM contact aligner, YES Asher, odd-hour evaporator, PT770, P10 profilometer

Abstract:

In this work, double barrier GaN/AlN heterostructures have been grown by molecular beam epitaxy (MBE) on single-crystal GaN substrates. The device structures were fabricated into resonant tunneling diodes (RTDs) using a newly developed mask design. The quantum transport characteristics of these devices have been studied as a function of temperature down to 77 K. Multiple resonances in the current-voltage characteristics are observed over a wide range of temperatures showing that coherent tunneling transport of carriers is enabled by multiple subbands. These results raise hopes for the realization of room temperature III-Nitride based terahertz (THz) emitters such as RTD oscillators and quantum cascade lasers (QCLs).

Summary of Research:

Resonant tunneling transport of electrons in III-Nitride quantum heterostructures has been studied during the last fifteen years with limited success. GaN/AlN resonant tunneling diodes (RTDs)—being the simplest device to study resonant transport—have been under scrutiny by several research groups [1-3]. However, these devices usually exhibit a negative differential resistance (NDR) that degrades over several scans or present hysteresis, which limits their performance as active devices [2]. On the other hand, GaN/AlGaN RTDs, with low aluminum composition barriers, grown on single-crystal GaN substrates have been also reported in the literature [2]. However, their NDR is observed only at cryogenic temperatures due to the presence of current leakage paths through screw dislocations. In this work, III-Nitride RTDs exhibiting repeatable room temperature NDR are studied over a wide range of temperatures. Furthermore, multiple resonances in the current-voltage (I-V) characteristics are observed at cryogenic temperatures. We speculate that these resonances might result from hole resonant tunneling transport across the active region.

GaN/AlN double barrier heterostructures were grown by molecular beam epitaxy (MBE) on the c-plane of commercially available n-type single-crystal GaN substrates. Metal-rich growth conditions were employed during the whole process to promote step-flow growth mode and minimize the roughness of the epitaxial layers. The device structure was grown at a constant substrate temperature of ~ 750°C and a nitrogen plasma power of 200 W was used to achieve a ~ 3 nm/min growth rate. The RTD heterostructure comprises two degenerately doped n-GaN layers of ~ 200 and ~ 100 nm of thickness, which act as contact layers [See Figure 1a]. Unintentionally doped (UID) spacer layers were also introduced next to each of the contact layers to minimize dopant diffusion into the active region. An asymmetric spacer scheme was employed to reduce the extension of the collector depletion layer in the top electrode. Thus, a 6 nm thick UID GaN collector spacer was introduced, whereas the emitter spacer features a 12 nm UID GaN layer. The

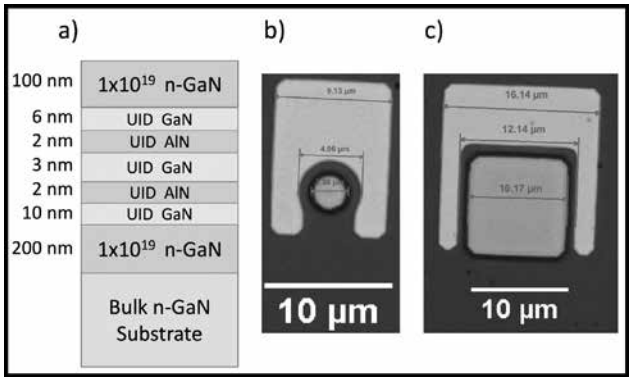

Figure 1: a) Schematic of the device structure grown by molecular beam epitaxy. b) and c) Fabricated RTDs featuring different mesa areas.

active region comprises two ultrathin 2 nm thick AlN barriers confining the quantum states of a 3 nm thick GaN quantum well. These thicknesses were measured by fitting a simulated x-ray diffraction pattern with the experimental pattern measured in the vicinity of the (002) peak.

The samples were fabricated by conventional contact lithography using an ABM contact aligner. Device mesas with areas between 2 × 2 μm^2 and 18 × 18 μm^2 were defined by a dry etching process using the $Cl_2/BCl_3/Ar$ gas mixture. Figures 1b) and 1c) show the fabricated devices featuring circular and square mesa geometries respectively. Figure 2 shows the equilibrium band diagram of the device structure calculated using a Schrodinger-Poisson solver [4]. From this diagram, we expect up to three resonant peaks due to the three electron bound states present in the quantum well. However, as shown in Figure 3, up to five resonances have been measured at cryogenic temperatures.

At this point, the origin of these multiple resonances is unknown. However, we can see from Figure 2 that hole bound states are also present in the collector side due to the thin GaN spacer and the high doping present in the top contact. Thus, additional resonant features might appear when these hole states get aligned with the hole bound-states in the quantum well. However, further studies will be necessary to confirm the origin of the resonances.

Temperature-dependent I-V characteristics were measured using a cryogenic probe station. Figure 3 shows the I-Vs curves obtained from a device with an area of 16 × 16 μm^2. At room temperature and under forward bias, only two resonances are clearly distinguished; in contrast reverse bias operation does not present any resonant peaks. This asymmetric I-V is a direct consequence of the strong spontaneous and piezoelectric polarization fields present in the polar heterostructure. As the temperature is lowered, additional resonances are resolved in forward bias and the largest peak-to-valley-current-ratio of 1.41 was measured at 77 K.

To summarize, we have experimentally investigated III-Nitride RTDs exhibiting multiple resonant features over a wide range of temperatures. Two of these resonances persist all the way up to room temperature with the highest peak current density recorded at ~ 7 kA/cm^2. These results represent a stepping stone for the future realization of room temperature III-Nitride based terahertz (THz) emitters.

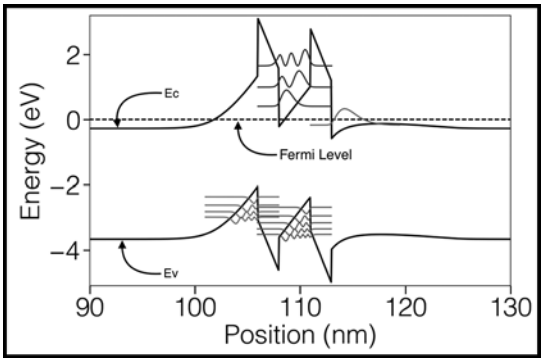

Figure 2: Equilibrium band diagram calculated using a Schrodinger-Poisson solver.

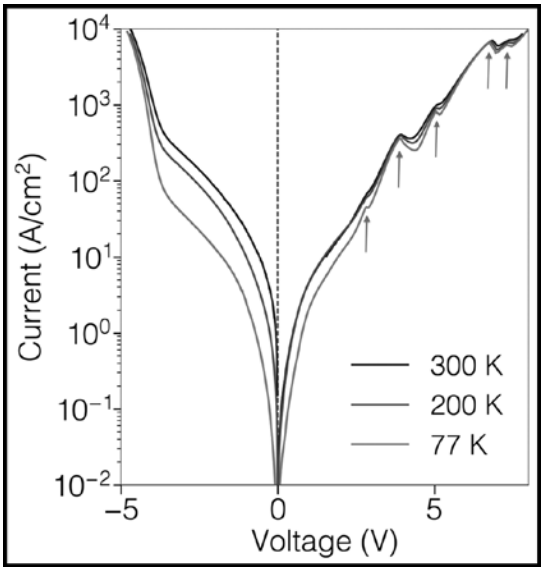

Figure 3: Temperature dependent current-voltage characteristics showing up to five resonances in forward bias.

References:

[1] K. Kishino, A. Kikuchi, H. Kanazawa, and T. Tachibana, Applied Physics Letters 81, 1234(2002).

[2] M. Nagase, T. Takahashi, and M. Shimizu, Japanese Journal of Applied Physics 54, 034201 (2015).

[3] D. Li, J. Shao, L. Tang, C. Edmunds, G. Gardner, M. J. Manfra, and O. Malis, Semiconductor Science and Technology 28, 074024 (2013).

[4] I. Tan, G. L. Snider, L. D. Chang, and E. L. Hu, Journal of Applied Physics 68, 4071 (1990).

High Temperature Epitaxial Growth of AlN/GaN/AlN Quantum Well HEMTs on SiC

CNF Project Number: 2470-16
Principal Investigator: Prof. Debdeep Jena
Users: Reet Chaudhuri, Austin Hickman

Affiliation: Electrical and Computer Engineering, Cornell University
Primary Source of Research Funding: Low Energy Systems Technology
Contact: djena@cornell.edu, rtc77@cornell.edu, alh288@cornell.edu
Primary CNF Tools Used: Veeco Icon AFM, photolithography set, SC4500, AG610 RTA, PT770 ICP, Oxford 81

Abstract:

This work is focused on the growth of a GaN quantum well high electron mobility transistor (HEMT) structure on the AlN/SiC platform. The AlN platform provides a number of advantages over the conventional AlGaN/GaN HEMTs that are on GaN platform. We report mobilities of 216/372 cm^2/V-s (300K/77K), which are suitable for decent transistor performance.

Summary of Research:

AlN/GaN/AlN heterostructures are rich in terms of previously unseen transport phenomena in III-V nitrides. Previous work has shown GaN quantum well (QW) FETs to have promising performance [1], but this was realized on AlN-on-sapphire templates that have low thermal conductivity. Moving to AlN/SiC platform is hence advantageous for use in high power applications. In our project, we have grown AlN/GaN/AlN QW structure using high temperature MBE growth of AlN on SiC to improve the crystal quality, improving upon the previous work done in our group on the SiC platform.

The GaN QW HEMT structure consists of a thin and strained GaN layer between relaxed layers of AlN acting as the buffer and barrier. A thick AlN buffer (~1 μm) is grown on SiC substrate and the top AlN barrier is capped with thin layer of GaN to prevent oxidation. The epi-structure with typical thicknesses is shown in Figure 1. As seen in the band diagram, a 2D electron gas is obtained at the GaN-AlN interface, which can be utilized as a channel in a processed FET. The samples were grown by plasma assisted molecular beam epitaxy (PA-MBE). The 6H-SiC substrates were back-coated with 500 nm of titanium to ensure uniform heat distribution on the growth surface. Standard Ga and Al solid source effusion cells were used along with an N_2 plasma source for the crystal growth. The structure was grown in two stages.

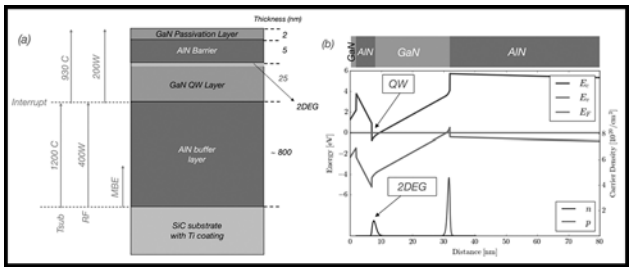

Figure 1: (a) Schematic structures of grown samples (b) Energy Band diagram showing the expected 2DEG.

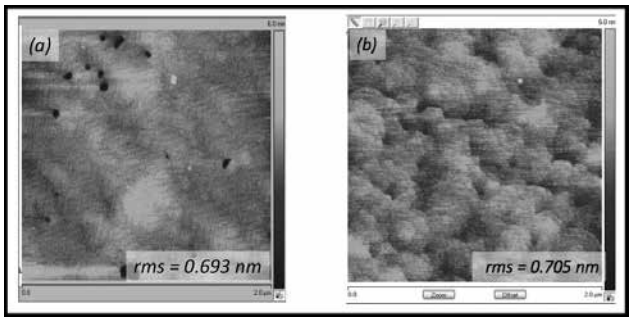

Figure 2: AFM images showing the MBE growth surfaces of (a) AlN on SiC and (b) complete QWHEMT structure on SiC with corresponding RMS roughness values.

The thick AlN buffer layer was grown at a substrate temperature of 1200°C and high growth rate of 600 nm/hour. The growth was then interrupted and excess Al on the surface was consumed completely using nitrogen. This was monitored by tracking the RHEED intensity. The substrate was then cooled to around 930°C for the active region growth at 300 nm/hour for better thickness control. The GaN quantum well region was grown in slightly metal rich condition. Throughout the growth, RHEED monitoring was performed to ensure the surface smoothness and optimized growth conditions.

Post growth, x-ray diffraction (XRD) and atomic force microscopy (AFM) were performed in the Cornell NanoScale Facility (CNF) for characterizing the growth quality. The transport characteristics were obtained through Hall measurements (Van der Pauw with indium contacts) at both room temperature and 77K. The GaN layer thickness, as well as the active region substrate temperature were varied during the growth to optimize the electron mobilities.

The highest mobilities obtained through Hall measurements were 216/372 cm^2/V-s (300K/77K) with sheet charge densities of 6e13/5.1e13 cm^{-2} (300K/77K), which is some of the highest charge densities reported for this structure. The Hall data also confirmed the presence of electrons. The sample also had a smooth surface morphology, with a root mean square (RMS) roughness of 0.705 nm (Figure 2).

Further characterization and growths are being investigated to improve the electronic transport. We are also developing fabrication process to make transistors from the structure and take advantage of the inherent physics it offers.

References:

[1] G. Li, et al., Appl. Phys. Lett, vol. 104, p. 193506 (2014).

Molybdenum Diselenide MOSFET and CMOS Integration

CNF Project Number: 2509-16

Principal Investigator: James C.M. Hwang

User: Kuanchen Xiong, Lei Li

Affiliation: Department of Electrical and Computer Engineering, Lehigh University

Primary Sources of Research Funding: This work was supported in part by the U.S. Office of Naval Research under Grant N00014-14-1-0653 and the Air Force Office of Scientific Research and the National Science Foundation EFRI 2-DARE Grant No. 1433459-EFMA

Contact: jh00@lehgih.edu, kux214@lehigh.edu, lel216@lehigh.edu

Primary CNF Tools Used: ABM contact aligner, Autostep I-line stepper, PT720-740, SC4500, P10 profilometer

Abstract:

We've used an alternative approach to the current practice of mechanical exfoliation and e-beam lithography in fabricating transitional metal dichalcogenide (TMD) metal-oxide-semiconductor field-effect transistors (MOSFETs). The alternative uses complementary metal-oxide-semiconductor (CMOS) back-end-of-line (BEOL) process and low-temperature molecular beam epitaxy (MBE). The BEOL process allows buried gates as short as 0.1 μm and high-quality gate insulator to be fabricated before TMD deposition (Figure 1). MBE offers large-scale deposition of TMDs at low temperature tolerable by CMOS BEOL process. After further photolithography, approximately 3,000 RF-probable molybdenum diselenide ($MoSe_2$) MOSFETs were fabricated on each chip (Figure 1(c)). The resulting MOSFETs were then characterized and show promising performance.

Summary of Research:

Figure 2 shows the designed process. Starting from chips fabricated by the CMOS foundry, high-dielectric-constant (κ) aluminum oxide was deposited on the substrate by atomic layer deposition (ALD) to 30 nm, as the gate dielectric (Figure 2. (a)). Then $MoSe_2$ was deposited onto the dielectric by MBE at 400. (Figure 2. (b)). A metal evaporation and lift-off process followed to form a 10 nm/160 nm Ti/Al contact to $MoSe_2$ (Figure 2. (c)). Finally, passivation by photo resist S1813 was spun coated and patterned to expose the contact pads (Figure 2. (d)).

Device performance was measured across several chips. The results show variable performance characteristics. Figure 3 shows a typical transfer characteristic of the $MoSe_2$ MOSFET. Although the current capacity is low, on/off ratio of 1000 is achieved. The device shows ambipolar characteristics as functions of both gate and drain biases. The $MoSe_2$ MOSFET drain characteristics are shown in Figure 4.

These preliminary results prove the feasibility of large-scale integration of TMD and CMOS technology. Further process improvement is needed to yield uniform and high-performance MOSFETs.

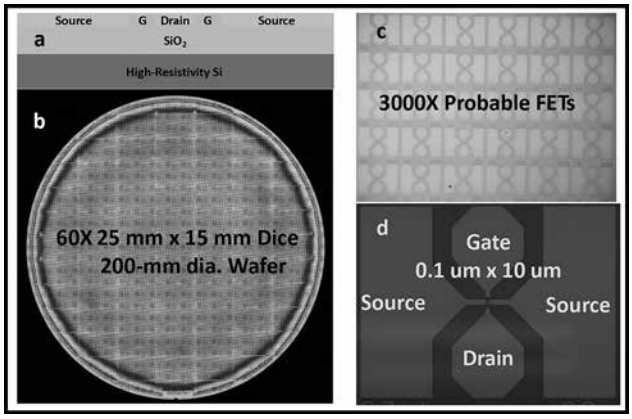

Figure 1: (a) Cross section schematic of a buried-gate MOSFET and micrographs of (b) a 200-mm dia. wafer, (c) a 25-mm by 15-mm chip, and (d) a MOSFET.

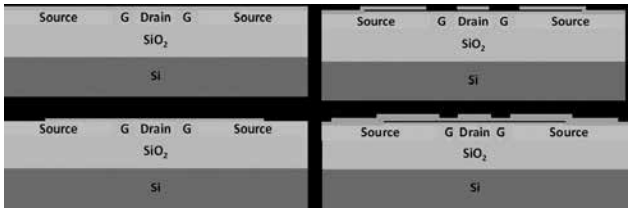

Figure 2: (a) Isolation layer by ALD Al_2O_3, (b) $MoSe_2$ layer transferred and patterned, (c) Ti/Al contact metal layer evaporated and lifted-off, and (d) S1813 photoresist passivation layer spun-on and patterned.

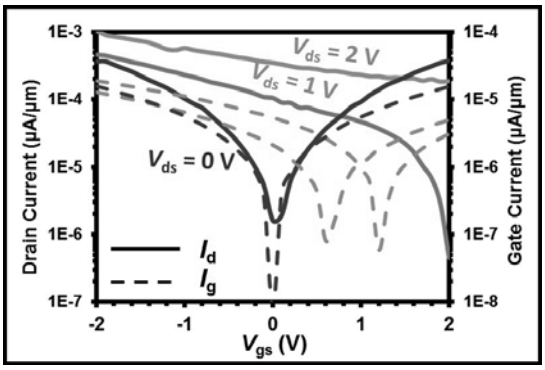

Figure 3: Transfer characteristics of a MBE-grown $MoSe_2$ MOSFET. V_{ds} = 0 V, 1 V, 2 V.

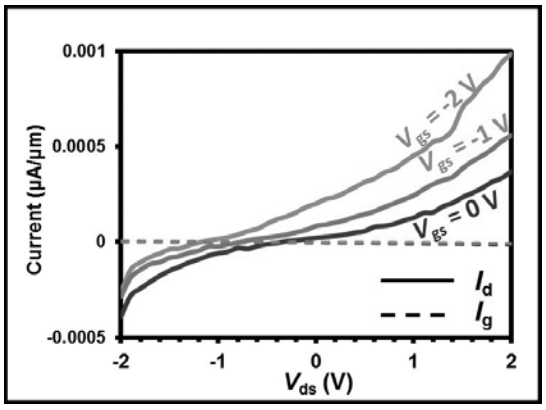

Figure 4: Drain characteristics of a MBE-grown $MoSe_2$ MOSFET. V_{gs} = 0.2 V, 0.1 V, 0 V.

Description of the Exploratory Etching and Electrodeposition Project

CNF Project Number: 2527-17
Principal Investigator: Dr. David Crouse
User: Golsa Mirbagheri

Affiliation: Electrical and Computer Engineering Department, Clarkson University
Primary Source of Research Funding: CFM
Contact: dcrouse@clarkson.edu, mirbagg@clarkson.edu
Primary CNF Tools Used: Oxford 81, 82 and 100, AJA, ALD, Electroplating Cu, ASML, Gamma

Abstract:

The project was to deposit a 1.5 µm thick silicon oxide layer on top of a silicon wafer, then etch an array of 0.5 µm diameter holes down to the silicon surface. Following the etching, we deposited a conformal and thin metal layer that was used as a seed layer for subsequent electrodeposition of metal into the holes and over the rest of the film. Following the electrodeposition, we took the wafer back to Clarkson and performed a chemical mechanical polishing to remove the metal on top of the silicon oxide film, leaving only the metal in the holes.

Summary of Research:

This is the first part of a potentially larger project that involves fabricating a wire mesh array that will function as a hyperbolic metamaterial.

However, for this proposed project, we focus on the core component of what will eventually become a hyperbolic metamaterial. In this project, we aim to show that electrodeposition in holes is a viable fabrication pathway; variations in hole size or incomplete filling are much less of a concern compared to demonstrating the overall technical merit of the fabrication approach outlined below.

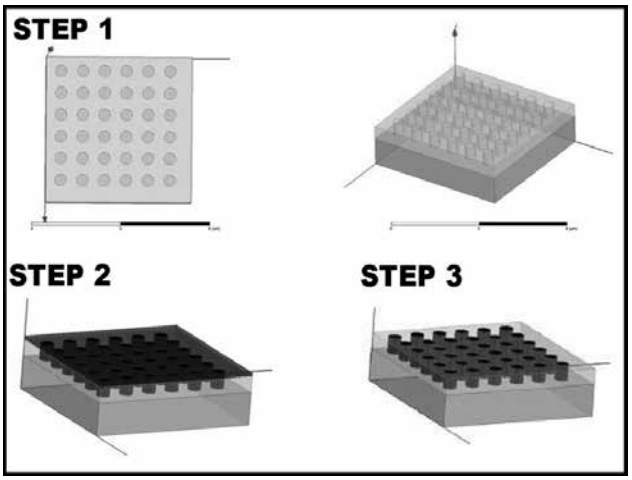

Figure 1: Step 1 (at the CNF): The SiO_2 film is deposited, patterned and etched. The holes are 0.5 µm in diameter and the SiO_2 layer is 1.5 µm thick. The holes go all the way down to the silicon wafer. Step 2 (at the CNF): The seed metal layer is deposited, followed by overfill electrodeposition of the metal (either Ag, Au, or CU). Step 3 (at Clarkson): The wafer will be chemically mechanically polished to remove the top metal layer, leaving only the metal in the holes.

Multi-Functional Platform for Characterization of Nanostructured Polymer Brushes

2017 CNF REU Intern: Michael E. Klaczko

CNF REU Affiliation: Chemistry, SUNY College of Environmental Science and Forestry

CNF Project: Cornell NanoScale Science & Technology Facility Research Experience for Undergraduates (CNF REU) Program

CNF REU Principal Investigator: Dr. Christopher Ober, Materials Science and Engineering, Cornell University

CNF REU Mentor: Wei-Liang Chen, School of Chemical and Biomolecular Engineering, Cornell University

Primary Source of Research Funding: National Science Foundation via the NNCI Grant No. ECCS-1542081

Contact: mklaczko@syr.edu, christopher.ober@cornell.edu, wc497@cornell.edu

Website: http://www.cnf.cornell.edu/cnf5_reuprogram.html

Primary CNF Tools Used: AJA Sputter, Hot Piranha Hamatech, Oxford PECVD, Gamma Developer, ASML Stepper, AFM, SEM. Oxford 81 and 100

Abstract:

Polymer brushes have been of interest because of their unique ability to act as a functional coating. The unique structure of polymer brushes allows them to be used for several applications including antifouling, cell adhesion, resistance to nonspecific binding, and biosensing. With the realized applications of polymer brushes, it has become more important to understand their fundamental structure and the resultant stimuli-responsive behavior. This project aims to create a way to observe the polymer brushes at the molecular level by putting polymer brushes onto the sidewalls of diffraction gratings. Once successful, completed observation can be done on the macro scale by observing the diffraction of light through the gratings, and on the molecular scale by observing the scattering of neutron beams across the sides of the diffraction gratings. These measurements are exemplified in Figure 1. By successfully utilizing photolithography and subsequent multiple etching steps for pattern transfer on a sandwich structure to create our multi-functional platform, the base platform has been created and the process to reaching this goal has been furthered.

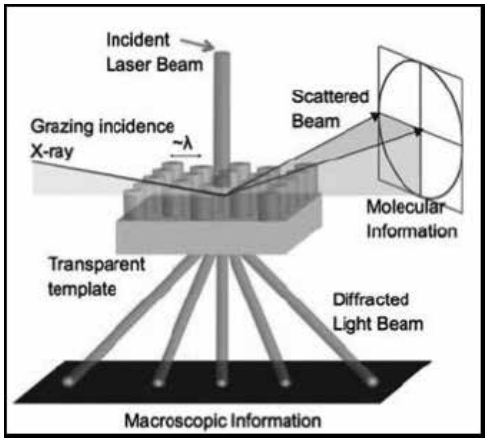

Figure 1: Diagram showing how laser diffraction and neutron beam scattering can be used to gain macroscopic and microscopic information on the polymer brushes grown on the multi-functional platform.

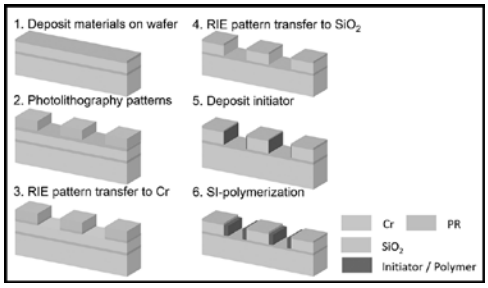

Figure 2: Wafer development process to create the multi-functional platform.

Summary of Research:

The focus of this summer's research was on developing a multi-functional platform which could be used to characterize nanostructured polymer brushes. As shown in Figure 2, this was done by developing a sandwich structure on top of a fused silica wafer which could be manipulated through photolithography and etching to create a structure which only had silicon dioxide exposed on the sidewalls of the structure. Since the small molecule initiator which is for the polymerization of polymer brushes can only bind to hydroxyl groups, it will only bind to the sidewalls which has exposed silanol groups. This in turn creates a structure that only has polymer brushes on its sidewalls after polymerization.

The structure was characterized with atomic force microscopy (AFM), scanning electron microscopy (SEM), and laser diffraction. These characterization techniques were also used throughout the fabrication process to correct problems along the way and to determine whether the process was being completed successfully.

Results and Conclusions:

In the end, this process was completed successfully as determined using AFM, SEM, and laser diffraction.

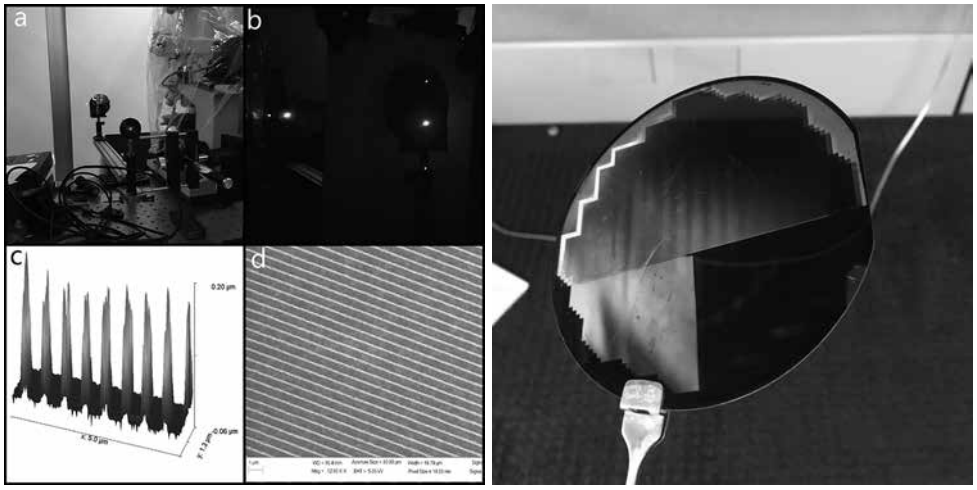

Figure 3, left: a) the laser diffraction setup b) a laser being diffracted by the final structure of the multi-functional platform c) An AFM image of the pattern on the final structure form d) An SEM image of the pattern on the final structure form. Figure 4, right: The multi-functional platform after its process completion. Differences in chrome etch time were measured on this wafer but the top half portion is where the pattern was successfully developed and processed.

The multi-functional structure was made so that a diffraction grating was created. As shown in Figure 3a and 3b, this structure was proven after a beam of green laser light with 532 nm was diffracted when shone through the pattern. Figure 3c and 3d further support this conclusion by showing the diffraction grating through their imaging process. During the creation of the platform it was found that layer uniformity, layer cleanliness, wafer flatness, ARC/resist type, and coating were all very important to the success of the structure. After completing the process, it was determined that layer uniformity and wafer flatness both worked together to counteract the advances made in photolithography. With a high numerical aperture, it was necessary for the overall shape of the wafer to be very homogeneous and uniform. To fix this the numerical aperture was lowered and the chromium was coated with a plasma bias, which made the film denser and more uniform.

The problem of layer cleanliness was fixed by cleaning and seasoning the chamber of the Oxford plasma enhanced vapor deposition (PECVD) before depositing the silicon dioxide onto the wafer, and by cleaning the wafer before each layer deposition with a hot piranha clean. After trying both negative and positive resists and several types of anti-reflective coatings (ARC), the resist UV210-0.6 was used with the ARC DUV-42P.

The successful completion of this project now allows for a more comprehensive observation and understanding of polymer brushes to be reached which would have never been reached had such a platform never been created. Figure 4 shows what the completed structure looks like.

Future Work:

Using this multi-functional platform, experiments can now be done which isolate the polymer brushes to the sidewalls of the structure which will ultimately enhance our knowledge of polymer brushes and how they work. Initiator will be deposited onto the structure and if it only attaches to the sidewalls like it is supposed to, polymer brushes will be grown here and laser diffraction as well as neutron beam scattering experiments will be able to be done on them. If it is found that the initiator does not only bind to the sidewalls but other areas as well, then the structure will be re-evaluated and recreated in a way that allows us to achieve this structure with silicon dioxide only exposed on the sidewalls. Using laser diffraction and neutron beam scattering information, the study of several different types of polymer brushes can be completed. From the greater understanding of polymer brushes given by these studies, research can be done on applying polymer brushes to their realized applications and to developing new ways that they could be used.

Acknowledgements:

I would like to thank Dr. Christopher Ober for allowing me to work in his research group this summer, my mentor Wei-Liang Chen for guiding through the field of nanotechnology and providing the support for my success in this program, Melanie-Claire Mallison for creating such a welcoming and loving environment, and the staff at CNF for all their expert help and support. I would also like to thank my peers in the REU program for their support throughout the program, and for their continued support moving forward. Finally, the National Nanotechnology Coordinated Infrastructure (NNCI) Grant No. ECCS-1542081 for funding the Research Experience for Undergraduates (CNF REU) Program.

References:

[1] W-L. Chen, R. Cordero, H. Tran, and C. K. Ober. 50th Anniversary Perspective: Polymer Brushes: Novel Surfaces for Future Materials. Macromolecules 2017 50 (11), 4089-4113.

[2] Swann, J. M. G.; Bras, W.; Howse, J. R.; Topham, P. D.; Ryan, A. J. Quantifying Hydrogel Response Using Laser Light Scattering. Soft Matter 2010, 6 (4), 743–749.

Texturing and Electrical Performance of CAAC IGZO Thin Film Transistors

CNF Project Number: 150-82
Principal Investigator: Michael O. Thompson
Users: David M. Lynch, Katherine K. Quinn

Affiliation: Materials Science and Engineering, Cornell University
Primary Source of Research Funding: Corning, Incorporated
Contact: mot1@cornell.edu, dml346@cornell.edu, kkq2@cornell.edu
Website: http://thompson.mse.cornell.edu/
Primary CNF Tools Used: Furnace B2, Oxford 100, PT 720, CHA, SÜSS MicroTec MA6, Everbeing EB-6 DC Probe Station

Abstract:

We report on the effect of substrate temperature during RF sputter deposition of IGZO films on the crystallographic texturing and the field-effect carrier mobility. Elevated temperatures are required to induce crystallinity in IGZO films and to achieve mobilities ~ 2 cm^2/Vs, and optimal texturing is observed at a substrate temperature of 315°C. Above 315°C, a degradation in c-axis alignment is observed, corresponding approximately to the sharp increase in mobility at temperatures above 340°C.

Summary of Research:

Amorphous $InGaO_3(ZnO)m$ (a-IGZO) has demonstrated tremendous potential as a replacement for amorphous silicon as an active channel material in thin film transistors (TFTs) for display applications due to a relatively high electron mobility, low processing temperatures, uniformity, and low leakage currents. Recently, focus has shifted to the reduction of long-term instability (on-voltage shifts in device transfer characteristics) in IGZO-based transistors due to material defects. One promising method incorporates *in situ* substrate heating during the deposition process to produce a textured crystalline microstructure, called c-axis aligned crystalline (CAAC) IGZO. While devices fabricated from CAAC IGZO have demonstrated vastly improved transfer characteristics, a systematic study of the effect of substrate temperature and film texturing has not been conducted.

Bottom-gate top-contact TFT structures were fabricated on heavily doped p-type Si wafers (used as TFT gate) with ~ 100 nm of thermally grown SiO_2 used gate dielectric (Furnace B2). IGZO films were RF sputtered from a sintered polycrystalline $InGaO_3(ZnO)$ target in a 10% O_2 in Ar mix with an RF power of 120W onto a rotating, temperature-controlled substrate (varied substrate temperature T_{sub}). The IGZO film backchannel surface was protected by a thin ~ 30 nm SiO_2 film (Oxford 100 PECVD). The SiO_2:IGZO active channel was patterned using fluorine-based dry etching (PlasmaTherm 720) and wet etching using 2 wt% HCl (for IGZO), and source/drain contacts were deposited (CHA Evaporator) and patterned lithographically (SÜSS MicroTec MA6) using liftoff. Devices were all annealed in dry air for 30 minutes prior to measurement (Everbeing EB-6 DC Probe Station). As-deposited film structures are characterized using x-ray diffraction (XRD).

Films deposited under similar deposition conditions were also structurally characterized using 2D XRD using a Bruker-AXS D8 General Area Detector Diffraction System (GADDS), which measures scattered x-ray intensity both as a function of 2θ (standard XRD) and as a function of χ, which gives a measure of texturing similar to an XRD rocking curve. Integrating scattering intensity over 2θ gives intensity vs. χ, shown in Figure 1, which represents the c-axis alignment distribution of the CAAC IGZO film. The full-width at half-maximum (FWHM) of this distribution is used to quantitatively compare the degree of alignment between films with lower FWHM values indicating stronger texturing.

Typical room temperature depositions yield amorphous IGZO films with the onset of crystallization occurring at a substrate temperature of ~ 200°C. Both crystallinity (determined quantitatively by diffraction peak intensity) and texturing improve with increasing temperature up to about 315°C. At higher substrate temperatures, an increased nucleation rate during film growth leads to reduced texturing and increasingly

polycrystalline films, shown in Figure 2. The film microstructure formed under optimal conditions (T_{sub} = 315°C) is shown in Figure 3.

TFTs fabricated from the IGZO films were electrically characterized using DC measurements of the output characteristics (I_{DS} vs. V_{DS} at fixed V_{GS}) of the transistors. The field-effect carrier mobility (μ) was extracted from the linear regime of the output characteristics by fitting the linear regime conductance to the MOSFET equation using the small-signal approximation.

The electron mobility as a function of substrate temperature during deposition is shown in Figure 4. Devices fabricated from α-IGZO films deposited at room temperature exhibit extremely low μ values (<1 cm^2/Vs). However, with the introduction of *in situ* heating, the mobility is observed to increase to about 2 cm^2/Vs. Above 340°C, the mobility unexpectedly increases to approximately 9 cm^2/Vs. This temperature regime with increased mobility (Figure 4) corresponds to the decrease of crystallographic texturing (Figure 2).

The mechanism for the increase in carrier mobility has yet to be fully understood, and may have one of several origins. Elevated temperatures also yield an increase in film crystallinity, and it may be that the crystalline domains shown in Figure 3 reach full percolation at temperatures above 340°C. Zinc desorption during film growth is yet another possibility, as it has been shown that as-deposited Zn fraction decreases linearly with substrate temperature — even when deposited from a stoichiometric target. Thus, a relatively higher In content can lead to a higher μ. However, an inexplicable link between texturing and mobility cannot yet be ruled out, and further study is required to determine the origin of the increase in carrier mobility at elevated deposition temperatures.

References:

[1] K. Nomura, et al., Nature 432, 488 (2004).

[2] J. S. Park, et al., Thin Solid Films 520, 1679 (2012).

[3] S. Yamazaki, SPIE Newsroom (2012).

[4] D. Lynch, et al., Appl. Phys. Lett. 105, 262103 (2014).

[5] D. Lynch, et al., SID Symposium, 308 (2015).

[6] B. Zhu, et al., ECS J Solid State Sci. Technol. 5, P368 (2016).

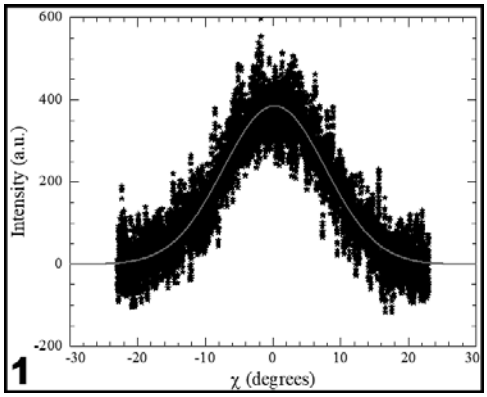

Figure 1: X-ray scattering intensity (integrated over 2θ space) as a function of azimuthal angle χ measured using GADDS, representing the crystallographic alignment distribution of the CAAC IGZO film deposited with T_{sub} = 315°C. The overlaid curve is a Gaussian function fit used to quantitatively determine the FWHM of the distribution.

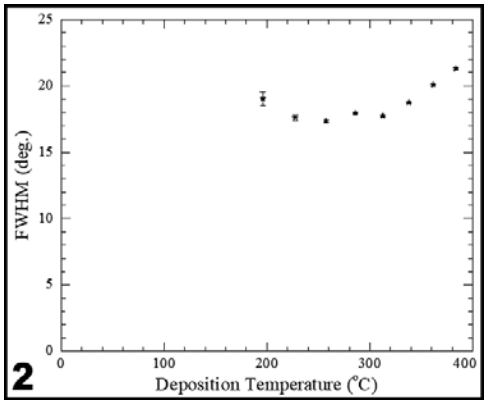

Figure 2: GADDS FWHM as a function of substrate temperature during deposition. Films exhibiting an amorphous as-deposited film structure are not shown. Films show strong texturing up to ~ 315°C; above this temperature, nucleation events lead to reduced alignment and increasingly polycrystalline characteristics.

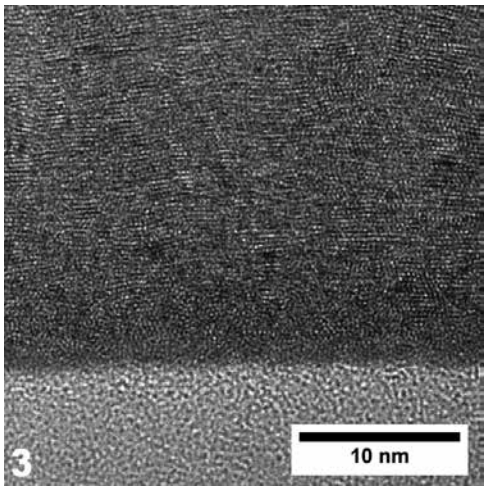

Figure 3: Cross-section HRTEM image of the CAAC IGZO film at the IGZO/SiO_2 interface deposited using a substrate temperature of 315°C.

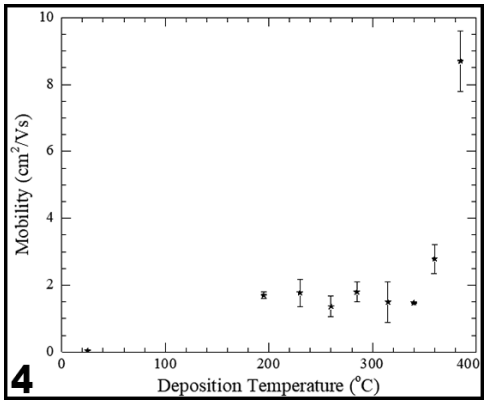

Figure 4: Electron mobility as a function of substrate temperature during deposition. Some* in situ *heating is required for improved device performance. At high temperatures, mobility is observed to increase almost fivefold.

Oxide Nanoparticle EUV (One) Photoresist Studies

CNF Project Number: 386-90
Principal Investigator: Christopher K. Ober
Users: Hong Xu, Kazuki Kasahara

Affiliation: Department of Materials Science and Engineering, Cornell University
Primary Source of Research Funding: JSR Micro
Contact: cko3@cornell.edu, hx49@cornell.edu
Primary CNF Tools Used: ABM contact aligner, ASML stepper, Zeiss Ultra SEM

Abstract:

Photo-acid generators (PAGs), key components in chemically amplified photoresists, are decomposed under mid-UV or deep-DV light to release strong acid. Such strong acid catalyzes the deprotection reaction or decomposition reaction of polymer resists, and leads to solubility changes between exposed and unexposed areas. However, PAGs are designed to absorb mid- or deep-UV, and strong acids are less-efficient in inducing solubility changes in metal-oxide nanoparticle resists, which are promising candidates in extreme ultra-violet (EUV) lithography. In this work, click chemistry is introduced into lithography to achieve high-contrast patterns under extremely low exposure dose, e.g., 7.5 mJ/cm^2, which is 10-20 times lower than the dose used in PAG resist chemistry. Under UV exposure, double bond modified zirconium oxide nanoparticles can quickly react with di-thiol compounds to form insoluble crosslinked networks and lead to clear patterns upon solvent development.

Summary of Research:

In a conventional lithography process, strong acids released by PAGs catalyze the deprotection reaction or decomposition reaction of the polymer resists and induce dissolution differences between exposed and unexposed areas. However, PAGs are usually aromatic compounds that are designed to absorb in the mid- or deep-UV regions, and strong acids are less-efficient in inducing solubility changes to metal-oxide nanoparticle resists. Utilizing zirconium/hafnium oxide (ZrO_2 or HfO_2) nanoparticles, the Ober group has developed a series of hybrid nanoparticles composed of an inorganic core with ZrO_2 or HfO_2 and various organic ligands [1]. These hybrid nanoparticles demonstrate excellent patterning efficiency under extreme ultraviolet (EUV) exposure conditions, due to their much smaller molecular size and higher EUV absorption than polymer resists.

However, the precise patterning mechanism is unclear, due to subtle changes that happen to these metal-oxide nanoparticles, and the role of PAG is rather confusing: PAG can improve the patterning performance; however, it is not an indispensable component in metal-oxide-nanoparticle EUV lithography. Patterns can be obtained without PAG, although there is a considerable decrease in quality; considering PAG's inefficiency on absorbing EUV light, the entire mechanism becomes quite complicated, and thus leads to difficulty on improving patterning performance.

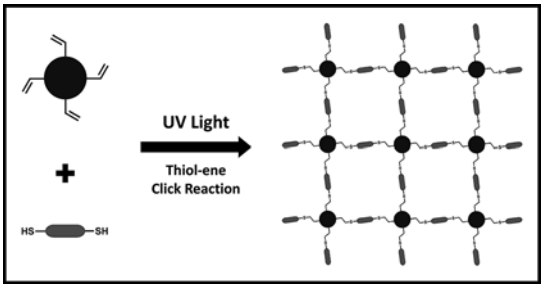

Figure 1: Scheme of thiol-ene click-crosslinking mechanism.

In this work, click chemistry is introduced into lithography, and high-contrast patterns under extremely low exposure dose are achieved. Thiol-ene click chemistry is a highly efficient, photo-initiated free-radical addition reaction, and under UV exposure, double bond modified zirconium oxide nanoparticles can quickly react with di-thiol compounds to form insoluble crosslinked networks (as shown in Figure 1) and lead to clear patterns upon development.

Middle Ultraviolet (mid-UV) Lithography. To demonstrate the dissolution behavior difference between the non-click and click reaction systems, preliminary lithographic evaluations were carried out using the CNF ABM contact aligner. For the non-click reaction test, the resist formulation contains 5 wt%

double bond modified nanoparticles, and propylene glycol monomethyl ether acetate (PGMEA) as solvent. The resist was spin-coated onto a silicon wafer at 2000 rpm for 1 min and then exposed with 254 nm mid-UV at 150 mJ/cm^2. For the click reaction system, the test resist formulation contains 5 wt% double bond modified nanoparticles, 0.5 wt% di-thiol compound as crosslinking agent and PGMEA as solvent. To highlight its superior sensitivity, the film was exposed with mid-UV at 150 and 7.5 mJ/cm^2, respectively.

For the non-click film, after being developed with 4-methyl-2-pentanone (4M2P) for 5s, negative tone patterns can be observed, however, with lots of residues (Figure 2A). Further development, e.g., 7s and 10s (Figure 2B and 2C), still allows the residue to be removed, but the desired patterns become weak and finally completely dissolved when developed for 15s (Figure 2D). For the case of the click reaction based film, after being exposed at the normal dose 150 mJ/cm^2, high-contrast patterns can be observed, even the film was developed in a much stronger solvent — acetone. Thiol-ene click reaction is a UV-sensitive and highly efficient reaction, meanwhile the reaction products are crosslinked networks (Figure 1), which are recognized for bad solubility or are totally insoluble in common developers. As a result, even the exposure dose was further decreased to 7.5 mJ/cm^2 — 20 times lower than the normal dose, clear patterns can be observed after being developed in acetone for 15s. It is noteworthy that the solubility change was remarkable, the pattern can be very well preserved after being developed in acetone for 12 or 24 hours (Figure 3C and 3D). Such obvious solubility change has not been observed in previous reports, although the dose used here is extremely low.

Deep Ultraviolet (deep-UV) Lithography. Using same the film fabricating condition, the click-reaction film was exposed using CNF ASML stepper (248 nm KrF laser). After being exposed at 25 mJ/cm^2 and developed in acetone for 15s, well-defined negative tone patterns were obtained, as indicated by scanning electron microscope (SEM) images (Figure 4), taken by CNF Zeiss Ultra SEM. 1:1 line-and-space patterns with the feature size from 1000 nm to 300 nm (Figure 4), in which the exposed area is slightly broader than the target feature size, suggest patterns are over-exposed, although the used dose is quite low.

In summary, click chemistry was introduced into lithography, and achieved high-contrast patterns under extremely low exposure dose. Utilizing click reaction between double bond modified ZrO_2 nanoparticles with di-thiol compound, good patterning performance was obtained under deep-UV exposure. Meanwhile, considering the thiol-ene click reaction is free-radical based reaction while the EUV-photoelectron and secondary electrons are good initiator for free-radicals, this preliminary work indicates such click reaction based patterning are promising candidates for EUV lithography.

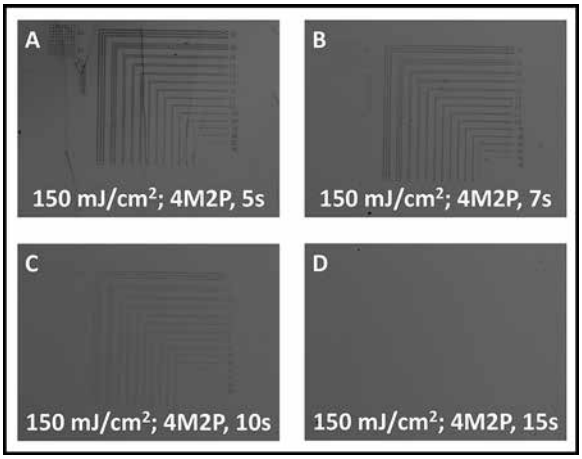

Figure 2: Optical microscopic images of non-click ZrO_2 nanoparticles.

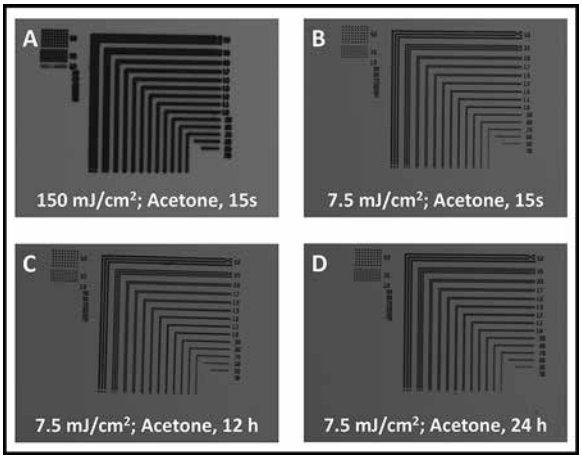

Figure 3: Optical microscopic images of click-crosslinking ZrO_2 nanoparticles.

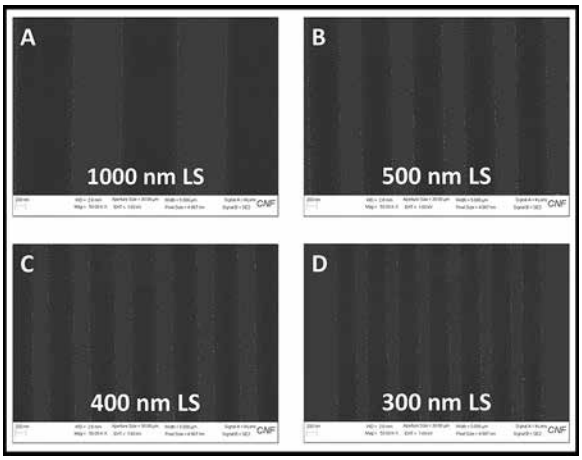

Figure 4, bottom: SEM images of click-crosslinking ZrO_2 nanoparticles.

References:

[1] Trikeriotis, M.; et al., Photopolym. Sci. Tech. 2012, 25, 583-586.

Approaching the Ultimate Size-Limit of Organometallic Silver-Thiolate $AgSC_n$ 2D Lamellae: Synthesis and Characterization

CNF Project Number: 522-94

Principal Investigator: Leslie H. Allen

User: Zichao Ye

Affiliation: Materials Science and Engineering, University of Illinois at Urbana-Champaign

Primary Sources of Research Funding: National Science Foundation Division of Materials Research (#1409953, #1006385 and #0735286); University of Illinois Research Board (#13187)

Contact: l-allen9@illinois.edu, zye3@illinois.edu

Website: http://allen.matse.illinois.edu

Primary CNF Tools Used: Photolithography (aligner, developer, spinner, baking), e-beam evaporator, Oxford RIE, wet etching hood, NH3 image reversal chamber

Abstract:

Approaching the ultimate lower limits of material sizes provides a unique path for designing new functional materials with extraordinary properties [1-7]. We demonstrate the first systematic synthesis [1] and characterization [2] study of a wide range of highly ordered silver alkanethiolate ($AgSC_n$, *n* = 1-16) aliphatic lamellae. Two-dimensional (2D) materials generate "golden nuggets" in nanoscience — materials exhibit extraordinary properties when their dimensions approach the ultimate scale limits. Graphene shows remarkably high electrical conductivity as compared with its "multilayer parent" — graphite. Indium nanoparticles show discrete "magic size" melting when their radii are smaller than 10 nm [2,3]. The quantum-size effect predicts the opening of band gaps in metal particles with decreased sizes. Metal-thiolate lamellae are currently of increasing scientific and technological interest, which has arisen from the other two more widely studied organometallic systems: self-assembled monolayers (SAM) and monolayer protected clusters (MPC or 3D SAM). The two-dimensional (2D) nanoconfinement of metal-aliphatic layers is fostering potential applications in lithography, nanoelectronics, biophysics and liquid crystals [6].

Summary of Research:

Synthesis [1] of single crystalline multilayer of ultimate-limit $AgSC_n$ is accomplished using a modified solution reaction method. Hot toluene recrystallization and/or Ostwald ripening enhances the structural ordering of the lamellar crystals. This work approaches the chain length limit of aliphatic lamellae by synthesizing highly ordered $AgSC_n$ (*n* = 1-3) with extremely short chains. All lamellae form single crystals with well-registered interlayer interfaces, similar to other alkyl-based lamellae but different from polyethylene lamellae. $AgSC_2$ with a layer thickness of 1.08 nm is the thinnest organometallic layer ever reported.

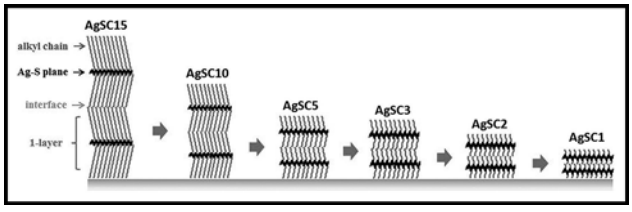

Figure 1: Schematic shows the methodology used in this research. The ultimate size limit of $AgSC_n$ lamellae is approached by systematically shortening chain lengths from $AgSC_{15}$ to $AgSC_1$ using a new synthesis method. Single layer or multilayer crystals can be formed having an Ag–S central plane with alkyl chains extending on both sides. Interlayer interfaces that form between adjacent layers exert extraordinary control over physical (e.g. melting) properties.

The composition, morphology, decomposition and structure of the lamellae are comprehensively studied. A new method quantifies the composition of the residual Ag and Ag_2S contents after the decomposition of the $AgSC_n$: all of the Ag, none of the C and a fraction of the S remain in the residue. The structural orderings of the $AgSC_n$ crystals, which are probed by electron diffraction for the first time, are characterized in terms of chain conformation, interlayer lamellar ordering and intralayer lattice ordering. All $AgSC_n$ (*n* = 2-16) layers, except for $AgSC_1$, possess a common lattice packing and the same inorganic network structure.

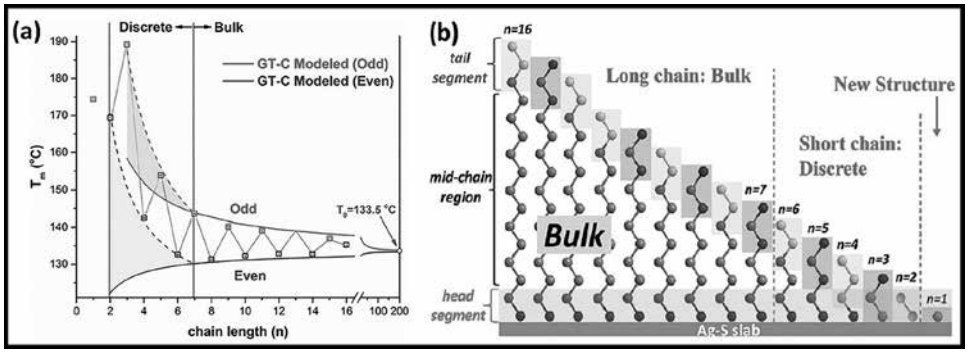

Figure 2: (Left) Plot of size dependent melting temperature vs chain length of $AgSC_n$. (Right) Schematic visualization of chain length dependent segmentation of alkyl chains: (1) gray atoms: mid-chain region, (2) dark/light [red] atoms of head segment, and (3) dark/light [blue/green] atoms off tail segment in odd/even chains. Critical length occurs for length n_{cr} = 7.

Characterization [2] of the short-chained $AgSC_n$ shows anomalous changes of physical properties in an abrupt bulk-to-discrete transition in layered silver alkanethiolate ($AgSC_n$, n = 1-16). A critical chain length of n_{cr} = 7 marks the sharp boundary between the bulk (uniform, $n \geq 7$) and discrete (individualistic, $n \leq 6$) forms of $AgSC_n$. Solid-state 13C NMR analysis reveals that none of the carbons share identical chemical environment in the discrete range, making each $AgSC_n$ with n = 2-6 uniquely different material, even though the crystal structure is preserved throughout. Extraordinary changes of thermodynamic properties appearing at this bulk-to-discrete transition include ~ 500% increases of melting enthalpy (ΔH_m), ~ 50°C increases of melting point (T_m), and an atypical transition between size-dependent T_m depression and T_m enhancement.

We develop a new comprehensive Gibbs-Thomson model with piecewise excess free energy (ΔG_{excess}) to predict the nature of the abrupt size effect melting. A new 3D spatial model is constructed to divide the aliphatic chains of $AgSC_n$ into three bulk or discrete segments: (a) tail segment containing three carbons, (b) head segment containing two carbons, and (c) bulk mid-chain segment containing (n - 5) carbons. Odd/even effect of T_m and DH_m is described by a constant ΔG_{excess} over the entire chain length range of $AgSC_n$ and is exclusively attributed to the localized tail segment. Bulk-to-discrete transition occurs when material properties are dominated by the discrete head and tail segments at $n < n_{cr}$. Values of n_{cr} are independently measured by both calorimetry and 13C NMR. This analysis is generalized to other aliphatic layers including n-alkanes with $n_{cr} \approx 11$.

This work is seminal to the design of novel aliphatic layers with tailorable properties (e.g., T_m) and has applications in molecular electronics [7] and biophysics.

References:

[1] Z. Ye, L. de la Rama, M. Y. Efremov, J-M. Zuo, L. H. Allen, "Approaching size limit of organometallic layers: synthesis/characterization of ultra-short chain lengths $AgSC_n$", Dalton Trans. 2016, 45, 18954-18966.

[2] Z. Ye, L. de la Rama, M. Y. Efremov, J-M. Zuo, A. Sutrisno and L. H. Allen, "Critical Size for Bulk-to-Discrete Transition Aliphatic Layers: Calorimetry Solid-state ^{13}C NMR" J. Phys. Chem,-C, 2017, in press.

[3] M.Y. Efremov, E. A. Olson, M. Zhang, F. Schiettekatte, Z. Zhang, and L. H. Allen; "Ultrasensitive, fast, thin-film differential scanning calorimeter" Review of Scientific Instruments, 2004. 75(1): p. 179.

[4] L. Hu, L. de la Rama, M. Y. Efremov, Y. Anahory, F. Schiettekatte, L. H. Allen; "Synthesis and Characterization of Single-Layer $AgSC_n$ Lamellar Crystals" J. Am. Chem. Soc., 133 4367 (2011) http://pubs.acs.org/doi/abs/10.1021/ ja107 817 x.

[5] S. L. Lai, J. Y. Guo, V. Petrova, G. Ramanath and L.H. Allen; "Size-dependent melting properties of small Tin particles: Nanocalorimetric measurements", Phys. Rev. Lett. 77, 99 (1996). http://prl.aps.org/abstract/PRL/v77/i1/p99_1.

[6] de la Rama, L.P., et al., "Size Effect and Odd-Even Alternation in the Melting of Single and Stacked $AgSC_n$ Layers: Synthesis and Nanocalorimetry Measurements" J. Am. Chem. Soc., 135, 14286 (2013). http://pubs.acs.org/doi/abs/10.1021/ ja40 599 58.

[7] Z. Ye, Z. Ma and L.H. Allen, Chapter 20. "Application of *in situ* resistance and Nanocalorimetry measurements for nanoelectronic TF materials", Metrology Diagnostic Techniques Nanoelectronics, ISBN 978-981-4745-08-6,1013 (2016).

Transferable Gyroidal Mesoporous Resin/Carbon Thin Films as Potential 3D Templates

CNF Project Number: 1356-05

Principal Investigator: Ulrich Wiesner

Users: Qi Zhang, Fumiaki Matsuoka, Peter Beaucage

Affiliation: Department of Materials Science and Engineering, Cornell University

Primary Sources of Research Funding: Defense Threat Reduction Agency (DTRA) funding # HDTRA1-13-C-0003; National Science Foundation Single Investigator Award (DMR-1409105); NSF Graduate Research Fellowship Program (DGE-1650441)

Contact: ubw1@cornell.edu, qz224@cornell.edu, fm388@cornell.edu, pab275@cornell.edu

Website: http://wiesner.mse.cornell.edu/

Primary CNF Tools Used: VCA Optima contact angle measurement tool, CHA evaporator

Abstract:

In this work, we introduced two types of gyroidal mesoporous network structures in thin film form achieved via co-assembly of poly(isoprene)-*block*-poly(styrene)-*block*-poly(ethylene oxide) (ISO) and resorcinol/phenol formaldehyde resols. The structures are resistant to high temperatures provided an inert atmosphere. Tunable hydrophilicity was achieved by pyrolyzing at different temperatures. A transfer technique was developed for these mesoporous thin films in order to meet the requirement of different substrates depending on the type of application. For example, these gyroidal mesoporous resin/carbon thin films have great potential as templates for on-chip 3D batteries.

Summary of Research:

Materials with three-dimensional (3D) network structures have seen great potential in photonics [1,2] and mechanics [3,4] related applications. However, direct fabrication of these 3D structures is often challenging due to materials limitations under suitable processing conditions. As a result, 3D porous templates are typically employed [1]. In this work 3D gyroidal mesoporous resin (GMR) thin films were obtained using ISO terpolymer directed resorcinol/phenol formaldehyde resols. Block copolymer self-assembly enables access to 3D structures with periodicities below 100 nm. Resorcinol or phenol formaldehyde resols as a carbon precursor provide structure stability at high temperatures or in severe processing environments.

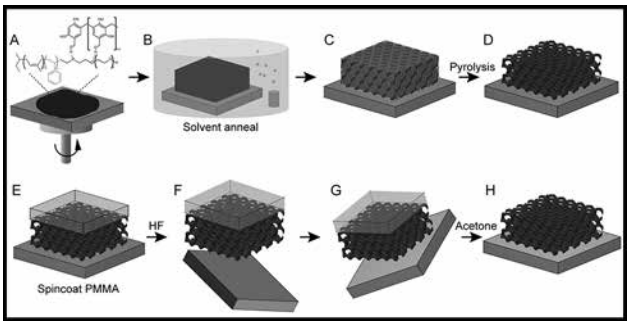

Figure 1: Illustration of fabrication and transfer procedures of mesoporous gyroidal resin thin films.

The formation steps of GMR thin films with either alternating gyroid or double gyroid structure are illustrated in Figure 1A-D. A solution mixture of ISO block copolymer and resorcinol/phenol-formaldehyde resols was first spin-coated onto a Si wafer resulting in a thin film with a thickness of around 500 nm (Figure 1A). The as-spun film was then solvent annealed to achieve the desired structure (Figure 1B,C). The block copolymer-resol hybrid film was then brought to 110-120°C to thermally crosslink the resols. Lastly, a heat treatment at 450°C under inert atmosphere further condensed the crosslinked resols into a polymeric resin material while decomposing the structure directing block copolymer, ISO, resulting in the desired GMR thin film (Figure 1D).

These highly ordered GMR thin films could be transferred onto different substrates (Figure 1E-H). To that end PMMA was spin-coated on top of the GMR thin film as protective layer while the native oxide layer of the Si substrate served as a sacrificial layer. (Figure 1E) Buffered oxide etch (BOE) 6:1 solution delaminated the thin film from the substrate by gradually etching away the sacrificial layer, leaving the thin film floating on the solution surface (Figure 1F). The desired substrate was then used to scoop out the floating thin film (Figure 1G). The transfer process was completed by removal

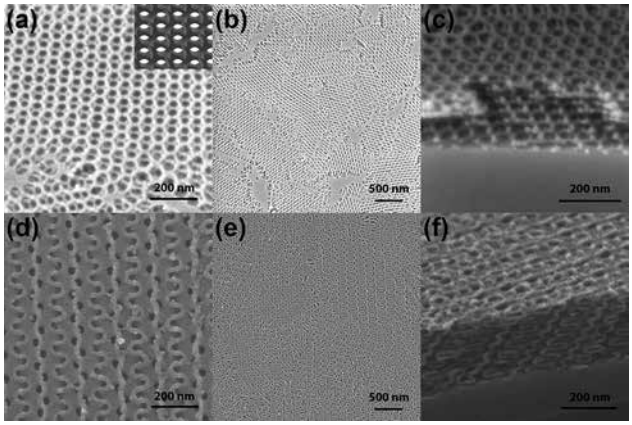

Figure 2: SEM characterization of (a-c) alternating and (d-f) double gyroidal mesoporous resin thin films.

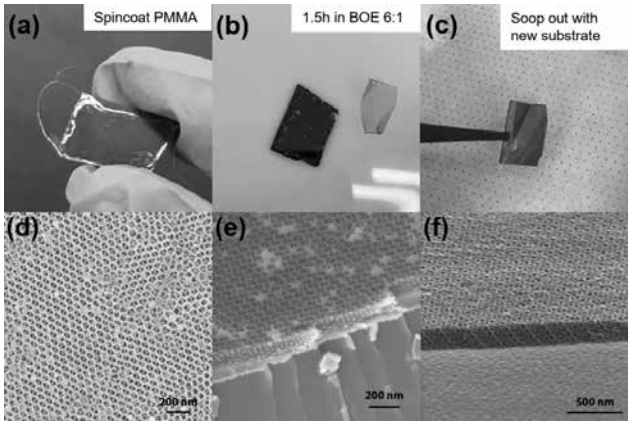

Figure 4: Photos of transfer process (a-c) and SEM characterization of G^AMR and (d-f) G^DMR thin films after transfer onto gold coated substrates.

of the PMMA layer through soaking the film in acetone overnight (Figure 1H).

Scanning electron microscopy (SEM) characterization of the two types of GMR thin films with alternating gyroid (G^AMR) and double gyroid (G^DMR) structures are shown in Figure 2. Figure 2A-C show top surface morphology, grain structure and cross-section of a G^AMR thin film. The highly-ordered pattern observed in the top surface SEM in Figure 2A is the <110> face of the alternating gyroid. Figure 2D-F displays top surface morphology, grain structure, and cross-section of a G^DMR thin film. The top surface SEM in Figure 2D shows the <211> face with double wavy pattern characteristic for the double gyroid morphology.

The advantage of GMR thin films generated in this work in comparison to previously reported polymer based films is that such resin-based materials can endure severe processing environments such as nonoxidative strong acids, and can withstand very high temperatures under inert atmospheres.

GMR thin films have tunable hydrophilicity when pyrolyzed at different temperatures. Contact angle measurements were taken for dense resin/carbon thin films (Figure 3a) and alternating gyroidal mesoporous resin/carbon thin films (Figure 3b) treated at different temperatures. Both sets of data indicate an increase in hydrophilicity as the pyrolysis temperature increased. Tunable hydrophilicity is beneficial to material deposition into the small meso-scale pores by matching the surface energy of the templates to that of the back-filling material.

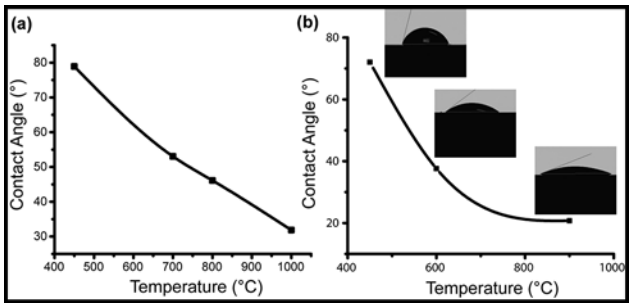

Figure 3: Contact angle measurements at different temperatures of (a) dense resin/carbon thin films and (b) alternating gyroidal mesoporous resin/carbon thin films.

Figure 4 shows photos of the transfer process (Figure 4a-c) described before and SEM images of GMR thin films after transfer onto new substrates, i.e., a gold coated wafer. Top surface and cross-sectional images (Figure 4d-f) confirm that both G^AMR and G^DMR structures were maintained after being transferred onto the gold coated wafer. The ability to transfer such films onto any desired substrate expands the back-filling choice even further, and also has a crucial influence on the final templated film quality if epitaxial growth is involved. Together with the tunable hydrophilicity and high temperature resistance, the GMR thin films reported in this work present a new platform to explore the 3D templating potential of highly ordered network structures on the sub-100 nm length scale.

References:

[1] P. V. Braun, Materials chemistry in 3D templates for functional photonics. Chem. Mater. 26, 277-286 (2013).

[2] K. Hur, Y. Francescato, V. Giannini, S. A. Maier, R. G. Hennig, U. Wiesner, Three-Dimensionally Isotropic Negative Refractive Index Materials from Block Copolymer Self-Assembled Chiral Gyroid Networks. Angew. Chem. Int. Ed. 50, 11985-11989 (2011).

[3] J. Bauer, A. Schroer, R. Schwaiger, O. Kraft, Approaching theoretical strength in glassy carbon nanolattices. Nat. Mater. 15, 438-443 (2016).

[4] J. H. Lee, J. P. Singer, E. L. Thomas, Micro/Nanostructured Mechanical Metamaterials. Adv. Mater. 24, 4782-4810 (2012).

[5] T. H. Epps, E. W. Cochran, T. S. Bailey, R. S. Waletzko, C. M. Hardy, F. S. Bates, Ordered network phases in linear poly (isoprene-b-styrene-b-ethylene oxide) triblock copolymers. Macromol. 37, 8325-8341 (2004).

Nanostructured Polymer Brushes

CNF Project Number: 1757-09

Principal Investigators: Christopher K. Ober[2], Jürgen Rühe[3], Oswald Prucker[3]

Users: Wei-Liang Chen[1], Matthias Menzel[3]

Affiliations: 1. School of Chemical and Biomolecular Engineering, Cornell University; 2. Department of Materials Science and Engineering, Cornell University; 3. IMTEK, University of Freiburg

Primary Sources of Research Funding: National Science Foundation, Deutsche Forschungsgemeinschaft

Contact: ck03@cornell.edu, wc497@cornell.edu

Website: http://cober.mse.cornell.edu/index.html

Primary CNF Tools Used: ASML 300C DUV Stepper, AFM - Veeco Icon, Oxford PlasmaLab 80+ RIE System

Abstract:

The degrafting phenomena of polyelectrolyte brushes (PEBs) were studied under patterned conditions. PEBs with different monomers and linking groups were fabricated and their degrafing was compared under different degrafting temperatures. It is determined that the lateral relaxation of PEBs could effectively reduce the degrafting extent, and under certain brush configurations, the time scale of the polymer relaxation might be too long to have a significant effect. It is proven that the interplay between degrafting and relaxation determines the stability of the PEB.

Summary of Research:

Polyelectrolyte brushes have many applications including surfaces for anti-fouling, lubrication and charge transportation [1]. The specific properties of the PEBs originate from densely surface-attached polyelectrolyte chains that then contribute to high charge density. When immersed in an aqueous solution, the high osmotic pressure leads to strong stretching of the polymer chains and such configurations repel most adhering species. However, such stretching also enhances the hydrolysis reaction of the chemical group at the polymer-surface interface by so-called 'mechano-facilitated hydrolysis' and thus reduces the stability of the PEBs [2]. Many studies up to today focus on non-patterned polyelectrolytes where polymer chains are confined by their neighboring chains whereas in this study we focus on patterned PEBs, where polymer chains could relax into the free spaces created by patterning. It was expected that with the stress-relaxation provided the PEBs should experience less degrafting and thus help to gain deeper realization for the phenomena.

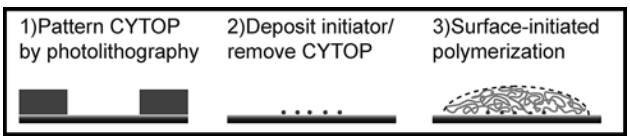

Figure 1: Process chart for the fabrication of the patterned PEB.

As shown in Figure 1, PEBs were synthesized by either radical-chain polymerization (RCP)[3] or Cu(0)-mediated living radical polymerization (CuLRP) [4]. Based on the differences between these two methods, the former method produces high molecular weight / low grafting density brushes while the latter makes brushes of low molecular weight / high grafting density. Patterned brushes were fabricated first by patterning fluorinated polymer, CYTOP (Asahi Glass) by photolithography. By taking advantage of the chemical orthogonality of the fluorinated polymer, which dissolves in neither hydrophobic nor hydrophilic solvents, the integrity of the pattern could be preserved during the initiator deposition process. Residual materials were removed and subsequently patterned brushes were obtained after polymerization. Patterned brush lines with width from 0.2 to 50 μm were then subject to degrafting test in water at different temperature for a given time. The cross-sectional areas before/after degrafting were captured using AFM in the dry state to evaluate degrafting.

The first test was conducted with poly{[2-(methacryloyloxy)ethyl]trimethylammonium chloride} (PMETAC) synthesized by CuLRP with a multi-linkage initiator. Such initiators could form more than one linkage to either the surface or other initiators and the stability would increase as a consequence. Figure 2 shows the area ratio of the brushes after the degrafting experiments for 24h at different pattern sizes. The

area ratio was defined as the cross-sectional area after degrafting over that before degrafting. It can be seen that the degrafting extent decreased as the pattern size shrank, which could be reasonably explained by the fact that more and more fraction of the brushes could relax into the free spaces at the smaller patterns. As temperature increased, the degrafting became more aggressive but the general trend did not change, which proved our hypothesis.

To further prove if the idea of lateral relaxation could be applied to PEBs with different configurations, patterned poly(4-methyl-vinylpyridinium iodide) (PMeVP) brushes were synthesized by CRP with a mono-linkage initiator that could form only single linkage to the surface. A similar degrafting test was conducted at room temperature (RT, 22°C). However, opposite degrafting trends were observed as shown in Figure 3 where more polymer chains degrafted at smaller pattern sizes.

In order to figure out the mechanism, PMeVP brushes were also synthesized by CuLRP with a similar initiator and tested. In Figure 4, it seems like that the degrafting trend does not change along different pattern sizes. Considering the difference between brushes synthesized by these two methods, the relaxation time of the FRP brushes should be longer than the other due to their high molecular weight ($\tau \sim M^3$). If the polymer relaxation rate is a lot slower than the degrafting rate, then the PEBs should degraft without even experiencing the effect of patterning, as we could see in the case of CuLRP synthesized PMeVP brushes.

In the case of CuLRP synthesized PMETAC brushes, the slow degrafting rate (24h) allows polymer relaxation to work against it and reduce the degrafting extent. Additional test at lower temperatures (14°C, 0°C) supports this hypothesis. As shown in Figure 3, when temperature went down, the degrafting trend at smaller patterns changed from more degrafting to less degrafting, showing the recovery of the stress relaxation as degrafting rate decreased. Similarly, Figure 4 shows the recovery of the stress relaxation at 0°C even though the scattering of the data at smaller patterns, which might be caused by the short degrafting time.

In its current stage, these data show that the degrafting of the PEBs is highly related to the dynamic of polymer relaxation. Thoroughly understanding these results could help to solve the puzzle in the mechanism of the PEB degrafting and it will be done in the ongoing study.

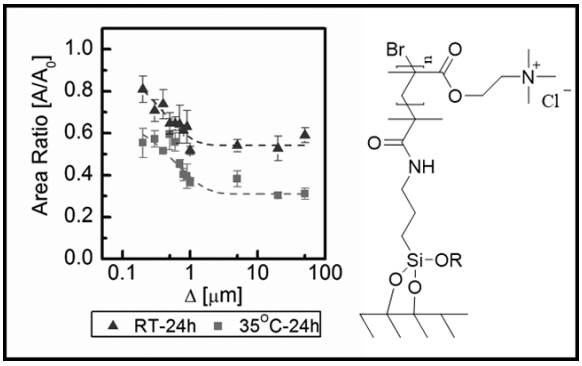

Figure 2: Degrafting condition of CuLRP synthesized PMETAC brushes.

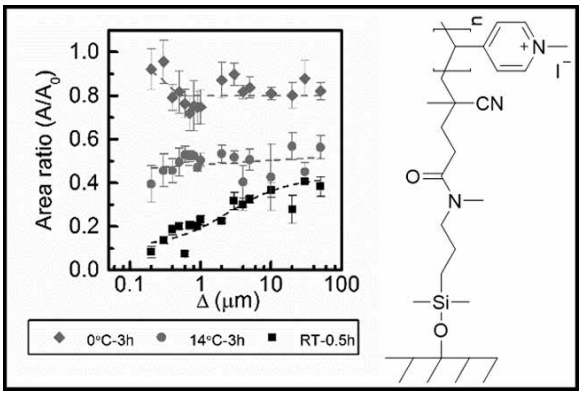

Figure 3: Degrafting condition of CRP synthesized PMeVP brushes.

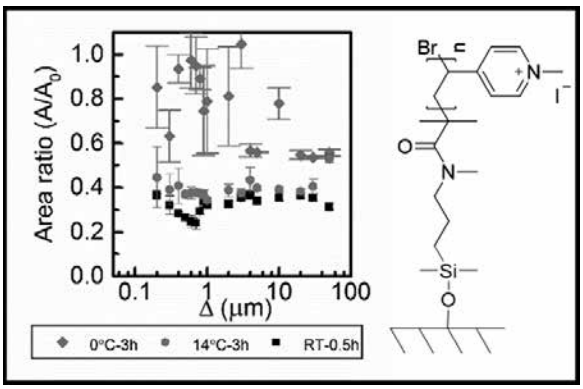

Figure 4: Degrafting condition of CuLRP synthesized PMeVP brushes.

References:

[1] Brittain, W., et al.; Polymer Brushes; 2004.

[2] Galvin, C. J.; Bain, E. D.; Henke, A.; Genzer, J. Macromolecules 2015, 48 (16), 5677-5687.

[3] Prucker, O.; Rühe, J. Macromolecules 1998, 31 (3), 592-601.

[4] Zhang, T.; Du, Y.; Müller, F.; Amin, I.; Jordan, R. Polym Chem 2015, 6 (14), 2726-2733.

Patterning of Liquid Crystal Elastomers

CNF Project Number: 1757-09
Principal Investigator: Christopher K. Ober
User: David Ditter

Affiliation: Department of Materials Science and Engineering, Cornell University

Primary Sources of Research Funding: Deutsche Forschung Gemeinschaft (DFG), National Science Foundation (NSF)

Contact: cko3@cornell.edu, daditter@uni-mainz.de (dd529@cornell.edu)

Website: https://cober.mse.cornell.edu/

Primary CNF Tools Used: ABM contact aligner, Autostep i-line stepper, Heidelberg mask writer DWL 2000, P10 profilometer, optical inspection microscopes, Trion etcher, spin coater

Abstract:

Liquid crystal elastomers (LCEs) combine the properties of polymeric elastomers with the self-organization of liquid crystals. Their actuation capacities through the anisotropy-to-isotropy change of macromolecular chains make them a unique class of shape memory materials. Since they show greater actuation, but smaller forces than piezo-materials and have a speed advantage compared to stimuli-responsive hydrogels, because no mass transport of solvent is needed, LCEs are a promising alternative in microelectromechanical systems (MEMS) [1,2]. In this work we want to present a method to structure 300-3500 nm thick LCE films in the micrometer range. Therefore, we developed a multilayer spin-coating process. A water soluble sacrificial layer, a photoalignment layer and a previous described LCE formulation [3], consisting of a liquid crystal monomer (4'-acryloyloxybutyl-2,5-(4'-butyloxybenzoyloxy)benzoate), a crosslinker (1,6-hexanediol diacrylate) and an initiator (diphenyl(2,4,6-trimethylbenzoyl)phosphine oxide), were spin-coated on top of each other. The LCE formulation was heated to its liquid crystal phase and polymerized by ultraviolet (UV)-light. The resulting LCE films showed reversible three-dimensional bending and twisting and two-dimensional shrinkage and elongation actuations up to 50% between 90 and 120°C in dependence of their thicknesses. We could pattern the LCE layers in an oxygen plasma with a resolution of 1.5-2.0 µm in a photolithographic process. Up to 600-700 nm a similar to previous reported fluorinated positive photoresist layer [4], which is orthogonal to all other layers and for thicker films a hard mask process with hydrogen silsesquioxane (HSQ) as a hardmask was used for the procedure. To our knowledge, this is the first time that LCEs were patterned in a photolithographic process with such a precision.

Summary of Research:

Thicknesses and homogeneities of all spin-coated layers were analyzed by profilometry. Polyacrylic acid (PAA) was used as a watersoluble sacrificial layer and 40-100 nm thick layers of ROP108 from Rolic Technologies as a photoalignment layer. Roughness-values R_q of 4-6 nm and waviness-values W_t of 30-70 nm were measured after spin-coating of both layers. 300-3500 nm thick LCE layers, which were spin-coated on top of them, showed R_q-values of 150-250 nm and W_t-values of 20-150 nm. The alignment of the liquid crystal monomers was evidenced by polarized optical microscopy that showed an extinction of light when one of the polarizers was aligned with the monomers and transmission when the alignment axis was oriented at 45° to the crossed polarizers.

OSCoR 5001 (from Orthogonal, Inc.) fluorinated photoresist was used for the patterning of up to 600-700 nm thick LCE layers through spin-coating, UV-light irradiation in contact or non-contact mode, development, etching in an oxygen plasma and stripping of the photoresist. The orthogonality to the other layers was proofed since no effect on the homogeneities, no swelling of the LCE layers and no loss of alignment, which would have a negative effect on the actuation properties, was observed. In contact mode we could achieve a resolution of 5 µm and in non-contact mode of 1.5-2.0 µm (Figure 1).

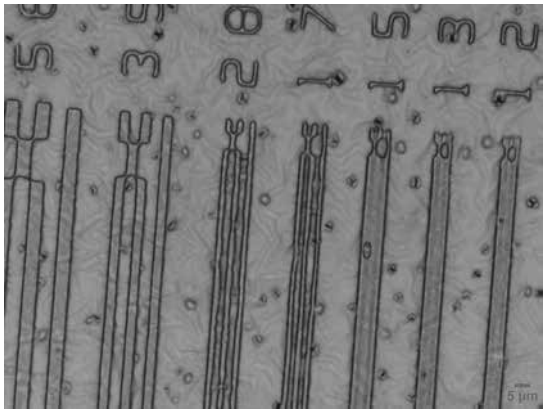

Figure 1: Resolution in non-contact mode.

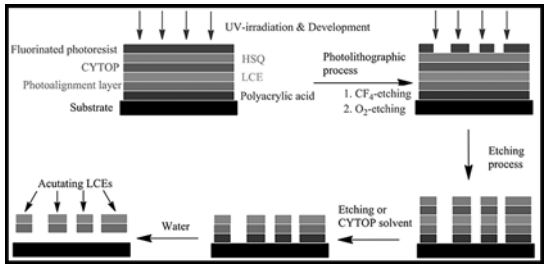

Figure 2: Hard mask spin-coating and patterning process.

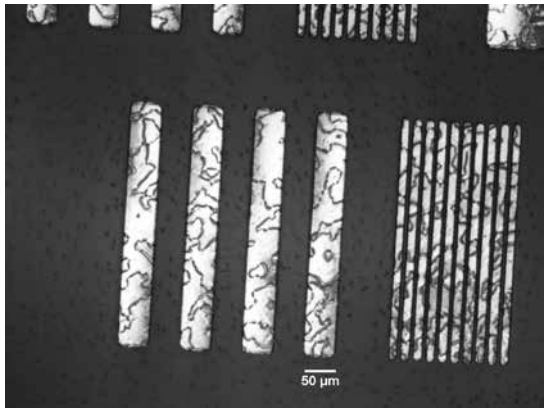

Figure 3: Example of patterning: LCE stripes patterned in contact mode.

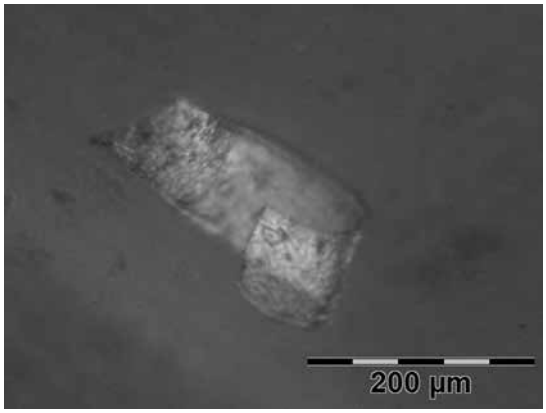

Figure 4: Bending motion of a LCE stripe.

Since there is a maximum thickness of 1.5 µm for OSCoR 5001 photoresist and the etching rate of it (9.90 nm/s) is higher than the etching rate of the LCE material (4.25 nm/s) under the used oxygen plasma conditions, it was not possible to etch thicker films with this method. That is why we developed a hard mask process where cyclized transparent optical perfluoropolymer (CYTOP) as a second sacrificial layer was spin-coated on the LCE films and HSQ as a hard mask afterwards. OSCoR 5001 still worked as photoresist. After development HSQ was etched in a tetrafluoromethane plasma and CYTOP and LCE layers below were etched in an oxygen plasma afterwards without affecting the areas protected by HSQ. In a last step, we could remove CYTOP and HSQ either through etching or through dissolution of CYTOP in an appropriate fluorinated solvent. The whole process is shown in Figure 2.

We constructed LCE stripes with different thicknesses and with different orientations referred to the liquid crystal alignment director to investigate the actuation properties and actuation directions. One example of those LCE stripe structures is shown in Figure 3.

Last but not least, the LCE stripes were removed from the substrate by dissolution of the sacrificial layer in water and their actuation motions were investigated. In dependence of the alignment director, the stripes showed three-dimensional twisting and bending motions above one micron thickness. Thinner films did not show any actuations. Both is probably observed because the photoalignment layer that is still attached to the stripes works as a resistance. An example of a bending motion is shown in Figure 4.

However, no two-dimensional shrinkage and elongation motions could be observed anymore after the etching processes. We believe that fluorinated solvents could give the used LCE network a better mobility and thus a better alignment on their surfaces than before. That additional alignment gradient could explain the observed bending motions.

All in all, LCE films up to 3500 nm thickness could be synthesized and patterned with no mechanical spin coating, photolithographic and etching techniques in the micrometer range. In a next step, we are going to demonstrate the patterning process on possible applications like a replica of a human iris. Through this we want to bring LCEs a step closer to the use in MEMS devices.

References:

[1] C. Ohm, M. Brehmer and R. Zentel, Adv. Mater. 2010, 22, 3366-3387.

[2] H. Yang, G. Ye, X. Wang and P. Keller, Soft Matter 2011, 7, 815.

[3] D. L. Thomsen III, P. Keller, J. Naciri, R. Pink, H. Jeon, D. Shenoy, and B. R. Ratna, Macromolecules 2001, 34, 5868-5875.

[4] P. G. Taylor, J.-K. Lee, A. A. Zakhidov, M. Chatzichristidi, H. H. Fong, J. A. DeFranco, G. G. Malliaras, and C. K. Ober, Adv. Mater. 2009, 21, 2314-2317.

Nanotwins in Copper Thin Films

CNF Project Number: 2103-12
Principal Investigator: Shefford Baker[1]
User: Nathaniel Rogers[2]

Affiliations: 1. Department of Materials Science and Engineering,
2. Sibley School of Mechanical and Aerospace Engineering; Cornell University

Primary Source of Research Funding: National Science Foundation Grant DMR 1411024

Contact: spb14@cornell.edu, ngr27@cornell.edu
Website: https://baker.mse.cornell.edu/

Primary CNF Tools Used: MOS hood for wafer cleaning, AJA sputtering system

Abstract:

Reliable control of the properties of thin metallic films have enabled modern technologies such as satellites, various optical devices and microelectronics. A microstructural defect called a nanotwin has been proposed as having the unique ability of increasing a film's strength and ductility simultaneously, possibly opening a path to many new novel applications previously thought impossible. However, a quantitative understanding of nanotwin formation is lacking due to the absence of the careful systematic variation of process parameters during film growth. In this project, we varied the deposition power over a range of five Cu films on Si substrates to produce a corresponding change in deposition rate. Transmission electron microscope (TEM) images were taken of the cross section of one of these films that suggests that the average twin boundary spacing may be much lower than reported elsewhere in the literature. Further imaging of the remaining films will inform a predictive model of nanotwin formation that will enable engineers to build applications that take advantage of this unique material defect.

Summary of Research:

Thin metallic films are critical in many technologies from the optical coatings on the world's most advanced satellites to the processers that power the world's fastest supercomputers. Control of the structure of these thin films at the micro and nano scale allows engineers to design materials that meet the demanding property specifications that modern technological applications require. A microstructural defect known as a nanotwin has been proposed to produce a previously impossible combination of desirable properties, high strength and high ductility [1]. While many have published results exploring the properties of nanotwined materials, the origins and control of these defects (and thus the properties of the films they inhabit) remain elusive.

In this project, we have developed methods to systematically vary the nanotwin density in sputtered copper thin films so that variations in deposition parameters can inform a quantitative model that describes nanotwin formation. 525 μm thick, 4-inch diameter silicon wafers with an RCA Clean (without HF) were used in the AJA Sputter System as a substrate for the films. The film stack consisted of an approximately 100 nm Ta diffusion barrier that was sputtered at 400W at an Ar gas pressure of 20 mTorr for 261 seconds, followed by a Cu layer sputtered at either 400, 325, 250, 175, or 100 W at an Ar gas pressure of 3 mTorr for 1.5, 5400, 7200, 9000, or 10,800 seconds (1.5, 2.0, 2.5, or 3.0 hours). A separate witness sample, patterned with photoresist was also exposed with each sample, so that the thickness of each film could be better estimated. While all of the films will be examined with a transmission electron microscope (TEM), only the 400W Cu film has been imaged at the writing of this report.

Figure 1 shows a cross section of the 400 W Cu film imaged via TEM. The growth direction of the film extends from the top left corner of the imaged towards the bottom right. The material region in the top left of the film is the Si substrate. It is separated from the Cu film that takes up the bulk of the image by a thin dark stripe. This stripe is the Ta diffusion barrier. Within the Cu film, there appear to be large grains that have gown close to the Ta layer and have spread rightward towards the surface of the film. Near the surface, small grains can be barely made out. Figure 2 is a magnified image of one of these grains. The orientation of the image in Figure 2. Is the same as that of Figure 1. The growth direction of the film proceeds from the top left to the

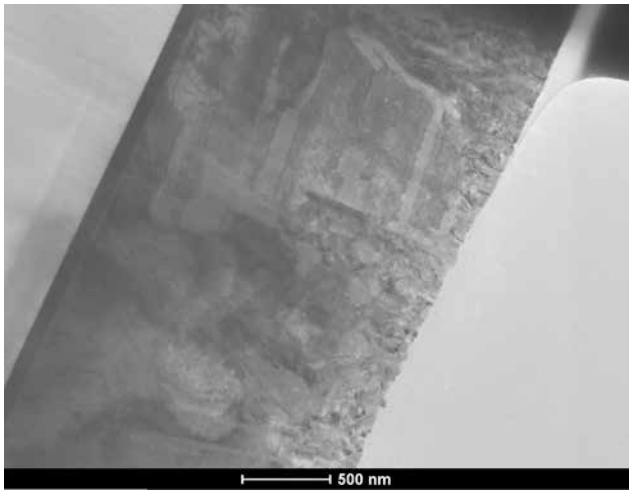

Figure 1: TEM cross section of Cu film sputtered at 400 W. Si substrate and Ta diffusion barrier are visible on the left side of the image. The growth direction of the film is thus from the top left of the image towards the bottom right. Note that large twinned grains seem to have grown from near the Ta layer up through the film towards the newer grains near the surface on the right.

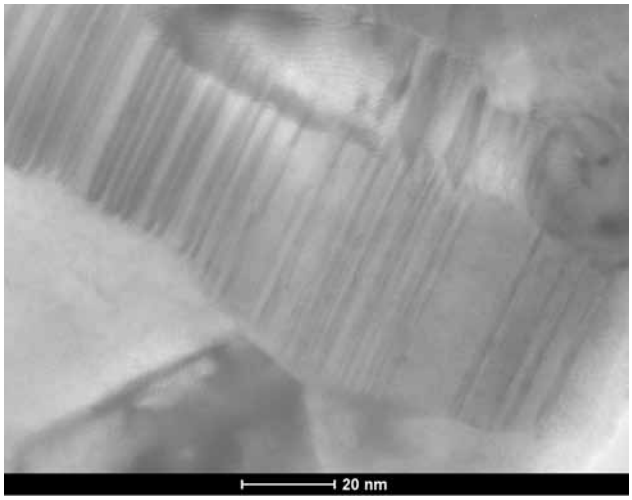

Figure 2: A magnified TEM image of one of the small grains near the surface of the Cu film visible in Figure 1. This image shows coherent twin boundaries (alternating dark and light striped regions) that occur with an average spacing of about 1 nm or less.

bottom right of the image. It is therefore plain to see that in this magnified image of one of the smaller grains near the surface, there are many nanotwins that have grown perpendicular to the growth direction of the film. Judging by the alternating light and dark contrast regions, these nanotwins are very small, mostly 1 nm or smaller in size. This is smaller than what is reported elsewhere in the literature [2], and is important to compare with any observed nanotwins in the four other copper films.

If a correlation between twin boundary spacing and deposition rate (via sputter power) can be quantitively determined, this could provide enough information to develop a predicative nanotwin formation model useful for the development of novel thin film technologies that exhibit both high strength and high ductility.

References:

[1] Shen, Y. F., Lu, L., Lu, Q. H., Jin, Z. H. and Lu, K. Tensile properties of copper with nano-scale twins. Scr. Mater. 52, 989-994 (2005).

[2] Zhang, X., et al. Enhanced hardening in Cu/330 stainless steel multilayers by nanoscale twinning. Acta Mater. 52, 995-1002 (2004).

MBE Selective Area Growth of N-polar GaN Nanowires

CNF Project Number: 2470-16
Principal Investigator: Dr. Debdeep Jena
User: Alexander Chaney

Affiliation: Department of Electrical Engineering, Cornell University
Primary Source of Research Funding: LEAST
Contact: djena@cornell.edu, aac227@cornell.edu
Primary CNF Tools Used: JEOL 6300, Oxford 81 RIE, CVC SC4500 e-gun evaporation system

Abstract:

In this work, the impact of various growth parameters, and titanium (Ti) mask preparation on the selective area growth (SAG) of GaN nanowires by plasma-assisted molecular beam epitaxy (PAMBE) is discussed. By varying the substrate temperature, highly selective nanowire growth was found to occur for substrate temperatures near 915°C. Adjusting the V/III ratio provided control over the lateral growth rate of the nanowires, with the smallest rate being 1 nm/hr for a V/III ratio of six. Changing the N_2 flow rate gave control over the vertical growth rate. The highest rate of 94 nm/hr was achieved using a flow rate of 2.5 sccm. Finally, improper Ti etch conditions lead to the formation of fluoropolymers that prevent SAG.

Summary of Research:

The growth of gallium nitride (GaN) nanowires has historically been achieved through a self-aligned process using silicon (Si) as a substrate [1]. Since then, growth has moved to a multitude of substrates including SiO_x [2] and Ti [3]. However, there is no direct control over the uniformity and diameter of the grown wires. SAG solves this by using a mask to limit the growth of wires to pre-defined regions giving complete control over all aspects of the nanowires.

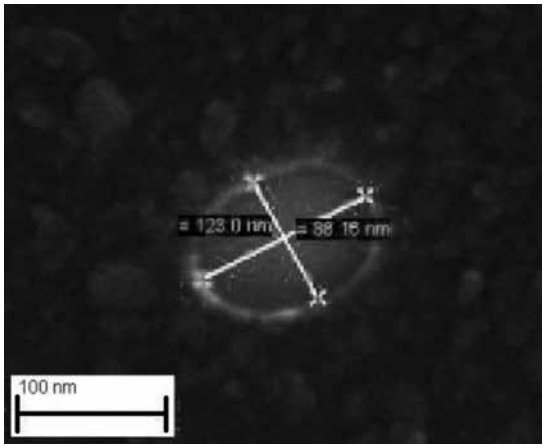

Figure 1: SEM of hole in Ti mask post RIE etch. Oblong shape is owed to slight charging during e-beam exposure.

Patterning of the mask began with evaporation of 7 nm of Ti onto bulk N-polar GaN substrates via the CVC evaporator. Following metal deposition, a mask consisting of holes and lines (for wires and fins, respectively) is defined using electron beam lithography. Use of the JEOL 6300 enabled holes of diameters down to 20 nm to be made. Lastly, the Ti was etched using CF_4 chemistry in the Oxford 81 RIE system. Figure 1 shows a hole that is formed in the Ti.

PAMBE growth of the nanowires was done in a Veeco Gen Xplor system. Ga atoms were provided by an effusion cell, while atomic nitrogen was supplied from a remote RF plasma source. Prior to growth, samples were nitridated at 400°C for 10 minutes. Growth proceeded at temperatures ranging from 880-925°C, under nominally nitrogen rich conditions. In this work, the V/III ratio is defined as the impinging active N flux divided by the impinging Ga flux, both measured as partial pressure. Plasma power was held constant at 400 W for all growths.

For substrate temperatures below 900°C, all selectivity in the growth was lost as the Ga adatoms not involved in the nanowire growth do not have sufficient energy to desorb before nucleating on the Ti mask. Increasing T_{sub} past 900°C enabled selective growth. At, 925°C or higher, the nanowires experience incomplete growth

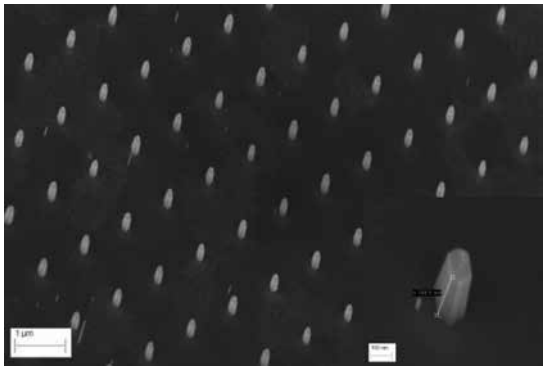

Figure 2: SEM of wires grown with a growth temperature of 915°C, a V/III ratio of 10 and a nitrogen flow of 2.5 sccm. Inset shows wire height of 188 nm after two hours of growth.

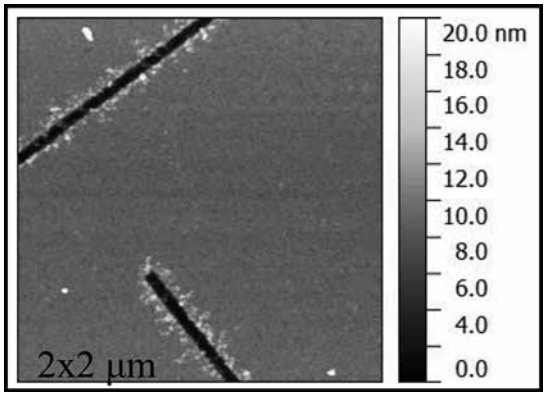

Figure 3: AFM of Ti mask following RIE etch. High areas near etch edge show post-etch fluoropolymers due to improper etch conditions.

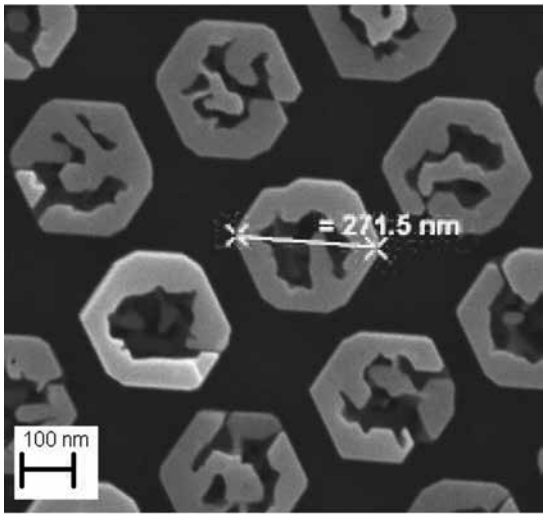

Figure 4: SEM after growth on sample where Ti etch conditions left post-etch residue. Original hole diameter was 180 nm.

as the GaN decomposition rate exceeds the growth rate. Ideal growth conditions were found to occur at 915°C, shown in Figure 2. It can be seen that the growth is limited to only those locations where there is a hole in the Ti, with the mask itself seeing little to no parasitic growth.

Increasing the V/III ratio from 6 to 12 led in a decrease in the wire lateral growth rate from 15 nm/hr to 1 nm/hr. Changing the N_2 flow rate directly affects the vertical growth rate. A flow of 1 sccm resulted in a rate of 50 nm/hr, and increasing the flow to 2.5 sccm increased the rate to 94 nm/hr. As higher N_2 flow rates create larger growth chamber pressures, 1.8×10^{-5} torr at 1 sccm vs 2.3×10^{-5} at 2.5 sccm, the desorption of Ga is suppressed, increasing its diffusion length on the Ti, which translates to higher Ga incorporating into the wire.

During the RIE etching of the mask, if the etch conditions are not ideal, fluoropolymers will form at the etch edge, leading to a local increase in the surface roughness, shown in Figure 3. This local roughening severely limits the adsorption of Ga into the etched hole, causing Ga to pool at the edge instead. During growth, this accumulation of Ga serves as a nucleation site, leading to the ring like shape that is shown in Figure 4. At this point SAG cannot be recovered.

In conclusion, PAMBE SAG of GaN nanowires was achieved using a 7 nm Ti mask. By fine tuning the growth conditions, a vertical growth rate of 94 nm/hr was obtained while lateral growth rates were suppressed to 1 nm/hr resulting in ~ 200 nm tall wires that are 74 nm in diameter. These thin wires will enable strong electrostatic control in FETs while enabling high quality tunneling based devices due to their intrinsic high material quality.

References:

[1] M. A. Sanchez-Garcia, E. Calleja, E. Monroy, F. J. Sanchez, F. Calle, E. Munoz, and R. Beresford, "The effect of the III/V ratio and substrate temperature on the morphology and properties of GaN- and AlN-layers grown by molecular beam epitaxy on Si <111>," J. Cryst. Growth, vol.183, pp. 23-30, 1998.

[2] S. Zhao, M. G. Kibria, Q. Wang, H. P. T. Nguyen and Z. Mi, "Growth of large-scale vertically aligned GaN nanowires and their heterostructures with high uniformity on SiO_x by catalyst-free molecular beam epitaxy," Nanoscale, vol. 5, pp. 5283-5287, 2013.

[3] G. Calabrese, P. Corfdir, G. Gao, C. Pfüller, A. Trampert, O. Brandt, L. Geelhaar, and S. Fernández-Garrido, "Molecular beam epitaxy of single crystalline GaN nanowires on flexible Ti foil," Appl. Phys. Lett, vol. 108, 202101, 2016.

Nanotube Transistor Arrays on a TEM Substrate

CNF Project Number: 2486-16, 900-00

Principal Investigators: Jonathan S. Alden, Paul L. McEuen

Users: Jonathan S. Alden, Alejandro J. Cortese

Affiliations: Esper Biosciences Inc.; Department of Physics, Cornell University

Primary Sources of Research Funding: National Institutes of Health, National Science Foundation

Contact: jonathan.alden@gmail.com, mceuen@ccmr.cornell.edu, ajc383@cornell.edu

Primary CNF Tools Used: Low pressure chemical vapor deposition (LPCVD) furnaces (oxide, nitride), Autostep i-line stepper, ABM contact aligner, SC4500 Evaporators, Oxford 80 RIE

Abstract:

We use photolithography to fabricate nanotube transistor devices on substrates with thin nitride windows, which can be imaged using transmission electron microscopy (TEM). Our device architecture permits us to characterize a given nanotube both electrically, and by high-resolution TEM. In low-dimensional systems, such as nanotubes, where nanoscale surface and defect structure can have profound influences on the electrical properties, we expect this combined nanoscale imaging and electrical characterization to yield insights that will inform the design of nanoscale sensors.

Summary of Research:

The study of low-dimensional materials, such as carbon nanotubes, graphene, and molybdenum disulfide, has been an area of growing interest over the past decades, in part due to their promise as molecular sensors. Due to their one-to-few-atom thickness, the properties of such materials often depend sensitively on surface adsorbates, substrate-surface interaction and defect structure.

Improving sample cleanliness, for example, enabled the first observations of spin-orbit coupling in carbon nanotubes [1] and, more recently, the fractal quantum Hall effect, known as Hofstadter's butterfly, in graphene [2]. In order to understand these nanoscale structures and subsequently design improved sensors, a device architecture is needed that combines the atomic-level characterization afforded by TEM with the electronics characterization ability enabled by a gated, transistor-like geometry. We demonstrate that we can produce arrays of gated nanotube sensors devices, with reasonably high yield that can be characterized afterwards by TEM. Our design also keeps parasitic capacitance from our electrodes to the highly resistive silicon substrate low enough to enable electronic measurements of our transistors at speeds up the MHz range.

We fabricate nanotube devices on TEM grids using a combination of photolithography and standard nanotube growth and transfer techniques [3]. Figure 1 shows one of such devices, having 26 source-drain electrode pairs and two top gates. Between a few of the electrode pairs are individual nanotubes, which have been transferred prior to the deposition of a gate dielectric, and top-gate. The device fabrication involves using nine masks to define the various structures, which have been designed to yield nanotube devices with good gating characteristics, as well as low capacitive coupling between nearby electrodes.

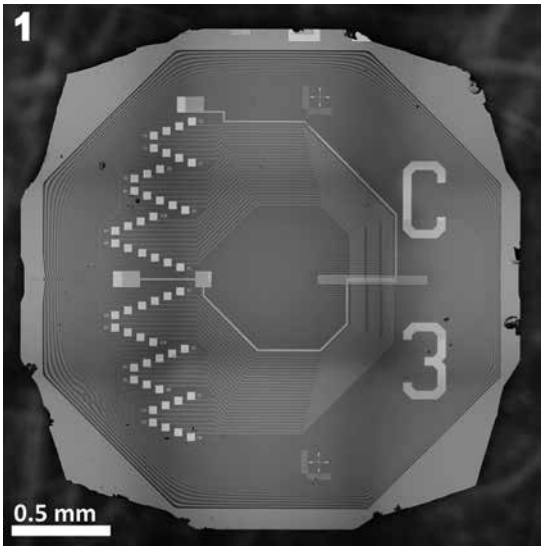

Figure 1: Optical image of microfabricated TEM grid with 26 pairs of source-drain electrodes, a top gate, and a thin nitride window for TEM imaging after top-gate is removed via chemical etching.

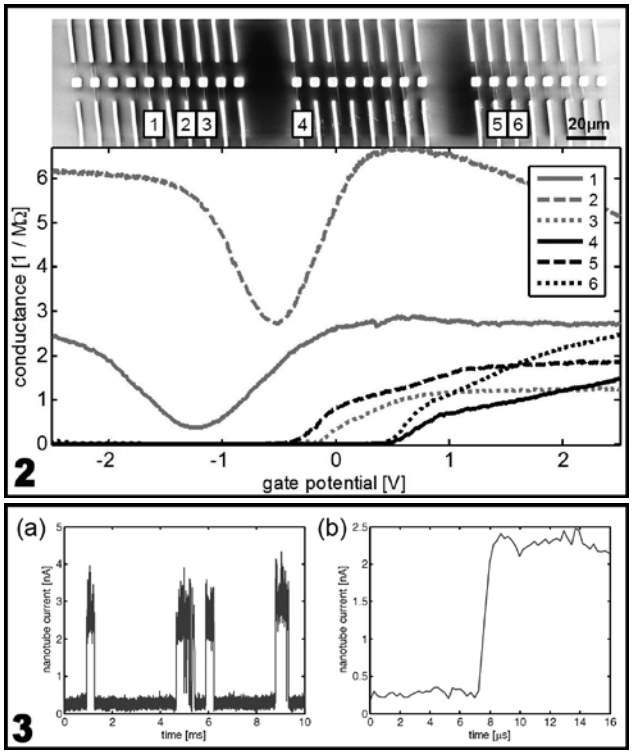

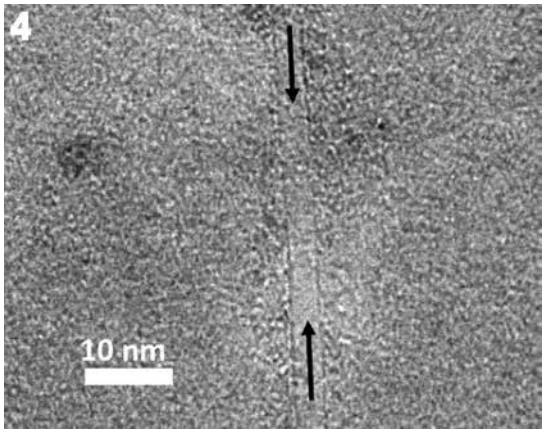

Figure 2, above left: Upper: Scanning electron microscope image of nanotubes between source-drain electrodes, passing over thin nitride windows. Lower: Corresponding conductance measurements as a function of top gate voltage showing six conducting nanotubes with varying characteristics.

Figure 3, left: High-speed measurement of nanotube random telegraph signal showing (a) fluctuations in nanotube current and (b) measured rise time of less than 1 μs.

Figure 4, above: TEM image of a nanotube imaged through a thin nitride window, after top-gate removal.

The outline of the fabrication procedure is as follows. We begin by using low pressure chemical vapor deposition (LPCVD) to deposit the low-stress nitride on a 300 μm-thick silicon substrate, which will ultimately become our TEM window. We later deposit electrodes, and use backside alignment followed by reactive ion etching (RIE) to expose rectangles on the back of the wafer which will later be used for a potassium hydroxide (KOH) through-etch. Arrays of parallel nanotubes are grown by CVD on a separate quartz substrate, coated with poly(methyl methacrylate) (PMMA), lifted off with KOH, and transferred onto the device substrate [3], where unwanted areas are patterned and etched using RIE. We use atomic layer deposition (ALD) to deposit a gate dielectric, after which we pattern and evaporate a gold top-gate. The surface is then coated with a KOH protection layer, and the devices are placed in hot KOH, which etches the silicon exposed on the back, to both release individual grids and to etch the silicon away from behind the nitride window. Later, the nanotube devices will be imaged through this window using TEM. The protection layer is then removed, and the grids are cleaned with oxygen plasma. Our fabrication process typically yields at least one electrically-connected, gated nanotube on 75% of the TEM grids.

Figure 2 shows an SEM image of nanotubes patterned between the source-drain electrode pairs, imaged prior to top-gate deposition. The squares in the center are thin nitride windows for low-background TEM imaging. After completion of the device fabrication, these nanotubes are characterized electrically, shown in the lower portion of Figure 2. All of these nanotubes can be gated to have resistance lower than 1MΩ (50kΩ/μm) showing that they have a low defect density, and good coupling to the top gate. Nanotubes 1 and 2 can be seen to be metallic, while nanotubes 3-6 are semiconducting.

Furthermore, we can probe the electrical characteristics at high speeds in the MHz range. Previous research has shown that single charge fluctuations in a dielectric can be detected by semiconducting carbon nanotubes as random telegraph signals [4]. As shown in Figure 3, our devices are also capable of measuring such signals, but at higher speeds with rise times less than 1 μs.

After characterizing the nanotubes electronically, we can etch away the gold top-gate, and image them by TEM to determine, for example, the nanotube diameter. Figure 3 shows one such nanotube, which can be seen to be single-walled (single dark lines running parallel to the arrows), and 4 nm in diameter (the width between those lines).

In principle, our fabrication procedure can be applied to many different CVD-grown low-dimensional materials with only minor modifications, and may lead to the development of improved nanoscale sensors capable of high-speed molecular sensing.

References:

[1] F. Kuemmeth, et al., Nature 452 448-452 (2008).
[2] C. R. Dean, et al., Nature 497, 598-602 (2013).
[3] L. Jiao, et al., J. Am. Chem. Soc. 130, 12612-12613 (2008).
[4] T. Sharf, et al., Nano Lett. 14 (9) 4925-4930 (2014).

Transient Fiber Mats of Electrospun Poly(Propylene Carbonate) Composites with Remarkable Mechanical Strength

CNF Project Number: 2489-16

Principal Investigators: Amit Lal, Christopher K. Ober

User: Alexander Ruyack

Affiliations: Electrical and Computer Engineering, Material Science and Engineering; Cornell University

Primary Sources of Research Funding: Defense Advanced Research Projects Agency (DARPA) project: Inbound, Controlled, Air-Releasable, Unrecoverable Systems (ICARUS)

Contact: amit.lal@cornell.edu, cko3@cornell.edu, arr68@cornell.edu

Primary CNF Tools Used: Zeiss SUPRA scanning electron microscope (SEM), Hummer Au/Pd sputtering system

Abstract:

Polymers with a triggered decomposition are attractive for an array of applications ranging from patterning to transient packaging materials as well as for environmental protection. This works UV and thermally triggered transience in fiber mats using poly(propylene carbonate) (PPC) composites. The electrospun PPC-composite fiber mats combine excellent decomposition performance (due to the high surface to volume ratio) with high stiffness and thus represent a new class of materials enabling innovative applications such as transient filter materials, short-time plant protection materials, as well as temporary lightweight materials for aerospace engineering. Thermally and UV-triggerable additives (protected acids or base) have been used in different concentrations to tune the transience performance of the fiber mats over a wide range (75-212°C). The addition of organo-modified clay (OMMT) enhanced mechanical stability and prevented shrinkage at room temperature. Different annealing methods have been used to improve the mechanical properties even further (tensile strength: 2-12 MPa, Young's modulus: 55-747 MPa) making these fiber mats attractive for a broad field of applications. An Ashby plot of Young's modulus versus degradation temperature for electrospun fiber mats is shown, revealing much lower degradation temperatures with higher moduli for PPC composites compared to other electrospun polymers.

Summary of Research:

We report novel electrospun transient fiber mats whose decomposition is triggered by UV irradiation and heat treatment. Beside a fast decomposition, these fiber mats also showed excellent mechanical strength. The latter is important for the major application of electrospun nonwovens as filter materials [1]. Furthermore, the transient properties demonstrated enables innovative vanishing filters for highly toxic materials. However, due to the high mechanical strength of these transient fiber mats further applications such as temporary plant protection materials in agriculture, packaging materials and lightweight materials for aerospace engineering can be envisaged. We recently demonstrated thin film decomposition of poly(propylene carbonate) (PPC) catalyzed with a thermal acid generator (TAG) or a photo acid generator (PAG) under mild conditions [2]. These findings along with the accessibility and mechanical toughness of PPC motivated us to produce transient fiber mats with this material. Inspired by the research of Jung, et al., on base-catalyzed hydrolyses of PPC [3], we also investigated the effect of a photo base generator (PBG) on the decomposition of PPC in addition to PAG and TAG. The ratio of acid or base generator to PPC has been varied to minimize the degradation temperature of the composite fiber mat.

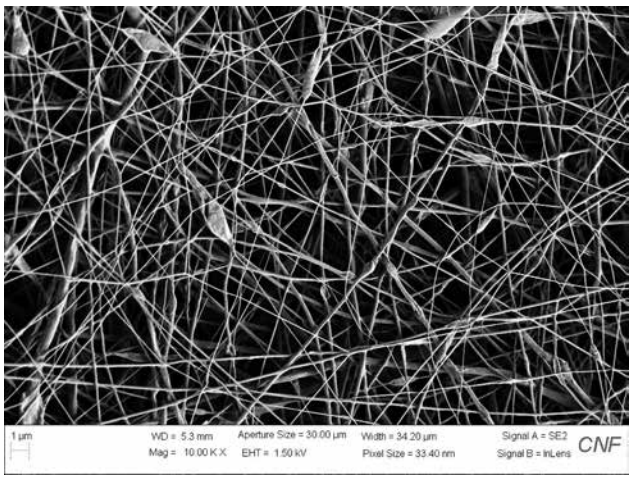

Figure 1: SEM image of electrospun PPC fiber mat with 10 wt.% PPC, 5% PBG, 10% clay.

Our studies on transient polycarbonate films imply that the mechanical strength of pure PPC fibers is probably still too low for many applications (e.g. transient filters), although the processing via electrospinning will influence mechanical stiffness due to polymer chain alignment. Organo-modified montmorillonite (OMMT) was selected to improve stiffness and to increase the glass transition temperature (T_g) of PPC in fiber mats. OMMT worked well for our PPC-composite films due to the preparation of the polymer/OMMT composite not requiring high temperatures (no release of the protected acids/bases). The amount of OMMT was kept to a minimum that guarantees stable fiber mats at room temperature without significantly affecting the decomposition temperature. Composite preparation, electrospinning conditions, as well as post-processing have been modified to tailor the mechanical properties of the PPC-composite fiber mats for the desired applications.

Blends from poly(propylene carbonate) with organo-modified montmorillonite (OMMT) and a thermal/UV-triggerable additive, which release either a strong acid or base, were electrospun successfully. The use of 5 wt% (relative to PPC) photo base generator, which releases the strong base TBD, reduces the thermostability of PPC significantly and enables the transience of PPC under relatively mild conditions. Fiber mats that have been irradiated with UV light (254 or 365 nm, for either 10 min before annealing or the entire time during annealing) showed full decomposition within 25 minutes at 75°C. Besides this behavior, the addition of OMMT enhances the mechanical stability and prevents shrinkage at room temperature. Tensile strength and Young's modulus were improved by pre-annealing of the spinning composition, electrospinning at ≥ 40°C as well as post-annealing of the fiber mats. Post-annealing showed the best improvement.

A 30 min post-annealing at 50°C while fiber mat remained on the collector plate covered by a thin aluminum plate showed no shrinkage or folding and led to a tensile strength of ~ 12 MPa and Young's modulus of ~ 747 MPa. Consequently, these transient composite fiber mats are suitable for a wide range of applications in the field of transient packaging materials, transient plant protection material, transient filter systems for toxic materials, and any application where a lightweight transient material with good mechanical strength is needed (e.g. in aerospace engineering).

SEM micrographs of 3 nm gold sputtered samples were captured on a ZEISS SUPRA 55VP SEM using the ZEISS SmartSEM software with an accelerating voltage of 1.5 kV and the SE2 detector. For additional information on solution preparation and spinning parameters, please contact the author.

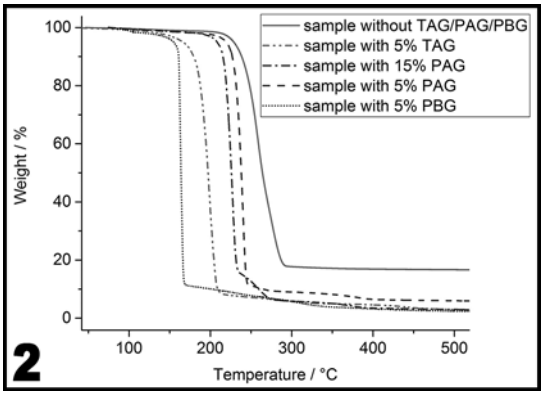

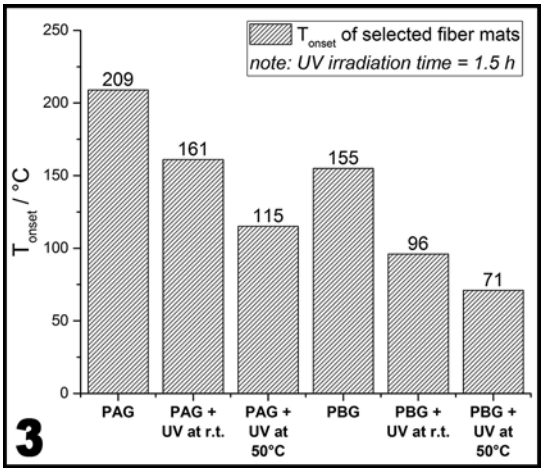

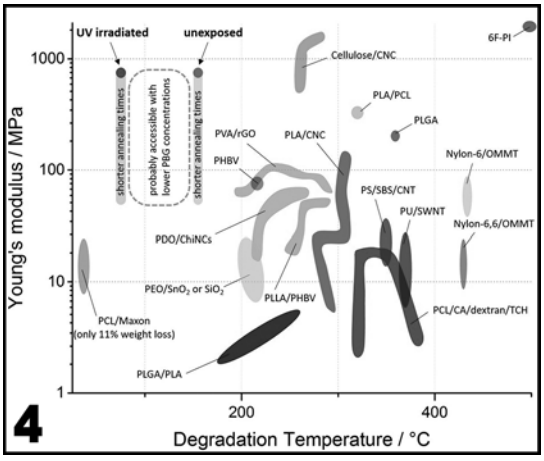

Figure 2: TGA traces of selected, unexposed PPC-composite fiber mats. All samples shown here contain 5% OMMT.

Figure 3: Tonset of unexposed and UV-irradiated (□ = 254 nm) fiber mats with 15% PAG and 5% PBG. UV-exposed fiber mats with lower amounts of PAG or higher amounts of PBG showed increased degradation temperatures.

Figure 4: Ashby plot of Young's modulus as a function of degradation temperature for electrospun fiber mats. PPC/OMMT/PBG fiber mats cover a huge area of materials with high stiffness and low degradation temperature.

References:

[1] Bognitzki, M., et al.; Nanostructured Fibers via Electrospinning. Adv. Mater. 2001, 13, 70-72.

[2] Camera, K., et al.; Transient materials from thermally-sensitive polycarbonates and polycarbonate nanocomposites. Polymer 2016, 101, 59-66.

[3] Jung, J. H.; Ree, M.; Kim, H. Acid- and base-catalyzed hydrolyses of aliphatic polycarbonates and polyesters. Catal. Today 2006, 115, 283-287.

Surface Morphology of Heavily Doped GaN-Based p-n Diodes

CNF Project Number: 2501-16
Principal Investigator: Debdeep Jena
User: Henryk Turski

Affiliation: Electrical and Computer Engineering, Cornell University
Primary Source of Research Funding: Department of Defense
Contact: djena@cornell.edu, henryk@cornell.edu
Primary CNF Tools Used: AFM, Veeco Icon

Abstract:

Studies were carried out to identify optimal growth conditions for GaN:Mg layers with high magnesium (Mg) concentrations. High quality p-type layers are essential part of standard light emitting diodes (LEDs) but also of tunnel junctions that can be used as an alternative way of highly resistive p-type contact on nitride-based LEDs. Investigated structures consisted of highly doped p- and n-type layers and were obtained by plasma-assisted molecular beam epitaxy.

Summary of Research:

White LEDs and blue laser diodes (LDs), obtained using nitrides heterostructures, have revolutionized optoelectronics [1]. Even though LEDs and LDs are now commercially mature, there are several possible new approaches to nitride structures that can prove to be revolutionary.

Presently, all industrial efforts are dedicated to crystal structures grown by metal-organic vapor phase epitaxy. Which has many commercial advantages over its counterparts, but has one major drawback. Due to the use of precursors, it cannot produce active p-type GaN layers overgrown with n-type material. Growth of subsequent layers, due to high hydrogen background, results in complete compensation of dopants in p-GaN layers below. This problem provoked the whole spectrum of emerging devices like: stacks of LEDs (possibly covering the whole visible light spectrum), tunnel junctions or hetero bipolar transistors, that require the p-type nitride layers to be covered with n-type layers. Fortunately, such structures can be grown by molecular beam epitaxy.

Two main parameters of p-type layers important for the use in tunnel junction structures are high enough p-type doping to assure thin depletion region to make the tunneling possible and smooth enough morphology to be able to grow subsequent layers.

Simple simulations of p-n junction with different doping concentrations indicate that n-type doping of 4×10^{19} atoms/cm^3 and p-type doping of 4×10^{19} atoms/cm^3 should result in depletion region thickness of less than 10 nm. To calibrate magnesium and silicon incorporation as a function of atomic fluxes and growth temperature, a calibration sample for second ion mass spectroscopy was grown. Conditions that allow for high enough Mg concentrations were identified in that way.

To investigate morphology of GaN:Mg layers that can be then applied in tunnel junctions three different samples were grown. Schematic structure of those layers is presented in Figure 1. It consists of 150 nm GaN:Si buffer layer follow by 100 nm GaN:Mg layers grown at different conditions. For the case of first sample GaN:Mg layer was grown at the same temperature as GaN:Si layer below (750°C) using rather high Mg flux that would result in Mg concentration of about 2×10^{19} atoms/cm^3. During the growth of the other two samples GaN:Mg layers were grown using much lower growth temperature (670°C) and indium instead of gallium as a surfactant that is known to enhance layers morphology at lower growth temperatures [2].

For the case of second and third samples, magnesium concentration was controlled by Mg atomic flux and was chosen to be at the level of 4×10^{19} atoms/cm^3 and 6×10^{19} atoms/cm^3, respectively.

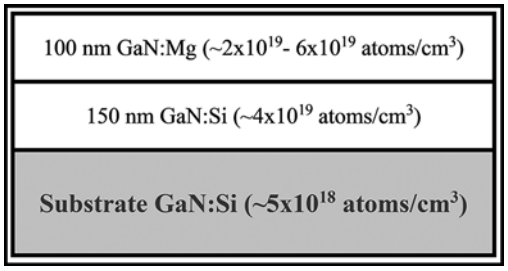

Figure 1: Schematic picture of the grown tunnel junction layers' structure. Next to layer composition concentration of specific dopant is indicated.

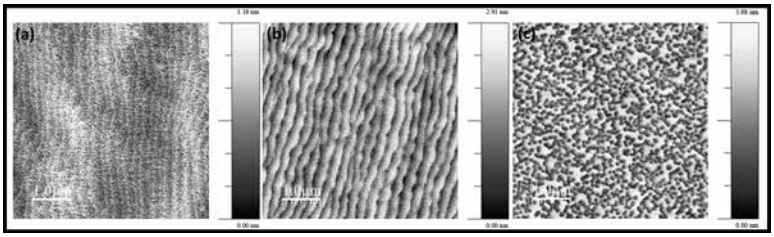

Figure 2: Surface morphology obtained by atomic force microscopy for sample with Mg concentration (a) 2 × 10^{19} atoms/cm^3, (b) 4 × 10^{19} atoms/cm^3, and (c) 6 × 10^{19} atoms/cm^3.

After the growth, samples were investigated using atomic force microscope available at CNF. Surface morphologies of obtained GaN:Mg layers are presented in Figure 2. Surface roughness measured as standard deviation of height obtained for those layers was (a) 0.2 nm, (b) 0.5 nm, and (c) 1.2 nm.

This way growth conditions that lead to Mg concentrations of 2-4 × 10^{19} atoms/cm^3 were identified as those that can be used in the growth of Mg layers for tunnel junctions with smooth surface morphology by molecular beam epitaxy.

References:

[1] S. Nakamura, S. Pearton, and G. Fasol, Measurement Science and Technology, 12(6) 755, 2001.

[2] J. Neugebauer, T. K. Zywietz, M. Scheffler, J. E. Northrup, H. Chen, and R. M. Feenstra, Physical Review Letters, (90) 056101, 2003.

CVD Graphene Growth on Copper and Refractory Metal Substrates

CNF Project Number: 2528-17

Principal Investigator and User: Brian J. Kennedy

Affiliation: Kennedy Labs

Primary Source of Research Funding: Self Paid

Contact: brian.kennedy@kennedylabs.tech

Website: www.kennedylabs.tech

Primary CNF Tools Used: CVD Equipment/First Nano graphene furnace for growth, Zeiss SEM and optical microscopes for characterization, wet benches for substrate cleaning

Abstract:

We used CNF's graphene furnaces to attempt direct CVD graphene growth on refractory metal and copper/refractory metal alloy substrates. Varying sizes and substrates thicknesses were deposited, with the goal of depositing graphene on refractory metal directly (copper was included for benchmarking).

After deposition, we used the CNF scanning electron microscope to inspect our substrates. Other equipment (cutting tables, lab desks, vacuum packing) was used to clean and prepare samples for deposition, and to package and seal our samples after deposition in the CNF clean room.

At a later date, we plan to return to do work on encapsulation techniques.

Summary of Research:

As an early manufacturer in the production and sale for graphene to world markets through sales channels such as Digikey, our products have focused on graphene on copper substrates, and manually transferred graphene onto substrates other than copper (silicon, PET, poly, etc.).

As our customers move from experimentation in research environments to commercial industry, handling, quality and cost constraints have created a need to eliminate the manual transfer of graphene where possible. Semiconductor applications using baseplates for high power RF and power gallium nitride (GaN) semiconductor devices in satellite communication and cellular base stations are one such example.

In this case, the coefficient of thermal expansion (CTE) of GaN (6) is mismatched to copper (18) traditionally used to mount and cool die, and baseplates of refractory metals (tungsten or molybdenum) or their alloys with matching CTE's are substituted to prevent failures due to CTE mismatch (premature cracking between die and flanges). However, while thermal stress problems are resolved, thermal conductivity plummets and die have to be powered down, or derated to shorter life spans. Graphene addresses this issue when combined with refractory metal, as thermal effectiveness of the baseplates climbs back up when graphene is added to metal stacks.

By growing graphene on tungsten and molybdenum baseplates directly, we will be able to avoid copper growth and manual transfer steps to refractory metal, as coated substrates will ultimately remain in end customer product systems. Direct growth eliminates costly and time consuming manual transfer steps of the graphene on copper process, and *in situ* deposition improves quality and eliminates PMMA residue which can contaminate the graphene and decrease performance.

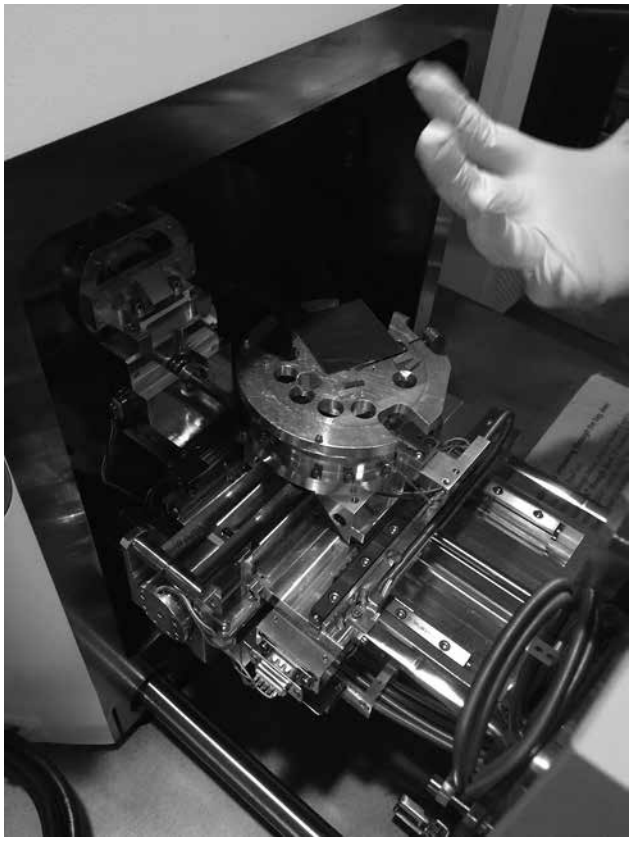

Figure 1: Metals being loaded into SEM after growth for analysis.

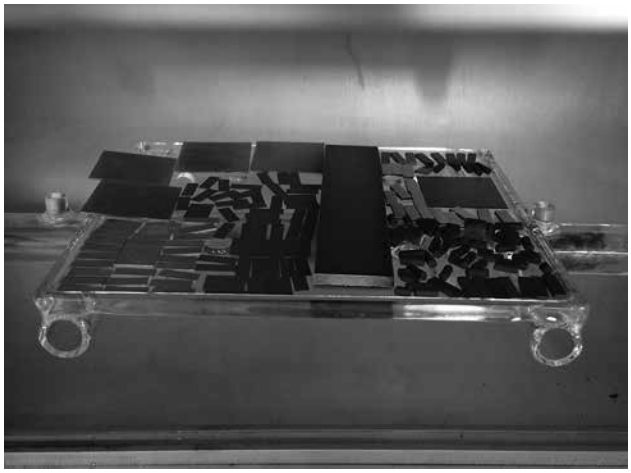

Figure 2: Mixed material (molybdenum, tungsten, Mo and W copper alloys, titanium, etc.) baseplates being loaded into the First Nano graphene furnace.

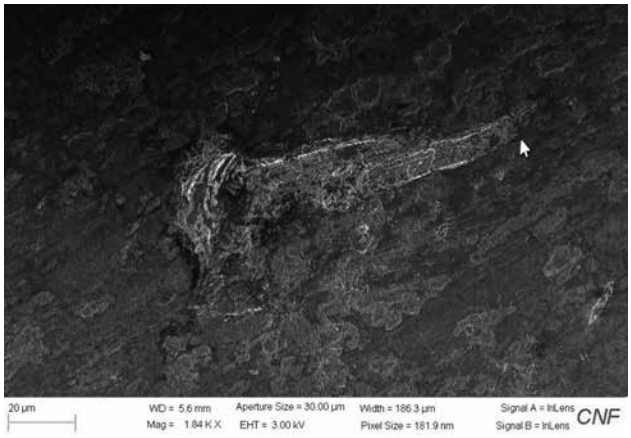

Figure 3: Interesting SEM image resembling T-Rex dinosaur found during SEM work.

Zero-Power Sensors with Near-Zero-Power Wakeup Switches for Reliable Sensor Platforms

CNF Project Number: 1122-03

Principal Investigator: Prof. Amit Lal

Users: Visarute Pinrod, Leanna Pancoast, Benyamin Davaji, Sunwoo Lee, Robin Ying, Alyosha Molnar, Amit Lal

Affiliation: School of Electrical and Computer Engineering, Cornell University, Ithaca, NY, USA

Primary Source of Research Funding: Defense Advanced Research Projects Agency (DARPA), NZERO Program

Contact: amit.lal@cornell.edu, vp239@cornell.edu

Primary CNF Tools Used: Furnace MOS clean anneal 2 - B1, furnace boron doping - D1, ASML 300C DUV stepper, Heidelberg DWL2000, Zeiss Ultra SEM, Zeiss Supra SEM, CVC sputter deposition, Oxford 81/82 etcher, Oxford 100 etcher, AJA ion mill, Hamatech hot piranha, Primaxx vapor HF etcher, PT deep Si etcher, Uniaxis 770 deep Si etcher, DISCO dicing saw, critical point dryer, wire bonder

Abstract:

The near zero-power sensor node solution is presented with piezoelectric sensors and DC tunable threshold electrostatic switches. A sensor suite measuring acceleration, rotation, and magnetic field based on PZT lateral bimorphs is used with nanoelectromechanical systems (NEMS) switches for the detection of a desired signal pattern and generating a wakeup trigger. The sensors are capable of detecting physical signals from 5 Hz to 1.5 kHz, with sourcing load capacitances as high as 200 pF. The sensor sensitivities achieved are: 0.1 V/g for the accelerometer, 31 mV/Gauss for the magnetic field, and 0.31 mV/(°/s) for rotation. NEMS switches, with threshold voltages in the mV to 15V range, can combine multiple sensor outputs through multi-gate actuation to detect desired event specific features. Using the sensors, we demonstrate the detection of a portable electrical generator in its different operational modes (On/Off state and the Eco mode).

Summary of Research:

Introduction. Sensor node reliability is limited by the longevity of the energy sources used to power them [1]. In order to have sensor nodes operational for extended periods of time, power consumption has to be minimized. The power consumed by the sensors of the sensor node is especially critical because the sensors must operate all the time, and generate wakeup trigger for the digital and communication components. MEMS sensors made of piezoelectric materials hold the promise of sensing signals without *any* power consumption, owing to charge being generated as a result of strain in the materials [2]. At the same time, the zero power sensors can trigger near-zero power consuming electrostatic switches that in turn generate a digital trigger as shown in Figure 1 [3].

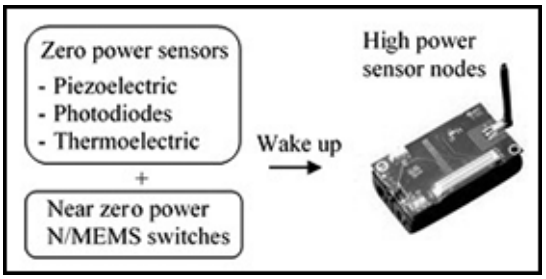

Figure 1: Zero power low-accuracy multi-sensor suite with near zero power N/MEMS switches wake up high power sensor nodes with higher accuracy sensors, communications, and computation, saving battery energy increasing sensor node lifetime.

Passive filter networks and multi-gate NEMS switches can provide a weighted combination of sensor outputs to allow the tuning of the system for identification of a desired signal pattern. In this work, a combination of the piezoelectric inertial and magnetic sensors with a multi-gate NEMS lateral switch is used to generate a wake-up trigger, thus proving a key component of advanced near-zero power consuming sensor nodes.

Near-Zero Power Wakeup Switch. The NEMS switches used to detect the signals are laterally actuated electrostatic switches. A single photomask process (Figure 2a) is used to fabricate the NEMS switches on SOI substrate, where the patterned structures are

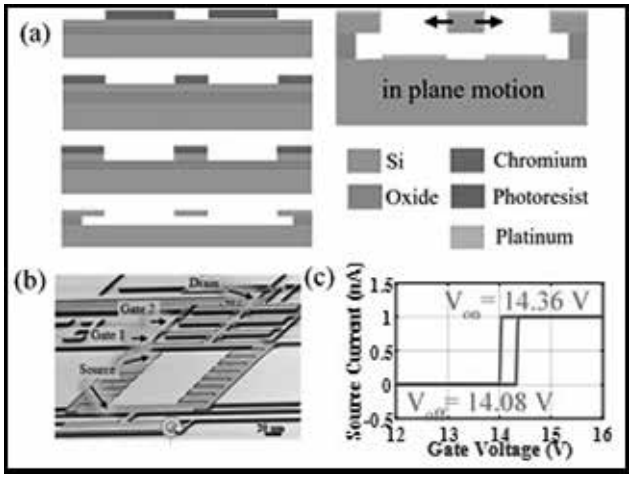

Figure 2: (a) Fabrication process flow. (b) SEM image of NEMS switch. (c) Switching hysteresis plot.

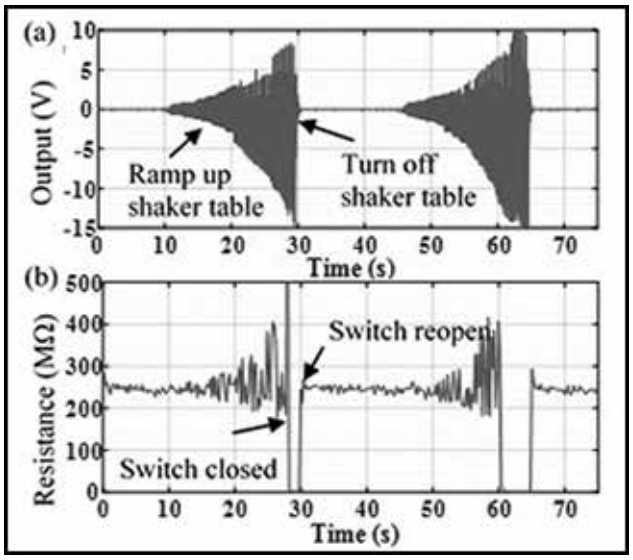

Figure 3: (a) PZT accelerometer output voltage. (b) NEMS switch resistance indicating switch close for trigger.

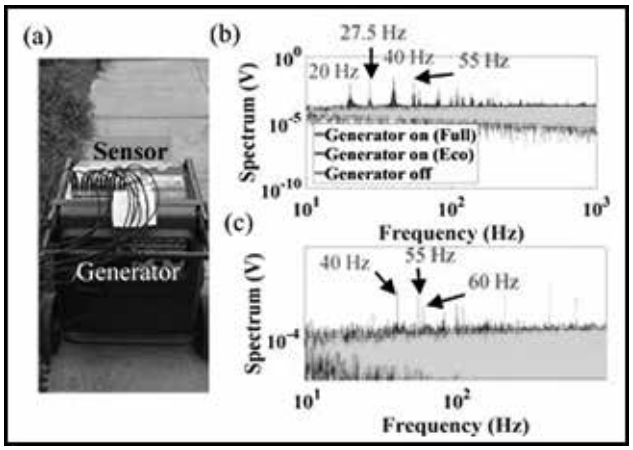

Figure 4: Field test by using zero power sensor for generator detection. (a) Photograph of sensors on top of generator. (b) Spectrum of PZT accelerometer for generator detection. (c) Spectrum of PZT magnetometer for generator detection.

etched by reactive ion etching (RIE) and released by vapor HF, followed by a metal deposition for reliable switching.

A completed switch is shown in Figure 2b. Multiple sized gates are used to actuate the switch to enable a lower turn on voltage and weighing of input signals [3]. Initial testing shows a turn on voltage of 14.36 V and turn off voltage of 14.08 V when actuating with only the largest area gate, shown in Figure 2c. In the shaker table test, a bias lower than the found turn on voltage is applied to the largest area gate and the sensor is connected to the second largest area gate.

The combined operation of the switch with pre-biased gates generates the digital wake up signal. Figure 3 shows a z-axis PZT accelerometer with added proof mass, directly coupled to a gate of a pre-biased NEMS switch, closing the switch to generate a wakeup signal. The switch was pre-biased at 10V, and the accelerometer was actuated by a shaker table at 280 Hz with an amplitude of 0.12 G. The total power consumption of the wakeup systems is estimated to be < 5 nW, mainly dominated by the 10V bias power supply leakage current.

Field Testing. In order to measure the efficacy of the zero-power sensor triggered NEMS switches, the fabricated sensors are used to monitor the operation of an internal combustion engine powered portable electrical generator by measuring the physical signals (Figure 4a). Figures 4b-c show the clear frequency signature difference in acquired spectrum signal between different modes.

References:

[1] J. Yick, B. Mukherjee, and D. Ghosal. "Wireless sensor network survey," Computer networks 52, no. 12 (2008): pp 2292-2330.

[2] S. K. Gupta, V. Pinrod, S. Nadig, B. Davaji and A. Lal. "Vibration Powered RF-Transponder for Sensing Low Frequency Motion Events," PowerMEMS 2016.

[3] K. Amponsah, N. Yoshimizu, S. Ardanuc, and A. Lal, "Near-kT switching-energy lateral NEMS switch," IEEE NEMS 2010, pp. 985-988.

The Nanoaquarium – A Device for *in situ* Electron Microscopy of Processes in Liquids

CNF Project Number: 1542-07
Principal Investigator: Haim H. Bau
User: Joseph M. Grogan

Affili0ation: Mechanical Engineering and Applied Mechanics, the University of Pennsylvania, Philadelphia, PA, USA
Primary Source of Research Funding: National Science Foundation-CBET 1066573 and NSF CMMI 1129722
Contact: bau@seas.upenn.edu, joegrogan@gmail.com
Website: http://bau.seas.upenn.edu
Primary CNF Tools Used: Chemical-mechanical polisher, direct wafer bonder

Abstract:

The nanoaquarium is a nanofluidic platform for *in situ* electron microscopy of objects and processes in liquid media. The nanoaquarium consists of a hermetically sealed, thin (~100 nm tall) liquid cell sandwiched between two electron-transparent silicon nitride membranes. The nanoaquarium is equipped with micro patterned electrodes. The device has been used to image electrochemical deposition and etching, growth and dissolution of nanoparticles, diffusion limited aggregation, crystallization, nucleation and bubble growth, nanobubble migration, interfacial phenomena, to assess the interactions between electron radiation and fluids, and to pattern nanostructures without a need for a mask.

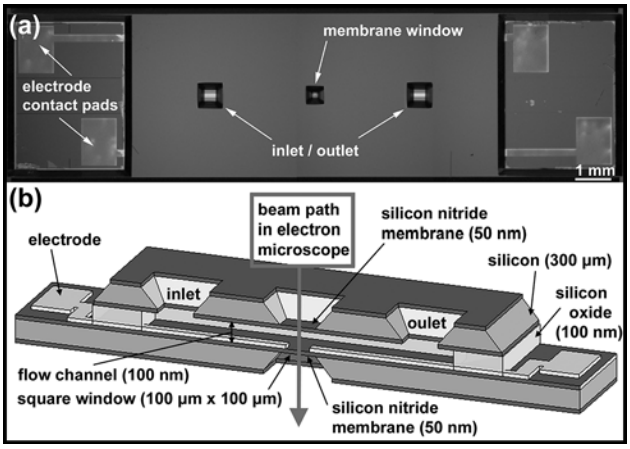

Figure 1: A photograph of the nanoaquarium (top) and a schematic of the nanoaquarium's cross-section (bottom).

Summary of Research:

The nanoaquarium is a custom-designed, micro-fabricated, nanofluidic device for *in situ* electron microscopy of processes taking place in liquids and of objects submerged in liquids (Figure 1). Two thin (<50nm), electron-transparent silicon nitride membranes sandwich a thin liquid layer, ranging in thickness from tens of nanometers to a few microns. The cell is hermetically sealed from the vacuum environment of the electron microscope. Due to its small thickness, the liquid layer does not significantly scatter electrons, allowing nanoscale resolution imaging of objects suspended in the confined liquid. The nanoaquarium contains electrodes patterned on the silicon nitride membrane for electrochemical measurements and for actuation.

The fabrication of the device was accomplished with direct bonding of silicon wafers coated with silicon nitride. One of the wafers contains a thin film of patterned silicon oxide that defines the shape and height of the imaging chamber and the liquid conduits. The use of direct wafer bonding eliminates risk from potential contamination from glue, epoxy, and other sealing materials and assures a hermetic seal. Use of a dielectric material as the spacer allows electrodes to be directly incorporated into the device. A schematic of the nanoaquarium is depicted in Figure 1. The fabrication process has been previously described [1]. Our lab, in collaboration with others, has used nanoaquariums to study nanoparticle aggregation and colloidal crystal growth dynamics [2-4]; interactions of nanoparticles with moving interfaces [5]; electron beam-induced radiolysis [12-14]; bubble nucleation, growth and detachment [6,10,12]; crystallization [8,16]; and electroplating [9,11,17]. We have also demonstrated the use of the electron beam as a "pen" to pattern nanowires without a need for a mask [12]. The device was patented [18].

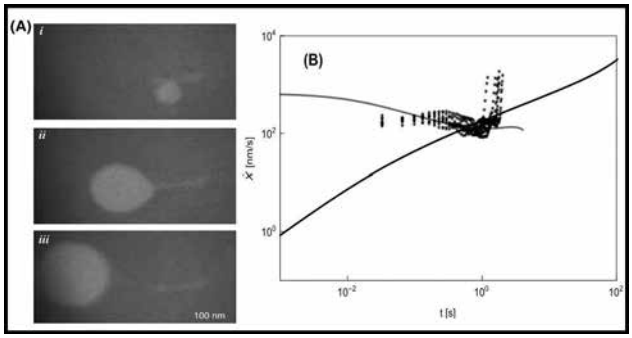

Figure 2: (A) a series of bright field transmission electron microscopy images of a bubble growing and migrating towards a region of lower confinement. (B) Velocity of the center of mass of the bubble as a function of time. The gray and dark solid lines correspond, respectively, to theoretical predictions for partially pinned and unpinned bubbles; and the symbols correspond to experimental data.

Since *in situ* electron microscopy produces large quantities of data, we have developed automated image processing algorithms to extract useful quantitative measures of the observed phenomena [17,19].

In our experiments, we observed spontaneous motion of bubbles. Interestingly, the electron beam plays a dual role in these experiments. E-beam induced radiolysis generates gas that induces bubble nucleation and growth and the beam provides a means to image the bubbles. To better understand and interpret our experimental data, we constructed a model, based on Blake-Haynes theory and predicted bubbles' shapes, growth rates, and migration. Consistent with experimental data, our model predicts that in the presence of confinement, growth rates are orders of magnitude slower compared with bubbles [20]. Figure 2 compares the predicted and experimentally observed velocity of bubble's center of mass as a function of time.

Acknowledgements:

Electron microscopy was performed at the Penn Regional Nanotechnology Facility at the University of Pennsylvania and at the IBM TJ Watson Research Center.

References:

[1] Grogan, J. M. and Bau, H. H., 2010, The Nanoaquarium: A Platform for *in situ* TEM in Liquid Media. Journal of Microelectromechanical Systems 19, 885-894.

[2] Grogan, J. M., Rotkina, L. and Bau, H. H., 2011, *In situ* liquid-cell electron microscopy of colloid aggregation and growth dynamics. Phys. Rev. E 83, 061405.

[3] Grogan, J., Schneider N., Ross, F., and Bau, H. H., 2012, The Nanoaquarium: A New Paradigm in Electron Microscopy, Journal of the Indian Institute of Science 92:2.

[4] Grogan, J., and Bau, A H. H., 2010, Nanoaquarium for *in situ* Electron Microscopy in Liquid Media http://arxiv.org/abs/1010.3286,

[5] Grogan, J. M., and Bau, H. H., 2011, Real Time Electron Microscope Imaging of Nanoparticle Motion Induced by a Moving Contact Line. http://arxiv.org/abs/1110.3273.

[6] Grogan, J. M., Ross, F., M., Bau, H, H., 2012, Electron Beam Artifacts in Liquid-Cell Electron Microscopy, http://arxiv.org/abs/1210.3380.

[7] Grogan, J.M., and Bau, H.H., 2011: *In situ* Liquid Cell TEM/STEM with the Nanoaquarium, Microscopy and Microanalysis 17, Supplement S2, 532-533.

[8] Park, J. H., Grogan, J. M., Bau, H.H., Kodambaka, S., and Ross, F.M., 2012, *In situ* Liquid Cell TEM Observation of Electron Beam Induced Au Crystal Growth in a Solution, Microscopy and Microanalysis 18, Supplement S2, 1098-1099.

[9] Grogan, J.M., Park, J.H., Ross, F.M. and Bau, H.H., 2012, Liquid Cell *in situ* Electron Microscopy: Interfacial Phenomena and Electrochemical Deposition, Microscopy and Microanalysis 18, Supplement S2, 1160-1161.

[10] Grogan, J., Ross, F., and Bau, H., H., 2013, Beam-Sample Interactions during Liquid Cell Electron Microscopy, Microscopy and Microanalysis, 19 (Suppl. 2), 408-409.

[11] Schneider, N., et al., 2013, *In situ* Electrochemical Measurements in the Nanoaquarium, Microscopy and Microanalysis, 19 (Suppl. 2), 422-423.

[12] Grogan, J.; Schneider, N.; Ross, F.; Bau, H.H., 2014, Bubble and pattern formation in liquid induced by an electron beam, Nano Letters 14 (1), 359-364.

[13] Schneider N., Norton, M., M., Mendel, B., Grogan, J., M., Ross, F., and Bau, H.H., 2014, Electron-Water Interactions and Implications for Liquid Cell Electron Microscopy, Journal Physical Chemistry Part C. 118, 22373-22382.

[14] Schneider, N.M., et al., 2014, "Radiolysis during Liquid Cell Electron Microscopy," Microscopy and Microanalysis 20, Supplement S3, pp 1516-1517.

[15] Schneider, N.M., et al., 2014, "Visualization of Active and Passive Control of Morphology during Electrodeposition," Microscopy and Microanalysis 20, Supplement 3, pp 1530-1531.

[16] Park, J., et al., 2015, Control of Electron Beam-Induced Au Nanocrystal Formation Kinetics through Solution Chemistry, Nano Letters 15 (8) 5314-20. DOI: 10.1021/acs.nanolett.5b01677.

[17] Schneider, N.M.; J.H. Park; M.M. Norton; F.M. Ross; H.H. Bau, 2016, Automated Analysis of Evolving Interfaces during *in situ* Electron Microscopy. Advanced Structural and Chemical Imaging 2:2. DOI: 10.1186/s40679-016-0016-z.

[18] Grogan, J., and Bau, H., H., "Flow Cells For Electron Microscope Imaging With Multiple Flow Streams," United States Patent 9,196,457. Awarded 11/24/2015.

[19] Schneider, N.M.; Quantitative-Image-Analysis. In: github.com. https://github.com/NMSchneider/Quantitative-Image-Analysis. Accessed 13 Feb 2015.

[20] Norton, M., et al., 2017, Growth-Induced Translation of a Nanobubble in a Tapered Conduit in the Asymptotic Limit of Zero Capillary and Bond Numbers, in preparation.

Hydrophobic/Hyrophilic Nanoscale Patterns for Enhanced Pool Boiling

CNF Project Number: 2123-12
Principal Investigator: Shalabh Maroo
Users: Geoffrey Vaartstra, An Zou

Affiliation: Department of Mechanical and Aerospace Engineering, Syracuse University
Primary Source of Research Funding: Reneé Crown Honors Program Crownwise Funding
Contact: scmaroo@syr.edu, gavaarts@syr.edu
Website: http://maroo.syr.edu
Primary CNF Tools Used: ASML 300C DUV stepper, Zeiss Ultra SEM, MVD 100

Abstract:

Raising pool boiling capacity via increase of critical heat flux is critical to emerging technology as ever-higher heat flux is demanded for operation. Power generation systems are stretching the limits of boiler output and more rapid cooling is needed to accommodate the newest generation of electronic devices. Researchers are seeking critical heat flux enhancement on modified surfaces which are durable and capable of being scaled up to industrial application. Critical heat flux enhancement has been attained by increasing surface wickability, adding surface roughness, creating thermal gradients, and introduction of capillary pumping effects. In this work, surfaces with nanoscale hydrophobic/hydrophilic patterns were created using current nanofabrication techniques to pattern hydrophobic silane onto a silicon dioxide surface. Improvement in critical heat flux was achieved by evaporation of the microlayer, which resulted in an elevated bubble growth rate that caused a delay in the onset of dry out. The highest performance observed in this study was a surface capable of evaporating off ~ 300 nm of microlayer height early, yielding a critical heat flux of 124.4 ± 1.5 W/cm^2, a 53% enhancement. These surfaces demonstrated pool boiling enhancement with no increase in surface area, capillary pumping effects, thermal gradients, additional roughness, nor complex/fragile nanostructures.

Summary of Research:

Boiling is a widely used heat transfer process in industrial power generation and commercial applications since it is a simple method to transfer large amounts of thermal energy. In pool boiling, the primary mechanism of heat transfer is the nucleation and growth of vapor bubbles on the heated surface. As these bubbles grow and detach, latent heat is imparted to the stationary fluid. Because heat flux through the surface is proportional to the rate of nucleation and vapor expansion, this flux is capped at the limit when bubbles do not depart quickly enough and coalesce into a film on the surface. This film, referred to as "dry out," insulates the fluid from the heating surface, causing a rapid drop in heat flux and in surface temperature. Critical heat flux is the maximum rate of heat transfer achieved before the dry out phenomenon occurs; industrial boilers must operate well below CHF as the temperature spike would damage the surface.

Manipulation of the boiling surface to raise CHF and improve the heat transfer coefficient (HTC), or rate of heat transfer per unit superheat (temperature difference between the surface and fluid), is necessary to meet the demand for increasing heat flux in power generators and electronics [1].

For this study, surfaces targeting CHF enhancement were fabricated using standard nanofabrication techniques on silicon wafers. The surfaces were comprised of a base layer of hydrophilic silicon dioxide (SiO_2) with nanoscale patterns of a hydrophobic silane. This resulted in variation of wettability across the surface. In order to test these samples in pool boiling experiments, a 500 nm film of copper was deposited on the back of the sample to be soldered to a copper heating rod in the boiling chamber.

Samples were fabricated at Cornell NanoScale Science and Technology Facility (CNF), a National Nanotechnology Infrastructure Network site. All materials and supplies were purchased from the cleanroom at CNF. The nanoscale patterns were fabricated onto the

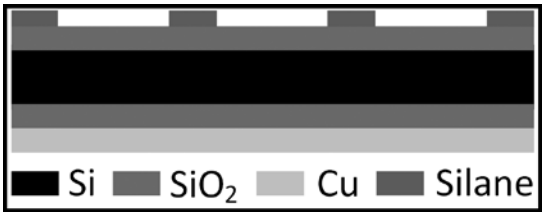

Figure 1, above: Cross-sectional schematic of the fabricated samples.

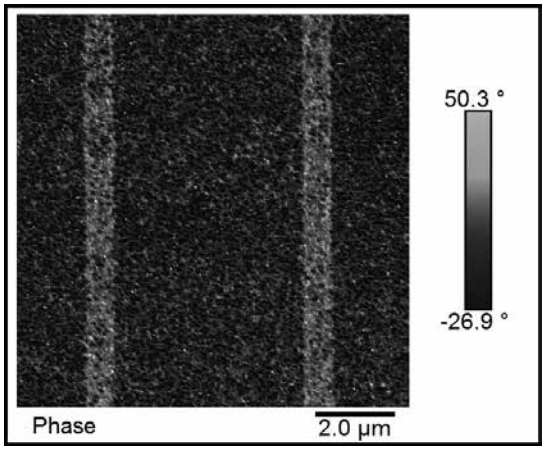

Figure 2, right: AFM image of nanoscale silane patterns on SiO_2 (top view).

front side of silicon wafers and a layer of copper (Cu) was deposited on the backside for coupling with a heater (Figure 1). Standard 100 mm N/Ph silicon wafers were cleaned per the semiconductor industry standard RCA clean, which is comprised of acid and base dips.

The wafers were first dipped for 10 minutes in a base bath of ammonium hydroxide and hydrogen peroxide held at 70°C. After rinse in deionized (DI) water, wafers were dipped in a bath of hydrochloric acid and hydrogen peroxide to remove metallic impurities. The wafers were then processed in a wet/dry oxide furnace to grow a uniform, 125 nm thick layer of SiO_2 on both front and back surfaces of the wafer. Oxide was grown in wet conditions (with the addition of steam to the furnace) at 900°C for 54 minutes. Immediately before Cu was deposited on the backside of the wafers, both front and back were cleaned under oxygen plasma for 60 s in an Aura 1000. A 10 nm adhesion layer of titanium (Ti) was deposited to provide strong adhesion between SiO2 and Cu. A 500 nm film of Cu was subsequently evaporated onto the substrate.

The evaporation chamber was initially pumped down to 2.0×10^{-6} Torr and vacuum was held through both Ti and Cu evaporation. The nanoscale patterns were then transferred to the front side SiO_2 surface via photolithography (Figure 1). An anti-reflective coating (ARC) was spin-coated onto the surface before photoresist deposition to improve exposure accuracy. DSK 101-312, a developer soluble ARC, was used for compatibility with the lift-off procedure and stability of silane. A 500 nm thick layer of negative photoresist (UVN 2300) was spun over the ARC and baked.

The pattern was transferred to the resist by deep ultraviolet (DUV) exposure in an ASML 300C DUV Stepper at an exposure intensity of 17 mJ/cm^2 and 0 µm focus; these parameters were determined by scanning electron microscope (Zeiss Ultra SEM) analysis for precision to the desired pattern dimensions. After development, silane was deposited in an MVD 100 molecular vapor deposition chamber for 10 minutes of reaction time. The lift-off procedure was completed by stripping the photoresist in an acetone bath and developing off the ARC, yielding a SiO_2 surface patterned with silane (Figure 2).

References:

[1] Yen-Wen Lu and Satish G. Kandlikar. Nanoscale surface modification techniques for pool boiling enhancement a critical review and future directions. Heat Transfer Engineering, 32(10):827-842, 2011.

Pool Boiling Critical Heat Flux Enhancement by Early Evaporation of Microlayer

CNF Project Number: 2123-12

Principal Investigator: Shalabh C. Maroo

User: An Zou

Affiliation: Department of Mechanical and Aerospace Engineering, Syracuse University, Syracuse, NY 13244

Primary Sources of Research Funding: Startup funds from Department of Mechanical and Aerospace Engineering at Syracuse University, and National Science Foundation Career Award NO. 1454450

Contact: scmaroo@syr.edu, azou@syr.edu

Website: http://maroo.syr.edu

Primary CNF Tools Used: Heidelberg DWL2000, Gama Tool, ASML stepper, Unaxis Si etcher, PVD75 sputter, CVC sputter, B2 furnace, DISCO dicing saw, SEM

Abstract:

Microlayer evaporation is one of the major heat transfer mechanisms of boiling. In our work, the boiling heat transfer is enhanced by affecting microlayer evaporation. The microlayer evaporates sooner due to the presence of ridges of a few micrometer high, leading to the increase in bubble growth rate, heat transfer, departure frequency, and critical heat flux. Approximately 120% enhancement of critical heat flux is obtained with only ~ 18% increase in area. This new mechanism is validated by comparing the growth rate of a laser created bubble on a ridge-structured surface and a plain surface, and the corresponding prediction of the critical heat flux is found to be in good agreement with the experimental boiling data. This work was published in Langmuir in 2016 [1].

Summary of Research:

Boiling has been widely used in industry as it utilizes the high latent heat of vaporization of a liquid to transfer large amounts of heat over a small surface area. Boiling occurs due to the heterogeneous nucleation and growth of vapor bubbles. Increasing the heat flux leads to more rapid formation and coalescence of the bubbles, an operation limit is reached when the bubble generation rate overcomes its removal rate, causing a vapor film to cover the surface. This limit, which is known as the critical heat flux (CHF), determines the highest heat flux that can be reached by pool boiling. CHF causes a drastic increase in surface temperature as the heat cannot be removed by the liquid due to the insulating vapor film. Thus, enhanced CHF is extremely demanding as high heat flux removal is required to achieve next generation energy and electronic devices.

Microlayer is a thin liquid film trapped underneath the vapor bubble. Microlayer evaporation is one of the major heat transfer mechanisms in boiling. The heat transfer rate in the microlayer region was identified as 1-2 orders higher than the overall value [2]. Thus, affecting microlayer evaporation to enhance boiling heat transfer performance becomes attractive. In our work, we utilized ridges with a few micrometer high to partition the microlayer into to water slabs and to disconnect it from the bulk liquid. The separation of the microlayer leads to an increase in its energy, thus causing it to evaporate due to the higher surface temperature. Compared to a plain surface, the microlayer evaporates sooner on a ridge-structured surface, resulting in an increase in bubble growth rate, bubble departure frequency and therefore critical heat flux.

The ridges were fabricated on the top surface of a Si substrate by deep ultraviolet photolithography, followed by plasma etching. A 125 nm thick thermal oxide layer was subsequently grown to achieve SiO2

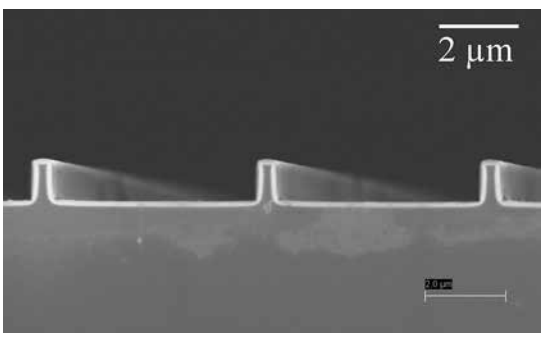

Figure 1: SEM image of ridges.

ridges. A thin film of indium tin oxide (ITO) was deposited on the back side of the wafer by physical vapor deposition, and served as the heater. Copper electrodes were patterned on the ITO using chemical vapor deposition. The wafer was diced into 2 cm × 2 cm sample. Figure 1 shows the images of ridges using scanning electron microscopy. In boiling experiments, the sample was attached on top of a polycarbonate holder located inside a liquid chamber and immersed in a pool of deionized water. The water was degassed by boiling it for one hour. After degassing, the water was maintained at saturation conditions during the experiments. Boiling on the sample was achieved by supplying power to ITO heater. The temperature of the ITO heater was measured by a T-type thermocouple. CHF was obtained when an incremental increase in the power resulted in a sudden and dramatic increase of the heater temperature.

Figure 2 shows the boiling curves for plain SiO_2 and ridge-structured surfaces. A boiling curve is a plot of heat flux versus superheat, which is defined as temperature difference between the surface and the saturated liquid. 177.2 ± 3.3 W/cm^2 of CHF was achieved on a ridge-structured surface, which is ~ 120% enhancement with only ~ 18% increase in surface area compared to a plain surface (78.8 ± 1.6 W/cm^2). Considering the heat flux based on the wetted area, 62% enhancement in CHF was attained, which is one of the highest values among reported values in literature (Figure 3) [3,4].

To verify the early evaporation of the microlayer with independent experimental data, the growth rate of a vapor bubble is measured on a ridge-structured surface and a plain surface. As mentioned above, the early evaporation of the microlayer is expected to increase the bubble growth rate and thus the bubble departure frequency, leading to CHF enhancement. As shown in Figure 4, the bubble growth rate is ~ 5.25 times faster on the ridge-structured surface than on the plain surface. According to Mikic's model [5], the CHF on the ridge-structured surface will be enhanced by 1.80 to 2.24 times that on a plain surface, which is in very good agreement with the CHF increase of 2.19 times achieved in boiling experiments.

In summary, we reported a new boiling heat transfer mechanism, which is early evaporation of the microlayer due to the presence of ridges, and this new mechanism was validated by independent experimental data of the growth rate of the laser created bubble.

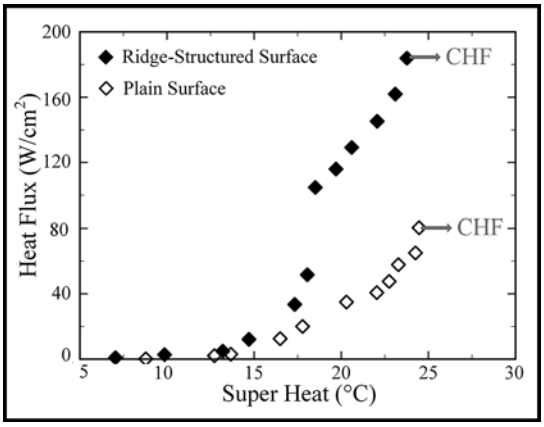

Figure 2: Boiling curves.

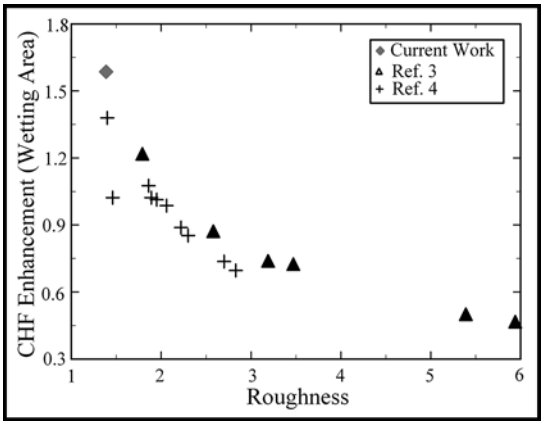

Figure 3: Comparison of CHF enhancement of our work with literature [3, 4].

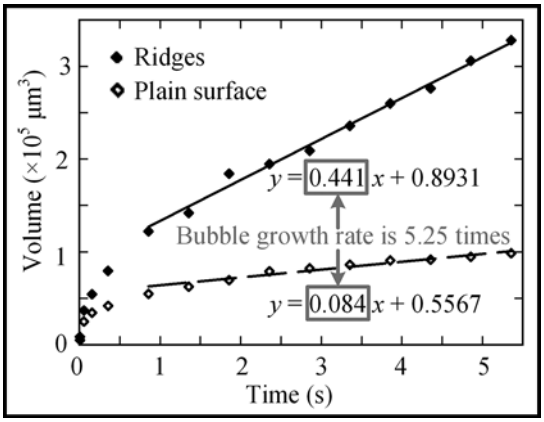

Figure 4: Comparison of bubble growth rate on a ridge-structured surface and a plain surface.

References:

[1] A. Zou, D. P. Singh, and S. C. Maroo, Langmuir 32, 10808-10814 (2016)

[2] S. Jung and H. Kim, Heat Transfer Eng. 36, 1001-1012 (2015).

[3] K. Chu, R. Enright, and E. N. Wang, Appl. Phys. Lett. 100, 241603 (2012).

[4] D. Cooke and S. G. Kandlikar, Int. J. Heat Mass Tran. 55, 1004-1013 (2012).

[5] B. Mikic, W. M. Rohsenow, and P. Griffth, Int. J. Heat Mass Tran. 13, 657-666 (1970).

Making a Microfluidic Device to Mimic Flow Through Porous Medium

CNF Project Number: 2385-15
Principal Investigator: Brian Kirby
User: Katherine Polhemus

Affiliation: Mechanical and Aerospace Engineering, Cornell University
Primary Source of Research Funding: IGERT Program for Earth Energy
Contact: kirby@cornell.edu, kcp44@cornell.edu
Primary CNF Tools Used: CAD L-Edit, Heidelberg DWL2000, ABM contact aligner, CNF hot press

Abstract:

With the rapid depletion of known oil reserves, detecting properties of the oil reservoirs and optimizing oil extraction is critical. By measuring the aqueous properties of the reservoirs, decisions can be made on which reservoirs to drill and the available quantity of oil to extract, with minimal environmental impact. Utilizing hairy nanoparticles in testing can provide a variety of information about the reservoir. The objective of the proposed work is to characterize the behavior of hairy nanoparticles at the oil-water interface in order to optimize their use as subsurface sensors. In order to complete the optimization, a microfluidic model for the environment needs to be developed. This past year's work involved making microfluidic devices to mimic water flowing through the subsurface and oil trapped in pores. The design and mold to make the mold was developed in the Cornell NanoScale Facility — first using photolithography to create a mold with negative photoresist that was used to make microfluidic channels out of polydimethylsiloxane and later using positive photoresist and etching to create a mold to make microfluidic channels out of polypropylene.

Summary of Research:

The work in the CNF has consisted of using microfabrication techniques to make a microfluidic device. Using the cad software L-Edit, we make patterns to transfer to a mask using the Heidelberg mask writer. In the past year, we have made two types of masks: one for positive photoresist and the other for negative photoresist. The first set of microfluidic devices were made using the negative photoresist SU-8 to make a mold. The process of making a mold with photoresist (photolithography) consist of the steps; 1] Pour and spin photoresist onto a wafer (using CNF spinner), 2] Bake photoresist (using CNF hot plates), 3] Wait time, 4] Expose photoresist (using ABM contact aligner), 5] Second wait time, 6] Development photoresist. At the end of the process, we have a mold out of SU-8 on top of a wafer.

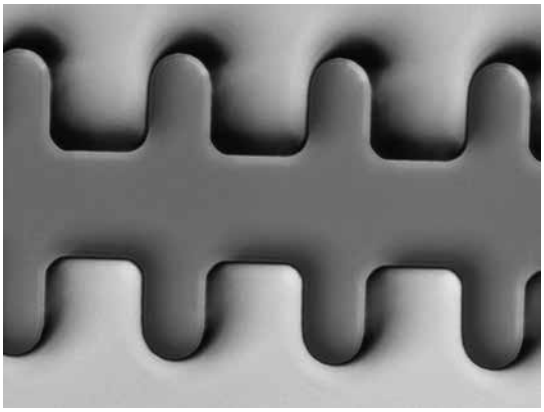

Figure 1: Developed positive resist pattern on wafer.

In the Kirby research group's lab, microfluidic devices were made by pouring PDMS on top of the mold and baking, then attaching the molded PDMS to a glass slide through plasma cleaning. Unfortunately for our application, the PDMS needs to be very hydrophobic and PDMS was not hydrophobic enough for our purposes. Therefore, we switched to making devices out of a polypropylene — a much more hydrophobic material — and to make molded polypropylene pieces we used hot embossing, which is done on the CNF hot press. Because of the large pressure applied during embossing, a stronger mold than SU-8 was needed, so we switched to making molds out of silicon.

To make a mold out of silicon, a positive photoresist is used (instead of negative) and after the photolithography process the wafer was etched on the deep reactive ion etcher in the CNF. The Si mold is then used in the CNF hot press to hot emboss the pattern onto polypropylene, which is then bonded, again using the hot press.

Graphene-Based Bimorphs for the Fabrication of Micron-Sized, Autonomous Origami Machines

CNF Project Number: 2416-16

Principal Investigators: Itai Cohen, Paul L. McEuen

Users: Marc Z. Miskin, Kyle J. Dorsey, Baris Bircan, Michael F. Reynolds

Affiliations: Laboratory of Atomic and Solid State Physics, School of Applied and Engineering Physics, Kavli Institute for Nanoscale Science; Cornell University

Primary Sources of Research Funding: National Science Foundation (DMREF DMR-1435999), Air Force Office of Scientific Research (MURI FA 9550-16-1-0031)

Contact: itai.cohen@cornell.edu, plm23@cornell.edu, mm2325@cornell.edu, kjd96@cornell.edu, bb625@cornell.edu

Primary CNF Tools Used: Oxford ALD FlexAL, Oxford 81 etcher, ABM contact aligner, SC4500 odd-hour evaporator, Glen 1000 resist strip, Heidelberg DWL2000

Abstract:

Origami is a powerful and general platform that can be used to fabricate three-dimensional structures from two-dimensional sheets. Drawing from the intrinsic scalability of origami, we use nanometer thin, quasi-two-dimensional, self-folding sheets made of graphene and SiO_2 to realize dynamic, micron-sized folds. Devices built using these actuators rapidly respond to changes in temperature, pH and ion concentration by self-folding.

Summary of Research:

Origami can be used to make arbitrarily complex structures from thin sheets at the macroscale [1]. The use of origami design principles and actuators that drive folding makes it possible to design very complicated macroscopic structures that assemble themselves through self-folding [2,3]. We have produced a platform to build microscopic three-dimensional (3D) structures through origami by developing ultra-thin bimorph bending actuators, which are two layer stacks made of graphene and 2 nm of SiO_2. A bimorph bending actuator switches between flat and bent states in response to external stimuli that cause a strain mismatch between the two bimorph layers. The operation principle of a bimorph is presented in Figure 1.

The bimorph bending response is a mechanism that can be used to actuate folds. By fabricating nanometer thin graphene-SiO_2 two layer stacks that have been optimized to produce maximum curvature, we have established an actuation mechanism that can rapidly form radii of curvature of 10 μm and less in response to changes in temperature, pH and ion concentration of its environment. The atomic thickness of these bimorph actuators enables them to attain such high curvatures without fracturing. Figure 2 shows the response of a graphene-SiO_2 bimorph to heating by a 1064 nm laser. Curvature is reduced to a certain minimum as the laser power is turned down.

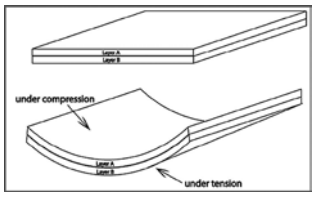

Figure 1, right: Schematic illustration of bimorph bending mechanism.

Figure 2, below: Graphene bimorph bending in response to temperature. Observed curvature increases linearly with temperature.

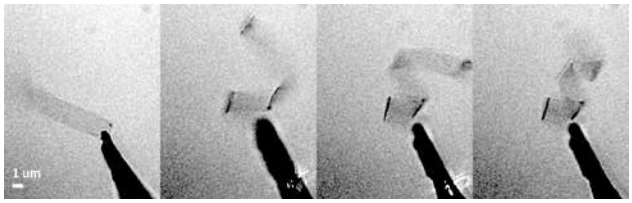

To fabricate 3D self-folding structures, we evaporate an aluminum release layer on fused silica substrates, and grow a 2 nm thick film of SiO_2 using one of CNF's two atomic layer deposition (ALD) tools, the Oxford ALD FlexAL. We transfer graphene on top of the SiO_2 film, and use contact photolithography and plasma etching to pattern graphene-SiO_2 bilayer hinges. We also lithographically pattern rigid SU-8 pads that define the flat surfaces of the 3D target geometries. By wet etching the aluminum release layer, we release our devices into an aqueous solution where they are free to fold. Figure 3 shows a set of devices that are bound down to their substrate in their flat states.

Once they are released from their substrate, our graphene-SiO_2 bimorph actuator based devices respond to external stimuli by folding and unfolding. Figure 4 shows a cube that folds itself in an acidic medium. When NaOH is added to the medium, the cube unfolds. These structures can be made to fold and unfold by repeatedly changing the pH of the medium. This dynamic behavior makes these micron-sized machines a good candidate for origami inspired fabrication at the micro/nanoscale.

Currently, we are exploring the possible functionalities that can be built into this fabrication platform. By substituting ALD HfO_2 instead of graphene, we are developing a pH sensitive folding method to achieve bidirectional and sequential folds, which will enable us to produce more complicated geometries at the microscale. We are also developing Pt-SiO_2 bimorph based systems, which have been shown to be electrically actuatable.

With these efforts, we aim to develop a general platform for three-dimensional microfabrication with different sensing and actuation capabilities that can be incorporated into self-folding devices that will be part of an extensive toolkit.

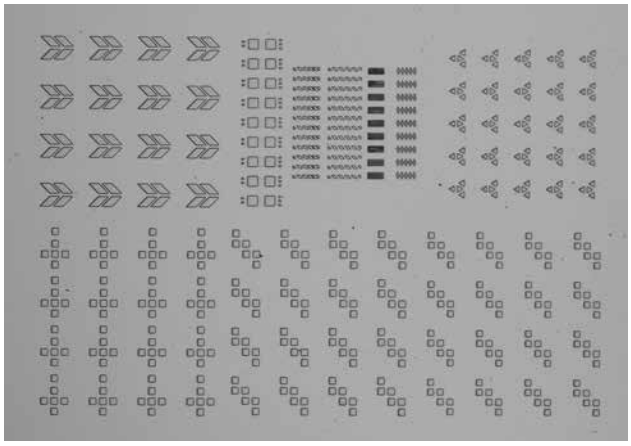

Figure 3: Array of microscopic self-folding devices bound to a substrate in their flat state.

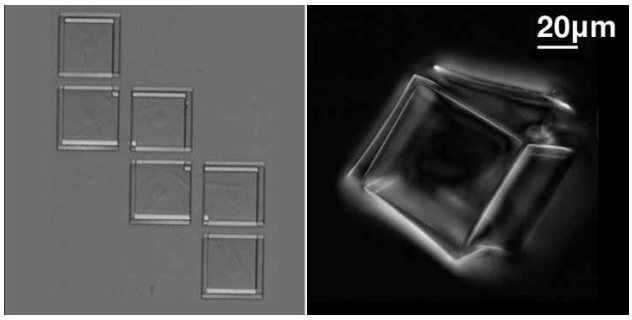

Figure 4: A microscopic self-folding cube in its unfolded and folded states. The cube folds itself in response to a change in the pH of its environment.

References:

[1] Benbernou, N., Demaine, E. D., Demaine, M. L. and Ovadya, A. A universal crease pattern for folding orthogonal shapes. arXiv preprint arXiv:0909.5388 (2009).

[2] Hawkes, E., et al. Programmable matter by folding. Proceedings of the National Academy of Sciences 107, 12441-12445 (2010).

[3] Felton, S., Tolley, M., Demaine, E., Rus, D. and Wood, R. A method for building self-folding machines. Science 345, 644-646 (2014).

Silicon-Based Variable Capacitors for Sound Energy Harvesting

CNF Project Number: 2452-16
Principal Investigator: Diana Borca-Tasciuc
Users: Jinglun Li, Gregory James (graduated)

Affiliation: Mechanical, Aerospace, and Nuclear Engineering, Rensselaer Polytechnic Institute

Primary Source of Research Funding: Los Alamos National Lab

Contact: BORCAD@rpi.edu, LIJ31@rpi.edu

Primary CNF Tools Used: Anatech resist strip, DISCO dicing saw, Oxford 81 etcher, Oxford PECVD, SUSS MA6-BA6 contact aligner, Unaxis 770 deep Si etcher

Abstract:

The objective of this project is to develop microscale power sources for wireless sensors. The proposed power sources will harvest energy from sound and convert it to electricity using variable capacitors that have electrodes moving relative to each other in the direction normal to the plane of the wafer. An array of such harvesters could be energized by a single sound source (such as a high-power loudspeaker) to provide energy to wireless sensors, eliminating the need for a battery or wiring along with the associated maintenance or infrastructure cost. Potential applications of such sensor networks include monitoring underground nuclear waste deposit sites.

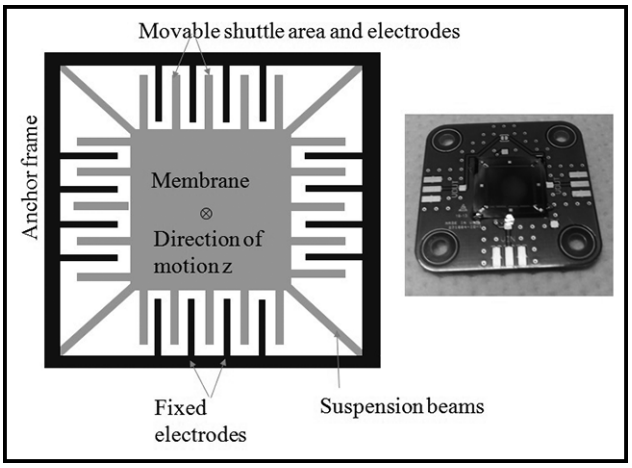

Figure 1: Device schematic and picture of a fabricated device.

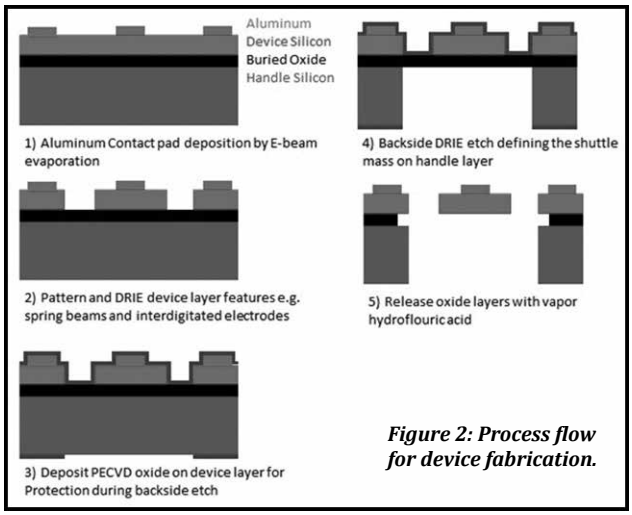

Figure 2: Process flow for device fabrication.

Summary of Research:

A schematic of the device along with a picture of the fabricated device mounted on a printed circuit board is shown in Figure 1. The device shuttle mass has an area of 1 cm square and has interdigitated electrodes on all four sides of the device supported by four cantilever beams. The device is designed to respond with relatively large displacements (of order 10 μm) to a 25 Pa sound force. Multiple device designs were attempted, where the dimension of the electrode fingers and suspension beams was varied. Only the successful attempt is discussed here.

In this device, the interdigitated electrodes are of 650 μm in length and 6 μm wide with a device layer depth of 58 μm. The gap between the fingers is 10 μm.

The process flow of the device fabrication is shown in Figure 2. The process starts with a silicon-on-insulator (SOI) wafer. The first step is to deposit chromium and aluminum by electron-beam evaporation to form the contact pads on the device layer. The next step is to create a mask for the device layer structures so the DRIE etching only removes the desired material. This mask

is patterned with thick resist that has high selectivity during the plasma etch step of the Botch process. The next step is the actual DRIE etching of the device layer. Then, a PECVD oxide is deposited to protect the deep etch trenches from the SF_6 plasma. After that, the wafer is flipped over and a backside etch is performed. The final step is to release the buried oxide by vapor hydrofluoric acid.

The successful devices were tested in a simple setup as discussed below. The device was mounted close (~1 cm) and parallel to the surface of a sound speaker. Electrically, the variable capacitor was mounted in series with a resistance load and a direct current (DC) voltage source. The DC voltage source imposes a constant voltage condition across the circuit during sound actuation. Thus, when the capacitance changes due to the motion of the electrodes in response to the sound force, charge is forced in and out of the capacitor, producing an alternative current (AC) voltage output across the series resistor, which is recorded. The power output of the devices is then quantified as the peak voltage output squared divided to the series resistor. This is the typical setup for assessing the power output of electrostatic power harvesters [1,2].

For sound harvesting, the voltage output is expected to be in sync with the sound wave. This behavior is recorded here, as shown in the screen capture of the oscilloscope in Figure 3, which graph the input signal to the speaker [in yellow] and the voltage output across the series resistor [in green].

Finally, Figure 4 shows the voltage output as function of frequency for different tilts of the speaker relative to the device surface. As can be seen from this figure, and as expected, the maximum output voltage is produced when the device is parallel to the speaker (tilt 0 degrees). Based on these preliminary experiments, the maximum amount of power was calculated to be approximately 10 μW, a promising level given the fact that it was obtained for the first generation devices.

Efforts are underway to improve device design and maximize power output per 1 centimeter squared area devices.

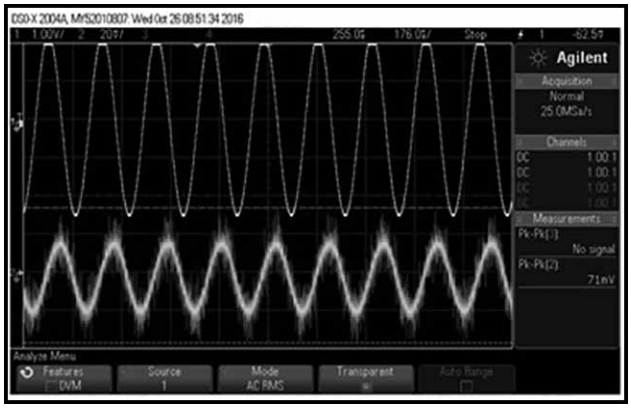

Figure 3: Screen capture from the oscilloscope: [green] is the voltage drop across the 2MΩ resistor in series with the device and the [yellow] is the input signal to the sound speaker.

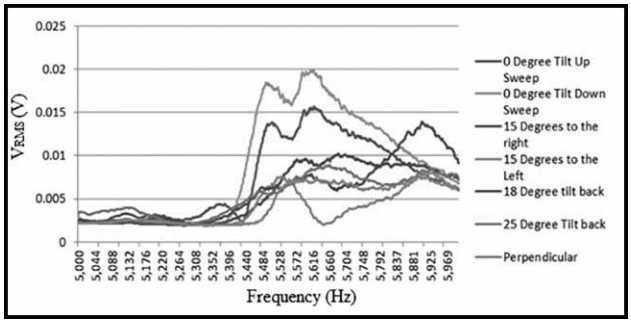

Figure 4: Root mean square (RMS) voltage output across the series resistor as function of sound frequency for different tilts of the speaker.

References:

[1] Oxaal, J., Hella, M., Borca-Tasciuc, D.-A., "Electrostatic MEMS vibration energy harvester for HVAC applications with impact-based frequency up-conversion," Journal of Micromechanics and Microengineering Vol. 26 (2016) p. 124012 (13pp) doi:10.1088/0960-1317/26/12/124012

[2] Oxaal, J., Foster, D., Hella, M. M., and Borca-Tasciuc, D.-A., "Investigation of gap-closing interdigitated capacitors for electrostatic vibration energy harvesting," Journal of Micromechanics and Microengineering, Vol. 25, p. 105010 (2015).

Investigation of Atomic Layer Deposition for Distributed Bragg Reflectors

2017 CNF REU Intern: Jonathan Chandonait

CNF REU Affiliation: Nanoscale Engineering, Colleges of Nanoscale Science and Engineering, SUNY Polytechnic Institute

CNF Project: Cornell NanoScale Science & Technology Facility Research Experience for Undergraduates (CNF REU) Program

CNF REU Principal Investigator: Prof. Huili Grace Xing, Department of Electrical and Computer Engineering, Department of Materials Science and Engineering, Cornell University

CNF REU Mentor: Shyam Bharadwaj, Department of Electrical and Computer Engineering, Cornell University

Primary Source of Research Funding: National Science Foundation via the NNCI Grant No. ECCS-1542081

Contact: jchandonait@sunypoly.edu, grace.xing@cornell.edu, sb2347@cornell.edu

Website: http://www.cnf.cornell.edu/cnf5_reuprogram.html

Primary CNF Tools Used: AFM, SEM, Filmetrics, JA Woollam Ellipsometer, Oxford ALD, P7 profilometer, ICP-RIE

Abstract:

Distributed Bragg Reflectors (DBRs) have been proposed as a method for increasing the external quantum efficiency (EQE) of light emitting diodes (LEDs) in the UV-C wavelength range (200-270nm). The DBR essentially works as mirror, collecting photons emitted in the active region of the device and reflecting them to an area where they can be extracted from the device. DBRs can be fabricated using molecular beam epitaxy (MBE) using alternating layers of AlGaN with varied composition [1]. However, atomic layer deposition (ALD) provides an alternative with several possible advantages. ALD allows the growth of dielectric films that may improve the effectiveness of these DBRs [3]. ALD also allows easier access to a much broader range of materials thanks to the flexibility of the tools. Here, we discuss preliminary efforts to evaluate ALD as a method for the fabrication of DBRs.

Summary of Research:

In current UV-C LEDs, the external quantum efficiency, or the ratio of generated photons that leave the device to electrons passing through, is currently low due to absorption losses and total internal reflection within the device. Distributed Bragg reflectors have been proposed to mitigate these issues. By using periodic quarter wavelength layers with a high refractive contrast, a mirror stack can be created with very high reflectance (Figure 1). Therefore, a large majority of the photons that reach the mirror stack will be reflected out of the device, improving the EQE of the device.

Currently there is little variety in the fabrication of DBRs for DUV LEDs. Most use MBE to grow varying compositions of AlGaN, although recently more groups have started to explore more possibilities. There are a few novel methods to change the formula, such as incorporating boron, but choices of materials are limited with MBE. Using ALD broadens the choice of materials, allowing us to take advantage of high-index contrast dielectrics, which could possibly increase the overall reflectance over a standard DBR.

Our goal was to investigate some of the advantages and obstacles involved with using ALD as a method for fabricating DBRs. In the future, the goal is to develop a dielectric mirror stack fabricated by ALD with a reflectance of > 99.9% in order to prove the viability of the method.

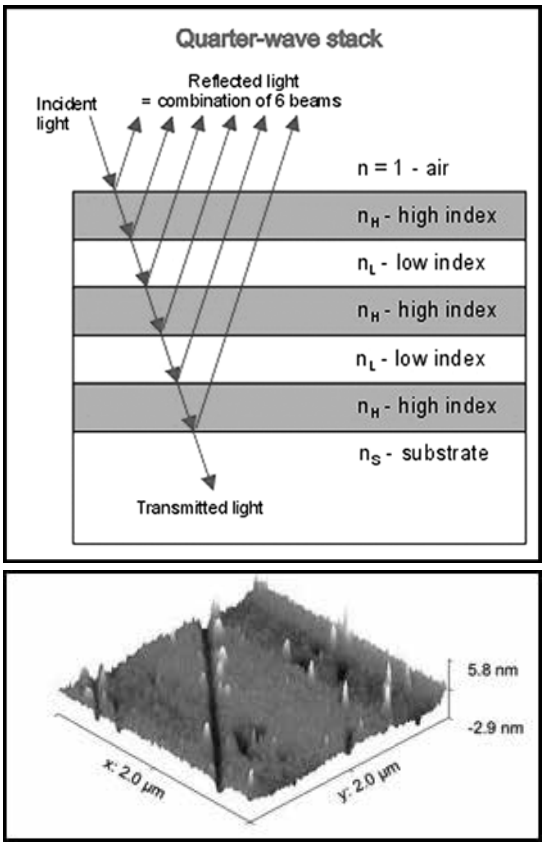

Figure 1, top: Shows the structure of a DBR and behavior of the photons that enter [2]. Figure 2. bottom: 3D AFM image of 35 nm Ta_2O_5 deposited on an AlN-on-sapphire template substrate. Shows desirable smooth surface.

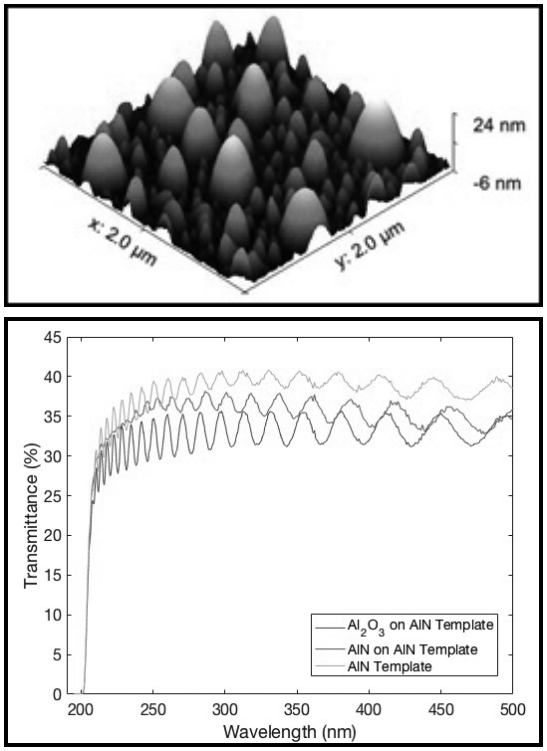

Figure 3, top: 3D AFM image of 35 nm AlN deposited on an AlN-on-sapphire template substrate. Shows undesirable rough surface. Figure 4, bottom: Graph showing the transmission spectra of our substrate, an Al_2O_3 ALD deposition, and a AlN ALD deposition.

Results and Conclusions:

Three different ALD materials were examined for surface roughness. AFM was used to characterize the surface roughness of the deposition for each material. All three depositions were carried out using 300°C plasma ALD. Ta_2O_5 showed the best results (Figure 2), giving an RMS surface roughness of 0.1 nm. Al_2O_3 showed the next best surface roughness with an RMS of 0.7 nm. AlN showed the worst surface roughness with 1.0 nm RMS (Figure 3). Varying the deposition conditions such as growth temperature can affect these results. This shows that ALD is capable of depositing materials with ultrasmooth surfaces, which is important for achieving high reflectivity.

Figure 4 shows a graph of the transmission spectra of the basic substrate (sapphire with AlN template) and depositions of Al_2O_3 and AlN with the substrate. The graph shows both films are reasonably transparent, which is essential for use in DBRs. The similarity of the two films with the substrate show that extinction is not a big issue. However, the graph also shows that the substrate itself is not very transparent, only transmitting approximately 40% of the light. This might suggest that a future possible step could be to remove the substrate through etching or lift off.

In studying growth rates between MBE and ALD, ALD demonstrates considerably slower growth rates at similar plasma powers. It is well known that ALD generally produces inferior crystal structure quality when compared to other growth methods, presenting a challenge if fabricating devices with ALD materials. However, ALD allows for atomically precise thickness control due to the monolayer nature of the process. This makes it possible to finely tune layer thicknesses to achieve complete constructive interference, which gives the highest possible measured peak reflectance.

Future Work:

There are still several factors that need to be explored to determine the viability of ALD as a method for fabrication of DBRs. The main problem that remains is the problem of crystallinity. With a typical epitaxial design consisting of the DBR being inserted between the substrate and the n-type semiconductor region, the low quality or amorphous crystal structures that are often produced by ALD can lead to defects later in the fabrication of the device. One way of getting around this problem would be to use different designs that move the mirror stack to a position in the device where it would have no effect on the structure of the rest of the device. Possible designs may include a dual-DBR stack, a flip-chip design, and several other possibilities. Other future work will involve characterization of film strain as a possible concern. Also, the dielectric properties of ALD DBRs are an important factor to explore. Furthermore, using different profiles at layer interfaces in place of flat surfaces should be explored. Finally, given the many possibilities that ALD offers, many other materials should be explored as options for fabricating DBRs.

Acknowledgements:

This work was funded by the NSF (NNCI grant no. ECCS-1532081). Special thanks to the Cornell NanoScale Science and Technology Facility and their staff for making this work possible. Also thanks to Prof. Grace Xing, Shyam Bharadwaj, and Dr. SM (Moudud) Islam for their help and support throughout the project. Finally, thank you to the NNCI for providing the opportunity to present this research at the NNCI REU Convocation in Atlanta, GA.

References:

[1] Kneissl, M., and Rass J. (2016). "III-Nitride Ultraviolet Emitters". Springer Series in Materials Science.

[2] Zhong, Y., Fu, S., Yan, S., Chen, P., and Lin, A. (2015). "Arbitrarily-Wide-Band Dielectric Mirrors and Their Applications to SiGe Solar Cells.

[3] Triani, G., Evans, P. J., Mitchell, D. RG., Attard, D. J., Finnie, K., James, M., Hanley, T., Latella, B., Prince, K. and Bartlett, J. (2005). Atomic layer depostion of TiO_2/Al_2O_3 films for optical applications. SPIE Conference on Optics and Photonics.

Process Optimization for Silicon Photonic Device Fabrication

CNF Project Number: 1850-09
Principal Investigator: Stefan Preble
User: Jeffrey Steidle

Affiliation: Microsystems Engineering, Rochester Institute of Technology
Primary Source of Research Funding: National Science Foundation
Contact: sfpeen@rit.edu, jas2518@rit.edu
Website: nanophotonics.rit.edu
Primary CNF Tools Used: JEOL JBX9500FS E-Beam, Oxford 82 Etcher, Oxford Cobra ICP Etcher, Oxford 100 PECVD System

Abstract:

Waveguide propagation loss is a very important metric for determining the viability of a silicon photonic fabrication process. Presented here are the results of optimizing two of the process steps in an effort to minimize sidewall roughness, the dominant contributor to propagation loss. Through use of a highly concentrated developer along with a pre-etch mask curing step, waveguide loopbacks and ring resonators were fabricated exhibiting a propagation loss of 5.35 dB/cm and quality factors of up to 75k. This process will continue to undergo optimization to further improve waveguide propagation loss.

Summary of Research:

For silicon photonic circuits, one of the key figures of merit is propagation loss. Propagation loss in silicon waveguides is primarily due to scattering from sidewall roughness. Presented here is the development of a fabrication process to minimize waveguide sidewall roughness.

The process for fabricating passive silicon photonic circuits consists of only three steps: electron beam lithography for writing the pattern in a mask, dry etching to translate the mask to the silicon, and deposition of a silica cladding. While each of these steps can impact the propagation loss of the circuit, the focus here will be on the electron-beam lithography as well as the dry etch.

The electron beam lithography was performed with the JEOL JBX9500FS with a 10 nA beam current and an 8 nm shot pitch. A 6% solution of hydrogen silsesquioxane (HSQ) was used as a negative resist (XR.1541 from Dow Corning) and was spun at 2000 rpm for 60s with a 1000 rpm/s ramp. The HSQ was baked at 170°C for two minutes prior to exposure. A concentrated solution (25%) of tetramethylammonium hydroxide (TMAH) was used to develop the HSQ at room temperature with a duration of 60s under constant agitation. This developer was chosen as it has been demonstrated to enable the fabrication of small, high contrast features [1]. The next parameter to optimize was the exposure dose. To do so, a grid of test features was exposed with sixteen different doses ranging from 1000 to 5000 μC/cm^2. Upon imaging the resulting HSQ masks, it was found that a dose of 2250 μC/cm^2 most closely matched the designed pattern (Figure 1).

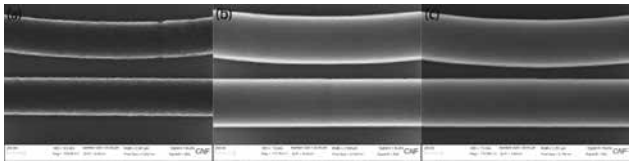

Figure 1: Scanning electron micrographs of the exposed and developed HSQ mask. The exposure doses are (a)1000 μC/cm^2, (b) 2250 μC/cm^2, and (c) 3500 μC/cm^2.

The silicon etch was carried out with the recently acquired Oxford Cobra ICP etcher using an HBr etch recipe (named 'HBr SOI 1' on the tool). Due to the thickness of the HSQ mask and the low selectivity between HSQ and silicon, an HSQ curing step was required prior to the silicon etch. This was done by exposing the piece to an oxygen plasma in the Oxford 82 etcher for one minute. A side effect of the curing process is some oxidation of the silicon surface. As a result, the first 30 s of the etch process did not etch any of the silicon and a total etch time of 150 s was required to fully etch the waveguides. A partially etched

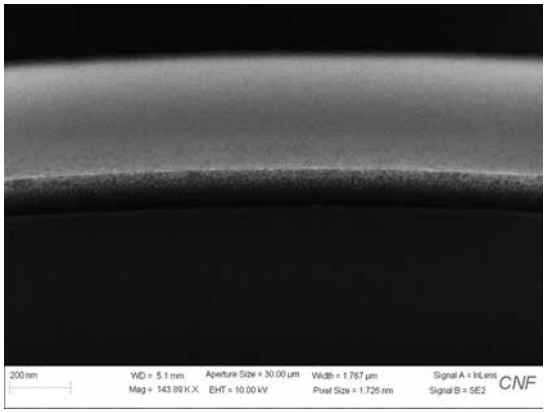

Figure 2: A scanning electron micrograph of a partially etched silicon ring resonator taken with a 45 degree tilt.

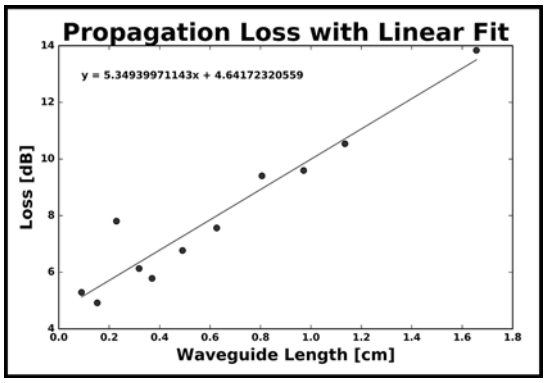

Figure 3: Comparison between total insertion loss and waveguide length. The overlaid linear fit was used to extract the coupling and propagation losses.

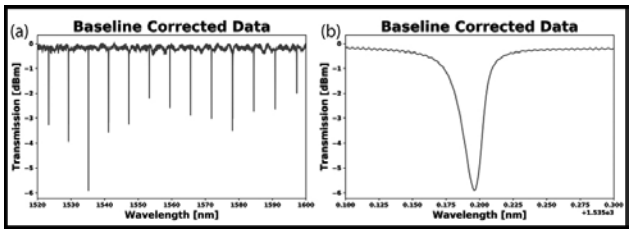

Figure 4: Transmission spectrum of a silicon ring resonator with a radius of 15 µm and waveguide/ring gap of 225 nm with wavelength ranges of (a) 80 nm and (b) 0.2 nm.

silicon ring resonator is shown in Figure 2, showing a smooth, vertical sidewall. The spotted pattern on the sidewall seemed to be a result of the HSQ mask and was removed after etching with a short (~20s) hydrofluoric acid dip prior to cladding.

In order to quantify the progress that had been made, a layout was designed that included waveguide loopbacks with lengths ranging from 900 µm to 1.6 cm as well as some single-bus ring resonators with ring radii of 15 µm and waveguide/ring gaps ranging from 150 nm to 300 nm. Upon measuring the total insertion loss for each of the waveguide loopbacks and performing a linear fit to the resulting data, the coupling loss and propagation loss were found to be 2.32 dB/facet and 5.35 dB/cm respectively (Figure 3). The ring resonators were also measured (Figure 4) and exhibited quality factors of up to 75k, indicative of low propagation loss.

In conclusion, two of the steps of a silicon photonic fabrication process have been optimized to minimize sidewall roughness and, in turn, reduce propagation loss. Propagation loss was measured to be 5.35 dB/cm and single-bus ring resonators were fabricated to exhibit quality factors of up to 75k. Further optimization will involve initial wafer cleaning procedures, electron-beam multi-patterning, and trying different cladding recipes to push the propagation loss even lower.

References:

[1] W. Henschel, Y. M. Georgiev, and H. Kurz, Study of a high contrast process for hydrogen silsesquioxane as a negative tone electron beam resist, J. Vac. Sci. Technol. B 21, 2018 (2003).

Quaternary Semiconductors for Integrated Nonlinear Optics

CNF Project Number: 1862-10

Principal Investigators: Robert Boyd[1], Ksenia Dolgaleva[2], Antonio Badolato[3]

User: Kashif Masud Awan[4]

Affiliations: 1. The Institute of Optics, University of Rochester; 2. Canada Research Chair in Integrated Photonics, University of Ottawa; 3. Physics and Astronomy, University of Rochester; 4. Electrical Engineering, University of Ottawa

Primary Source of Research Funding: Canada Excellence Research Chairs Program

Contact: boydrw@mac.com, ksenia.dolgaleva@uottawa.ca, antonio.badolato@gmail.com, kashifmasudawan@gmail.com

Website: http://www.quantumphotonics.uottawa.ca/

Primary CNF Tools Used: JEOL 9500, Zeiss Ultra, PT770, Oxford PECVD, SC4500, Oxford 100, Trion

Abstract:

We propose strip-loaded and nanowire waveguides on quaternary III-V semiconductor InGaAsP for integrated nonlinear optics. III-V Quaternary semiconductors have been widely used for laser sources and multilayer mirrors such as Bragg reflectors. However, their nonlinear optical properties yet remain unexplored, while the materials definitely hold promise for nonlinear photonics on-a-chip, since III-V compounds tend to exhibit high values of the nonlinear optical susceptibilities, while the nonlinear absorption in these materials can be minimized in the wavelength range of interest through a proper selection of the material composition. We designed waveguide structures based on InGaAsP and show that the effective mode area as small as 1.0 μm² can be achieved through the optimized design. We also present fabrication process for these waveguides and optical transmission loss measurements along with self-phase modulation data are also presented.

Summary of Research:

All-optical wavelength conversion can be achieved through nonlinear optical effects, such as four-wave mixing, cross-phase modulation, or a two-step $\chi^{(2)}$ process involving a difference-frequency generation followed by a sum-frequency generation [1]. Several material platforms have been used to demonstrate all-optical wavelength conversion and other operations of optical signal processing. Among these materials, III-V semiconductor compound, such as, aluminum gallium arsenide (AlGaAs), demonstrated the best potential for nonlinear photonic devices [2]. In the present study, we extend the quest for suitable nonlinear optical materials to III-V quaternary semiconductor: indium gallium arsenide phosphide ($In_{1-x}Ga_xAs_yP_{1-y}$), whose relative composition (x and y) add another degree of freedom (compared to tertiary semiconductors, such as AlGaAs) to control optical linear and nonlinear properties.

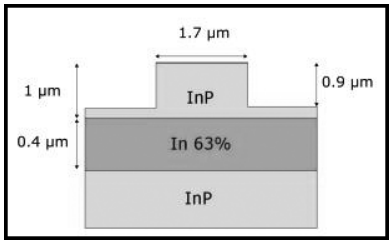

Figure 1: Schematic of InGaAsP waveguide with wafer composition.

InGaAsP passive nonlinear waveguides can be used in combination with integrated InGaAsP lasers to extend their range of operation to longer wavelengths (2 μm and beyond). Such sources can be of interest in spectroscopy and environmental sensing, specifically for lab-on-chip applications that are of interest specially for biosensing [3]. This motivates our studies on the nonlinear optical performance of InGaAsP.

Designs of the material composition and waveguide geometry were optimized to achieve high confinement, while being suitable for epitaxial growth on lattice-matched substrates, indium phosphide in this case. For high confinement, material compositions with high refractive index contrast between core and cladding layers was selected. Numerical simulations of the Eigenmode were performed using finite-difference Eigenmode method. Figure 1 shows a schematic of the designed strip-loaded waveguide along with wafer composition for substrate, core and cladding layers. Simulated effective modal area of this waveguide design was 1.0 μm².

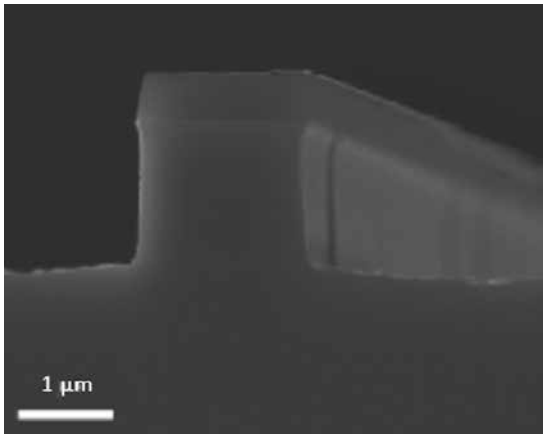

Figure 2: SEM image of fabricated InGaAsP waveguide.

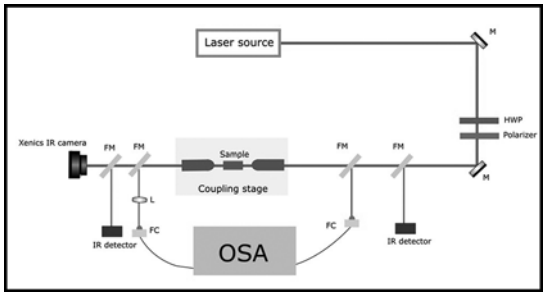

Figure 3: Optical setup for self-phase modulation experiment.

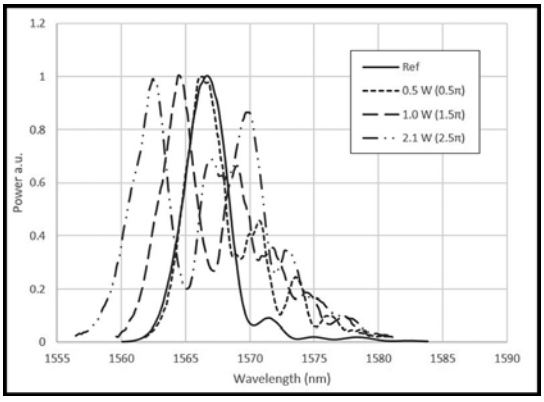

Figure 4: Power spectra showing self-phase modulation in InGaAsP waveguide, nonlinear phase shift and power in waveguides is listed.

Strip-loaded InGaAsP waveguides were fabricated with waveguide widths ranging from 1.5 µm to 1.9 µm. Wafer was grown by a commercial vendor using molecular beam epitaxy. 250 nm of silica was deposited by plasma enhanced chemical vapor deposition, followed by 50 nm of chromium deposited using electron-beam evaporation. Negative tone e-beam resist HSQ was spin-coated and patterned using 100 kV JEOL electron beam lithography system. Waveguide pattern was etched into chromium layer using inductively coupled plasma reactive ion etching (ICP-RIE) to generate mask for etching silica layer. Silica layer was then etched using another ICP-RIE to form silica mask, which was finally used to etch InGaAsP. Scanning electron microscopy images of fabricated structures are shown in Figure 2.

Fabry-Perot method was used for measuring propagation losses [4]. Measured propagation loss for 1.7 µm wide waveguide was 1.5 dB/cm, which is lower than any published data for InGaAsP waveguides, to the best of our knowledge. To demonstrate nonlinear optical process in such waveguides, self-phase modulation measurements were performed using setup shown in Figure 3, spectral broadening is shown in Figure 4, showing power in waveguides in watts (W) and also approximate nonlinear phase shift. These measurements hint at efficient nonlinear effect in InGaAsP waveguides, detailed measurements to determine quantitative efficiency are in progress.

This study demonstrates InGaAsP as a suitable candidate for integrated nonlinear optics targeting optical applications in mid-infrared band. Low propagation losses were achieved using our fabrication process and self-phase modulation was demonstrated.

References:

[1] RW Boyd, Nonlinear Optics, 3rd Edition, AP (2008).

[2] K Dolgaleva, et al., Opt. Express 19, 12440-12455 (2011).

[3] M. Ka.uráková, et al., Carb. Polymers 44, 291-303 (2001).

[4] RJ Deri, et al., IEEE J. Quantum Electron. 27, 626–640 (1991).

Visible Three-Dimensional Metallic Photonic Crystal

CNF Project Number: 1880-10
Principal Investigators: Professor Shawn-Yu Lin
Users: Ping Kuang, Brian Frey

Affiliation: Physics Department, Rensselaer Polytechnic Institute
Primary Source of Research Funding: Department of Energy, Office of Science, Basic Energy Science
Contact: sylin@rpi.edu, freyb2@rpi.edu
Primary CNF Tools Used: CVD silicon deposition, reactive ion beam etcher, deep UV lithography

Abstract:

In this work, a novel Teepee-like photonic crystal (PC) structure on crystalline silicon (Si) is experimentally demonstrated. Our PC structure is shown to exhibit 98.5% solar absorption over λ = 400-1000 nm spectral range for 500 μm-thick silicon. By reducing the silicon solid content by 50 times to only 10 μm thick, we still achieve a 94.7% averaged solar absorption. This data represents, to the best of our knowledge, the best average absorption for such a super-thin Si.

Summary of Research:

In summary, we proposed and demonstrated a new Teepee-like PC design with broadband, wide-angle near-unity solar energy absorption, which is achieved by novel light trapping mechanisms: (1) Gaussian-type gradient-index interface profile and (2) near-orthogonal parallel-to-interface negative refraction. The Teepee-like PC structure is realized by a unique but simple photolithography patterning and RIE dry etching process, which is repeatable and IC-technology compatible for large-area, high-throughput wafer-scale fabrications. The funnel-like geometry of the PC structure with greater vertical depth and higher sidewall angle means it can achieve better light trapping than typical KOH-etched inverted pyramid structures.

Teepee-like PC on 500-μm crystalline silicon can already achieve a broadband near-zero reflection and near-unity absorption (A=98.5%) in λ = 400-1000 nm. For Teepee-like PC on much thinner c-Si (t=10μm), the average absorption is ~ 94.7%. Even for near IR wavelengths (λ=800-1000nm), the average absorption is sustained at ~ 90.5%. The main reason for enhanced light trapping and significantly improved near IR absorption in much thinner c-Si is the parallel-to-interface refraction effect, which creates near-90° optical refraction and vortex-like energy circulation patterns concentrated inside absorbing material. Therefore, the Teepee-like photonic crystal shows excellent promise for achieving greater efficiency improvement in both conventional and thin film crystalline silicon solar cells towards the Shockley-Queisser limit.

References:

[1] P. Kuang, S. Eyderman, M.-L. Hsieh, A. Post, S. John, and S.-Y. Lin, "Achieving an Accurate Surface Profile of a Photonic Crystal for Near-Unity Solar Absorption in a Super Thin-Film Architecture", ACS Nano, 10, pp 6116-6124 (2016).

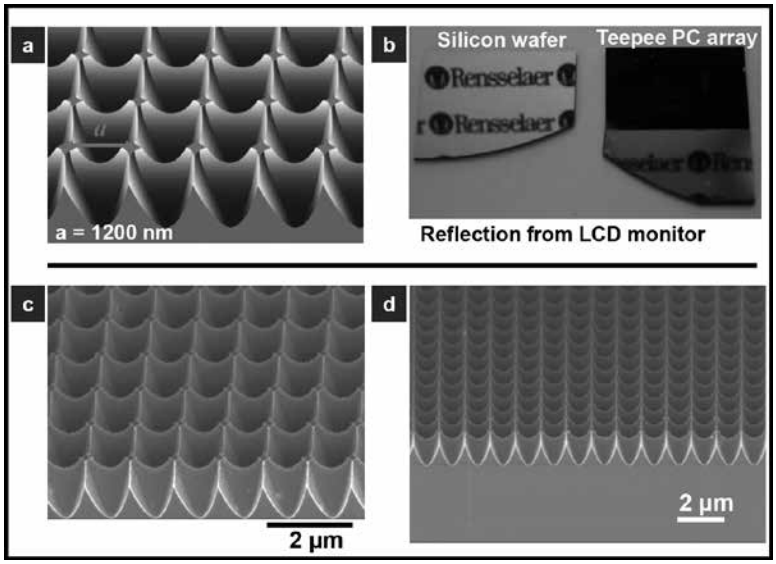

Figure 1: (a) Schematic representation of the Teepee-like photonic crystal structure. (b) Optical reflection from polished, planar silicon wafer surface and from the Teepee-like photonic crystal structure surface. (c) SEM image of the Teepee-like photonic crystal structure at slanted view. (d) SEM image of the photonic crystal at front side view.

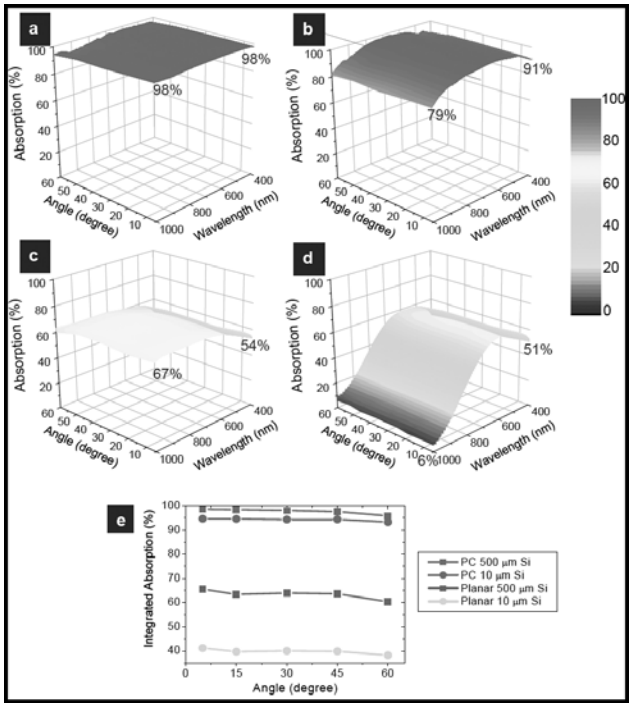

Figure 2: 3D contour plots of measured total absorption of (a) Teepee-like photonic crystal structure on 500 μm thick silicon with 60 nm SiO_2 AR coating, (b) Teepee-like photonic crystal on 10 μm thick silicon with 60 nm SiO_2 AR coating and 200 nm Ag back reflector, (c) planar 500 μm thick silicon, and (d) planar 10 μm thick silicon at different incident angles. (e) Measured integrated absorption of the four samples for λ = 400-1000 nm at different incident angles.

Lithium Niobate Micro-Structures

CNF Project Number: 1997-11
Principal Investigator: Qiang Lin
Users: Rui Luo, Hanxiao Liang, Yang He

Affiliation: Department of Electrical and Computer Engineering, University of Rochester
Primary Source of Research Funding: National Science Foundation (ECCS-1509749, ECCS-1610674)
Contact: qiang.lin@rochester.edu, ruiluo@rochester.edu, hanxiao.liang@rochester.edu, yhe26@ur.rochester.edu
Website: http://photonlab.hajim.rochester.edu/
Primary CNF Tools Used: JEOL 9500, AJA Ion Mill

Abstract:

Lithium niobate, with its wide applications in optics and mechanics, is a chemically inert material, and fabrication techniques for microscale and nanoscale structures of lithium niobate are to be developed. In this report, we demonstrate fabricating high-quality lithium niobate microdisk resonators and nanobeam photonic crystal cavities, using electron beam lithography and ion milling. Our devices exhibit high optical quality (*Q*) factors, paving the way for cavity nonlinear optics and cavity opto-mechanics of lithium niobate.

Summary of Research:

Lithium niobate, $LiNbO_3$, with its large optical nonlinearities, wide transparency window, high optical damage threshold, and high mechanical stiffness, has been widely studied in the fields of optics and mechanics for decades. Recently, $LiNbO_3$ on insulator thin film wafers are available, giving us opportunities to study optical, mechanical and electrical properties of $LiNbO_3$ in the microscale. However, since $LiNbO_3$ does not efficiently react with commonly used etching chemicals, its fabrication is nontrivial. A variety of fabrication techniques have been explored to make optical waveguides or resonators with $LiNbO_3$, including titanium diffusion [1], hybrid waveguiding [2-4], machining [5], laser writing [6], and direct ion etching [7-10]. Direct ion etching, which uses standard electron beam lithography and ion milling, is potentially capable of defining microscale and nanoscale lithium niobate structures with high optical confinement and small footprints, and thus is selected by us to fabricate microdisk resonators and nanobeam photonic crystal cavities. Our devices show high optical qualities ($Q > 10^6$ for microdisk resonators and $Q > 10^5$ for nanobeam photonic crystal cavities), and are promising for on-chip nonlinear optics, quantum photonics, and opto-mechanics.

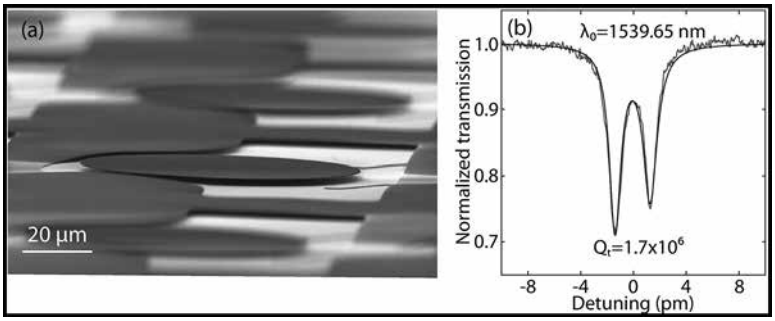

Figure 1: (a) A scanning electron microscopy picture, and (b) a telecom-band cavity resonance and its Lorentzian fitting, of a typical fabricated lithium niobate microdisk resonator. (See cover!)

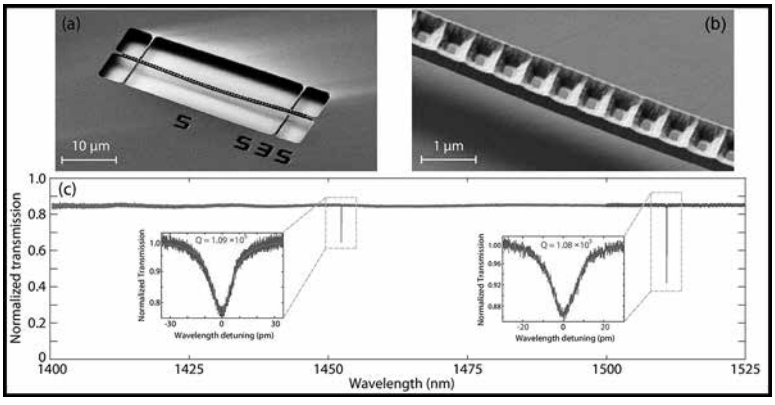

Figure 2: (a) (b) SEM pictures, and (c) broadband transmission spectrum, of a typical fabricated lithium niobate nanobeam photonic crystal cavity. Insets: zoom-in cavity resonances and Lorentzian fittings.

The fabrication process of our devices is pretty standard. First, we start with an x-cut lithium niobate-on-insulator wafer, which has a device layer of 300 nm sitting on a buried silicon oxide layer of 2 μm; then we spin ZEP-520A on the top of the wafer, and pattern with JEOL 9500 electron beam lithography. Second, $LiNbO_3$ is etched with AJA ion milling, with ZEP-520A as the mask. Next, the remaining resist is removed by YES Asher oxygen plasma etcher. Finally, diluted hydrofluoric acid is utilized to remove buried silicon oxide and release our suspended structures.

Figure 1 shows our fabricated microdisk resonators and a typical cavity resonance. The resonance in the telecom band, shown in Figure 1(b), is from a microdisk with a radius of 45 μm, and exhibits a loaded optical Q of 1.7×10^6, which to our best knowledge is the highest record among reported microscale lithium niobate microdisk resonators.

The high optical quality indicates good etching of our fabrication techniques, and gives us opportunities to make more delicate structures. Thus, we design nanobeam photonic crystal cavities and do the fabrication with the same method. Our fabricated nanobeam, shown in Figure 2 (a), consists of multiple aligned rectangular holes, with their sizes the smallest in the center, and gradually growing up towards the two ends. The non-uniform lattice forms a defect in a one-dimensional photonic crystal, and thus is able to support high-Q optical modes that are tightly confined around the center of the nanobeam. Figure 2(b) gives more details of the nanobeam, of which the width is 750 nm and rectangular openings are around 200 nm × 100 nm. Sidewalls are pretty smooth, and exhibit a non-vertical slant angle, resulting from the ion milling process. Figure 2(c) shows the transmission spectrum of a typical nanobeam photonic crystal cavity, with two cavity resonances. Both resonances show Q's of over 10^5, which confirms the robustness of our design and the capability of making sub-microscale structures with our fabrication method.

In conclusion, we have developed fabrication on lithium niobate-on-insulator platform using electron beam lithography and ion milling. High-quality etching of lithium niobate is verified by our microdisk resonator with Q of 1.7×10^6 and nanobeam photonic crystal cavity with Q of 1.1×10^5. Our work is of great potential for nonlinear optics, quantum photonics, and opto-mechanics of lithium niobate on chip.

References:

[1] M. Fukuma, et al, J. Appl. Phys. 49, 3693 (1978).
[2] L. Chen, et al, Optica 1, 112 (2014).
[3] J. Chiles, et al, Optica 1, 350 (2014).
[4] L. Chang, et al, Optica 3, 531 (2016).
[5] A. A. Savchenkov, et al, Appl. Phys. Lett. 88, 241909 (2006).
[6] J. Lin, et al, Sci. Rep. 5, 8072 (2015).
[7] A. Guarino, et al, Nature Photon. 1, 407 (2007).
[8] C. Wang, et al, Opt. Express 22, 30924 (2014).
[9] W. C. Jiang, et al, Sci. Rep. 6, 36920 (2016).
[10] R. Luo, et al, Opt. Lett. 42, 1291 (2017).

Fabrication of Silicon Single-Photon Avalanche Diodes (SPADs)

CNF Project Number: 2232-13
Principal Investigator: Massimo Ghioni
User: Angelo Gulinatti

Affiliation: Dipartimento di Elettronica, Informazione e Bioingegneria, Politecnico di Milano
Primary Source of Research Funding: National Institutes of Health, Grant 5R01-GM095904
Contact: massimo.ghioni@polimi.it, angelo.gulinatti@polimi.it
Primary CNF Tools Used: Oxford 82, GSI PECVD, AJA Sputter Deposition, GCA Autostep 200

Abstract:

Single photon avalanche diodes (SPADs) are devices capable of signaling the arrival of a photon by means of a synchronous electrical pulse. They are enabling technologies for many applications in fields ranging from quantum physics to life science. Our aim is to develop new generations of SPAD detectors to meet the requirements of most demanding applications in terms of single pixel performance and multi-pixel integration.

Summary of Research:

Many applications in fields ranging from biology to material science, from quantum physics to astronomy, from biochemistry to quantum cryptography require the detection of single photons in the visible and near-infrared region of the spectrum.

Although single-photon detection has been achieved for many years by using photo-multipliers tubes (PMTs), in the last years single photon avalanche diodes (SPADs) emerged as a valid alternative to PMTs and, thanks to their remarkable performance, in the last decade they started replacing PMTs in the most demanding applications like single molecule analysis, quantum cryptography, laser ranging, etc. A SPAD is a p-n junction reverse biased above the breakdown voltage in a metastable state in which no current flows. When a photon is absorbed into the device active area, a self-sustained avalanche is triggered by the photo-generated electron-hole pair. The macroscopic current that results from this process allows for a simple detection of the photon itself [1].

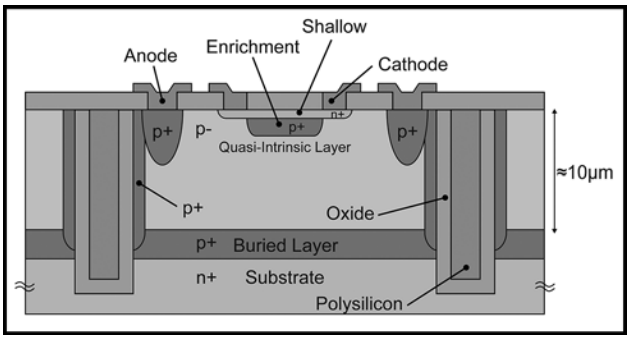

Figure 1: Cross-section of a red-enhanced SPAD with deep trenches.

During years 2014-2015 we fabricated devices with the structure represented in Figure 1. Compared to thin SPADs [1], these detectors provide higher photon detection efficiency (PDE) in the red/near-infrared region of the spectrum thanks to an increased thickness of the absorption layer (about 12 µm vs. 5 µm) [2]. However, they require the introduction of deep trenches for attaining electrical isolation between multiple devices on monolithic arrays [3] and may also require guard rings (not shown in Figure 1) to be operated at high bias voltages without suffering of edge breakdown.

The experimental characterization of the red-enhanced SPADs manufactured during years 2014-2015 highlighted a few technological problems related to the last steps of the fabrication process (backend technology). These resulted in: a) a reduced thickness of the antireflective coating; b) guard-rings shorted with the cathode; c) interconnection metals broken in some regions of each wafer. Since all these issues are related to the last steps of the fabrication, during years 2015-2016 we reworked part of the affected wafers, with the aim of attaining working devices and gaining a better understanding of the problems. Rework consisted essentially in stripping the aluminum interconnection layer and the antireflective coating, then in re-depositing and patterning them with a different process flow and by using different tools [4].

The experimental characterization showed the effectiveness of the reworking in solving the outlined issues [3]. This allowed us to build a 32 × 1-pixel SPAD-array module currently used in a high-throughput Single Molecule Analysis setup developed in collaboration with Prof. Weiss and Dr. Michalet group at University of California Los Angeles (UCLA) [5].

A remarkable drawback of the 2015-2016 reworking process is an increase in the dark count rate (DCR) of the detectors (see Figure 2), that poses some limitations for their use in most demanding applications, like single molecule analysis. In order to better understand this issue we decided to rework some additional wafers. In particular, to narrow down the list of the processes potentially responsible for the increase in the DCR, during year 2017 we performed only the part of the reworking needed to fix the issue with the antireflective coating. So we stripped the defective oxide layer by means of plasma etching (Oxford 82), we re-deposited a suitable layer of oxide by either GSI plasma-enhanced chemical vapor deposition or by AJA sputter deposition, then we removed the oxide from the bonding pads (GCA Autostep 200 and Oxford 82).

Preliminary characterization showed that wafers reworked during 2017 did not experience an increase in the DCR. In particular, Figure 3 shows the DCR distribution measured on the same devices before and after reworking. The apparent small decrease in the DCR after reworking is only due to a slightly different measurement temperature. Additional investigation will be carried out to further clarify the mechanisms the led to the increase in the DCR during 2015-2016 rework and to find out possible solutions.

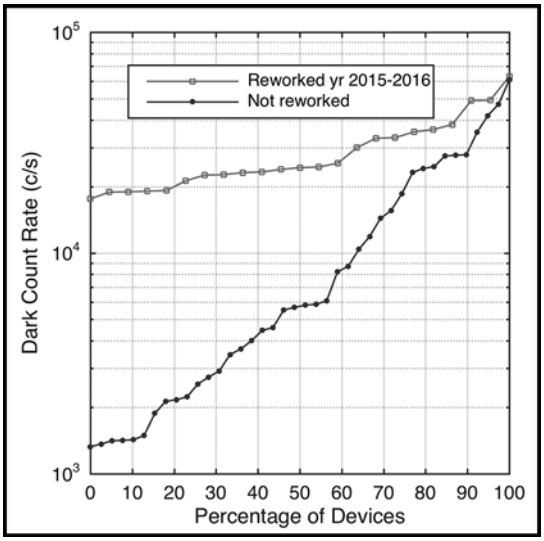

Figure 2: Dark count rate distribution before and after 2015-2016 reworking.

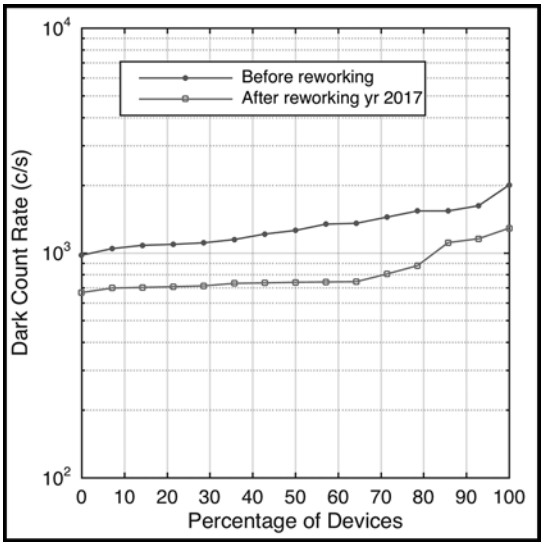

Figure 3: Dark count rate distribution before and after 2017 reworking.

References:

[1] M. Ghioni, et al., "Progress in Silicon Single-Photon Avalanche Diodes," IEEE J. Select. Topics Quantum Electron., vol. 13, pp. 852-862, 2007.

[2] A. Gulinatti, et al., "New silicon SPAD technology for enhanced red-sensitivity, high-resolution timing and system integration," J. Modern Optics, vol. 59, pp. 1489-1499, 2012.

[3] A. Gulinatti, et al., "Silicon technologies for arrays of Single Photon Avalanche Diodes," presented at the SPIE Commercial + Scientific Sensing and Imaging, 2016, vol. 9858, p. 98580A.

[4] A. Gulinatti, "Fabrication of Silicon Single-Photon Avalanche Diodes (SPADs)," 2015-2016 CNF Research Accomplishment, pp. 136-137, 2016.

[5] X. Michalet, et al., "Silicon Photon-Counting Avalanche Diodes for Single-Molecule Fluorescence Spectroscopy," IEEE J. Sel. Top. Quantum Electron. vol. 20, 3804420, 2014.

Silicon-Based PN Junction Linear Modulator

CNF Project Number: 2325-15
Principal Investigator: Zhaoran Rena Huang
User: Lingjun Jiang

Affiliation: Department of Electrical, Computer and Systems Engineering, Rensselaer Polytechnic Institute

Primary Source of Research Funding: Army Research Lab

Contact: zrhuang@ecse.rpi.edu, jiangl2@rpi.edu

Primary CNF Tools Used: JEOL 9500 e-beam lithography, UNAXIS 770 deep Si etcher, Oxford ALD FlexAL, YES Asher, Oxford PECVD, DISCO dicing saw

Abstract:

We have designed and fabricated silicon-based optical waveguides and Bragg gratings over the past year in CNF. E-beam lithography is used to define the patterns and several issues have been solved for e-beam exposure. The waveguides and gratings are tested with a tunable laser and the transmission spectrum has met our expectations.

Summary of Research:

Our project goal is to fabricate optical modulators on silicon-on-insulator (SOI) substrate. Modulators are usually optical waveguides that incorporate PN junctions for electrical control. In order to make the device shorter, we take advantage of the slow light effect of Bragg gratings at wavelengths near the band edge. This report focuses on the fabrication and testing of Bragg gratings.

The top Si layer of the SOI substrate is 250 nm thick, and the etching depth is 200 nm, which leaves a 50 nm-thick Si slab for electrical connection. According to our simulation, the grating pitch is chosen to be around 300 nm to keep the band edge at telecommunication wavelengths. Apodization is used to improve spectrum quality.

The most important processing step is e-beam lithography that defines the gratings. There are three main issues that we have encountered during fabrication is from the JEOL 9500 e-beam lithography:

(1) The geometry parameters usually have a small variation with respect to the layout in our .gds file. The most critical parameter of the Bragg grating is its pitch size and filling factor. Since SOI substrate is a high index contrast material, a small change in the pitch size and filling factor will result in significant change in the transmission spectrum. Once the band edge falls outside the range of our C band tunable laser, the gratings cannot be tested. In order to reduce the variation proximity effect correction is applied when preparing the .v30 file. We also do a testing exposure every time and manually add an offset to the layout to balance out the variation.

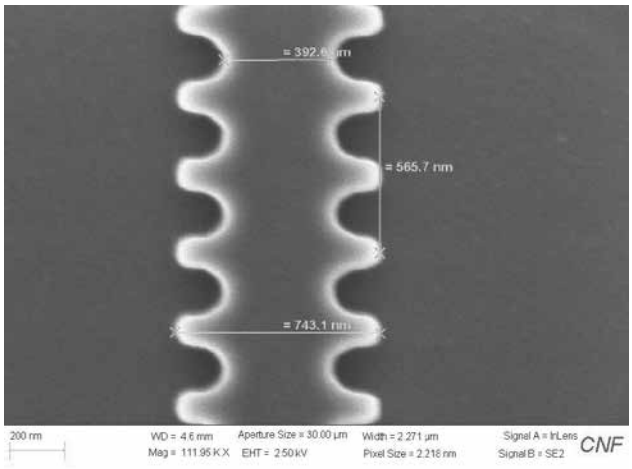

Figure 1: Rounded corners of a grating due to poor focus.

(2) The condition file is sometimes not maintained on time and will result in a bad beam alignment, a poor focus, and a low current level. The AE mark on the stage may also fail when the beam is trying to focus. If the pattern is exposed using a bad condition file, it will be out of shape. Our grating structures which have rectangle-shaped pitches, end up with a rounded corner due to poor focus, as shown in Figure 1.

(3) For long waveguide fabrication, large stitching error often occurs during exposure when there are

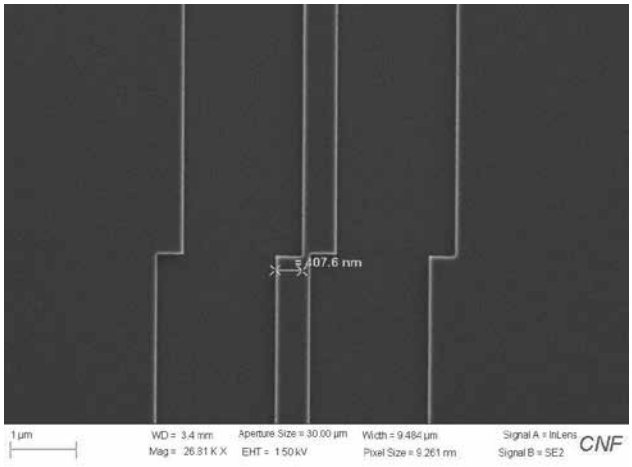

Figure 2: Field stitching error of ~ 400 nm in a Bragg grating.

over 100 fields and the writing time is over two hours. The stitching error can be as large as 400 nm for a single mode waveguide, which will totally block light propagation, as shown in Figure 2. The problem has been solved by using the "multipath" function in Layout Beamer, which exposes the pattern twice and removes the stitching error by taking the average. However, this is at the cost of longer writing time.

Other processing steps are very straightforward. We use a photonic etch recipe with UNAXIS deep Si etcher, whose etching rate is about 200 nm/min. Then we use both atomic layer growth (ALD), and Plasma-enhanced chemical vapor deposition (PECVD) to deposit a top SiO_2 cladding layer. ALD is necessary because PECVD cannot fill up the grating pitches. Every step is first characterized carefully on dummy samples before processing on real samples. The samples will be diced and polished before we test them. Figure 3 shows an image of a portion of a fabricated grating device.

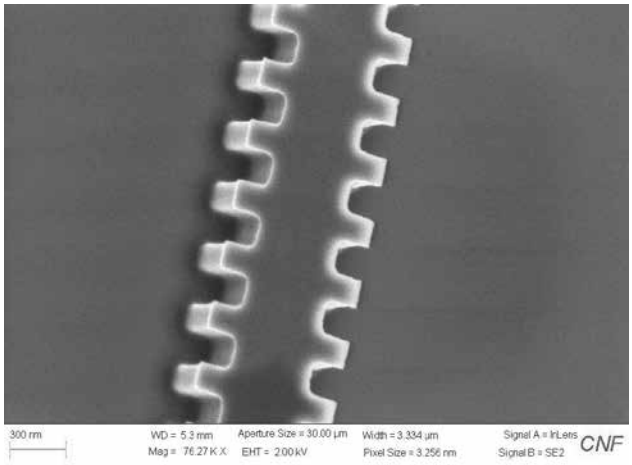

Figure 3: Image of a fabricated Bragg grating segment.

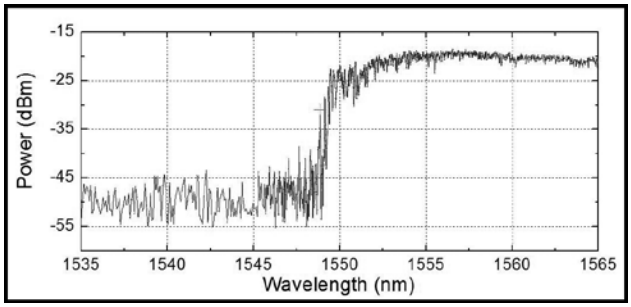

Figure 4: Transmission spectrum of a Bragg grating.

The gratings are tested for their transmission spectrum and wavelength-dependent group index at telecommunication wavelengths. TE mode is used. Figure 4 shows an example of the measurement results.

The optical band gap edge is found at λ = 1548.8 nm, and there is ~ 30 dB extinction ratio between pass band and the band gap. The fringes near the band edge come from the parasitic FP cavities. Possible sources include chip facets and grating mode mismatch. Insertion loss is mostly from the fiber-to-chip coupling loss, which is estimated to be 10 dB per facet. We measure the propagation loss of single mode waveguides for TE polarization as well and it's around 4 dB per cm. The scattering loss could be decreased by using thermal oxidation to reduce surface roughness.

Other than gratings, we have also fabricated some building blocks of photonic circuits, such as Y splitters, direction couplers, Mach-Zehnder interferometer (MZI), inverse tapers, etc. Careful design of these basic structures can remove parasitic Fabry-Perot (FP) cavities in the optical path. We are looking forward to adding electrical part of the device by ion-implantation, via etching and metallization in near future.

Pixelated Polarizer for IR Focal Plane Array

CNF Project Number: 2359-15

Principal Investigator and User: Lori Lepak

Affiliation: Phoebus Optoelectronics, LLC

Primary Source of Research Funding: Department of Defense

Contact: llepak@phoebusopto.com

Website: www.phoebusopto.com

Primary CNF Tools Used: JEOL 9500 electron beam lithography, DWL2000 photomask writer, ASML DUV stepper, SC4500 evaporator, AJA ion mill, Zeiss SEM

Abstract:

Since 2003, Phoebus Optoelectronics has enabled custom R&D solutions in the fields of metamaterials, plasmonics, antennas, and sensors. We work closely with our customers throughout device development, from product realization to small volume manufacturing. Our R&D portfolio spans the spectral ranges of visible light, infrared, terahertz, and microwave radiation, for applications in high resolution infrared imaging systems, wavelength and polarization filtering, tunable optical components, beam forming and steering, solar cells and renewable energy devices, and chemical and biological toxin sensors. Our agile team makes extensive use of the resources at the CNF for our nano/micro fabrication and testing, to provide cost efficiency and rapid turnaround. In this report, we discuss the ongoing development of a metamaterial-based pixelated focusing polarizing device.

Summary of Research:

Extraordinary optical transmission (EOT) is a phenomenon in which light is transmitted through apertures much smaller than the incident wavelength, at anomalously large intensities relative to the predictions of conventional aperture theory. EOT was first observed by T.W. Ebbesen in 1998 [1], setting off a flurry of research into metamaterials and anomalous transmission, into which Phoebus Optoelectronics was an early entrant. For over 10 years, Phoebus has successfully incorporated metasurfaces into devices used to perform light filtering [2-3], photon sorting [4-5], polarimetric detection [6], high speed optical detection [7], optical sensing of biological and chemical toxins [8], and other light controlling tasks. In the present report, we present recent developments toward the development of a metamaterial-based pixelated focusing polarizer.

The current industry standard for pixelated polarizers is a wire grid geometry. However, this decades-old technology has been developed to its full potential, in that the further optimization of wire grid pixels is limited by optical physics itself. Each wire grid diffracts light very strongly, so that as the transmission of individual pixels increases, the cross talk between neighboring pixels increases as well, which decreases resolution.

We have developed an on-chip pixelated polarimeter device that *sidesteps this fundamental tradeoff between cross talk and transmission*, by using metasurfaces in place of wire grids, to simultaneously minimize diffraction and better collimate the transmitted light. In our first-generation IR polarimeter, which is currently commercially available, each pixel has the structure shown in Figure 1, with four arrays of wires oriented at 0°, 45°, 90°, and 135° to each other. Each array is capable of acting as a graded index lens to focus and collimate transmitted light. At the same time, the phase delay produced by the four arrays together allow the pixel as a whole to behave as a polarizer to control the phase of the light. A higher magnification image of a typical array (Figure 2) illustrates the high aspect ratios and smooth sidewalls that are essential for the high-quality performance of our metasurface structures. We are currently developing additional metasurface structures, such as the second generation design shown in Figure 3, which are tailored to operate in other spectral ranges.

Preliminary computer simulations, shown in Figure 4, demonstrate the ability of our metasurface structures to simultaneously deliver higher transmittance and lower cross talk between pixels than the current generation of wire-grid-based pixelated polarimeters. Our meta-structures combine the advantages of extremely high extinction ratios (>10000:1), high transmission, and lower cross talk between pixels than the current state-of-the-art wire grid technology.

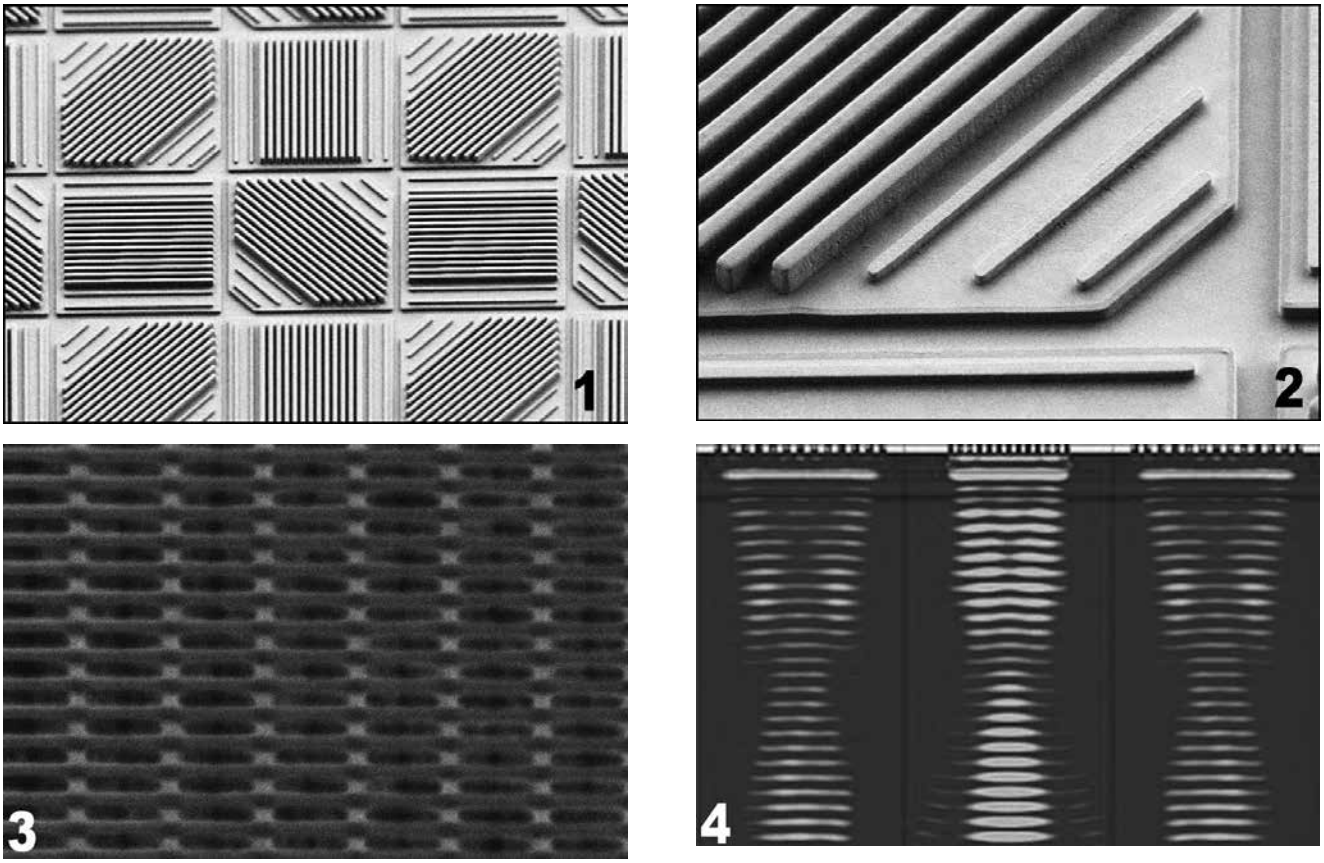

Figure 1: SEM image of metasurface-based IR polarimeter, currently commercially available from Phoebus, and initially developed at CNF. Figure 2: A single sub-pixel at higher magnification. These high aspect ratio features with smooth sidewalls were fabricated at CNF using the ASML DUV stepper and dry etch tools. Figure 3: Another candidate metasurface structure for a second-generation focusing polarimeter device currently in development, fabricated at CNF using the JEOL 9500 e-beam lithography system. Figure 4: Numerical simulation of three adjacent pixels of our IR polarimeter device, indicating minimal crosstalk between pixels.

References:

[1] Ebbesen, T.W., et al., "Extraordinary optical transmission through sub-wavelength hole arrays." Nature, (1998). 391(6668): p. 667-669.

[2] Crouse, D. "Numerical modeling and electromagnetic resonant modes in complex grating structures and optoelectronic device applications." Electron Devices, IEEE Transactions on 52.11 (2005): 2365-2373.

[3] Crouse, D., and Keshavareddy, P. "Polarization independent enhanced optical transmission in one-dimensional gratings and device applications." Optics Express 15.4 (2007): 1415-1427.

[4] Lansey, E., Crouse, D., et al. "Light localization, photon sorting, and enhanced absorption in subwavelength cavity arrays." Optics Express 20.22 (2012): 24226-24236.

[5] Jung, Y.U; Bendoym, I.; Golovin, A.B.; and Crouse, D.T. "Dual-band photon sorting plasmonic MIM metamaterial sensor." Proc. SPIE 9070, Infrared Technology and Applications XL, 90702X (June 24, 2014); doi:10.1117/12.2050620.

[6] Crouse, D., and Keshavareddy, P. "A method for designing electromagnetic resonance enhanced silicon-on-insulator metal-semiconductor-metal photodetectors." Journal of Optics A: Pure and Applied Optics 8.2 (2006): 175.

[7] Mandel, I.; Gollub, J.; Bendoym, I; Crouse, D. Theory and Design of A Novel Integrated Polarimetric Sensor Utilizing a Light Sorting Metamaterial Grating. Sensors Journal, IEEE, (2012): Vol. PP, 99.

[8] Lepak, L., et al. "Handheld chem/biosensor using extreme conformational changes in designed binding proteins to enhance surface plasmon resonance (SPR)" Proc. SPIE 9862, Advanced Environmental, Chemical, and Biological Sensing Technologies XIII, 9862-7 (April 17, 2016); doi:10.1117/12.2222305.

Wide Bandgap Semiconductor Deep UV Devices

CNF Project Numbers: 2387-15, 2438-16

Principal Investigator: Debdeep Jena

Users: Kevin Lee, Shyam Bharadwaj

Affiliation: School of Electrical and Computer Engineering, Cornell University

Primary Source of Research Funding: Designing Materials to Revolutionize and Engineer our Future, E70-8276

Contact: djena@cornell.edu, KL833@cornell.edu, sb2347@cornell.edu

Website: https://sites.google.com/a/cornell.edu/photonic-devices/home

Primary CNF Tools Used: Veeco Icon AFM, ABM contact aligner, photolithography tools (spinners, hot plates, solvent hoods), SC4500 e-beam evaporators, AG610 RTA, PT770 ICP etcher, YES Asher, Oxford 81 RIE, Profilometers, Filmetrics

Abstract:

Our main research goal is to improve and fabricate deep UV photonic devices (ex. LEDs and Lasers). We grow the thin film by molecular beam epitaxy (MBE). The material system we're focusing on is III-Nitride semiconductors. For deep UV devices, wide bandgap materials such as AlN, GaN and AlGaN are the typical materials. High quality AlN epitaxy on bulk and AlN-on-sapphire template substrates is investigated, and subsequently, UV LED performance on both substrates is compared.

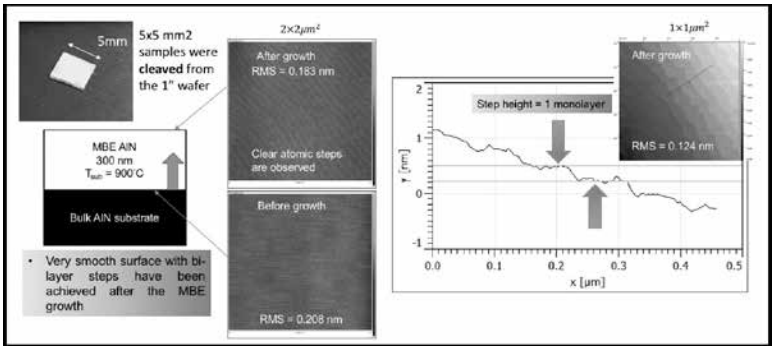

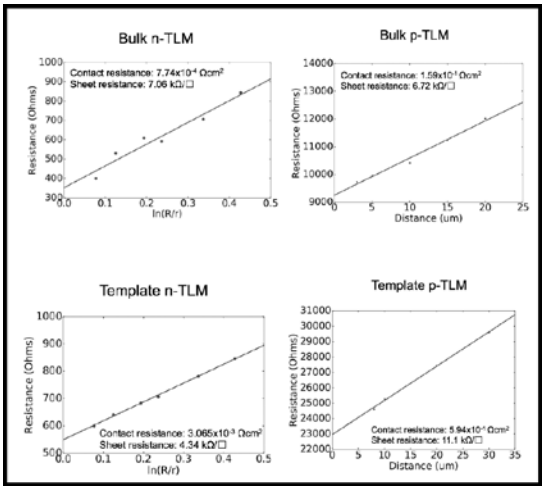

Figure 1, above: AFM images of grown AlN film on single crystal bulk AlN substrate. Figure 2, right: TLM measurements for the LED structures for both n-and p-contacts. Bulk sample shows slightly improved contact resistances.

Summary of Research:

We have performed high temperature (>900°C) aluminum nitride (AlN) epitaxy on bulk AlN substrates using plasma-assisted MBE. The high growth temperature ensures good nucleation and subsequent AlN growth with few extended dislocations and defects. The growth conditions have been optimized on both bulk single crystals and AlN on sapphire templates for comparison. Two different growth rates, 300 nm/hr and 600 nm/hr, were investigated. A 300 nm AlN layer grown on a bulk crystal exhibited atomic steps and smooth surface (0.18 nm RMS roughness over 2 × 2 μm^2) shown in Figure 1, while 500 nm AlN films grown on AlN templates are rougher (~0.5 nm RMS roughness over 2 × 2μm^2). X-ray diffraction based rocking curve analysis shows a FWHM of ~10 arc sec along the <002> and <012> directions for epitaxial AlN films on bulk crystals. Further structural characterization and defect analysis using transmission electron microscopy is under investigation.

Upon optimization of the AlN nucleation layer, UV-LED structures with quantum disk (QD) active regions were grown. UV LEDs based on AlGaN materials require high quality AlN nucleation layers to reduce leakage. In order to measure the grown LEDs, fabrication of mesas is necessary. 100 × 100 μm^2 mesas were defined using ICP-RIE etching, and n-and p-ohmics were deposited via e-beam evaporation. The qualities of deposited

contacts along with resistivities of grown cladding layers were measured via transmission line method (TLM) measurements. Figure 2 shows the contact and layer resistances extracted from TLM measurements.

JV measurements and electroluminescence measurements were performed on fabricated devices to characterize the sharpness of emission, location of emission peak, and leakage current. 100 × 100 μm^2 devices grown on both bulk AlN and AlN-on-sapphire (co-loaded in the MBE system to ensure that the layer structure is identical) were measured in order to determine whether LEDs on low threading dislocation density (TDD<$10^4/cm^2$) bulk substrates show better performance than those grown on AlN-on-sapphire (~$1010/cm^3$). Figure 3 shows measured electroluminescence data for the devices. Both LEDs displayed emission peaks around 248 nm, as expected based on the two monolayer GaN QD active regions. Broad low-energy (>350nm) emission was suppressed for the LED grown on bulk AlN as compared to the one grown on AlN-on-sapphire, likely due to the lower TDD and thus fewer deep levels present in the substrate for recombination. The LED grown on bulk AlN also displayed a lower FWHM for the 248nm peak (11nm) and fewer side-peaks, likely due to lower TDD and thus increased homogeneity of the active region.

JV measurements (Figure 4) show similar forward bias characteristics for both devices, with turn-on around 6V (as expected based off the 5eV emission) and around 40 A/cm^2 at 12V. Leakage in the reverse bias is suppressed in the LED grown on bulk AlN by around an order of magnitude. Overall, performance is superior for the LED grown on bulk substrates.

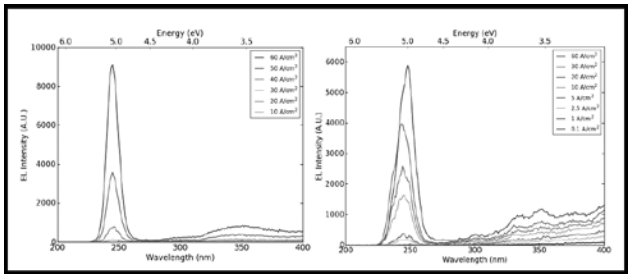

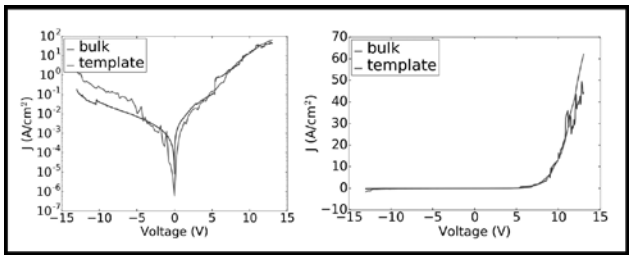

Figure 3, top: Electroluminescence spectra for LEDs grown on bulk AlN (left) and AlN-on-sapphire template substrates (right). Samples are 100 × 100 μm^2, and the FWHM for LED on bulk is 11 nm, while FWHM for LED on template is 14 nm.

Figure 4, bottom: JV characteristics (log scale on left, linear scale on right) for two identical LED structures grown on different substrates (bulk AlN and AlN-on-sapphire substrates). The LED grown on bulk AlN shows lower leakage in the reverse bias.

Xenon Difluoride Release of MEMS Three-Dimensional Micro-Mirror

CNF Project Number: 2406-15
Principal Investigator: David L. Dickensheets
User: Tianbo Liu

Affiliation: Department of Electrical and Computer Engineering, Montana State University
Primary Source of Research Funding: National Institutes of Health
Contact: davidd@montana.edu, tianbo.liu@msu.montana.edu
Primary CNF Tools Used: Xactix xenon difluoride etcher, Oxford 100 etcher

Abstract:

Xenon difluoride was utilized to complete the final release of a MEMS three-dimensional scanner. Bulk silicon was removed to allow freedom of motion in three axes.

Summary of Research:

A MEMS micro-mirror scanning device that is capable of performing two-dimensional scanning as well as focus adjustment in the third dimension is constructed on a silicon on insulator wafer. For the final release process, the Xactix xenon difluoride etcher was used to remove the sacrificial silicon.

The Oxford 100 etcher was used to remove the buried oxide following the xenon difluoride etch process [1].

Figure 1: MEMS three-dimensional micro-mirror post release.

References:

[1] Liu, Tianbo, and David L. Dickensheets. "Three-dimensional beam scanner for a handheld confocal dermoscope." Optical MEMS and Nanophotonics (OMN), 2016 International Conference on. IEEE, 2016.

Development of Single and Double Layer Anti-Reflective Coatings for Astronomical Instruments

CNF Project Number: 2458-16

Principal Investigator: Gordon Stacey[1]

Users: Nicholas Cothard[2], Kenny Vetter[3]

Affiliations: 1. Department of Astronomy, 2. Applied and Engineering Physics, 3. Department of Physics; Cornell University

Primary Source of Research Funding: NASA Grant NNX16AC72G

Contact: stacey@cornell.edu, nc467@cornell.edu, kjv35@cornell.edu

Primary CNF Tools Used: FilMetrics F50-EXR, FleXus Film Stress Measurement, Zygo optical profilometer, ABM contact aligner, ASML 300C deep UV stepper, Gamma automatic coat-developer, Heidelberg DWL2000, Oxford PECVD, Anatech resist strip, Oxford 82 etcher, Unaxis 770 Deep Si etcher, Hamatech-Steag mask processors, Hamatech-Steag wafer processors

Abstract:

In the past year, we have developed methods to fabricate single and double layer anti-reflection coatings at multiple wavelengths that have potential to be used in sub-millimeter and millimeter astronomical instruments. Our methods center on the use of deep reactive ion etching devices at CNF to produce quarter-wavelength metamaterial anti-reflection coatings on silicon wafers. We've published a paper in Applied Optics that describes the fabrication methods and optical testing of our samples. Since the publication, we've continued developing our recipe for double-layer anti-reflection coatings centered on multiple wavelengths and we are nearly ready to fabricate new optical quality samples. In the coming months, we will use various metrology tools at CNF to improve our etched geometry and we will test the optical efficiency of samples that have been fabricated at CNF.

Summary of Research:

The goal for this project is to fabricate single and double-layer anti-reflection coatings (ARCs) on silicon wafers by etching sub-millimeter features into the silicon using deep reactive ion etching (DRIE). These anti-reflection coatings are designed for sub-millimeter and far-infrared astronomical instruments that observe the cosmic microwave background and early star and galaxy formation.

This project is a continuation and expansion of a previous CNF Project ("Development of Quarter Wavelength Anti-Reflective Coatings at CNF," with Professor Michael Niemack). The previous project by Prof Niemack developed single-layer ARCs. This project develops methods to create double-layer ARCs, which offer increased bandwidth and optical performance over a single-layer.

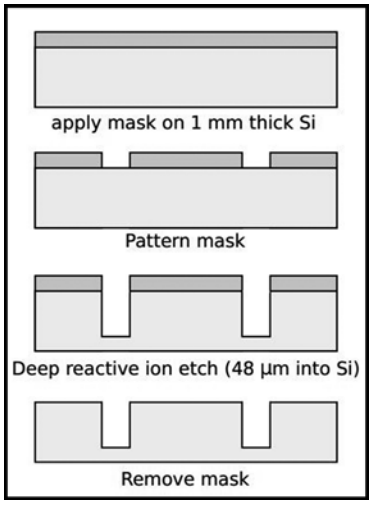

Figure 1: Process flow for fabricating a single-layer ARC on a silicon wafer. Steps from top to bottom. Dark grey represents photoresist. Light grey represents the silicon wafer.

Our major accomplishment of the year is our publication in Applied Optics that presented the fabrication and optical testing of single-layer ARCs as well as the fabrication of a prototype double-layer ARC [1]. The ARCs in this paper were designed to be highly transmissive at the far-infrared wavelength of 350 µm.

Figure 1 shows the recipe used in fabricating a single-layer ARC. Figure 2 shows the optical transmission through wafer with a single-layer ARC on both sides of the wafer. Notice the sub-percent reflection within the central bandwidth.

At the end of our Applied Optics paper, we present the first prototype double-layer ARC that we fabricated at CNF last fall. Figure 3 shows the recipe used to fabricate the double-layer ARC. A challenge in designing this recipe was learning how to deposit and pattern a layer of thermal oxide that could be used as an etch mask during our DRIE processes. To do this, we use the Oxford plasma enhanced chemical

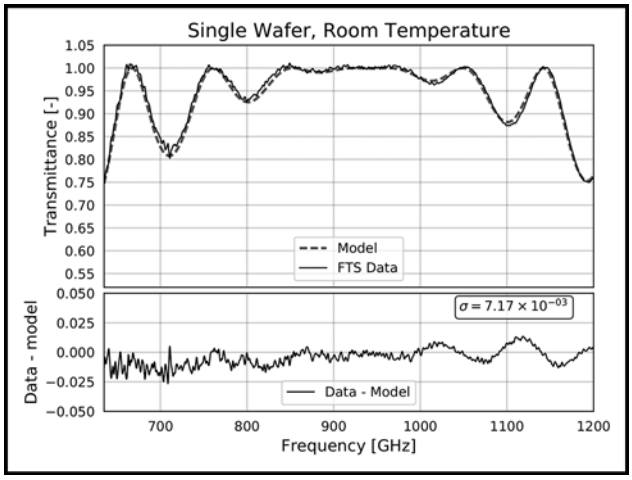

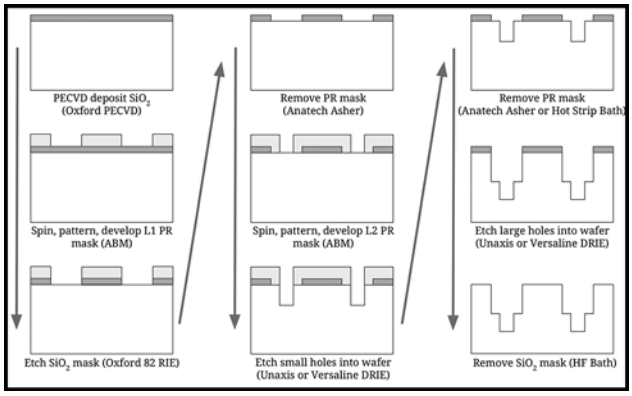

Figure 2, above: Room temperature FTS transmission measurements of a wafer with a single-layer ARC on both sides. Black line shows raw FTS data. [Blue] line shows our best fit parameter Fresnel model. Figure 3, below: Process flow for fabricating a double-layer ARC on a silicon wafer. Dark grey represents thermal oxide. Light grey represents photoresist. White represents the silicon wafer.

vapor deposition (PECVD) tool to deposit oxide and the Oxford 82 etcher to etch a pattern into the oxide. With this oxide etch mask and a photoresist etch mask, we use the Unaxis 770 deep silicon etcher to etch two layers of features into the silicon wafer using DRIE. Figure 4 shows a three-dimensional reconstruction of surface geometry of our first prototype double-layer ARC. The data used in this reconstruction was taken using the Zygo optical profilometer at CNF. Since the Applied Optics publication, we have been developing methods to fabricate double-layer ARCs tuned for center wavelengths of 102 μm and 1.2 mm. The 102 μm ARC is being designed for use in the etalon of an astronomical Fabry-Perot interferometer.

These Fabry-Perot interferometers will be used for spectroscopy of proto-planetary disks in the High-Resolution Mid-InfraRed Spectrometer (HIRMES) instrument, which will fly in NASA's airborne Stratospheric Observatory for Infrared Astronomy (SOFIA) [2]. Two wafers with ARC on one side and a metalized layer on the other side will form the resonant cavity of a Fabry-Perot.

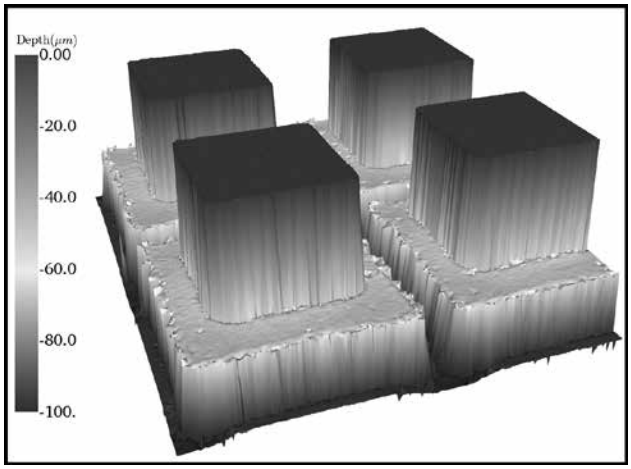

Figure 4: Prototype double-layer anti-reflection coating with a pillar geometry fabricated using DRIE in the Unaxis 770 deep silicon etcher. The 3D image is reconstructed based on depth measurements with a Zygo optical profilometer.

As we move to ARCs at shorter wavelengths, our feature sizes also become smaller. As a result, we have been learning to use the ASML deep-ultraviolet stepper to pattern photoresist with smaller features.

The 1.2 mm ARC is being designed for lens coatings for use in the optics of the ground-based CCAT-Prime telescope that will observe the sky at sub-millimeter and millimeter wavelengths [3]. The features on this sample are approximately 350 μm deep, requiring long deep silicon etch times using the Unaxis 770. The depth of the sample also makes it difficult to characterize the surface geometry using the Zygo optical profilometer. We are exploring options to use one of CNF's scanning electron microscopes (SEMs) to obtain precision metrology of the surface geometry.

In the past year, we have made great steps towards achieving our goals at CNF. We have demonstrated our ability to fabricate many double-layer ARCs for three different bandwidths using the tools at CNF. Our next steps are to learn about and use the advanced metrology tools, such as an SEM at CNF, to better characterize our etched geometries and inform us as to how we can improve our fabrication flow. We will then test the optical performance of our samples using Fourier transform spectrometry (FTS).

References:

[1] P.A. Gallardo, B.J. Koopman, N.F. Cothard, S.M.M. Bruno, G. Cortes-Medellin, G. Marchetti, K.H. Miller, B. Mockler, M.D. Niemack, G. Stacey, and E.J. Wollack, "Deep reactive ion etched anti-reflection coatings for sub-millimeter silicon optics," Appl. Opt. 56, 2796-2803 (2017).

[2] https://www.nasa.gov/feature/nasa-selects-next-generation-spectrometer-for-sofia-flying-observatory

[3] http://www.ccatobservatory.org/

Large Area Electrically Tunable Metasurface Lens

CNF Project Number: 2471-16
Principal Investigator: Federico Capasso
Users: Alan She, Shuyan Zhang

Affiliation: John A. Paulson School of Engineering and Applied Sciences, Harvard University
Primary Source of Research Funding: Air Force Office of Scientific Research
Contact: capasso@seas.harvard.edu, ashe@seas.harvard.edu, shuyanzhang@seas.harvard.edu
Website: https://www.seas.harvard.edu/capasso/
Primary CNF Tools Used: Heidelberg Mask Writer DWL2000

Abstract:

Our tunable optics technology enables dynamic tuning with voltage-resolved precision. We have demonstrated electrically controlled focal length tuning of over 100% with a metasurface lens 2 cm in diameter.

Summary of Research:

Introduction. Planar optical elements control the wavefront of light by using arrays of fixed optical phase shifters, amplitude modulators, or polarization changing elements, which are patterned on a surface to introduce a desired spatial distribution of optical phase, amplitude, and/or polarization. By tailoring the properties of each element of the array, one can spatially control these properties of the transmitted, reflected, or scattered light and consequently mold the wavefront [1]. Based on this concept, various functionalities have been demonstrated including lenses, axicons, blazed gratings, vortex plates and wave plates [2]. These devices are thin and lightweight. Recently, a new class of optical components based on metasurfaces has been developed that are based on subwavelength-spaced phase shifters. We introduce a new technology in which metasurface lenses are made tunable by an applied voltage.

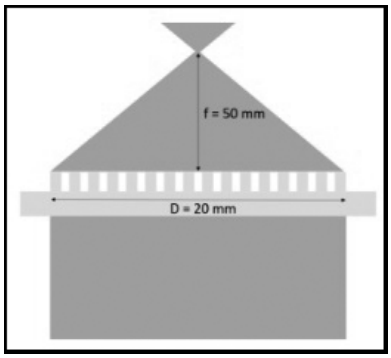

Figure 1: Schematic of the designed metasurface lens.

Lens Description. Requirements for practical devices include high efficiency, controllability, repeatability, and ruggedness. A practical device should also be readily extendable for large-area fabrication. The lens we have constructed is a transmission-based, polarization-independent, infinity-corrected spherical lens. The design is based on pillars in the material amorphous silicon for the wavelength of 1550 nm and focal length of 50 mm (Figure 1). The lens diameter is 2 cm (Figure 2), giving a large diameter to metasurface unit cell ratio greater than 10,000.

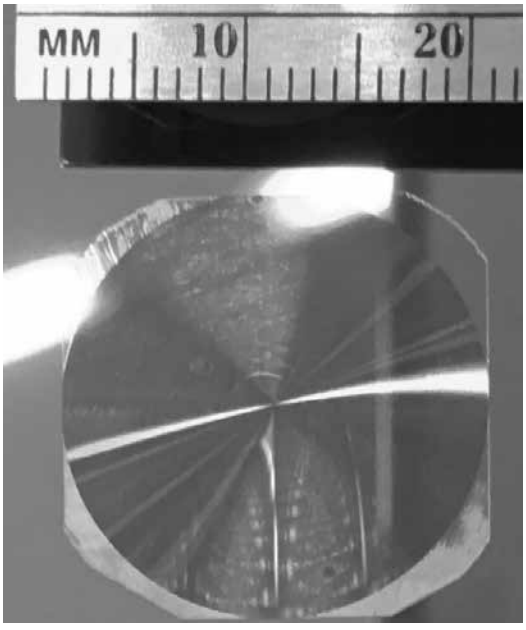

Figure 2: Our metasurface lens with diameter of 2 cm.

Tuning Description. The lens was designed with an initial focal length of 50 mm and in experiment displayed a focal length tuning range from 52 mm to 107 mm (Δf/f=106%) when the applied voltage

was increased (Figure 3). With this method, focal length tuning of the metasurface lens maintains a good focus. Spherical aberration can be quantified as the deviation of the resulting phase profile from the ideal hyperbolic phase function. Our calculations reveal that increasing the focal length introduces a built-in suppression of spherical aberration. The magnitude of spherical aberration can be mathematically expressed to follow an inverse quartic function to the applied voltage. This allows for flat, highly tunable lens devices with excellent immunity to aberration.

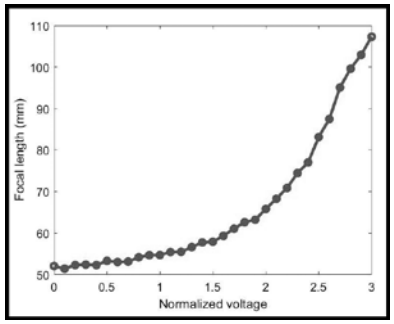

Figure 3: The focal length response of one of our tunable metasurface lens to an applied voltage.

Applications. This technology enables long sought-after applications, in which dynamic and high-speed tuning can be done with voltage-resolved precision in an analog or digital manner. It brings into focus embedded optical zoom for chip-scale image sensors (e.g. cell phone cameras) as well as optical zoom and adaptive focus with lightweight form factors for head mounted optics, such as everyday eyeglasses, virtual reality and augmented reality hardware, heads-up displays, projectors, and optical disc drives. In other applications, it allows for optical zoom and focal plane scanning for cameras, telescopes, and microscopes without the need for motorized parts. Furthermore, its flat construction and inherently lateral actuation allows for highly-stackable systems, such as compound optics.

References:

[1] Nanfang Yu, Patrice Genevet, Mikhail A. Kats, Francesco Aieta, Jean-Philippe Tetienne, Federico Capasso, Zeno Gaburro, "Light propagation with phase discontinuities: Generalized laws of reflection and refraction", Science 334, 333 (2011).

[2] Nanfang Yu and Federico Capasso, "Flat optics with designer metasurfaces", Nature Materials 13, 139 (2014).

Tunable Semiconductor Metasurfaces for Mid-Infrared Photonics

CNF Project Number: 2472-16
Principal Investigator: Gennady Shvets
User: Maxim Shcherbakov

Affiliation: School of Applied and Engineering Physics, Cornell University
Primary Source of Research Funding: Office of Naval Research
Contact: gs656@cornell.edu, mrs356@cornell.edu
Primary CNF Tools Used: JEOL 9500, even hour evaporator, Oxford Cobra, J.A. Woollam ellipsometer

Abstract:

We report on fabrication and characterization of 300-nm-thick germanium metasurfaces exhibiting thermally tunable high-quality resonances in the mid-infrared.

Summary of Research:

One of the most promising, yet unresolved, opportunities in wearable electronics is to serve as a platform for chemical sensing [1] and to be able to monitor critical biochemical parameters of our body and/or environment, such as glucose concentration, oxygenation, and hazardous gas presence, to name a few. Each molecule of the substance to be detected has a certain "fingerprint"—a set of spectral absorption lines in the mid-infrared by which many molecules can be distinguished. A compact infrared (IR) spectrometer can, therefore, be an ultimate tool to fulfill the goal; however, the most wide-spread mid-IR spectroscopy approaches are realized in costly and bulky devices. A miniature mid-IR spectrometer is a game changer that will potentially enable wearable breath analyzers, bodily fluid analyzers and environmental probes. In many spectroscopic applications, having a narrow spectrum of the light source is of paramount importance. Currently, the available light sources in the mid-IR are either cheap and broadband (thermal sources, light emitting diodes) or monochromatic, yet expensive and bulky (quantum cascade lasers, parametric generators and amplifiers). Controlling and tuning the bandwidth of mid-IR radiation is key to compact mid-IR spectroscopy, leading to devices with no expensive detector arrays or sensitive and cumbersome diffraction elements.

In this project, we aim at design, fabrication and characterization of novel types of ultrathin nanostructured materials based on high-index semiconductors, which allow narrowband and tunable optical response in the mid-IR. It is known that designed arrays of nanoparticles—so called metasurfaces—can significantly alter the spectral, spatial and polarization properties of light [2,3]. We build on the vast experience of using metasurfaces for mid-IR spectroscopy of ultralow substance concentrations, both in plasmonic [4] and all-dielectric [5] metaphotonics. In our effort, we push the boundaries of conventional metasurfaces, which possess broadband Mie or plasmonic resonances with typical quality factors of the resonances of < 10^2, by using strong coupling between adjacent nanoparticles that results in theoretical quality (Q)-factors of up to 10^4, allowing to distinguish individual gas absorption lines, which typically have the linewidth on the order of 1 nm.

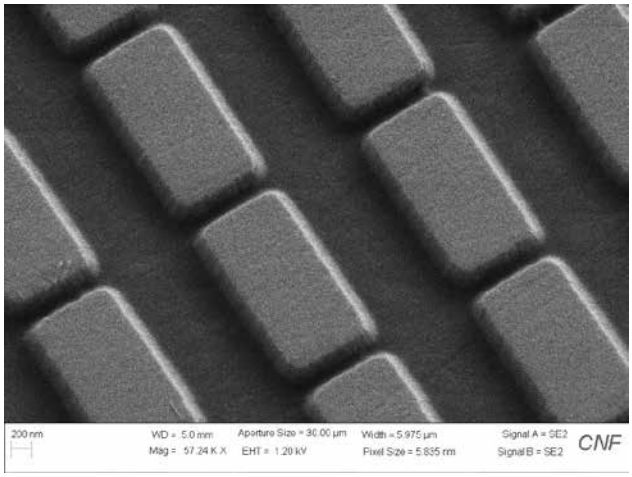

Figure 1: A scanning electron microscope image of a typical Ge-based mid-IR high-Q metasurface on a CaF2 substrate.

The following process is applied to define the metasurfaces under study: standard two-layer PMMA spin-coating, baking, and e-beam exposure at 1000 µC/cm^2; development; electron-beam evaporation of 300 nm of Ge; liftoff in sonicated acetone. A typical example of the proof-of-concept samples under study is shown in Figure 1. Using advanced nanofabrication tools

available at Cornell NanoScale Facility, and up-to-date testing, we have so far experimentally demonstrated metasurfaces with strong spectral features with widths of down to 20 nm in the mid-IR. Being applicable as wavelength filters for high-resolution compact mid-IR spectroscopy, these metasurfaces are also highly thermally tunable, owing to the large thermo-optic coefficient of germanium. The samples comprise amorphous germanium rectangle patches situated on a calcium fluoride substrate, with the gap between the patches being responsible for the *Q*-factor of the mid-IR resonance.

Mid-IR transmittance and reflectance of the metasurfaces were characterized using Fourier-transform microspectroscopy with a Bruker Vertex 80 spectrometer. The spectra were recorded in the range of 600-10000 cm^{-1} with polarization differentiation. The spectrometer was operating in the external mode, where the IR beam is sent outside and detected with a mercury cadmium telluride detector, opening opportunities for beam conditioning, including shaping its spatial spectrum and polarization. The temperature of the sample was controlled with a heating stage formed by a ceramic heating element and a thermistor attached to the surface of the sample. Typical temperature-dependent transmittance spectra of a metasurface are given in Figure 2, showing a wavelength shift of more than a full width at half-maximum.

We envision applications of such metasurfaces as tunable notch filters for compact mid-IR spectroscopy devices.

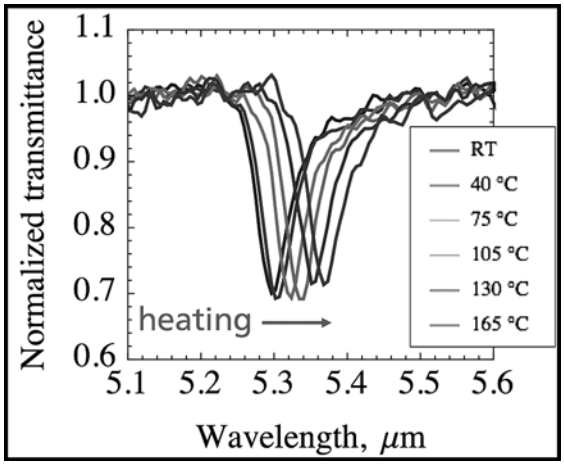

Figure 2: Experimental mid-IR transmittance spectra of the metasurface, revealing thermally tunable notch-filter operation at 5.3-5.4 μm with a Q-factor of about 130.

References:

[1] Amay J. Bandodkar and Joseph Wang, "Non-invasive wearable electrochemical sensors: a review," Trends in Biotechnology 32, 363 (2014).

[2] Nina Meinzer, William L. Barnes and Ian R. Hooper, "Plasmonic meta-atoms and metasurfaces," Nature Photonics 8, 889 (2014).

[3] Arseniy I. Kuznetsov, Andrey E. Miroshnichenko, Mark L. Brongersma, Yuri S. Kivshar, Boris Luk'yanchuk, "Optically resonant dielectric nanostructures," Science 354, aag2472 (2016).

[4] Chihhui Wu, Alexander B. Khanikaev, Ronen Adato, Nihal Arju, Ahmet Ali Yanik, Hatice Altug, and Gennady Shvets, "Fano-resonant asymmetric metamaterials for ultrasensitive spectroscopy and identification of molecular monolayers," Nature Materials 11, 69 (2012).

[5] Chihhui Wu, Nihal Arju, Glen Kelp, Jonathan A. Fan, Jason Dominguez, Edward Gonzales, Emanuel Tutuc, Igal Brener, and Gennady Shvets, "Spectrally selective chiral silicon metasurfaces based on infrared Fano resonances," Nature Communications 5, 3892 (2014).

[6] S. Hossein Mousavi, Iskandar Kholmanov, Kamil B. Alici, David Purtseladze, Nihal Arju, Kaya Tatar, David Y. Fozdar, Ji Won Suk, Yufeng Hao, Alexander B. Khanikaev, Rodney S. Ruoff, and Gennady Shvets, "Inductive Tuning of Fano-Resonant Metasurfaces Using Plasmonic Response of Graphene in the Mid-Infrared," Nano Letters 13, 1111 (2013).

III-Nitride and Light-Emitting Diodes

CNF Project Number: 2479-16

Principal Investigator: Hieu Pham Trung Nguyen

Users: Moab Rajan Philip, Hieu Pham Trung Nguyen

Affiliation: Department of Electrical and Computer Engineering, New Jersey Institute of Technology

Primary Source of Research Funding: U.S. Army

Contact: hieu.p.nguyen@njit.edu, mrp66@njit.edu

Website: https://web.njit.edu/~hpnguyen

Primary CNF Tools Used: Plasma-enhanced chemical vapor deposition, JEOL 9500 electron beam lithography, ASML 300C DUV (248nm) stepper, Oxford 81, PlasmaTherm PT 770, SEM

Abstract:

In this project, we have focused on fabricating full-color light-emitting diodes (LEDs) and laser diodes using III-nitride nanostructures. III-nitride LEDs with the incorporation of InGaN/AlGaN nanowire heterostructures were grown directly on Si <111> substrates by molecular beam epitaxy (MBE) while laser diodes were grown on patterned substrates. Multiple color emissions across nearly the entire visible wavelength range were realized by varying the *In* composition in the InGaN quantum dot active region. Moreover, multiple AlGaN shell layers are spontaneously formed during the growth of InGaN/AlGaN quantum dots, leading to the drastically reduced nonradiative surface recombination, and enhanced carrier injection efficiency. Such core-shell nanowire structures exhibit significantly increased carrier lifetime and massively enhanced photoluminescence intensity compared to conventional InGaN/GaN nanowire LEDs. A high color rendering index of ~ 98 was recorded for white-light emitted from such phosphor-free core-shell nanowire LEDs.

Summary of Research:

For our research, the Veeco GEN II MBE system was employed to grow vertically aligned InGaN/AlGaN dot-in-a-wire core-shell LEDs on Si substrates. Figure 1(a) depicts the schematic structure of an InGaN/AlGaN core-shell nanowire LED structure on Si substrate. The inset presents detailed LED structure.

First, 0.4 μm GaN:Si nanowire was grown at ~ 770°C, followed by ten coupled InGaN/AlGaN dots grown at relatively low temperatures of 640°C - 680°C to enhance *In* incorporation in the InGaN dots. Emission wavelength of LEDs can be precisely controlled by varying the *In* composition in the InGaN/AlGaN active region, reported in Figure 2(a). We report that, to dramatically reduce surface recombination, AlGaN barriers have been grown in the active region instead of GaN barriers.

During the growth process of AlGaN barrier, an AlGaN downward-bending shell layer was also formed around the InGaN dot due to the diffusion-controlled growth process [1]. The barrier of each quantum dot was also modulation doped p-type using Mg to enhance hole transport [2]. Finally, 0.2 μm GaN:Mg section was grown on top of the LED structure. Figure 1(b) is a 45 degree-

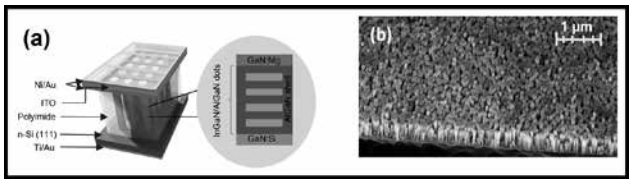

Figure 1: (a) Schematic illustration of an InGaN/AlGaN naowire LED heterostructure on Si substrate. (b) A 45° tilted SEM of a typical InGaN/AlGaN core-shell nanowire LED sample.

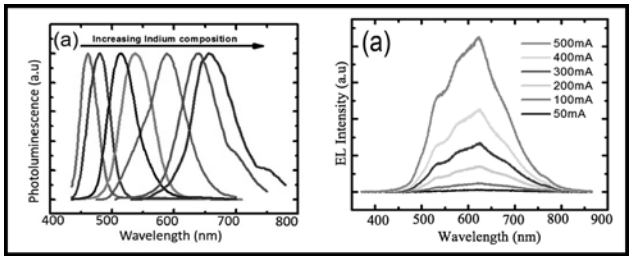

Figure 2: (a) Normalized room temperature PL spectra of multiple emission colors from InGaN/AlGaN nanowire LEDs. (b) Room temperature EL spectra of an InGaN/AlGaN core-shell LED under different injection current levels.

tilted scanning electron microscopy (SEM) image for a typical InGaN/AlGaN core-shell sample. Highly uniform nanowires on Si substrate were achieved. The variation of In concentration in the InGaN dots ranges from 8% to more than 50% [2]. For the ideal performance scenario of InGaN/AlGaN core-shell LEDs, the best Al composition in the AlGaN barrier is predicted to be in range of 15% to 20%.

The device fabrication route of InGaN/AlGaN dot-in-a-wire core-shell devices comprises of the following steps. First, nanowire arrays were spin-coated with polyimide resist for planarization and passivation, which is followed by O_2 dry etching to expose the top region of the nanowires. The exposed GaN:Mg surface were then deposited with layers including Ni (5nm)/ Au(5nm)/indium tin oxide (ITO) to form top metal contacts. Afterwards to form the backside and topside contacts respectively, Ti/Au (10nm/100nm) and Ni/ Au (10nm/100nm) layers were evaporated on the backside of the Si substrate and top of ITO respectively.

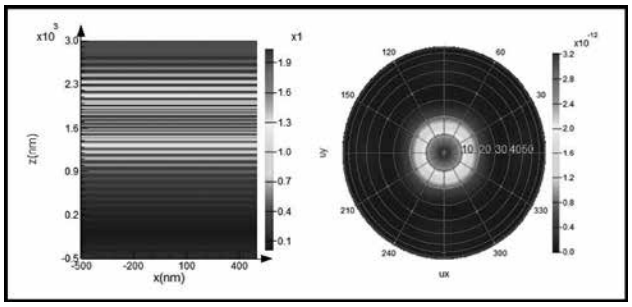

Figure 3: (a) The side view of simulated mode profile that shows strong light confinement in the cavity region and the leaked light through DBR structure, (b) Far field radiation pattern from top showing the directional emission from the top surface of the laser structure.

Our preliminary results show that the unique core-shell nanowire LED heterostructure has been developed by employing axial self-organized InGaN/ AlGaN heterostructure and exhibit significantly improved carrier injection efficiency and output power, compared to conventional nanowire LEDs. These core-shell nanowire LED arrays were grown by MBE, where the device light emission properties, including the correlated color temperature (CCT) and color rendering index (CRI) can be readily engineered by varying the size and composition of the InGaN dots in a single epitaxial growth step. The electroluminescence (EL) spectra show a very broad spectral linewidth and fully covers the entire visible spectrum, shown in Figure 2(b). Additionally, the InGaN/AlGaN LEDs exhibit good current-voltage characteristic. Phosphor-free InGaN/ AlGaN nanowire white-LEDs hold high CRI up to ~ 98, which is more efficient compared to the current phosphor-based white-LED technologies [3].

We have also systematically developed green laser diodes using MBE. In this program, we focused on design, epitaxial growth and prototype fabrication of patterned substrates for green laser fabrication. Figure 3 shows the cavity mode for the surface emitting laser designs, which is lasing at 550 nm. Figure 3(a) presents the side view of the electric field intensity distribution for the proposed laser. It is seen that the light is mostly confined in the cavity region rather than surrounding top and down DBRs structure. The radiation pattern calculated by the FDTD showed the directional emission from top surface of structure in Figure 3(b). The simulated far field radiation pattern from top at 550 nm shows that the nanowire bandgap laser emits up to 20° from the surface normal direction.

References:

[1] Nguyen, H. P. T.; Djavid, M.; Woo, S. Y.; Liu, X.; Connie, A. T.; Sadaf, S.; Wang, Q.; Botton, G. A.; Shih, I.; Mi, Z. Scientific Reports 2015, 5, 7744.

[2] Nguyen, H. P. T.; Zhang, S.; Cui, K.; Han, X.; Fathololoumi, S.; Couillard, M.; Botton, G. A.; Mi, Z. Nano Letters 2011, 11, 1919.

[3] Philip, M. R.; Choudhary, D. D.; Djavid, M.; Bhuyian, M. N.; Piao, J.; Pham, T. T.; Misra, D.; Nguyen, H. P. T. Journal of Vacuum Science and Technology B, 2017, 35, 02B108.

L-Couplers for Efficient Fiber-Chip Coupling

CNF Project Number: 2557-17
Principal Investigator: Zhaolin Lu
User: Peichuan Yin

Affiliation: Microsystems Engineering, Rochester Institute of Technology
Primary Source of Research Funding: National Science Foundation
Contact: zxleen@rit.edu, pxy7717@rit.edu
Primary CNF Tools Used: ASML PAS 5500/300C DUV stepper, microscopes, SEM

Abstract:

Efficient fiber-to-waveguide light coupling has been a key issue in integrated photonics for many years. The main challenge lies in the large mode mismatch between an optical fiber and a single mode waveguide. Several techniques have been developed including grating coupling, inverse tapers, evanescent couplers and vertical tapering, but they are either difficult to fabricate, large or have poor efficiency. In our previous report we presented results on a novel fiber-to-waveguide coupler — named "L-coupler" — through which the light fed from the top of a chip can bend 90° with low reflection and is then efficiently coupled into an on-chip Si_3N_4 waveguide within a short propagation distance (< 20 μm) as is seen in Figures 1 and 2. We experimentally demonstrated a 20% coupling efficiency that was primarily limited by the multimode operation of the Si_3N_4 waveguides, particularly in 90° bend.

Summary of Research:

In our new designs, we have optimized for single-mode mode conversion and optimized the experimental setup so that light will be coupled in/out through a fiber array. By deploying a fiber array on top of the structure, the output of this structure can be coupled back into fiber instead of scattering into air. The improved fabrication process also uses deep-UV lithography technology that can yield better tolerances. Furthermore, the new design includes numerous variations of design parameters, which can be used to investigate the actual impact of imperfections.

However, fabrication by using deep-UV lithography tool (ASML PAS 5500/300C DUV Stepper) has encountered multiple challenges. First, in order to get high resolution patterning the DUV stepper requires anti-reflective coating (ARC) between substrate and photoresist. The ARC needs to be removed by using oxygen plasma after every step. However, we discovered that the silver L-Coupler is not compatible with an oxygen plasma and will result in silver oxide (Ag_2O), which causes issues for further deposition steps. The microscope and SEM images of deposited silver peeling off from oxidized layer are shown in Figure 4.

Secondly, the L-coupler requires multiple steps that use 2 μm thick photoresist. However, DUV lithography is not suitable for such a thick photoresist that causes significant resolution degradation that inadvertently caused most of the waveguide terminals to be buried by silver, as shown in Figure 3. This prevents light from being able to be coupled into the nitride waveguide. Lastly, we found that the DUV stepper is very sensitive to the wafer's flatness, which created issues with the silicon nitride waveguide deposition. Consequently, we have decided to re-design the layout for better tolerance to fabrication errors and return to using i-line lithography. While the resolution is not as high it is still sufficient for the L-coupler and is better suited to the fabrication process.

References:

[1] Zhaolin Lu, Peichuan Yin, Kaifeng Shi, "Bent Metal-Clad Waveguides for Fiber-to-Waveguide and 3D Chip-to-Chip Light Coupling Applications," Frontiers in Optics, Rochester, NY, Oct. 2016.

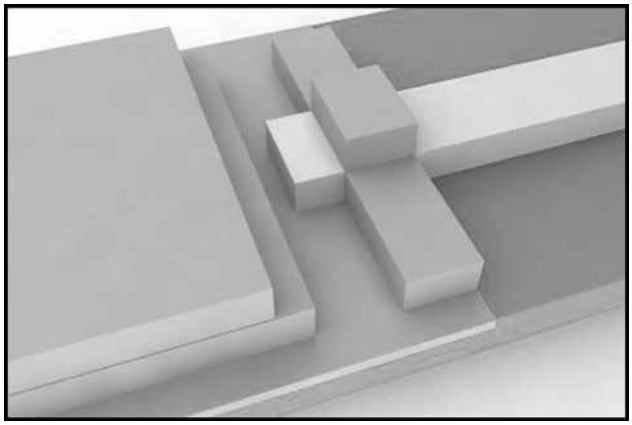

Figure 1: Three-dimensional rendering of L-coupler structure.

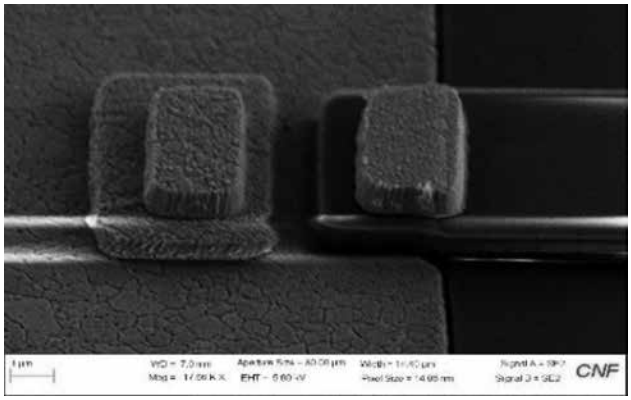

Figure 2: SEM image of L-coupler.

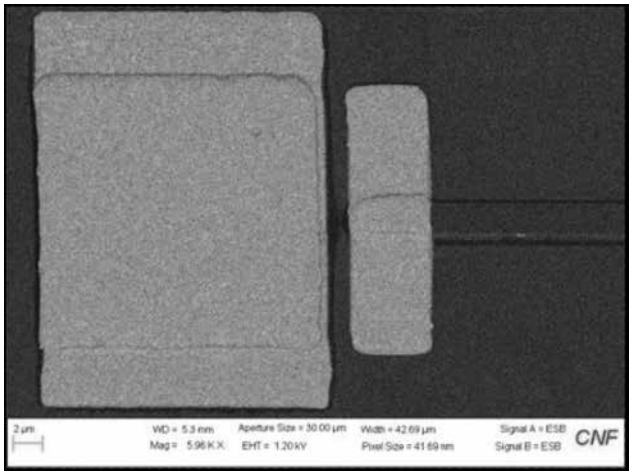

Figure 3: The new image showing the waveguide is covered by silver due to low precision.

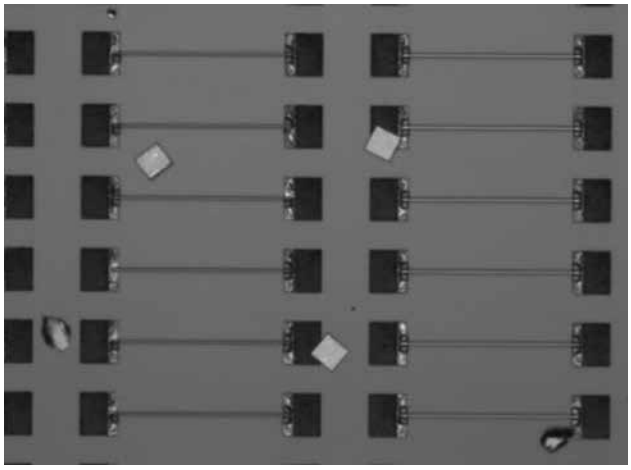

Figure 4: The microscope image shows the silver oxidation during fabrication.

Efficient Switching of Three-Terminal Magnetic Tunnel Junction Devices Powered by the Giant Spin Hall Effect of PtHf Alloys

CNF Project Number: 111-80
Principal Investigator: Robert A. Buhrman
User: Minh-Hai Nguyen

Affiliation: Applied and Engineering Physics, Cornell University
Primary Source of Research Funding: Samsung Electronics Co.
Contact: rab8@cornell.edu, mn455@cornell.edu
Primary CNF Tools Used: ASML 300C, JEOL 6300, AJA sputter deposition

Abstract:

The three-terminal magnetic tunnel junction (3T-MTJ) structure based on the spin Hall effect has become a promising candidate for power efficient non-volatile memory applications. We demonstrate that by using the $Pt_{85}Hf_{15}$ alloy for the channel, in combination with a thin Hf spacer, we achieve a low switching critical current density of 3.4×10^{11} A/m^2 and the pulse switching time can be below 2 ns. This large reduction is the combined effect of the strong spin Hall effect in the channel and the role of the Hf spacer in reducing the magnetic damping.

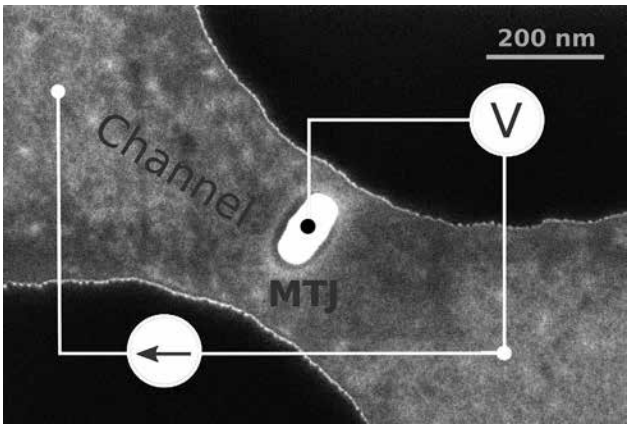

Figure 1: Tilted SEM image of a 3T-MTJ device.

Summary of Research:

The spin Hall effect (SHE), a mechanism by which a transverse spin current is induced by an electrical current in certain heavy metals, has provided a convenient means for charge-spin conversion and has enabled a new class of magneto-resistive memory called three-terminal magnetic tunnel junctions (3T-MTJs) [1]. Figure 1 shows the tilted scanning electron microscope (SEM) image of a 3T-MTJ device fabricated at CNF using deep UV photolithography (ASML 300C), e-beam lithography (JEOL 6300) and AJA sputter deposition. The device consists of a 30 nm × 115 nm CoFeB/MgO/CoFeB MTJ nanopillar on top of a 200 nm channel made by a strong SHE material such as Pt, Ta or W. The parallel (P) and anti-parallel (AP) states of the MTJ are determined by relative value of the MTJ resistance, measured by reading the drop voltage across the MTJ tunnel barrier while applying a small current through it. For writing, an electrical current is applied through the SHE channel from which a transverse current is generated by the SHE and switches the magnetization of the free layer of the MTJ via spin-transfer torque.

For in-plane magnetized 3T-MTJ devices, the critical current density is proportional to the Gilbert magnetic damping and inversely proportional to the spin torque efficiency of the channel, which is the ratio of the SHE-induced spin current density flowing into the free layer and the electrical one in the channel. Thus, for power efficient applications, it is important to reduce the magnetic damping and use strong SHE materials for the channel. Previously we demonstrated that a thin, ~ 0.5 nm, Hf spacer between the channel and the MTJ can help reduce the magnetic damping by more than a factor of two [2] and the 3T-MTJ devices using Pt channel and a thin Hf spacer exhibit a low pulse critical current density of 6.3×10^{11} A/m^2 and a fast pulse switching speed of less than 2 ns [3]. We also showed by harmonic Hall measurements on perpendicularly magnetized samples that due to the dominant intrinsic SHE mechanism in Pt, the spin torque efficiency of Pt can be enhanced by more than two times by alloying Pt with Hf [4]. Therefore, it is of technological importance to study the performance of the in-plane magnetized 3T-MTJ devices having a PtHf channel.

The pulse switching results of our 3T-MTJ device having a PtHf channel and thin 0.7 nm Hf spacer are shown in Figure 2. The color represents the switching probability from 0 [red] to 1 (black) at different values of pulse duration and pulse amplitude. The device can be switched within 2 ns by pulses of high enough amplitude, about 1.5 V. The right asymptote of the 50% probability boundary (white area) indicates the (pulse) critical voltage to be about 1.1 V, which is translated to a current density of 3.4×10^{11} A/m^2, about two times lower than that of the device having pure Pt channel. Our ferromagnetic resonance and DC switching analyses show that the spin torque efficiency of the PtHf device is 0.11, which is two times higher than that of the Pt device (0.55).

Our results suggest that it is possible and promising to enhance the spin torque efficiency by alloying the spin Hall material (Pt in our case) to reduce the critical current density in 3T-MTJ structures for low power spintronic applications.

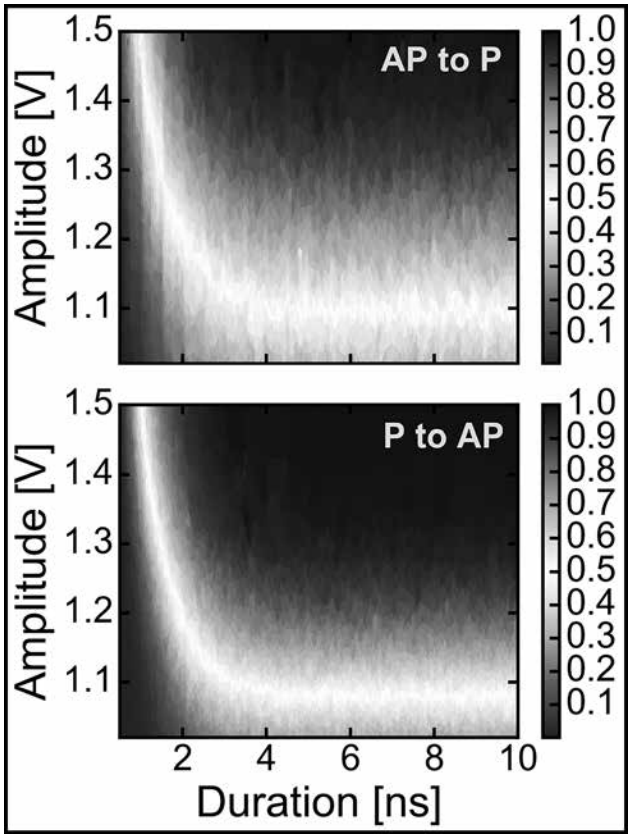

Figure 2: Switching phase diagrams of the PtHf 3T-MTJ device.

References:

[1] L. Liu, C.-F. Pai, Y. Li, H. W. Tseng, D. C. Ralph, and R. A. Buhrman, Science 336, 555 (2012).

[2] M.-H. Nguyen, C.-F. Pai, K. X. Nguyen, D. A. Muller, D. C. Ralph, and R. A. Buhrman, Appl. Phys. Lett. 106, 222402 (2015).

[3] S. V. Aradhya, G. E. Rowlands, J. Oh, D. C. Ralph, and R. A. Buhrman, Nano Lett. 16, 5987 (2016).

[4] M.-H. Nguyen, M. Zhao, D. C. Ralph, and R. A. Buhrman, Appl. Phys. Lett. 108, 242407 (2016).

Tuning Write Current in Tungsten Based Magnetic Tunnel Junctions with an Ultrathin Hf Insertion Layer

CNF Project Number: 111-80

Principal Investigator: Robert. A. Buhrman

Users: Shengjie Shi, Yongxi Ou

Affiliation: Applied and Engineering Physics, Cornell University

Primary Source of Research Funding: Department of Defense; Intelligence Advanced Research Projects Activity

Contact: buhrman@cornell.edu, ss2882@cornell.edu, yo84@cornell.edu

Primary CNF Tools Used: ASML, JEOL6300, AFM Veeco Icon, even-hour evaporator, Oxford 81 etcher, AJA sputtering system

Abstract:

Higher demand for high capacity, high speed and reliable memory cell has motivated intensive study in various emerging magnetic memory structures. The large spin current from spin Hall effect (SHE) provides an efficient way to manipulate magnetic states compared to traditional spin transfer torque structures. SHE driven three terminal magnetic tunnel junctions (MTJ) possess some key advantages, including non-volatility, scalable size and easy read-out without read disturbance, which make them a good candidate for future applications. In an SHE MTJ, write current strongly depends on spin Hall angle (SHA) of the spin source, in-plane magnetic anisotropy of the free layer represented by demagnetization field (M_{eff}) and magnetic damping. We demonstrate an efficient way to lower the write current by insertion of an ultrathin Hf layer (Hf dusting) between the ferromagnetic layer (FM) and the magnesium oxide barrier (MgO) that effectively reduces demagnetization field through enhancement of interfacial perpendicular magnetic anisotropy (PMA). We show significantly lower switching current density in tungsten-based MTJs with this Hf dusting layer and demonstrate wide range of application of Hf dusting technique.

Summary of Research:

For an in-plane magnetized magnetic heterostructure, a key property, the strength of in plane magnetic anisotropy M_{eff} is set by saturation magnetization and perpendicular magnetic anisotropy, which can change dramatically depending on the FM/MgO interface. Ou, et al., report that a few angstroms of Hf insertion layer between FM and oxide capping layer, can significantly change interfacial property and induce robust PMA [1]. This strong induced PMA can in principle lower the Meff in in-plane MTJ systems and reduce the switching current.

We fabricate the two MTJ stacks A and B into three terminal MTJ devices with deep UV lithography defined spin Hall channel and e-beam defined nanopillars. As shown by Figure 1, around a 20 nm tall MTJ sits on top of tungsten spin Hall channel where DC current or RF pulses can flow. We apply a lock-in method across the top terminal and one of the bottom terminals to measure the resistance of the MTJ during the sweep of magnetic field or electric current. By comparing high and low resistances, we determine anti-parallel (AP) and parallel (P) states. For comparison, we present here the results of stack A and B from 390 × 100 nm elliptical pillars on 500 nm channels, annealed at 300°C in air furnace for one hour.

First we sweep the external field parallel to the easy axis of the nanopillar and get a hysteresis loop (minor loop), which shows switching of the free layer by field. Figure 2 shows minor loops for two devices taken from wafer A and B with a top subplot showing the device with Hf dusting and bottom dashed subplot showing the device without Hf dusting. Both devices show clear, abrupt switching between P and AP states. We then apply DC current in the tungsten channel and monitor MTJ resistance change during current sweep. Figure 3 shows current induced switching of the free layer resulting in change in resistance from P (AP) to AP (P) state with negative (positive) current. The polarity of the switching is consistent with negative spin Hall sign of tungsten as opposed to platinum. As shown by the narrowing of the hysteresis loop for device A, the current needed to switch the device is significantly reduced in the Hf dusted structure compared to the structure without Hf dusting.

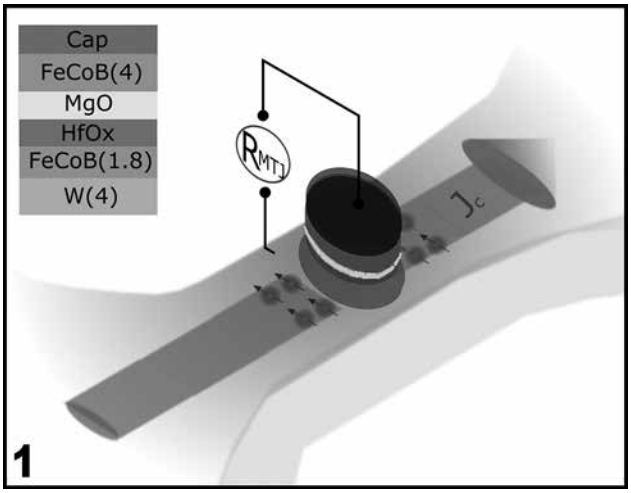

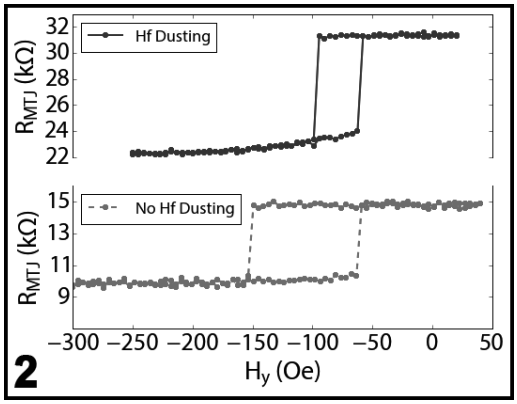

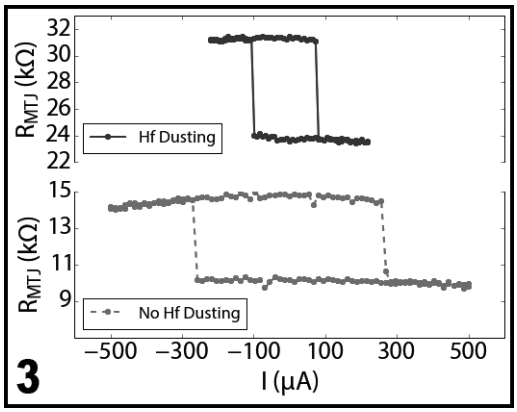

Figure 1, above: Schematic picture of the three terminal MTJ and measurement technique. Figure 2, top right: Magnetic minor loop of devices A and B, with (top) and without (bottom, dashed) Hf dusting. Figure 3, bottom right: Current induced switching of magnetic free layer in MTJs with (top) and without (bottom, dashed) Hf dusting.

We took current ramp rate measurements to obtain the zero-temperature critical current, and determined the critical current density in the Hf dusted device to be 7.8×10^6 A/cm^2, compared to 18.5×10^6 A/cm^2 for the device without Hf dusting. Results with Hf dusting have five times reduction of switching current compared to platinum based three terminal MTJs reported to date [2].

References:

[1] Ou, Yongxi, Ralph, D.C., and Buhrman, R. A. Strong perpendicular magnetic anisotropy energy density at Fe alloy/HfO2 interfaces. Arxiv Prepr. 192403, 1-16 (2017).

[2] Aradhya, S. V., Rowlands, G. E., Oh, J., Ralph, D. C., and Buhrman, R. A. Nanosecond-Timescale Low Energy Switching of In-Plane Magnetic Tunnel Junctions through Dynamic Oersted-Field-Assisted Spin Hall Effect. Nano Lett. 16, 5987-5992 (2016).

Reduction of the Spin Hall Angle in Oxygen-Doped Beta Tungsten

CNF Project Number: 111-80
Principal Investigator: Robert A. Buhrman
User: Ryan Tapping

Affiliation: Applied and Engineering Physics, Cornell University
Primary Sources of Research Funding: The Office of Naval Research and the National Science Foundation
Contact: buhrman@cornell.edu, rct76@cornell.edu
Primary CNF Tools Used: GCA 5x stepper, AJA sputtering tool, Veeco Icon AFM

Abstract:

Spintronic devices rely on spin currents that can be generated from charge currents flowing through certain non-magnetic metals. The spin Hall angle (SHA) is a measure of a materials' efficiency of this charge to spin current conversion. Tungsten is useful because the thin films have been shown to have a very large SHA of over 0.30, but only when the tungsten is ordered in the A15 structure (β-W) [1]. It has been previously shown that incorporation of oxygen into the tungsten during deposition can promote β-W growth and increase the SHA. Using spin-torque ferromagnetic resonance (ST-FMR) [2], we demonstrate that the SHA may actually decrease from over 0.30 to 0.10 or less as the oxygen concentration increases. We also show that the roughness of the tungsten films is approximately 0.19 ± 0.03 nm and is not significantly affected by the oxygen incorporation.

Summary of Research:

Thin film samples were deposited onto 100 mm silicon wafers using our magnetron sputtering system. The structure was W(8)/$Fe_{60}Co_{20}B_{20}(t_{FeCoB})$/MgO(2)/Ta(1) with numbers in parenthesis representing the thickness of the layer in nanometers and t_{FeCoB}, the thickness of FeCoB, was varied between 2 and 4 nm. Oxygen was incorporated only during the sputtering of tungsten, with the percentage corresponding to the relative amount of oxygen to argon.

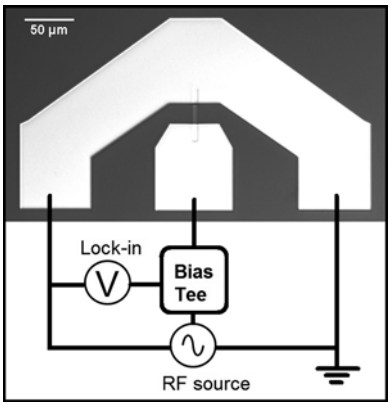

Figure 1: Microstrip after fabrication with a schematic of the ST-FMR measurement.

Stacks were then patterned into 20 × 5 µm^2 microstrips using photolithography with the 5X g-line stepper at CNF and etched using our own ion milling system. The contacts were made using the AJA sputtering system at CNF. An optical image of the microstrip is shown in Figure 1.

X-ray diffraction measurements were done on the tungsten thin films to verify that the sputtering techniques yielded β-W. Peaks were found corresponding to mostly β phase tungsten composition, and with some mixed phase α-W likely present. Resistivity measurements, using the Van der Pauw method, also confirmed that the films were majority β phase, where β-W typically has a resistivity of between 100-300 µΩ·cm [1]. Resistivities ranged from 127 µΩ·cm for tungsten films with no oxygen incorporation to 329, 306, and 723 µΩ·cm for tungsten with 1.6%, 2.4% and 4.0% oxygen respectively.

The spin hall angle (SHA) was determined using spin-torque ferromagnetic resonance (ST-FMR) with analysis described by Pai, et al. for determination of the SHA [2]. This technique works by driving a microwave frequency (RF) current through the microstrip, which induces magnetic precession in the ferromagnetic layer via the spin transfer torque. A magnetic field is swept from -3000 to 3000 Oe at 45° to the microstrip and the voltage is measured by a lock-in amplifier, then the measurement is repeated for various frequencies. A lineshape analysis is done by fitting a

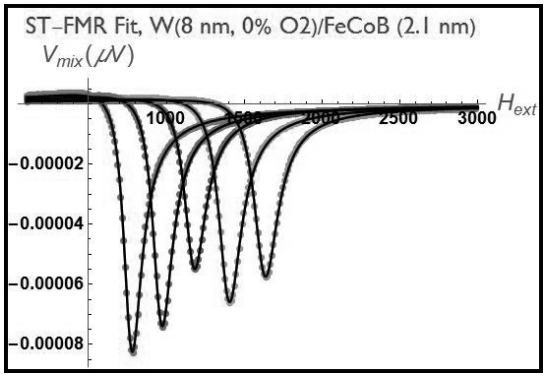

Figure 2: Voltage output from a magnetic field sweep from ST-FMR. Fits are also shown at 8,9,10,11, and 12 GHz frequencies.

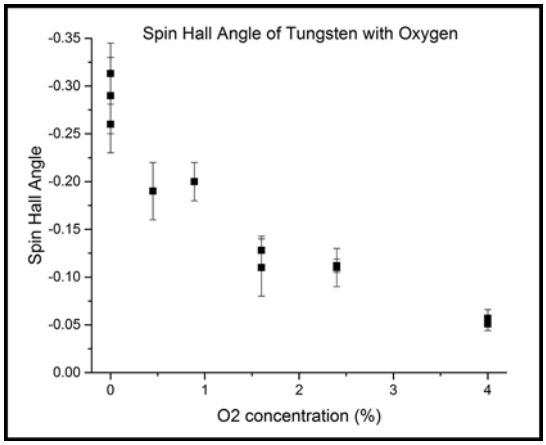

Figure 3: The spin hall angle (SHA) vs oxygen incorporation in tungsten films.

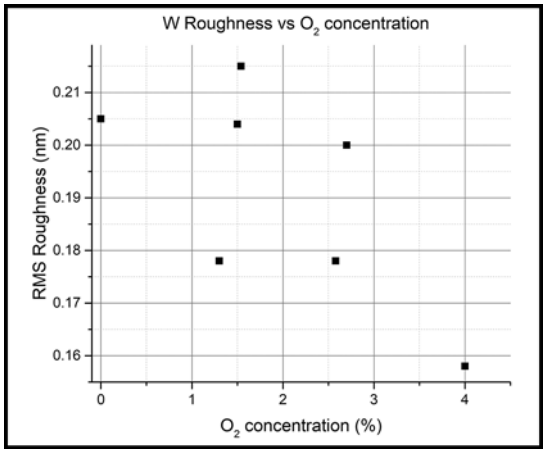

Figure 4: The roughness of tungsten films vs oxygen incorporation shows no significant variation.

Lorentzian function with symmetric (S) and antisymmetric (A) components as shown in Figure 2. The ratio of the prefactors S and A yield ξ_{FMR}, the spin torque efficiency. By fitting $1/\xi_{FMR}$ vs $1/t_{FeCoB}$, the SHA is extrapolated.

For pure tungsten films with no oxygen incorporation, the SHA was found to be 0.31 ± 0.03. However, as oxygen incorporation increased, the SHA was found to decrease, with values of 0.13 ± 0.02 and 0.06 ± 0.01 for tungsten with 1.6% and 4.0% oxygen respectively. The results of the SHA vs. oxygen incorporation for several samples are shown in Figure 3. Despite resistivity data demonstrating potentially enhanced β-W growth, the SHA reduces as oxygen is incorporated. The roughness of pure tungsten films with varying oxygen concentration were measured using the Veeco Ion AFM at CNF and all films had an rms roughness of 0.19 ± 0.03 nm, independent of oxygen concentration, as shown in Figure 4. An explanation for the reduction in the SHA may be that the pure tungsten films were already grown in the β phase, and thus adding oxygen could not enhance the growth further. Rather, the oxygen may have only oxidized the tungsten, which would also explain the increase in resistivity. This result contradicts the findings of K. Demasius, et al., which showed an enhancement of the SHA with oxygen incorporation [1].

References:

[1] Kai-Uwe Demasius, Timothy Phung, Weifeng Zhang, Brian P. Hughes, See-Hun Yang, Andrew Kellock, Wei Han, Aakash Pushp, and Stuart S.P. Parkin, Nat. Comm. 7, 10644 (2016).

[2] Chi-Feng Pai, Yongxi Ou, Luis Henrique Vilela-Leão, D.C. Ralph, and R.A. Buhrman, Phys. Rev. B. 92, 064426 (2015).

Anomalous Hall Generation of Spin Currents with Controllable Spin Polarization

CNF Project Number: 598-96

Principal Investigators: Daniel C. Ralph, Robert A. Buhrman

Users: Jonathan D. Gibbons, David MacNeill

Affiliation: Physics, Cornell University

Primary Sources of Research Funding: National Science Foundation/Division of Materials Research, Western Digital

Contact: dcr14@cornell.edu, buhrman@cornell.edu, jg833@cornell.edu, djm398@cornell.edu

CNF Tools Used: GCA 5x stepper, resist spinners, Heidelberg DWL2000, AFM – Veeco Icon, AJA sputter deposition

Abstract:

We have measured the out-of-plane field-like spin torque exerted on a magnetic sensor layer, resulting from a spin current generated through the anomalous Hall effect in a magnetic source layer. We have further demonstrated that the spin polarization direction of the generated spin current can be reoriented by turning the magnetization direction of the spin source layer. This new capability may be used to improve the efficiency of next-generation magnetic memory devices that are operated by spin-transfer torques exerted by spin currents.

Summary of Research:

Background. The spin Hall effect has proven to be an interesting and potentially useful means of generating spin torques for controlling magnetic layers and nano-magnets, a field with significant interest for the advancement of modern day computing, and particularly for the development of effective implementations of magnetic random access memory (MRAM). However, the spin Hall effect has several practical limitations. The spin polarization direction of the spin current (and hence the types of spin torques one can generate) are defined by the geometry of the device. If the spin polarization direction were controllable, the spin torques generated could be much more versatile.

The spin-orbit interactions that give rise to the spin Hall effect in normal materials also analogously give rise to the anomalous Hall effect in ferromagnets, generating a sizable charge current, but also a sizable spin current. Taniguchi, et al. [1], predicted that this spin current would have a spin polarization parallel to the direction of the magnetization of the source ferromagnet. By using an exchange biased ferromagnetic source layer, we can control the magnetization of the source ferromagnet, and hence control the direction of the spin polarization. A diagram of this effect in our sample is shown in Figure 1.

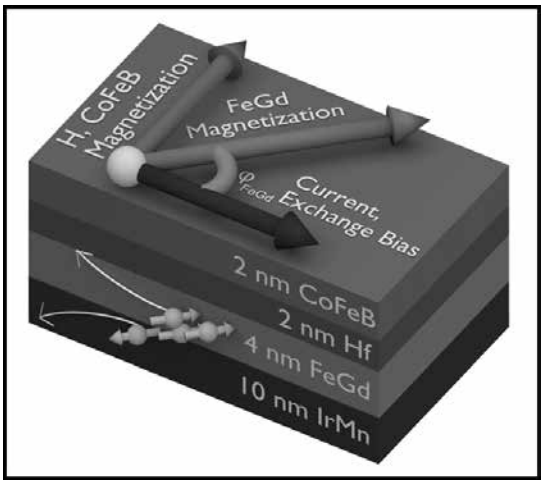

Figure 1: An anomalous Hall effect diagram. Spin carriers are deflected in a direction dependent on their sign, while remaining parallel to the magnetization of the source layer.

Fabrication. We sputter an IrMn (10 nm)/FeGd (4 nm)/Hf (2 nm)/CoFeB (2 nm)/Hf (3 nm) stack in a CCMR/Ralph Group sputter system. We use IrMn to exchange bias the FeGd layer, which is the spin source layer, and a hafnium spacer to magnetically isolate the FeGd and CoFeB layers.

We pattern 120 μm by 20 μm Hall bars using the CNF photolithography tools, with photo masks made at CNF. We then etch the Hall bars using a Buhrman-group ion mill. We then again use photolithography to define contact pads via a lift-off process. The material for the contact pads is sputtered using the CNF AJA

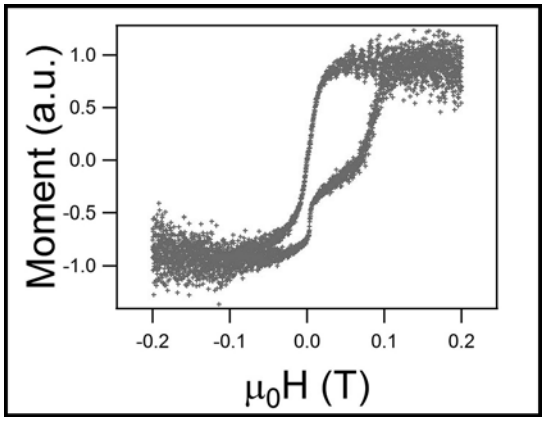

Figure 2: VSM data clearly showing the presence of one exchange biased magnetic layer and one free magnetic layer.

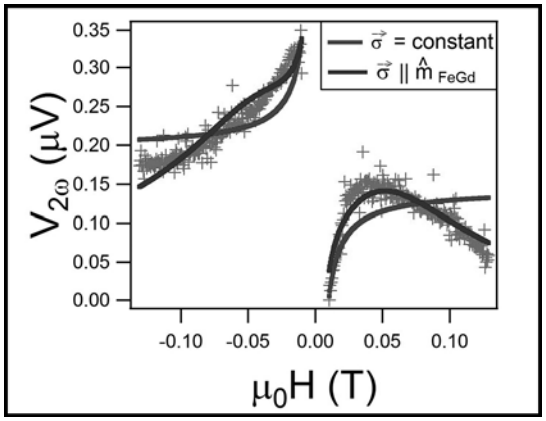

Figure 3: Measured second harmonic Hall data, with a fit to our predicted model for spin orientations parallel to the magnetization. Also shows a fit using the standard second harmonic Hall model, which is considerably worse than our model.

system. We characterize the sample using the CNF atomic force microscope and a CCMR vibrating sample magnetometer (VSM). The VSM data are shown in Figure 2.

Experiment. We use a lock-in amplifier to apply a slowly-varying (effectively DC) current to the Hall bars and detect the Hall voltage transverse to the applied current. At the same time, we use a magnetic field perpendicular to the exchange bias direction to control the magnetization of the source FeGd layer. The applied current generates a spin current with controllable orientation, which exerts an out-of-plane field-like torque on the CoFeB sensor layer, generating a rotation (in-plane) of its magnetization direction. This rotation is detected through the planar Hall effect by locking into the second harmonic Hall signal. We then use the known magnetic properties of our materials to model the system and fit to the expected behavior in order to make a quantitative measurement of the spin torque generated.

Results:

In our experimental geometry, spin torques produced by known mechanisms including the spin Hall effect would by symmetry not produce any signal. The fact that we do observe a clearly measurable signal (Figure 3) therefore indicates that a magnetic layer acting as a source of spin current produces an output with a different symmetry than a non-magnetic metal. As can be seen in Figure 3, our measured second harmonic Hall signal agrees well with the result expected due to the anomalous Hall effect within the model of Taniguchi, et al. [1]. To illustrate the consequences of turning the direction of the source-layer magnetization, we also include a fit to the data assuming that the spin-torque from the magnetic source layer is independent of the applied magnetic field – the result does not capture the behavior of our measured data.

We conclude that we have demonstrated the generation of spin-current with controllable spin polarization direction. Further, from our data, we can extract the size of the spin current generated in the source layer and extract a lower bound on the spin torque efficiency of -1.8 ± 0.4% for FeGd.

References:

[1] T. Taniguchi, J. Grollier, and M. D. Stiles, Phys. Rev. Appl. 3, 044001 (2015).

Creating Skyrmions Using Spin Transfer Torque

CNF Project Number: 598-96
Principal Investigator: Daniel C. Ralph
Users: Jennifer Grab, Alison Rugar

Affiliation: Department of Physics, Cornell University

Primary Source of Research Funding: National Science Foundation

Contact: dcr14@cornell.edu, jlg373@cornell.edu, aer245@cornell.edu

Primary CNF Tools Used: JEOL 6300, ion mill, even hour evaporator, Oxford 81 plasma etcher, AJA sputter system

Abstract:

Skyrmions are topologically protected quasiparticles in the form of stable spin textures in a magnetic material. Because skyrmions can be smaller than the domain size in a ferromagnet, they are promising candidates for high density information storage. Finding an efficient way to create and annihilate individual skyrmions under ambient conditions is an important first step toward realizing skyrmion-based technologies. In this project, we attempt to create skyrmions using a spin valve like device. If this work is successful, it will offer a relatively simple method for creating isolated magnetic skyrmions for further study and manipulation.

Summary of Research:

Skyrmions are encountered in a number of different material systems. Of particular interest experimentally are systems with a strong Dzyaloshinskii Moriya Interaction (DMI), which favors helical spin textures. Skyrmion lattices have been observed in materials with bulk DMI, for example manganese silicide [1] and iron germanium [2], at cryogenic temperatures. More recently, isolated skyrmions have been created and observed in heavy metal / ultrathin ferromagnet systems with perpendicular magnetic anisotropy (PMA) and strong interfacial DMI [3,4].

Our devices consist of a cobalt (Co) / platinum (Pt) multilayer and copper spacer patterned into a nanopillar on top of a bulk Co/Pt bilayer with strong DMI (Figure 1). The purpose of the nanopillar is to generate a spin polarized current, which is expected to reverse the magnetization of the film underneath the pillar via spin transfer torque. Micromagnetic simulations predict that we should be able to excite a skyrmion breathing mode, which will have a large resistance signal distinguishable from the switching of the entire bottom layer. Both the multilayer and bilayer have PMA as confirmed by vibrating sample magnetometry and Hall measurements. Imaging of our bilayer films using magnetic force microscopy in the Veeco Icon shows that they have a helical domain structure (Figure 2), which is favorable for the formation of skyrmions.

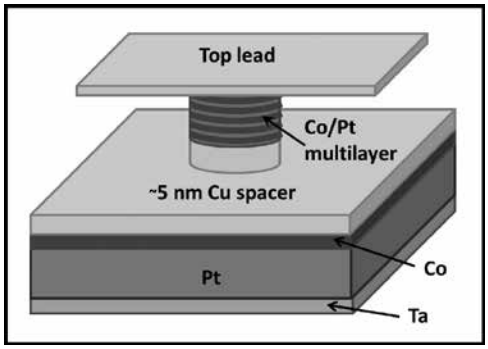

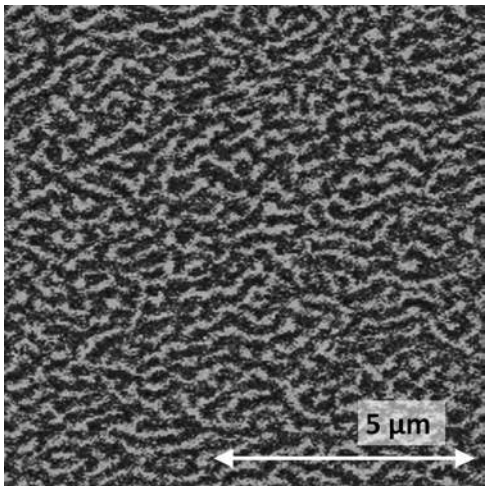

Figure 1, top: Device geometry. Figure 2, below: Magnetic force microscopy image showing helical stripe domains in one of our Co/Pt bilayer films.

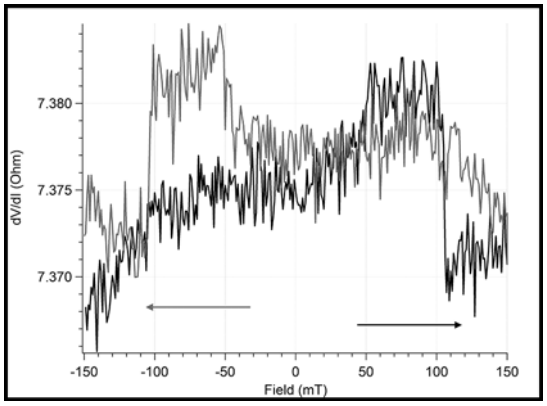

Figure 3: Example four-point magnetoresistance data demonstrating switching of the free and fixed layers in a device. The lower resistance state corresponds to the fixed and free layers aligned parallel to each other, while the higher resistance state corresponds to antiparallel alignment.

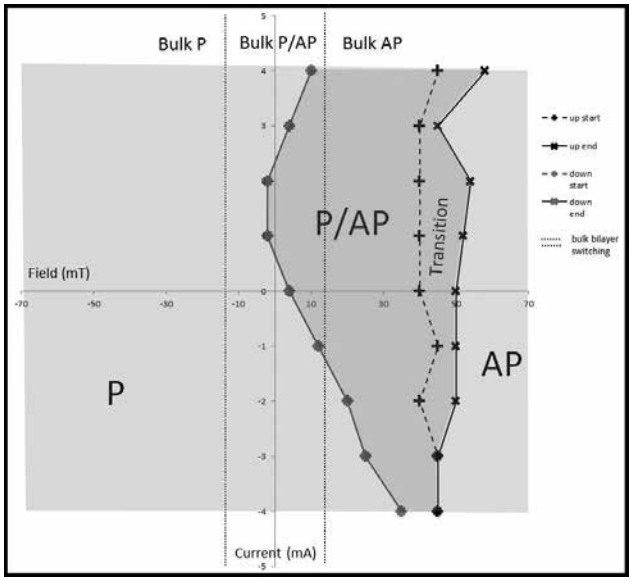

Figure 4: Phase diagram for the Co/Pt bilayer in the region immediately under the pillar, with the pillar fixed in the negative field direction. The dotted lines show where the bulk bilayer switches. "P" corresponds to parallel alignment with the pillar, and "AP" corresponds to antiparallel alignment.

Fabrication Process:

First, the entire material stack is grown using magnetron sputtering in our group's Kurt J. Lesker sputter system. Then, photolithography and ion milling are used to etch all the way to the substrate and define the bottom leads. Nanopillars are fabricated using a negative resist recipe in the JEOL 6300 electron beam lithography system, and then endpoint detection in the ion mill is used to etch down to the copper spacer. A thin protective layer of aluminum is deposited *in situ* immediately after etching. The sample is then quickly transferred to the Even Hour Evaporator, and about 80 nanometers (nm) of silicon dioxide is deposited to protect the sides of the pillar from oxidizing. The silicon dioxide is removed from the top of the pillar via liftoff and the bottom leads using the Oxford 81 plasma etcher. Next, we deposit an additional 70 nm layer of silicon dioxide around the pillar to prevent the top and bottom leads from shorting together. Lastly, we deposit top and bottom contacts using the AJA sputter system and liftoff.

Results and Conclusion:

Four-point magnetoresistance measurements of completed devices show switching of the free and fixed layers, as expected (Figure 3). To study the behavior of the bilayer local to the pillar, we hold the nanopillar in a fixed direction and conduct minor field loop scans as a function of applied DC current through the pillar. We separately monitor the state of the bulk bilayer away from the pillar using the Anomalous Hall Effect. These results are summarized in a phase diagram (Figure 4). It is interesting to note that the behavior of the bilayer local to the pillar is completely different from the behavior of the bulk. The coercive field is shifted to the right relative to the bulk bilayer, indicating that the field from the pillar might be locally favoring parallel alignment. Secondly, there is evidence of spin transfer torque induced switching. That is, the phase diagram is not symmetric with respect to the sign of the DC current.

These results indicate that there is a domain under the pillar that is switching independently of the rest of the bilayer. Because of the strong DMI demonstrated in these films, the domain is likely to be a skyrmion, but we are working on additional measurements to prove this. If the domain is indeed a skyrmion, then this will be the first experimental demonstration of skyrmion creation using a nanopillar and spin transfer torque.

References:

[1] X. Z. Yu, et al., Nano Lett., 13 (8), 3755 (2013).
[2] X. Z. Yu, et al., Nature Materials 10, 106-109 (2011).
[3] S. Woo, et al., Nature Materials 15, 501-506 (2016).
[4] W. Jiang, et al., Science 349 (6245), 283-286 (2015).

Platforms for Probing the Electronic Properties of Covalent Organic Frameworks

CNF Project Number: 598-96
Principal Investigator: Daniel C. Ralph
Users: Ruofan Li, Gregory Stiehl, David MacNeill

Affiliation: Physics, Cornell University

Primary Source of Research Funding: Army Research Office (W911NF-15-1-0447)

Contact: dcr14@cornell.edu, rl643@cornell.edu, gms263@cornell.edu, djm398@cornell.edu

Primary CNF Tools Used: 5x G-line Stepper, Oxford 80s, KOH Hood, SC4500 Even-Hour Evaporator, Oxford PECVD System, Veeco Icon AFM, Zeiss Supra SEM

Abstract:

Two-dimensional (2D) organic polymers provide a unique template for engineering material properties on the nanoscale. Our focus is on the synthesis and characterization of stable, single-monomer-thick 2D covalent organic frameworks (COFs) with novel optical and electronic properties. Development of these new materials requires rapid characterization and iteration, and often must be performed *in situ*. We report the fabrication details of two main device types — stencil masks and graphene-based platforms — that we use for *in situ* probing of the electronic properties for COFs grown in ultra-high vacuum.

Summary of Research:

The synthesis of 2D covalent organic frameworks (COFs) [1,2] is an exciting development in the field of nanotechnology, with broad implications for engineering 2D materials with unique mechanical, electrical and optical properties from the bottom up. COFs are comprised of individual monomer molecules that link deterministically to form 2D crystalline polymer films. COFs are typically grown in solvent/monomer solutions, but are occasionally evaporated under ultra-high vacuum for scanning tunneling microscopy (STM) studies. However, many COFs pose significant challenges in regard to compatibility with standard lithography techniques, such as sensitivity to water or air exposure, and are easily contaminated by other polymers. Here, we discuss two methods for studying the electronic properties of COFs with minimally invasive techniques: patterning electrical leads using stencil masks, and graphene-based platforms for *in situ* COF growth and characterization.

To engineer COFs with interesting and useful electronic properties, a robust method for measuring conductivity that minimizes contamination from processing is required. One promising approach is to deposit metal leads on top of COFs through a lithographically defined stencil mask. This produces cleaner interfaces than resist based lithography, and is an efficient means to explore different metals to reduce contact resistances.

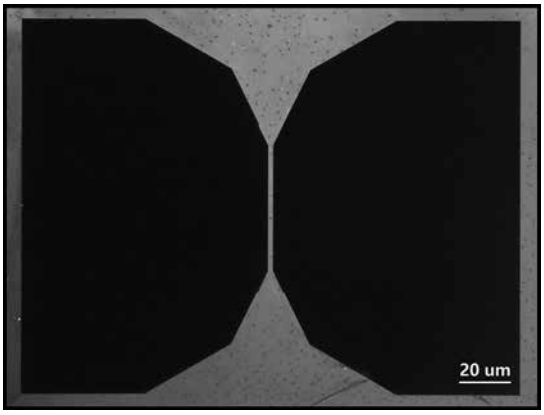

Figure 1: SiN stencil mask with 2 µm of bridge.

We fabricated two distinct types of stencil masks, a silicon nitride membrane stencil mask and a silicon stencil mask.

High-resolution stencil masks are typically fabricated from low-stress silicon nitride, which can be used to deposit metallic features on the scale of tens of nanometers [3]. Figure 1 shows one of our silicon nitride shadow masks consisting of two holes separated by a thin bridge two micrometers wide. When metal is deposited through the mask, the large holes create

contact pads that allow resistance measurements across a pristine COF region (under the bridge). To fabricate the mask, we start with a double side polished silicon wafer with low stress silicon nitride on both sides. Large area (1.21 mm2) squares are defined on one side using photolithography (5x g-line stepper) and transferred to silicon nitride with reactive-ion etching (RIE) (Oxford 80). The membrane is released by a heated KOH etch, creating arrays of windows. Photolithography (5x g-line stepper) is then used to define the shape of the actual shadow mask on the suspended windows. Finally, the photoresist pattern is transferred into the suspended silicon nitride membrane by a final RIE etch.

For large features (above 100 μm), stencil masks are instead made with whole silicon wafers due to their increased robustness. To make silicon stencils, thin silicon wafers (200 μm thick) are patterned and etched through. Since the smallest distance between the openings in the desired pattern is around 10 μm, which couldn't be achieved with a KOH etch, deep reactive-ion etching (DRIE) is performed using Unaxis 770 Deep Si Etcher. In this etch, alumina is used as a mask, while alumina and silicon dioxide are used as stopping layers. Here alumina is deposited using SC4500 even-hour evaporator and silicon dioxide is deposited using the CNF's Oxford plasma enhanced chemical vapor deposition system (Oxford PECVD). Since the etching rate is feature dependent, several dimensions of the design are still being explored to get the best outcome.

One interesting application of COFs is the prospect of integration into heterostructures with other 2D materials. Earlier work has shown that graphene can be used as a growth template for some COFs [4], but it remains an open question as to how a COF can be used to modify the electronic band structure of graphene. As a first attempt to explore the interaction between COFs and other 2D materials, we make graphene-based platforms for STM and transport studies. Figure 2 shows the design of our heterostructure. Graphene flakes are transferred on the top of hexagonal boron nitride (hBN) flakes and their cleanliness is checked both before and after the transfer with atomic force microscope (AFM-Veeco). After that the contacts are patterned by e-beam lithography (Nabity, Supra SEM). Finally, Ti and Pt metal pads are deposited by lift-off.

In conclusion, due to the chemical sensitivity of COFs, rapid characterization and iteration often must be performed *in situ*. Our research has provided procedures for fabricating two kinds of stencil masks as well as a graphene-based platform that can enable *in situ* COF growth and characterization in ultra-high vacuum.

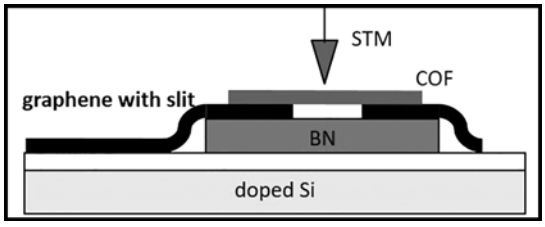

Figure 2: Design of graphene-based platforms for STM studies of COF assembly and transport properties.

References:

[1] Colson, J. W.; Dichtel, W. R. "Rationally synthesized two-dimensional polymers." Nature Chem. 5, 453-465 (2013).

[2] Sakamoto, J.; van Heijst, J.; Lukin, O.; Schlüter, A. D. "Two-Dimensional Polymers: Just a Dream of Synthetic Chemists?" Angew. Chem. Int. Ed. 48, 1030-1069 (2009).

[3] Kim, G. M.; van den Boogaart, M. A. F.; Brugger, J. Fabrication and Application of a Full Wafer Size Micro/Nanostencil for Multiple Length-Scale Surface Patterning. Microelectron. Eng. 67.68, 609.614 (2003).

[4] Colson, J. W.; Woll, A. R.; Mukherjee, A.; Levendorf, M. P.; Spitler, E. L.; Shields, V. B.; Spencer, M. G.; Park, J.; Dichtel, W. R. "Oriented 2D Covalent Organic Framework Thin Films on Single-Layer Graphene." Science 332, 228-231 (2011).

Spin Hall Effect in $YbAl_3$

CNF Project Number: 598-96
Principal Investigators: Daniel C. Ralph, Darrell Schlom, Kyle Shen
Users: Neal Reynolds, Shouvik Chatterjee, Ariel Seidner

Affiliations: Laboratory of Atomic and Solid State Physics, Materials Science and Engineering; Cornell University
Primary Source of Research Funding: National Science Foundation
Contact: dcr14@cornell.edu, schlom@cornell.edu, kmshen@cornell.edu, ndr37@cornell.edu
Primary CNF Tools Used: 5x G-line stepper, AJA sputter deposition tool, Heidelberg DWL2000

Abstract:

The spin Hall effect results in a spin current that flows transverse to an applied electric field in non-magnetic materials, and that can be used to apply an efficient spin-transfer torque in magnetic memory devices. Recent experimental and theoretical work has shown that the magnitude of the spin Hall effect should be enhanced by the presence of 4*f*-derived bands near the Fermi level. $YbAl_3$ is a rare-earth mixed-valence system, in which the ytterbium (Yb) 4*f* states become increasingly itinerant at low temperatures. This is accompanied by a shift of the 4*f* derived bands towards the Fermi level and an enhanced 4*f* contribution to the $YbAl_3$ Fermi surface, as temperature is lowered. In this report we discuss the measurement of the spin Hall effect in $LuAl_3/YbAl_3$/Fe/Al multilayers as a function of temperature.

Summary of Research:

The spin Hall effect arises from spin-dependent interaction of electrons with the electronic band structure of a given material, the so-called "intrinsic" contributions, and from asymmetric spin scattering off of impurities, the "extrinsic" contributions. Intrinsic contributions to the spin Hall effect are generally large when the material has large spin-orbit coupling and avoided crossings at the Fermi level. Materials that are expected to have large intrinsic spin Hall effects are then the late transition metals (those with 5*d* valence), and the *f*-valent lanthanides and actinides. Much work measuring the spin Hall effect in the 5*d* metals has indeed shown a large spin Hall effect [1], but it is only recently that any work has been to corroborate this understanding in the lanthanide (4*f*) metals [2]. To further our understanding of the effect of the 4*f* orbital-derived bands on the intrinsic spin Hall effect, we measured the spin Hall effect as a function of temperature in $YbAl_3$, a material system in which the 4*f*-derived bands move through the Fermi level and become itinerant as temperature is decreased. Because of this temperature dependence of the 4*f*-derived states, we expect that the intrinsic spin Hall effect should increase as the temperature of the $YbAl_3$ is decreased.

$LuAl_3/YbAl_3$/Fe/Al multilayers were grown on MgO substrate using molecular beam epitaxy (MBE) in collaboration with the Schlom group. Micron-scale devices were patterned out of the films via photolithography using the 5x g-line stepper. Argon ion milling was then used to define the devices. Ti/Pt liftoff leads were applied via photolithography, again with 5x g-line stepper, and the AJA sputter deposition tool. An optical image of a finished device is shown in Figure 1.

Measurements of the spin Hall effect as a function of temperature were done using spin torque-ferromagnetic resonance (ST-FMR) [3,4] in a custom He-flow cryostat. ST-FMR uses a microwave frequency signal (6-20 GHz) to excite resonant dynamics of the magnetic Fe layer that then leads to a measureable voltage that is proportional to the strength of the spin Hall effect. We report the strength of the spin Hall effect as a dimensionless efficiency calculated as the ratio of the measured spin current to applied charge current. We find a strong enhancement of the spin Hall effect as temperature is decreased, consistent with the hypothesis that the *f*-orbital-derived states should enhance the spin Hall effect as their presence at the Fermi level is increased (Figure 2).

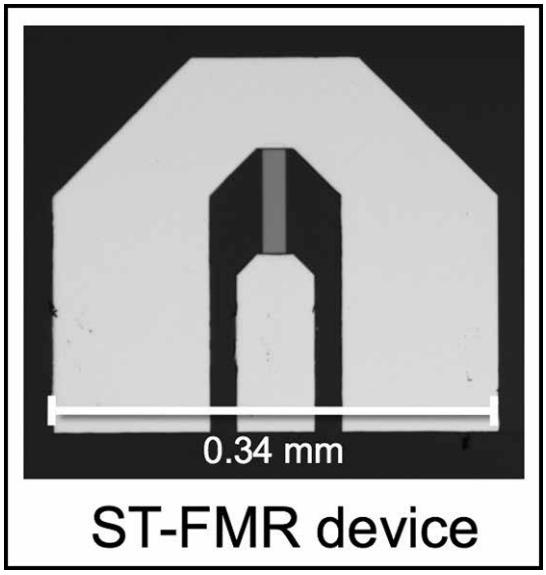

Figure 1: An optical image of a finished device used to measure the spin Hall effect via ST-FMR.

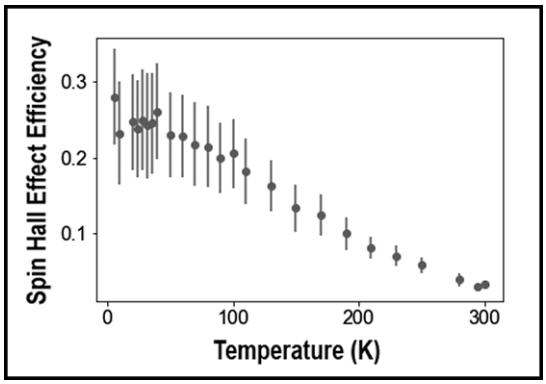

Figure 2: Spin Hall effect efficiency as a function of temperature measured by ST-FMR of a $LuAl_3/YbAl_3/Fe/Al$ multilayer. A strong increase in the spin Hall effect efficiency is observed going from 300 K down to 10 K.

References:

[1] H. L. Wang, C. H. Du, Y. Pu, R. Adur, P.C. Hammel, and F. Y. Yang, Phys. Rev. Lett. 112, 197201 (2014).

[2] N. Reynolds, P. Jadaun, J. T. Heron, C. L. Jermain, J. Gibbons, R. Collette, R. A. Buhrman, D. G. Schlom, and D. C. Ralph, Phys. Rev. B 95, 064412 (2017).

[3] L. Liu, T. Moriyama, D. C. Ralph, and R. A. Buhrman, PRL 106, 036601, (2011).

[4] L. Liu, C. F. Pai, Y. Li, H. W. Tseng, D. C. Ralph, and R. A. Burhman, Science 366, 555 (2012).

Magnetic Actuation of Graphene Microstructures

CNF Project Number: 900-00

Principal Investigator: Paul McEuen

Users: Tanner Pearson, Kyle Dorsey, Lei Wang

Affiliations: School of Applied and Engineering Physics, Laboratory of Atomic and Solid State Physics, Kavli Institute for Nanoscale Science; Cornell University

Primary Sources of Research Funding: Airforce Office of Scientific Research (MURI FA 9550-16-1-0031), National Science Foundation (DMREF DMR-1435999)

Contact: plm23@cornell.edu, tgp34@cornell.edu, kjd96@cornell.edu, lw2379.columbia@gmail.com

Website: http://www.mceuengroup.lassp.cornell.edu/

Primary CNF Tools Used: Oxford ALD FlexAL, odd/even-hour evaporators, ABM contact aligner, Autostep i-line stepper, Heidelberg DWL2000, Yes Vapor Prime Oven, P7 profilometer, Zeiss Ultra/Supra SEMs, Anatech resist strip, Oxford 81 etcher

Abstract:

The principles of origami and kirigami provide an exciting platform for the development of robotic devices and metamaterials. While these principles have been utilized in macroscale devices, the scale-invariance of origami designs and their compatibility with conventional lithography techniques makes them ideally suited for micron-scale fabrication. We investigate the potential for magnetic actuation of graphene kirigami structures using superparamagnetic Fe3O4 nanoparticles suspended in SU-8 photoresist. This technique can be used to understand the mechanics of out-of-plane buckling in square graphene frames by relating the magnetic force to the displacement in the corner-to-corner length of the frames.

Summary of Research:

We are investigating techniques using magnetic forces to automate folding and buckling in graphene. Macroscopic magnetically actuated folding has been demonstrated with magneto-active elastomers, with the potential for unidirectional locomotion, and in computer-programmable sheets for predetermined design construction [1,2,3]. Microscale actuation has also been exhibited in hinged microstructures to create optical components [4,5]. However, no equivalent work has been done with graphene. This two-dimensional material has a Föppl-von Kármán number comparable to that of paper, making it a suitable choice for devices that emulate traditional origami on the micron-scale [6]. Furthermore, graphene's conductivity suggests applications involving the integration of electrical components in deployable three-dimensional graphene origami structures.

Recent advances in our group have demonstrated localizable strain-induced bending of graphene-glass bimorphs [7]. We are complementing these efforts with the effects of superparamagnetic nanoparticles. In the absence of an external magnetic field, superparamagnetic nanoparticles exhibit zero net magnetization as their magnetic moments randomly orient with thermal fluctuations. In the presence of an external field, however, their moments point in the direction of the field, creating an attractive force towards the source of the field. The resulting lack of hysteresis in the magnetization versus magnetic field curve of superparamagnetic nanoparticles makes them an ideal material for reversible magnetic actuation in devices that have a built-in restoring force. One example we are interested in is a "trampoline" of square frames etched in graphene (Figure 1). These frames represent the universal unit of many of our kirigami structures, exhibiting an out-of-plane buckling as they are pulled at their corners (Figure 2). We strive to understand the mechanics of this buckling in terms of force-distance curves obtained by controlled superparamagnetic actuation.

Previous attempts at accomplishing this goal were focused on the use of ferromagnetic pads evaporated in the center of the graphene structures (Figure 1). Currently we are replicating results from literature that achieve magnetic manipulation with magnetite (Fe_3O_4) superparamagnetic nanoparticles suspended in SU-8 matrices [8]. We vortex mix a solution of 15 nm core Fe_3O_4 nanoparticles in SU-8 photoresist. Using standard photolithography techniques, we pattern this SU-8/nanoparticle composite on SiO_2 slides with Al_2O_3 and

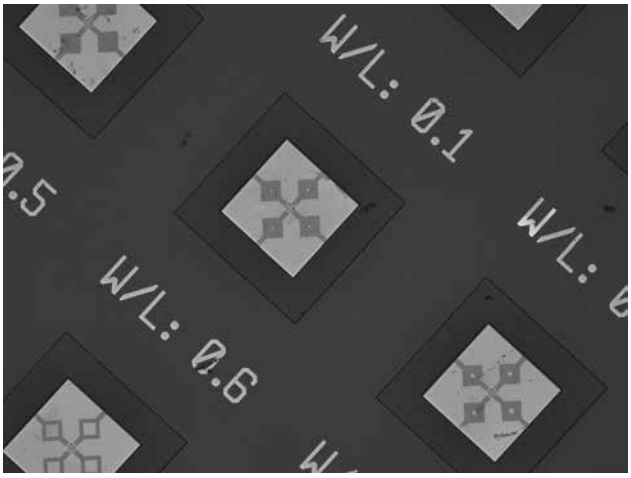

Figure 1: Early prototype of graphene frames. Arrays of frames with varying ratios of inner length (W) to outer length (L) were etched in graphene. An Fe pad was evaporated in the center of the trampoline for parallel manipulation of the square frames. The graphene is pinned at the edge to the substrate with SiO_2.

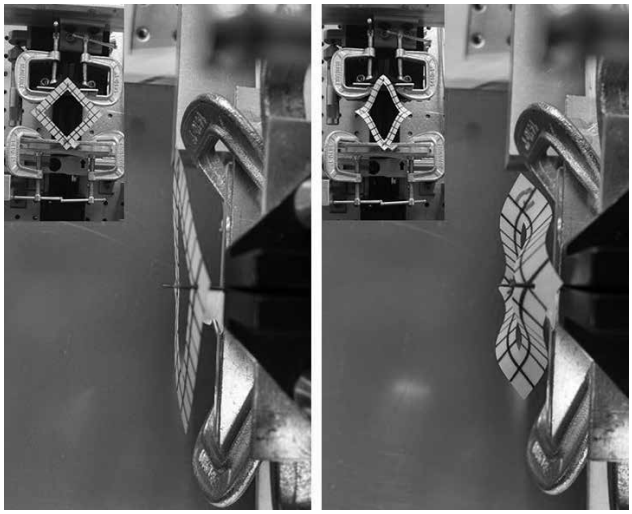

Figure 2: Paper models exhibiting the out-of-plane buckling in square frames. Left image shows an unstrained, two-dimensional frame from the side and top (inset). Right image shows the buckling of a frame under tension from the side and top (inset).

graphene. The graphene is etched into the appropriate designs using oxygen plasma. The Al_2O_3 is etched in the final step as a sacrificial layer, releasing the graphene devices from the substrate so that they can be manipulated with probes and actuated with magnetic fields. One of the primary challenges in this fabrication has been the existence of a post-development SU-8/Fe_3O_4 residual layer that connects all the devices. This layer is tens of nanometers thick and is robust enough that it prevents etching of the graphene and causes our devices to release in continuous sheets rather than individually. We have ameliorated this issue with the use of a second release layer of Cr on top of Au. This release layer is designed such that, after patterning our SU-8/Fe_3O_4 composite, we can etch the Au to release the Cr, which in turn detaches the composite residue from our primary features (Figure 3).

Our current twofold release mechanism has been successful in removing the residual composite connections between a portion of our devices. Moving forward, we will improve this technique further to increase yield. Once a repeatable fabrication recipe has been established, we will begin performing magnetic actuation tests using solenoidal magnetic probes to investigate the mechanical properties of these graphene frames.

References:

[1] P. V. Lockette and R. Sheridan, Folding Actuation and Locomotion of Novel Magneto-active Elastomer (MAE) Composites (2013).

[2] E. Hawkes, B. An, N. M. Benbernou, H. Tanaka, S. Kim, E. D. Demaine, D. Rus, and R. J. Wood, PNAS 107, 12441 (2010).

[3] M. Boncheva, S. A. Andreev, L. Mahadevan, A. Winkleman, D. R. Reichman, M. G. Prentiss, S. Whitesides, G.M. Whitesides, Proceedings of the National Academy of Sciences, 102, 3924 (2005).

[4] Y. Yi and C. Liu, Journal of Microelectromechanical Systems 8, 10 (1999).

[5] Y. W. Yi and C. Liu, Sensors and Actuators A: Physical 78, 205 (1999).

[6] M. K. Blees, A. W. Barnard, P. A. Rose, S. P. Roberts, K. L. McGill, P. Y. Huang, A. R. Ruyack, J. W. Kevek, B. Kobrin, D. A. Muller, and P. L. McEuen, Nature 524, 204 (2015).

[7] M. Z. Miskin, K. Dorsey, B. Bircan, Y. Han, D. Mulller, P. McEuen, and I. Cohen, 2017 (submitted).

[8] M. Suter, O. Ergeneman, J. Zürcher, C. Moitzi, S. Pané, T. Rudin, S. E. Pratsinis, B. J. Nelson, C. Hierold, Sensors and Actuators B: Chemical 156, 433 (2011).

Vortex Dynamics in Nanofabricated Superconducting Devices

CNF Project Number: 1314-05
Principal Investigator: Britton L.T. Plourde
Users: Kenneth Dodge, JJ Nelson

Affiliation: Department of Physics, Syracuse University
Primary Source of Research Funding: Army Research Office
Contact: bplourde@syr.edu, krdodgej@syr.edu, jjnelson@syr.edu
Website: http://plourdelab.syr.edu
Primary CNF Tools Used: ASML, JEOL 9500, PlasmaTherm 720/740

Abstract:

We fabricate superconducting microwave devices for studying the dynamics of vortices and quasiparticles at low temperatures. Vortices are quantized bundles of magnetic flux that thread many different superconductors over a particular range of applied magnetic field. Our experiments are aimed at investigating loss mechanisms that can limit the performance of superconducting circuits for quantum information processing. In addition to probing the loss in these circuits that arises from trapped magnetic flux, we are also studying techniques for coupling superconducting digital control circuitry to superconducting qubits for control of the quantum state.

Summary of Research:

Superconducting microwave circuits play an important role in quantum information processing. Circuits composed of Josephson junctions and capacitors with superconducting electrodes can serve as qubits, the fundamental element of a quantum computing architecture. Various loss mechanisms limit the ultimate performance of these devices, including trapped magnetic flux vortices and quasiparticles. Vortices can be trapped in the superconducting electrodes when background magnetic fields are present and contribute to dissipation when driven with microwave currents [1].

Quasiparticles are excitations above the super--conducting ground state and also result in microwave losses in superconducting electrodes. Various mechanisms can lead to the generation of excess quasiparticles, including the operation of superconducting digital control circuitry in close proximity to qubits [2]. Thus, techniques for controlling the trapping of vortices and the mitigation of quasiparticles are critical to the development of large-scale quantum information processors with superconducting circuits.

We are fabricating a system of microwave resonators using a variety of superconducting thin films, including Nb and TiN, for studying the loss contributed by trapped flux in these materials over the frequency range from 1.5-11 GHz [3]. By cooling the resonators in different magnetic fields, we are able to probe the loss from vortices as a function of field at the resonance frequencies contained in our design.

We are also working on fabricating and testing devices containing superconducting quantum circuits as well as digital control circuitry for cryogenic control of the quantum state of superconducting qubits [2]. The qubits are fabricated at the CNF and Syracuse with Al-AlOx-Al junctions and the superconducting digital circuits are fabricated by collaborators at the University of Wisconsin, Madison with a Nb-based process [4,5]. We have demonstrated techniques for mitigating the effects on qubit coherence due to stray quasiparticles from the operation of the digital control circuitry [6]. The qubit junctions for these devices are currently patterned on the JEOL9500, but we are pursuing a parallel approach with an all-photolithography process on the ASML for defining the junction electrodes.

We fabricate our microwave resonators from various superconducting films, including aluminum, deposited onto silicon wafers in our electron-beam evaporator at Syracuse University. We define the patterns on the ASML stepper and transfer them into the films with a combination of reactive ion etching and wet-etch processing. We define the electrodes for our Josephson tunnel junctions with electron-beam lithography on the JEOL9500 and ASML. We measure these circuits at temperatures of 100 mK and below in our lab at Syracuse University.

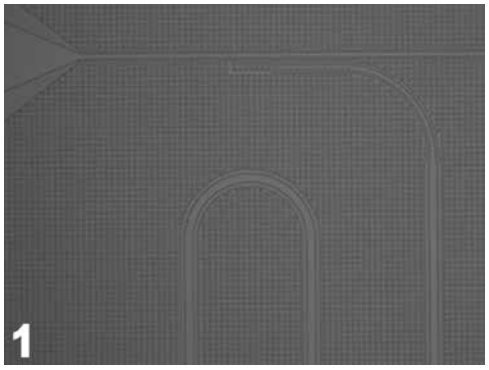

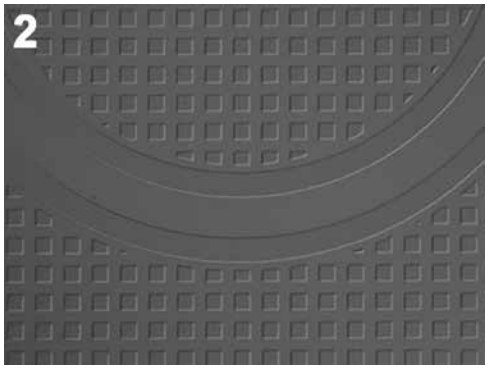

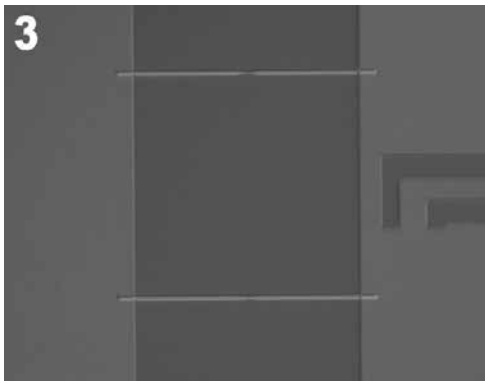

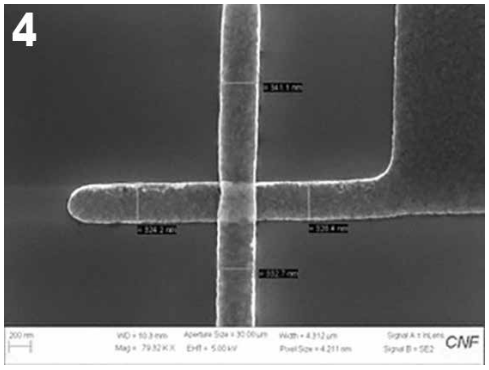

References:

[1] Song, C., Heitmann, T.W., DeFeo, M.P., Yu, K., McDermott, R., Neeley, M., Martinis, John M., Plourde, B.L.T.; "Microwave response of vortices in superconducting thin films of Re and Al"; Physical Review B 79, 174512 (2009).

[2] McDermott, R., Vavilov, M.G.; "Accurate Qubit Control with Single Flux Quantum Pulses"; Physical Review Applied 2, 014007 (2014).

[3] Dodge, K., Plourde, B.L.T.; "Microwave response of vortices in superconducting Nb resonators"; Bull. Am. Phys. Soc. 2017, http://meetings.aps.org/Meeting/MAR17/Session/L51.11.

[4] Beck, Matthew, Leonard, Edward Jr., Thorbeck, Ted, Zhu, Shaojiang, Howington, Caleb, Nelson, JJ, Plourde, Britton, McDermott, Robert; "Superconducting Qubit with Integrated Single Flux Quantum Controller Part I: Theory and Fabrication"; Bull. Am. Phys. Soc. 2017, http://meetings.aps.org/Meeting/MAR17/Session/C46.4.

[5] Leonard, Edward Jr., Beck, Matthew, Thorbeck, Ted, Zhu, Shaojiang, Howington, Caleb, Nelson, JJ, Plourde, Britton, McDermott, Robert; "Superconducting Qubit with Integrated Single Flux Quantum Controller Part II: Experimental Characterization"; Bull. Am. Phys. Soc. 2017, http://meetings.aps.org/Meeting/MAR17/Session/C46.5.

[6] Patel, U., Pechenezhskiy, Ivan V., Plourde, B.L.T., Vavilov, M.G., McDermott, R.; "Phonon-Mediated Quasiparticle Poisoning of Superconducting Microwave Resonators"; arXiv:1610.09351.

Figure 1: Optical micrograph of superconducting titanium nitride microwave resonator for low-temperature experiments probing the effects of magnetic flux vortices on microwave loss.

Figure 2: Zoomed-in optical micrograph of portion of superconducting titanium nitride microwave resonator. Square holes in ground plane ensure that magnetic flux vortices are trapped in the coplanar waveguide center conductor during field-cooling measurements.

Figure 3: Optical micrograph of Al-AlOx-Al superconducting tunnel junctions and Nb capacitor pads for a superconducting transmon qubit for investigations of qubit control with digital superconducting electronics.

Figure 4: Scanning electron micrograph of superconducting Al-AlOx-Al tunnel junction fabricated with photolithography on the ASML stepper.

Fabrication of Nanofluidic Cavities for Superfluid ^{3}He Studies

CNF Project Number: 1520-07

Principal Investigator: Jeevak M. Parpia

Users: Abhilash Thanniyil Sebastian, Nikolay Zhelev, Roberto DeAlba

Affiliation: Department of Physics, Cornell University

Primary Source of Research Funding: National Science Foundation

Contact: jmp9@cornell.edu, at654@cornell.edu

Website: http://parpia.lassp.cornell.edu

Primary CNF Tools Used: Karl Suss MA6 contact aligner, Heidelberg DWL 2000, Oxford 81/82 etchers, Uniaxis 770 Deep Si etcher, CMOS wet oxide

Abstract:

We have demonstrated nanoscale cavities that have proven to be capable of being cycled to ultralow temperatures, are pressure tight, and maintain their integrity. The devices were designed at Cornell, fabricated at the CNF, and cooled down to mK temperatures to investigate properties of superfluid ^{3}He at Cornell and at Royal Holloway in the UK. The surfaces of the cavities are nearly pristine having well characterized surface roughness (well under 1 nm). Their bowing under pressure was also characterized. We have also fabricated novel nanostrings from high stress silicon nitride. The devices are then coated with niobium that will be superconducting at low temperatures. Their optomechanical behavior was investigated at room temperature. These structures will be used to investigate the energy gap of the ^{3}He superfluid state.

Summary of Research:

Superfluid ^{3}He is a unique system for study of exotically paired condensed matter systems. Unlike the more common isotope ^{4}He, ^{3}He is a Fermion (like electrons), but its pairing into the superfluid state is more complex than its electronic counterparts. This complexity allows for a multiplicity of superfluid phases. In the bulk two phases the anisotropic A phase and the isotropically gapped B phase emerge. Confinement favors the A phase over the B phase but a so called Stripe Phase is also predicted [1] to emerge at the interface between the A and B phases. The superfluid state is attained at a variety of pressures between 0 and 35 bar and the pairing length is also highly tunable by varying the pressure. Because of its extreme purity and exotic pairing ^{3}He can serve as a model system for exotically paired systems.

Cavities of depths 50, 100, 200, 300, 600, 1100 nm have been fabricated. Confinement alters the phase diagram and as the ^{3}He is progressively restricted to smaller sizes, the B phase should yield to the A phase and new phases should emerge. Surface quality is very important as roughness or scratches can pin the A-B transition boundary.

Thus far we have investigated a 700 nm tall ^{3}He filled cavity using NMR [2], (Figure 1) a 1080 nm tall cavity using a torsion pendulum [3] (Figure 2), and are actively investigating a 200 nm cavity using NMR at Royal Holloway and a 1100 nm cavity using thermal conductivity. As yet these reveal no new phases of ^{3}He but show that the strong coupling that favors the stability of the A phase is larger than previously estimated even at low pressure. Further the supercooling of the A phase as it transitions to the B phase is remarkably small. It is possible that this small supercooling is indicative of an intrinsic nucleation mechanism for example by resonant tunneling [4]. Resonant tunneling has been invoked as an explanation for efficient transformations of state during the inflationary epoch following the big-bang. This raises the exciting possibility of carrying out experiments in the lab that may provide new insights for the evolution of the early universe. Some of these results will appear shortly in Nature Communications.

We have also examined the opto-mechanics of a very narrow wire (Figure 3), which, by its construction and design has features that lead to a significant thermo-opto-mechanical coupling. Under illumination

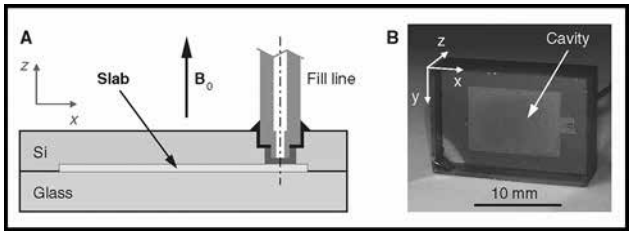

Figure 1: A Schematic of the cavity design. B. Bonded NMR cavity viewed from the glass side.

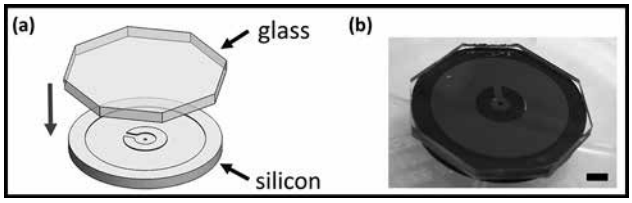

Figure 2: (a) Schematic of the design of torsion oscillator head. (b) Actual Torsion pendulum head. The cavity to contain the 3He is readily visible. Scale bar is 2 mm. From Reference [3].

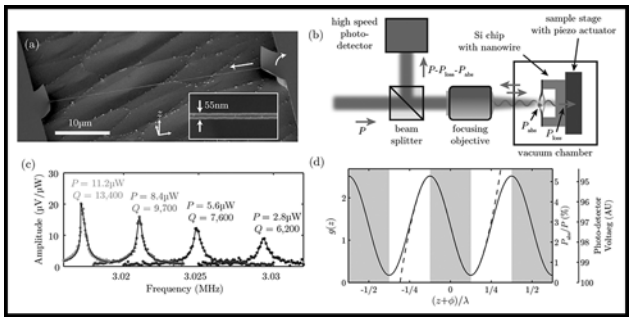

Figure 3: (a) False color image of Niobium coated wire (b) set up for drive and detection of wire (c) narrowing of resonance and frequency shift on illumination with red laser (d) regions in pink showing where photothermal feedback is positive. From Reference [5].

at very low laser-light power, this structure exhibits self-oscillation and linewidth narrowing. This can be attributed to a significant change in tension of the wire due to thermal expansion that in-turn leads to a vertical (out of plane) displacement of the wire and positive optical feedback amplifying the resonant motion. The results at room temperature are described in Reference [5].

References:

[1] Crystalline order in superfluid ^{3}He Films; J. A. Sauls, and A.B. Vorontsov, Phys. Rev. Lett. 98, 045301 (2007). DOI:https://doi.org/10.1103/PhysRevLett.98.045301

[2] Phase Diagram of the Topological Superfluid ^{3}He Confined in a Nanoscale Slab Geometry; L. V. Levitin, R. G. Bennett, A. Casey, B. Cowan, J. Saunders, D. Drung, Th. Schurig, J. M. Parpia, Science 340, 841 (2013) DOI: 10.1126/science.1233621

[3] The A-B transition in superfluid helium-3 under confinement in a thin slab geometry; N. Zhelev, T.S. Abhilash, E.N. Smith, R.G. Bennett, X. Rojas, L. Levitin, J. Saunders, and J.M. Parpia, Nature Comm, in press.

[4] Resonant tunneling in superfluid He; S.-H.H. Tye, and D. Wohns, Phys. Rev. B 84, 184518 (2011). DOI:https://doi.org/10.1103/PhysRevB.84.184518

[5] Low-Power Photothermal Self-Oscillation of Bimetallic Nanowires; Roberto De Alba, T. S. Abhilash, Richard H. Rand, Harold G. Craighead, and Jeevak M. Parpia, Nano Letters DOI: 10.1021/acs.nanolett.6b04769

Fabrication of Nanoscale Josephson Junctions for Quantum Coherent Superconducting Circuits

CNF Project Number: 1735-08

Principal Investigator: Britton L.T. Plourde

Users: Caleb Howington, Matthew Hutchings, Indrajeet, JJ Nelson, Haozhi Wang

Affiliation: Department of Physics, Syracuse University

Primary Source of Research Funding: Army Research Office

Contact: bplourde@syr.edu, cjhowing@syr.edu, mdhutc01@syr.edu, indraje@syr.edu, jjnelson@syr.edu, hwang42@syr.edu

Website: http://plourdelab.syr.edu

Primary CNF Tools Used: ASML, JEOL 9500, PlasmaTherm 720/740

Abstract:

We fabricate nanoscale superconductor tunnel junctions and other structures for experiments involving quantum coherent circuits. Such circuits have shown great promise in recent years for explorations of quantum mechanics at the scale of circuits on a chip and for forming qubits, the foundational elements of a quantum computer. The quantum state of these superconducting qubits can be manipulated with microwave radiation at low temperatures. In addition, we are developing alternative techniques for probing the state of these qubits, as well as superconducting metamaterial structures with novel microwave mode spectra for coupling to superconducting qubits.

Summary of Research:

The unique properties of nanoscale Josephson junctions enable a wide range of novel superconducting circuits for investigations in many diverse areas. In recent years, circuits composed of such junctions have emerged as promising candidates for the element of a quantum computer, due to the low intrinsic dissipation from the superconducting electrodes and the possibility of scaling to many such qubits on a chip [1]. The quantum coherent properties of the circuits are measured at temperatures below 50 mK with manipulation of the qubit state through microwave excitation.

We are currently working on a variety of experiments involving these nanoscale Josephson junctions and other superconducting structures that will allow us to probe novel quantum effects in our microwave circuits. With particular combinations of superconducting lumped-circuit elements, it is possible to engineer metamaterial transmission lines that exhibit novel mode structures characteristic of left-handed materials [2]. We are fabricating such metamaterial transmission lines from Al and Nb films on Si and characterizing these at low temperatures [3-4]. We are working on experiments to couple these left-handed lines to superconducting qubits for experiments involving the exchange of microwave photons [5]. In addition, we are fabricating other superconducting circuits for forming low-temperature detectors of single microwave photons and for implementing a new scheme for the efficient readout of the quantum state of superconducting qubits [6-7].

We pattern these circuits at the CNF with nanoscale structures defined with electron-beam lithography integrated with photolithographically defined large-scale features. The junctions are fabricated using the standard double-angle shadow evaporation technique, in which a resist bilayer of copolymer and PMMA is used to produce a narrow PMMA airbridge suspended above the substrate. Evaporation of aluminum from two different angles with an oxidation step in between forms a small Al-AlOx-Al tunnel junction from the deposition shadow of the airbridge. We have developed a process for defining these junctions with electron-beam lithography and we perform the aluminum evaporations in a dedicated chamber at Syracuse. We pattern large-scale features using the ASML stepper, with electron-beam evaporation of Al, sputter-deposition of Nb, and PECVD deposition of SiO_2. Measurements of these circuits are performed in cryogenic systems at Syracuse University, including dilution refrigerators for achieving temperatures below 30 mK.

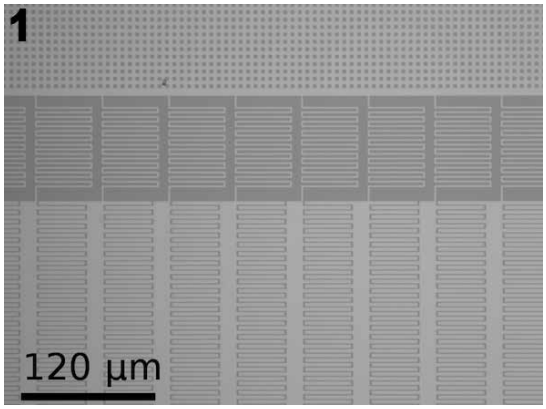

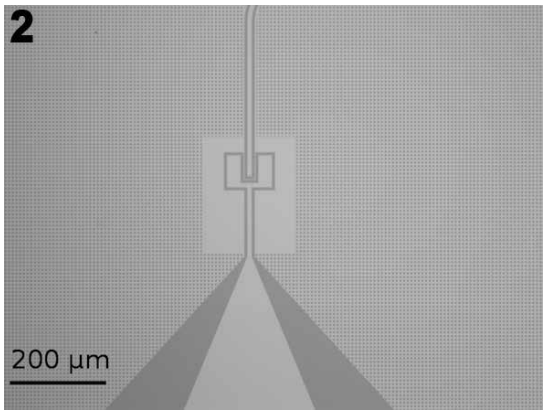

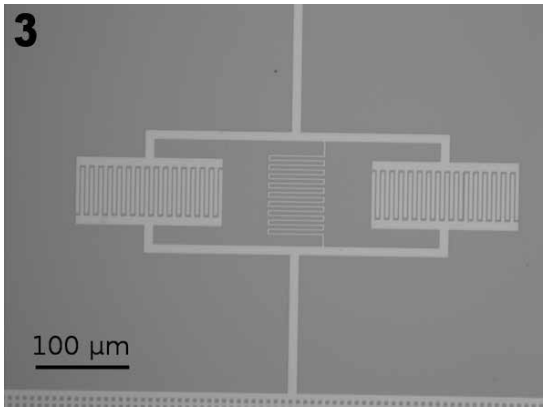

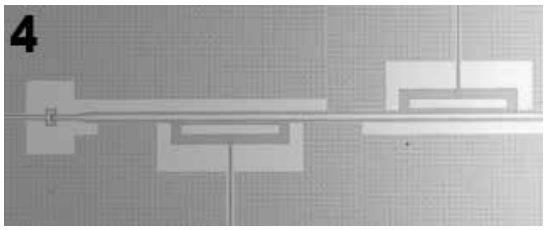

References:

[1] Clarke, J. and Wilhelm, F.K.; "Superconducting quantum bits"; Nature, 453, 1031 (2008).

[2] Egger, D.J. and Wilhelm, F.K.; "Multimode Circuit Quantum Electrodynamics with Hybrid Metamaterial Transmission Lines"; Physical Review Letters 111, 163601 (2013).

[3] Plourde, B.L.T., Wang, Haozhi, Rouxinol, Francisco, LaHaye, M.D.; "Superconducting metamaterials and qubits"; Proceedings of the SPIE 9500, Quantum Information and Computation XIII, 95000M (2015).

[4] Wang, Haozhi, Hutchings, Matthew, Indrajeet, Sagar, Rouxinol, Francisco, LaHaye, Matthew, Plourde, B.L.T., Taketani, Bruno G., Wilhelm, Frank K., Zhuravel, Alexander, Ustinov, Alexey; "Superconducting metamaterial resonators: analysis of mode structure"; Bull. Am. Phys. Soc. 2017, http://meetings.aps.org/Meeting/MAR17/Session/F51.5.

[5] Indrajeet, Sagar, Hutchings, Matthew, Wang, Haozhi, Plourde, Britton, Taketani, Bruno, Wilhelm, Frank; "Multi-mode Experiments with Superconducting Qubits and Metamaterial Resonators"; Bull. Am. Phys. Soc. 2017, http://meetings.aps.org/Meeting/MAR17/Session/F51.6.

[6] Govia, L.C.G., Pritchett, Emily J., Xu, Canran, Plourde, B. L. T., Vavilov, Maxim G., Wilhelm, Frank K., McDermott, R.; "High-fidelity qubit measurement with a microwave-photon counter"; Physical Review A 90, 062307 (2014).

[7] Howington, Caleb, Opremcak, Alex, Pechenezhskiy, Ivan, Schöndorf, Marius, Wilhelm, Frank, McDermott, R., Plourde, B.L.T.; "Parity detection of multiple superconducting qubits"; Bull. Am. Phys. Soc. 2017, http://meetings.aps.org/Meeting/MAR17/Session/S51.13.

Figure 1: Optical micrograph of Nb superconducting metamaterial transmission line resonator, patterned photolithographically on ASML stepper showing multiple unit cells of interdigitated capacitors and meander-line inductors.

Figure 2: Zoomed-in optical micrograph of input launcher and coupling capacitor on superconducting Nb transmission line resonator.

Figure 3: Optical micrograph of Nb superconducting lumped-element test oscillator for characterization of circuit elements for metamaterial structures.

Figure 4: Optical micrograph of device with Nb ground plane and microwave resonator plus Al-AlOx-Al tunnel junctions for superconducting qubits for coupling to microwave photon detector.

Development of Superconductor Circuits for Readout of Quantum Nanomechanical Resonators

CNF Project Number: 1851-09

Principal Investigator: Prof. Matthew LaHaye

User: Yu Hao

Affiliation: Department of Physics, Syracuse University

Primary Sources of Research Funding: National Science Foundation Faculty (NSF) Early Career Development Program (CAREER) Grant, number 1056423; NSF Materials World Network Grant 1312421

Contact: mlahaye@syr.edu, yuhao@syr.edu; rouxinol@gmail.com

Website: http://lahayelab.syr.edu

Primary CNF Tools Used: ASML 300C Stepper, JEOL 9500, Oxford 81 / 82, PT740 etcher

Abstract:

The LaHaye lab (Syracuse University) has been utilizing the nanofabrication facilities at Cornell NanoScale Science and Technology Facility (CNF) to develop a new hybrid quantum system that involves the integration of nanomechanical systems with state-of-the-art technology from the field of superconducting quantum computing. In recent years, the LaHaye group began studying the complex behavior of this quantum electromechanical system, and is currently following up on these initial experiments with plans to optimize the system to serve as a platform for generating and studying non-classical states of motion at the nanoscale [1]. With further development, this system could have applications for quantum information processing, quantum thermodynamics, and the study of fundamental topics that are of central interest to emerging quantum-enabled technologies.

Summary of Research:

Hybrid quantum systems — systems consisting of multiple elements with distinct functionality that each behave quantum mechanically — are being developed for a range of quantum-enabled applications, including quantum information processing and quantum-limited sensing [2,3]. They also offer prospects for studying fundamental topics of direct relevance to these applications, such as quantum decoherence [4-6] and quantum fluctuation theorems [7,8].

The LaHaye group is developing a particular hybrid quantum system that could serve as a versatile platform for pursuing many of these directions (Figures 1 and 2). The system is composed of three devices: a superconducting quantum bit (qubit) [9], superconducting microwave resonator (SMR) [10], and flexural nanomechanical resonator (nanoresonator) [1]. These components are integrated on a silicon wafer and can be coupled together and probed via the application of DC and microwave signals. This architecture is analogous to that of systems used in cavity and circuit quantum electrodynamics, where atoms and artificial atoms — such as superconducting quantum bits — are used for studying the quantum properties of light [10]. It is thus expected that this electromechanical analog should enable exploration of quantum behavior of the nanoresonator [5,6,11]. For instance, it should allow for the creation and measurement of nanoresonator superposition states, which would enable experiments to probe decoherence with the nanoresonator [5,6] and also be an important step toward utilizing the nanoresonator as quantum coherent circuit element (such as quantum switch [12], transducer [13], or memory device [14]).

In the first series of experiments pursued by the LaHaye group in 2015 and 2016, the qubit served as an element for measuring the nanoresonator; similarly, the SMR functioned to control and probe the state of the qubit. In the last year, the LaHaye group published results that characterized the interactions between the components of this tripartite system at milli-Kelvin temperatures — temperatures where each element resides near its quantum ground state [1]. These measurements were performed in the weak coupling limit between the nanoresonator and qubit, where the strength of

their mutual interaction is weaker than the relaxation rate of the nanoresonator, which is dominated by elastic energy loss through the nanoresonator's structural supports to the substrate. In this limit, the nanoresonator acts like a thermal bath absorbing and imparting energy to the qubit [1].

Building on these initial results, the LaHaye group is planning new experiments to access the strong-coupling regime between the mechanical resonator and qubit. The new experiments will utilize electromechanical devices that incorporate membrane-style nanoresonators (Figure 3). These membrane resonators are designed to improve the interaction strength between the qubit and nanoresonator, and to decrease the clamping loss that dominates the nanoresonator's dissipation in current experiments. Such modifications should make this hybrid quantum electromechanical system a viable candidate for the many research directions outlined above.

Our devices are patterned on 4-inch, <100>-oriented silicon wafers (>10 kΩ.cm resistivity). We pattern large-scale features, including the SMR (Figure 1), using CNF's ASML 300C Stepper. The qubit and first generation nanoresonators are fabricated using electron-beam lithography (Figure 2). This has been accomplished using CNF's electron beam writer JEOL 9500, followed by a double-angle evaporation of aluminum at SU; the nanoresonators are released by a reactive ion etch process using CNF's Oxford 82. Fabrication of the second generation of nanoresonators (Figure 3) is accomplished in a multi-step process utilizing the ASML, the PT740 etcher, and Oxford 81 or 82.

Acknowledgements:

This work was funded by a National Science Foundation CAREER grant, grant number 1056423, and a NSF Materials World Network grant, grant number 1312421.

References:

[1] F. Rouxinol, et al. Nanotechnology 27, 364003 (2016).
[2] G. Kurizki, et al. Proc. Natl. Acad. Sci. USA 112, 3866 (2015).
[3] Z. Xiang, et al. Phys. Rev. Lett. 85, 623 (2013).
[4] M. Aspelmeyer, et al. Phys. Today 65 (7), 29 (2012).
[5] A. Armour and M.P. Blencowe, New J. Phys. 10, 095005 (2008).
[6] D.W. Utami and A.A. Clerk, Phys. Rev. A 78, 042323 (2008).
[7] M. Campisi, P. Hanggi, and P. Talkner, Rev. Mod. Phys. 83, 771 (2011).
[8] F. Brito, et al. New J. Phys. 17, 075002 (2015).
[9] J. Clarke and F.K. Wilhelm, Nature 453, 1031 (2008).
[10] M.H. Devoret and R.J. Schoelkopf, Science 339, 1169 (2013).
[11] E.K. Irish and K.C. Schwab, Phys. Rev. B 68, 155311 (2003).
[12] M. Mariantoni, et al. Phys. Rev. B 78, 104508 (2008).
[13] J. Bochmann, et al. Nat. Phys 9, 712 (2013).
[14] T.A. Palomaki, et al. Nature 495, 210 (2013).

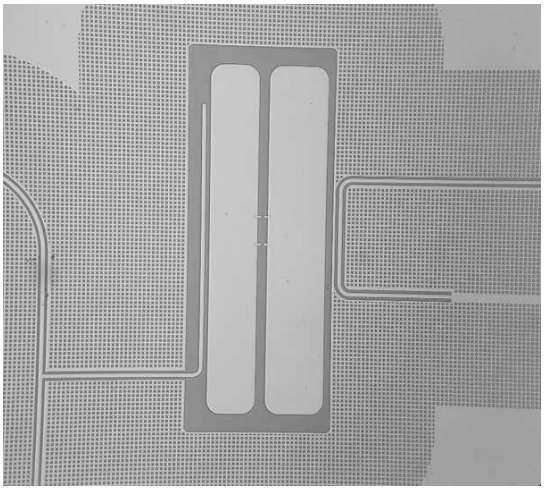

Figure 1: An optical image displaying a birds-eye-view of the type of superconducting qubit and SMR resonator used in the new hybrid quantum system. The SMR is a superconducting coplanar waveguide microwave cavity. The qubit is based on the standard transmon design [10]. The device was fabricated at CNF and Syracuse by the LaHaye group.

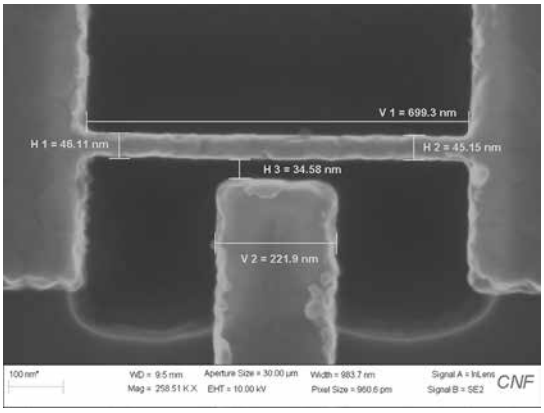

Figure 2: A scanning electron micrograph illustrating the nanostructure in one of the LaHaye group's quantum electromechanical devices. The suspended nanostructure is fabricated from aluminum; the third in-plane mode of this beam serves as the nanoresonator in this work [1].

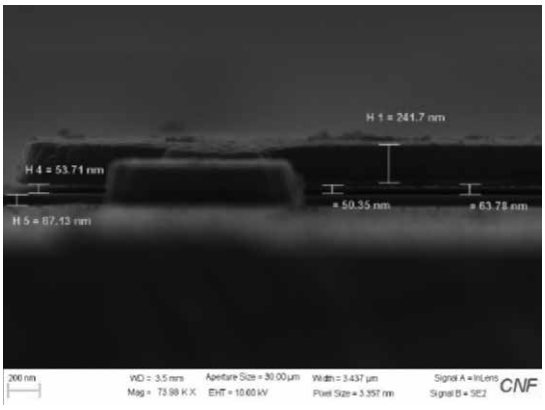

Figure 3: A scanning electron micrograph of the new generation of nanoresonators being developed by the LaHaye group. Here the nanoresonator is formed from a suspended aluminum plate.

Fabrication of Superconducting Devices for Quantum Information Science

CNF Project Number: 1873-10
Principal Investigator: Britton L.T. Plourde
Users: Matthew Hutchings, Jaseung Ku, Yebin Liu

Affiliation: Department of Physics, Syracuse University
Primary Source of Research Funding: Intelligence Advanced Research Projects Agency
Contact: bplourde@syr.edu, mdhutc01@syr.edu, jku102@syr.edu, yliu166@syr.edu
Website: http://plourdelab.syr.edu
Primary CNF Tools Used: ASML, JEOL 9500, PlasmaTherm 720/740

Abstract:

We are fabricating nanoscale superconductor tunnel junctions and microwave resonators for investigations in quantum information science. Such circuits have shown great promise in recent years for forming qubits, the elements of a quantum computer. We are developing architectures involving multiple superconducting qubits and microwave resonators. This involves a combination of photolithographic processing and etching of large-scale features and electron-beam lithography for the tunnel junctions.

Summary of Research:

In recent years, circuits composed of nanoscale Josephson junctions have emerged as promising candidates for the foundational element of a quantum computer, due to the low intrinsic dissipation from the superconducting electrodes and the possibility of scaling to many such qubits on a chip [1]. The quantum coherent properties of the circuits are measured at temperatures below 50 mK with manipulation of the qubit state through microwave excitation.

We are working to develop architectures involving multiple superconducting qubits coupled to multiple low-loss microwave resonators [2-4]. We probe the coupling between each qubit and resonator by measuring the dispersive shift of the resonator frequency with the qubit detuned from the resonator. Some of our experiments are aimed at developing qubit designs that have reduced sensitivity to low-frequency magnetic flux noise that can lead to decoherence [2]. We are also investigating alternative qubit designs [3] that may lead to more efficient two-qubit gates for generating entanglement between circuits [4].

We pattern these circuits at the CNF with nanoscale structures defined with electron-beam lithography integrated with photolithographically defined large-scale features on Si and sapphire substrates. The junctions are fabricated using the standard double-angle shadow evaporation technique, in which a resist bilayer of copolymer and PMMA is used to produce a narrow PMMA airbridge suspended above the substrate. Evaporation of aluminum from two different angles with an oxidation step in between forms a small Al-AlOx-Al tunnel junction from the deposition shadow of the airbridge. We have developed a process for defining these junctions with electron-beam lithography on the JEOL 9500 and we perform the aluminum evaporations in a dedicated vacuum chamber at Syracuse. We pattern large-scale features using the ASML, with sputter deposition of superconducting Nb films in a dedicated vacuum system at Syracuse University. Microwave measurements of these circuits are performed in cryogenic systems at Syracuse University, including dilution refrigerators for achieving temperatures below 30 mK.

References:

[1] Clarke, J. and Wilhelm, F.K.; "Superconducting quantum bits"; Nature, 453, 1031 (2008).

[2] Hutchings, M. D. Hertzberg, Jared B., Liu, Y., Bronn, Nicholas T., Keefe, George A., Chow, Jerry M., Plourde, B.L.T.; "Tunable Superconducting Qubits with Flux-Independent Coherence"; arXiv:1702.02253.

[3] Ku, Jaseung, Hutchings, Matthew, Liu, Yebin, Plourde, B.L.T., Hertzberg, Jared B., Sandberg, Martin, Brink, Markus, Magesan, Easwar, Solgun, Firat, Chow, Jerry M.; "Capacitively Shunted Flux Qubits for Multi-qubit Architectures"; Bull. Am. Phys. Soc. 2017, http://meetings.aps.org/Meeting/MAR17/Session/Y51.8.

[4] Corcoles, A.D., Gambetta, J.M., Chow, J.M., Smolin, J.A., Ware, M., Strand, J.D., Plourde, B.L.T., Steffen, M.; "Process verification of two-qubit quantum gates by randomized benchmarking"; Physical Review A 87, 030301(R) (2013).

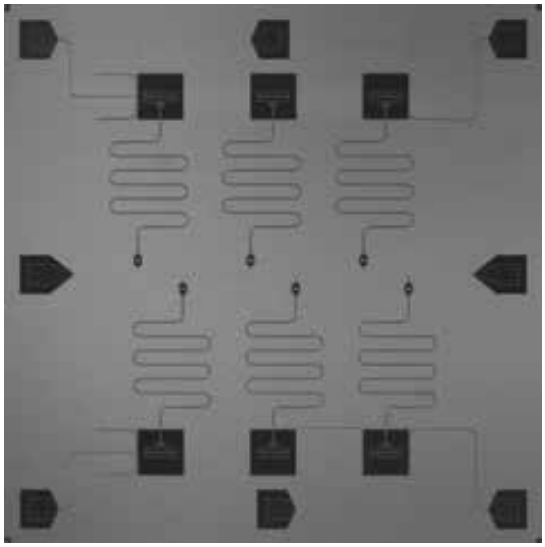

Figure 1: Optical micrograph of chip containing six superconducting qubits, each of which is coupled to a coplanar waveguide readout resonator for microwave measurements through a common feedline along the center of the image.

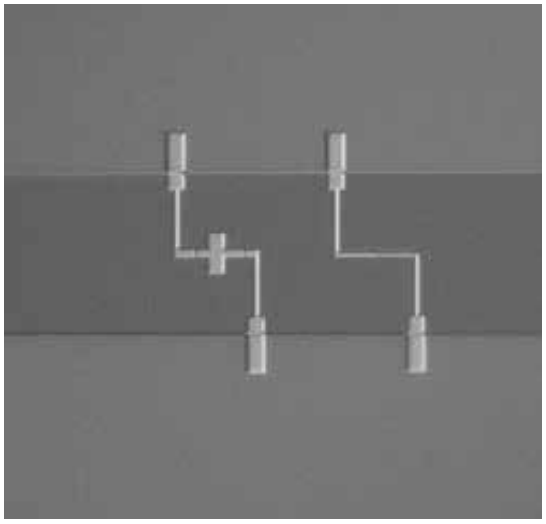

Figure 3: Optical micrograph of Al-AlOx-Al superconducting tunnel junctions and leads coupled to Nb capacitor pads.

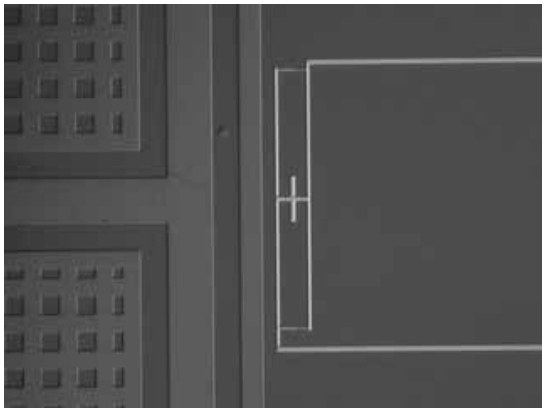

Figure 2: Optical micrograph of Al superconducting qubit loop with Nb on-chip bias lead and ground plane.

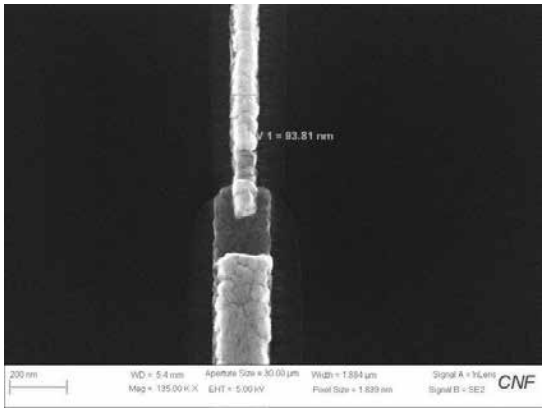

Figure 4: Scanning electron micrograph of Al-AlOx-Al tunnel junction for superconducting qubit; electron-beam lithography performed on JEOL9500.

Imaging Magnetization Structure and Dynamics in Ultrathin YIG/Pt Bilayers with High Sensitivity Using the Time-Resolved Longitudinal Spin Seebeck Effect

CNF Project Number: 2091-11

Principal Investigators: Gregory D. Fuchs[1], Daniel C. Ralph[2]

Users: Jason M. Bartell[1], Colin L. Jermain[2], Sriharsha V. Aradhya[2]

Affiliation(s): 1. School of Applied and Engineering Physics, 2. Department of Physics; Cornell University

Primary Sources of Research Funding: U.S. Air Force Office of Scientific Research, under Contract No. FA9550-14-1-0243, U.S. National Science Foundation under Grants No. DMR-1406333

Contact: gdf9@cornell.edu, dcr14@cornell.edu, jb864@cornell.edu, clj72@cornell.edu, sva24@cornell.edu

Website: http://fuchs.research.engineering.cornell.edu/

Primary CNF Tools Used: AJA Sputter Deposition, GCA 5x Stepper, Westbond wirebonder

Abstract:

We demonstrate the time-resolved longitudinal spin Seebeck (TRLSSE) effect microscope: an instrument for time-resolved magnetic imaging that is highly sensitive to the in-plane magnetization state and dynamics of thin-film bilayers of magnetic insulators and spin-orbit metals such as yttrium iron garnet ($Y_3Fe_5O_{12}$,YIG)/Pt. In this TRLSSE microscopy, we detect the local, in-plane magnetic orientation of YIG by focusing a picosecond laser that creates a thermally-driven spin current from the YIG into the via by the longitudinal spin Seebeck effect. The inverse spin Hall effect (ISHE) of Pt then to transduces this spin current to a voltage, which we monitor as our signal. We find that TRLSSE microscopy has sub-micron spatial resolution, sub-100 ps temporal resolution and a sensitivity to magnetic orientation below 0.3 deg/√Hz in ultrathin YIG.

Summary of Research:

Ultrathin bilayers of the magnetic insulator YIG that are interfaced with a heavy, non-magnetic metal such at Pt, are being studied intensely for the development of devices [1] and for understanding the physics of spin transport [2,3]. To advance in both areas, it will be useful to have a local, high-sensitivity, and high-speed probe of magnetization in the YIG layer. Techniques for this type of magnetic microscopy, however, are lacking. We address this problem by developing the TRLSSE microscope.

The principle behind the TRLSSE microscope, shown schematically in Figure 1, is the generation and detection of a thermally generated local spin current. For the case of YIG/Pt, a local thermal gradient perpendicular to the film plane is generated by laser heating of Pt. The gradient creates a thermally-induced spin current that is proportional to the local magnetization [4]. The spin current that flows into the Pt is detected with the ISHE in which spin-orbit coupling leads to a spin-dependent transverse electric field.

We demonstrate the capability of our microscope by studying 4 μm × 10 μm Yig (20 nm)/Pt (6 nm) wires. The YIG was growth by off-axis sputtering onto <110>-oriented gadollinum gallium garnet (Gd3Ga5O12, GGG), [5] followed by *ex situ* deposition of 6 nm of Pt with a 2 nm Ru capping layer. Photolithography and ion milling were used to pattern wires and contacts for wire-bonding.

First we characterize the temporal properties, temporal resolution, and sensitivity of TRLSSE microscopy. To generate the necessary thermal gradient, we focus a Ti:Sapphire 780 nm laser pulse with a fluence of 5.8 mJ/cm^2 (0.606 μm spot diameter), temporal full-with at half-maximum (FWHM) of 3 ps, and a repetition rate of 25.5 MHz onto a YIG/Pt sample. Each laser pulse heats the platinum film by ~ 50 K at peak, generating a thermal gradient with a FWHM of 100±10 ps. We also find a noise-limited sensitivity to the in-plane magnetization of 0.3 deg/√Hz [6].

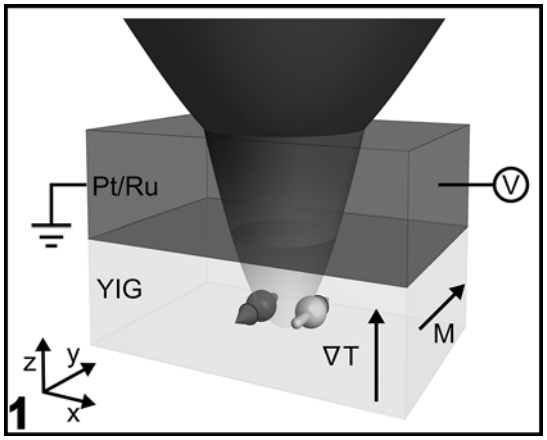

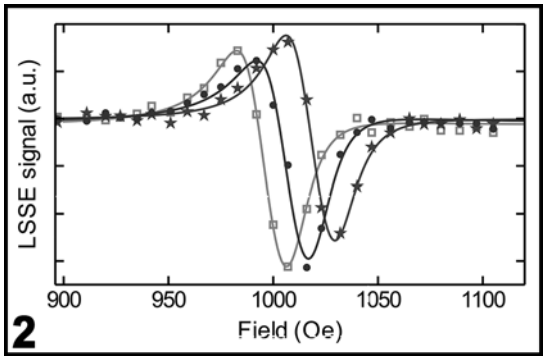

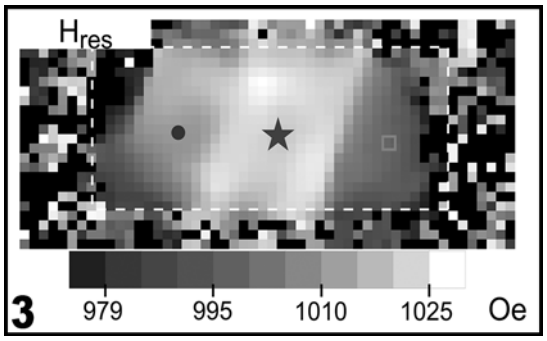

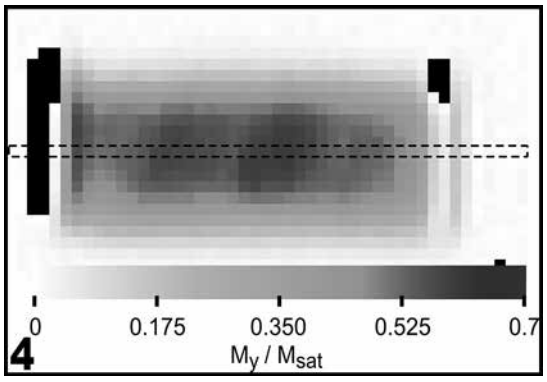

Figure 1: Schematic of our TRLSSE measurement.

Figure 2: FMR spectra at three locations on the YIG/Pt wire.

Figure 3: Spatial maps of fitted FMR resonance field for the 4 μm wide wire, the symbols mark the pixels corresponding to the FMR spectra shown in Figure 2.

Figure 4: Images of the 4 μm wide YIG/Pt wire at remnant magnetization.

The sub-100 ps spin current lifetime in our experiment is short enough that the TRLSSE is useful for stroboscopic measurements of YIG magnetization dynamics. To image ferromagnetic resonance (FMR) of YIG, we excite magnetic precession by applying a microwave current to the Pt, which drives YIG dynamics through both the associated Oersted magnetic field torque and through spin-orbit torque. We synchronize the microwave current with laser repetition rate to create a continuous phase relationship between the precessing magnetization and the sensing heat pulse. In our FMR measurements, we align the wire axis parallel to the external magnetic field as we drive the 1.2 ± 0.1 mA, 4.9 GHz current into the wire. In this configuration, the TRLSSE signal is stroboscopically sensitive to the magnetic projection, My, at a particular phase of the magnetic precession about the x-axis. We image the dynamical magnetization at a series of magnetic fields near the resonance field by scanning the laser and measuring

the TRLSSE voltage point-by-point and fitting the FMR spectra of each pixel. We show a selection of FMR spectra from individual pixels in Figure 2. Figure 3 show a spatial map of the fitted resonance field, Hres, in which we notice a variation of ~30 Oe as a function of position.

To better understand to magnetic properties of wire we also measure the static magnetization of the wire near zero-field after applying a saturating field. The image (Figure 4) shows magnetic texture that indicates non-uniform canting of the device magnetization that is qualitatively similar to the variation in the resonance field shown in Figure 3. Together, these measurements confirm the presence of locally varying magnetic anisotropy and they quantify both static and dynamic magnetic properties in each region.

References:

[1] B. Behin-Aein, D. Datta, S. Salahuddin, and S. Datta, Proposal for an all-spin logic device with built-in memory, Nat. Nanotechnol. 5, 266 (2010).

[2] K. Uchida, J. Xiao, H. Adachi, J. Ohe, S. Takahashi, J. Ieda, T. Ota, Y. Kajiwara, H. Umezawa, H. Kawai, G. E. W. Bauer, S. Maekawa, and E. Saitoh, Spin Seebeck insulator, Nat. Mater. 9, 894 (2010).

[3] G. E. W. Bauer, E. Saitoh, and B. J. van Wees, Spin caloritronics., Nat. Mater. 11, 391 (2012).

[4] M. Weiler, M. Althammer, F. D. Czeschka, H. Huebl, M. S. Wagner, M. Opel, I.-M. Imort, G. Reiss, A. Thomas, R. Gross, and S. T. B. Goennenwein, Local Charge and Spin Currents in Magnetothermal Landscapes, Phys. Rev. Lett. 108, 106602 (2012).

[5] H. L. Wang, C. H. Du, Y. Pu, R. Adur, P. C. Hammel, and F. Y. Yang, Large spin pumping from epitaxial Y3Fe5O12 thin films to Pt and W layers, Phys. Rev. B 88, 100406 (2013).

[6] J. M. Bartell, D. H. Ngai, Z. Leng, and G. D. Fuchs, Towards a table-top microscope for nanoscale magnetic imaging using picosecond thermal gradients, Nat. Commun. 6, 8460 (2015).

Imaging of Topological Spin Textures by Time-Resolved Anomalous Nernst Effect in FeGe

CNF Project Number: 2091-11

Principal Investigator: Gregory D. Fuchs

Users: Emrah Turgut, Isaiah Gray, Jason Bartell

Affiliation: Applied and Engineering Physics, Cornell University

Primary Source of Research Funding: Department of Energy

Contact: gdf9@cornell.edu, et329@cornell.edu

Primary CNF Tools Used: Heidelberg DWL 2000, GCA 5x stepper, even and odd evaporators, AJA ion mill, dicing saw

Abstract:

We study local spin dynamics in patterned FeGe, a non-collinear helimagnet, with time-resolved anomalous Nernst effect (TRANE) microscopy. We compare the local spin dynamics with the global resonances measured using flip-chip ferromagnetic resonance. We find that although the uniform mode appears at similar magnetic fields and frequencies, the low-field helical resonance in 5 μm wide patterned channel is distinct from the global helical resonance of the film. This suggests that TRANE is applicable for studying non-collinear magnets as well.

Summary of Research:

Transition metal germanides (TMGs) have a non-centrosymmetric crystal structure, which creates a non-vanishing asymmetric exchange energy in addition to the common symmetric exchange in ferromagnets. In an external magnetic field asymmetric exchange can stabilize chiral and topological spin textures, including magnetic skyrmions, merons, and helices. These spin textures are functionally a magnetic quasi-particle in which information can be stored and manipulated with a very low energy as compared to other magnetic storage modalities.

The potential application in energy-efficient storage and logic applications makes understanding the local spin dynamics in these TMGs crucial. We use TRANE microscopy to probe TMG spin dynamics with submicron spatial resolution and GHz bandwidth. The local magnetization is probed through focused laser heating, which creates a local thermal gradient that is transduced into an electrical signal proportional to the transverse in-plane magnetization component via the anomalous Nernst effect [1].

Figure 1a shows a sketch of the TRANE microscope. A 3-ps laser pulse is focused onto our 176 nm thick FeGe sample that capped with a 5 nm Al layer using a 0.4 NA objective. This generates a thermal gradient that lasts approximately 100 ps within the 1.2 μm-size spot. The thermal gradient produces an electric field, on the same time scale, that is proportional to the local magnetization My. We detect the resulting voltage using a lock-in technique. To probe magnetic resonance dynamics, we also apply an RF current to the sample to initiate precession at 4.2 GHz frequency. In addition, we collect the reflected light from the sample and show a reflectivity image of 5 μm wide FeGe channel in Figure 1a.

In Figure 1b, we show the spin configuration of the FeGe under low and high magnetic fields. When the applied field is less than the critical field Hc, a spin helix forms due to the asymmetric exchange energy. Larger fields (H>Hc) force the film into a uniform magnetization. Furthermore, helical state unwrapping occurs only below the critical temperature Tc of 273 K. Above the critical temperature, our FeGe films are paramagnetic near zero field, but can be polarized by large magnetic fields.

First, we study the local magnetic hysteresis of the FeGe film, without RF excitation. In Figure 2a, we show the magnetic hysteresis as a function of field for different temperatures. As seen in previous bulk magnetometry studies [2], the magnetization has strong variation

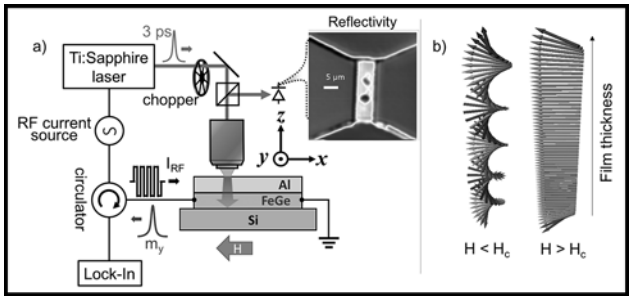

Figure 1: a) Schematic of TRANE microscopy. A 3-ps long laser pulse creates a thermal gradient that lasts ~ 100 ps. This thermal gradient generates an electrical signal that is proportional to the local magnetization. We excite ferromagnetic resonance dynamics by injecting microwave current. The reflected light from the sample is collected by a fast photodiode to visualize the device. b) Spin configuration of FeGe below and above the critical field, at which a helical state unwraps into a field polarized state.

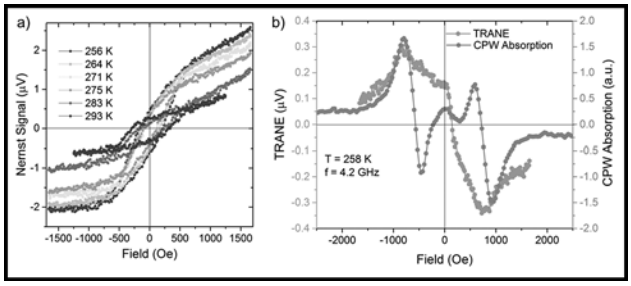

Figure 2: a) Static magnetic hysteresis of the FeGe at different temperatures. The critical temperature of the sample is 273K, determined by vibrating magnetometry measurements. We find close agreement with local hysteresis measurements using TRANE microscopy. b) The orange curve shows the resonance of the whole film measured by flip-chip FMR at 258 K and 4.2 GHz microwave frequency. The blue curve shows the local resonances at the laser spot at the same temperature and frequency.

around the Tc of 273 K. Next, we turn on the RF excitation to initiate resonant precession of spins around their equilibrium condition. In Figure 2b, we show both global resonance measurements obtained with a coplanar waveguide and the local magnetic resonance obtained with TRANE microscopy, all at 258 K and 4.2 GHz. The uniform ferromagnetic resonance at -1000 and 1000 Oe fields corresponds well in both measurements.

In conclusion, we have examined a new approach to probing the local spin dynamics in thin films of the chiral magnet FeGe. We find good agreement between the uniform spin dynamics and global magnetic resonance of the film and look forward to understanding the local, dynamic magnetic properties of thin-film chiral magnetic materials.

References:

[1] Bartell, et al, Nat. Comm. 6, 8460 [2015].

[2] Turgut, et al, PRB 95, 134416 [2017].

Properties of Isolated Defects in Hexagonal Boron Nitride

CNF Project Number: 2126-12
Principal Investigator: Gregory D. Fuchs
User: Nicholas Ryan Jungwirth

Affiliation: Applied and Engineering Physics, Cornell University
Primary Source of Research Funding: National Science Foundation
Contact: gdf9@cornell.edu, nrj32@cornell.edu
Website: http://fuchs.research.engineering.cornell.edu
Primary CNF Tools Used: Scanning electron microscope

Abstract:

We investigate the optical properties of sharp, zero-phonon emission from defect-based single photon sources in multilayer hexagonal boron nitride (h-BN) flakes. We observe sharp emission lines from optically active defects distributed across an energy range that exceeds 500 meV. Spectrally-resolved photon-correlation measurements of individual lines verify single photon emission, even though multiple emission lines are simultaneously excited. We present a detailed study of the temperature-dependent linewidth for two different zero-phonon lines (ZPLs) centered at 575 nm and 682 nm. Our results are well described by a lattice vibration model that considers piezoelectric coupling to in-plane acoustic phonons. Lastly, we perform polarization measurements of absorption and emission for 103 different ZPLs and compare our findings with a Huang-Rhys model involving two electronic states. Our survey reveals that a two-level Huang-Rhys model succeeds at describing excitations mediated by the creation of one phonon but fails in general at describing excitations that require the creation of multiple phonons.

Summary of Research:

Two-dimensional materials and associated layered solids including graphene, hexagonal boron nitride (h-BN), and transition metal dichalcogenides (TMDs) possess attractive mechanical, electrical, thermal, chemical, and optical properties. Unlike graphene and TMDs, h-BN is a wide bandgap (~6 eV) electrical insulator, making it a key component in many van der Waals heterostructures. This feature also makes h-BN an ideal host for optically active defect centers [1,2].

Isolated color centers in wide bandgap semiconductors are single photon sources with potential applications in quantum optics, precision sensing, and quantum information processing technologies. Recently, ultrabright and polarized single photon emission from isolated defects in monolayer and multilayer h-BN has been reported [3-5]. These observations add h-BN to the growing collection of wide bandgap materials (diamond, SiC, and ZnO) that host defect-based room temperature single photon sources. Whereas isolated defects in monolayer h-BN show broad spectral emission and unreliable photostability in our measurements, single defects in multilayer h-BN appear to be absolutely photostable and exhibit sharp zero-phonon lines (ZPLs) with a small Huang-Rhys factor. These properties potentially make multilayer h-BN defects attractive sources of indistinguishable single photons. At present, defect centers in both monolayer and multilayer h-BN remain poorly understood, which motivates investigation of the properties of defects within each material.

In this work [4,5] we study the temperature dependence of spectrally narrow ZPLs from point defects in multilayer h-BN. First, we characterize the distribution and intensity of sharp spectral emission in the range ~ 570-740 nm at cryogenic temperatures. This survey reveals a forest of sharp spectral features across a wide range of energy. Spectrally-resolved photon-correlation measurements enable us to unambiguously identify emission lines that correspond to single photon emission from individual defects. Figure 1 shows one such ZPL positioned at ~ 575 nm. Here three spectra are presented, which were acquired at 4.5 K, 210 K, and 360 K. Evidently the ZPL broadens and red-shifts as temperature is increased.

For two ZPLs (575 nm and 682 nm) we thoroughly investigate the temperature-dependent linewidth, line shift, excited state lifetime, and intensity. The linewidth data for these two lines in displayed in Figure 2. Despite having an energy difference of over 300 meV, both lines

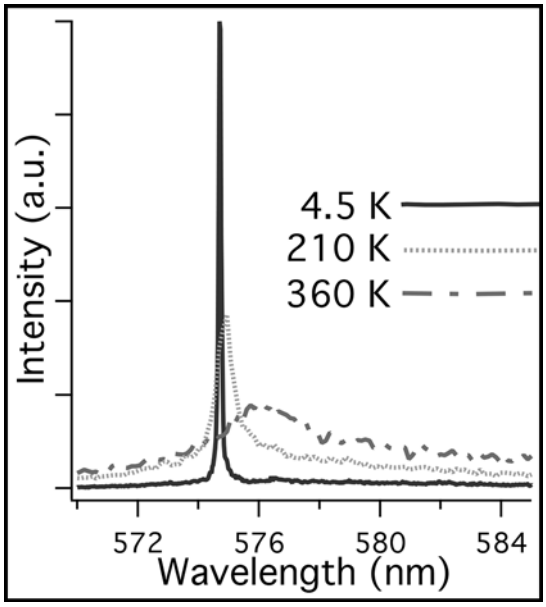

Figure 1: Emission spectrum of a narrow ZPL taken at the temperatures indicated. As temperature is increased the ZPL broadens and red-shifts.

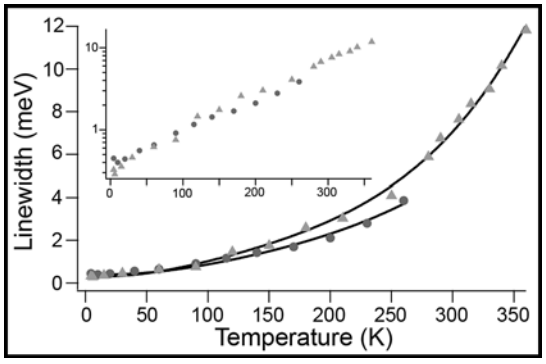

Figure 2: Temperature-dependent linewidth of two ZPLs positioned at 575 nm (triangles) and 682 nm (circles). The inset, which is the same data on a log scale, reveals that the linewidth broadens exponentially with temperature.

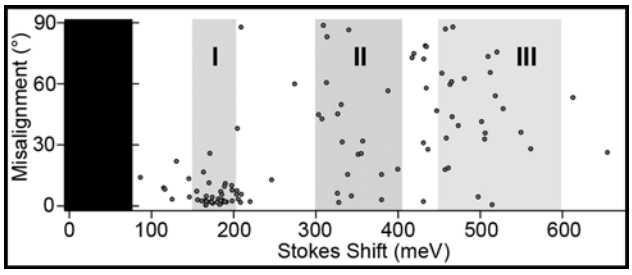

Figure 3: Scatter plot relating the misalignment angle between the absorption and emission dipole of a ZPL to its Stokes shift from the exciting light for 103 defects.

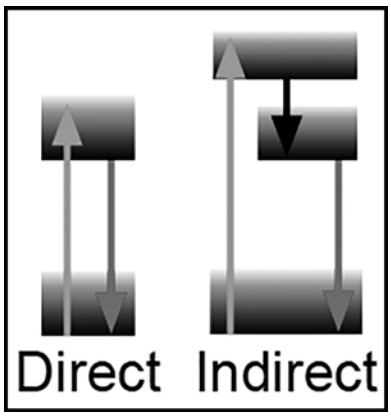

Figure 4: Two energy-level diagrams illustrating direct (left) and indirect (right) excitation mechanisms.

exhibit similar temperature-dependent broadening. In particular, the linewidth of each increases exponentially, a property that may be modeled by considering piezoelectric coupling to in-plane acoustic phonons.

We also perform polarization spectroscopy [5,6] measurements of absorption and emission on 103 ZPLs and compare our findings with the predictions of a Huang-Rhys model. The result of this polarization survey is shown in Figure 3, which compares the Stokes shift of each ZPL to the misalignment angle between its absorption and emission dipole. We find that when the Stokes shift of the ZPL from the exciting light is less than the maximum phonon energy in h-BN (Region I), the absorption and emission dipole tend to be aligned and that the polarization properties are well-explained by a Huang-Rhys model with two electronic states. Conversely, when the Stokes shift of the ZPL exceeds the maximum phonon energy, a Huang-Rhys model with two electronic states fails at explaining the observed behavior. These findings suggest that ZPL emission may be mediated by an intermediate electronic state. This possibility is shown in Figure 4, which contrasts a direct transition, where the absorption and emission dipoles are aligned, with an indirect transition, were the dipoles may be misaligned.

References:

[1] J. R. Weber, W. F. Koehl, J. B. Varley, A. Janotti, B. B. Buckley, C. G. Van de Walle, and D. D. Awschalom, Proc. Natl. Acad. Sci. 107, 8513 (2010).

[2] N. R. Jungwirth, Y. Y. Pai, H. S. Chang, E. R. MacQuarrie, K. X. Nguyen, and G. D. Fuchs, J. Appl. Phys. 116, 043509 (2014).

[3] T. T. Tran, K. Bray, M. J. Ford, M. Toth, and I. Aharonovich, Nat. Nanotechnol. 11, 37 (2015).

[4] N. R. Jungwirth, B. Calderon, Y. Ji, M. G. Spencer, M. E. Flatté, and G. D. Fuchs, Nano Lett. 16, 6052 (2016).

[5] N. R. Jungwirth and G. D. Fuchs, ArXiv Prepr. ArXiv170405536 (2017).

[6] N. R. Jungwirth, H.-S. Chang, M. Jiang, and G. D. Fuchs, ACS Nano 10, 1210 (2016).

Fabrication of Aligned Substrates and Suspended Membranes

CNF Project Numbers: 2343-15, 2344-15, 2345-15
Principal Investigators: James Hone, Jeffrey Kysar
Users: Cheng Tan, Christopher DiMarco

Affiliation: Department of Mechanical Engineering, Columbia University

Primary Source of Research Funding: MRSEC, INDEX, AFOSR-2D

Contact: jh2228@columbia.edu, jk2079@columbia.edu, cheng.tan@columbia.edu, csd2117@columbia.edu

Website: http://hone.me.columbia.edu/

Primary CNF Tools Used: Gamma automatic coat-develop tool, ASML 300C stepper, Anatech plasma etcher, Heidelberg DWL2000, Hamatech HMR

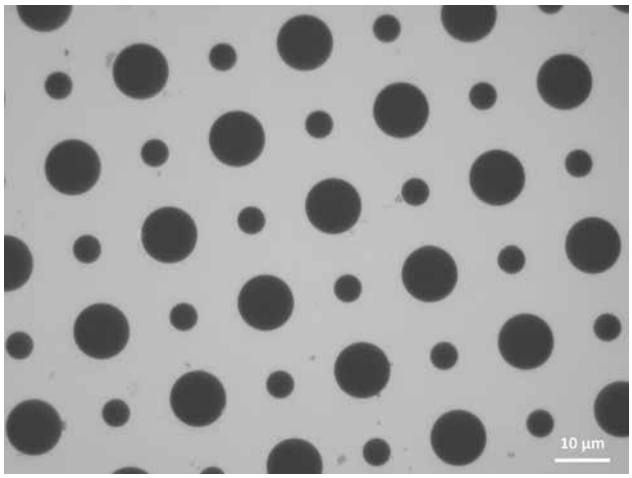

Summary of Research:

To support our efforts at Columbia University, we have ongoing projects at Cornell NanoScale Facility (CNF) to fabricate alignment marks on SiO2/Si wafers. To fabricate these wafers, the Gamma automatic coat-develop tool (Gamma) is used to coat the wafers with photoresist, as well as to develop the photoresist post-exposure. To pattern the wafers, ASML 300C Deep Ultra Violet Stepper was used to expose the photoresist. Post development, the wafers were descummed using the Anatech plasma etcher. The alignment metals were then evaporated using Nanobiotechnology Center's (NBTC) batch evaporation system. Post evaporation, the wafers underwent lift off followed by a resist strip in both the bath and the Anatech plasma etcher.

The purpose of these alignment marks is to facilitate the electron beam lithography processes here at Columbia, where we prepare and transfer samples to the prepared wafers, and align them using the marks. By using the wafer scale processing at CNF, we are able to produce large numbers of wafers in a relatively short amount of time, speeding up our processes as a whole.

We also use CNF for the fabrication of a large number of square silicon/silicon nitride grids with a hole-patterned suspended silicon nitride membrane. The goal was to fabricate six different membrane types, each with a different set of alternating through-hole diameters: (1) 100 and 50 µm, (2) 50 and 25 µm, (3) 25 and 10 µm, (4) 10 and 5 µm, (5) 5 and 2 µm, and (6) 2 and 1 µm (see Figure 1).

Each membrane window was designed to be 500 µm and the grid itself to be 3 mm on the diagonal. The Heidelberg DWL2000 mask writer was used to write the patterns on each mask. After the masks were written, the photoresist was developed and the underlying chrome etched using the Hamatech HMR 900 chemical processes tool. The photoresist was removed and the masks were cleaned using the hot strip bath setup. A 220 nm thick low-stress nitride layer was grown on bare four-inch diameter silicon wafers using the LPCVD furnace after the wafers were MOS cleaned.

In CNF's photolithography area, the top-side was spun coated and cured with a layer photoresist and then the SÜSS MA6-BA6 contact aligner was used to expose the wafer with the top-side mask (i.e., the membrane holes). The photoresist was developed effectively using a Hamatech HMR 900 chemical processes tool. The Oxford Plasma 81 was used to etch the exposed nitride until the underlying silicon was revealed.

Once the holes were confidently etched through the nitride with verification of the P-10 profilometer, the photoresist mask was removed and the wafer was cleaned again using the hot strip bath. This process was then repeated for the back-side of the wafer with the bottom-side mask (i.e. the membrane window and the grid break-lines).

Once the patterning was completed, the patterned nitride was used as a mask to etch the silicon in order to suspend the nitride membranes and break-lines. This was accomplished using CNF's heated KOH etch setup and the chemical resistant wafer holder, used to protect the membranes during the process.

These membrane substrates will be used in nanoindentation tests for suspended graphene and graphene-based composites. The batch processing of the substrates allows us to expedite our experimental research here at Columbia.

Development of Scanning Graphene Hall Probes for Magnetic Microscopy

CNF Project Number: 2361-15
Principal Investigator: Katja C. Nowack
User: Brian T. Schaefer

Affiliation: Laboratory of Atomic and Solid-State Physics, Department of Physics, Cornell University

Primary Sources of Research Funding: Cornell Center for Materials Research with funding from the NSF MRSEC program (DMR-1120296), President's Council of Cornell Women Affinito-Stewart Grant, National Science Foundation Graduate Research Fellowship under Grant No. DGE-1650441

Contact: kcn34@cornell.edu, bts72@cornell.edu

Website: http://nowack.lassp.cornell.edu/

Primary CNF Tools Used: Veeco Icon AFM, Zeiss Supra SEM/Nabity, odd-hour evaporator, Oxford 82 etcher

Abstract:

We discuss our progress on developing scanning Hall probes fabricated from graphene encapsulated in hexagonal boron nitride, with the goal to image magnetic fields with submicron resolution. Our devices demonstrate high carrier mobility at low carrier densities, enabling low-noise measurements in the regime in which the device is most sensitive to small changes in magnetic field. We present transport measurements demonstrating the high quality of these devices, with a carrier mobility exceeding 100,000 $cm^2/V{\cdot}s$ and mean free path exceeding 1 μm at 4 Kelvin. We outline our plans for adapting these devices for scanning, including characterization of the point spread function with a scanned current loop and fabrication of a deep-etched structure that enables positioning the sensitive area within 100 nm of the sample surface.

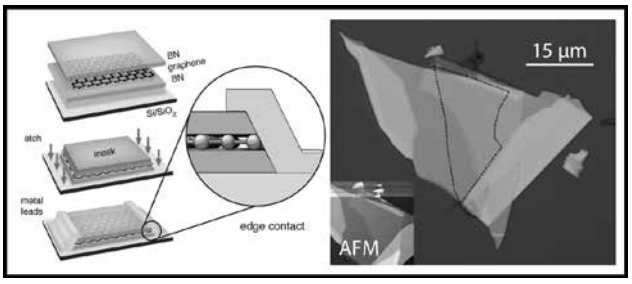

Figure 1: (left) Overview of process from [3], used with permission. (right) A graphene flake (dotted outline) sandwiched between flakes of hexagonal boron nitride (inset: AFM image, scaled down).

Summary of Research:

Magnetic imaging provides a direct spatial map of the magnetic landscape above the surface of a material, arising from local magnetic features or the distribution of electronic currents through a device. Currently, the superconducting quantum interference device (SQUID) is the most sensitive magnetic probe, but only at low temperatures and sub-tesla magnetic fields [1]. Moreover, lithographical challenges limit the spatial resolution of SQUID microscopy to about a micron [2]. Hall probes permit measurements in a strong magnetic field, over a much larger temperature range, and with potentially higher spatial resolution than SQUIDs [2]. To compete with the field sensitivity of a SQUID and to enable in-house fabrication, we choose to fabricate Hall probes from graphene encapsulated in hexagonal boron nitride (hBN) with one-dimensional edge contacts (Figure 1). Devices made with this architecture demonstrate low contact resistance and high mobility at low carrier densities [3].

Our process closely follows the steps described in [3]. We exfoliate graphene and hBN flakes onto SiO2 (285 nm)/Si p++ and select uniform flakes using optical and atomic-force microscopy (AFM). Using the van der Waals assembly technique [4], we use a polymer stamp to sequentially pick up and stack a hBN/graphene/hBN heterostructure (Figure 1). We use electron-beam lithography and reactive-ion etching to pattern the flakes into a Hall bar, and then in a second electron-beam lithography step, we pattern, deposit, and lift off 5 nm Cr/70 nm Au contacts. A second etch directly before the metal deposition exposes a clean graphene edge untouched by resist, decreasing the contact resistance [5]. This step is the primary difference between the process here and the process in [3], and is necessary for matching the quality of the devices described therein.

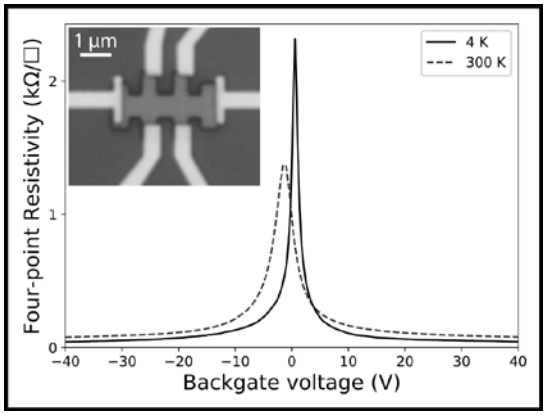

Figure 2: Four-terminal resistivity versus backgate voltage. Inset: optical image of the device.

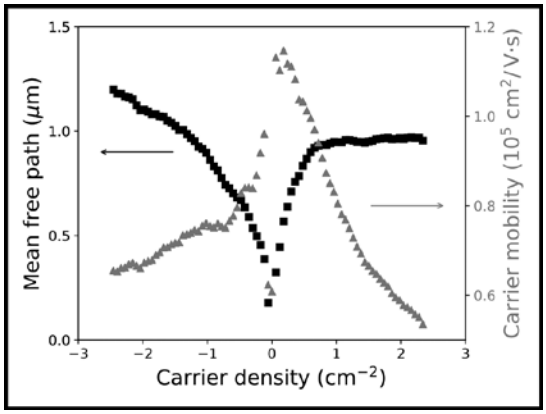

Figure 3: Mean free path (black squares) and carrier mobility (gray triangles) for the device in Figure 2.

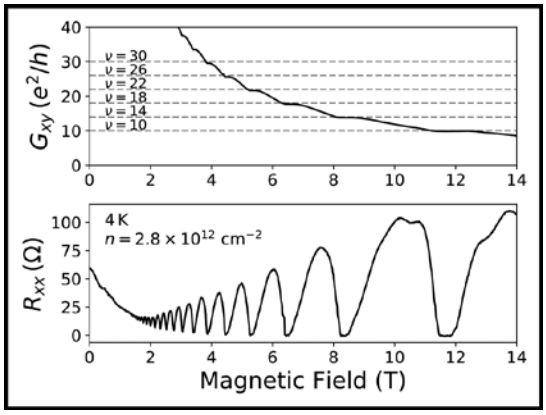

Figure 4: Transverse (Hall) conductance (upper panel) and longitudinal resistance (lower panel) versus magnetic field. Dashed lines mark the expected quantized conductance plateaus for monolayer graphene.

In Figures 2-4, we summarize electrical transport measurements demonstrating the high quality of these devices. Figure 2 shows four-terminal resistivity versus silicon backgate voltage, with a sharp peak at the charge neutrality point, indicating homogeneity of carrier density throughout the device [6]. From the resistivity, we calculate the total resistance of the device channel and subtract it from the two-terminal resistance over the whole device, yielding an edge contact resistance of ~ 400 Ω·μm at high carrier density, neglecting the small resistance of the metal leads. This is comparable to the contact resistance achieved in [3].

The usual metrics for overall device quality are the carrier mobility and mean free path, which we extract from the Drude resistivity and carrier density (Figure 3). At 4 Kelvin, the carrier mobility exceeds 100,000 cm2/V·s and the mean free path exceeds 1 μm. The devices described in this report match or outperform graphene devices with alternative geometries, including suspended graphene [7] and graphene on hBN [6], but do not yet match the best fully encapsulated, edge-contacted devices [3]. Further improvements will focus on eliminating bubbles, wrinkles, and tears introduced when stacking the graphene and hBN flakes, which introduce disorder into the system and decrease the mobility and mean free path.

A last indicator for high device quality is the quantum Hall effect: the appearance of plateaus in the transverse (Hall) resistivity at high magnetic field, quantized to certain integer multiples of the conductance quantum (Figure 4). These features further demonstrate that the density of electronic states is uniform over the two-dimensional electronic system.

Our next goal is to characterize the response of the device to a small, locally-applied magnetic field, an experiment which will guide our eventual development of scanning Hall probes. Initial tests show that the devices are sensitive not only to local changes in magnetic field, but also to local changes in the electrostatic environment. We use a small current loop to apply a local magnetic field, but the metallic loop acts as a local gate and introduces nonuniformity in the current density that masks any response from the magnetic field. We therefore plan to add a top gate or uniform metal layer on top of the device to electrostatically shield the device, thereby reducing local gating effects. Lastly, we plan to add a deep etch around the device to ensure that the sensitive area of the device can scan as close as possible to the sample surface.

References:

[1] M. E. Huber et al., Rev. Sci. Inst. 79, 053704 (2008).

[2] J. R. Kirtley et al., Rep. Prog. Phys. 73, 126501 (2010).

[3] L. Wang et al., Science 342, 614 (2013).

[4] P. J. Zomer et al., Appl. Phys. Lett. 105, 013101 (2014).

[5] M. Ben Shalom et al., Nat. Phys. 12, 318 (2016).

[6] C. R. Dean et al., Nat. Nanotechnol. 5, 722 (2010).

[7] K. I. Bolotin et al., Phys. Rev. Lett. 101, 096802 (2008).

Tailoring the Spin-Orbit Torques in PtPd/FeCoB Bilayers by Composition

CNF Project Number: 2444-16

Principal Investigator: Robert A. Buhrman

User: Lijun Zhu

Affiliation: School of Applied and Engineering Physics, Cornell University

Primary Source of Research Funding: Samsung Electronics Corporation

Contact: rab8@cornell.edu, lz442@cornell.edu

Primary CNF Tools Used: GCA 5X stepper, AJA sputtering system, Bruker EDS

Abstract:

Current-induced spin-orbit torques (SOTs) in heavy metal/ferromagnet bilayers have attracted considerable attention due to the great application potential in magnetization manipulation [1-3]. Here we report our recent progress on the controllable spin orbit torques in Pt_xPd_{1-x}/FeCoB bilayer samples fabricated at the Cornell NanoScale Science &Technology Facility.

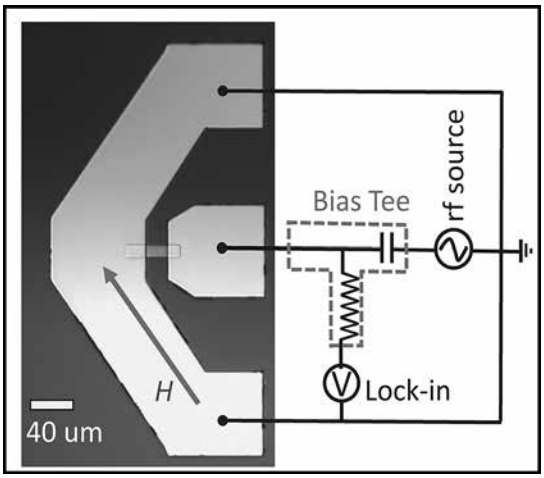

Figure 1: Spin torque ferromagnetic resonance devices.

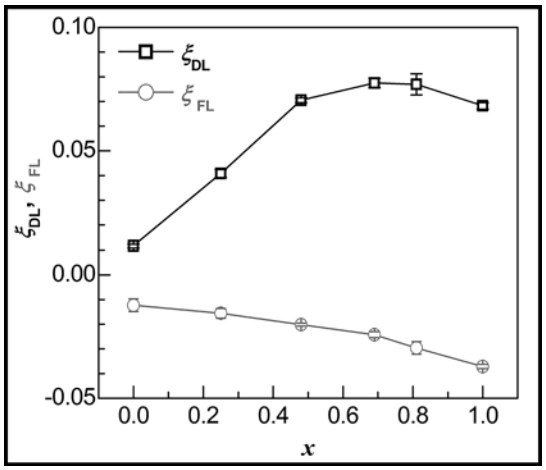

Figure 2: Dampinglike and fieldlike spin orbit torques of Pt_xPd_{1-x}/FeCoB bilayers plotted as a function of Pt concentration x.

Summary of Research:

We fabricated the spin torque ferromagnetic resonance devices schematically shown in Figure 1. Firstly, the magnetic stacks of Ta 1/ Pt_xPd_{1-x} 4/ $Fe_{0.6}Co_{0.2}B_{0.2}$ 1.5-5/ MgO 2/Ta 1.5 (numbers are thicknesses in nm) were sputtered on 4-inch oxidized Si <100> substrate with DC and RF magnetron sputtering. Secondly, the samples were patterned into 10 μm stripes with ion milling etching after ultraviolet photolithography using the GCA 5X stepper. Finally, the electrical contacts were made sequentially by photolithography, deposition of 5 nm Ti/150 nm Pt by AJA sputtering system, and liftoff in acetone. The chemical composition of Pt_xPd_{1-x} alloys was determined to be x = 0, 0.25, 0.49, 0.69, 0.81, and 1 by the Bruker EDS.

After fabrication, the devices were measured at room temperature by spin torque ferromagnetic resonance at different microwave frequencies with magnetic field swept between ± 3500 Oe along the direction that is 45° with respect to the magnetic strips. Figure 2 summarizes the determined fieldlike (ξ_{FL}) and dampinglike (ξ_{DL}) spin orbit torques as a function of the Pt concentration x, from which a strong effect of SOC strength can be found. ξ_{FL} is negative in the whole composition range, while its magnitude decreases monotonically from 0.037 to 0.012 with x decreasing from 1 to 0. The suppression of a negative fieldlike torque of a spin Hall source material is highly desirable for the fast and reliable switching of three-terminal

SOT-MRAMs via a reduction of the incubation delay and micromagnetic processes. More intriguingly, the ξ_{DL} increases from 0.012 to 0.078 as *x* increases from 0 to 0.69 and drops slightly to 0.068 as *x* increases to 1. Further detailed studies show that the peak behavior of ξ_{DL} in the intermediate composition is a consequence of competition of the spin Hall conductivity, resistivity, and interfacial spin memory loss.

From the viewpoint of the SOT-MRAM applications, the enhanced dampinglike spin torque ($\xi_{DL} \sim 7.8\%$) and the reduced fieldlike torque ($\xi_{FL} \sim -0.024$) makes the $Pt_{0.69}Pd_{0.31}$ alloy a more efficient and more reliable spin Hall material than Pt ($\xi_{DL} \sim 0.069$, $\xi_{FL} \sim -0.037$). $Pt_{0.69}Pd_{0.31}$ alloy is also more efficient than Pt in electrically detecting spin currents via inverse spin Hall effect and in generating spin current for manipulation of magnetization, magnetic domain wall, and skyrmions. The ability to continuously tune the fieldlike torque of Pt_xPd_0 alloys simply by controlling the composition while without significantly changing the structural and magnetic properties of the spin Hall material and adjacent ferromagnetic layer is interesting as it allows for controllable experimental study of the roles of fieldlike torque in various spinorbitronic phenomena, e.g. interplay of the fieldlike torque and micromagnetic processes of SOT-MRAMs in the nanosecond scale.

References:

[1] L. Liu, C.-F. Pai, Y. Li, H. W. Tseng, D. C. Ralph, and R. A. Buhrman, Science 336, 555 (2012).

[2] W. Jiang, P. Upadhyaya, W. Zhang, G. Yu, M. B. Jungfleisch, F. Y. Fradin, J. E. Pearson, Y. Tserkovnyak, K. L. Wang, O. Heinonen, S. G. E. Velthuis, A. Hoffmann, Science 349, 283-286 (2015).

[3] P. P. J. Haazen, E. Muré, J. H. Franken, R. Lavrijsen, H. J. M. Swagten, and B. Koopmans, Nat. Mater. 12, 299 (2013).

Heusler B_2-Co_2MnSi-Based Magnetic Tunneling Junctions on Silicon

CNF Project Number: 2444-16, 111-80

Principal Investigator: Robert A. Buhrman

Users: Lijun Zhu, Ryan C. Tapping

Affiliation: School of Applied and Engineering Physics, Cornell University

Primary Source of Research Funding: Samsung Electronics Corporation

Contact: rab8@cornell.edu, lz442@cornell.edu, rct76@cornell.edu

Primary CNF Tools Used: ASML stepper, Heidelberg masker writer DWL-2000, even-hour electron-beam evaporator, AJA sputtering system, Bruker EDS, Veeco Icon AFM, Zeiss Supra/Ultra SEMs

Abstract:

The Heusler alloy Co_2MnSi (CMS) with a $B2$- or $L2_1$-order has attracted a great deal of attention in the field of spintronics due to the half metallicity of the fully ordered structure [1,2]. The fabrication of $B2$- or $L2_1$-ordered CMS on silicon has so far remained challenging, which is a critical obstacle for its potential magnetic random access memory application that requires the devices being compatible with current CMOS techniques. Here we report our latest successes on the sputtering growth of <001>-orientated $B2$-CMS films on oxidized silicon wafers as well as their application in magnetic tunneling junction devices fabricated at the Cornell NanoScale Science &Technology Facility.

Summary of Research:

We successfully fabricated the magnetic tunneling junction devices schematically shown in Figure 1(a). Magnetic stacks of MgO 7/Cr 40/ CMS 3/MgO 2/CoFe 5/IrMn 12/Ru 5 (numbers are thicknesses in nm) were firstly sputtered on 4-inch oxidized Si <100> wafers with DC and RF magnetron sputtering. Here we use the 3 nm CMS layer as the free layer (FL) and use the CoFe layer pinned by IrMn as reference layer (RL). Secondly, we defined the pillars with ion milling etching after deep ultraviolet (DUV) photolithography using the ASML stepper and a mask written by Heidelberg masker writer DWL-2000. Thirdly, an insulating layer of 100 nm SiO_2 was deposited by even hour electron-beam evaporator, followed by lift-off in PG remover. Finally, the electrical contacts were made sequentially by DUV photolithography, deposition of 50 nm Ti/200 nm Pt by AJA sputtering system, and liftoff in PG remover. In addition, Veeco Icon atomic force microscopy and Zeiss Supra/Ultra Scanning electron microscopy (SEM) were heavily used for observing the devices during fabrication. The Bruker EDS was used to determine the composition of the samples.

After fabrication, the devices were measured as a function of external magnetic field along the pillar long axis (y direction) at room temperature by lock-in amplifier. As an example, we show the magnetization switching behaviors for a series of magnetic tunneling devices with roughly the same short axis of ~ 300 nm, but different aspect ratios. As examples, we show in Figure 1(b) the scanning electron images for two of the pillars, the aspect ratios of which are 1.9:1 and 2.5:1, respectively. From Figure 2, one can see that all the devices show tunneling magnetoresistance (TMR) of ~10% and good pinning of the CoFe reference layer along negative y direction. The coercivity (H_c) of Co_2MnSi free layers was successfully tuned by controlling the shape anisotropy via their aspect ratios, i.e., H_c is 142, 245, 286, to 325 Oe for the aspect ratio of 1.9:1, 2.6:1, 3.1:1, and 4.5:1, respectively. Further efforts are needed in the future in order for improved sample quality and enhanced TMR.

References:

[1] M. Jourdan J. Minár, J. Braun, A. Kronenberg, S. Chadov, B. Balke, A. Gloskovskii, M. Kolbe, H.J. Elmers, G. Schönhense, H. Ebert, C. Felser, and M. Kläui, Nat. Commun. 5, 3974 (2014).

[2] Y. Sakuraba, M. Ueda, Y. Miura, K. Sato, S. Bosu, K. Saito, M. Shirai, T. J. Konno, and K. Takanashi, Appl. Phys. Lett. 101, 252408 (2012).

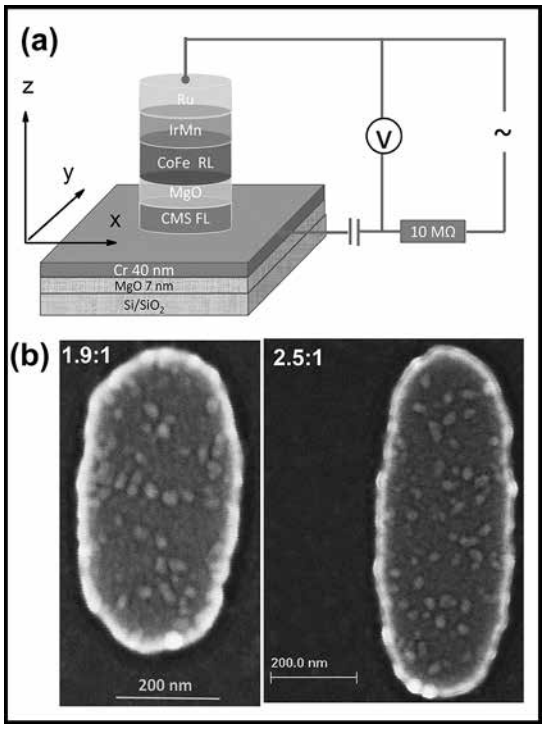

Figure 1: (a) schematic of the magnetic tunneling junction device; (b) Scanning electron microscopy images for elliptical magnetic pillars with aspect ratio of 1.9:1 and 2.5:1.

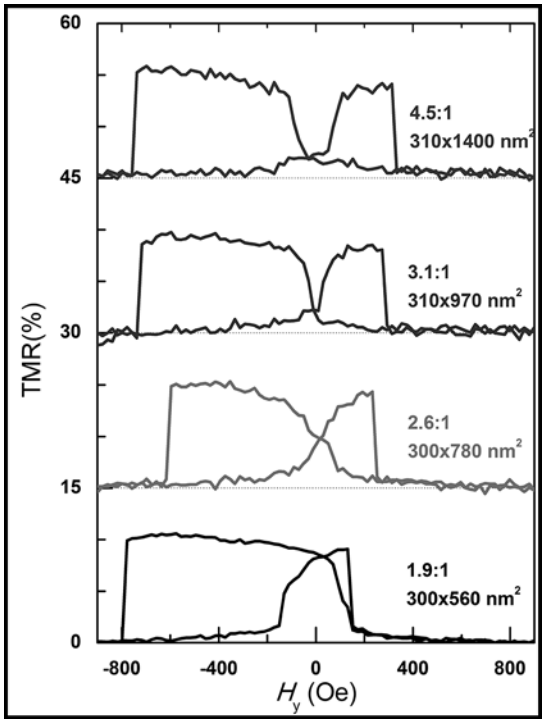

Figure 2: Magnetic field switching behaviors for the Co2MnSi magnetic tunneling junctions with pillar aspect ratios of 1.9:1, 2.6:1, 3.1:1, and 4.5:1, respectively.

Two-Dimensional Devices to Probe Emergent Properties of Ionic Liquid Interfaces

CNF Project Number: 2476-16

Principal Investigator: Paul McEuen

Users: Menyoung Lee, Jun Wei Lam

Affiliations: Department of Physics, Laboratory of Atomic and Solid State Physics, Kavli Institute for Nanoscale Science; Cornell University

Primary Source of Research Funding: Air Force Office of Scientific Research (MURI FA 9550-16-1-0031)

Contact: PLM23@cornell.edu, ML2475@cornell.edu, JL2576@cornell.edu

Primary CNF Tools Used: SÜSS MJB4, SC4500 odd-hour and even-hour evaporators, Heidelberg DWL2000, Glen 1000, YES Asher, Zeiss Supra and Ultra SEMs, Nabity PG system, Class 1 and Class 2 spinners

Abstract:

We take advantage of graphene's excellent sensitivity to local electrical environment to probe the electric double layers of room temperature ionic liquids, which are expected to exhibit novel emergent behaviors driven by strong mutual interactions between its constituent ions. We fabricate graphene-ionic liquid electric double layer transistors and demonstrate their ability to monitor the charge state of the interface, which is responsive to the applied electrode potential. We can monitor the device noise caused by fluctuations as well as the time-domain dynamics of double layer charging and discharging, and are studying these properties in detail to elucidate the mechanisms and processes.

Summary of Research:

Graphene and many other two-dimensional (2D) materials can be prepared in single-layer form, or close to it. Such an atomically thin sheet is entirely its own surface without a three-dimensional (3D) bulk interior. The ultimate thinness and all-surface nature of 2D materials imply that their physical (electrical, optical, and mechanical) properties are susceptible to influence from their interaction with directly adjacent environment. This sensitivity presents challenges for device engineering, but ultimately promises devices which, if they can be prepared well enough, can function as great sensors for information about the local physical environment to reveal nanoscale effects previously not accessible to experiment.

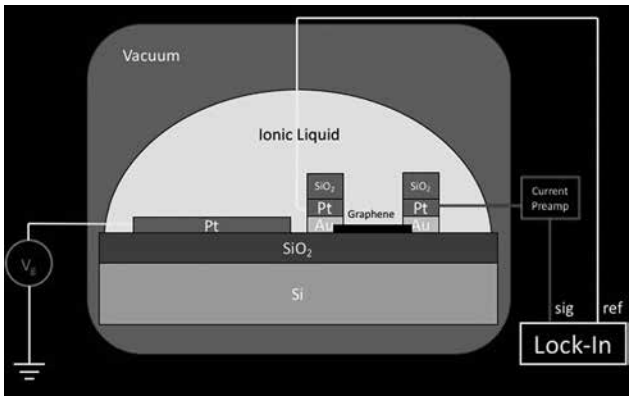

Figure 1: Cartoon cross section of a graphene-ionic liquid electric double layer transistor (EDLT) and the electrical characterization schematic.

Graphene sensors have many promising applications, including chemical detection and electrophysiology; our objective is to use its sensing functionality to reveal the physical properties of the electric double layer (EDL) of room temperature ionic liquids. The EDL is the interface region on the surface of solid electrodes immersed in an electrolyte, and ionic liquids are electrolytes that lack any solvent, i.e. are composed entirely of charged ions that are mobile and conduct electricity. Unlike electrons in metals or electrolyte salts in dilute solution, the ions of an ionic liquid reside in a crowded and strongly correlated environment, so the structure and dynamics of the arrangement of these ions may be expected to exhibit novel, collective behaviors driven by the mutual interactions, where both steric constraints and electrostatic forces are relevant. Examples of emergent phenomena expected to occur in ionic liquid interfaces include abrupt symmetry breaking phase transitions and metastable charge density wave configurations.

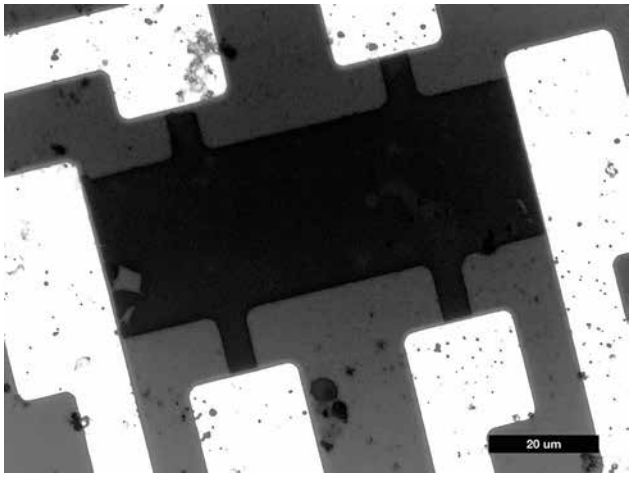

Figure 2: Optical micrograph of a Hall bar-shaped graphene device, rinsed and dried after the being immersed and characterized in ionic liquid.

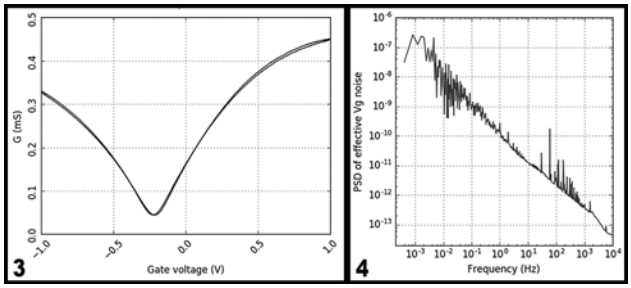

Figure 3, left: Typical EDLT transfer curve of graphene conductance (G) as a function of counter electrode gate voltage applied to ionic liquid 1-butyl-3-methylimidazolium hexafluorophosphate. Figure 4, right: Power spectral density (PSD) of the graphene conductance fluctuations in time (converted into equivalent fluctuations of electrolyte gate voltage V_g) that exhibits 1/f noise spectrum.

The electric double layer transistor (EDLT) is constructed by attaching source and drain electrodes onto the graphene and immersing the device in electrolyte. The electric potential of the electrolyte, and hence the potential drop across the EDL, is set by the voltage of the counter electrode, which may be considered the gate electrode of the EDLT. Figure 1 shows a cross-sectional schematic of the device structure and a typical electrical characterization experiment. All fabrication steps after graphene synthesis by chemical vapor deposition and before immersion into electrolyte are carried out in Cornell NanoScale Science & Technology Facility. Figure 2 shows an optical micrograph of a simple Hall bar-shaped graphene device with six ohmic contacts fabricated on an oxidized silicon substrate, rinsed and dried after characterization in ionic liquid.

The EDL and the 2D electrode are in intimate contact and interact electrostatically, acting as two plates of a capacitor. Normally the EDL capacitance is measured by its impedance, but we can in addition use the charge sensing function of graphene. When the device is held at a cathodic potential relative to the electrolyte, i.e. the counter/gate electrode is at positive voltage relative to the device, then cations accumulate in the EDL. Correspondingly the graphene sheet experiences electron doping, which is detected by the change of its conductivity. Conversely, hole doping is detected when the device is at an anodic potential.

Figure 3 shows a typical transfer curve of the graphene-ionic liquid EDLT, showing the conductivity minimum when the graphene is in its charge neutral state (the Dirac point of the band structure). It is expected that some emergent function of the EDL, such as a surface phase transition or a density wave formation, if it changes the net interface charge density, would be directly detectable as a sharp change in the conductance of the device. At this point in the development of the experiment, we can fabricate and characterize EDLT devices, including the EDL charging and discharging characteristics in the time domain, and are searching for sharp electrical signatures of emergent behaviors, which are predicted by theory and hinted at by probes of surface structure, such as x-ray reflectivity.

We can also monitor the fluctuations of the graphene EDLT conductance in time while the electrolyte potential is fixed. The dependence of EDLT output noise power on operating frequency exhibits the familiar 1/f-like spectrum (Figure 4), similar to the noise encountered in many solid state devices. We are carrying out further experiments to understand the relationship between the physical properties of the EDL and the EDLT noise, as it may be mediated by fluctuations in the electrolyte, which may require new descriptions distinct from the case of solid dielectrics.

Improving Dopant Activation in III-V Materials using LSA

CNF Project Number: 150-82
Principal Investigators: Michael Thompson, Paulette Clancy
Users: Hsien-Lien Huang, Emily R. Cheng, Victoria C. Sorg

Affiliations: Materials Science and Engineering, Chemical and Bimolecular Engineering; Cornell University

Primary Sources of Research Funding: Semiconductor Research Corporation (SRC), National Science Foundation (NSF)

Contact: mot1@cornell.edu, pc@icse.cornell.edu, vcs26@cornell.edu, hh596@cornell.edu, erc77@cornell.edu

Primary CNF Tools Used: Oxford PECVD, manual resist spinners, ABM contact aligner, SÜSS MA6-BA6 contact aligner, CHA evaporator

Abstract:

The high temperatures and short annealing times (sub-millisecond to millisecond) of laser spike annealing (LSA) have the potential to increase activation of ion-implanted compound semiconductors to levels necessary for use in future generations of CMOS technology as well as power electronics. These conditions enable access to both metastable activation levels after ion implantation, and extended process temperatures without deactivation from *in situ* doped metastable films. Single stripe LSA scans were conducted to probe thermal damage behavior and electrical characteristics as a function of peak annealing temperature and heating dwell. Temperatures under LSA were measured directly using the known decomposition behavior of a polymer and gold melt. These measurements thermal damage limits are crucial to establish conditions for future studies of dopant activation by LSA.

Summary of Research:

As silicon transistor technology is pushing material limits, major scaling challenges remain. Ultimately, a shift towards a new device architectures and geometries are needed, but a possible short-term solution to continue scaling is to replace silicon with materials that are better suited for a particular device. Compound semiconductors are strong candidates, e.g. $In_{0.53}Ga_{0.47}As$ (InGaAs) for low power, n-type materials for transistor channels and source/drain contacts and GaN for power electronics for high temperature and voltage applications. However, challenges arise when attempting to maximize dopant activation during thermal processing due to thermal budget limitations.

In this project, sub-millisecond and millisecond (sub-ms to ms) LSA was investigated as a method to improve the activation of ion-implanted dopants and to limit deactivation of grown-in dopants in InGaAs and GaN. LSA uses a continuous-wave, line focused laser scanned over a sample to rapidly heat and quench samples (rates of 10^6 K/s and 10^5 K/s, respectively). Using spatially resolved measurements perpendicular to the single laser annealing scan, a continuous range of annealing temperatures can be tested from room temperature to the highest annealing temperature reached [1]. Two types of samples were used to study the laser annealing damage threshold and dopant behavior with LSA; ion-implanted and molecular beam epitaxy (MBE) grown samples (either unintentionally doped and intentionally doped).

The thermal processing limits and peak laser annealing temperature calibration was determined for gallium nitride (GaN) using the known thermal decomposition behavior of a polymer and melting behavior of gold dots. The polymer decomposition served as a rough estimate for peak annealing temperatures, which were then further explored by using the melting of gold dots. The GaN samples were annealed using a 10.6 μm wavelength CO2 laser.

A block copolymer (poly(styrene-*block*-methyl methacrylate), 70 wt.% polystyrene), with complete thermal decomposition of 850°C, was spun to a thickness of 60 nm on GaN samples (GaN-on-GaN or GaN-on-sapphire) and laser annealed at power conditions ranging from 32-56 W, all with 1 ms dwells. The peak temperature GaN reached before thermally induced damage was established to be in the 1400-1600°C range for GaN-on-sapphire.

After obtaining approximate peak annealing temperatures from the polymer decomposition experiment, more specific temperature calibrations were achieved

using the gold dot method. Gold dots with diameters on the order of 2-5 μm were fabricated using photolithography using a standard liftoff procedure. A 50 nm SiN_x layer was deposited on the GaN substrates using Oxford plasma enhanced chemical vapor deposition (PECVD) (to limit N evaporation at high annealing temperatures). The dots were photolithographically patterned and metal was deposited using thermally evaporated chrome (10 nm for adhesion) and gold (25 nm). The samples with gold dots were laser annealed at conditions ranging from 10-30 W with a 1 ms dwell. An example annealed stripe is shown in Figure 1. Results from the gold dot experiment show the samples reaching temperatures above the gold melt threshold (1064°C).

To gain a better understanding of the laser annealing damage behavior of GaN on sapphire substrates, a sapphire sample was laser annealed. The sapphire (Al_2O_3) substrate was prepared by removing silicon thin film layer from a silicon-on-sapphire sample by etching with a 50% KOH solution for three minutes at 80°C. A CO_2 laser was scanned with a 1 ms dwell, at 22.5 W. The resulting laser annealing damage has a crosshatch texture shown in Figure 2. The crystalline slip damage along the annealing direction is most likely the result of the combination of poor thermal conductivity compared to other candidates (Si:150, GaN:130, InP:68, Al_2O_3:23.1 W/m-K), and high light absorbance of sapphire with thermally-induced strain that causes damage before reaching the melting point of sapphire at 2050°C.

The dopant activation behavior of laser annealed, ion-implanted, thin InGaAs film on an InP substrate was explored for ultra-shallow junction applications. A 20 nm InGaAs thin film was ion-implanted with silicon and capped with 3 nm Al_2O_3 layer to prevent arsenic evaporation at high temperatures. The sample was annealed with a 980 nm diode laser with a 5 ms dwell at 75 Amps. Based on the decomposition behavior of the polymer, the sample reached a peak temperature of 1060°C before it cracked (Figure 3), likely due to InP melting point based on previous annealing results.

Overall, the damage threshold and peak temperatures reached during laser annealing of compound semiconductors was explored. These studies set the basis for future annealing studies and characterization of how electrical properties are affected by annealing time and temperature.

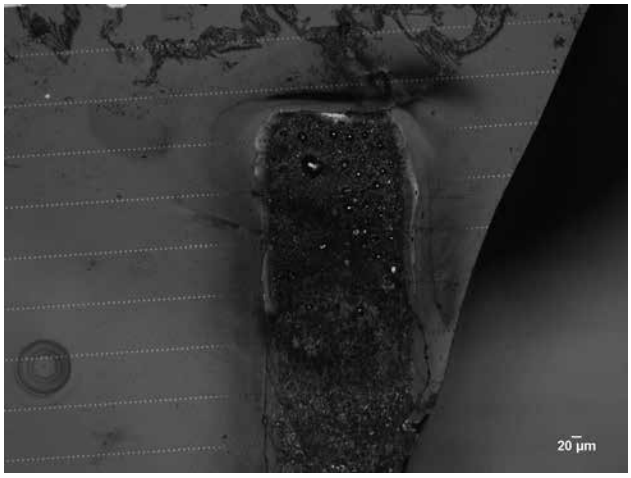

Figure 1: Bright field micrograph of GaN on sapphire sample with gold dots annealed with a single laser scan.

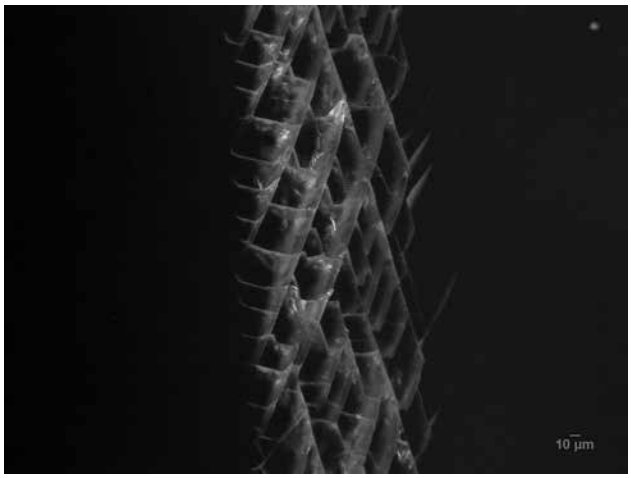

Figure 2: Dark field micrograph of laser annealed sapphire.

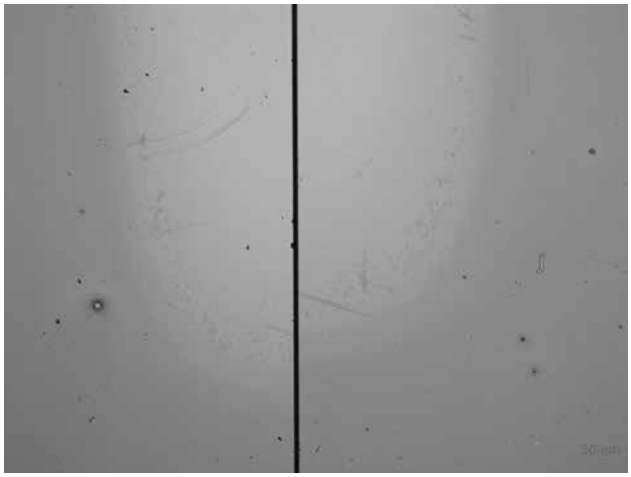

Figure 3: Bright field micrograph of LSA InGaAs on InP.

References:

[1] R.T. Bell, A.G. Jacobs, V.C. Sorg, B. Jung, M.O. Hill, B.E. Treml, and M.O. Thompson, ACS Comb. Sci. 18, 548 (2016).

Vector Electric field Measurements Using Position-Modulated Kelvin Probe Force Microscopy

CNF Project Number: 863-00

Principal Investigator: Prof. John Marohn

Users: Ryan Dwyer, Ali Tirmzi

Affiliation: Department of Chemistry and Chemical Biology, Cornell University

Primary Source of Research Funding: National Science Foundation, Division of Materials Research (NSF-DMR 1006633)

Contact: jam99@cornell.edu, rpd78@cornell.edu, st759@cornell.edu

Website: marohn.chem.cornell.edu

Primary CNF Tools Used: MOS thermal oxidation furnace, SC4500 evaporator, Autostep i-line stepper

Abstract:

High-quality local measurements of electric fields are critical to understanding charge injection, charge transport, and charge trapping in semiconducting materials. Here, we report a new variation of frequency-modulated Kelvin probe force microscopy that enables local measurements of electric field along multiple directions simultaneously by employing position modulation and lock-in detection instead of numeric differentiation of the surface potential. This technique is simple to implement and should be especially useful for studying electric fields in spatially inhomogeneous samples like organic transistors and photovoltaic blends. We demonstrate the technique on a organic field-effect transistor (bottom-gate, bottom-contact) made from the hole-transporting small molecule DPh-BTBT.

Summary of Research:

We report a simple modification of frequency-modulated Kelvin force microscopy (FM-KPFM) that enables the direct spatial imaging of electric fields near a surface along multiple directions simultaneously. The lateral electric field in a FM-KPFM measurement is typically obtained by numerically differentiating the measured surface potential versus position to obtain a plot of electric field versus position [1-3]. This microscopically measured electric field can be helpful for understanding both device physics and materials properties.

Many KPFM measurements derive information mainly from contrast in surface potential images or the average difference in surface potential over different regions of the sample. These properties are relatively insensitive to feedback loop dynamics, noise and surface potential fluctuations. In contrast, these sources of error affect the calculated electric field dramatically. If the scan speed is carefully optimized, low-frequency surface potential noise along the scan axis can be avoided without distorting the measured electric field significantly. In a 2D raster scan, however, the electric field measured along the slow-scan axis will still be subject to large low-frequency surface potential noise caused by position hysteresis and surface potential fluctuations.

To avoid this low-frequency noise, we modify the FM-KPFM measurement by adding a small position modulation $\delta\vec{r}$. We use a modulation $\delta r(t) = A_{pm} \sin(2\pi f_{pm} t)$ with A_{pm} the modulation amplitude and f_{pm} the modulation frequency. We detect the electric field as an oscillating potential at the modulation frequency with amplitude $A_{pm}E_{pm}$. We call the technique *position-modulated* Kelvin probe force microscopy (PM-KPFM).

To calculate the electric field from the position-modulation signal, we processed the raw surface potential data using a software lock-in amplifier at the position-modulation frequency f_{pm} = 4.5 Hz. We used a 0.8 Hz bandwidth lock-in amplifier filter. The measured electric field is $E_{pm} = X_{LI}/A_{pm}$, where X_{LI} is the in-phase channel of the phased lock-in amplifier output.

Figure 1 shows our DPh-BTBT thin-film transistor. To fabricate the transistor, we evaporated 100 nm of DPh-BTBT onto a transistor substrate. The transistor substrate was a highly n-doped silicon gate, a 300 nm thermally grown silicon oxide insulator layer (wet oxide deposited using MOS thermal oxidation furnace), and 40 nm thick thermally evaporated gold source and drain electrodes (SC4500 evaporator, Autostep i-line Stepper). The channel width was 5 µm.

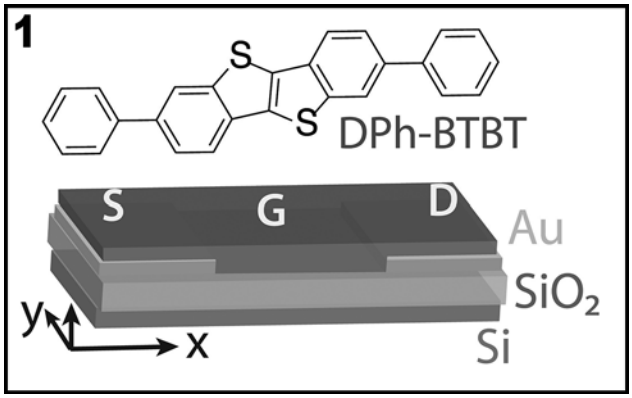

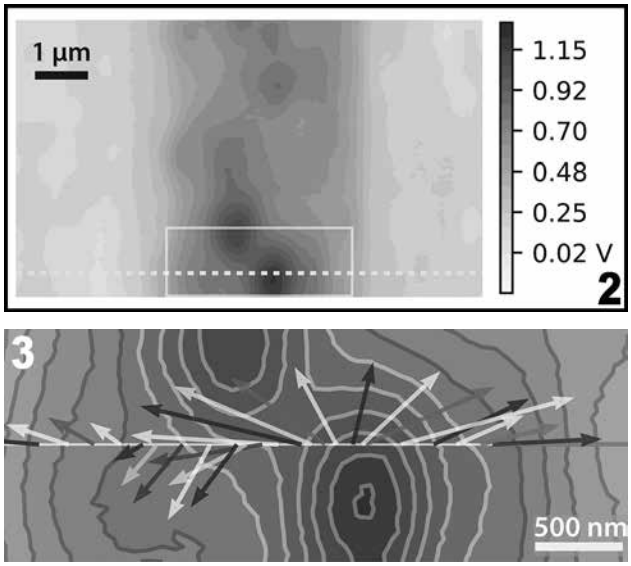

Figure 1, above: Cartoon of the transistor. Figure 2, top right: FM-KPFM image of the transistor channel with $V_S = V_D = V_G = 0$. Contours are shown every 75 mV. Figure 3, bottom right: FM-KPFM surface contours from Figure 2 with the vector electric field calculated from a PM-KPFM linescan.

Figures 2 and 3 demonstrate using PM-KPFM to measure the electric field along the slow-scan axis more precisely. We collected a KPFM image over the DPh-BTBT transistor with source, gate, and drain electrodes off (Figure 2). The KPFM image revealed pockets of trapped charge in the transistor channel.

To probe the electric field near these trapped charges, we took a PM-KPFM linescan. We applied the position modulation *perpendicular* to the scan direction so that we simultaneously measured E_x, the electric field along the fast scan direction, and E_y, the electric field along the slow scan direction. The electric field E_x was determined by numerically differentiating the measured surface potential with respect to the fast-scan direction while E_y was obtained from XLI as discussed above. Figure 3 shows the KPFM image contours along with the in-plane electric field vector (E_x, E_y) measured by PM-KPFM. One consequence of the electric field being the negative gradient of the electrostatic potential is that the electric field vector at location $\vec{r}$ must be perpendicular to a line tangent to the constant-$\phi(x, y)$ surface passing through $\vec{r}$. This perpendicular relationship is clearly evident in Figure 3, demonstrating PM-KPFM's ability to serve as a *vector electrometer*.

We anticipate that the simple modification of FM-KPFM introduced here will be useful for electric field measurements in a variety of systems. Although we demonstrate its use for measuring lateral electric fields, it should also be possible to measure vertical electric fields with an additional vertical position modulation. The 2D electric field images demonstrated here are already an advance from lateral electric field line scans, and we envision applying the PM-KPFM technique to measure local electric fields in bulk heterojunction solar cell blends. The 2D electric field scans could show the current flow direction at domain boundaries near the open-circuit voltage V_{OC}.

References:

[1] Burgi, L.; Sirringhaus, H.; Friend, R. Appl. Phys. Lett. 2004, 80, 2913-2915.

[2] Silveira, W.; Marohn, J. Phys. Rev. Lett. 2004, 93, 116104.

[3] Ng, T. N.; Silveira, W. R.; Marohn, J. A. Phys. Rev. Lett. 2007, 98, 066101.

Fabrication of Semiconductor Nanostructured Thin Film Using Inkjet Printing

CNF Project Number: 1645-08

Principal Investigator: Tobias Hanrath

Users: Qiannan Wen, Eliad Peretz

Affiliations: School of Applied and Engineering Physics, Sibley School of Mechanical Engineering and Aerospace Engineering, Robert Frederick Smith School of Chemical and Biomolecular Engineering; Cornell University

Primary Source of Research Funding: National Science Foundation

Contact: th358@cornell.edu, qw97@cornell.edu, ep442@cornell.edu

Primary CNF Tools Used: Dimatix printer, Zeiss Supra SEM, ABM contact aligner, Heidelberg DWL2000, MVD 100

Abstract:

Semiconductor nanocrystals (NCs) have size dependent optical and electronic properties. The assembly of NCs building blocks into superlattice has opened up materials library by design. The fundamental processes governing the assembly and attachment of NCs into coherent artificial solids are not well understood due to the complexity of the system. Here we demonstrate the application of inkjet printing to form ordered lead sulfide NCs from sub-monolayer to multi-layer structures. The optimization of NCs/substrate interaction by surface functionalization, and the controlled liquid diffusion by confined area printing give insights into the nucleation and growth mechanisms of NCs superlattice. The printing technique shows the potential of decoupling reaction kinetics on small scale and advancing nano-patterning on flexible substrates in semiconductor microelectronics.

Summary of Research:

Semiconductor nanocrystals (SC NCs) have a size smaller than the bulk Bohr radius and quantum confined properties tuned by size, shape and surface chemistry. The self-organization of the NC building blocks forms connected-but-confined structure with their distinct electronic properties [1]. Among various thin film deposition methods, the printing technology is particularly interesting due to its compatibility with flexible electronics and large-scale device manufacture.

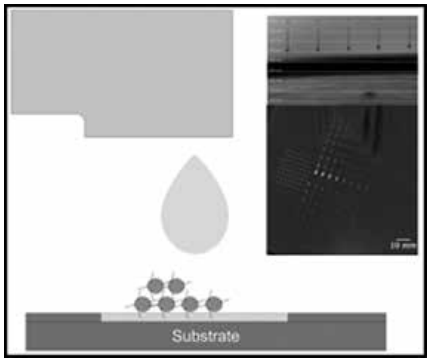

Figure 1: Illustration of inkjet printing of colloidal NCs on a functionalized substrate. Inset shows the jetting of solvent at 10pL each from Dimatix cartridge nozzles and the hydrophilic/hydrophobic patterning of Si/SiO_2 substrate.

Minemawari, et al. [2,3], reported the formation of organic single crystal thin film using anti-solvent coupled inkjet printing and resolved the liquid contact dynamics triggering its crystallization. The NCs system however, is more complicated due to the multiple interaction pathways between the NCs core, ligand and solvent [4]. An understanding of the fundamental principle in NCs assembly and attachment is still lacking.

We demonstrated the fabrication of lead sulfide (PbS) NCs thin film using a Dimatix printer. A silicon wafer with a thin layer of oxide is deposited with a layer of S1818 and exposed to a mask with various pattern shapes (of dimension 100-1000 μm). The unmasked regions are coated with hydrophilic groups by UV-Ozone treatment. Another option is to grow monolayer of 3-mercaptopropyltrimethoxysilane (MPTMS) by molecular vapor deposition to increase the adhesion of nanoparticles to the substrate.

The Dimatix printer uses a disposable cartridge with 16 piezo-actuated nozzles controlled by a user-defined waveform. We dissolve the PbS NCs in dichlorobenzene. The ink is dispensed at 10 pL for each droplet at 2 m/s adjusted by the firing voltage. The printing protocol developed here is applicable to materials of the same class. Figure 1 is an illustration of the colloidal NCs inkjet printing on functionalized

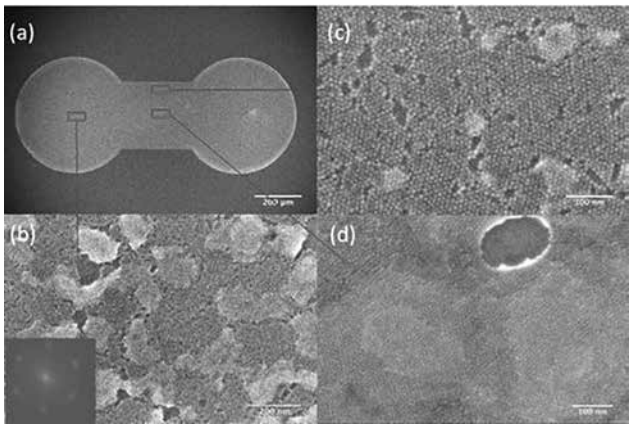

Figure 2: SEM images of the PbS NC thin film printed on MPTMS treated Si substrate with film morphologies controlled by liquid flow on the confined pattern.

substrates. The inset presents the liquid jetting from cartridge nozzle and the hydrophilic/hydrophobic patterned substrate we use for printing.

The PbS NCs with size of 6 nm are assembled into hexagonal geometry with film thickness from sub-monolayer to multiple layers. Figure 2(a-d) show scanning electron microscopy (SEM) images taken on a dumbbell pattern deposited with PbS NCs. The variations in the film structures are correlated with the controlled liquid flow. In most regions of the pattern, the film forms monolayer to bilayer structures as shown in Figure 2(b). Inset is the Fourier transform showing hexagonal lattice. Figure 2(c-d) shows the sub-monolayer formation near the edge where solvent drying is initiated, and the multi-layer structures with array of holes at the center towards which liquid flow from the surroundings.

While the solvent evaporation driven assembly is a simple method for thin film deposition, the fast evaporation rate poses a major problem to the long range ordering of the NCs. Other limitations include difficulties in delivering chemical triggers for the superlattice transformation, *in situ* ligand exchange and multi-component assembly.

One of our ongoing research goals is to transfer the conventional liquid-air interface assembly in big troughs to the small scale experiments on a printer. Our preliminary test has been successful in depositing ethylene glycol as non-solvent on confined hydrophilic patterns, while the deposition of the NCs layer has more challenges regarding undesired mechanical perturbation and non-uniform spreading. Solving these problems will give further insights into the NCs assembly kinetics and promote the application of coherent NCs solid in semiconductor thin film technology. Our other investigations include the substrate functionalization that specifically address the surface chemistry of NCs during assembly and attachment, and different coating techniques applicable to large scale manufacture while preserving long range ordering of the NCs superlattice.

References:

[1] Whitham, K.; Yang, J.; Savitzky, B. H.; Kourkoutis, L. F.; Wise, F.; Hanrath, T. Nat. Mater. 2016, 15 (February), 1-8.

[2] Minemawari, H.; Yamada, T.; Matsui, H.; Tsutsumi, J.; Haas, S.; Chiba, R.; Kumai, R.; Hasegawa, T.; Sun, M.; Paciga, J. E.; Feldman, R. I.; Yuan, Z. Q.; Coppola, D.; You Yong Lu; Shelley, S. A.; Nicosia, S. V.; Cheng, J. Q. Nature 2011, 475 (7356), 364-367.

[3] Noda, Y.; Minemawari, H.; Matsui, H.; Yamada, T.; Arai, S. Adv. Funct. Mater. 2015, 4022-4031.

[4] Choi, J. J.; Bealing, C. R.; Bian, K.; Hughes, K. J.; Zhang, W.; Smilgies, D.-M.; Hennig, R. G.; Engstrom, J. R.; Hanrath, T. J. Am. Chem. Soc. 2011, 133 (9), 3131-3138.

Microfabricated Germanium X-Ray Optics for the Cornell High Energy Synchrotron Source (CHESS)

CNF Project Number: 2172-12

Principal Investigators: Arthur Woll[1], Joel Brock[1,3], Ernie Fontes[1]

User: David Agyeman-Budu[2]

Affiliations: 1. Cornell High Energy Synchrotron Source (CHESS), Cornell University; 2. Materials Science and Engineering, Cornell University; 3. Applied and Engineering Physics, Cornell University

Primary Sources of Research Funding: CHESS is supported by the NSF and NIH/NIGMS via NSF award DMR-1332208

Contact: aw30@cornell.edu, jdb20@cornell.edu, ef11@cornell.edu, da76@cornell.edu

Website: http://www.chess.cornell.edu/

Primary CNF Tools Used: Plasma-Therm Versaline® Deep Si Etcher

Abstract:

With microfabrication and deep reactive ion etching, we have developed an x-ray optic called the Collimating Channel Array (CCA) for confocal x-ray fluorescence (CXRF) using germanium substrates. This builds on our previous efforts where these optics were fabricated out of silicon and demonstrated to have a depth resolution of 1.7 µm. The etch mechanisms and comparison between Si and Ge substrates are highlighted.

Summary of Research:

Confocal x-ray fluorescence (CXRF) is a depth resolved x-ray microprobe technique used to spatially resolve the elemental and chemical speciation of thin films or virtual cross sections of materials that cannot be thinned. The technique is realized by isolating a probe volume formed by the overlap of the foci of a focusing optic and a collection optic. CCAs are excellent collection optics in this regard since its depth resolution is nearly energy independent and more flexible to design [1-5].

CCAs contain a set of radially arranged, collimating channels that point to a single source position at the focus. The channel geometry, which collects the fluorescent x-ray photons from the defined probe volume to the detector, is defined with staggered pillars. The range of energy where these optics are useful is limited by attenuation losses at higher energies with silicon substrates. Optics fabricated from germanium (Ge) substrates as an alternative can operate well up to 30 keV compared to 12 keV with silicon (Si).

Since there are very few publications on plasma etching of germanium and even fewer on deep etching, a study was done to compare the etch performance of Ge with Si. The etch chemistry of Ge to SF_6 is similar and comparable to that of Si and as such, deep reactive ion etch recipes for Si also work well with germanium substrates. Using the Plasma-Therm Versaline® deep silicon etcher, a Taguchi L9 orthogonal partial factorial Design Of Experiment (DOE) was conducted to compared the trends of the etch rates by varying the ICP power of the three processing steps; polymer deposition, polymer removal etch, isotropic Si/Ge etch, and the peak-to-peak voltage of the polymer removal etch step.

The etch comparison done for 4 µm and 40 µm features shown in Figures 1 and 2 suggests that the etch mechanisms for Ge differ from Si and that accounts for the difference in the etch rates and trends of the Ge and Si. The Ge etch rate is higher for the larger 40 µm features and *smaller* for the 4 µm features when compared to the Si etch rates as shown in Figure 3.

There is a strong aspect ratio dependent etching (ARDE) effect with Ge compared to Si and this suggests that the Ge etch is more chemically dependent process and as such, more susceptible to RIE-LAG. This unusual etch response actually also makes Ge a preferred substrate for fabricating CCA optics as the optic design inherently imposes a variable loading effect. The desired larger features are preferred to etch as deep as possible while maintaining the structural integrity of smaller features to survive the etch.

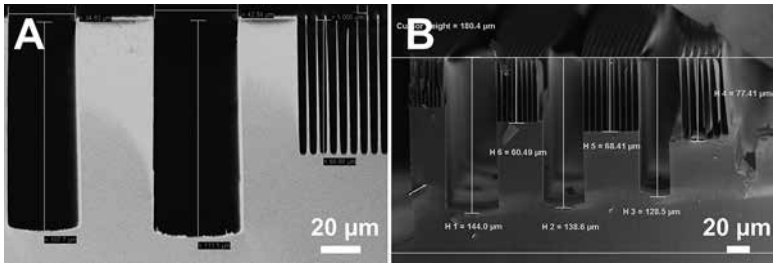

Figure 1: SEM profile of the etched 40 µm and 4 µm features in Si (A) and Ge (B).

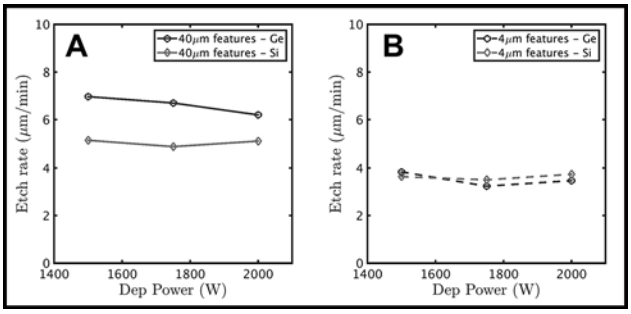

Figure 2: Etch rate dependence on the Dep ICP power for the Si and Ge. The etch rate for the 40 µm features (A) is higher for Ge compared to Si but lower for the 4 µm features (B).

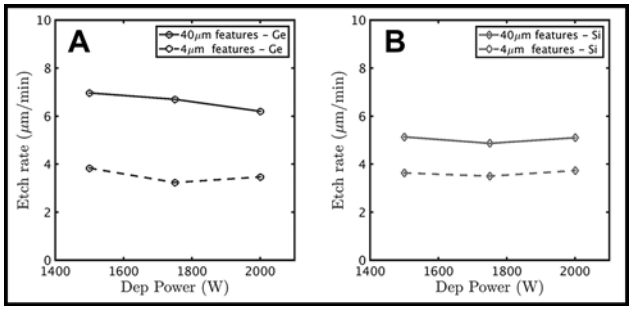

Figure 3: Comparison of ARDE with Ge (A) and Si (B) substrates demonstrating the differential etch rates for 4 µm and 40 µm trenches.

References:

[1] A. R. Woll, J. Mass, C. Bisulca, M. Cushman, C. Griggs, T. Wanzy and N. Ocon, Stud Conserv 53 (2), 93-109 (2008).

[2] A. R. Woll, J. Mass, C. Bisulca, R. Huang, D. H. Bilderback, S. Gruner and N. Gao, Applied Physics a-Materials Science and Processing 83 (2), 235-238 (2006).

[3] L. Vincze, B. Vekemans, F. E. Brenker, G. Falkenberg, K. Rickers, A. Somogyi, M.Kersten and F. Adams, Analytical Chemistry 76 (22), 6786-6791 (2004).

[4] B. Kanngiesser, W. Malzer and I. Reiche, Nuclear Instruments and Methods in Physics Research Section B-Beam Interactions with Materials and Atoms 211 (2), 259-264 (2003).

[5] A R. Woll, D. Agyeman-Budu, D. H. Bilderback, D. Dale, A. Y. Kazimirov, M. Pfeifer, T. Plautz, T. Szebenyi, and G. Untracht, SPIE Optical Engineering + Applications, 8502, 85020K-85021-85014 (2012).

Nanocale Periodic Features with DUV Stepper Backside Alignment

CNF Project Number: 2217-13
Principal Investigator: Ioannis Kymissis
User: Tanya Garza

Affiliation: Department of Electrical Engineering, Columbia University, New York, NY
Primary Source of Research Funding: National Science Foundation
Contact: johnkym@ee.columbia.edu, tcg2112@columbia.edu
Website: http://kymissis.columbia.edu
Primary CNF Tools Used: ASML 300C DUV, GCA 5x stepper, Oxford 100, P10 profilometer

Abstract:

Lithography with the ASML 300C DUV stepper has been used in previous years to produce pillar features with diameters including 232 nm, 306 nm, 408 nm, and 446 nm on the wafer frontside. This past year work with the ASML 300C DUV stepper was expanded to include backside features aligned to the frontside using the ASML 300C DUV backside alignment system. A process was developed where tool auto alignment could be done with backside alignment features etched into a fused silica wafer.

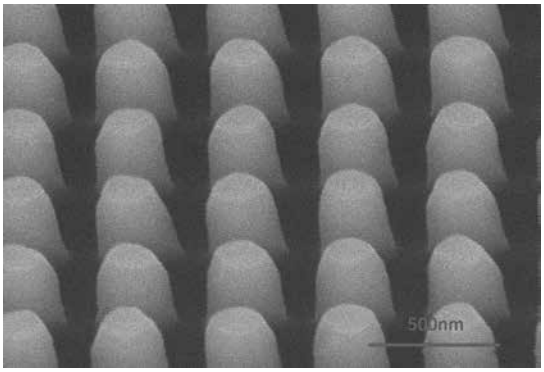

Figure 1: SEM image of photonic crystal pattern, nominally with 270 nm pillar features, fabricated fused silica with process developed with ASML 300C DUV stepper.

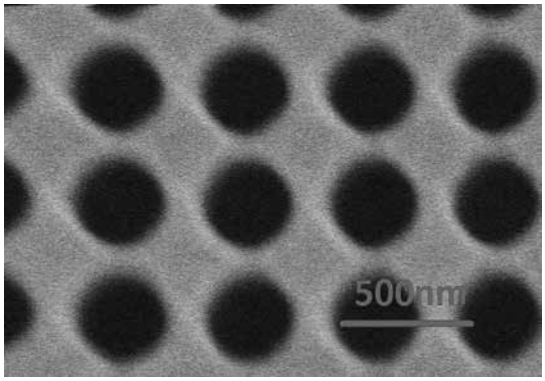

Figure 2: SEM image of photonic crystal pattern, nominally with 306 nm hole features, fabricated in fused silica with a process developed with ASML 300C DUV stepper.

Summary of Research:

In previous years, a process for patterning nanophotonic pillar and hole structures was developed at CNF that used the ASML 300C DUV stepper and the GCA 5x stepper. These features were etched into the substrate material using the patterned resist as an etch mask. The ASML 300C DUV stepper process has been used to pattern 4-inch borosilicate float glass wafers ("borofloat"), 4-inch fused silica wafers, and 4-inch silicon wafers. Pillar features like those shown in Figure 1 were fabricated with diameters of 232 nm, 270 nm, 306 nm, 408 nm, 612 nm and 816 nm. Hole features like those shown in Figure 2 were fabricated with design diameters of 306 nm, 408 nm, and 446 nm. Optimal depth of focus (DOF), exposure dose, and etch time were determined for nanophotonic patterns in fused silica by varying these parameters incrementally and examining the resultant features. Photonic crystal geometry was examined in the SEM and photonic crystal performance was assessed optically via extraction of waveguided light. Prelimary work was done with the GCA 5x stepper process to pattern 4-inch fused silica wafers for minimum hole feature sizes of 408 nm and 446 nm. The best results of a coarse DOF and exposure dose variation study on the GCA 5x stepper are shown in Figure 3.

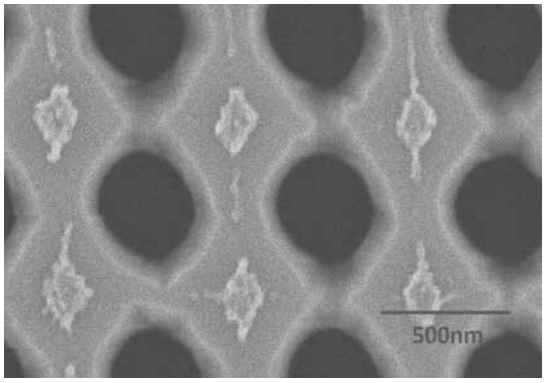

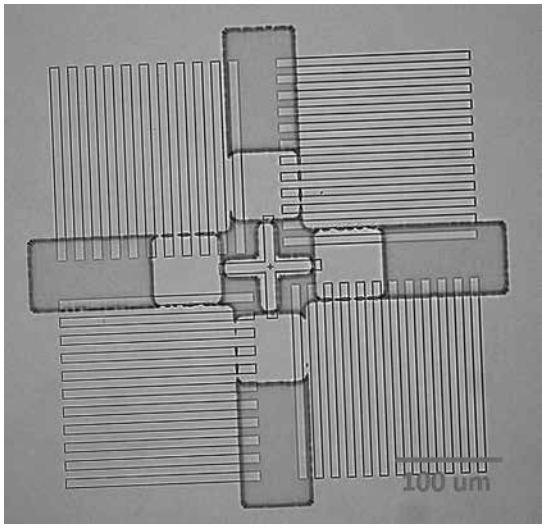

Figure 3, above: SEM image of photonic crystal pattern, nominally with 446 nm hole features, fabricated in fused silica with a process developed with GCA 5x stepper. Figure 4, right: Microscope image of cross alignment mark in photoresist aligned by contact lithography to AMSL diffraction alignment mark etched into fused silica wafer.

This past year work was done to enable front and backside patterning of 4-inch fused silica wafers on the ASML 300C DUV stepper. Typically backside alignment is done in silicon with four ASML defined alignment patterns etched on four corners of the wafer backside. These ASML marks are diffraction gratings that reflect a laser light focused onto a sensor. These marks are etched to a target depth of 160 nm for bare silicon to optimize the signal strength on the sensor [1].

Two possible methods were considered to achieve backside alignment on fused silica. Since fused silica is highly transparent, processes where the ASML patterns in the material were coated with a thin 60 nm layer of aluminum were considered in addition to patterns in the bare fused silica. One minute of the oxide etch recipe on the Oxford 100 tool produced etched depths of 150 nm as measured by the P10 profilometer. With these etch conditions, alignment to three out of the four backside alignment marks was obtained. This level of alignment was found satisfactory. Repetition of this processes would sometimes yield alignment to only two out of the four backside alignment marks but this level of alignment was also considered satisfactory. Tests with aluminum over the alignment marks on fused silica have not yet been done.

Two ASML alignment marks were patterned on the wafer backside in addition to the four used for automated alignment on the DUV stepper. These additional alignment marks were used for contact lithography on the wafer backside in addition to the projection lithography done on the DUV stepper. Figure 4 shows an optical microscope image of contact alignment marks in resist overlaid on the ASML diffraction grating alignment marks etched into the wafer backside.

In summary, the process previously developed to pattern fused silica wafers with nanophotonic pillar and hole structures was expanded to include automated backside alignment on the ASML 300C DUV stepper. Work done to enable backside alignment was achieved for up to three out of four ASML alignment marks etched into bare fused silica to a depth of 150 nm.

References:

[1] Berge, PT. (2007, February 28). 3DAlignTM: Recent developments in double sided alignment and back-side alignment, ASML 200mm/Special Application - SPIE Technical Symposium. Retrieved from https://staticwww.asml.com/doclib/misc/asml_20070323_04_SA_Tech._Symp._presentation_3D Align_v2.pdf.

Efficient Template-Based Nano Manufacturing of Carbon Nanotube Arrays

CNF Project Number: 2334-15
Principal Investigator: Dr. Michael Schrlau
User: Devarsh Shah

Affiliation: Mechanical Engineering, Rochester Institute of Technology
Primary Source of Research Funding: NIH-R21 Grant
Contact: mgseme@rit.edu, dxs1199@rit.edu
Primary CNF Tools Used: PT-740 etcher, Oxford 81 etcher

Abstract:

Carbon nanotube arrays have been found to be highly effective at carrying out the intracellular delivery of cargo at high efficiencies while ensuring cell viability. Template-based chemical vapor deposition is an efficient two-step process to synthesize carbon nanotubes (CNTs) for a wide range of applications. In this process, the choice of template dictates certain physical features of the carbon nanotubes (CNTs), such as length and outer diameter, while the process itself affects other features, such as tube wall thickness, carbon deposition rate, and carbon morphology. In this report, the manufacturing and fabrication process of carbon nanotube arrays is being described.

Summary of Research:

Carbon nanotubes (CNT) arrays are fabricated using commercially available anodized aluminum oxide (AAO) membranes. Anodized aluminum oxide (AAO) membranes are annealed in air at 730°C for 4 h and placed in a three-stage chemical vapor deposition (CVD) tube furnace. After purging the furnace with Argon, 30/70 (vol%/vol%) ethylene/helium precursor gas was flowed at 60 sccm into the furnace at 700°C for 5 h to deposit a thin film of carbon on all surfaces of the anodized aluminum oxide (AAO) membrane, including the walls of the membrane pores to form carbon nanotubes (CNTs) embedded in the anodized aluminum oxide (AAO) template.

The carbon layer on one side of the membrane was then removed using plasma etching (Oxford 81) at 300 mTorr, RF 250 W, and oxygen flow rate of 50 sccm for 45 sec. Carbon nanotubes (CNTs) were then partially exposed by selectively etching the anodized aluminum oxide (AAO) template using reactive ion etching (PT-740) with boron trichloride (BCl_3) at 15 mTorr, RF 500 W, and BCl_3 flow rate of 80 sccm for six hours.

The resultant carbon nanotube (CNT) array as shown in Figure 1, consisted of millions of carbon nanotubes (CNTs). This is the first step of the process — as seen in Figure 1, the nanotubes are uneven in height and are not coplanar. From studies conducted previously, we have shown that cells like coplanar surface of nanotubes [1], so to an achieve even and coplanar height of the carbon nanotubes (CNTs), we again used plasma etching (Oxford 81) at 300 mTorr, RF 250 W, and oxygen flow rate of 50 sccm for 45 sec. and again carbon nanotubes (CNTs) were then partially exposed by selectively etching the anodized aluminum oxide (AAO) template using reactive ion etching (PT-740) with boron trichloride (BCl_3) at 15 mTorr, RF 500 W, and BCl_3 flow rate of 80 sccm for six hours.

The resultant carbon nanotubes (CNTs) array is as shown in Figure 2, with an average tip diameter of 205 ± 42 nm, tube wall thickness of 28 ± 5 nm, tube-to-tube spacing of 187 ± 36 nm protruding 176 ± 34 nm from the surface of the 13-mm diameter anodized aluminum oxide (AAO) membrane. Figure 3 shows the diagram of how the carbon nanotubes look after the first and second steps, for better understanding.

Dozens of carbon nanotubes (CNT) arrays devices were produced in a single manufacturing run and stored until needed for transfection.

References:

[1] M. Golshadi, L.K.Wright, I.M.Dickerson, M.G.Schrlau; "High-Efficiency Gene Transfection of Cells through Carbon Nanotube Arrays"; small, p. 7, 2016. DOI: 10.1002/smll.201503878

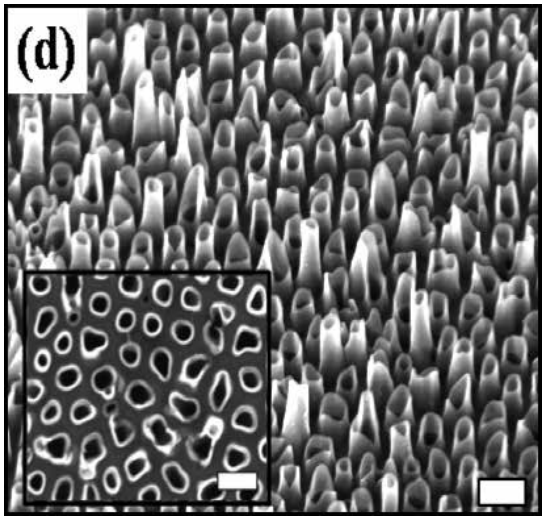

Figure 1: SEM of carbon nanotubes (CNTs) array after the first step of processing.

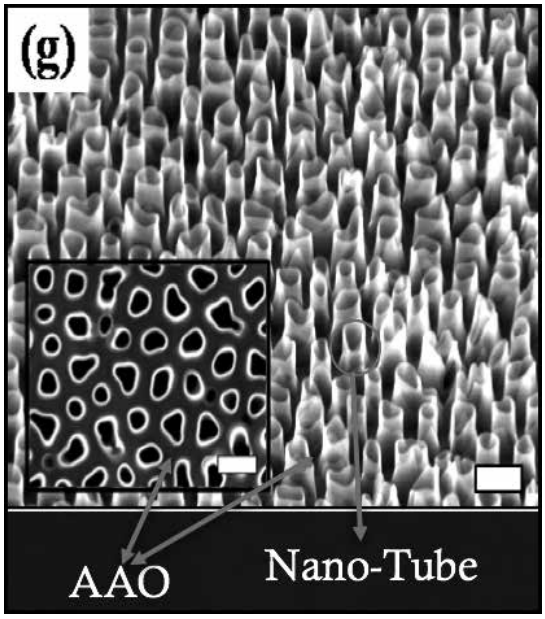

Figure 2: SEM of carbon nanotubes (CNTs) array after the second step of processing.

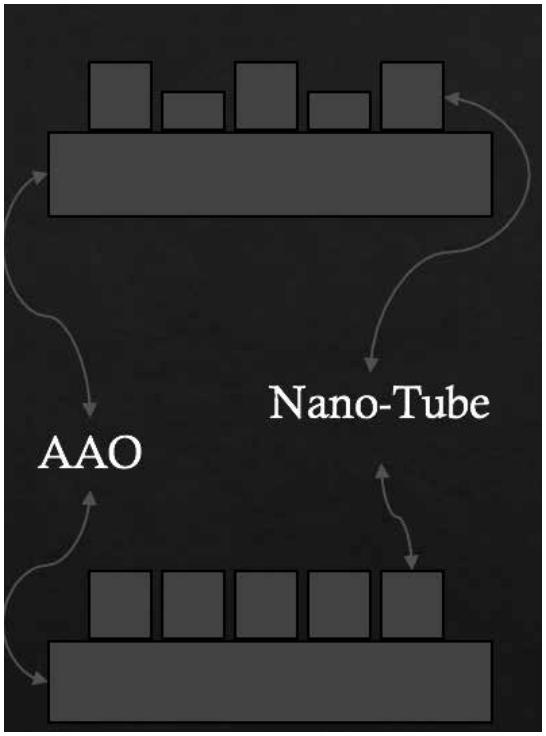

Figure 3: Schematics of anodized aluminum oxide after the first and second step for better understanding.

1.1kV GaN Vertical Power P-N Diodes on Ammonothermal GaN Substrates; Process Development and Device Characteristics

CNF Project Number: 2350-15

Principal Investigators: Huili Grace Xing, Debdeep Jena

Users: Zongyang Hu, Wenshen Li, Mingda Zhu, Hank Liu

Affiliations: Electrical and Computer Engineering, Material Science Engineering; Cornell University

Primary Source of Research Funding: ARPA-E Sixpoint

Contact: grace.xing@cornell.edu, zh249@cornell.edu

Primary CNF Tools Used: Oxford PECVD, Autostep i-line stepper, PT770 etcher, SC4500 evaporator,

Abstract:

Vertical GaN power p-n diode processes have been developed using the CNF. The project includes device fabrication, imaging and electrical test of GaN homoepitaxial p-n junction structures on ammothermal GaN substrates. High performance GaN-on-GaN vertical p-n diodes have been demonstrated. Large forward currents (forward turn-on voltage of 3.3V, forward current of 500 A/cm^2 at 4V and 1000 A/cm^2 at 4.5V), on-resistance of 0.72 mΩ·cm^2 and reverse breakdown voltage of 1172V have been measured in these devices. Baliga figure-of-merit is calculated to be 1.9 GW/cm^2. This is the first demonstration of high voltage GaN p-n diodes on ammono GaN substrate.

Summary of Research:

Gallium nitride (GaN) has been widely considered as one of the most promising wide band gap semiconductors for development of next generation power semiconductor devices. The theoretical power performance of GaN predicted by the Baliga's figure-of-merit is 1000x higher than that of Si and nearly 2x higher than SiC. Though record-high power diode performance has been demonstrated in GaN compared to all other semiconductor materials [1], the lack of low-cost, low-dislocation-density bulk substrate limits the feasibility of application for GaN based devices. The goal of the ARPA-E Sixpoint project is to develop high quality, inexpensive GaN substrates using ammonothermal method, and demonstrate high performance and repeatability of vertical GaN power devices. The development of fabrication processes for GaN based power devices is also acritical component in this project.

Device fabrication includes metal deposition (e-beam evaporation of Ti, Pd, Au), dry etching (Cl-based plasma etching), photolithography (Autostep i-line stepper), dielectric deposition (PECVD SiO_2). Device sizes are 50 μm ~ 700 μm. Optical microscope, profilometer and AFM are used frequently to observe sample surfaces during processes. The device processes and main CNF tools used are described briefly as the following:

1. Beveled p GaN mesa etching
   - *SiO_2 mask deposition (Oxford PECVD)*
   - *Litho and wet etching of SiO_2 (Autostep i-line Stepper)*
   - *Dry etching of p GaN (PT770 etcher)*
2. Top ohmic contact deposition
   - *Litho and Pd/Au ohmic contacts (SC4500 evaporator)*
3. Passivation
   - *Dielectric passivation (Spinner)*
   - *Lithography*
   - *Wet etch to open contact holes*
4. Field plate
   - *Litho and field plate deposition, liftoff*
5. Bottom contact deposition
   - *Photoresist coating and cleaning*
   - *Ti/Au back ohmic contacts, liftoff*

The schematic device structure is depicted in Figure 1. The epitaxial structure is grown by metalorganic chemical vapor deposition (MOCVD) on bulk GaN substrates. The thick (8 μm) n-GaN region is the most critical part for the electrical characteristics of the GaN p-n diodes. Compared to last year's devices, the MOCVD growth condition in the most recent runs has been

tuned to control the charge concentration in the n-GaN layer within 2E15-1E16 cm^{-3} ranges. Other device parameters have been kept largely the same. The beveled mesa and field plates are designed to mitigate electrical field crowding at the edge of the p-n junction and the corners of the mesa [2].

An optical image of the GaN device chip after fabrication is shown in Figure 2. The devices have sizes ranging from 50 μm to 700 μm (the largest device is not shown in the figure).

The forward current-voltage curve of a typical GaN p-n diode is plotted in Figure 3. The forward current at V < 2.4V is lower than the lower limit of the measurement system (semi-log scale plot is not shown). The diode turns on at ~ 3.3V, and the current reaches 500 A/cm^2 at 4V and more than 1000 A/cm^2 at 4.5V, which meets our project goal for the forward current density. Devices with and without field plates do not show significant difference under forward biases.

The reverse current-voltage characteristics of a group of GaN p-n diodes with 110 μm diameter are plotted in Figure 4. The highest breakdown voltage measured is 1172V. The Baliga's figure-of-merit (BFOM) is calculated to be 1.9 GW/cm^2, among the highest reported for GaN power p-n diodes. Capacitance-voltage measurement has been performed on these diodes, and charge distribution inside the n-GaN has been analyzed (results not shown due to limited space). The charge concentration ranges from 2×10^{15} cm^{-3} to 1×10^{16} cm^{-3} at different positions in the n-GaN. This is likely caused by gas flow fluctuation near edges of the 10 mm × 10 mm sample during the MOCVD growth, which leads to variations in impurity incorporation in the GaN layers.

Device mapping has been performed on the 10 mm × 10 mm GaN p-n diode sample. Breakdown voltages are measured between ~ 500V to ~ 1000V on different devices with the same size (110 μm diameter). It has been found that the surface roughness (instead of charge concentration in the n-GaN) is likely the main factor that leads to the non-uniform breakdown voltages.

Future work from Sixpoint will be growths on 2-inch ammono GaN substrates to demonstrate high breakdown voltage p-n diodes with good uniformity across the wafer.

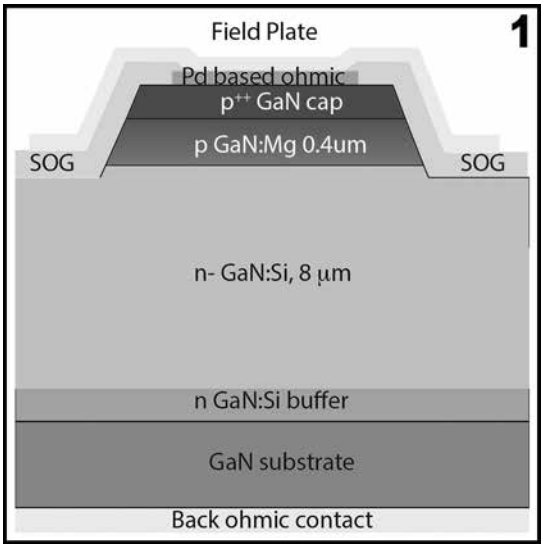

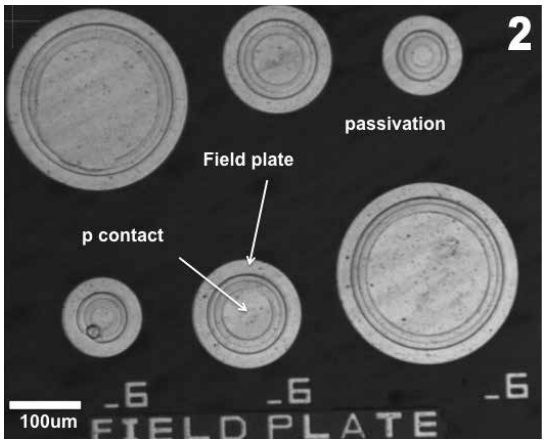

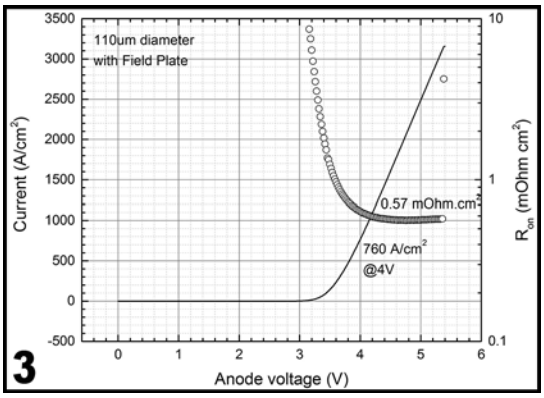

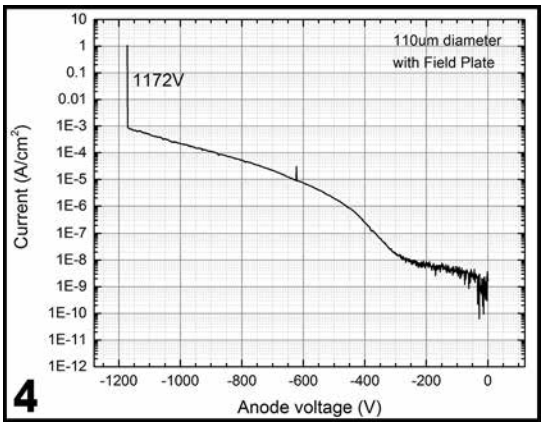

Figure 1: Schematic cross section of a vertical GaN power p-n diode with field plate edge termination. Figure 2: Part of a GaN power p-n diode chip imaged under the optical microscope. Figure 3: Forward current-voltage characteristics of a vertical GaN power p-n diode. Figure 4: Reverse current-voltage characteristics of a vertical GaN power p-n diode with a breakdown voltage of 1172V.

References:

[1] Z. Hu, K. Nomoto, B. Song, M. Zhu, M. Qi, M. Pan, X. Gao, V. Protasenko, D. Jena and H.G. Xing, Appl. Phys. Lett. 107, 243501 (2015).

[2] K. Nomoto, Z. Hu, B. Song, M. Zhu, M. Qi, R. Yan, V. Protasenko, E. Imhoff, J. Kuo, N. Kaneda, T. Mishima, T. Nakamura, D. Jena and H. Xing, IEEE International Electron Devices Meeting (IEDM), 9.7.1 (2015).

Deep-Tissue Photonic Needles

CNF Project Number: 2364-15
Principal Investigator: Michal Lipson
User: Romy Fain

Affiliations: Electrical and Computer Engineering, Cornell University; Electrical Engineering, Columbia University

Primary Source of Research Funding: National Science Foundation

Contact: ML3745@columbia.edu, rmf98@cornell.edu

Primary CNF Tools Used: Woollam spectroscopic ellipsometer, ABM and SÜSS MA6-BA6 contact aligners, ASML 300C DUV stepper, Heidelberg DWL2000, Zeiss Supra and Ultra SEMs, GSI PECVD, Oxford ALD and PECVD

Abstract:

We demonstrate a new platform for minimally invasive, light delivery probes leveraging the maturing field of silicon photonics, enabling massively parallel fabrication of photonic structures. These photonic needles probes have sub-10.m cross-sectional dimensions, lengths greater than 3 mm — surpassing 1000 to 1 aspect ratio, and are released completely into air without a substrate below. We show the photonic needles to be mechanically robust when inserted into 2% agarose. The propagation loss of these waveguides is low — on the order of 4dB/cm.

Summary of Research:

The use of light for biological imaging and stimulation, in the near and far field, has an array of useful applications, but due to combined scattering and absorption effects in tissue, current techniques require significant damage to the tissue when reaching past a couple of millimeters into deep tissue.

Ground-breaking early light delivery probe schemes have included large chip shank-like designs [1-3] reminiscent of traditional electrode on chip platforms [4,5] fiber-like devices [6,7] or designs with traits of both [8,9]. When these schemes reach deep tissue they have large cross-sections on the order of 100 μm across or more. They are destructive to the biological tissue, inducing an immunological response, disrupting the system we want to measure, but also impeding the signal response collected [10-12]. Our approach is to provide high aspect ratio Photonic Needles long enough to reach deep-tissue, but narrow enough to provoke minimal immune response.

High quality photonic signals can be guided in nano-waveguides as small as a few hundreds of nanometers in cross-section, but how small of a cross-section can we make before buckling occurs and a deep tissue probe fails, either mechanically or optically?

We have demonstrated:

- *1000:1 aspect ratio*
- *3.5 mm long released, no substrate*
- *Concurrent mechanical and optical robustness*
- *Minimum cross-section 3 μm wide, up to 3.5 mm long*
- *Mechanical stability down to 3μm × 10μm × 3.25mm long*
- *Array of 18 photonic needles*
- *Low loss: 4 dB/cm average*

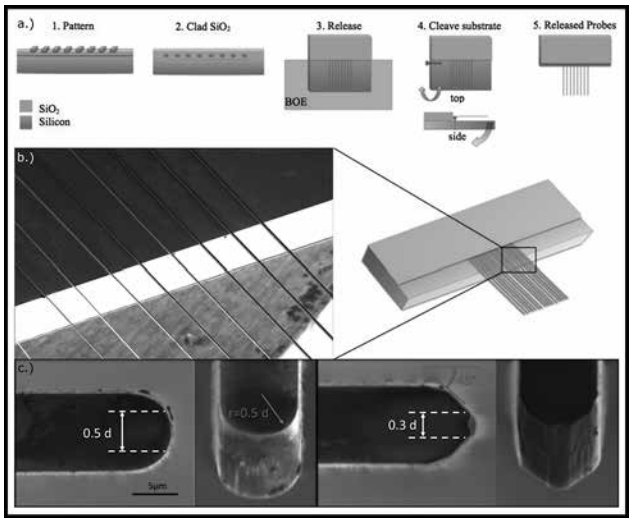

Figure 1: Details of the Photonic Needle fabrication using the mechanical substrate removal (MSR) process. a.) The MSR is shown here left to right. b.) SEM (left) shows the pristine cleaved silicon face, post-MSR. Scale bar is 300 μm. Diagram (right) shows the SEM location on the chip. c.) SEMs of Photonic Needle tips show top view and 45° at the tip, with radiused tip (left), angled tip (right). Scale bar is 5 μm.

Ultra long and narrow photonic needles could enable longer-term chronic studies and insertion of very large arrays of needles by:

- *Displacing only a negligible volume of tissue*
- *Providing stronger signals and more accurate data*
- *Allowing the stimulation and imaging of individual neurons across large volume cell circuits in real time*

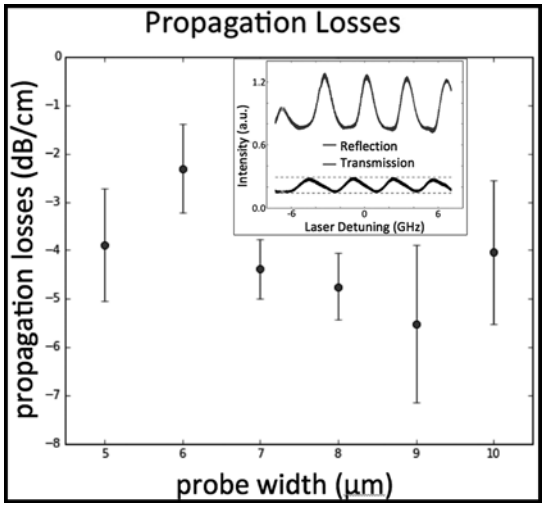

Figure 2: Optical loss testing results. This graph shows the measured propagation losses in waveguides with dimensions that survived mechanical testing without buckling using the Fabry-Perot cavity between the input and output facets.

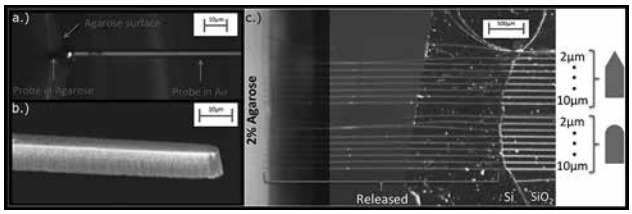

Figure 3: The mechanical testing of Photonic Needles. Images (left) are of a 3 × 10 μm cross-section probe approximately 3.25 mm long, with a.) microscope image of it being inserted into 0.5% agarose, and b.) angled SEM of tip. c.) Composite microscope image demonstrates a full double set of released probes being inserted into 2% agarose, to simulate mouse cortex with dura [24,25]. Buckling needles are colorized in [red].

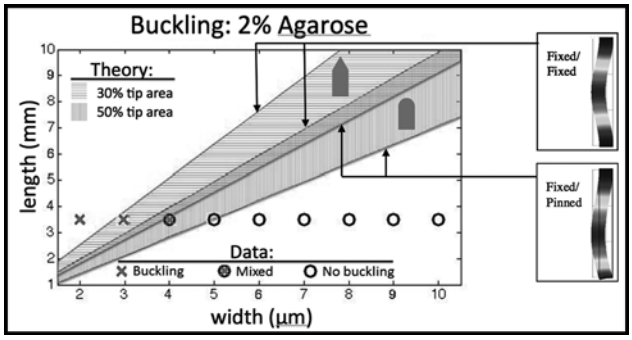

Figure 4: Buckling results for Photonic Needles. This graph describes the mechanical testing results from the insertion of a full chip array of Photonic Needles into 2% agarose (see also photo Figure 2c.), as compared with applied theory. Angled and radiused tips have an estimated 30% and 50% tip area respectively, compared to a blunt tip surface area (see also SEMs in Figure 1c). Blunt tip critical force [20] is scaled for decreased cross-sectional tip area. Theoretical shaded areas are bounded by Euler buckling theory for fixed/fixed above and fixed/pinned below.

References:

[1] Zorzos, Boyden, Fonstad; Opt. Lett. 2010, 35, 4133-4135.

[2] Stark, Koos, Buzsaki; J. Neurophysiol. 2012, 108, 349-363.

[3] Wu, Yoon, et. al.; J. Neural Eng. 2013, 10, 056012.

[4] Wise, Angell, Starr; Biomed. Eng. IEEE Trans. Bio-Med. Eng. 1970, 3, 238-247.

[5] Masmanidis, Du, Roukes, Laurent; Google Patents, 2013.

[6] Barretto, Messerschmidt, Schnitzer; Nat. Methods 2009, 6, 511-512.

[7] Doronina-Amitonova, Zheltikov, et. al.; Sci. Rep. 2013, 3.

[8] Anikeeva, Deisseroth, et. al.; Optetrode: Nat. Neurosci. 2011, 15, 163-170.

[9[Abaya, Solzbacher, et. al.; Biomed. Opt. Express 2012, 3, 3087-3104.

[10] Szarowski, Craighead, Turner, Shain, et. al.; Brain Res. 2003, 983, 23-35.

[11] Biran, R.; Martin, D. C.; Tresco, P. A. Exp. Neurol. 2005, 195, 115-126.

[12] Williams, Hippensteel, Dilgen, Shain, Kipke; J. Neural Eng. 2007, 4, 410-423.

[13] Farrar, Wise, Fetcho, Schaffer; Biophys. J. 2011, 100, 1362-1371.

[14] Ji, Sato, Betzig; Proc. Natl. Acad. Sci. 2012, 109, 22-27.

[15] Horton, Wang, Kobat, Clark, Wise, Schaffer, Xu; Nat. Photonics 2013, 7, 205-209.

[16] Theer, Denk; JOSA A 2006, 23, 3139-3149.

[17] Popov; 2nd ed.; Prentice Hall: Upper Saddle River, N.J, 1998.

[18] Hosford; Cambridge University Press: Cambridge; New York, 2008.

[19] Bower; CRC Press: Boca Raton, 2010.

[20] Sharp, Ortega, Restrepo, Curran-Everett, Gall; IEEE Trans. Biomed. Eng. 2009, 56, 45-53.

[21] Hecht; Optics; 4th ed.; Addison-Wesley: Reading, Mass, 2002.

[22] Park, Kim, et. al.; J. Appl. Phys. 1995, 78, 6318.

[23] Taebi, Khorasaninejad, Saini; Appl. Opt. 2008, 47, 6625-6630.

[24] Normand, Lootens, Amici, Plucknett, Aymard; Biomacromolecules 2000, 1, 730-738.

[25] Chen, Suki, An; J. Biomech. Eng. 2004, 126, 666.

[26] Griffith, Cardenas, Poitras, Lipson; Opt. Express 2012, 20, 21341-21345.

Quest for X-Ray Transparent Multilayer Graphene

CNF Project Number: 2386-15
Principal Investigator: Sol M. Gruner
User name: Gabrielle Illava

Affiliation: Macromolecular Diffraction Facility at Cornell High Energy Synchrotron Source (MacCHESS); Biophysics/Physics Department, Cornell University

Primary Sources of Research Funding: MacCHESS is funded by the National Institutes of Health, under grant GM-103485 from the National Institute of General Medical Sciences

Contact: smg26@cornell.edu, GL432@cornell.edu

Website: http://bigbro.biophys.cornell.edu/

Primary CNF Tools Used: First Nano Carbon Nanotube and Graphene (CNT/Graphene) Furnace, Zeiss Ultra SEM

Abstract:

This project centers on the incorporation of multilayer graphene with ultrathin polymer support as x-ray transparent vacuum-tight window material. Possible applications include microcrystallography and biological small angle x-ray scattering (bioSAXS) flow cells for use in diffraction studies at the Macromolecular Diffraction Facility at the Cornell High Energy Synchrotron Source (MacCHESS). Graphene is a 2D hexagonal carbon lattice that has remarkable electrical and mechanical properties. Due to extraordinary tensile strength graphene has shown much promise as being able to hold vacuum at a thickness of just a few atoms [1]. This is important because reduction of material within the x-ray beam path can reduce the background scatter that is highly problematic in microcrystallography and bioSAXS.

Summary of Research:

The goal of this work was to explore the fabrication of graphene-based vacuum-tight windows for x-ray specimen cells. The areas that need to be covered span tenths of a millimeter, thereby necessitating multilayer graphene. The need for > 20-25 layers of graphene to achieve the goals of this project led to several different methods for obtaining multilayers of graphene. During the initial stages of this project, mono-bi-trilayer graphene was used for manual assembly of layers [2]. The process of manual layer assembly is both time intensive and highly delicate, with a low yield of intact and useable graphene-based pieces. One of the solutions to this problem is to grow large grain multi-layer graphene (LGMLG) that is strong enough to stand alone with no polymer backing, see Figure 1. The LGMLG covering the 150 μm diameter windows remained intact through diffraction data collection.

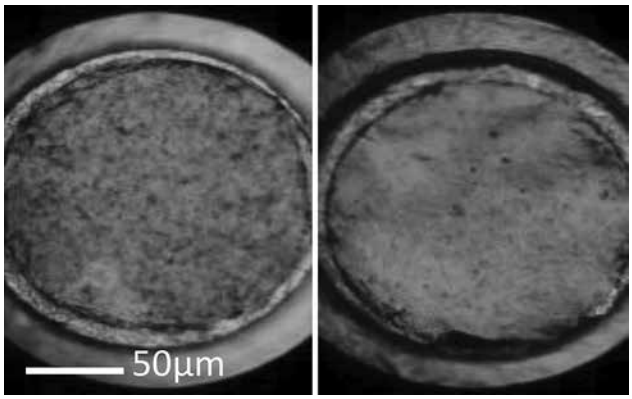

Figure 1: Optical image of free-standing LGMLG windows over 150 μm diameter windows after diffraction data was taken.

This was accomplished by adapting a chemical vapor deposition (CVD) process using the First Nano Carbon Nanotube and Graphene (CNT/Graphene) Furnace with the help of Phil Infante. We combined several graphene recipes to optimize the characteristics of LGMLG. The initial multilayer graphene recipe could produce greater than tetra-layer graphene on copper by increasing the pressure within the growth chamber during the growth step [3]. This was accomplished by increasing the hydrogen gas flow to the maximum rate while also reducing the power of the vacuum pump. Analysis with Raman spectroscopy showed that graphene growths done at 240 mTorr produced non-uniform layers that were sometimes bilayer and often greater than four layers of graphene. These results were confirmed through scanning electron microscopy (SEM), using the Zeiss Ultra high-resolution field emission SEM at CNF.

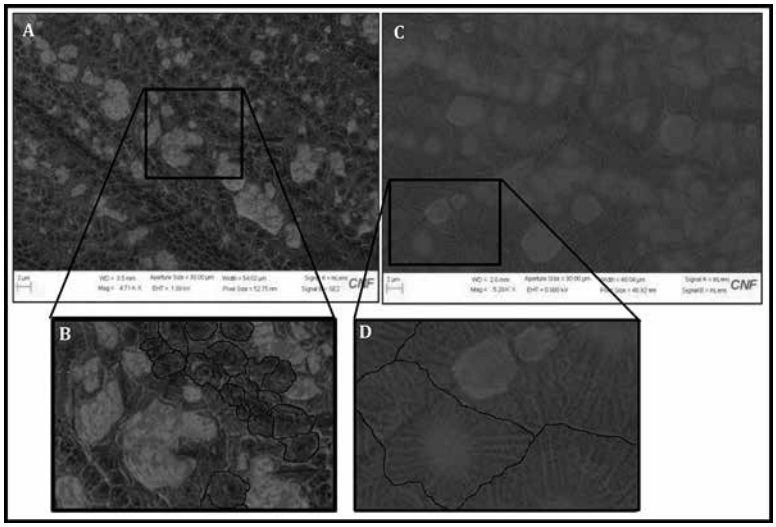

Figure 2: Final result of optimization compared to MLG with no oxidation step. A,B) No oxidation, 15min growth. C,D) 2 min oxidation, 90 min growth. In B and D, several grain boundaries are highlighted with black outline.

Since graphene is weakest at the grain boundaries [1], and the size of the windows exceeded the size of the grains we were producing, we attempted to increase grain size in hopes of growing larger grains. Introducing an oxidation step before the growth step has been shown to increase grain size and thus reduce the occurrence of boundaries over large mono-layer growths [4]. Our recipe combined the multilayer inducing pressure increase, with an oxidation step to produce LGMLG.

In Figure 2, A/B is multilayer growth without an oxidation step, and C/D is after optimization of the oxidation step. This comparison shows that the irregularities in grain size were reduced and that overall grain size was increased. However, it was not a significant enough increase and the LGMLG was not able to hold vacuum. We then tried growing LGMLG with a thin PMMA polymer backing layer, under the rationale that the graphene would serve as a layer that was gas and water vapor impermeable and the PMMA would add sufficient strength to hold the vacuum. The graphene-PMMA material was indeed vacuum tight, but when tested for x-ray scatter it was realized that the material had significant SAXS, possibly due to carbon particles produced during the synthesis. Figure 3 shows the SAXS from kapton, glass, and graphene-PMMA windows. It is observed that commercially available Kapton® and glass windows have lower SAXS backgrounds than the graphene-PMMA windows.

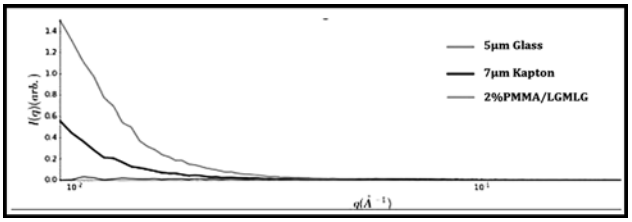

Figure 3: Comparison of SAXS from graphene-based 2%PMMA/ LGMLG, 7 μm Kapton, and 5 μm glass across a 150 μm diameter aperture.

Conclusions:

We failed to produce a graphene-based x-ray window that was both strong enough to withstand vacuum over a 150 μm diameter aperture and yet had a lower SAXS background than commercially available alternative window materials. Further work is required to make better multilayer graphene sheets that do not require a polymer support.

References:

[1] Lee, C. (2008). "Measurement of the Elastic Properties and Intrinsic Strength of Monolayer Graphene". Science 321 (385), 385-388.

[2] J. L. Wierman, J. S. Alden, C. U. Kim, P. L. McEuen, and S. M. Gruner, "Graphene as a protein crystal mounting material to reduce background scatter.," J. Appl. Crystallography., vol. 46, no. Pt 5, pp. 1501-1507, Oct. 2013.

[3] Sun, Z. et al. (2012). "Large-Area Bernal-Stacked Bi-, Tri-, and Tetralayer Graphene" ACS Nano (11), 9790-9796.

[4] Lee, G.-H. et al. (2013) "High-Strength Chemical-Vapor-Deposited Graphene and Grain Boundaries," Science, (340), 6136, 1073-1076.

INDEX OF REPORTS BY CNF PROJECT NUMBER

2017 CNF REU Intern Reports 2, 4, 82, 110, 150
111-80 ..... 180, 182, 184, 218
150-82 ..... 112, 222
386-90 114
522-94 116
598-96 ..... 186, 188, 190, 192
657-97 66
731-98 6
762-99 8
863-00 ..... 70, 80, 224
900-00 ..... 10, 128, 194
1119-03 12
1122-03 136
1239-04 72
1255-04 14
1262-04 84
1278-04 16
1314-05 196
1356-05 118
1371-05 74
1520-07 198
1540-07 16
1542-07 138
1645-08 ..... 86, 226
1735-08 200
1738-08 ..... 18, 20
1757-09 ..... 22, 120, 122
1850-09 152
1851-09 202
1858-10 24
1859-10 26
1862-10 154
1872-10 28
1873-10 204
1880-10 156
1923-10 30
1936-10 76
1940-10 ..... 32, 34
1970-10 78
1997-11 158
2065-11 36
2068-11 38
2091-11 ..... 206, 208
2103-12 124
2123-12 ..... 140, 142
2125-12 80
2126-12 210
2172-12 228
2214-13 40
2217-13 230
2232-13 160
2249-13 42
2260-13 44
2293-14 46
2298-14 ..... 48, 50
2307-14 ..... 88, 90
2324-15 92
2325-15 162
2334-15 232
2343-15 212
2344-15 212
2345-15 212
2349-15 52
2350-15 ..... 94, 234
2359-15 164
2361-15 214
2364-15 ..... 54, 236
2385-15 144
2386-15 238
2387-15 166
2406-15 168
2416-16 146
2428-16 96
2430-16 56
2435-16 98
2438-16 166
2440-16 100
2443-16 102
2444-16 ..... 216, 218
2452-16 148
2458-16 170
2460-16 58
2461-16 60
2467-16 62
2470-16 ..... 104, 126
2471-16 172
2472-16 ..... 64, 174
2476-16 220
2479-16 176
2486-16 128
2489-16 130
2501-16 132
2504-16 66
2509-16 106
2518-17 46
2527-17 108
2528-17 134
2531-17 68
2557-17 178

Index of Reports by CNF Principal Investigators & Users

A

Acharya, Rohan 48
Agyeman-Budu, David 228
Alden, Jonathan 128
Allen, Leslie H. 116
Alpha, Christopher 68
Aradhya, Sriharsha V. 206
Awan, Kashif Masud 154

B

Badman, Ryan 4, 18, 20
Badolato, Antonio. 154
Baker, James E. 4, 18
Baker, Shefford 124
Bartell, Jason M. 206, 208
Bau, Haim H. 138
Beaucage, Peter 118
Bharadwaj, Shyam 150, 166
Bircan, Baris 146
Black II, Winston L. 12
Boone, Carl 68
Borca-Tasciuc, Diana 148
Boucher, Michael 70, 80
Boyd, Robert 154
Brock, Joel 228
Buhrman, Robert 180, 182, 184, 186, 216, 218
Butcher, Jonathan 30

C

Calderon, Brian 98
Capasso, Federico 172
Chandonait, Jonathan 150
Chaney, Alexander 126
Chatterjee, Shouvik 192
Chaudhuri, Reet 104
Chen, Chen-yu 6
Chen, Jiun-Ruey 72
Chen, Wei-Liang 110, 120
Cheng, Emily R. 222
Clancy, Paulette 222
Cohen, Itai 146
Cordero, Roselynn 22
Cortese, Alejandro J. 128
Cosgrove, Benjamin D. 60
Costello, Cait M. 48, 50
Cothard, Nicholas 170
Craighead, Harold G. 6, 8
Crouse, David 108
Curley, Elizabeth 70, 80

D

Davaji, Benyamin 136
De Micheli, Andrea J. 60
DeAlba, Roberto 198
DelNero, Peter 16
Dickensheets, David L. 168
DiMarco, Christopher 212
Ditter, David 122
Dodge, Kenneth 196
Dolgaleva, Ksenia 154
Dorsey, Kyle J. 146, 194
Dutta Gupta, Shourya 64
Dwyer, Ryan 224

E

Encomendero, Jimy 102
Engstrom, James R. 72
Erickson, David 24, 28

F

Fain, Romy 236
Fischbach-Teschl, Claudia. 16
Fontes, Ernie 228
Frey, Brian 156
Fuchs, Gregory D.. . . . . 206, 208, 210

G

Gao, Xiang. 18
Garza, Tanya 230
Ghioni, Massimo 160
Gibbons, Jonathan D.. 186
Gillilan, Richard E. 32, 34
Gingerich, Marcus 66
Grab, Jennifer 188
Gray, Isaiah 208
Grogan, Joseph M.. 138
Gruner, Sol M. 238
Guisado, Gabriel. 2
Gulinatti, Angelo 160
Gund, Ved 84

H

Hanrath, Tobias.. . . . . 86, 226
Hao, Yu. 202
He, Yang.. 158
Hernandez, Christopher J. 2, 78
Herzog, Walter. 14
Hickman, Austin. 104
Hoffmann, Roald 74
Hone, James 212
Hopkins, Jesse.. 34
Howington, Caleb 200
Hu, Zongyang 96, 234
Huang, Hsien-Lien 222
Huang, Manjie.. 32
Huang, Meng.. . . . . 44, 58
Huang, Yu Ling. 38
Huang, Zhaoran Rena 162
Hutchings, Matthew 200, 204
Hwang, James C.M. 106

I

Illava, Gabrielle 238
Indrajeet 200
Isaac, Corinne E.. 80

J

Jadhav, Vivek 40
James, Gregory 148
Jena, Debdeep
. . . . . 90, 94, 96, 98, 104, 126, 132, 166, 234
Jermain, Colin L.. 206
Ji, Xingchen 54
Jiang, Lingjun 162
Jungwirth, Nicholas Ryan 210

K

Kasahara, Kazuki.. 114
Keil, Wolfgang.. 46
Kelp, Glen 64
Kennedy, Brian J. 134
Kirby, Brian J. 52, 144
Klaczko, Michael E. 110
Kriksunov, Irina 62
Ku, Jaseung 204
Kuang, Ping. 156
Kwasnica, Marek Andrzej. 48
Kymissis, Ioannis.. 230
Kysar, Jeffrey 212

L

LaHaye, Matthew 202
Lal, Amit. 82, 84, 130, 136
Lam, Jun Wei.. 220
Lammerding, Jan 36
Lee, Hyunjea.. 92
Lee, Kevin 166
Lee, Menyoung. 220
Lee, Sunwoo 100, 136
Leonard, Timothy. 14
Lepak, Lori.. . . . . 56, 164
Li, Jinglun 148
Li, Lei. 106
Li, Mingda. 92

Li, Ruofan 190
Li, Wenshen 88, 234
Li, Xiang 92
Liang, Hanxiao 158
Lin, Qiang 158
Lin, Shawn-Yu 156
Lindau, Manfred 44, 58
Ling, Lu 16
Lipson, Michal 54, 236
Liu, Hank 234
Liu, Tianbo 168
Liu, Yebin 204
López Martínez, Mónica M. 4
Lu, Zhaolin 178
Luo, Rui 158
Lynch, David M. 112

M

Ma, Minglin 42
MacMullan, Melanie 32
MacNeill, David 186, 190
March, John C. 48, 50
Marohn, John A. 70, 80, 224
Maroo, Shalabh C. 140, 142
Matsuoka, Fumiaki 118
McEuen, Paul L. 10, 128, 146, 194, 220
McGill, Kathryn L. 10
Menzel, Matthias 120
Miller, Paula 6
Mirbagheri, Golsa 108
Miskin, Marc Z. 146
Mohanty, Aseema 54
Molnar, Alyosha C. 100, 136
Morgan, John 16

N

Nelson, JJ 196, 200
Nguyen, Hieu Pham Trung 176
Nguyen, Minh-Hai 180
Nomoto, Kazuki 90, 96
Norris, Samantha 10
Nowack, Katja C. 214
Nurmukhanov, Aibar 22

O

Ober, Christopher K. . . 22, 110, 114, 120, 122, 130
Ou, Yongxi 182

P

Pancoast, Leanna 136
Parpia, Jeevak M. 198
Pearson, Tanner 194
Peretz, Eliad 226
Petersen, Poul B. 76
Philip, Moab Rajan 176
Pinrod, Visarute 136
Plourde, Britton L.T. 196, 200, 204
Polhemus, Katherine 144
Preble, Stefan 152
Prucker, Oswald 120

Q

Quinn, Katherine K. 112

R

Rahm, Martin 74
Ralph, Daniel C. 186, 188, 190, 192, 206
Reinhart-King, Cynthia A. 26
Reinholt, Sarah 8
Resnick, Brett 30
Rey, Elizabeth 28
Reynolds, Michael F. 10, 146
Reynolds, Neal 192
Roberts, Melanie F. 2, 78
Robin, Antoine 12
Rogers, Nathaniel 124
Rugar, Alison 188
Rühe, Jürgen 120
Ruyack, Alexander 82, 130

S

Sanders, Stephanie 76
Santiago-Pinero, Michael 12
Sawatsky, Andrew 14
Schaefer, Brian T. 214
Schlom, Darrell 192

Schrlau, Michael. 232
Sehgal, Prateek 52
Seidner, Ariel. 192
Shah, Devarsh 232
Shaham, Shai. 46
Shcherbakov, Maxim 174
She, Alan 172
Shen, Kyle 192
Shi, Shengjie 182
Shin, Jae Ho. 94
Shire, Douglas 66
Shuler, Michael L. 6
Shvets, Gennady 64, 174
Siggia, Eric D. 46
Skvarla, Michael. 46
Snodgrass, Ryan 24
Song, Wei 42
Sorg, Victoria C. 222
Stacey, Gordon 170
Steidle, Jeffrey 152
Stiehl, Gregory. 190
Stroock, Abraham D. 12, 16
Suh, Taewon 72
Sun, Peter 70
Szebenyi, Marian 62

T

Tan, Cheng 212
Tanen, Nicholas 96
Tapping, Ryan C. 184, 218
Teal, Daniel 82
Thanniyil Sebastian, Abhilash 198
Thompson, Michael O. 112, 222
Tian, Harvey C. 8
Tirmzi, Ali 224
Turgut, Emrah 208
Turski, Henryk 132

V

Vaartstra, Geoffrey 140
VanderBurgh, Jacob 26
Vetter, Kenny 170
Vincent, Olivier 12
Vishwanath, Suresh 92

W

Wang, Haozhi 200
Wang, Lei 194
Wang, Lucy 78
Wang, Michelle D. 4, 18, 20
Wang, Ying 6
Wanunu, Meni 40
Wen, Qiannan 226
Whitham, Kevin 86
Wiesner, Ulrich 118
Windsor, Aaron 36
Woll, Arthur 228
Wu, Mingming 38

X

Xing, Huili Grace
. . . . . 88, 90, 92, 94, 96, 102, 150, 234
Xiong, Kuanchen 106
Xu, Hong. 114

Y

Yan, Rusen 92
Ye, Fan 20
Ye, Zichao 116
Yin, Peichuan 178
Ying, Robin 136

Z

Zhang, Liheng 96
Zhang, Qi 118
Zhang, Shuyan 172
Zhelev, Nikolay 198
Zhu, Lijun 216, 218
Zhu, Mingda 96, 234
Zhu, Siyu 12
Zou, An. 140, 142

The 2016-2017 CNF Research Accomplishments reports were formatted by Ms. Melanie-Claire Mallison and proof-read by the CNF Staff. We welcome your comments at mallison@cnf.cornell.edu

The reports are also online at http://www.cnf.cornell.edu/cnf_2017ra.html


NSF